UC San Diego
UC San Diego Electronic Theses and Dissertations

Title

Heterogeneous chemistry of atmospheric mineral dust particles and their resulting cloud-nucleation properties

Permalink

https://escholarship.org/uc/item/89c072pv

Author

Sullivan, Ryan Christopher

Publication Date

2008

Peer reviewed|Thesis/dissertation

UNIVERSITY OF CALIFORNIA, SAN DIEGO

Heterogeneous chemistry of atmospheric mineral dust particles and their resulting
cloud-nucleation properties

A dissertation submitted in partial satisfaction of the requirements for the degree

Doctor of Philosophy

in

Chemistry

by

Ryan Christopher Sullivan

Committee in charge:

      Professor Kimberly Prather, Chair
      Professor Lynn Russell
      Professor Amit Sinha
      Professor Mark Thiemens
      Professor William Trogler

2008

The dissertation of Ryan Christopher Sullivan is approved, and it is acceptable in quality and form for publication on microfilm and electronically:

_____

_____

_____

_____

Chair

University of California, San Diego

2008

For my Parents

TABLE OF CONTENTS

LIST OF ABBREVIATIONS

APS	aerodynamic particle sizer
ART-2a	adaptive resonance theory-2a
ATOFMS	aerosol time-of-flight mass spectrometer
CCN	cloud condensation nuclei
CCNc	cloud condensation nuclei counter
CN	condensation nuclei
CPC	condensation particle counter
DMA	differential mobility analyzer
EDX	energy dispersive x-ray analysis
HC	hierarchical classification
IC	ion chromatography
ICP-MS	inductively coupled plasma mass spectrometry
IN	ice nuclei
LDI	laser desorption/ionization
RH	relative humidity
SEM	scanning election microscopy
SMPS	scanning mobility particle sizer
SPMS	single-particle mass spectrometer

LIST OF SYMBOLS

C	solubility (volume solute/volume water)
C_c	Cunningham slip correction
D	particle diameter
D_a	aerodynamic diameter
D_{ca}	critical activation diameter
D_{dry}	dry diameter
D_g	geometric diameter
D_m	mobility diameter
D_p	physical diameter
DRH	deliquescence relative humidity
dT	temperature gradient
D_{ve}	volume-equivalent diameter
g	asymmetry parameter
k	chemical rate constant
K_{sp}	solubility product
M	molecular weight
N	complex index of refraction
n	number of moles
PM	particulate matter mass
p_w	water vapor pressure
Q	light scattering efficiency
R	ideal gas constant
S	water saturation ratio
s_c	critical supseraturation
SS	supersaturation
T	temperature
x	component dissolved fraction
a_w	activity of water
α	mass accommodation coefficient
ε	component volume fraction

γ	reactive uptake coefficient
κ	hygroscopicity parameter
κ_{app}	apparent hygroscopicity
κ_{intr}	intrinsic hygroscopicity
μ	gas viscosity
σ	standard deviation
ρ	density
ν	van't Hoff factor
χ	dynamic shape factor
ω	single scattering albedo (SSA)

LIST OF TABLES

ACKNOWLEDGEMENTS

background in environmental chemistry. Finally, I would like to thank my high school chemistry teacher, Innis Akmens, for kindling and nourishing my intial interest in chemistry, which led me to continue to study it in undergraduate and graduate school.

I am very grateful to all my family back in Canada for their support and help with my move to California and during my graduate studies. I am very lucky and fortunate to have had the support of so many good friends back in Toronto, and to have made countless new friends in San Diego, both at UCSD and outside of grad school. All of my friends made my move to the United States much easier and more enjoyable than I would have imagined, and thus greatly improved my graduate school experience. I am particularly indebted to all the friends and colleagues I met at UCSD for their regular advice and support.

The text and figures of Chapter 3 are a reprint of a published paper, Sullivan RC, Guazzotti SA, Sodeman DA, and Prather KA, "Direct observations of the atmospheric processing of Asian mineral dust" Atmospheric Chemistry and Physics 7, 1213-1236, FEB 22 2007. I was the primary researcher and author.

The text and figures of Chapter 4 are a reprint of a published paper, Sullivan RC, Guazzotti SA, Sodeman DA, Tang Y, Carmichael GR, and Prather KA, "Mineral dust is a sink for chlorine in the marine boundary layer" Atmospheric Environment 41, 7166-7179, NOV 2007. I was the primary researcher and author, and Sergio Guazzotti contributed significantly to the analysis and writing.

The text and figures of Chapter 5 are a reprint of a published paper, Sullivan RC, and Prather KA, "Investigations of the diurnal cycle and mixing state of oxalic acid in individual particles in Asian aerosol outflow" Environmental Science & Technology 41 (23), 8062-8069, OCT 24 2007. I was the primary researcher and author.

The contents of Chapter 6 compose part of a submitted manuscript: Sullivan RC, Moore MJK, Petters MD, Kreidenweis SM, Roberts GC, and Prather KA, Hygroscopicity and cloud nucleation ability of calcium mineral dust particles – 1. Importance of chemical mixing state, submitted to Journal of Physical Chemistry A; and a manuscript in preparation: Sullivan RC, Moore MJK, Petters MD, Kreidenweis SM, Qafoku O, Laskin A, Roberts GC, and Prather KA, Hygroscopicity and cloud nucleation ability of calcium mineral dust particles – 2. Effect of water and hydrate formation, to be submitted to Journal of Physical Chemistry A.

The contents of Chapter 7 are part of a manuscript in preparation, Sullivan RC, Moore MJK, Petters MD, Kreidenweis SM, Roberts GC, and Prather KA.: Timescale for hygroscopic conversion of mineral dust particles after heterogeneous reaction with nitric acid, 2008, to be submitted.

VITA

June 2002	Hon.B.Sc. Environmental Chemistry, University of Toronto
2000-2003	Research Assistant, Department of Chemistry, University of Toronto
2003-2004	Teaching Assistant, Department of Chemistry & Biochemistry, University of California, San Diego
December 2006	M.S. Chemistry, Department of Chemistry & Biochemistry, University of California, San Diego
2003-2008	Graduate Student Researcher, Department of Chemistry & Biochemistry, University of California, San Diego
December 2008	Ph.D. Chemistry, Department of Chemistry & Biochemistry, University of California, San Diego

PUBLICATIONS

Sullivan, R.C., Thornberry, T., and Abbatt, J.P.D. Ozone decomposition kinetics on alumina: effects of ozone partial pressure, relative humidity and repeated oxidation cycles, *Atmospheric Chemistry and Physics*, 4, 1301-1310, 2004.

Chang, R.Y.-W., Sullivan, R.C., and Abbatt, J.P.D. Initial uptake of ozone on Saharan dust at atmospheric relative humidities, *Geophysical Research Letters*, 32 (14), doi:10.1029/2005GL023317, 2005.

Sullivan, R. C., and Prather, K. A. Recent advances in our understanding of atmospheric chemistry and climate made possible by on-line aerosol analysis instrumentation, *Analytical Chemistry*, 77 (12), 3861-3885, 2005.

Arimoto, R., Kim, Y.J., Kim, Y.P., Quinn, P.K., Bates, T.S., Anderson, T.L., Gong, S., Uno, I., Chin, M., Huebert, B.J., Clarke, A.D., Shinozuka, Y., Weber, R.J., Anderson, J.R., Guazzotti, S.A., Sullivan, R.C., Sodeman, D.A., Prather, K.A., and Sokolik, I.N. Characterization of Asian Dust during ACE-Asia, *Global and Planetary Change*, 52 (1-4), 23-56, 2006.

Sullivan, R.C., Guazzotti, S.A., Sodeman, D.A., and Prather, K.A. Direct observations of the atmospheric processing of Asian mineral dust, *Atmospheric Chemistry and Physics*, 7, 1213-1226, 2007.

Sullivan, R.C., Guazzotti, S.A., Sodeman, D.A., Tang, Y.H., Carmichael, G.R., and Prather, K.A. Mineral dust is a sink for chlorine in the marine boundary layer, *Atmospheric Environment*, 41 (34), 7166-7179, 2007.

Sullivan, R.C., and Prather, K.A. Investigations of the diurnal cycle and mixing state of oxalic acid in individual particles in Asian aerosol outflow, *Environmental Science & Technology*, 41 (23), 8062–8069, 2007.

Sullivan, R.C., Moore, M.J.K., Petters, M.D., Kreidenweis, S.M., Roberts, G.C., and Prather, K.A. Hygroscopicity and cloud nucleation ability of calcium mineral dust particles – 1. Importance of chemical mixing state*,* submitted to *Journal of Physical Chemistry A*, 2008.

ABSTRACT OF THE DISSERTATION

Heterogeneous chemistry of atmospheric mineral dust particles and their resulting
cloud-nucleation properties

by

Ryan Christopher Sullivan

Doctor of Philosophy in Chemistry

University of California, San Diego, 2008

Professor Kimberly Prather, Chair

Mineral dust particles are a major component of tropospheric aerosol mass and affect regional and global atmospheric chemistry and climate. Dust particles experience heterogeneous reactions with atmospheric gases that alter the gas and particle-phase chemistry. These in turn influence the warm and cold cloud nucleation ability and optical properties of the dust particles. This dissertation investigates the atmospheric chemistry of mineral dust particles and their role in warm cloud nucleation through a combination of synergistic field measurements, laboratory experiments, and theoretical modeling. In-situ measurements made with a single-particle mass spectrometer during the ACE-Asia field campaign in 2001 provide the motivation for this work. The observed mixing state of the individual ambient particles with secondary organic and inorganic components is described in Chapter 2. A large Asian dust storm occurred during the campaign and produced dramatic changes in the aerosol's composition and mixing state. The effect of particle size and

mineralogy on the atmospheric processing of individual dust particles is explored in Chapters 3 & 4. Sulfate was found to accumulate preferentially in submicron iron and aluminosilicate-rich dust particles, while nitrate and chloride were enriched in supermicron calcite-rich dust. The mineral dust (and sea salt particles) were also enriched in oxalic acid, the dominant component of water soluble organic carbon. Chapter 5 explores the roles of gas-phase photochemistry and partitioning of the diacids to the alkaline particles in producing this unique behavior. The effect of the dust's mixing state with secondary organic and inorganic components on the dust particles' solubility, hygroscopicity, and thus warm cloud nucleation properties is explored experimentally and theoretically in Chapter 6. Cloud condensation nucleation (CCN) activation curves revealed that while calcium nitrate and calcium chloride particles were very hygroscopic and CCN-active, due to the high solubility of these compounds, calcium sulfate and calcium oxalate were not. Particles composed of these two sparingly soluble compounds had apparent hygroscopicities similar to pure calcium carbonate. This implies that the commonly made assumption that all dust particles become more hygroscopic after atmospheric processing must be revisited. Calcium sulfate and oxalate represent two forms of aged mineral dust particles that remain non-hygroscopic and thus have poor CCN nucleation ability. The particle generation method (dry versus wet) was found to significantly affect the chemistry and hygroscopicity of the aerosolized particles. Finally, in Chapter 7 the timescale for the atmospheric conversion of insoluble calcite particles to soluble, CCN-active calcium nitrate particles was derived from aerosol flow tube experiments. The reaction rate is rapid was used to estimate the conversion of calcite particles to very hygroscopic particles can occur in just a few hours of exposure to tropospheric levels of nitric acid. This process will therefore be controlled by the availability of nitric acid and its precursors, as opposed to the available atmospheric reaction time.

Chapter 1

Introduction

1.1 Atmospheric aerosols

An aerosol is defined as the suspension of solid or liquid particles in a gaseous medium. While the aerosol includes both the gas and condensed phases, typically the term refers to the condensed phase only. Aerosol particles represent a significant component of the Earth's atmosphere and profoundly impact global and regional climate, by absorbing and scattering radiation (direct aerosol climate effects) as well as acting as seeds for cloud droplet formation, which alters cloud albedo, cloud cover, and the hydrological cycle (indirect aerosol climate effects) (Kanakidou et al., 2005; Lohmann and Feichter, 2005; Ramanathan et al., 2005; Ramanathan et al., 2001; Seinfeld and Pandis, 2006). Aerosols also alter the chemical composition of the atmosphere through heterogeneous and multiphase chemistry with trace gases (Abbatt, 2003; Finlayson-Pitts, 2003; Kolb et al., 2002; Maria et al., 2004; Martin et al., 2003; Molina et al., 1996; Ravishankara, 1997), deteriorate visibility by scattering light, and adversely affect human health (Oberdorster et al., 2004; Pietropaoli et al., 2004; Pope, 2000; Utell and Frampton, 2000). Atmospheric aerosols are complex mixtures of organic and inorganic compounds produced by both natural and anthropogenic activities. Their sizes span over five orders of magnitude, ranging from 1 nm to greater than 100 μm in diameter when cloud/fog droplets are considered. Single-particle measurements have revealed their composition to vary widely between individual particles even of the same size (Murphy et al., 2006; Sullivan and Prather, 2005). Their chemical composition is determined by the complex interplay between sources, size, atmospheric age, and chemical processing of aerosols that

1

occurs during transport. Due to this interplay, the physicochemical properties of aerosols, including their size, density, morphology, hygroscopicity, and optical properties, are constantly evolving with time. These properties dictate the important environmental effects of aerosols including the absorption and scattering of radiation (direct climate effects), interactions with clouds (indirect climate effects), reaction rates and mechanisms with trace gases, as well as their toxicological properties. The role of aerosols in all of these important environmental impacts remains poorly constrained due to their complex, constantly evolving, and difficult to measure composition.

1.2 Sources of atmospheric aerosols

Aerosols are directly released into the atmosphere through both combustion and mechanical processes (primary aerosols), and are also formed and modified by gas- and multiphase-chemical reactions involving gas-to-particle conversion, which produces secondary aerosol mass. Their chemical components can be readily divided into organic and inorganic compounds.

1.2.1 Inorganic aerosols

Primary inorganic aerosol particles are typically dominated by those produced from mechanical forces, i.e. mineral dust particles lofted by winds, and sea salt particles released from the oceans by wave action. Their production is largely controlled by wind speed, as well as soil moisture and composition in the case of mineral dust loess. Due to the mechanical generation processes, these particles are typically quite large and are most abundant in the supermicron size range. Both sea salt and dust can also have smaller but significant submicron aerosols modes.

Sulfuric and nitric acids dominate secondary inorganic aerosol mass, formed through heterogeneous/multiphase reactions of atmospheric trace gases including SO_2, H_2SO_4, NO_x ($NO + NO_2$), HNO_3, NO_3, and N_2O_5 with existing aerosols. Ammonia gas partially or fully neutralizes these aerosol-phase acids, producing ammonium sulfate and nitrate salts. Sulfuric acid and it's ammonium salts, $(NH_4)_2SO_4$ and NH_4HSO_4, typically dominate the smallest submicron aerosol modes, as the uptake of sulfuric acid is diffusion-limited and thus controlled by the maximum in the available aerosol surface area (Bassett and Seinfeld, 1984a). Sulfuric acid and its salts are non-volatile at typical atmospheric temperatures and thus their gas-to-particle conversion is irreversible. Ammonium nitrate, however, is very sensitive to ambient temperature and relative humidity (RH), and readily partitions between the gas and aerosol phases. As nitric acid is a weaker acid than sulfuric acid, and because nitric acid and its ammonium salts are semi-volatile, these compounds tend to dominate in a somewhat larger range of the submicron aerosol size distribution (Bassett and Seinfeld, 1984a; Song and Carmichael, 1999). Other secondary inorganic aerosol components include chlorine and bromine compounds, whose gases are displaced from sea salt particles that become acidified by reaction with the stronger sulfuric and nitric acids. Iodine compounds, released from the oceans, have also been implicated in new particle formation events (O'Dowd et al., 2002).

Some trace atmospheric gases can also participate in nucleation, leading to new particle formation through the growth of molecular clusters. Sulfuric acid, nitric acid, ammonia, water, amines, and possibly some organic acids have been identified as playing a major role in particle nucleation (Kurten et al., 2008; Smith et al., 2005; Zhang et al., 2004). These newly formed particles are very small initially, < 3 nm in diameter, but quickly grow through gas-to-particle conversion and/or coagulation with existing particles (Kulmala et al., 2004; McMurry et al., 2005).

1.2.2 Organic aerosols

Carbon-containing (carbonaceous) compounds represent a widely varied and significant fraction of atmospheric aerosols, and therefore also present difficult analytical measurement challenges (Seinfeld and Pankow, 2003). From a measurement perspective, the carbonaceous aerosol component is frequently sub-divided into organic carbon (OC), and elemental carbon (EC), or black carbon (BC). OC refers to the organic compounds that include hydrogen, oxygen, and other atoms in addition to carbon in their chemical structure and can typically be extracted using various organic solvents or water in the case of water soluble organic compounds (WSOC). Organic species possess a wide range of polarities and and some undefined fraction exist as large polymers or oligomers. EC refers to a graphitic non-molecular form of carbon that is typically associated with soot from combustion. It is primarily composed of carbon atoms in an sp^2 lattice arrangement with other atoms possibly occupying interstitial sites. Due to the chemical structure, soot is extremely non-polar and insoluble in water and organic solvents. The high degree of conjugation also causes it to be highly light absorbing across the UV-Vis-IR spectrum. BC is operationally defined based on its optical properties as opposed to an actual chemical structure, and refers to the light absorbing fraction of carbonaceous species, which can be either EC or OC (Bond and Bergstrom, 2006). Light-absorbing organic carbon is often referred to as "brown carbon". It typically has a chemical structure similar to humic substances, though it is often formed through aqueous/cloud processing (Andreae and Gelencser, 2006; Graber and Rudich, 2006).

Primary carbonaceous aerosols are predominantly produced by combustion processes including the burning of fossil fuels, biofuels for residential cooking and heating, and biomass burning. The resulting aerosol is a complex mixture of elemental and organic carbon, and inorganic compounds, whose chemical composition is determined by the fuel source and

burning conditions (Reid et al., 2005). As elemental carbon is only a primary aerosol component, it is solely produced by combustion processes. Primary organic carbon aerosols (POA) may also be produced by resuspension of plant debris, and from the surfactant surface microlayer that resides on bodies of water, in addition to other mechanisms (Seinfeld and Pankow, 2003). POA can react in the atmosphere with oxidants such as O_3 and OH and be converted to oxidized organic aerosol (OOA). Some sources of POA inherently contain highly oxidized organic compounds such as dicarboxylic acids; using oxidized species to distinguish different formation pathways may not be entirely accurate (Kawamura and Kaplan, 1987). Recently, previous assumptions regarding the low volatility of POA have been called into question. POA was found to have a dynamic volatility profile in which some components of POA evaporate from the aerosol phase as the combustion plume becomes diluted with ambient air (Robinson et al., 2007). The semivolatile organic compounds (SVOCs) that have evaporated from the POA can subsequently be rapidly oxidized to produce secondary organic aerosol that re-partitions back to the particle phase.

Secondary organic aerosol (SOA) is formed in the atmosphere by the oxidation of volatile and semivolatile organic compounds (VOCs), yielding products with significantly reduced vapor pressures, causing them to condense onto existing particles or nucleate to produce new particles (Seinfeld and Pankow, 2003). Heterogeneous/multiphase reactions of organic compounds also occur in the aerosol phase. Secondary organic aerosol (SOA) is an extremely complex, important, and still poorly understood aerosol component that frequently composes a large and highly variable fraction of submicron aerosols, and also has supermicron components (Fuzzi et al., 2006). The relative contributions of anthropogenic versus biogenic (from plants and trees) VOCs to SOA formation is an important and as of yet undetermined question. The mechanisms and reversibility of SOA formation are an area of intense

investigation as model predictions of SOA formation routinely underestimate the measured SOA mass. The organic compounds that have been found to compose aerosols possess a wide range of polarities, functionalities, and an undefined fraction exists as large polymers or oligomers. However, only a small fraction of organic aerosol mass has been quantified at the molecular level, the remainder has yet to be fully characterized (Jacobson et al., 2000).

1.2.3 Aerosol size distribution

The size of an aerosol particle is an important parameter that controls the rates of diffusion, coagulation, and gravitational settling, and several other important properties including how a particle interacts with radiation, forms cloud droplets, and penetrates into the lungs (Seinfeld and Pandis, 2006). Due to the fact that particles such as elemental carbon and mineral dust have an extensive number of potentially complicated non-spherical shapes and settling properties, there are a number of metrics used to describe particle size including physical (D_p), Stokes, and mobility diameter (D_m) (DeCarlo et al., 2005). When the diameter or size of a particle is discussed, in this dissertation it refers to the aerodynamic diameter, D_a, unless otherwise stated. Equivalent size metrics are often referenced to the physical diameter of a volume equivalent sphere, D_{ve}, which is the diameter a particle of the same volume would have if melted into a sphere while preserving any internal void space. D_{ve} is equal to D_p for spherical particles. The aerodynamic diameter, D_a, is defined as the diameter of a spherical particle with unit density that has the same terminal velocity as the particle under consideration (Seinfeld and Pandis, 2006). Thus D_a is the most appropriate measure to describe a particle's motion in the atmosphere and depends on it's shape and density, and is generally defined as:

$$\rho_0 D_a^2 C_c(D_a) = \frac{\rho_p}{\chi} D_{ve}^2 C_c(D_{ve})$$

(1.1)

where ρ_0 is the unit density (1 g cm^{-1}), C_c is the Cunningham slip correction, ρ_p is the particle's density, including any internal voids, and χ is the dynamic shape factor. X equals 1 for spheres and is > 1 for nonspherical particles; χ is the ratio of the resistive or drag force on the nonspherical particle divided by the resistive force on a volume equivalent sphere (DeCarlo et al., 2005).

The equation that governs D_a is dependent on the flow regime that the measurement is made under. In the free molecular regime the vacuum aerodynamic diameter, D_{va}, is used:

$$D_{va} = \frac{\rho_p D_{ve}}{\rho_0 \chi} .$$
(1.2)

Equation 1.2 applies to instruments that use an aerodynamic aerosol inlet, such as the aerosol mass spectrometer (AMS) (DeCarlo et al., 2005) and the UF-ATOFMS (described below). Instruments that determine D_a at higher pressure operate under the continuum regime, and the continuum aerodynamic diameter, D_{ca}, is defined as:

$$D_{ca} = D_{ve} \sqrt{\frac{\rho_p}{\rho_0 \chi}} .$$
(1.3)

Equation 1.3 applies to instruments such as the aerodynamic particle sizer (APS) (see below). Note that in all cases the aerodynamic diameter depends on both shape and density. For spheres with unit density D_a equals D_{ve}.

The electrical mobility diameter, D_m, is another common metric that describes a particle's size when measured in the presence of an electric field (see below). D_m is defined as:

$$\frac{D_m}{C_c(D_m)} = \frac{D_{ve} \chi}{C_c(D_{ve})} .$$
(1.4)

Note that mobility diameter is sensitive to shape but not density, while aerodynamic diameter depends on both shape and density. A spherical particle of any density will have D_m equal to

D_{ve}. A differential mobility analyzer (DMA), otherwise known as an electrostatic classifier, measures mobility diameter, as discussed below. Mobility diameter (D_m) and aerodynamic diameter (D_a) are equal for spheres ($\chi = 1.0$) with $\rho_p = 1.0$. The relationship between a spherical particle's vacuum aerodynamic and mobility diameters is (DeCarlo et al., 2005):

$$D_m = D_{va} \frac{\rho_0}{\rho_p} . \tag{1.5}$$

Coupling of a differential mobility analyzer and a vacuum aerodynamic diameter based instrument such as the AMS or UF-ATOFMS permits the determination of the particle's density and dynamic shape factor using this relationship (DeCarlo et al., 2005; Spencer et al., 2007; Zelenyuk et al., 2006a). Note that D_a depends on shape (χ) and density (ρ_p), while D_m only depends on shape. For nonspherical particles of unit density, $D_m > D_{ve} > D_a$.

The sources and formation pathways described above determine in large part the resulting size and concentration profile of atmospheric aerosols. In general, when the atmospheric number concentration is plotted versus the particle diameter several log-normal modes are observed with distinct sources and physicochemical properties. Figure 1.1 displays a representative size distribution of atmospheric aerosols displaying the typical size modes. Plotting by both number and mass concentration demonstrates that particle numbers are typically dominated by the smallest nuclei and ultrafine (or Aitken) modes, while particle mass is dominated by the larger accumulation and coarse modes (Seinfeld and Pandis, 2006). The smallest size mode is the nucleation mode and applies to particles with $D_a < 10$ nm. As the nucleation mode is formed from nucleation events in which the condensation of vapors leads to new particle formation they are typically composed of inorganic compounds, ammonium sulfate in particular, and some organic compounds (Kulmala et al., 2004). These nuclei rapidly grow by condensation or coagulation into the larger ultrafine and accumulation
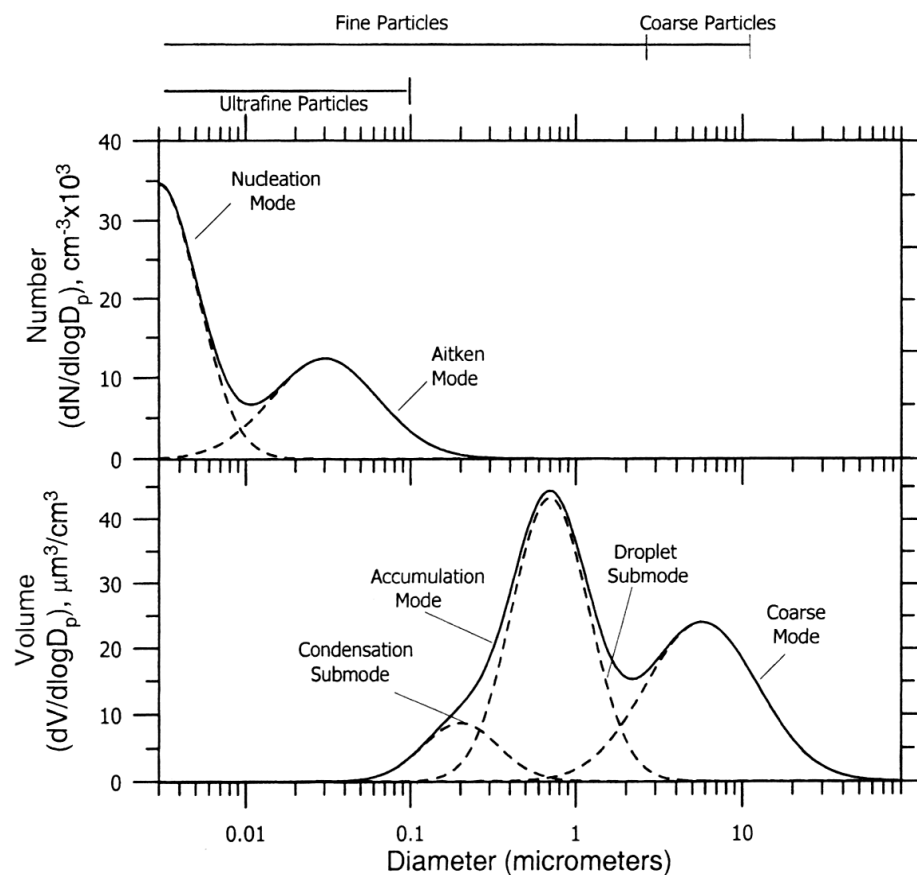
Figure 1.1. Typical size distribution of atmospheric aerosols and their representative modes based on particle number (top) and particle mass (bottom). The mass distribution displays the frequently observed condensation and droplet submodes in the accumulation mode. (Figure taken from Seinfeld & Pandis (2006), © 2006 by John Wiley & Sons, Inc.)

size modes. The ultrafine, or Aitken mode has D_a of 10-100 nm, and is typically composed of primary combustion particles in addition to nucleation mode particles that have grown into this size mode. They can also be composed of ultrafine metal particles from industrial sources. The accumulation mode has sizes between 100 nm $< D_a <$ 1000 nm (1 μm) and are dominated by organic and inorganic components that have formed through gas-to-particle conversion. Ultrafine combustion and metal particles that have coagulated or experienced condensational growth can also occupy this size mode. The accumulation mode is referred to as such because the rates of the major aerosol removal pathways, condensational growth and coagulation, and

gravitational settling, are minimized in this size range. The accumulation mode therefore typically has the longest atmospheric lifetime. The accumulation mode is often bimodal. The smaller mode is referred to as the condensation mode; it is produced by gas-to-particle conversion processes. The larger mode is the droplet mode, which is a subset of the condensation mode that has grown hygroscopically and experienced cloud or fog processing before dissipating (Kerminen and Wexler, 1995; Meng and Seinfeld, 1994). The formation of non-volatile aerosol mass during these fog/cloud processing cycles causes the droplet mode to be larger than the original condensation mode.

The largest particles compose the coarse mode. The split between the accumulation and coarse modes is somewhat variable, typically defined as $D_a > 1.0$ or > 2.5 µm. The US EPA defines the fine aerosol mode as $D_a < 2.5$ µm and thus this includes the nuclei, ultrafine and accumulation modes, while coarse aerosols are defined as those with $D_a > 2.5$ µm. These definitions are used by the EPA to formulate national ambient air quality standards based on $PM_{2.5}$ mass, which will be predominantly determined by the relatively small number of larger particles. The break between volume-based fine and coarse aerosol modes is variable and typically does not occur at 2.5 µm (Seinfeld and Pandis, 2006). More recent measurements, particularly those using single particle mass spectrometers to measure particle numbers, often detect the chemical distinction between modes to be near the 1.0 µm breakpoint (Liu et al., 2003; Noble and Prather, 1996a; Pastor et al., 2003). To avoid confusion, these size modes will be referred to in this dissertation as submicron ($D_a < 1.0$ µm) and supermicron ($D_a > 1.0$ µm) particles and maintain the previous fine and coarse definitions based on the EPA $PM_{2.5}$ standard definition 2.5 µm division. The supermicron and submicron size modes typically show significant differences in their chemical composition. This can be attributed to different formation mechanisms of the particles in the two size modes. Coarse aerosols are also referred
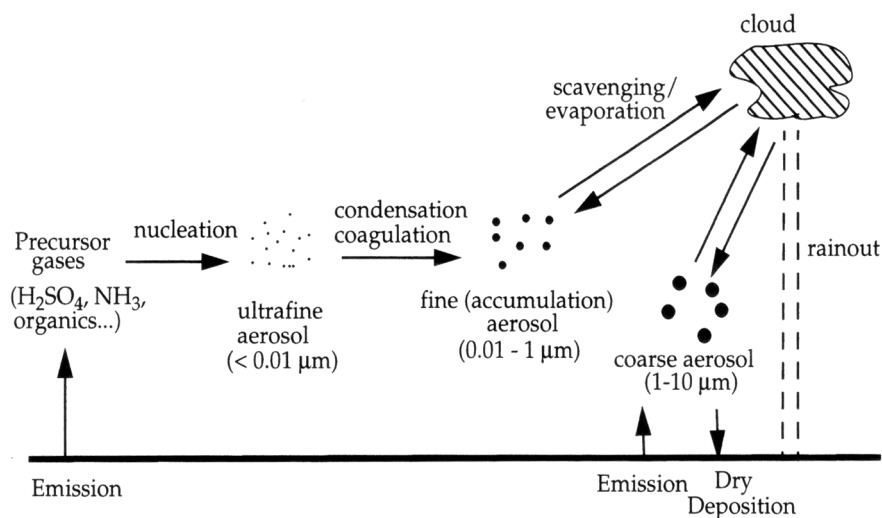
Figure 1.2. Simplified schematic of typical aerosol sources, sinks, and transformation pathways that produce the aerosol size distribution shown in Figure 1.1. (Figure taken from Jacob (1999), © 1999 by Princeton University Press)

to as supermicron aerosol, while the nucleation, ultrafine and accumulation modes combined compose the submicron aerosol. The coarse/supermicron mode is typically dominated by mechanically generated primary inorganic aerosols such as mineral dust and sea salt. Secondary inorganic and organic components can also condense onto these primary inorganic aerosols. The submicron mode is dominated by primary and secondary carbonaceous aerosol components and secondary inorganic compounds such as sulfate and nitrate salts. However, contributions to submicron aerosol from mineral dust, sea salt, and industrial metallic particles should not be ignored. Figure 1.2 is a simplified representation of the principle sources, sinks, and transformation pathways of atmospheric aerosols that produce the aerosol size distribution and modes discussed above.

1.2.4 Aerosol mixing state

The distribution of various aerosol chemical components between individual particles in the same aerosol population plays an important role in determining the physicochemical

properties of the aerosol. The existence of pure single-component particles appears to be a very rare occurrence from single-particle measurements, particularly for particles larger than ~100 nm (Andreae et al., 1986a; Moffet et al., 2008a; Murphy et al., 2006; Noble and Prather, 1996b; Whiteaker et al., 2002). Ultrafine and nucleation mode particles may have simple compositions due to their relatively young atmospheric age and production from single sources such as combustion, industrial processes, and nucleation (Smith et al., 2005; Smith et al., 2004; Tolocka et al., 2005). The growth of these nanoparticles through the various chemical and physical processes described below greatly increases the complexity of their chemical composition as they become internally mixed with other types and chemical species. An externally mixed aerosol is comprised of individual particles that are composed of one chemical component, though the different individual particles do not all have to be composed of the same component. It can also be defined as each particle originating from one single source or production pathway. An internally mixed aerosol is composed of individual particles that all have the same chemical composition at a given size. Individual atmospheric aerosols frequently contain multiple chemical components when measured using single-particle techniques. Large variations exist in their chemical composition within narrow size bins. An example of this behavior is described in Chapter 2. Therefore, atmospheric aerosols can generally be described as a complex external mixture of internally mixed chemical aerosol components.

1.2.5 Hygroscopic and cloud nucleating properties

Atmospheric particles frequently contain soluble hygroscopic components that allow them to absorb water and undergo hygroscopic growth (Swietlicki et al., 2008). This behavior has important consequences for visibility reduction caused by aerosols as well as the

interaction of particles with radiation (see below) and the ability of particles to grow into cloud droplets (McFiggans et al., 2006).

At equilibrium a particle's water content, expressed through its water activity, α_w, is equal to the surrounding air's relative humidity (RH) if the Kelvin effect of particle curvature is neglected. The particle will absorb more water and grow as the ambient RH increases to maintain this equilibrium. Soluble chemical components will undergo a spontaneous phase change from solid to liquid, a process called deliquescence, as RH is increased (Martin, 2000). This deliquescence relative humidity (DRH) occurs when the ambient RH equals the water activity of the saturated salt solution at that temperature (Seinfeld and Pandis, 2006). Deliquescence is typically accompanied by a large and rapid increase in particle size, after which the particle will readily continue to absorb water vapor. A deliquesced particle can undergo a liquid to solid phase transition, efflorescence, when the ambient RH is decreased. The efflorescence or crystallization RH typically occurs well below the DRH (Martin, 2000; Seinfeld and Pandis, 2006). This is because efflorescence is a kinetically limited process while
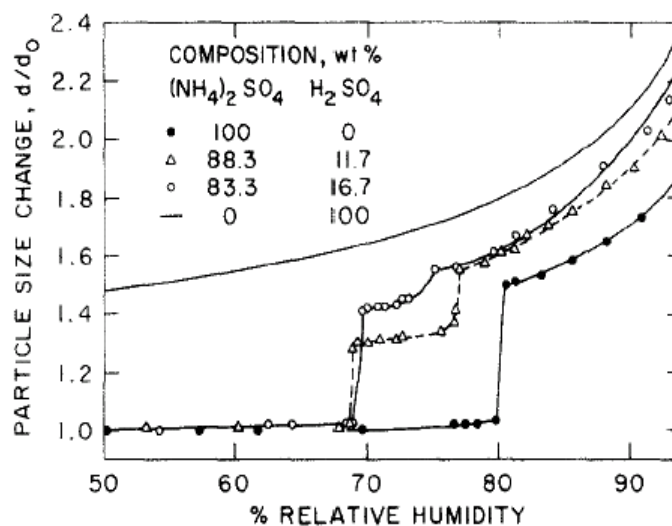
Figure 1.3. Deliquescence and hygroscopic growth of mixed $H_2SO_4/(NH_4)_2SO_4$ particles of varying composition. (Figure taken from Tang et al. (1978), © 1978 by Elsevier.)

deliquescence is controlled purely by thermodynamics, and therefore a hysteresis develops. Figure 1.3 demonstrates the deliquescence and hygroscopic growth of mixed ammonium sulfate/sulfuric acid particles of varying composition. The two-staged growth curve for the mixed particles is caused by the presence of letovicite, which deliquesces at 69% RH, and ammonium bisulfate, which deliquesces later at a compositionally dependent RH, allowing the particle to experience unconstrained hygroscopic growth (Tang et al., 1978). Pure sulfuric acid is always in a quasi-liquid state and experiences continuous hygroscopic growth over the entire RH range.

Figure 1.4 displays the idealized hygroscopic growth and deliquescence, and evaporation and efflorescence, of a simple soluble salt particle. The presence of the hysteresis requires knowledge of the particle's history as its hygroscopic behavior and phase depends on whether the it is on the lower or upper (metastable) branch. Some components do not display sharp phase transitions, such as H_2SO_4 that experiences smooth hygroscopic growth over all
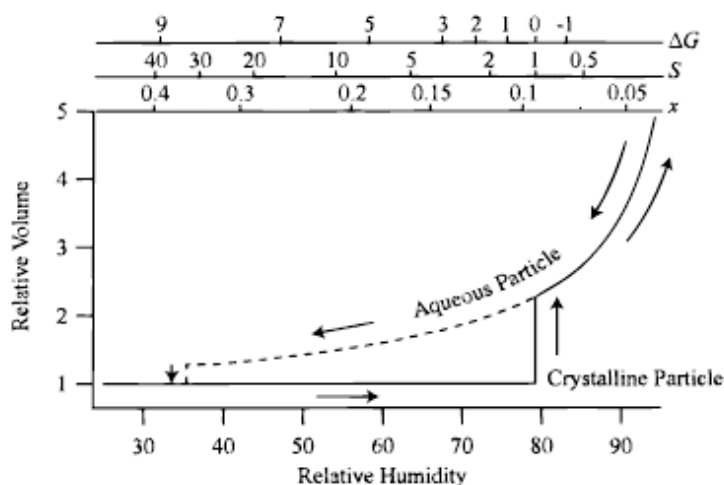
Figure 1.4. Idealized phase transitions and hygroscopic growth of an ammonium sulfate particle. The dashed line represents the upper branch as the deliquesced metastable droplet undergoes evaporation and efflorescence. Thermodynamic parameters including change in Gibbs free energy (ΔG), saturation ratio with respect to crystalline ammonium sulfate (S), and particle salt mole fraction (x) are displayed at the top. (Figure taken from Martin (2000), © 2000 American Chemical Society.)

RH ranges (Figure 1.3). Other insoluble and/or non-hygroscopic components, such as metal oxides and pure elemental carbon, do not experience hygroscopic growth in subsaturated (RH < 100%) conditions. Multicomponent particles, which are more realistic representations of atmospheric aerosols, typically display more complex hygroscopic growth and phase transitions. The DRH of a mixed salt particle is always lower than the DRH of the particle's individual components, due to the formation of eutonic mixtures (Seinfeld and Pandis, 2006). Evaporation and crystallization of multicomponent particles can exhibit several plateaus caused by the crystallization of the various components at their respective efflorescence RHs (Xiao et al., 2008).

Particles can continue to grow hygroscopically when the ambient water vapor becomes supersaturated such as in a rising air parcel. Eventually the critical activation diameter, D_{ca}, is reached at which point increasing water supersaturation is no longer required
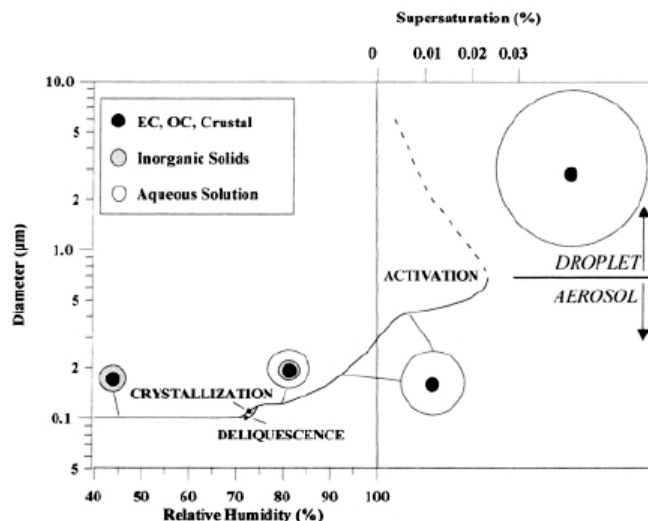
Figure 1.5. Schematic of the hygroscopic growth of a representative internally mixed atmospheric aerosol particle composed of an insoluble core, and a mixture of solid and aqueous inorganic salts. The deliquescence and efflorescence/crystallization processes occur at subsaturated RH, while droplet activation occurs at supersaturated RH. Note the change in scale at 100% RH. There are no equilibrium states available after activation (dashed line) A small hysteresis between deliquescence and crystallization is also shown. (Figure taken from Pandis (1995), © 1995 American Chemical Society.)

for the particle to continue to grow and remain in equilibrium with its surroundings. At this point, the droplet can continue to grown spontaneously constrained only by the availability of water vapor. Figure 1.5 displays the hygroscopic growth and droplet activation of an internally mixed particle composed of insoluble mineral dust and elemental carbon, organic carbon, and a mixture of soluble inorganic salts. The processes of deliquescence, efflorescence, and droplet activation are all displayed to demonstrate the connection between hygroscopic growth under sub- and supersaturated conditions.

The critical activation diameter is chiefly determined by particle size and chemical composition, particularly the volume fraction of soluble hygroscopic components (McFiggans et al., 2006; Petters and Kreidenweis, 2007; Seinfeld and Pandis, 2006). Köhler theory (Kohler, 1936) describes the water vapor saturation ratio, s, required to keep a particle in equilibrium as:

$$\ln(s) = \ln\left(\frac{p_w}{p_w^{\circ}}\right) - 1 = \frac{4 M_w \sigma_w}{RT \rho_w D_p} - \frac{6 n_s M_w}{\pi \rho_w D_p^3} \tag{1.6}$$

where p_w is the water vapor pressure, p_w° is the saturated water vapor pressure at T over a flat surface, M_w is the molecular weight of water, σ_w, is the surface tension of water, R is the ideal gas constant, T is the temperature, ρ_w is the density of water, D_p is the particle's physical diameter, and n_s is the number of moles of solute in the particle. The first parameter on the right side of Equation 1.6 is proportional to D_p and describes the Kelvin effect of particle curvature, which states that the vapor pressure over a curved surface is always larger than that over a flat surface. The second parameter is proportional to D_p^3 and accounts for the reduction in vapor pressure caused by the presence of solute, governed by Raoult's law. Solving Equation 1.6 for an aqueous salt particle produces the classic Köhler growth curve displayed in Figure 1.6.
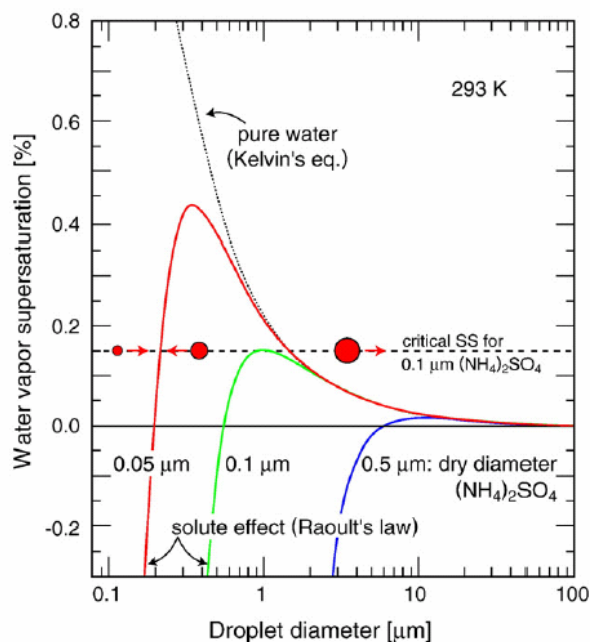
Figure 1.6. Köhler growth curves of pure ammonium sulfate particles of three different dry diameters, showing the particle's equilibrium water vapor supersatuatation. (Taken from Andreae and Rosenfeld (2008), used under the Creative Commons License.)

The growing droplet will activate into a stable droplet if the ambient supersaturation exceeds the critical supersaturation (s_c) at the maximum of the growth curve. The droplet diameter at this maximum is defined as the critical diameter (D_c). Once past this size, the droplet will continue to experience spontaneous growth even as the ambient supersaturation decreases. Experimentally, the critical activation diameter (D_{ca}) is often determined, defined as the dry diameter at which 50% of the particles activate under a specific critical supersaturation. In general, particles with larger initial dry diameters and that contain higher volume fractions of soluble hygroscopic material will activate at smaller critical supersaturations. It is important to note that only deliquesced components can participate in hygroscopic growth and the Raolut term of Eq. 1.6, while insoluble components reduce the Kelvin term by increasing the particle's size (Bilde and Svenningsson, 2004; Petters and

Kreidenweis, 2008; Shulman et al., 1996). The role of insoluble components and the cloud activation properties of mixed particles are discussed in detail in Chapter 6.

1.2.5.1 *Single-parameter of hygroscopicity:* κ

Recently a single-parameter for particle hygroscopicity and CCN activation was proposed by Petters and Kreidenweis (2007) and has already been adopted by several research groups (Andreae and Rosenfeld, 2008). κ describes the particle's water activity, a_w, as:

$$\frac{1}{a_w} = 1 + \kappa \frac{V_s}{V_w},$$

(1.7)

where V_s is the volume of the dry particle mass and V_w is the volume of water. A choice of dry diameter (D_{dry}) and κ enable calculation of the expected supersaturation – wet diameter relationship (Köhler curve):

$$S(D) = \frac{D^3 - D_{dry}^3}{D^3 - D_{dry}^3 (1-\kappa)} \exp\left(\frac{A}{D}\right),$$

(1.8)

where S is the water saturation ratio over the aqueous droplet, D is the droplet diameter, and A
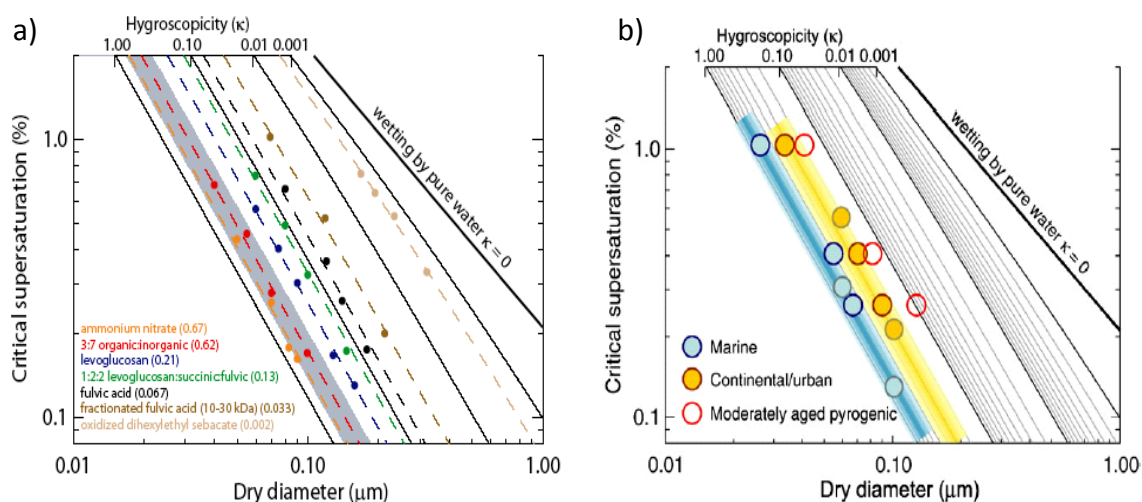
Figure 1.7. s_c–D_{dry} relationships with κ isolines of laboratory generated test particles summarized by Petters and Kreidenweis (2007) (a, left), and of ambient aerosol particles measured in a variety of air masses summarized by Andreae and Rosenfeld (2008) (b, right). (Figures used under the Creative Commons License)

$= 2.1 \times 10^{-9}$ m is a constant evaluated for a surface tension of 0.072 J m^{-2} (pure water) and temperature of 298.15 K. The maximum in the curve described by Eq. 1.8 is identified as the critical saturation ratio for activation of the chosen dry diameter (critical supersaturation, $s_c = S$-1). κ ranges from 1.4 to 0 for typical atmospheric components. Particles composed of sufficiently soluble and highly hygroscopic material such as inorganic salts have κ values that approach 1.4. NaCl has $\kappa = 1.2$ and (NH$_4$)SO$_4$ has $\kappa = 0.6$, for example. Completely insoluble but wettable particles, such as pure elemental carbon and metal oxides, have $\kappa \sim 0$, and activate according to the Kelvin effect of particle curvature only. Further details on the important roles that solubility (Petters and Kreidenweis, 2008) and particle phase play in determining a particle's observed hygroscopicity are discussed in Chapter 6.

Plotting the critical supersaturation, s_c, versus the particle dry diameter, D_{dry}, in log-log space reveals a consistent relationship between the two properties. Isolines of constant kappa can be overlaid on log s_c–log D_{dry} plots to help organize and compare CCN experimental data. Points along a kappa isoline all have the same hygroscopicity and therefore should exhibit the same CCN activation properties. At large kappa values, for the most CCN-active systems, the kappa isolines follow the -3/2 slope predicted by Köhler theory (Seinfeld and Pandis, 2006). However, as kappa approaches zero the slope of the kappa isoline decreases and approaches -1, which is predicted when particle activation is determined by the Kelvin effect alone. Figure 1.7a displays the hygroscopicities of several representative atmospheric aerosol components in log s_c–log D_{dry} space with κ isolines to demonstrate the available range of aerosol hygroscopicity (Petters and Kreidenweis, 2007). Figure 1.7b is a similar plot of aerosol hygroscopicity but measured for ambient aerosols in a variety of locations summarized by Andreae et al. (2008). The hygroscopicity and CCN activation of atmospheric aerosols and their climate effects are discussed further below.

1.2.6 Optical properties

Aerosol particles also directly affect climate by absorbing and reflecting (or scattering) incident solar and terrestrial radiation. The interactions of particles with radiation are controlled by size, shape, and complex index of refraction, which is determined by chemical composition and hygroscopicity. The complex index of refraction is defined as

$$N = n + ik \qquad (1.9)$$

where n is the real (nonabsorbing) and k the imaginary (absorbing) component of refraction and both are a function of wavelength. These optical properties determine the role of aerosols in visibility reduction and the redistribution of solar and terrestrial radiation throughout the atmosphere. Mie theory governs the majority of the interactions between aerosols and terrestrial and solar radiation wavelengths for most atmospheric particles sizes. This causes the scattered light functions to have complex angular dependences (Seinfeld and Pandis, 2006). The key parameters used to describe these optical properties include the single scattering albedo (SSA) and asymmetry parameter. SSA, ω, is defined as the scattering efficiency, Q_{scat}, divided by the extinction efficiency (sum of absorption + scattering), Q_{ext}:

$$\omega = \frac{Q_{scat}}{Q_{ext}} \qquad (1.10)$$

The asymmetry parameter, g, captures the angular dependence of the scattered light and is defined as the intensity-weighted average of the cosine of the scattering angle:

$$g = \frac{1}{2}\int_0^\pi \cos\theta P(\theta)\sin\theta d\theta \qquad (1.11)$$

where θ is the angle between the incident and scattered light, and $P(\theta)$ is the angular distribution of the scattered light at θ (the phase function).

1.3 Atmospheric processing of aerosol particles

Aerosol particles represent a dynamic component of the atmosphere whose physicochemical properties constantly evolve during their entire atmospheric lifetime. Changes in the particles' chemical composition alter other important properties such as size, morphology, optical properties, density, hygroscopicity, and toxicology. Before discussing the various chemical processing mechanisms that occur in the atmosphere, some key physical processes are reviewed below.

1.3.1   Dynamics of aerosol populations

New particles are produced by nucleation, and emission from combustion and mechanical processes. Very small particles have high rates of diffusion, causing them to coagulate with other existing aerosol particles. Coagulation reduces aerosol number concentration while conserving aerosol mass and shifting the size distribution towards larger particle sizes (Pandis et al., 1995). The rate of coagulation is minimized for particles of the same size and maximized for two particles of greatly differing size (Seinfeld and Pandis, 2006). Larger particles are removed through gravitational settling leading to dry deposition on surfaces. The major particle sinks, coagulation and gravitational settling, are minimized in the accumulation size mode ($0.1 < D_a < 1.0$ μm). This causes particles in this size range to have the longest atmospheric lifetimes of several weeks to a month. Wet deposition also removes particles when they become activated into cloud droplets through hygroscopic growth and are rained out, or are washed out by falling rain droplets below a precipitating cloud. The ability of particles to activate into cloud droplets is discussed further below and in Chapter 6. Chemical processes including condensational growth and cloud/fog processing also modify the size distribution of aerosol populations. Condensational growth preserves particle numbers while increasing particle size and mass. These effects are discussed in the following section.

1.3.2 Condensational growth

Semi-volatile compounds can partition from the gas to the aerosol phase when the compound's partial vapor pressure exceeds its saturated vapor pressure, and re-evaporate when its partial vapor pressure drops below saturation. The available aerosol surface area largely controls condensation, causing condensable aerosol species to typically maximize in the submicron aerosol. Note that condensation is treated as a simple chemical partitioning phenomenon in which the chemical composition of the available aerosol does not influence the process. When reactive uptake mechanisms are involved this is not the case, as discussed below. Ambient temperature and relative humidity (RH) play important roles in gas-particle partitioning of many compounds, ammonium nitrate in particular. The partitioning of $NH_4NO_3(s) \rightleftharpoons NH_3(g) + HNO_3(g)$ is strongly shifted towards the particle phase (left side) at low ambient temperature and high RH (Stelson et al., 1979). The condensation of ammonium nitrate is therefore typically favored at night. Sometimes this process is also referred to as heterogeneous nucleation (Korhonen et al., 2003).

1.3.3 Cloud/fog processing

Particles that contain sufficient volume fractions of soluble hygroscopic compounds can experience hygroscopic growth by absorbing ambient water vapor. A supersaturated water vapor environment, such as in a rising air parcel, can cause such a particle to exceed is activation diameter and form a stable cloud droplet, as described above. Fog formation involves similar processes. The absorption of large amounts of water caused by cloud/fog droplet formation significantly dilutes the particle's existing chemical components. Trace gases therefore partition to the dilute droplets to reestablish gas-particle equilibrium. Many of these gases participate in aqueous chemistry in the droplets, including SO_2, NO_x, HNO_3, N_2O_5, H_2O_2, O_3, and a wide range of water-soluble organics (Ervens et al., 2004; Finlayson-Pitts and

Pitts, 2000). The products of these aqueous reactions typically have much lower vapor pressures than their precursors. Most cloud systems experience numerous cloud growth and dissipation cycles. This entire process is referred to as cloud processing and is generally the major pathway for particulate sulfate production, as the rate of aqueous conversion of $SO_2 \rightarrow H_2SO_4$ exceeds the homogeneous gas-phase oxidation rate (Finlayson-Pitts and Pitts, 2000). Cloud processing is responsible for the droplet submode in the accumulation mode discussed above (Kerminen and Wexler, 1995; Meng and Seinfeld, 1994). Scavenging of non-activated interstitial particles by cloud droplets within clouds leads to a high degree of internal aerosol mixing that is retained when the cloud droplets dissipate. Scavenging during cloud processing is responsible for the large degree of internal mixing of sea salt and mineral dust particles (Andreae et al., 1986a; Niimura et al., 1998), for example.

1.3.4 Heterogeneous and multiphase reactions

Particles undergo chemical reactions with trace atmospheric gases during transport (Abbatt, 2003; Poschl, 2005). A heterogeneous reaction involves a gas molecule striking and reacting with a particle's surface, while a multiphase reaction involves chemistry between and within the gas, aqueous, and particle phases (Ravishankara, 1997). Unlike condensation and cloud processing described above, the individual particle's chemical composition plays an important role in dictating the reaction mechanisms and rates at which these processes occur. Heterogeneous/multiphase reactions are important because they change the chemical balance of trace atmospheric gases (Bauer et al., 2004; Dentener and Crutzen, 1993) while also altering the chemical composition and associated properties of aerosol particles (Petters et al., 2006a), and increase aerosol mass through particle growth (Gelencser and Varga, 2005; Heald et al., 2006; Maria et al., 2004).
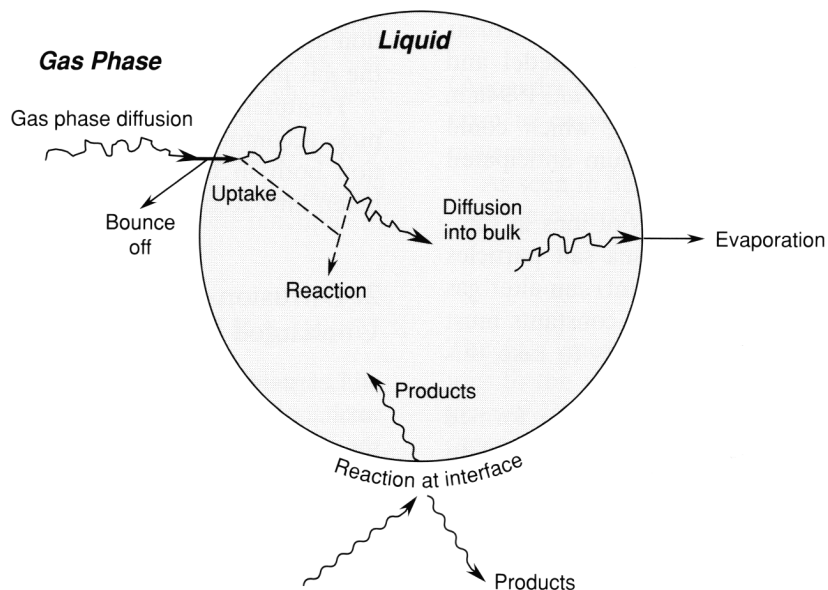
Figure 1.8. Schematic of various chemical and physical processes involved in the uptake and reaction of atmospheric gases with aqueous particles. (Figure taken from Finlayson-Pitts and Pitts (2000), © 2000 Academic Press.)

Gas-particle reactions involve several steps, particularly in aqueous particles, including diffusion of the reactant gas to the particle surface, mass accommodation across the air-particle interface, and transport and reaction within the particle (Finlayson-Pitts and Pitts, 2000; Kolb et al., 2002; Poschl et al., 2007; Worsnop et al., 2002). These processes are summarized in Figure 1.8. The gas-particle reaction mechanism is typically described using a resistor model analogy in which each process represents a potential rate limiting step in the overall circuit, such as shown in Figure 1.9. The reactive uptake coefficient, γ, is a commonly reported parameter used to describe the reaction probability of various gases with different aerosol surfaces. γ is defined as the fraction of gas-particle collisions that lead to a chemical reaction. The mass accommodation coefficient, α, is the fraction of gas molecules that are transported across the gas-particle interface upon collision, but it does not require a chemical reaction to occur. Transport to and from the interface to the aerosol's bulk, and aqueous phase

reactions may also occur. The net overall resistant, or rate, $(\gamma_{net})^{-1}$, is the sum of the individual resistances displayed in Figure 1.9:

$$\frac{1}{\gamma_{net}} = \frac{1}{\Gamma_g} + \frac{1}{\alpha} + \frac{1}{\Gamma_{rxn} + \Gamma_{sol}} \, . \tag{1.12}$$

 A variety of aerosol flow tube (Thornton et al., 2003), Knudsen cell (Underwood et al., 2001a), and falling droplet apparatuses (Li et al., 2001) are typically used to experimentally measure these parameters.

Numerous experimental studies on a wide variety of gas-particle systems have measured the relevant reaction kinetics and mechanisms and are too numerous to summarize here. Important general conclusions include the role that particle composition, physical phase, and water content play in determining these reaction rates and mechanisms (Poschl, 2005). For example, the reactive uptake of N_2O_5 on organic aerosols and sea salt particles, and HNO_3 on $CaCO_3(s)$ and $NaCl(s)$ particles was significantly enhanced at elevated RH and when the
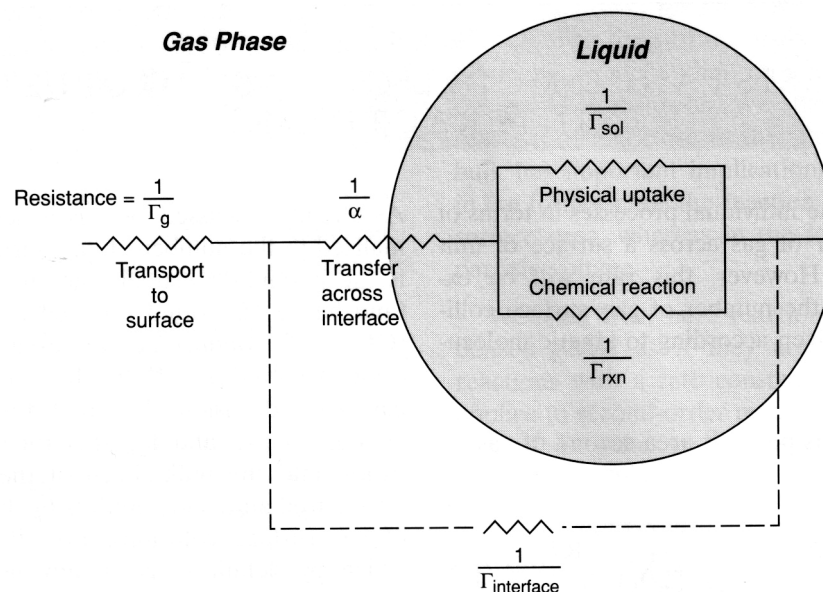
Figure 1.9. Resistance model of gas diffusion, uptake, reaction, and transport within an aqueous droplet. (Figure taken from Finlayson-Pitts and Pitts (2000), © 2000 Academic Press)

organic and sea salt particles were in a deliquesced aqueous state. Thornton et al. (2005; 2003) measured γ of N_2O_5(g) equal to < 0.001 and 0.005 on dry crystalline malonic acid and sea salt particles, versus 0.03 and 0.03 on the same wet, aqueous aerosols. Recent reactive uptake experiments have been performed on mixed aerosol particles that better represent the chemical composition of realistic aerosols (Knopf et al., 2005). A great deal of research into the effects of chemical composition, physical phase (Hearn and Smith, 2007), particle morphology, photochemistry, and secondary reactions within the particle are still required to improve our understanding of heterogeneous chemistry. New heterogeneous processes continue to be discovered (e.g. Karagulian et al., 2008; Stemmler et al., 2006).The role of a organic surfactant coating around an aerosol particle on reactive uptake and mass transport from the gas to particle phase has been a particular recent emphasis (Tabazadeh, 2005; Thornton and Abbatt, 2005). Our understanding of the complex heterogeneous and multiphase reactions that organic compounds undergo during photochemical oxidation is particularly lacking (Fuzzi et al., 2006).

1.4 Cloud nucleation properties of aerosol particles

All cloud droplets and ice crystals form on a nucleating aerosol particle, i.e. cloud condensation nuclei (CCN). The aerosol indirect climate effects produced via aerosol-cloud interactions remain one of the most poorly understood aspects of anthropogenic contributions to global climate change (IPCC, 2007; Lohmann and Feichter, 2005). These include altering cloud albedo (Twomey, 1977) and lifetime (Albrecht, 1989), as well as suppressing or enhancing precipitation (Rosenfeld, 2000). The complex and heterogeneous physicochemical nature of atmospheric aerosols is the primary cause of our poor understanding of these processes. Furthermore, we do not fully understand the interactions of the wide range of

aerosol compositions with water (Kanakidou et al., 2005; Sotiropoulou et al., 2006), particularly under freezing conditions (Cantrell and Heymsfield, 2005). These issues are made more complex by heterogeneous and multiphase chemistry that particles experience with gaseous and aqueous-phase reactants, causing further changes in their physicochemical properties during atmospheric transport (Maria et al., 2004; Petters et al., 2006a). Human activities alter aerosol-cloud interactions through the emission of primary combustion aerosol (Adams and Seinfeld, 2003), the production of secondary aerosol (via gas-to-particle conversion) (Maria et al., 2004; Petters et al., 2006a), and through the modification of natural aerosol such as sea salt and mineral dust through reaction with trace pollutant gases (Laskin et al., 2005a). Measurement of the chemical composition of individual particles across the size distribution and knowledge of how the various components, and their mixtures, interact with water under warm and cold cloud conditions are therefore required to reduce the uncertainty in the aerosol indirect climate effect (Andreae and Rosenfeld, 2008; Cantrell and Heymsfield, 2005; McFiggans et al., 2006).

Aqueous cloud droplets dominate warm and mixed phase clouds, while cirrus clouds are composed of ice crystals. While the mechanisms of cloud droplet versus ice crystal growth and formation are very different, both involve the exposure of an aerosol population to a supersaturated water vapor environment. A particle becomes "activated" when it grows large enough through a period of unstable equilibrium to become a stable cloud droplet or ice crystal. The chemical composition and size are the primary factors that control the activation properties, as well as the ambient temperature and supersaturation with respect to liquid water or ice (Andreae and Rosenfeld, 2008; McFiggans et al., 2006). Köhler theory (Kohler, 1936) can describe and predict the activation properties of aqueous droplets, as previously described above. Köhler theory has been extended to account for the presence compounds with limited

solubility that are frequently present in atmospheric particles (Bilde and Svenningsson, 2004; Raymond and Pandis, 2003; Shulman et al., 1996). The presence of surface-active components that lower the surface tension at the particle-air interface also need to be considered in some situations (Facchini et al., 1999; Ming and Russell, 2004).

Understanding of aerosol interactions with warm clouds has improved greatly in the last decade, with a particular focus on the complex organic fraction (Kanakidou et al., 2005). In general the CCN activity of most aerosol components can be accurately predicted via Köhler theory modified to account for solubility, surface tension, and metastable hydrates (Petters and Kreidenweis, 2008; Sotiropoulou et al., 2006). The hygroscopicity of soluble inorganic salts are well-understood and can be accurately predicted. Until recently, sparingly soluble inorganic compounds, such as those abundant in mineral dust particles, have been largely ignored in experimental CCN studies. The possible conversion of mineral dust particles from originally poor CCN into highly CCN-active particles through atmospheric processing and heterogeneous chemistry is of particular interest (Gibson et al., 2006a; Laskin et al., 2005a), as discussed in detail in Chapters 6 & 7.

CCN-activation of organic compounds pose a greater challenge due to their large diversity but in general can be divided into soluble and insoluble organic fractions, though the factors that control the production of each fraction are still not well known (Kanakidou et al., 2005). Within these fractions organic compounds exhibit a wide range of hygroscopicity which frequently cannot be accurately predicted by thermodynamics. Surface-active organics represent an additional challenging complexity (Facchini et al., 1999). The hygroscopic and cloud-nucleating properties of organic compounds in aerosols remain an intense area of investigation as a result. CCN closure in aged continental air masses can often be achieved by treating the entire aerosol simply as one composition and hygroscopicity, such that CCN

production is controlled primarily by particle size (Dusek et al., 2006). However, in situ CCN measurements made during cruises along the Californian coast (Furutani et al., 2008), during the San Diego 2007 Wildfires (Moore et al., 2008), and by other groups (Hudson, 2007; Quinn et al., 2008) have revealed a much larger variability in the aerosol's hygroscopicity in younger air masses close to their sources. The major remaining questions to improve the parameterizations of aerosol-warm cloud interactions in regional and global models are therefore:

1. What are the timescales and mechanisms for the conversion from a fresh, heterogeneous aerosol into a well-mixed aerosol with uniform hygroscopicity?

2. What is the variability of this timescale with location, meteorology, and seasonality?

3. How often can atmospheric aerosols be described by a single hygroscopicity, particularly at typical cloud base altitudes?

4. How do the cloud-nucleation properties vary for aerosols from different sources?

5. How similar are surface measurements of aerosol composition and hygroscopicity to those made at higher altitudes?

6. What are the controlling factors governing the solubility and hygroscopicity of the organic aerosol fraction?

7. How important are kinetic limitations to thermodynamic cloud droplet growth?

The ability of aerosol particles to freeze and act as **ice nuclei** (IN) is even less well understood than warm aerosol-cloud interactions. Ice clouds typically have a net positive (warming) radiative forcing. Cirrus clouds cover on average 20% of the atmosphere and are responsible for approximately 50% of precipitation (Baker, 1997; Cantrell and Heymsfield, 2005). IN can be produced through numerous homogeneous and heterogeneous nucleation mechanisms, and secondary production mechanisms. The efficient homogeneous nucleation of

aqueous salt particles that occurs at cold temperatures $< -35\,°C$ is reasonably well constrained (Koop et al., 2000). Heterogeneous nucleation, which can occur at warmer subzero temperatures than homogeneous nucleation, remains very poorly understood but seems to be most efficient on insoluble particles including mineral dust and soot particles (DeMott et al., 2003a), as well as solid ammonium sulfate (Abbatt et al., 2006). Mineral dust particles have been the most well studied heterogeneous IN in both laboratory studies and field measurements, yet large uncertainties remain. The dust's mineralogy appears to be a major factor in controlling IN properties. Furthermore, coating mineral dust particles with sulfuric acid to mimic atmospheric processing can increase or decrease IN activity, depending on the mineral (Archuleta et al., 2005). Recently attention has been drawn to the IN ability of biological particles, which remains a poorly understood process (Christner et al., 2008; Mohler et al., 2007). The major questions to address concerning **ice nucleation** in ice and mixed-phase clouds are:

1. What are the major IN-active particle types in different meteorological conditions (T and RH_{ice}), locations, seasons, and altitudes?

2. How does atmospheric processing and the resulting addition of secondary aerosol material alter the IN properties of these IN-active particle types?

3. In what circumstances can nucleation theory and thermodynamic properties such as water activity, contact angle, and activation barriers, predict the measured IN concentrations?

1.5 Major aerosol instrumentation used

Motivated by the substantial, yet poorly understood impacts aerosols have on the environment, significant advances are being made in the development of state-of-the-art

instruments and techniques used for aerosol characterization (Bluhm et al., 2006; Canagaratna et al., 2007; Hunt and Petrucci, 2002; Murphy, 2007; Noble and Prather, 2000; Pui et al., 2004; Shimmo et al., 2004; Smith et al., 2004; Suess and Prather, 1999; Wood and Prather, 1998; Ziemann, 1998). Of particular interest are instruments that measure important physicochemical properties of atmospheric aerosols in an on-line manner and thus require no to very little pre-conditioning of the particles before analysis. Such instruments are essential to advancing our understanding of atmospheric aerosol processes by providing information on their chemical composition, and temporal changes in chemistry with high temporal resolution. Many instruments operate at the single aerosol particle level, obtaining the size and composition of each particle being analyzed. Measurements performed in an on-line manner avoids potentially significant sampling artifacts caused by the loss (evaporation) or gain (adsorption or chemical reaction) of particulate species which occur when aerosols are collected for extended periods of time on substrates such as filters. Real-time analysis also allows the direct measurement of a rapidly changing aerosol population while sampling ambient air on moving platforms such as an aircraft or motor vehicle.

1.5.1 Aerosol time-of-flight mass spectrometry (ATOFMS)

Single-particle mass spectrometry (SPMS) is the major technique used for online individual particle analysis (Murphy, 2007; Murphy et al., 2006; Noble and Prather, 2000; Sullivan and Prather, 2005; Ziemann, 1998). These instruments measure the size and chemical composition of individual particles in an aerosol sample in real-time. The SPMS instrument used to perform the research described here is the Aerosol Time-of-Flight Mass Spectrometer (ATOFMS) (Gard et al., 1997). Single particle analysis is achieved by pulling the aerosol into a vacuum through an aerosol inlet. A converging nozzle inlet is used to study larger particles; it has a maximum transmission efficiency at $D_a \sim 1.7$ μm and can effectively sample particles
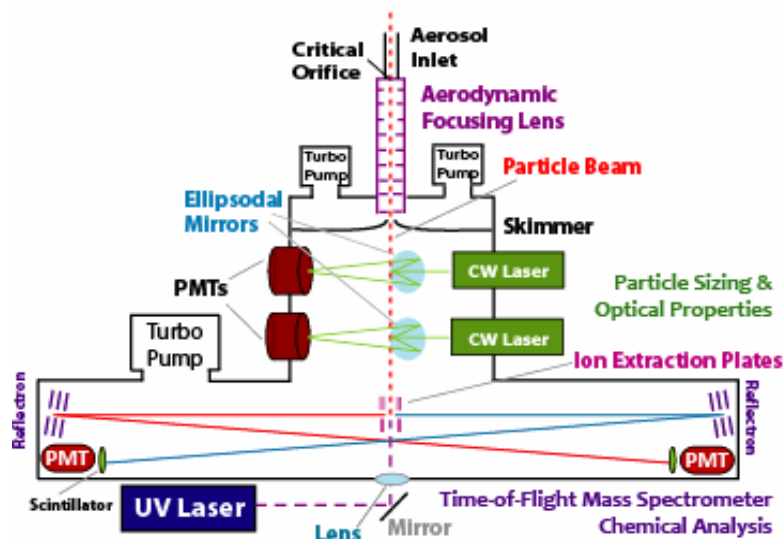
Figure 1.10. Schematic of the current UF-ATOFMS instrument for online submicron individual particle analysis. Blue and red lines are positive and negative ion trajectories, respectively.

from ca. 0.2-3.0 μm. The aerodynamic lens was recently developed as an efficient inlet for submicron aerosol particles (Liu et al., 1995). A series of plates with decreasing orifi collimates the aerosol into a tight beam. The aerodynamic lens has been coupled with the ATOFMS to develop the UF-ATOFMS for the analysis of ultrafine and accumulation mode aerosol particles between ca. 80 and 600 nm (Su et al., 2004). The UF-ATOFMS inlet uses lower aerosol sample flow rates and a longer transmission length than the nozzle inlet. The longer aerosol residence time typically leads to a greater degree of evaporation and particle drying with the aerodynamic lens inlet (Zelenyuk et al., 2006b).

The inlet accelerates each particle to a size- and shape-dependent terminal velocity. The particle then passes through two continuous-wave diode-pumped Nd:YAG laser beams (532 nm). An elliptical mirror collects the back-scattered laser light and focuses it onto a photomultiplier tube (PMT). An operational amplifier processes this signal and feeds it to a timing circuit. The timing circuit measures the time-of-flight between pulses from the first and second laser beams to determine particle velocity. Through a calibration of particle velocity

versus dry diameter using polystyrene latex spheres, the aerodynamic diameters can be determined from the time-of-flight measurement. The timing circuit also uses this velocity measurement to trigger the firing of a Q-switched Nd:YAG laser (4th harmonic, 266 nm). The lasers are aligned to maximize the probability that the laser desorption/ionization (LDI) laser pulse will intersect the sized particle in the source region of the mass spectrometer. The UV laser pulse rapidly desorbs and ionizes the chemical constituents in each particle. Positive and negative ions are passed into two separate ion flight tubes using a push-pull ion source for time-of-flight mass spectrometry. The ions enter a reflectron to increase the mass resolution before being deflected back towards the ion source. A microchannel plate facing the reflectron intercepts the ions and delivers the produced signal to a data acquisition board. Positive and negative ion mass spectra and aerodynamic size are thus determined for each individual particle. Recently the scattered laser light intensity from the sizing laser beams has been used to determine refractive index, effective density, and shape (Moffet and Prather, 2005; Moffet et al., 2008b). A schematic of the UF-ATOFMS is shown in Figure 1.10.

Laser desorption/ionization (LDI) methods can detect all typical aerosol components and allow single-particle measurements to be made in real-time. Quantification of chemical components has been demonstrated but can be challenging since the signals produced by LDI can be highly variable and experience significant matrix effects. The ion signals can be quantified by characterizing relative response factors for specific analytes in model aerosol standards (Gross et al., 2000). This approach has been used to quantify a number of cations and anions in sea salt particles and to measure the amount of OC on coated EC particles (Gross et al., 2000; Spencer and Prather, 2006). Quantification of at least 44 different chemical species in ambient particles has been achieved (Fergenson et al., 2001) and instrumental sensitivities can be calculated by comparing the on-line measurements with co-

located filter samples (Bhave et al., 2002a). These quantitative measurements have also been compared to model predictions of the size-dependent chemical composition of single particles with excellent agreement (Bhave et al., 2002b). Number concentrations of various particle types can also be obtained by scaling the measurements to atmospheric concentrations (Pastor et al., 2003; Wenzel et al., 2003) allowing the fraction of particles resulting from different sources to be determined (Bhave et al., 2002b; Vogt et al., 2003). In this dissertation, ATOFMS is primarily used to observe changes in particle chemical composition caused by atmospheric processing, heterogeneous chemistry in particular, occurring on mineral dust particles in controlled laboratory experiments and the real atmosphere.

1.5.1.1 *Single-particle data analysis and classification algorithms*

Recent improvements to the ATOFMS data acquisition systems permit the rapid collection of single-particle data, typically producing over one million single-particle mass spectra after a few days of sampling in polluted urban environments. The fast data collection rate allows for the analysis of changes in particle chemistry over small particle size bins (0.010-0.10 μm) and with high time resolution – as small as 10 minute bins. Modern data analysis tools are required to sort the large volume of data collected. Several different types of particle classification algorithms are commonly used in the SPMS community. The ART-2a algorithm is the most commonly used to sort ATOFMS single-particle mass spectra into clusters of particles with similar mass spectral features (Rebotier and Prather, 2007; Song et al., 1999). The algorithm operates by randomly selecting particles from the dataset and comparing the dot product of the mass spectra from two individual particles. If the dot product falls within the specified vigilance factor, both particles are placed into one cluster. The grouping procedure continues with the remaining particle mass spectra, until each particle is either placed in a matching particle cluster, or creates a new particle cluster to which future

particles may join. The clusters are regrouped at the end by testing the dot product of each cluster with one and other to reduce the overall number of particle clusters. A vigilance factor of 0.80 or greater is commonly used to properly distinguish between similar mass spectra that are actually from different particle sources. Typically at least the top 50-70 largest clusters representing more than 90% of the total particles are then manually inspected and classified by particle type based on the vast number of ATOFMS ambient measurements in prior ambient and source characterization studies (e.g. Angelino et al., 2001; Gross et al., 2005; Guazzotti et al., 2001a; Moffet et al., 2008a; Qin and Prather, 2006; Silva et al., 2000; Silva et al., 1999; Silva and Prather, 2000; Sodeman et al., 2005; Toner et al., 2006). Recently a hierarchical classification (HC) algorithm has also been applied to ATOFMS SPMS data (Rebotier and Prather, 2007). This involves grouping the particles into clusters that fall into a hierarchical tree based on the similarity of the clusters' to one another in mass spectral space. HC offers the advantage of more user control over the classification process as the degree to which the classification tree is divided can be manually inspected and controlled. This enables the relationships between similar clusters to be more readily apparent and the degree of separation to be specified on a cluster-to-cluster basis. HC has the disadvantages of consuming more computing resources, thus taking much longer than ART-2a, and breaking down for datasets larger than ~100,000 particles. Comparison to ATOFMS datasets previously classified by ART-2a with those classified by HC poses a further challenge.

After sorting and manual classification of the clusters into representative types or classes (including sea salt, mineral dust, elemental carbon, metals, organic carbon, K-biomass burning, others, and internal mixtures of these types), the analysis of ATOFMS data is not straightforward and dictated by the specific questions to be addressed. The high size and temporal resolution of the ATOFMS data collection permits the study of changes in particle

composition over fine particle size and time bins. Typically, the fractions of the various particle types are plotted versus time and particle size to study changes in their properties following diurnal cycles, meteorological changes, and specific atmospheric events such a pollution point sources, or precipitation. Searches for specific chemical markers in individual particles or particle classes are also performed. Liu et al. (2003), Moffet et al. (2008a), and Chapters 2 & 3 list some common mass-to-charge ratios used for such searches. More recently variations in specific ion peak areas with particle size and time have been used to investigate the atmospheric processing of aerosols as they evolve during transport. While the ATOFMS generally produces semi-quantitative data, changes in the relative amounts of specific chemical compounds can be inferred upon careful analysis of the ion peak area signals. Examples of such analysis are present in Chapters 2-5. More recently, laboratory studies have been conducted to quantify the absolute amount of specific compounds in specific particle types. These calibrations are applied to interpret ATOFMS data from laboratory experiments, such as in Chapter 7.

1.5.2   Aerosol size distribution and particle counting instrumentation

As discussed previously, an aerosol particle's size is an important parameter that reflects the particle's source and chemistry, and dictates its atmospheric behavior. Aerosol particles span over five decades of particle diameter, between approximately 1 nm to larger than 100 μm when fog/cloud droplets are considered. Numerous instruments exist to measure the concentration of aerosol particles in discrete size bins (size distribution) across this wide dynamic particle size range. McMurry (2000) presents an excellent review of many of these instruments.

1.5.2.1 Aerodynamic particle sizer (APS)

The APS determines the aerodynamic diameter of individual particles based on their time-of-flight between two continuous wave lasers once the particle has been accelerated to its terminal velocity. This is the same principle of operation as used in the ATOFMS sizing region. In the ATOFMS, the scattering lasers are placed further apart than in the APS, which permits a more accurate measurement of velocity and thus aerodynamic diameter. The lasers in the APS are aligned right next to each other in a double-crest, which reduces coincidence errors from overlapping particles traversing the laser beam(s), with a reduction in the sizing accuracy. The APS used in this research is a Model 3321 manufactured by TSI, Inc. (Volckens
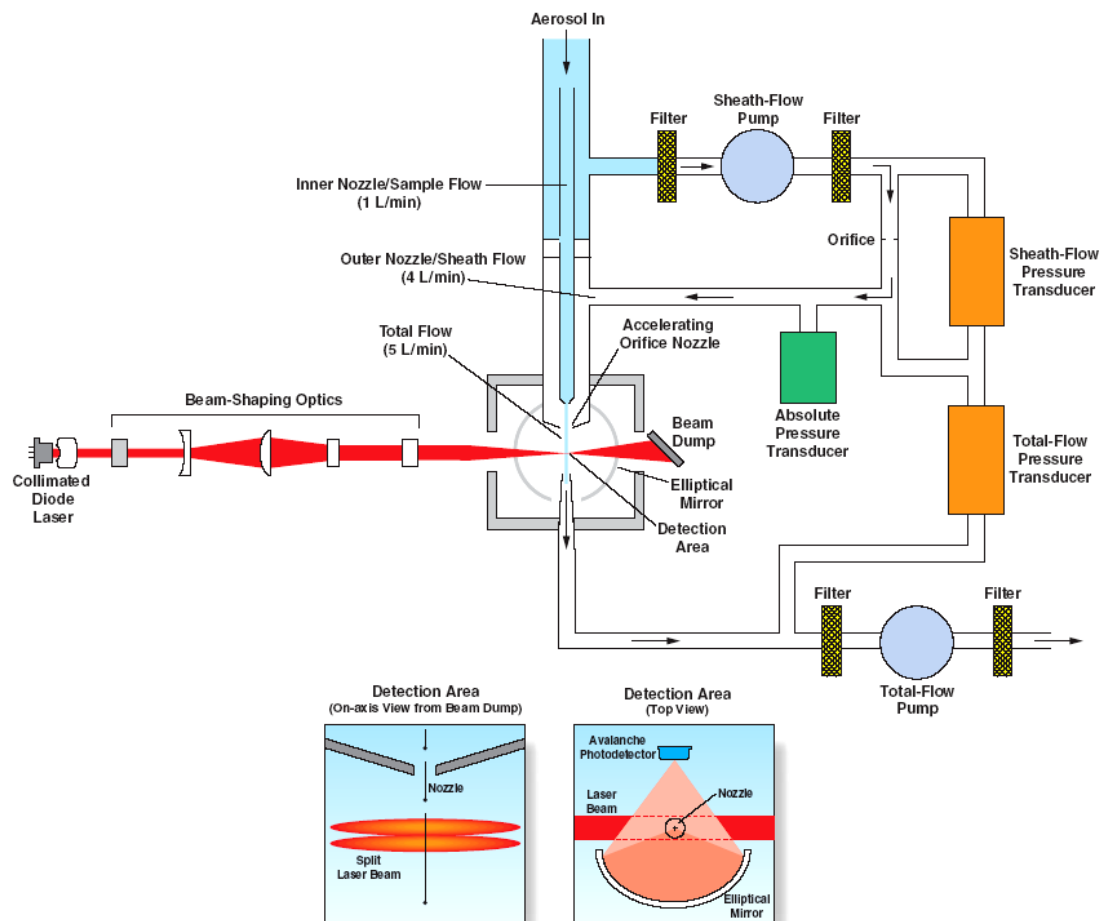
Figure 1.11. Schematic of the TSI Model 3321 Aerodynamic Particle Sizer (APS) capable of determining the size of particles between 0.5 and 20 μm. (Diagram courtesy of TSI, Inc.)

and Peters, 2005), a schematic is shown in Figure 1.11. The APS samples 5.0 Lpm of total aerosol flow, of which 4.0 Lpm is filtered and used as a sheath flow to surround the remaining 1.0 Lpm of aerosol sample flow through the detection region. It has a stated size resolution of ±0.02 μm at 1.0 μm. The APS groups the measured particle diameters into discrete size bins spanning from 0.523 to 20 μm. It also counts any measured particles smaller than 0.523 μm in one large unresolved bin.

1.5.2.2 *Differential mobility analyzer (DMA)*

A differential mobility ability analyzer, or electrostatic classifier, operates by transmitting a discrete particle size through the instrument. The DMA is based on mobility diameter, as opposed to aerodynamic diameter, as described above. Mobility diameter is sensitive to shape and size but not density. The aerosol first passes through a bipolar aerosol neutralizer, which exposes the aerosol to ionized gas generated by radioactive decay. The objective is to achieve charge equilibrium in the aerosol by exposing it to a high concentration of positive and negative ions. At charge equilibrium, the distribution of electrical charges across the aerosol size distribution can be accurately described using the Wiedensohler (1988) approximation to the corrected Fuchs charge distribution. The fraction of particles containing an electrical charge, and the number of changes per particle, increases exponentially with particle size. An appreciable fraction of particles larger than ~200 nm will have multiple charges, while the fraction of charged particles smaller than 100 nm is much less than 10% (Flagan, 2001). ^{85}Kr (*β*-emitter*)* or ^{210}Po (*α*-emitter) are commonly used radioisotopes. ^{210}Po emits about 10 times more energy than ^{85}Kr and can thus achieve charge equilibrium under faster flow conditions (Covert et al., 1997; Ji et al., 2004), but has a short half-life of 138.4 days, compared to 10.76 for ^{85}Kr.

After charge neutralization, the aerosol enters the cylindrical DMA tube. A portion of the aerosol flow is filtered in a recirculating loop and used as the sheath flow through the DMA. A variable negative electrical potential is applied to the rod at the center of the DMA. The electric field attracts positively charged particles flowing through the DMA towards the center of the cylinder. A small opening at the bottom of the DMA's tube allows a narrow portion of the sampled aerosol to exit the cylinder, all other aerosols impact on the surface of the cylinder or rod. The particle mobility diameter that exits the DMA is a function of the particle's physical size, shape, and number of charges as described by:

$$\frac{D_m}{C} = \frac{2neVL\chi}{3\mu q_{sh} \ln\frac{r_2}{r_1}} \tag{1.13}$$

where D_m is the mobility diameter, C is the Cunningham slip correction, n is the number of elementary charges, e, V is the rod voltage, L is the rod's length, χ is the particle's dynamic shape factor, μ is the gas viscosity, q_{sh} is the sheath flow rate, and r_1 and r_2 are the inner and outer radii of annulus space. Non-spherical particles $(\chi > 1)$ have larger mobility diameters than volume equivalent spherical particles due to the extra drag force experienced by non-spherical particles as they move towards the rod (DeCarlo et al., 2005).

The DMA used in this work is a Model 3081 manufactured by TSI, Inc., employing the Long DMA column to achieve the largest particle size range (Flagan, 2001; Knutson and Whitby, 1975). A schematic is shown in Figure 1.12. The optimum sheath-to-aerosol flow ratio is 10:1 for maximum size resolution. Typical sheath and aerosol flow rates used in this work are 10.0-15.0 and 1.0-1.50 Lpm. A lower sheath-to-aerosol flow rate is sometimes employed to increase the maximum particle size that can be selected. This model can effectively transmit particle sizes from ca. 20 to 1000 nm. Below 20 nm diffusional broadening seriously impairs the size resolution, while high enough voltages cannot be applied
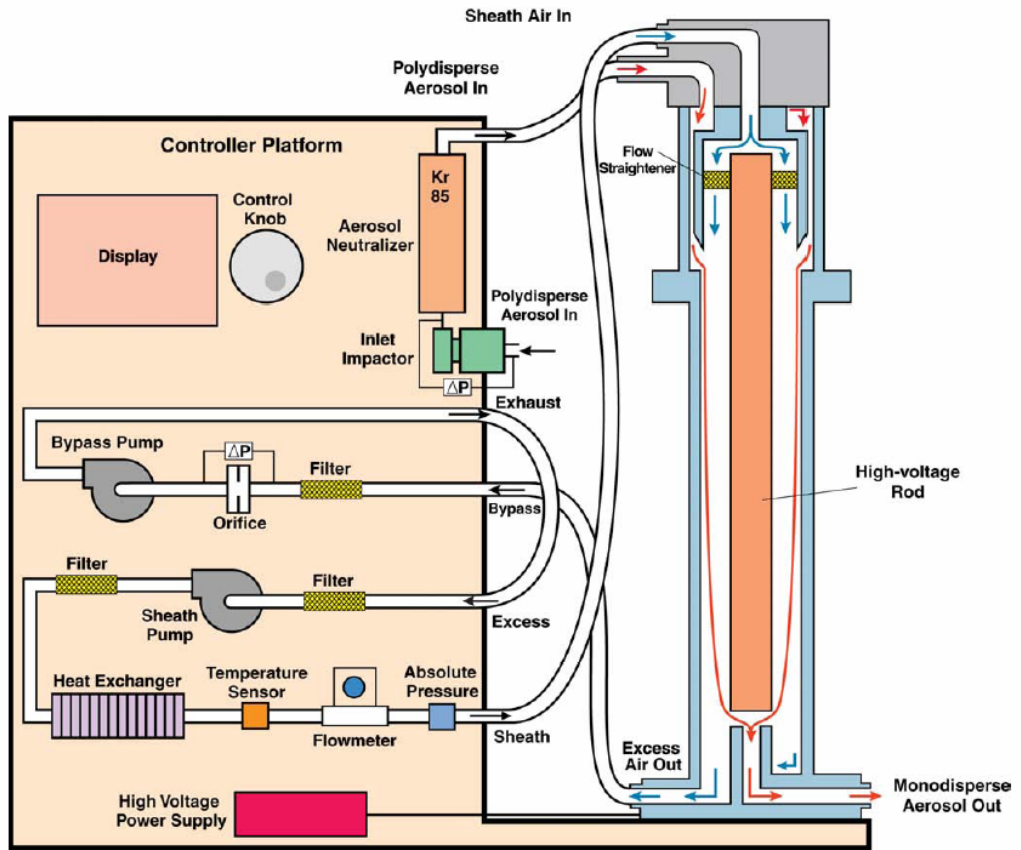
Figure 1.12. Schematic of the TSI Model 3081 Differential Mobility Analyzer (DMA). Orange lines show the flow path of the monodisperse aerosol, blue lines are the sheath flow. (Figure courtesy of TSI, Inc.)

to select and effectively transmit supermicron particles. The DMA can be operated to continuously select one mobility diameter by leaving the rod voltage, *V*, fixed, or the voltage can be continuously adjusted to scan across the submicron particle size range. In scanning more the DMA is typically coupled to a Condensation Particle Counter (CPC), described below, to measure the submicron size distribution.

1.5.2.3 Condensational particle counter (CPC)

The CPC can count all particles, regardless of their size, composition, or shape, above a certain nanoparticle size threshold. The instrument achieves this by forcing all particles to grow via condensation in a hot saturated vapor stream. An optical particle detector counts each
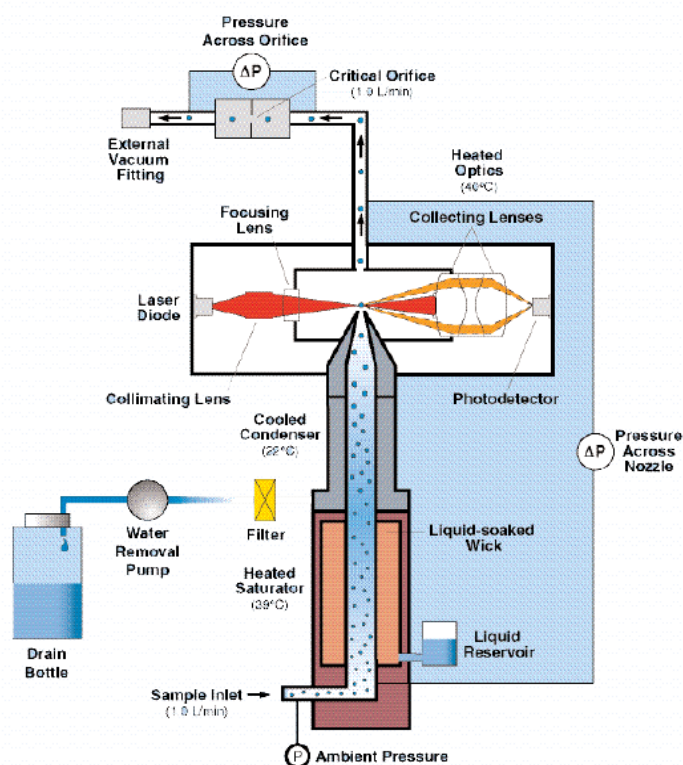
Figure 1.13. Schematic of the TSI Model 3772 Condensation Particle Counter (CPC), the successor to the Model 3010. The principle of design is the same and both models use 1-butanol as the working fluid. (Figure courtesy of TSI, Inc.)

condensationally grown particle through the scattering of light as the aerosol flow transects a continuous laser beam. The CPC used in this work is a Model 3010 manufactured by TSI, Inc. [(Mertes et al., 1995); a schematic is shown in Figure 1.13. This instrument uses 1-butanol as the working fluid to produce condensational growth. Recent versions now operate with water as the working fluid (Biswas et al., 2005). The model 3010 can count all particles larger than 10 nm, up to a particle concentration of 10,000 P/cm^3, and draws an aerosol sample flow of 1.0 Lpm. The CPC is frequently coupled with a DMA to measure submicron aerosol size distributions.

1.5.2.4 Scanning mobility particle sizer (SMPS)

The coupling of a DMA particle selector to a CPC particle counter produces a Scanning Mobility Particle Sizer (SMPS) that measures the size distribution of the submicron aerosol (Wang and Flagan, 1990). The DMA is operated in scanning voltage mode to transmit a steadily changing narrow range of particle sizes through the DMA column and transport these to the CPC. By counting the particle concentration in each DMA size bin the CPC determines the aerosol's size distribution. Accurate SMPS measurements require the use of transfer functions to invert the raw data to account for charge equilibrium, the probability of an aerosol being electrically charged as a function of particle size, and to account for multiply charged particles (Collins et al., 2004; Stolzenburg and McMurry, 2008). Referring to Equation 1.8, a particle with a particular mobility diameter and more than one charge will have a larger volume equivalent diameter than a singly-charged particle of the same mobility diameter. Thus it is important to account for the contribution of multiply-charged particles measured in each DMA size bin. The Model 3081 DMA and Model 3010 CPC used here can typically measure the aerosol size distribution between 20 and 660 nm using a sheath flow of 4.0 Lpm with a scan time of 5 minutes. Note that this overlaps well with the lower size limit of the APS of 532 nm, however the SMPS measures mobility diameter while the APS measures aerodynamic diameter (Khlystov et al., 2004).

1.5.3 Cloud condensation nuclei counter (CCNc)

A cloud condensation nuclei counter (CCNc) simulates cloud formation by exposing the flowing aerosol sample to a controlled water supersaturation and counting the number of particles that grow into cloud droplets (Nenes et al., 2001). The CCNc used in this work is a miniature continuous-flow streamwise thermal-gradient CCN chamber constructed at the Scripps Institution of Oceanography based on the design of Roberts and Nenes (2005). The
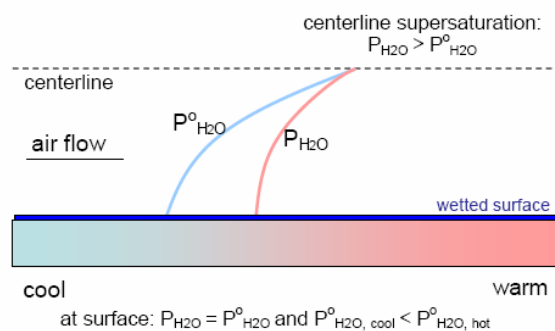
Figure 1.14. Development of a constant water supersaturation in the CCNc via a linear temperature gradient due to the different rates of diffusion of heat (which controls $P°_{H2O}$) and water vapor (which controls P_{H2O}). Figure courtesy of Greg Roberts.

aerosol sample is introduced into the center of the growth column surrounded by a sheath of filtered humidified air. A linear thermal gradient along the column's continuously wetted wall produces the water supersaturation. This develops due to the different gas diffusion rates of water vapor versus air, as depicted in Figure 1.14. In this manner the aerosol sample is exposed to a well-defined and controlled water supersaturation. This supersaturation is primarily a function of the column's thermal gradient (dT), and the total flow rate. Particles that absorb water and grow substantially are detected by an optical particle counter (OPC) at the end of the column from the scattered laser light signal. The OPC is calibrated to record particles with optical diameters greater than 1 μm. This corresponds to particles that have activated and are counted as CCN. The CCNc records the CCN concentration every second. The aerosol flow rate is 15.0 sccm while the sheath flow is adjusted to produce a total flow of 100.0 sccm. A bypass flow of 400 sccm is used to increase the initial sample flow to the top of the column and reduce particle losses.

Calibration of the CCNc's supersaturation (SS) as a function of column temperature gradient (dT) was carefully performed by atomizing a 1.0 g/L solution of ammonium sulfate (Sigma, 99.999%) and determining its activation diameter as a function of column dT. Köhler
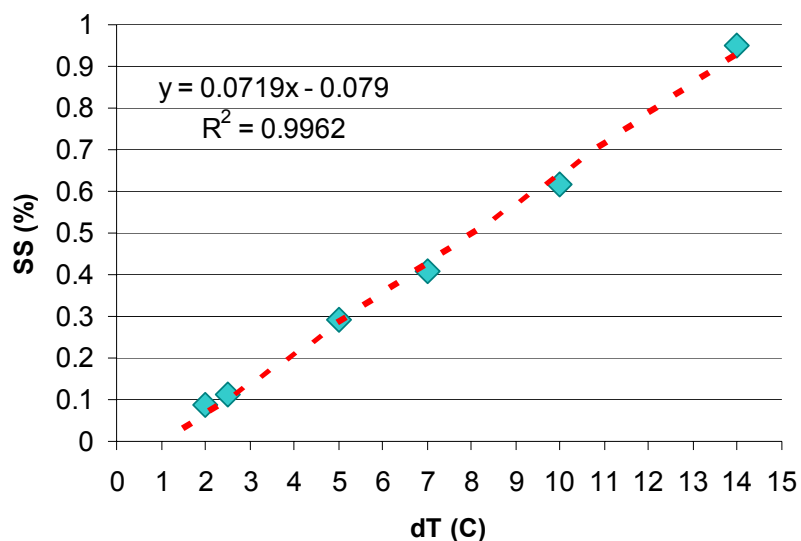
Figure 1.15. Calibration of the CCNc's water supersaturation (SS) versus the column's temperature gradient (dT) using pure ammonium sulfate aerosol.

theory using thermodynamic data from the aerosol inorganic model (AIM) (Wexler and Clegg, 2002) was used to calculate the supersaturation that corresponds to each activation diameter. This corresponds to a single-parameter hygroscopicity of $\kappa = 0.61$ (see below), and the particle shape factor was assumed to equal 1.0. A linear fit of critical supersaturation (s_c) versus column dT was then generated, typically with a $R^2 > 0.995$. A dT of 2.0 to 15.0 C generates a SS of approximately 0.08 to 1.0% (Figure 1.15).

1.6 Mineral dust particle chemistry

Mineral dust particles are one of the largest components of primary particle emissions by mass, with an estimated global annual source strength of 1500 to 2600 Tg (Cakmur et al., 2006). Large dust storms frequently develop in the world's major desert regions, including the Saharan, Gobi, Taklamakan, and Arabian deserts, creating very high atmospheric dust concentrations. These dust plumes can be transported trans-continentally (Duce et al., 1980; Thulasiraman et al., 2002; VanCuren, 2003) and consequentially affect the atmospheric

chemistry, radiative transfer, regional climate, visibility, and air quality over a large portion of the Earth (Bauer et al., 2004; Bian and Zender, 2003; Duce, 1995). Anthropogenic activities can also generate atmospheric dust particles through mechanical processes and this is estimated to contribute to 0 to 20% of the global dust burden (IPCC, 2007). More importantly, changes in land use and topography and the increasing desertification of the planet's surface are predicted to increase the future global dust emission strength (IPCC, 2007). Mineral dust particles scatter and absorb solar and terrestrial radiation, and also alter cloud properties, and thus are important climate-forcing agents (Satheesh and Moorthy, 2005; Sokolik et al., 2001; Tegen et al., 1996). As discussed previously, mineral dust particles are typically dominant in the supermicron particle size range due to their mechanical generation; however submicron dust particle modes can exist and should not be ignored (Gomes et al., 1990). The majority of the research described here focuses on the atmospheric chemistry of mineral dust particles with a particular focus on the unique chemistry of Asian mineral dust particles.

Mineral dust near the source region is composed of a large and variable mixture of different minerals. This can include insoluble aluminosilicate clays (e.g. kaolinite, montmorilinite, illite), metal oxides (e.g. hematite, silica), carbonates (e.g. calcite, dolomite), and sparingly soluble gypsum ($CaSO_4 \cdot 2H_2O$), as well as soluble halite (NaCl) salts (Jeong, 2008; Krueger et al., 2004; Shi et al., 2005). These mineral components often undergo chemical reactions during atmospheric transport, such as reactions with $SO_2(g)$ to produce sulfate, HCl(g) producing chloride, and nitrogen oxides such as $NO_2(g)$, $HNO_3(g)$, and $N_2O_5(g)$ to produce nitrate compounds (Cwiertny et al., 2008; Krueger et al., 2004; Usher et al., 2003a). Uptake of organic compounds such as carboxylic acids by dust is also possible (Falkovich et al., 2004b).

During long-range transport, the physical and chemical properties of mineral dust particles change due to heterogeneous reactions with trace gases, coagulation with other particles, and in-cloud processing (Andreae et al., 1986a; Dentener et al., 1996; Niimura et al., 1998; Okada et al., 1990; Wurzler et al., 2000; Zhang et al., 2003b). These processes affect the optical and hygroscopic properties of dust particles, and therefore influence their radiative (Satheesh and Moorthy, 2005; Sokolik and Toon, 1999; Sokolik et al., 2001), cloud nucleating (Gibson et al., 2006a; Kelly et al., 2007; Levin et al., 1996; Rudich et al., 2002b), and biogeochemical impacts (Houghton et al., 2001; Jickells et al., 2005). These processes also affect the cycles and chemical balances of important trace gases involved in the reactions (e.g., SO_2, NO_x, NO_y, O_3) (Bauer et al., 2004; Dentener et al., 1996), acid deposition, and the pH of precipitation. Mineral dust particles act as a vector for the long-range transport of various chemical components and pollutants through mixing and reacting with atmospheric gases and other particle types (Bauer and Koch, 2005). This is particularly important for the role of mineral dust particles as nutrient sources to remote ocean regions (Jickells et al., 2005).

Calcite ($CaCO_3(s)$) is generally regarded to be the most chemically reactive mineral component in aeolian dust particles (Laskin et al., 2005a; Tang et al., 2004b; Usher et al., 2003a). It can be found in the form of individual mostly-calcite particles, and also as calcite nanofibers distributed throughout mineral dust particles (Jeong and Chun, 2006). Its strong alkaline nature causes CaCO3 to react readily with acidic gases such as HNO_3, HCl, and SO_2. This converts calcium carbonate to other calcium salts such as calcium nitrate, calcium chloride, and calcium sulfate, respectively. Krueger et al. (2004; 2003) first demonstrated the conversion of insoluble calcium carbonate particles to deliquescent calcium nitrate through reaction with nitric acid vapor in laboratory experiments. This conversion has also been observed in recent field studies (Laskin et al., 2005a; Matsuki et al., 2005b; Shi et al., 2008).

Uptake and/or formation of nitrate and/or sulfate on mineral dust particles during transport has been observed in different locations (Bates et al., 2004; Fan et al., 1996; Jordan et al., 2003; Laskin et al., 2005a; Matsuki et al., 2005b; Shi et al., 2008), as well as in laboratory studies (Cwiertny et al., 2008; Usher et al., 2003a), and has been studied in several aerosol modeling efforts (Bauer et al., 2004; Dentener et al., 1996; Tang et al., 2004a; Tang et al., 2004b). Associations of sulfate and nitrate with mineral dust particles, from sorption and/or oxidation, or cloud processing, affect the local cooling effect of the aerosols and modify the ability of the mineral particles to become cloud condensation nuclei (CCN) and ice nuclei (IN), also altering the lifetime of the dust particles (DeMott et al., 2003a; Fan et al., 2004; Gibson et al., 2006a; Kelly et al., 2007; Levin et al., 1996; Rudich et al., 2002b). These associations can shift the partitioning of soluble species from smaller sized particles into larger dust particles, thus reducing the hygroscopicity and CCN capability of particles in the accumulation mode (D_a = 0.1-1.0 µm) (Arimoto et al., 2006; Tang et al., 2004a; Tang et al., 2004b).

1.6.1 Asian mineral dust storms

Major dust storm events typically develop in China in the spring, brought about by cold frontal systems and the Mongolian cyclonic depression (Sun et al., 2001). The Gobi Deserts in Mongolia and northern China, and the Taklimakan Desert in western China, are the two dominant source regions of dust in east Asia. These dust storms seriously impact the regional climate, visibility, and air quality of the surrounding regions. Once lofted to high altitudes, the dust can become entrained in the jet stream and may be transported long distances over the Pacific Ocean to North America (Cahill, 2003; Duce et al., 1980; Jaffe et al., 1999; Thulasiraman et al., 2002; VanCuren, 2003). The Asian Pacific Regional Aerosol Characterization Experiment (ACE-Asia) in 2001 was designed to study the impact these

spring dust events have on the physical, chemical and radiative properties of the Asian aerosol as it is transported over the mainland and the Pacific Ocean (Huebert et al., 2003a; Seinfeld et al., 2004). Observations of mineral dust chemistry obtained during the ACE-Asia campaign are described in Chapters 2-5.

1.6.2   Chemical reactions of mineral dust particles

Laboratory studies have demonstrated the uptake of reactive gases including O_3 (Chang et al., 2005; Hanisch and Crowley, 2003b; Sullivan et al., 2004; Usher et al., 2003b), NO_x (Grassian, 2002; Hanisch and Crowley, 2003a), NO_y (e.g. HNO_3, NO_3, N_2O_5) (Al-Hosney and Grassian, 2005; Hanisch and Crowley, 2001; Karagulian and Rossi, 2005; Krueger et al., 2004; Liu et al., 2008a; Santschi and Rossi, 2006; Seisel et al., 2005; Underwood et al., 2001b; Vlasenko et al., 2006), SO_2 (Ullerstam et al., 2003), and organics (Al-Hosney et al., 2005; Carlos-Cuellar et al., 2003) on dust particles (Usher et al., 2003a). Dust particles present a large surface area for heterogeneous reactions to occur on, and alter radiative transfer and rates of photolysis. Thus dust influences the chemical composition of the troposphere, as demonstrated by numerous field and modeling studies (Bauer et al., 2004; Bian and Zender, 2003; de Reus et al., 2000; Dentener et al., 1996; Seinfeld et al., 2004; Tang et al., 2004a). Mineral dust particles can become internally mixed with secondary species such as ammonium sulfate, ammonium nitrate, hydrochloric acid, sea salt, and biomass burning particles through coagulation, cloud processing, and heterogeneous reactions (Andreae et al., 1986b; Clarke et al., 2004; Guazzotti et al., 2001a; Korhonen et al., 2003; Mamane and Gottlieb, 1989; Mori et al., 1998; Song and Carmichael, 1999; Yin et al., 2002; Zhang and Iwasaka, 2004; Zhang et al., 2003a). These processes modify the chemical composition of the dust-laden aerosol and this can alter the radiative properties of the dust aerosol. The addition of water-soluble secondary species to a dust particle can affect its ability to act as a cloud or

ice nucleus and thus influences the indirect climate forcing of dust (Cziczo et al., 2004; DeMott et al., 2003b; Gibson et al., 2006a; Levin et al., 1996; Levin et al., 2005; Matsumoto et al., 2006; Perry et al., 2004; Rudich et al., 2002a; Yin et al., 2002). Mineral dust particles have been observed to increase cloudiness by producing more but smaller droplets, with potential reductions in precipitation (Kaufman et al., 2005; Rosenfeld et al., 2001). Photochemical processes and the uptake of secondary acids and organics can also increase the solubility and bioavailability of iron in dust particles, which is an important pathway for the fertilization of remote oceans with subsequent climate impacts (Bishop et al., 2002; Jickells et al., 2005; Meskhidze et al., 2003). Mineral dust mixed with nitrate is also an important vector for nitrogen fertilization of oceans (Baker et al., 2003; Prospero and Savoie, 1989).

Asian mineral dust particles at their original source location are primarily composed of mixtures of quartz, clays, micas, feldspars, carbonates (primarily calcite, $CaCO_3$), and other minor minerals (Gao and Anderson, 2001; Honda et al., 2004; Pye, 1987; Trochkine et al., 2003; Usher et al., 2003a; Yuan et al., 2004). The mineralogy of PM_{10} collected during severe Asian dust events in 2000 and 2002 in Beijing was determined by Shi et al. (2005) to be primarily clay minerals (>40%), followed by noncrystalline materials and quartz (both around 19%), with smaller amounts of calcite, plagioclase, K-feldspar, pyrite and other trace minerals. Jeong (2008) determined the single-particle mineralogy of individual Asian dust particles from their source to be predominantly clay aggregates (48%) that were often mixed with nanosized calcite, followed by particles of quartz (22%), plagioclase (11%), coarse calcite (6%), and K-feldspar (5%). The clay minerals in Asian dust were mostly illite and interstratified illite-smectite. Surface measurements made in Beijing by Matsuki et al. (2005a) classified 28% of the Asian dust particles as calcite. Calcite nanofibers are commonly found internally mixed with other Asian dust particles at the source (Jeong, 2008; Jeong and Chun, 2006). The high

carbonate fraction of Asian dust is significant and this alkaline mineral has been shown to react readily with acidic species such as HNO_3 to form $Ca(NO_3)_2$ and liberate $CO_2(g)$ (Hanisch and Crowley, 2001; Johnson et al., 2005; Kelly and Wexler, 2005a; Krueger et al., 2004; Laskin et al., 2005a; Liu et al., 2008a; Matsuki et al., 2005b; Song and Carmichael, 2001).

1.6.3   Climate effects of atmospheric mineral dust

Mineral dust particles, like other aerosols, can affect the planet's radiation balance and climate by directly absorbing and scattering solar radiation, and indirectly aerosol-cloud interactions. The optical properties of dust particles that determine their direct climate effects are a complex function of the particle's shape, size, and composition (Sokolik et al., 2001). Mineral dust particles are one of the few atmospheric particle types that can absorb solar radiation due to the presence of iron oxides such as hematite (α-Fe_2O_3) and goethite (α-FeO(OH)), and their clay aggregates (Lafon et al., 2006). Mineral dust particles can also absorb IR radiation, and this can cause the solar and infrared radiative forcing components of mineral dust to have opposite signs (Sokolik et al., 2001). Radiative forcing by dust particles can range from -27.9 to 11.4 W cm^{-2} (Sokolik and Toon, 1999), with uncertainties in these values due to complex chemical composition, shape, and evolution during transport. The net global direct radiative forcing due to mineral dust particles is currently estimated as -0.1 $\pm$ 0.2 W m^{-2} (IPCC, 2007).

Mineral dust particles can also play a significant but still poorly understood role in warm and cold cloud development. Mineral dust particles have been observed to be the most efficient heterogeneous ice nuclei in numerous experiments, freezing under the mildest thermodynamic conditions (Abbatt et al., 2006; Koehler et al., 2007; Mohler et al., 2005; Salam et al., 2006). Dust seed immersions can also accelerate the freezing of aqueous salt particles (Hung et al., 2003; Zuberi et al., 2002). The freezing ability of mineral dust particles

is a strong but poorly constrained result of the mineralogy and extent of atmospheric processing, such as coatings of sulfuric acid or organic compounds (Archuleta et al., 2005; Mohler et al., 2008). Numerous analyses of ice crystal residues collected in situ in cold clouds have found mineral dust particles to be the dominant tropospheric ice nucleator under heterogeneous freezing conditions (Chen et al., 1998; DeMott et al., 2003a; DeMott et al., 2003b).

Less attention has been paid to the warm cloud nucleation effects of atmospheric dust particles, until very recently. Several field and satellite measurements have implicated the role of mineral dust in contributing to cloud droplet formation and cloud properties (Kaufman et al., 2005; Levin et al., 1996; Roberts et al., 2006; Rosenfeld et al., 2001; Rudich et al., 2002b). However, very few laboratory studies have been conducted on the hygroscopicity and warm cloud nucleation ability of representative dust particles. Mineral dust is believed to act as an efficient CCN after soluble secondary material has accumulated on the dust from atmospheric processing (Gibson et al., 2007). The mineralogy of the dust particles and the potential conversion of insoluble minerals such as calcite to soluble salts such as calcium nitrate via reaction with nitric acid are other potential pathways for CCN production from mineral dust particles (Gibson et al., 2006a; Kelly et al., 2007; Laskin et al., 2005a; Shi et al., 2008). The hygroscopicity and CCN properties of mineral dust particles, and the effects of atmospheric process remain important questions requiring further investigation. Laboratory experiments investigating these questions are described in Chapters 6 & 7.

1.6.4 Major outstanding questions regarding atmospheric mineral dust particles

The atmospheric chemistry of mineral dust particles has received increased attention in the last decade as the important but largely unknown roles that dust particles play in

atmospheric trace gas chemistry, radiative transfer, biogeochemical cycles, and cloud formation have become more apparent (Bauer and Koch, 2005; Bian and Zender, 2003; Dentener et al., 1996; IPCC, 2007; Jickells et al., 2005). A particularly important development has been the growing recognition that mineral dust cannot be treated as one uniform chemical composition with one single chemical reaction rate and other physicochemical properties (Gibson et al., 2006a; Kelly et al., 2007; Krueger et al., 2004). The wide variety of mineralogical compositions that compose atmospheric dust particles and dictate their atmospheric processing and resulting physicochemical properties must be accounted for in atmospheric chemistry models. Some particularly pressing questions related to atmospheric mineral dust are:

1. Which factors control the production and size distribution of suspended atmospheric dust aerosol?

2. How does the size-resolved chemical composition and related physicochemical properties of mineral dust particles vary between dust/desert sources?

3. What are the mechanisms and timescales of atmospheric processing that mineral dust particles experience? What fractions of mineral dust particles contain significant amounts of secondary material and what is the variability in this?

4. What are the kinetic rates of reaction of various mineral dust particles with important trace gases under atmospheric conditions? How does the dust's mineralogy affect the kinetics and mechanisms of these reactions?

5. How does this chemical processing affect the important properties of dust including warm and cold cloud nucleation abilities, atmospheric lifetimes, optical properties, and the solubility of important trace metals such as iron?

6. How frequently are mineral dust particles internally mixed with carbonaceous components (elemental and organic carbon), which mechanisms cause this, and how does the amount of organic material associated with dust change the climate relevant properties of dust?

7. What are the direct and indirect climate effects of mineral dust particles on the regional and global scales?

The majority of the research described here focuses on the atmospheric chemistry of mineral dust particles and addresses many of the outstanding questions outlined above. Chapter 2 describes the chemical composition of individual aerosol particles sampled during the ACE-Asia campaign at sea level while traveling from Hawaii into the Sea of Japan. A major Asian dust storm was encountered towards the end of the research cruise. Chapter 3 investigates the atmospheric processing observed in the dust particles measured during ACE-Asia, while Chapter 4 focuses on the unique observation of secondary chlorine in the aged Asian dust particles during the campaign. Chapter 5 describes the presence and formation of secondary dicarboxylic acids in the Asian dust and other particle types measured during ACE-Asia. Chapter 6 investigates the warm cloud nucleation potential of mineral dust particles as a function of the dust's mineralogy through laboratory experiments. Chapter 7 describes the results of aerosol flow tube experiments that explore the timescale of the conversion of calcium carbonate particles to calcium nitrate by reaction with nitric acid vapor, and the resulting changes in the particles' hygroscopicity.

1.7 References

Abbatt, J. P. D.: Interactions of atmospheric trace gases with ice surfaces: Adsorption and reaction, Chemical Reviews, 103 (12), 4783-4800, 2003.

Abbatt, J. P. D., Benz, S., Cziczo, D. J., Kanji, Z., Lohmann, U., and Mohler, O.: Solid ammonium sulfate aerosols as ice nuclei: A pathway for cirrus cloud formation, Science, 313 (5794), 1770-1773, 2006.

Adams, P. J., and Seinfeld, J. H.: Disproportionate impact of particulate emissions on global cloud condensation nuclei concentrations, Geophys. Res. Lett., 30 (5), 2003.

Al-Hosney, H. A., Carlos-Cuellar, S., Baltrusaitis, J., and Grassian, V. H.: Heterogeneous uptake and reactivity of formic acid on calcium carbonate particles: a Knudsen cell reactor, FTIR and SEM study, Physical Chemistry Chemical Physics, 7 (20), 3587-3595, 2005.

Al-Hosney, H. A., and Grassian, V. H.: Water, sulfur dioxide and nitric acid adsorption on calcium carbonate: A transmission and ATR-FTIR study, Physical Chemistry Chemical Physics, 7 (6), 1266-1276, 2005.

Albrecht, B. A.: Aerosols, Cloud Microphysics, and Fractional Cloudiness, Science, 245 (4923), 1227-1230, 1989.

Andreae, M. O., Charlson, R. J., Bruynseels, F., Storms, H., Van Grieken, R., and Maenhaut, W.: Internal mixture of sea salt, silicates, and excess sulfate in marine aerosols, Science, 232 (4758), 1620-1623, 1986a.

Andreae, M. O., Charlson, R. J., Bruynseels, F., Storms, H., Vangrieken, R., and Maenhaut, W.: Internal mixture of sea salt, silicates, and excess sulfate in marine aerosols, Science, 232 (4758), 1620-1623, 1986b.

Andreae, M. O., and Gelencser, A.: Black carbon or brown carbon? The nature of light-absorbing carbonaceous aerosols, Atmos. Chem. Phys., 6, 3131-3148, 2006.

Andreae, M. O., and Rosenfeld, D.: Aerosol–cloud–precipitation interactions. Part 1. The nature and sources of cloud-active aerosols Earth Science Reviews, 89 (1-2), 13-41, 2008.

Angelino, S., Suess, D. T., and Prather, K. A.: Formation of aerosol particles from reactions of secondary and tertiary alkylamines: Characterization by aerosol time-of-flight mass spectrometry, Environ. Sci. Technol., 35 (15), 3130-3138, 2001.

Archuleta, C. M., DeMott, P. J., and Kreidenweis, S. M.: Ice nucleation by surrogates for atmospheric mineral dust and mineral dust/sulfate particles at cirrus temperatures, Atmos. Chem. Phys., 5, 2617-2634, 2005.

Arimoto, R., Kim, Y. J., Kim, Y. P., Quinn, P. K., Bates, T. S., Anderson, T. L., Gong, S., Uno, I., Chin, M., Huebert, B. J., Clarke, A. D., Shinozuka, Y., Weber, R. J., Anderson, J. R., Guazzotti, S. A., Sullivan, R. C., Sodeman, D. A., Prather, K. A., and Sokolik, I. N.: Characterization of Asian Dust during ACE-Asia, Global And Planetary Change, 52 (1-4), 23-56, 2006.

Baker, A. R., Kelly, S. D., Biswas, K. F., Witt, M., and Jickells, T. D.: Atmospheric deposition of nutrients to the Atlantic Ocean, Geophys. Res. Lett., 30 (24), doi:10.1029/2003GL018518, 2003.

Baker, M. B.: Cloud microphysics and climate, Science, 276 (5315), 1072-1078, 1997.

Bassett, M. E., and Seinfeld, J. H.: Atmospheric Equilibrium-Model Of Sulfate And Nitrate Aerosols .2. Particle-Size Analysis, Atmos. Environ., 18 (6), 1163-1170, 1984.

Bates, T. S., Quinn, P. K., Coffman, D. J., Covert, D. S., Miller, T. L., Johnson, J. E., Carmichael, G. R., Uno, I., Guazzotti, S. A., Sodeman, D. A., Prather, K. A., Rivera, M., Russell, L. M., and Merrill, J. T.: Marine boundary layer dust and pollutant transport associated with the passage of a frontal system over eastern Asia, J. Geophys. Res., 109 (D19), doi:10.1029/2003JD004094, 2004.

Bauer, S. E., Balkanski, Y., Schulz, M., Hauglustaine, D. A., and Dentener, F.: Global modeling of heterogeneous chemistry on mineral aerosol surfaces: Influence on tropospheric ozone chemistry and comparison to observations, J. Geophys. Res., 109 (D2), doi:10.1029/2003JD003868, 2004.

Bauer, S. E., and Koch, D.: Impact of heterogeneous sulfate formation at mineral dust surfaces on aerosol loads and radiative forcing in the Goddard Institute for Space Studies general circulation model, J. Geophys. Res., 110 (D17), doi:10.1029/2005JD005870, 2005.

Bhave, P. V., Allen, J. O., Morrical, B. D., Fergenson, D. P., Cass, G. R., and Prather, K. A.: A field-based approach for determining ATOFMS instrument sensitivities to ammonium and nitrate, Environmental Science & Technology, 36 (22), 4868-4879, 2002a.

Bhave, P. V., Kleeman, M. J., Allen, J. O., Hughes, L. S., Prather, K. A., and Cass, G. R.: Evaluation of an Air Quality Model for the Size and Composition of Source-Oriented Particle Classes, Environmental Science & Technology, 36 (10), 2154-2163, 2002b.

Bian, H. S., and Zender, C. S.: Mineral dust and global tropospheric chemistry: Relative roles of photolysis and heterogeneous uptake, J. Geophys. Res., 108 (D21), doi:10.1029/2002JD003143, 2003.

Bilde, M., and Svenningsson, B.: CCN activation of slightly soluble organics: the importance of small amounts of inorganic salt and particle phase, Tellus Series B-Chemical And Physical Meteorology, 56 (2), 128-134, 2004.

Bishop, J. K. B., Davis, R. E., and Sherman, J. T.: Robotic observations of dust storm enhancement of carbon biomass in the North Pacific, Science, 298 (5594), 817-821, 2002.

Biswas, S., Fine, P. M., Geller, M. D., Hering, S. V., and Sioutas, C.: Performance evaluation of a recently developed water-based condensation particle counter, Aerosol Sci. Technol., 39 (5), 419-427, 2005.

Bluhm, H., Andersson, K., Araki, T., Benzerara, K., Brown, G. E., Dynes, J. J., Ghosal, S., Gilles, M. K., Hansen, H. C., Hemminger, J. C., Hitchcock, A. P., Ketteler, G., Kilcoyne, A. L. D., Kneedler, E., Lawrence, J. R., Leppard, G. G., Majzlam, J., Mun, B. S., Myneni, S. C. B., Nilsson, A., Ogasawara, H., Ogletree, D. F., Pecher, K., Salmeron, M., Shuh, D. K., Tonner, B., Tyliszczak, T., Warwick, T., and Yoon, T. H.:

Soft X-ray microscopy and spectroscopy at the molecular environmental science beamline at the Advanced Light Source, J. Electron Spectrosc. Relat. Phenom., 150 (2-3), 86-104, 2006.

Bond, T. C., and Bergstrom, R. W.: Light absorption by carbonaceous particles: An investigative review, Aerosol Sci. Technol., 40 (1), 1-41, 2006.

Cahill, C. F.: Asian aerosol transport to Alaska during ACE-Asia, J. Geophys. Res., 108 (D23), doi:10.1029/2002JD003271, 2003.

Cakmur, R. V., Miller, R. L., Perlwitz, J., Geogdzhayev, I. V., Ginoux, P., Koch, D., Kohfeld, K. E., Tegen, I., and Zender, C. S.: Constraining the magnitude of the global dust cycle by minimizing the difference between a model and observations, J. Geophys. Res., 111 (D6), 2006.

Canagaratna, M. R., Jayne, J. T., Jimenez, J. L., Allan, J. D., Alfarra, M. R., Zhang, Q., Onasch, T. B., Drewnick, F., Coe, H., Middlebrook, A., Delia, A., Williams, L. R., Trimborn, A. M., Northway, M. J., DeCarlo, P. F., Kolb, C. E., Davidovits, P., and Worsnop, D. R.: Chemical and microphysical characterization of ambient aerosols with the aerodyne aerosol mass spectrometer, Mass Spectrometry Reviews, 26 (2), 185-222, 2007.

Cantrell, W., and Heymsfield, A.: Production of ice in tropospheric clouds - A review, Bulletin of the American Meteorological Society, 86 (6), 795-807, 2005.

Carlos-Cuellar, S., Li, P., Christensen, A. P., Krueger, B. J., Burrichter, C., and Grassian, V. H.: Heterogeneous uptake kinetics of volatile organic compounds on oxide surfaces using a Knudsen cell reactor: Adsorption of acetic acid, formaldehyde, and methanol on alpha-Fe_2O_3, alpha-Al_2O_3, and SiO_2, Journal Of Physical Chemistry A, 107 (21), 4250-4261, 2003.

Chang, R. Y. W., Sullivan, R. C., and Abbatt, J. P. D.: Initial uptake of ozone on Saharan dust at atmospheric relative humidities, Geophys. Res. Lett., 32 (14), doi:10.1029/2005GL023317, 2005.

Chen, Y. L., Kreidenweis, S. M., McInnes, L. M., Rogers, D. C., and DeMott, P. J.: Single particle analyses of ice nucleating aerosols in the upper troposphere and lower stratosphere, Geophys. Res. Lett., 25 (9), 1391-1394, 1998.

Christner, B. C., Morris, C. E., Foreman, C. M., Cai, R. M., and Sands, D. C.: Ubiquity of biological ice nucleators in snowfall, Science, 319 (5867), 1214-1214, 2008.

Clarke, A. D., Shinozuka, Y., Kapustin, V. N., Howell, S., Huebert, B., Doherty, S., Anderson, T., Covert, D., Anderson, J., Hua, X., Moore, K. G., McNaughton, C., Carmichael, G., and Weber, R.: Size distributions and mixtures of dust and black carbon aerosol in Asian outflow: Physiochemistry and optical properties, J. Geophys. Res., 109 (D15), doi:10.1029/2003JD004378, 2004.

Collins, D. R., Cocker, D. R., Flagan, R. C., and Seinfeld, J. H.: The scanning DMA transfer function, Aerosol Sci. Technol., 38 (8), 833-850, 2004.

Covert, D., Wiedensohler, A., and Russell, L.: Particle charging and transmission efficiencies of aerosol charge neutralizers, Aerosol Sci. Technol., 27 (2), 206-214, 1997.

Cwiertny, D. M., Young, M. A., and Grassian, V. H.: Chemistry and photochemistry of mineral dust aerosol, Annual Review of Physical Chemistry, 59, 27-51, 2008.

Cziczo, D. J., Murphy, D. M., Hudson, P. K., and Thomson, D. S.: Single particle measurements of the chemical composition of cirrus ice residue during CRYSTAL-FACE, J. Geophys. Res., 109 (D4), D04201, doi:10.1029/2003JD004032, 2004.

de Reus, M., Dentener, F., Thomas, A., Borrmann, S., Strom, J., and Lelieveld, J.: Airborne observations of dust aerosol over the North Atlantic Ocean during ACE 2: Indications for heterogeneous ozone destruction, Journal of Geophysical Research-Atmospheres, 105 (D12), 15263-15275, 2000.

DeCarlo, P. F., Slowik, J. G., Worsnop, D. R., Davidovits, P., and Jimenez, J. L.: Particle Morphology and Density Characterization by Combined Mobility and Aerodynamic Diameter Measurements. Part 1: Theory, Aerosol Science And Technology, 38, 1185-1205, 2005.

DeMott, P. J., Cziczo, D. J., Prenni, A. J., Murphy, D. M., Kreidenweis, S. M., Thomson, D. S., Borys, R., and Rogers, D. C.: Measurements of the concentration and composition of nuclei for cirrus formation, Proc. Natl. Acad. Sci. USA, 100 (25), 14655-14660, 2003a.

DeMott, P. J., Sassen, K., Poellot, M. R., Baumgardner, D., Rogers, D. C., Brooks, S. D., Prenni, A. J., and Kreidenweis, S. M.: African dust aerosols as atmospheric ice nuclei, Geophys. Res. Lett., 30 (14), doi:10.1029/2003GL017410, 2003b.

Dentener, F. J., Carmichael, G. R., Zhang, Y., Lelieveld, J., and Crutzen, P. J.: Role of mineral aerosol as a reactive surface in the global troposphere, J. Geophys. Res., 101 (D17), 22869-22889, 1996.

Dentener, F. J., and Crutzen, P. J.: Reaction Of N2O5 On Tropospheric Aerosols - Impact On The Global Distributions Of Nox, O3, And OH, J. Geophys. Res., 98 (D4), 7149-7163, 1993.

Duce, R. A., Sources, distributions, and fluxes of mineral aerosols and their relationship to climate, in *Aerosol forcing of climate*, edited by Charlson, R.J., and Heintzenberg, J., John Wiley & Sons Ltd., Chichester, England, 1995.

Duce, R. A., Unni, C. K., Ray, B. J., Prospero, J. M., and Merrill, J. T.: Long-range atmospheric transport of soil dust from Asia to the tropical North Pacific - temporal variability, Science, 209 (4464), 1522-1524, 1980.

Dusek, U., Frank, G. P., Hildebrandt, L., Curtius, J., Schneider, J., Walter, S., Chand, D., Drewnick, F., Hings, S., Jung, D., Borrmann, S., and Andreae, M. O.: Size matters more than chemistry for cloud-nucleating ability of aerosol particles, Science, 312 (5778), 1375-1378, 2006.

Ervens, B., Feingold, G., Frost, G. J., and Kreidenweis, S. M.: A modeling study of aqueous production of dicarboxylic acids: 1. Chemical pathways and speciated organic mass production, J. Geophys. Res., 109 (D15), 2004.

Facchini, M. C., Mircea, M., Fuzzi, S., and Charlson, R. J.: Cloud albedo enhancement by surface-active organic solutes in growing droplets, Nature, 401 (6750), 257-259, 1999.

Falkovich, A. H., Schkolnik, G., Ganor, E., and Rudich, Y.: Adsorption of organic compounds pertinent to urban environments onto mineral dust particles, J. Geophys. Res., 109 (D2), doi:10.1029/2003JD003919, 2004.

Fan, S. M., Horowitz, L. W., Levy, H., and Moxim, W. J.: Impact of air pollution on wet deposition of mineral dust aerosols, Geophys. Res. Lett., 31 (2), doi:10.1029/2003GL018501, 2004.

Fan, X. B., Okada, K., Niimura, N., Kai, K., Arao, K., Shi, G. Y., Qin, Y., and Mitsuta, Y.: Mineral particles collected in China and Japan during the same Asian dust-storm event, Atmos. Environ., 30 (2), 347-351, 1996.

Fergenson, D. P., Song, X. H., Ramadan, Z., Allen, J. O., Hughes, L. S., Cass, G. R., Hopke, P. K., and Prather, K. A.: Quantification of ATOFMS data by multivariate methods, Analytical Chemistry, 73 (15), 3535-3541, 2001.

Finlayson-Pitts, B. J.: The tropospheric chemistry of sea salt: A molecular-level view of the chemistry of NaCl and NaBr, Chemical Reviews, 103 (12), 4801-4822, 2003.

Finlayson-Pitts, B. J., and Pitts, J. N., Chemistry of the upper and lower atmopshere: Theory, experiments, and applications, Academic Press, San Diego, 2000.

Flagan, R. C., Electrical Techniques, in *Aerosol Measurement, 2nd Edition*, edited by Baron, P.A., and Klaus, W., Wiley-InterScience, Inc., Hoboken, New Jersey, 2001.

Furutani, H., Dall'osto, M., Roberts, G. C., and Prather, K. A.: Assessment of the relative importance of atmospheric aging on CCN activity derived from field observations, Atmos. Environ., 42 (13), 3130-3142, 2008.

Fuzzi, S., Andreae, M. O., Huebert, B. J., Kulmala, M., Bond, T. C., Boy, M., Doherty, S. J., Guenther, A., Kanakidou, M., Kawamura, K., Kerminen, V. M., Lohmann, U., Russell, L. M., and Poschl, U.: Critical assessment of the current state of scientific knowledge, terminology, and research needs concerning the role of organic aerosols in the atmosphere, climate, and global change, Atmos. Chem. Phys., 6, 2017-2038, 2006.

Gao, Y., and Anderson, J. R.: Characteristics of Chinese aerosols determined by individual-particle analysis, Journal Of Geophysical Research-Atmospheres, 106 (D16), 18037-18045, 2001.

Gard, E., Mayer, J. E., Morrical, B. D., Dienes, T., Fergenson, D. P., and Prather, K. A.: Real-time analysis of individual atmospheric aerosol particles: Design and performance of a portable ATOFMS, Anal. Chem., 69 (20), 4083-4091, 1997.

Gelencser, A., and Varga, Z.: Evaluation of the atmospheric significance of multiphase reactions in atmospheric secondary organic aerosol formation, Atmos. Chem. Phys., 5, 2823-2831, 2005.

Gibson, E. R., Gierlus, K. M., Hudson, P. K., and Grassian, V. H.: Generation of internally mixed insoluble and soluble aerosol particles to investigate the impact of atmospheric aging and heterogeneous processing on the CCN activity of mineral dust aerosol, Aerosol Sci. Technol., 41 (10), 914-924, 2007.

Gibson, E. R., Hudson, P. K., and Grassian, V. H.: Aerosol chemistry and climate: Laboratory studies of the carbonate component of mineral dust and its reaction products, Geophys. Res. Lett., 33 (13), doi:10.1029/2006GL026386, 2006.

Gomes, L., Bergametti, G., Coudegaussen, G., and Rognon, P.: Submicron desert dusts - a sandblasting process, J. Geophys. Res., 95 (D9), 13927-13935, 1990.

Graber, E. R., and Rudich, Y.: Atmospheric HULIS: How humic-like are they? A comprehensive and critical review, Atmos. Chem. Phys., 6, 729-753, 2006.

Grassian, V. H.: Chemical reactions of nitrogen oxides on the surface of oxide, carbonate, soot, and mineral dust particles: Implications for the chemical balance of the troposphere, Journal of Physical Chemistry A, 106 (6), 860-877, 2002.

Gross, D. S., Barron, A. R., Sukovich, E. M., Warren, B. S., Jarvis, J. C., Suess, D. T., and Prather, K. A.: Stability of single particle tracers for differentiating between heavy- and light-duty vehicle emissions, Atmos. Environ., 39 (16), 2889-2901, 2005.

Gross, D. S., Galli, M. E., Silva, P. J., and Prather, K. A.: Relative sensitivity factors for alkali metal and ammonium cations in single particle aerosol time-of-flight mass spectra, Analytical Chemistry, 72 (2), 416-422, 2000.

Guazzotti, S. A., Coffee, K. R., and Prather, K. A.: Continuous measurements of size-resolved particle chemistry during INDOEX-Intensive Field Phase 99, J. Geophys. Res., 106 (D22), 28607-28627, 2001.

Hanisch, F., and Crowley, J. N.: Heterogeneous reactivity of gaseous nitric acid on Al_2O_3, $CaCO_3$, and atmospheric dust samples: A Knudsen cell study, Journal of Physical Chemistry A, 105 (13), 3096-3106, 2001.

Hanisch, F., and Crowley, J. N.: Heterogeneous reactivity of NO and HNO_3 on mineral dust in the presence of ozone, Physical Chemistry Chemical Physics, 5 (5), 883-887, 2003a.

Hanisch, F., and Crowley, J. N.: Ozone decomposition on Saharan dust: an experimental investigation, Atmospheric Chemistry and Physics, 3, 119-130, 2003b.

Heald, C. L., Jacob, D. J., Turquety, S., Hudman, R. C., Weber, R. J., Sullivan, A. P., Peltier, R. E., Atlas, E. L., de Gouw, J. A., Warneke, C., Holloway, J. S., Neuman, J. A., Flocke, F. M., and Seinfeld, J. H.: Concentrations and sources of organic carbon aerosols in the free troposphere over North America, J. Geophys. Res., 111 (D23), doi:10.1029/2006JD007705, 2006.

Hearn, J. D., and Smith, G. A.: Ozonolysis of mixed oleic acid/n-docosane particles: The roles of phase, morphology, and metastable states, J. Phys. Chem. A, 111 (43), 11059-11065, 2007.

Honda, M., Yabuki, S., and Shimizu, H.: Geochemical and isotopic studies of aeolian sediments in China, Sedimentology, 51 (2), 211-230, 2004.

Houghton, J. T., Ding, Y., Griggs, D. J., Noguer, M., van der Linden, P. J., Dai, X., Maskell, K., and Jonhnson, C. A., Climate Change 2001: The Scientific Basis, Cambridge University Press, Cambridge, 2001.

Hudson, J. G.: Variability of the relationship between particle size and cloud-nucleating ability, Geophys. Res. Lett., 34 (8), doi:10.1029/2006GL028850, 2007.

Huebert, B. J., Bates, T., Russell, P. B., Shi, G. Y., Kim, Y. J., Kawamura, K., Carmichael, G., and Nakajima, T.: An overview of ACE-Asia: Strategies for quantifying the relationships between Asian aerosols and their climatic impacts, Journal Of Geophysical Research-Atmospheres, 108 (D23), doi:10.1029/2003JD003550, 2003.

Hung, H. M., Malinowski, A., and Martin, S. T.: Kinetics of heterogeneous ice nucleation on the surfaces of mineral dust cores inserted into aqueous ammonium sulfate particles, J. Phys. Chem. A, 107 (9), 1296-1306, 2003.

Hunt, A. L., and Petrucci, G. A.: Analysis of ultrafine and organic particles by aerosol mass spectrometry, Trac-Trends In Analytical Chemistry, 21 (2), 74-81, 2002.

IPCC, Climate Change 2007: The Physical Science Basis. Contribution of Working Group I to the Fourth Assessment Report of the Intergovernmental Panel on Climate Change, Cambridge University Press, Cambridge, 2007.

Jacob, D. J., Introduction to Atmospheric Chemistry, Princeton University Press, Princeton, NJ, 1999.

Jacobson, M. C., Hansson, H. C., Noone, K. J., and Charlson, R. J.: Organic atmospheric aerosols: Review and state of the science, Reviews Of Geophysics, 38 (2), 267-294, 2000.

Jaffe, D., Anderson, T., Covert, D., Kotchenruther, R., Trost, B., Danielson, J., Simpson, W., Berntsen, T., Karlsdottir, S., Blake, D., Harris, J., Carmichael, G., and Uno, I.: Transport of Asian air pollution to North America, Geophysical Research Letters, 26 (6), 711-714, 1999.

Jeong, G. Y.: Bulk and single-particle mineralogy of Asian dust and a comparison with its source soils, J. Geophys. Res., 113 (D2), doi:10.1029/2007JD008606, 2008.

Jeong, G. Y., and Chun, Y.: Nanofiber calcite in Asian dust and its atmospheric roles, Geophys. Res. Lett., 33 (L24802), doi:10.1029/2006GL028280, 2006.

Ji, J. H., Bae, G. N., and Hwang, J.: Characteristics of aerosol charge neutralizers for highly charged particles, Journal of Aerosol Science, 35 (11), 1347-1358, 2004.

Jickells, T. D., An, Z. S., Andersen, K. K., Baker, A. R., Bergametti, G., Brooks, N., Cao, J. J., Boyd, P. W., Duce, R. A., Hunter, K. A., Kawahata, H., Kubilay, N., laRoche, J., Liss, P. S., Mahowald, N., Prospero, J. M., Ridgwell, A. J., Tegen, I., and Torres, R.: Global iron connections between desert dust, ocean biogeochemistry, and climate, Science, 308 (5718), 67-71, 2005.

Johnson, E. R., Sciegienka, J., Carlos-Cuellar, S., and Grassian, V. H.: Heterogeneous uptake of gaseous nitric acid on dolomite ($CaMg(CO_3)_2$) and calcite ($CaCO_3$) particles: A knudsen cell study using multiple, single, and fractional particle layers, Journal Of Physical Chemistry A, 109 (31), 6901-6911, 2005.

Jordan, C. E., Dibb, J. E., Anderson, B. E., and Fuelberg, H. E.: Uptake of nitrate and sulfate on dust aerosols during TRACE-P, J. Geophys. Res., 108 (D21), doi:10.1029/2002JD003101, 2003.

Kanakidou, M., Seinfeld, J. H., Pandis, S. N., Barnes, I., Dentener, F. J., Facchini, M. C., Van Dingenen, R., Ervens, B., Nenes, A., Nielsen, C. J., Swietlicki, E., Putaud, J. P., Balkanski, Y., Fuzzi, S., Horth, J., Moortgat, G. K., Winterhalter, R., Myhre, C. E. L., Tsigaridis, K., Vignati, E., Stephanou, E. G., and Wilson, J.: Organic aerosol and global climate modelling: a review, Atmos. Chem. Phys., 5, 1053-1123, 2005.

Karagulian, F., Dilbeck, C. W., and Finlayson-Pitts, B. J.: Unusual oxidation of organics at interfaces from the bottom up and atmospheric implications, J Am Chem Soc, 130 (34), 11272-+, 2008.

Karagulian, F., and Rossi, M. J.: The heterogeneous chemical kinetics of NO_3 on atmospheric mineral dust surrogates, Phys. Chem. Chem. Phys., 7 (17), 3150-3162, 2005.

Kaufman, Y. J., Koren, I., Remer, L. A., Rosenfeld, D., and Rudich, Y.: The effect of smoke, dust, and pollution aerosol on shallow cloud development over the Atlantic Ocean, Proc. Natl. Acad. Sci. USA, 102 (32), 11207-11212, 2005.

Kawamura, K., and Kaplan, I. R.: Motor Exhaust Emissions As A Primary Source For Dicarboxylic-Acids In Los-Angeles Ambient Air, Environmental Science & Technology, 21 (1), 105-110, 1987.

Kelly, J. T., Chuang, C. C., and Wexler, A. S.: Influence of dust composition on cloud droplet formation, Atmos. Environ., 41 (14), 2904-2916, 2007.

Kelly, J. T., and Wexler, A. S.: Thermodynamics of carbonates and hydrates related to heterogeneous reactions involving mineral aerosol, Journal Of Geophysical Research-Atmospheres, 110 (D11), doi:10.1029/2004JD005583, 2005.

Kerminen, V. M., and Wexler, A. S.: Growth Laws for Atmospheric Aerosol-Particles - an Examination of the Bimodality of the Accumulation-Mode, Atmos. Environ., 29 (22), 3263-3275, 1995.

Khlystov, A., Stanier, C., and Pandis, S. N.: An algorithm for combining electrical mobility and aerodynamic size distributions data when measuring ambient aerosol, Aerosol Sci. Technol., 38, 229-238, 2004.

Knopf, D. A., Anthony, L. M., and Bertram, A. K.: Reactive uptake of O-3 by multicomponent and multiphase mixtures containing oleic acid, J. Phys. Chem. A, 109 (25), 5579-5589, 2005.

Knutson, E. O., and Whitby, K. T.: Aerosol classification by electric mobility: Apparatus, theory, and applications, Journal Of Aerosol Science, 6, 443-451, 1975.

Koehler, K. A., Kreidenweis, S. M., DeMott, P. J., Prenni, A. J., and Petters, M. D.: Potential impact of Owens (dry) Lake dust on warm and cold cloud formation, J. Geophys. Res., 112 (D12), D12210, doi:10.1029/2007JD008413, 2007.

Kohler, H.: The nucleus in and the growth of hygroscopic droplets, Trans. Faraday Soc., 32 (2), 1152-1161, 1936.

Kolb, C. E., Davidovits, P., Jayne, J. T., Shi, Q., and Worsnop, D. R.: Kinetics of trace gas uptake by liquid surfaces, Progress In Reaction Kinetics And Mechanism, 27 (1), 1-46, 2002.

Koop, T., Luo, B. P., Tsias, A., and Peter, T.: Water activity as the determinant for homogeneous ice nucleation in aqueous solutions, Nature, 406 (6796), 611-614, 2000.

Korhonen, H., Napari, I., Timmreck, C., Vehkamaki, H., Pirjola, L., Lehtinen, K. E. J., Lauri, A., and Kulmala, M.: Heterogeneous nucleation as a potential sulphate-coating mechanism of atmospheric mineral dust particles and implications of coated dust on new particle formation, J. Geophys. Res., 108 (D17), doi:10.1029/2003JD003553, 2003.

Krueger, B. J., Grassian, V. H., Cowin, J. P., and Laskin, A.: Heterogeneous chemistry of individual mineral dust particles from different dust source regions: the importance of particle mineralogy, Atmospheric Environment, 38 (36), 6253-6261, 2004.

Krueger, B. J., Grassian, V. H., Laskin, A., and Cowin, J. P.: The transformation of solid atmospheric particles into liquid droplets through heterogeneous chemistry: Laboratory insights into the processing of calcium containing mineral dust aerosol in the troposphere, Geophys. Res. Lett., 30 (3), doi:10.1029/2002GL016563, 2003.

Kulmala, M., Vehkamaki, H., Petajda, T., Dal Maso, M., Lauri, A., Kerminen, V. M., Birmili, W., and McMurry, P. H.: Formation and growth rates of ultrafine atmospheric particles: a review of observations, Journal Of Aerosol Science, 35 (2), 143-176, 2004.

Kurten, T., Loukonen, V., Vehkamaki, H., and Kulmala, M.: Amines are likely to enhance neutral and ion-induced sulfuric acid-water nucleation in the atmosphere more effectively than ammonia, Atmos. Chem. Phys., 8 (14), 4095-4103, 2008.

Lafon, S., Sokolik, I. N., Rajot, J. L., Caquineau, S., and Gaudichet, A.: Characterization of iron oxides in mineral dust aerosols: Implications for light absorption, J. Geophys. Res., 111 (D21), 2006.

Laskin, A., Iedema, M. J., Ichkovich, A., Graber, E. R., Taraniuk, I., and Rudich, Y.: Direct observation of completely processed calcium carbonate dust particles, Faraday Discussions, 130, 453-468, 2005.

Levin, Z., Ganor, E., and Gladstein, V.: The effects of desert particles coated with sulfate on rain formation in the eastern Mediterranean, Journal Of Applied Meteorology, 35 (9), 1511-1523, 1996.

Levin, Z., Teller, A., Ganor, E., and Yin, Y.: On the interactions of mineral dust, sea-salt particles, and clouds: A measurement and modeling study from the Mediterranean Israeli Dust Experiment campaign, J. Geophys. Res., 110 (D20), doi:10.1029/2005JD005810, 2005.

Li, Y. Q., Davidovits, P., Shi, Q., Jayne, J. T., Kolb, C. E., and Worsnop, D. R.: Mass and thermal accommodation coefficients of H2O(g) on liquid water as a function of temperature, J. Phys. Chem. A, 105 (47), 10627-10634, 2001.

Liu, D. Y., Wenzel, R. J., and Prather, K. A.: Aerosol time-of-flight mass spectrometry during the Atlanta Supersite Experiment: 1. Measurements, Journal Of Geophysical Research-Atmospheres, 108 (D7), 2003.

Liu, P., Ziemann, P. J., Kittelson, D. B., and McMurry, P. H.: Generating Particle Beams of Controlled Dimensions and Divergence .1. Theory of Particle Motion in Aerodynamic Lenses and Nozzle Expansions, Aerosol Sci. Technol., 22 (3), 293-313, 1995.

Liu, Y., Gibson, E. R., Cain, J. P., Wang, H., Grassian, V. H., and Laskin, A.: Kinetics of heterogeneous reaction of CaCO3 particles with gaseous HNO3 over a wide range of humidity, J. Phys. Chem. A, 112 (7), 1561-1571, 2008.

Lohmann, U., and Feichter, J.: Global indirect aerosol effects: a review, Atmos. Chem. Phys., 5, 715-737, 2005.

Mamane, Y., and Gottlieb, J.: Heterogeneous reactions of minerals with sulfur and nitrogen-oxides, Journal Of Aerosol Science, 20 (3), 303-311, 1989.

Maria, S. F., Russell, L. M., Gilles, M. K., and Myneni, S. C. B.: Organic aerosol growth mechanisms and their climate-forcing implications, Science, 306 (5703), 1921-1924, 2004.

Martin, R. V., Jacob, D. J., Yantosca, R. M., Chin, M., and Ginoux, P.: Global and regional decreases in tropospheric oxidants from photochemical effects of aerosols, Journal Of Geophysical Research-Atmospheres, 108 (D3), 2003.

Martin, S. T.: Phase transitions of aqueous atmospheric particles, Chem. Rev., 100 (9), 3403-3453, 2000.

Matsuki, A., Iwasaka, Y., Shi, G. Y., Chen, H. B., Osada, K., Zhang, D., Kido, M., Inomata, Y., Kim, Y. S., Trochkine, D., Nishita, C., Yamada, M., Nagatani, T., Nagatani, M., and Nakata, H.: Heterogeneous sulfate formation on dust surface and its dependence on mineralogy: Balloon-borne observations from ballon-borne measurements in the surface of Beijing, China, Water, Air, and Soil Pollution: Focus, 5, 101-132, 2005a.

Matsuki, A., Iwasaka, Y., Shi, G. Y., Zhang, D. Z., Trochkine, D., Yamada, M., Kim, Y. S., Chen, B., Nagatani, T., Miyazawa, T., Nagatani, M., and Nakata, H.: Morphological and chemical modification of mineral dust: Observational insight into the heterogeneous uptake of acidic gases, Geophysical Research Letters, 32 (22), 2005b.

Matsumoto, J., Takahashi, K., Matsumi, Y., Yabushita, A., Shimizu, A., Matsui, I., and Sugimoto, N.: Scavenging of pollutant acid substances by Asian mineral dust particles, Geophys. Res. Lett., 33 (7), doi:10.1029/2006GL025782, 2006.

McFiggans, G., Artaxo, P., Baltensperger, U., Coe, H., Facchini, M. C., Feingold, G., Fuzzi, S., Gysel, M., Laaksonen, A., Lohmann, U., Mentel, T. F., Murphy, D. M., O'Dowd, C. D., Snider, J. R., and Weingartner, E.: The effect of physical and chemical aerosol properties on warm cloud droplet activation, Atmos. Chem. Phys., 6, 2593-2649, 2006.

McMurry, P. H.: A review of atmospheric aerosol measurements, Atmos. Environ., 34 (12-14), 1959-1999, 2000.

McMurry, P. H., Fink, M., Sakurai, H., Stolzenburg, M. R., Mauldin, R. L., Smith, J., Eisele, F., Moore, K., Sjostedt, S., Tanner, D., Huey, L. G., Nowak, J. B., Edgerton, E., and Voisin, D.: A criterion for new particle formation in the sulfur-rich Atlanta atmosphere, J. Geophys. Res., 110 (D22), 2005.

Meng, Z. Y., and Seinfeld, J. H.: On the Source of the Submicrometer Droplet Mode of Urban and Regional Aerosols, Aerosol Sci. Technol., 20 (3), 253-265, 1994.

Mertes, S., Schroder, F., and Wiedensohler, A.: The Particle-Detection Efficiency Curve of the TSI-3010 CPC as a Function of the Temperature Difference between Saturator and Condenser, Aerosol Sci. Technol., 23 (2), 257-261, 1995.

Meskhidze, N., Chameides, W. L., Nenes, A., and Chen, G.: Iron mobilization in mineral dust: Can anthropogenic SO_2 emissions affect ocean productivity?, Geophys. Res. Lett., 30 (21), doi:10.1029/2003GL018035, 2003.

Ming, Y., and Russell, L. M.: Organic aerosol effects on fog droplet spectra, J. Geophys. Res., 109 (D10), 2004.

Moffet, R. C., de Foy, B., Molina, L. T., Molina, M. J., and Prather, K. A.: Measurement of ambient aerosols in northern Mexico City by single particle mass spectrometry, Atmos. Chem. Phys., 8, 4499-4516, 2008a.

Moffet, R. C., and Prather, K. A.: Extending ATOFMS measurements to include refractive index and density, Anal. Chem., 77 (20), 6535-6541, 2005.

Moffet, R. C., Qin, X. Y., Rebotier, T., Furutani, H., and Prather, K. A.: Chemically segregated optical and microphysical properties of ambient aerosols measured in a single-particle mass spectrometer, J. Geophys. Res., 113 (D12), doi:10.1029/2007JD009393, 2008b.

Mohler, O., Benz, S., Saathoff, H., Schnaiter, M., Wagner, R., Schneider, J., Walter, S., Ebert, V., and Wagner, S.: The effect of organic coating on the heterogeneous ice nucleation efficiency of mineral dust aerosols, Environ. Res. Lett., 3 (2), 2008.

Mohler, O., Buttner, S., Linke, C., Schnaiter, M., Saathoff, H., Stetzer, O., Wagner, R., Kramer, M., Mangold, A., Ebert, V., and Schurath, U.: Effect of sulfuric acid coating on heterogeneous ice nucleation by soot aerosol particles, J. Geophys. Res., 110 (D11), 2005.

Mohler, O., DeMott, P. J., Vali, G., and Levin, Z.: Microbiology and atmospheric processes: the role of biological particles in cloud physics, Biogeosciences, 4 (6), 1059-1071, 2007.

Molina, M. J., Molina, L. T., and Golden, D. M.: Enviromental chemistry (gas and gas-solid interactions): The role of physical chemistry, Journal Of Physical Chemistry, 100 (31), 12888-12896, 1996.

Moore, M., Sullivan, R. C., Roberts, G., Wang., Y., and Prather, K. A.: Single particle composition and CCN activity during the 2007 San Diego Wildfires, to be submitted, 2008.

Mori, I., Nishikawa, M., and Iwasaka, Y.: Chemical reaction during the coagulation of ammonium sulphate and mineral particles in the atmosphere, Science of the Total Environment, 224 (1-3), 87-91, 1998.

Murphy, D. M.: The design of single particle laser mass spectrometers, Mass Spectrometry Reviews, 26 (2), 150-165, 2007.

Murphy, D. M., Cziczo, D. J., Froyd, K. D., Hudson, P. K., Matthew, B. M., Middlebrook, A. M., Peltier, R. E., Sullivan, A., Thomson, D. S., and Weber, R. J.: Single-particle mass spectrometry of tropospheric aerosol particles, J. Geophys. Res., 111 (D23), doi:10.1029/2006JD007340, 2006.

Nenes, A., Chuang, P. Y., Flagan, R. C., and Seinfeld, J. H.: A theoretical analysis of cloud condensation nucleus (CCN) instruments, J. Geophys. Res., 106 (D4), 3449-3474, 2001.

Niimura, N., Okada, K., Fan, X. B., Kai, K., Arao, K., Shi, G. Y., and Takahashi, S.: Formation of Asian dust-storm particles mixed internally with sea salt in the atmosphere, Journal of the Meteorological Society of Japan, 76 (2), 275-288, 1998.

Noble, C. A., and Prather, K. A.: Real-time measurement of correlated size and composition profiles of individual atmospheric aerosol particles, Environmental Science & Technology, 30 (9), 2667-2680, 1996a.

Noble, C. A., and Prather, K. A.: Real-time measurement of correlated size and composition profiles of individual atmospheric aerosol particles, Environ. Sci. Technol., 30 (9), 2667-2680, 1996b.

Noble, C. A., and Prather, K. A.: Real-time single particle mass spectrometry: A historical review of a quarter century of the chemical analysis of aerosols, Mass Spectrometry Reviews, 19 (4), 248-274, 2000.

O'Dowd, C. D., Jimenez, J. L., Bahreini, R., Flagan, R. C., Seinfeld, J. H., Hameri, K., Pirjola, L., Kulmala, M., Jennings, S. G., and Hoffmann, T.: Marine aerosol formation from biogenic iodine emissions, Nature, 417 (6889), 632-636, 2002.

Oberdorster, G., Sharp, Z., Atudorei, V., Elder, A., Gelein, R., Kreyling, W., and Cox, C.: Translocation of inhaled ultrafine particles to the brain, Inhalation Toxicology, 16 (6-7), 437-445, 2004.

Okada, K., Naruse, H., Tanaka, T., Nemoto, O., Iwasaka, Y., Wu, P. M., Ono, A., Duce, R. A., Uematsu, M., Merrill, J. T., and Arao, K.: X-ray spectrometry of individual Asian dust-storm particles over the Japanese islands and the north Pacific-Ocean, Atmos. Environ., 24 (6), 1369-1378, 1990.

Pandis, S. N., Wexler, A. S., and Seinfeld, J. H.: Dynamics of Tropospheric Aerosols, Journal of Physical Chemistry, 99 (24), 9646-9659, 1995.

Pastor, S. H., Allen, J. O., Hughes, L. S., Bhave, P., Cass, G. R., and Prather, K. A.: Ambient single particle analysis in Riverside, California by aerosol time-of-flight mass spectrometry during the SCOS97-NARSTO, Atmospheric Environment, 37, S239-S258, 2003.

Perry, K. D., Cliff, S. S., and Jimenez-Cruz, M. P.: Evidence for hygroscopic mineral dust particles from the Intercontinental Transport and Chemical Transformation Experiment, J. Geophys. Res., 109 (D23), doi:10.1029/2004JD004979, 2004.

Petters, M. D., and Kreidenweis, S. M.: A single parameter representation of hygroscopic growth and cloud condensation nucleus activity, Atmos. Chem. Phys., 7 (8), 1961-1971, 2007.

Petters, M. D., and Kreidenweis, S. M.: A single parameter representation of hygroscopic growth and cloud condensation nucleus activity - Part 2: Including solubility, Atmos. Chem. Phys., 8, 6273–6279, 2008.

Petters, M. D., Prenni, A. J., Kreidenweis, S. M., DeMott, P. J., Matsunaga, A., Lim, Y. B., and Ziemann, P. J.: Chemical aging and the hydrophobic-to-hydrophilic conversion of carbonaceous aerosol, Geophys. Res. Lett., 33 (24), doi:10.1029/2006GL027249, 2006.

Pietropaoli, A. P., Frampton, M. W., Hyde, R. W., Morrow, P. E., Oberdorster, G., Cox, C., Speers, D. M., Frasier, L. M., Chalupa, D. C., Huang, L. S., and Utell, M. J.: Pulmonary function, diffusing capacity, and inflammation in healthy and asthmatic subjects exposed to ultrafine particles, Inhalation Toxicology, 16, 59-72, 2004.

Pope, C. A.: What do epidemiologic findings tell us about health effects of environmental aerosols?, Journal Of Aerosol Medicine-Deposition Clearance And Effects In The Lung, 13 (4), 335-354, 2000.

Poschl, U.: Atmospheric aerosols: Composition, transformation, climate and health effects, Angewandte Chemie-International Edition, 44 (46), 7520-7540, 2005.

Poschl, U., Rudich, Y., and Ammann, M.: Kinetic model framework for aerosol and cloud surface chemistry and gas-particle interactions - Part 1: General equations, parameters, and terminology, Atmos. Chem. Phys., 7 (23), 5989-6023, 2007.

Prospero, J. M., and Savoie, D. L.: Effect of continental sources on nitrate concentrations over the Pacific-Ocean, Nature, 339 (6227), 687-689, 1989.

Pui, D. Y. H., Flagan, R. C., Kaufman, S. L., Maynard, A. D., de la Mora, J. F., Hering, S. V., Jimenez, J. L., Prather, K. A., Wexler, A. S., and Ziemann, P. J.: Experimental methods and instrumentation, Journal Of Nanoparticle Research, 6 (2-3), 314-315, 2004.

Pye, K., Aeolian dusts and dust deposits, Academic Press, San Diego, 1987.

Qin, X., and Prather, K. A.: Impact of biomass emissions on particle chemistry during the California Regional Particulate Air Quality Study, International Journal Of Mass Spectrometry, 258 (1-3), 142-150, 2006.

Quinn, P. K., Bates, T. S., Coffman, D. J., and Covert, D. S.: Influence of particle size and chemistry on the cloud nucleating properties of aerosols, Atmos. Chem. Phys., 8 (4), 1029-1042, 2008.

Ramanathan, V., Chung, C., Kim, D., Bettge, T., Buja, L., Kiehl, J. T., Washington, W. M., Fu, Q., Sikka, D. R., and Wild, M.: Inaugural Article: Atmospheric brown clouds: Impacts on South Asian climate and hydrological cycle, PNAS, 102 (15), 5326-5333, 2005.

Ramanathan, V., Crutzen, P. J., Kiehl, J. T., and Rosenfeld, D.: Atmosphere - Aerosols, climate, and the hydrological cycle, Science, 294 (5549), 2119-2124, 2001.

Ravishankara, A. R.: Heterogeneous and multiphase chemistry in the troposphere, Science, 276 (5315), 1058-1065, 1997.

Raymond, T. M., and Pandis, S. N.: Formation of cloud droplets by multicomponent organic particles, J. Geophys. Res., 108 (D15), doi:10.1029/2003JD003503, 2003.

Rebotier, T. P., and Prather, K. A.: Aerosol time-of-flight mass spectrometry data analysis: A benchmark of clustering algorithms, Analytica Chimica Acta, 585 (1), 38-54, 2007.

Reid, J. S., Koppmann, R., Eck, T. F., and Eleuterio, D. P.: A review of biomass burning emissions part II: intensive physical properties of biomass burning particles, Atmos. Chem. Phys., 5, 799-825, 2005.

Roberts, G., Mauger, G., Hadley, O., and Ramanathan, V.: North American and Asian aerosols over the eastern Pacific Ocean and their role in regulating cloud condensation nuclei, J. Geophys. Res., 111 (D13), doi:10.1029/2005JD006661, 2006.

Roberts, G. C., and Nenes, A.: A continuous-flow streamwise thermal-gradient CCN chamber for atmospheric measurements, Aerosol Sci. Technol., 39 (3), 206-221, 2005.

Robinson, A. L., Donahue, N. M., Shrivastava, M. K., Weitkamp, E. A., Sage, A. M., Grieshop, A. P., Lane, T. E., Pierce, J. R., and Pandis, S. N.: Rethinking organic aerosols: Semivolatile emissions and photochemical aging, Science, 315 (5816), 1259-1262, 2007.

Rosenfeld, D.: Suppression of rain and snow by urban and industrial air pollution, Science, 287 (5459), 1793-1796, 2000.

Rosenfeld, D., Rudich, Y., and Lahav, R.: Desert dust suppressing precipitation: A possible desertification feedback loop, Proc. Natl. Acad. Sci. USA, 98 (11), 5975-5980, 2001.

Rudich, Y., Khersonsky, O., and Rosenfeld, D.: Treating clouds with a grain of salt, Geophys. Res. Lett., 29 (22), doi:10.1029/2002GL016055, 2002a.

Rudich, Y., Khersonsky, O., and Rosenfeld, D.: Treating clouds with a grain of salt, Geophysical Research Letters, 29 (22), doi:10.1029/2002GL016055, 2002b.

Salam, A., Lohmann, U., Crenna, B., Lesins, G., Klages, P., Rogers, D., Irani, R., MacGillivray, A., and Coffin, M.: Ice nucleation studies of mineral dust particles with a new continuous flow diffusion chamber, Aerosol Sci. Technol., 40 (2), 134-143, 2006.

Santschi, C., and Rossi, M. J.: Uptake of CO_2, SO_2, HNO_3 and HCl on calcite ($CaCO_3$) at 300 K: Mechanism and the role of adsorbed water, J. Phys. Chem. A, 110 (21), 6789-6802, 2006.

Satheesh, S. K., and Moorthy, K. K.: Radiative effects of natural aerosols: A review, Atmos. Environ., 39 (11), 2089-2110, 2005.

Seinfeld, J. H., Carmichael, G. R., Arimoto, R., Conant, W. C., Brechtel, F. J., Bates, T. S., Cahill, T. A., Clarke, A. D., Doherty, S. J., Flatau, P. J., Huebert, B. J., Kim, J., Markowicz, K. M., Quinn, P. K., Russell, L. M., Russell, P. B., Shimizu, A., Shinozuka, Y., Song, C. H., Tang, Y. H., Uno, I., Vogelmann, A. M., Weber, R. J., Woo, J. H., and Zhang, X. Y.: ACE-ASIA - Regional climatic and atmospheric chemical effects of Asian dust and pollution, Bulletin Of The American Meteorological Society, 85 (3), 367-380, 2004.

Seinfeld, J. H., and Pandis, S. N., Atmospheric Chemistry & Physics, John Wiley & Sons, Inc., New York, 2006.

Seinfeld, J. H., and Pankow, J. F.: Organic atmospheric particulate material, Annual Review of Physical Chemistry, 54 (1), 121-140, 2003.

Seisel, S., Borensen, C., Vogt, R., and Zellner, R.: Kinetics and mechanism of the uptake of N_2O_5 on mineral dust at 298 K, Atmos. Chem. Phys., 5, 3423-3432, 2005.

Shi, Z., Zhang, D., Hayashi, M., Ogata, H., Ji, H., and Fujiie, W.: Influences of sulfate and nitrate on the hygroscopic behaviour of coarse dust particles, Atmos. Environ., 42 (4), 822-827, 2008.

Shi, Z. B., Shao, L. T., Jones, T. P., and Lu, S. L.: Microscopy and mineralogy of airborne particles collected during severe dust storm episodes in Beijing, China, J. Geophys. Res., 110 (D1), doi:10.1029/2004JD005073, 2005.

Shimmo, M., Hyotylainen, T., Kallio, M., Anttila, P., and Riekkola, M. L.: Multidimensional and hyphenated techniques in aerosol analysis, Lc Gc Europe, 17 (12), 640-+, 2004.

Shulman, M. L., Jacobson, M. C., Charlson, R. J., Synovec, R. E., and Young, T. E.: Dissolution behavior and surface tension effects of organic compounds in nucleating cloud droplets, Geophys. Res. Lett., 23 (3), 277-280, 1996.

Silva, P. J., Carlin, R. A., and Prather, K. A.: Single particle analysis of suspended soil dust from Southern California, Atmos. Environ., 34 (11), 1811-1820, 2000.

Silva, P. J., Liu, D. Y., Noble, C. A., and Prather, K. A.: Size and chemical characterization of individual particles resulting from biomass burning of local Southern California species, Environ. Sci. Technol., 33 (18), 3068-3076, 1999.

Silva, P. J., and Prather, K. A.: Interpretation of mass spectra from organic compounds in aerosol time-of-flight mass spectrometry, Anal. Chem., 72 (15), 3553-3562, 2000.

Smith, J. N., Moore, K. F., Eisele, F. L., Voisin, D., Ghimire, A. K., Sakurai, H., and McMurry, P. H.: Chemical composition of atmospheric nanoparticles during nucleation events in Atlanta, J. Geophys. Res., 110 (D22), 2005.

Smith, J. N., Moore, K. F., McMurry, P. H., and Eisele, F. L.: Atmospheric measurements of sub-20 nm diameter particle chemical composition by thermal desorption chemical ionization mass spectrometry, Aerosol Sci. Technol., 38 (2), 100-110, 2004.

Sodeman, D. A., Toner, S. M., and Prather, K. A.: Determination of single particle mass spectral signatures from light-duty vehicle emissions, Environ. Sci. Technol., 39 (12), 4569-4580, 2005.

Sokolik, I. N., and Toon, O. B.: Incorporation of mineralogical composition into models of the radiative properties of mineral aerosol from UV to IR wavelengths, J. Geophys. Res., 104 (D8), 9423-9444, 1999.

Sokolik, I. N., Winker, D. M., Bergametti, G., Gillette, D. A., Carmichael, G., Kaufman, Y. J., Gomes, L., Schuetz, L., and Penner, J. E.: Introduction to special section: Outstanding problems in quantifying the radiative impacts of mineral dust, J. Geophys. Res., 106 (D16), 18015-18027, 2001.

Song, C. H., and Carmichael, G. R.: The aging process of naturally emitted aerosol (sea-salt and mineral aerosol) during long range transport, Atmos. Environ., 33 (14), 2203-2218, 1999.

Song, C. H., and Carmichael, G. R.: Gas-particle partitioning of nitric acid modulated by alkaline aerosol, J. Atmos. Chem., 40 (1), 1-22, 2001.

Song, X. H., Hopke, P. K., Fergenson, D. P., and Prather, K. A.: Classification of single particles analyzed by ATOFMS using an artificial neural network, ART-2A, Anal. Chem., 71 (4), 860-865, 1999.

Sotiropoulou, R. E. P., Medina, J., and Nenes, A.: CCN predictions: Is theory sufficient for assessments of the indirect effect?, Geophys. Res. Lett., 33 (5), doi:10.1029/2005GL025148, 2006.

Spencer, M. T., and Prather, K. A.: Using ATOFMS to determine OC/EC mass fractions in particles, Aerosol Sci. Technol., 40 (8), 585-594, 2006.

Spencer, M. T., Shields, L. G., and Prather, K. A.: Simultaneous measurement of the effective density and chemical composition of ambient aerosol particles, Environ. Sci. Technol., 41 (4), 1303-1309, 2007.

Stelson, A. W., Friedlander, S. K., and Seinfeld, J. H.: Note on the equilibrium relationship between ammonia and nitric-acid and particulate ammonium-nitrate, Atmos. Environ., 13 (3), 369-371, 1979.

Stemmler, K., Ammann, M., Donders, C., Kleffmann, J., and George, C.: Photosensitized reduction of nitrogen dioxide on humic acid as a source of nitrous acid, Nature, 440 (7081), 195-198, 2006.

Stolzenburg, M. R., and McMurry, P. H.: Equations governing single and tandem DMA configurations and a new lognormal approximation to the transfer function, Aerosol Sci. Technol., 42 (6), 421-432, 2008.

Su, Y. X., Sipin, M. F., Furutani, H., and Prather, K. A.: Development and characterization of an aerosol time-of-flight mass spectrometer with increased detection efficiency, Anal. Chem., 76 (3), 712-719, 2004.

Suess, D. T., and Prather, K. A.: Mass spectrometry of aerosols, Chemical Reviews, 99 (10), 3007-3036, 1999.

Sullivan, R. C., and Prather, K. A.: Recent advances in our understanding of atmospheric chemistry and climate made possible by on-line aerosol analysis instrumentation, Anal. Chem., 77 (12), 3861-3885, 2005.

Sullivan, R. C., Thornberry, T., and Abbatt, J. P. D.: Ozone decomposition kinetics on alumina: effects of ozone partial pressure, relative humidity and repeated oxidation cycles, Atmospheric Chemistry and Physics, 4, 1301-1310, 2004.

Sun, J. M., Zhang, M. Y., and Liu, T. S.: Spatial and temporal characteristics of dust storms in China and its surrounding regions, 1960-1999: Relations to source area and climate, Journal Of Geophysical Research-Atmospheres, 106 (D10), 10325-10333, 2001.

Swietlicki, E., Hansson, H. C., Hameri, K., Svenningsson, B., Massling, A., McFiggans, G., McMurry, P. H., Petaja, T., Tunved, P., Gysel, M., Topping, D., Weingartner, E., Baltensperger, U., Rissler, J., Wiedensohler, A., and Kulmala, M.: Hygroscopic properties of submicrometer atmospheric aerosol particles measured with H-TDMA instruments in various environments - a review, Tellus Series B-Chemical and Physical Meteorology, 60 (3), 432-469, 2008.

Tabazadeh, A.: Organic aggregate formation in aerosols and its impact on the physicochemical properties of atmospheric particles, Atmos. Environ., 39 (30), 5472-5480, 2005.

Tang, I. N., Munkelwitz, H. R., and Davis, J. G.: Aerosol growth studies - IV. Phase transformation of mixed salt aerosols in a mois atmosphere, Journal Of Aerosol Science, 9 (6), 505-511, 1978.

Tang, Y. H., Carmichael, G. R., Kurata, G., Uno, I., Weber, R. J., Song, C. H., Guttikunda, S. K., Woo, J. H., Streets, D. G., Wei, C., Clarke, A. D., Huebert, B., and Anderson, T. L.: Impacts of dust on regional tropospheric chemistry during the ACE-Asia experiment: A model study with observations, J. Geophys. Res., 109 (D19), doi:10.1029/2003JD003806, 2004a.

Tang, Y. H., Carmichael, G. R., Seinfeld, J. H., Dabdub, D., Weber, R. J., Huebert, B., Clarke, A. D., Guazzotti, S. A., Sodeman, D. A., Prather, K. A., Uno, I., Woo, J. H., Yienger, J. J., Streets, D. G., Quinn, P. K., Johnson, J. E., Song, C. H., Grassian, V. H., Sandu,

A., Talbot, R. W., and Dibb, J. E.: Three-dimensional simulations of inorganic aerosol distributions in east Asia during spring 2001, J. Geophys. Res., 109 (D19), doi:10.1029/2003JD004201, 2004b.

Tegen, I., Lacis, A. A., and Fung, I.: The influence on climate forcing of mineral aerosols from disturbed soils, Nature, 380 (6573), 419-422, 1996.

Thornton, J. A., and Abbatt, J. P. D.: N2O5 reaction on submicron sea salt aerosol: Kinetics, products, and the effect of surface active organics, J. Phys. Chem. A, 109 (44), 10004-10012, 2005.

Thornton, J. A., Braban, C. F., and Abbatt, J. P. D.: N2O5 hydrolysis on sub-micron organic aerosols: the effect of relative humidity, particle phase, and particle size, Phys. Chem. Chem. Phys., 5 (20), 4593-4603, 2003.

Thulasiraman, S., O'Neill, N. T., Royer, A., Holben, B. N., Westphal, D. L., and McArthur, L. J. B.: Sunphotometric observations of the 2001 Asian dust storm over Canada and the US, Geophys. Res. Lett., 29 (8), doi:10.1029/2001GL014188, 2002.

Tolocka, M. P., Lake, D. A., Johnston, M. V., and Wexler, A. S.: Size-resolved fine and ultrafine particle composition in Baltimore, Maryland, J. Geophys. Res., 110 (D7), -, 2005.

Toner, S. M., Sodeman, D. A., and Prather, K. A.: Single particle characterization of ultrafine and accumulation mode particles from heavy duty diesel vehicles using aerosol time-of-flight mass spectrometry, Environ. Sci. Technol., 40 (12), 3912-3921, 2006.

Trochkine, D., Iwasaka, Y., Matsuki, A., Yamada, M., Kim, Y. S., Nagatani, T., Zhang, D., Shi, G. Y., and Shen, Z.: Mineral aerosol particles collected in Dunhuang, China, and their comparison with chemically modified particles collected over Japan, Journal of Geophysical Research-Atmospheres, 108 (D23), doi:10.1029/2002JD003268, 2003.

Twomey, S.: Influence of Pollution on Shortwave Albedo of Clouds, Journal of the Atmospheric Sciences, 34 (7), 1149-1152, 1977.

Ullerstam, M., Johnson, M. S., Vogt, R., and Ljungstrom, E.: DRIFTS and Knudsen cell study of the heterogeneous reactivity of SO_2 and NO_2 on mineral dust, Atmospheric Chemistry And Physics, 3, 2043-2051, 2003.

Underwood, G. M., Li, P., Al-Abadleh, H., and Grassian, V. H.: A Knudsen cell study of the heterogeneous reactivity of nitric acid on oxide and mineral dust particles, J. Phys. Chem. A, 105 (27), 6609-6620, 2001a.

Underwood, G. M., Song, C. H., Phadnis, M., Carmichael, G. R., and Grassian, V. H.: Heterogeneous reactions of NO_2 and HNO_3 on oxides and mineral dust: A combined laboratory and modeling study, J. Geophys. Res., 106 (D16), 18055-18066, 2001b.

Usher, C. R., Michel, A. E., and Grassian, V. H.: Reactions on mineral dust, Chem. Rev., 103 (12), 4883-4939, 2003a.

Usher, C. R., Michel, A. E., Stec, D., and Grassian, V. H.: Laboratory studies of ozone uptake on processed mineral dust, Atmospheric Environment, 37 (38), 5337-5347, 2003b.

Utell, M. J., and Frampton, M. W.: Acute health effects of ambient air pollution: The ultrafine particle hypothesis, Journal Of Aerosol Medicine-Deposition Clearance And Effects In The Lung, 13 (4), 355-359, 2000.

VanCuren, R. A.: Asian aerosols in North America: Extracting the chemical composition and mass concentration of the Asian continental aerosol plume from long-term aerosol records in the western United States, J. Geophys. Res., 108 (D20), doi:10.1029/2003JD003459, 2003.

Vlasenko, A., Sjogren, S., Weingartner, E., Stemmler, K., Gaggeler, H. W., and Ammann, M.: Effect of humidity on nitric acid uptake to mineral dust aerosol particles, Atmospheric Chemistry And Physics, 6, 2147-2160, 2006.

Vogt, R., Kirchner, U., Scheer, V., Hinz, K. P., Trimborn, A., and Spengler, B.: Identification of diesel exhaust particles at an Autobahn, urban and rural location using single-particle mass spectrometry, Journal Of Aerosol Science, 34 (3), 319-337, 2003.

Volckens, J., and Peters, T. M.: Counting and particle transmission efficiency of the aerodynamic particle sizer, Journal of Aerosol Science, 36 (12), 1400-1408, 2005.

Wang, S. C., and Flagan, R. C.: Scanning electrical mobility spectrometer, Aerosol Sci. Technol., 13 (2), 230-240, 1990.

Wenzel, R. J., Liu, D. Y., Edgerton, E. S., and Prather, K. A.: Aerosol time-of-flight mass spectrometry during the Atlanta Supersite Experiment: 2. Scaling procedures, Journal Of Geophysical Research-Atmospheres, 108 (D7), 2003.

Wexler, A. S., and Clegg, S. L.: Atmospheric aerosol models for systems including the ions H+, NH4+, Na+, SO42-, NO3-,Cl-, Br-, and H2O, J. Geophys. Res., 107 (D14), 2002.

Whiteaker, J. R., Suess, D. T., and Prather, K. A.: Effects of meteorological conditions on aerosol composition and mixing state in Bakersfield, CA, Environ. Sci. Technol., 36 (11), 2345-2353, 2002.

Wiedensohler, A.: An Approximation of the Bipolar Charge-Distribution for Particles in the Sub-Micron Size Range, Journal of Aerosol Science, 19 (3), 387-389, 1988.

Wood, S. H., and Prather, K. A.: Time-of-flight mass spectrometry methods for real time analysis of individual aerosol particles, Trac-Trends In Analytical Chemistry, 17 (6), 346-356, 1998.

Worsnop, D. R., Morris, J. W., Shi, Q., Davidovits, P., and Kolb, C. E.: A chemical kinetic model for reactive transformations of aerosol particles, Geophys. Res. Lett., 29 (20), 2002.

Wurzler, S., Reisin, T. G., and Levin, Z.: Modification of mineral dust particles by cloud processing and subsequent effects on drop size distributions, J. Geophys. Res., 105 (D4), 4501-4512, 2000.

Xiao, H.-S., Dong, J.-L., Wang, L.-Y., Zhao, L.-J., Wang, F., and Zhang, Y.-H.: Spatially Resolved Micro-Raman Observation on the Phase Separation of Effloresced Sea Salt Droplets Environ. Sci. Technol., doi: 10.1021/es801181f 2008.

Yin, Y., Wurzler, S., Levin, Z., and Reisin, T. G.: Interactions of mineral dust particles and clouds: Effects on precipitation and cloud optical properties, Journal Of Geophysical Research-Atmospheres, 107 (D23), doi:10.1029/2001JD001544, 2002.

Yuan, H., Rahn, K. A., and Zhuang, G.: Graphical techniques for interpreting the composition of individual aerosol particles, Atmospheric Environment, 38 (39), 6845-6854, 2004.

Zelenyuk, A., Cai, Y., and Imre, D.: From agglomerates of spheres to irregularly shaped particles: Determination of dynamic shape factors from measurements of mobility and vacuum aerodynamic diameters, Aerosol Sci. Technol., 40 (3), 197-217, 2006a.

Zelenyuk, A., Imre, D., and Cuadra-Rodriguez, L. A.: Evaporation of water from particles in the aerodynamic lens inlet: An experimental study, Anal. Chem., 78 (19), 6942-6947, 2006b.

Zhang, D. Z., and Iwasaka, Y.: Size change of Asian dust particles caused by sea salt interaction: Measurements in southwestern Japan, Geophysical Research Letters, 31 (15), doi:10.1029/2004GL020087, 2004.

Zhang, D. Z., Iwasaka, Y., Shi, G. Y., Zang, J. Y., Matsuki, A., and Trochkine, D.: Mixture state and size of Asian dust particles collected at southwestern Japan in spring 2000, Journal Of Geophysical Research-Atmospheres, 108 (D24), doi:10.1029/2003JD003869, 2003a.

Zhang, D. Z., Iwasaka, Y., Shi, G. Y., Zang, J. Y., Matsuki, A., and Trochkine, D.: Mixture state and size of Asian dust particles collected at southwestern Japan in spring 2000, J. Geophys. Res., 108 (D24), doi:10.1029/2003JD003869, 2003b.

Zhang, Q., Stanier, C. O., Canagaratna, M. R., Jayne, J. T., Worsnop, D. R., Pandis, S. N., and Jimenez, J. L.: Insights into the chemistry of new particle formation and growth events in Pittsburgh based on aerosol mass spectrometry, Environ. Sci. Technol., 38 (18), 4797-4809, 2004.

Ziemann, P. J.: Particle mass and size measurement using mass spectrometry, Trac-Trends In Analytical Chemistry, 17 (6), 322-328, 1998.

Zuberi, B., Bertram, A. K., Cassa, C. A., Molina, L. T., and Molina, M. J.: Heterogeneous nucleation of ice in (NH4)(2)SO4-H2O particles with mineral dust immersions, Geophys. Res. Lett., 29 (10), doi:10.1029/2001GL014289, 2002.

Chapter 2

Chemical composition and mixing state of individual particles in the ACE-Asia aerosol at sea level

2.1 Synopsis

Single-particle measurements performed with an aerosol time-of-flight mass spectrometer (ATOFMS) on the R/V Ronald H. Brown during the ACE-Asia campaign are used to investigate the temporal variations in the chemical composition and mixing state of the sampled aerosol along a transect from Hawaii into the Sea of Japan. The particles were classified first by the general particle type, and then by the presence of secondary inorganic and organic components, as a function of particle size. Elemental carbon and organic carbon particles were always mixed with secondary inorganic compounds, while biomass particles were mixed to a lesser extent and showed more variability. Carbonaceous particles were more prevalent in submicron particles. The fraction of particles classified as OC was very low, however OC components were found mixed with a large fraction of other particle types. Supermicron particles were largely composed of mineral dust and sea salt particles, though both of these classes also had appreciable submicron contributions. A unique brief episode in which a substantial amount of pure submicron sulfate particles was observed in a volcanic-influenced air mass just prior to the arrival of the dust front. The arrival of a major dust storm caused mineral dust particles to dominate the supermicron particles, and also produced elevated concentrations of submicron particles. Unlike sulfate, nitrate was enriched in sea salt and mineral dust particles, as was oxalic acid, a secondary organic diacid. The observed aerosol mixing state can be largely explained by known atmospheric processing mechanisms.

The mixing state of the Asian outflow is summarized herein to provide improved inputs and comparisons for models of atmospheric chemistry, chemical transport, and climate.

2.2 Introduction

Major dust storm events typically develop in China in the spring, brought about by cold frontal systems and the Mongolian cyclonic depression (Sun et al., 2001). The Gobi Deserts in Mongolia and northern China, and the Taklimakan Desert in western China, are the two dominant source regions of dust in eastern Asia. Once lofted to high altitudes, dust can then become entrained in the jet stream and transported long distances over the Pacific Ocean to North America (Cahill, 2003; Duce et al., 1980; Jaffe et al., 1999; Thulasiraman et al., 2002). The Asian Pacific Regional Aerosol Characterization Experiment (ACE-Asia) in 2001 was designed to study the impact these spring dust events have on the physical, chemical and radiative properties of the Asian aerosol as it becomes transported over the mainland and the Pacific Ocean (Huebert et al., 2003a; Seinfeld et al., 2004). The region is characterized by significant pollution outflow from the continent, which can become mixed with these dust outbreaks, increasing the complexity of the analysis of the mixed aerosol and the resulting effects on regional atmospheric chemistry and climate.

The distribution of primary and secondary aerosol chemical components between individual particles as a function of size in a polydisperse aerosol (i.e. mixing state) has significant effects on the physicochemical properties of the ambient aerosol. Mixing state influences a particle's chemical composition, size, shape, density, physical phase, solubility, hygroscopicity, and complex index of refraction (Choi and Chan, 2002; Moffet et al., 2008b; Spencer et al., 2007; Zhang et al., 2008). These in turn determine a particle's optical properties (e.g. single scattering albedo and asymmetry parameter), warm and cold cloud nucleation

properties, atmospheric lifetime, and reaction rates and mechanisms with gaseous reactants (Bond et al., 2006; Furutani et al., 2008; Hearn and Smith, 2007; McFiggans et al., 2006; Thornton et al., 2003). The chemical mixing state is therefore required to accurately predict the direct and indirect climate effects of atmospheric aerosols (Chung and Seinfeld, 2002; Jacobson, 2001; Petters et al., 2006a; Pierce et al., 2007), as well as the effects on atmospheric chemistry (Bauer et al., 2004; Bian and Zender, 2003; Dentener and Crutzen, 1993; Tang et al., 2004a). This information can be compared to and used to refine chemical models of atmospheric chemistry and aerosol processing dynamics. Single-particle analysis such as single-particle mass spectrometry (SPMS) can directly measure the mixing state of individual particles within a polydisperse aerosol.

This chapter summarizes the chemical composition and mixing state of the ambient aerosol sampled during the NOAA R/V Ronald H. Brown's (RHB) research cruise from Hawaii into the Sea of Japan during the ACE-Asia campaign. In April 2001, a major dust storm event transported highly elevated levels of dust particles to the various ground, ship, and aircraft sampling platforms during ACE-Asia (Bates et al., 2004; Huebert et al., 2003b). The principal source regions of the dust during these events were the Taklimakan desert in Xinjiang Province, China and the desert regions in Mongolia, including the Gobi desert (Arimoto et al., 2006; Gong et al., 2003a). As the mineral dust aerosol was transported over China, Korea, and Japan to the ocean, it became mixed with anthropogenic, volcanic, and natural aerosols and aerosol precursor gases. When sampled onboard the R/V Ronald H. Brown in the Sea of Japan, the resulting aerosol was a complex mixture of mineral dust, organic carbon, elemental carbon, sulfates, nitrates, ammonium, and sea salt (Bates et al., 2004). The changes in the aerosol mixing state altered the aerosol's optical and hygroscopic

properties, and therefore its effect on regional climate (Arimoto et al., 2006; Seinfeld et al., 2004).

2.3 Experimental methods

2.3.1   Shipboard aerosol sampling

In situ aerosol measurements were performed from the NOAA R/V Ronald H. Brown (RHB) during its research cruise from Hawaii to Japan between 16 March 2001 (DOY 75) and 18 April 2001 (DOY 108). The RHB's cruise track from Hawaii to Japan is shown in Figure 2.1. The sampled ambient aerosol was drawn through a 6 m community inlet from ~18 m above sea level. The bottom 1.5 m of the mast was heated 5.1 C above ambient on average to maintain a relative humidity (RH) of 55 ± 5% (Bates et al., 2004). Air was only sampled when the relative wind speed and direction, and concentrations of particles larger than 15 nm indicated that the sampled air was free of local contamination. Several instruments sub-sampled from this mast, including the aerosol time-of-flight mass spectrometer (ATOFMS) SPMS instrument, and the aerosol filter samples collected by scientists from NOAA's Pacific Marine Environmental Laboratory (PMEL). The design and operation of the ATOFMS is described in Chapter 1. The instrument used here was capable of efficiently detecting particles between D_a = 0.2-3.0 μm. A total of 731,309 single-particle mass spectra were collected over the course of the campaign.

2.3.2   Single-particle analysis classification criteria

Analysis of the single-particle mass spectra collected by the ATOFMS was performed using the Matlab® based toolkit YAADA (http://www.yaada.org) to perform searches for particular mass spectral features within the dataset. An adaptive resonance theory-based neural
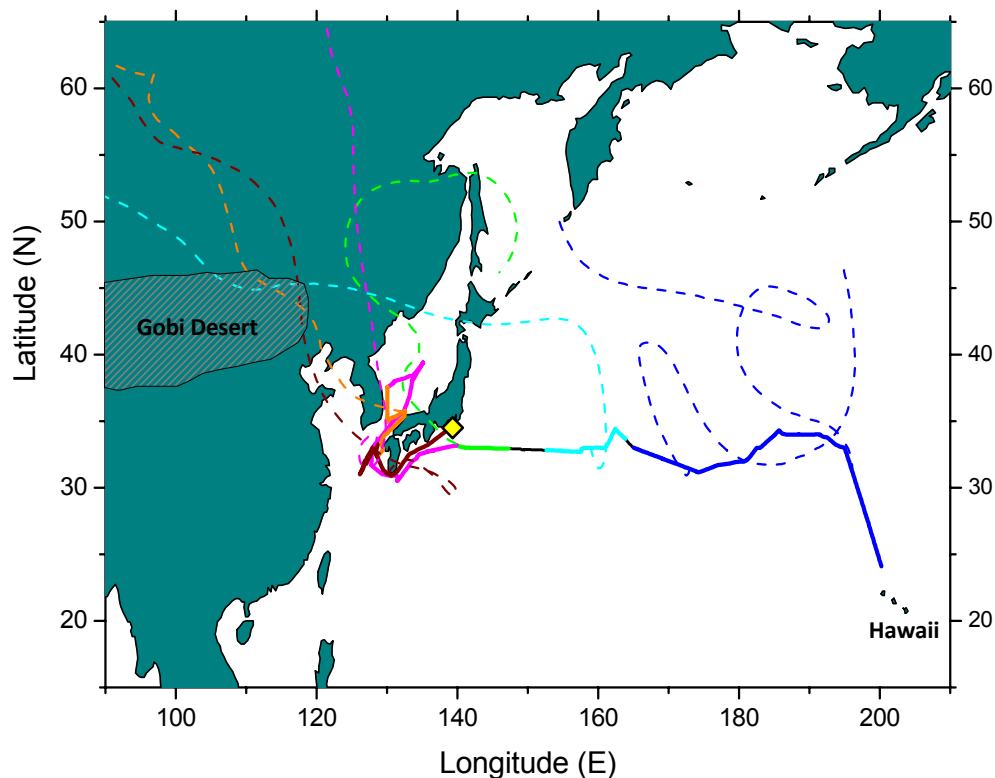
Figure 2.1. Cruise track of the *R/V Ronald H. Brown* (thick line), coloring represents the different broad air mass periods: Remote Marine, Polluted Marine, First Volcano, Pre-Frontal + Volcano, Dust Storm, Post-Frontal Continental. Dashed lines correspond to typical air mass back trajectories for those periods. The approximate location of the Gobi desert is included; the Taklimakan desert lies to the south-west.

network algorithm, ART-2a, was used to group the data into clusters of particles with similar

mass spectral features, using a vigilance factor of 0.80, and the clusters were then regrouped at

0.85 vigilance factor (Song et al., 1999). The regrouped clusters were manually sorted into

broad primary particle classes (mineral dust, sea salt, elemental carbon (EC), organic carbon

(OC), K-biomass, and marine-bio), these are described in detail below and displayed in Figure

2.2. The ART-2a algorithm produced a cluster containing a mixture of mineral dust and K-

biomass particles due to the large K^+ signal common to both particle types. This was resolved

using a Hierarchical Classification analysis (Rebotier and Prather, 2007) on that cluster, which

properly segregated it into K-mineral dust, K-EC-biomass, and K-OC-biomass sub-clusters.

The first sub-cluster was merged with the mineral dust class while the later two were merged with the K-biomass class. In all cases the presence or absence of secondary aerosol products including sulfate, nitrate, and ammonium were not used in the principal particle classification. The 60 largest clusters were manually classified into the broad particle classes as described below. This accounted for > 90% of the total particles detected.

Within these primary particle classes secondary aerosol components were queried including ammonium, nitrate, sulfate, and organic carbon. The ion peaks used to perform these searches are summarized in Table 2.1. A relative area criterion of 2% was typically used to classify particles as internally mixed with the various inorganic compounds, while a 1.0% or 0.5% criterion was used for organic carbon peaks. While the mass or mass fraction that corresponds to this criterion is not known, it is well above the detection limit and typical noise threshold (< 0.1 % relative area) in the single-particle mass spectra. This threshold thus represents a significant amount of that compound in the particle and has a very low probability or producing false positive caused by spurious noise. The same 2% relative area threshold was used in a previous analysis by Liu et al. (2000). Searches for ammonium were performed using a relative area criteria of > 1%, as the ATOFMS is generally less sensitive to detecting this compound in the positive ion mass spectrum. Oxalic acid was queried using a > 0.5% threshold, due to the generally smaller abundance of this compound. This criterion was found to give similar results but better counting statistics as a 1% or 2% threshold for oxalic acid (Chapter 5).

Single-particle measurements are typically divided between submicron ($0.2 < D_a < 1.0$ μm) and supermicron ($1.0 < D_a < 3.0$ μm) size ranges. This has been found to reduce most of the sampling bias caused by the ATOFMS particle transmission efficiency, which shows a maximum in the supermicron size mode at ~1.7 μm (Qin et al., 2006).

Table 2.1. Ion peak identities and relative peak area thresholds used to classify single-particle mixing state.

Compound	Ion peak criterion (m/z)
NH_4^- (ammonium)	$+18 > 1\%$
NO_3^- (nitrate)	$-62 > 2\%$
SO_4^- (sulfate)	$-97 > 2\%$
SO_4^- (sulfate in sea salt)	$-96 > 2\%$
C_3H^+ (general organics)	$+37 > 1\%$
$C_2H_3O^+$ (oxidized organics, OOA)	$+43 > 1\%$
$C_2O_4H^-$ (organic diacids)	$-89 > 0.5\%$

2.3.3   Aerosol size distributions

The number size distributions were measured by an ultrafine differential mobility particle sizer (UDMPS), a differential mobility particle sizer (DMPS) and an aerodynamic particle sizer (APS, TSI model 3320). The UDMPS measured size distributions between 3 and 26 nm, the SMPS between 20 and 670 nm, and the APS between 542 nm and 20 μm. Number size distributions were obtained by all the instruments every 15 minutes. The APS data was converted from aerodynamic to geometric (mobility) diameter using the procedure described by Bates et al. (2004) and combined with the UDMPS and DMPS measurements to produce a combined number size distribution from 3 nm to 10 μm.

2.3.4   Filter-based aerosol mass measurements

Two sets of aerosol samples for mass measurements were collected and analyzed by scientists from PMEL. All of the measurements described below, were analyzed by PMEL scientists and are available on their project website (http://saga.pmel.noaa.gov/data/ download.php?cruise=ACEASIA). A two-stage impactor with aerodynamic cutoff diameters,

D_{50}, of 1.1 and 10 μm collected submicron and PM_{10} aerosol samples for determination of total and speciated aerosol mass concentrations. Samples were typically collected for 2.5 to 7 hrs during the day and 4 to 12 hours at night. A seven-stage impactor collected aerosol samples with finer size segregation and cutoff diameters of 0.18, 0.31, 0.55, 1.1, 2.0, 4.1, and 10 μm. Longer sampling times of 12 to 36 hours were used for the seven-stage samples. The filters were weighed to measure total mass, and extracted into water for determination of inorganic ions including SO_4^{-2}, Cl^-, NO_3^-, and NH_4^+ by ion chromatography. Non-sea-salt sulfate (nss-SO_4^{-2}) concentrations were calculated from Na^+ concentrations and the ratio of SO_4^{-2} to Na^+ in seawater. Organic carbon (OC) and elemental carbon (EC) aerosol mass was determined from filter samples collected with an identical two-stage impactor and determined using a Sunset Labs EC/OC thermal/optical analyzer. Further details on the aerosol filter sampling and analysis is provided by Bates et al. (2004).

2.3.5 Aerosol optical properties

Aerosol light scattering was determined by a three-wavelength integrating nephelometer (TSI, Inc.) at 450, 550, and 700 nm at $55 \pm 5\%$ RH. Two single-stage impactors, one with a D_{50} of 1.1 μm and one with a D_{50} of 10 μm were placed upstream of the nephelometer. An automated valve switched between the two impactors every 15 min so that sampling alternated between sub-1 μm and sub-10 μm aerosol. The aerosol light absorption coefficient was measured by monitoring the change in transmission through a filter with a Particle Soot Absorption Photometer (PSAP, Radiance Research). The PSAP was downstream of the same impactors as the nephelometer. Further details are provided by Quinn et al. (2004).

2.3.6   Meteorological parameters and gas measurements

Sulfur dioxide gas concentrations were measured by a trace level pulsed fluorescence analyzer (Thermo Environmental Instruments model 43C) that recorded data every minute. Ozone, carbon monoxide, and radon were also determined. Meteorological parameters including surface temperature, RH, wind speed and direction were measured. Air mass back trajectories were calculated at three arrival altitudes (500, 2500, and 5500 m) for the position of the ship at 6 hour intervals. Trajectories were calculated with the hybrid-coordinate model HYSPLIT 4 (http://www.arl.noaa.gov/ready/hysplit4.html) using the Global FNL wind fields.

2.4   Results and discussion

2.4.1   Air masses sampled

The major air masses experienced during the RHB's research cruise from Hawaii to Japan are summarized as follows, with the air mass name given in parentheses, and the related air masses previously defined by Bates et al. (2004) (B04) also listed. These classifications are based on the air-mass back trajectories as well as the in situ meteorological, gas, and aerosol observations made on the ship. The RHB sampled relatively clean marine air during its cruise from Hawaii towards Japan over DOY 75-84 (Remote Marine; Marine in B04). Air-mass back trajectories and radon measurements indicated the air had not been in contact with continental land masses for at least five days. From DOY 84.5-87.5 the first notable continental pollution influences from Japan, Korea, and China were observed, mixed with the marine air (Polluted Marine). This period included frequent frontal activity, rain, high winds, and no well-defined marine boundary layer. From DOY 88.5-91.0 the RHB was passing near the active Miyakejima volcano which lies SE of Japan, and sampled increasingly polluted air that had passed over Japan and sometimes Korea, as well as greatly elevated SO_2 from the volcano

(First Volcano). From 91.0-99.2 increasingly polluted air was experienced with back trajectories coming first from Korea and/or Japan, and then air that had circulated over Japan for the last seven days as the ship cruised along the southern shore of Japan. Beginning on DOY 99.3 while sampling in the Sea of Japan air that had passed over the Miyakejima volcano and Japan was observed, with elevated $SO_2(g)$. A dust layer was also aloft at 5 km altitude. This air mass includes the Polluted Korea/Japan, Polluted Japan, and Polluted + Volcano air masses from B04 (Pre-Frontal + Volcano, DOY 91.0-100.75). Beginning at DOY 100.83 a frontal zone reached the RHB while in the Sea of Japan, bringing greatly elevated levels of mineral dust. Upper-level trajectories were from China and Mongolia dust regions, while lower-levels extended across China and Korea. This was the first time that both upper and lower back-trajectories indicated flow from dust source regions. Precipitation began on DOY 101.3. From this point until DOY 104.5 the ship continued to experience elevated dust concentrations during a massive dust event in the cloud-free air following the frontal passage. Back trajectories indicated an origin in the north China/Mongolia dust regions and flow over Korea at first, and then over Shanghai towards the end of the period (Dust Storm, includes Dust Frontal Passage, Dust + Korea, Dust + Shanghai from B04). Finally, from DOY 104.5-109.5 polluted continental air with reduced dust loadings was observed while sampling in the East China Sea and then near Honshu, Japan. 500 m trajectories included air passing over the Yellow Sea, Beijing, Shanghai, Japan and Korea (Post-Frontal Continental). The RHB's cruise track is shown in Figure 2.1 with the broad air mass time periods indicated and typical 500 m air mass back trajectories for each period shown. Further details on the air masses sampled and their origins are given by Bates et al. (2004).
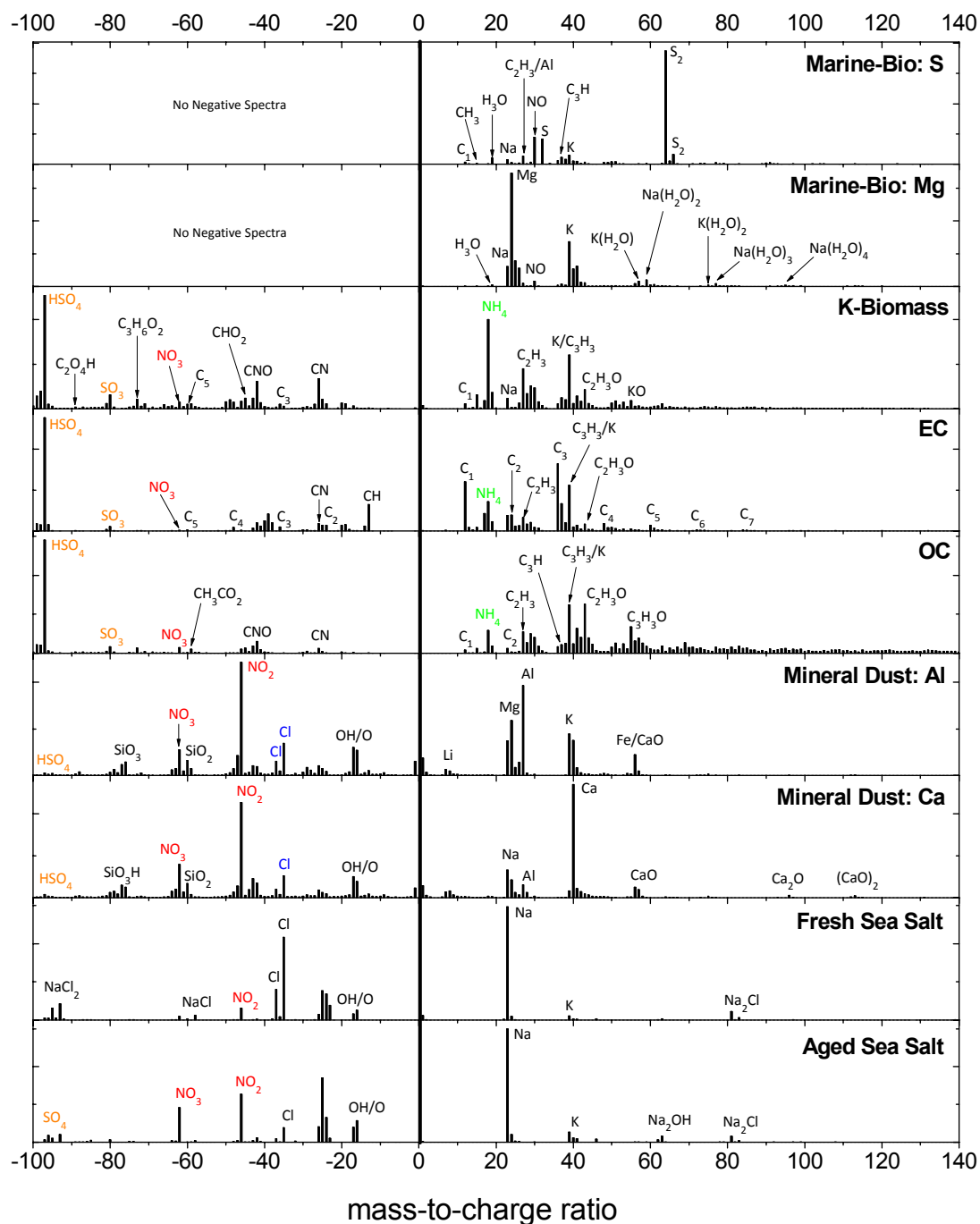
Figure 2.2. Representative average dual-polarity mass spectra of the major primary particle classes detected during ACE-Asia. Likely peak identities are given, and predominantly secondary components are indicated using colored labels. The y-axis is in an arbitrary unit that is the product of each ion's peak area and frequency of detection.

2.4.2   Principal particle classes

The particle clusters generated by the ART-2a sorting algorithm were manually regrouped into broad particle classes based on their similarity to other source characterization and field studies conducted with the ATOFMS (e.g. Guazzotti et al., 2001a; Moffet et al., 2008a; Silva et al., 1999; Toner et al., 2008), based on unique mass spectral features and their combinations. Representative average mass spectra of typical major clusters that comprise each particle class are displayed in Figure 2.2 and discussed below. The mass spectra include labels for major ion peaks used to classify each particle class.

2.4.2.1 Sea Salt

Sea salt particles were the most abundant particle type measured due to the marine sampling environment, and had the largest contribution in the supermicron mode. These particles are characterized by intense Na^+ and Cl^- peaks, as well as smaller K^+, Ca^+, Na_2Cl (m/z +81, +83) and $NaCl_2$ (m/z -93, -95, -97) markers. The sea salt class was the only class that was subdivided based on the presence of secondary compounds such as nitrate (m/z -46, -62) and sulfate (m/z -80, -96), indicators of heterogeneous processing of the particles by acidic vapors (Gard et al., 1998). The ART-2a algorithm accurately divides sea salt particles into fresh and aged clusters based on the presence or absence of these secondary products. This division provides an easy indication of the age of the marine air mass in the temporal particle counts shown below. Note that the largest sulfate peak occurs at m/z -96 (SO_4^-) in sea salt particles, while the largest sulfate peak occurs at m/z -97 (HSO_4^-) in the other particle classes.

2.4.2.2 Mineral dust

Mineral dust particles from northern China and Mongolia are the second most abundant particle class, predominantly in the supermicron mode but with significant submicron contributions as well. Dust produced a large number of individual clusters due to

complex mineralogical variations between individual dust particles, even from the same source region, and due to the large degree of fragmentation during the laser desorption/ionization (LDI) process. Two of the most abundant dust spectra are shown in Figure 2.2, a calcium-rich and an aluminosilicate-rich dust type. The calcium signal is likely from calcite ($CaCO_3$) and dolomite ($MgCa(CO_3)_2$). $CaCO_3$ cannot be directly observed via LDI as it fragments to $CaO^+ + CO_2(g)$, but its presence can be inferred from the Ca^+, CaO^+, Ca_2O^+, and $(CaO)_2^+$ ions. The Al-rich dust spectra contains several peaks indicative of aluminosilicate clays, including Al^+, Fe^+, and the silicate ion envelopes in the negative ions including SiO_2^- (m/z -60) and SiO_3H^- (m/z -77). Note that the Ca-rich dust spectrum also contains some of these silicate markers, demonstrating the complex mixed mineralogy at the single-particle level. The presence of chloride in the dust mass spectrum is predominantly from the uptake of chlorine-containing gases such as $HCl(g)$, as opposed to existing at the dust source; this is explored in detail in Chapters 3 & 4.

2.4.2.3 Organic carbon (OC)

Predominantly organic carbon particles were rarely detected during the study and were almost entirely found in the submicron mode. Typical organic carbon peaks include $C_2H_3^+$ (m/z +27), C_3H^+ (m/z +37), $C_3H_3^+$ (m/z +39), $C_2H_3O^+$ (m/z +43), and $C_3H_3O^+$ (m/z +55). Carbon fragments (C_1^+, C_2^+, C_3^+) that are either from elemental carbon contained in the OC particle, or from charring of OC to EC during the LDI process are also present. The negative ions include OC peaks such as CN^- (m/z -26), CNO^- (m/z -42), and CH_3CO_2 (m/z -59). Due to the lack of unique markers in the OC particles measured during this study it is not possible to speculate as to the sources of these particles (biogenic vs. anthropogenic, primary vs. secondary) in this case. These OC particles have similar mass spectral features to OC particles measured via ATOFMS in a wide variety of locations and source characterization

studies including during the INDOEX campaign in the Indian Ocean and Bay of Bengal (Guazzotti et al., 2001a), Mexico City (Moffet et al., 2008a), in various organic aerosol standards (Silva and Prather, 2000), and in EC particles coated by OC (Spencer and Prather, 2006).

2.4.2.4 Elemental carbon (EC)

Elemental carbon particles have a characteristic carbon fragment pattern (C_n) in both the positive and negative ion spectra and are also distinguished from other carbonaceous particles (e.g. OC, K-Biomass) by the C_3^+ (m/z +36) ion peak being larger than the $K^+/C_3H_3^+$ (m/z +39), C_2H_3 (m/z +27), and other OC peaks. The EC spectra do contain OC peaks including $C_2H_3^+$, C_3H^+, $C_3H_3^+$, $C_2H_3O^+$ (m/z +43), CH^- (m/z -13), and CN^- (m/z -26), which are either from organic carbon present at the source, or are added to the EC particles during atmospheric processing (Spencer and Prather, 2006). Other field and source studies with the ATOFMS have commonly observed Ca-EC particles, attributed to unburned lubricating oil from combustion engines, and V-EC particles, predominantly form ship emissions. These features were not predominant in the EC particle spectra observed during ACE-Asia. This could be due to the different fuels and lubricating oil packages used in the vehicles in this region compared to most previous ATOFMS studies that have been conducted in North America (e.g. Toner et al., 2008). Ca-EC and V-EC particle were also not detected in notable fractions by the ATOFMS during the INDOEX campaign in the Indian Ocean and Sea of Bengal (Guazzotti et al., 2001a). The term elemental carbon is used as it is based on its observed chemical structure of repeating carbon clusters, as opposed to labels used by other researchers including black carbon, soot, and light-absorbing carbon (Bond and Bergstrom, 2006).

2.4.2.5 K-biomass

Particles produced from biomass and biofuel combustion typically produce intense potassium signals, and are a complex mixture of EC, OC, and inorganic salts including KCl (Guazzotti et al., 2001a; Guazzotti et al., 2003; Silva et al., 1999). The K-biomass mass spectrum is characterized by a large K^+ (m/z +39) peak, which is greater than any EC (e.g. C_3^+) or OC peak (e.g. $C_2H_3^+$, $C_2H_3O^+$). The spectrum also contains EC carbon fragments (C_1^+, C_3^+, C_3^-, C_5^-) and OC peaks including $C_2H_3^+$, $C_2H_3O^+$, CN^-, CNO^-, and $C_2O_4H^-$ (m/z -89, oxalate). CHO_2^- (m/z -45, formate), CH_3CO_2 (m/z -59), and $C_3H_6O_2^-$ (m/z -73) peaks are also observed, they are commonly observed fragments of levoglucosan (Muhle et al., 2007; Qin and Prather, 2006; Silva et al., 1999), a sugar anhydride and common abundant molecular marker of biomass combustion particles (Schauer et al., 1996; Simoneit et al., 2004a). The biomass particle mass spectra and clusters contained varying signals from EC and OC components, reflecting the relative contributions of these two broad types of carbon.

2.4.2.6 Marine-Bio

The last major particle class detected is a unique particle type often observed by the ATOFMS in marine environments. These particles are believed to be biological particles released into the atmosphere from the ocean. Their abundance was correlated with measurements of marine productivity including DMS(g) during the RHB's cruise and are described in more detail in a forthcoming manuscript. This particle class is included here for completeness, as they did comprise notable periodic contributions to the aerosol loadings during the campaign. There are two general types of mass spectra in this class, as shown in Figure 2.2. One is characterized by an intense Mg^+ ion peak, while the other by a large S^+ peak. The Mg-type contains numerous cation-water clusters including $[K-H_2O]_n^+$ and $[Na-H_2O]_n^+$ with *n* ranging from 1 up to at least 5. The hydronium ion, H_3O^+ is also observed at

m/z +19. The S-type contains prominent $^{32}S^+$, $^{34}S^+$, $^{32}S_2^+$ (m/z +64) and $^{32}S^{34}S^+$ (m/z +66) ion peaks. This is a very rare observation of elemental sulfur ions/clusters in the positive-ion spectrum. Typically sulfur compounds are detected as sulfate via SO_3^- and HSO_4^- ions when analyzed by the ATOFMS. This indicates that these particles contain a unique form of reduced sulfur, possibly as disulfide bonds contained in proteins. The S-type particles also contain OC ion fragments including C_1^+, C_3^+, CH_3^+, $C_2H_3^+$, and the hydronium ion. Both types never produced a negative ion mass spectrum. This fact, as well as the hydronium ion and water cluster ion peaks, indicate that these particles were likely very hydrated because the presence of large amounts of water can suppress the formation of negative ions (primarily produced from electron attachment) when the wet particle is analyzed by LDI (Neubauer et al., 1998). The lack of a negative ion spectrum also precludes the analysis of the mixing state of these biological particles with secondary components, as most of these components appear in the negative ion mass spectrum. Therefore, these marine-bio particles are only included in the overall particle class number distributions.

2.4.3 Temporal evolution of principal particle classes

Hourly particle counts of the six principal particle types in the submicron and supermicron size ranges are shown in Figure 2.3. This includes the previously described division of the sea salt particle class into fresh and aged sea salt. The carbonaceous particle classes (OC, EC, and K-biomass, excluding the Marine-Bio class) are enriched in the submicron mode, as is typically observed (Guazzotti et al., 2001a; Moffet et al., 2008a; Pastor et al., 2003). The hourly counts of these particle types are widely variable with no obvious temporal (e.g. diurnal) patterns observable. While the total hourly counts of these particle types demonstrate great variability, the relative proportions of the three carbonaceous particle types to each other are quite constant. A large increase in the fraction of OC particles is noted
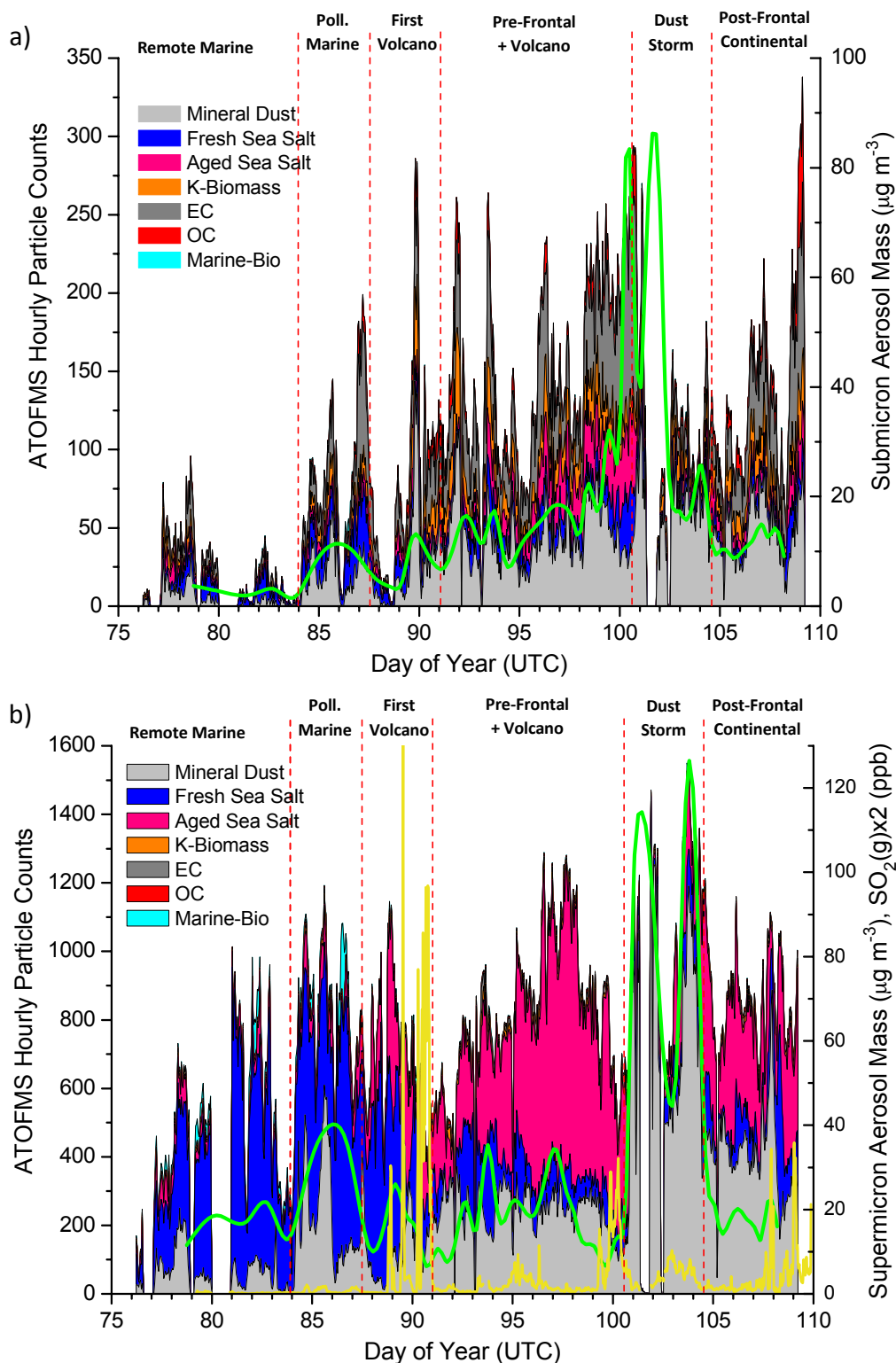
Figure 2.3. Hourly counts of principal particle types in submicron (a) and supermicron (b) size ranges, and the total aerosol mass from 4-6 hour filter samples for D_a < or > 1.1 μm (green line). The $SO_2(g)$ mixing ratio is also included (yellow line).

briefly at the onset of the Dust Storm (DOY 100.8) and at the end of the Post-Frontal Continental air mass. The contribution from OC particles compared to EC particles generally increases as the ship moves towards Japan. In general, the number fraction of OC particles is very low, well below what is typically observed by ATOFMS analysis in urban areas, for example (Liu et al., 2003; Moffet et al., 2008a; Pastor et al., 2003). This is a feature shared with other ATOFMS measurements made in marine areas that experience predominantly regional and long-range aerosol transport, including the INDOEX study (Guazzotti et al., 2001a), and recent measurements on Jeju Island, Korea during the PACDEX campaign (unpublished results).

K-biomass particles were a more consistent fraction of the detected carbonaceous particle classes and no notable biomass burning plumes were observed. The air mass back trajectories generally did not indicate substantial flow from the biomass-burning dominated regions of south-east Asia (Bates et al., 2004). The biomass particles observed here were likely predominantly produced by residential biomass/biofuel burning, as opposed to large-scale open biomass burning.

Mineral dust and sea salt particles make significant contributions to the submicron particle counts. The mineral dust fraction increases as the RHB approaches Japan, and dominates the submicron size mode during the Dust Storm air mass, and for several days afterwards. The fraction of mineral dust and carbonaceous particle classes increases with increasing air pollution levels, indicated by the submicron total aerosol mass loadings. Sea salt particles comprised periodic notable fractions of the submicron particle counts, and a clear shift from fresh to aged sea salt particles occurred as the RHB moved towards Japan and sampled increasingly polluted air. Submicron sea salt particles were highly diminished during

the Dust Storm air mass, as the winds were coming from aloft and suppressed the production of sea salt via wave action.

Supermicron particle counts were dominated by sea salt particles in the marine air masses, with increasing contributions and then dominance of mineral dust particles during the dust event. Carbonaceous particle types represented a minor fraction of the supermicron particle counts. This is a commonly observed split between submicron and supermicron single-particle types (Guazzotti et al., 2001a; Liu et al., 2003; Pastor et al., 2003; Spencer et al., 2008) as the former are produced via combustion and gas-to-particle conversion processes, while the later and mechanically generated by winds. Sea salt and mineral dust particles did have notable submicron components as well. The shift from fresh to aged sea salt is particularly evident in the supermicron size range as the air became increasingly polluted. Supermicron total aerosol mass is a poor indication of pollutant levels as the majority of the aerosol mass is composed of naturally produced sea salt. The dust event produced a rapid and prolonged increase in the total aerosol mass loading. During the Dust Storm air mass mineral dust particles were the dominant particle type and the contribution of sea salt particle was notably reduced, as previously discussed. The Marine-Bio particles were predominantly observed in the supermicron size range in the cleaner marine air masses early in the cruise. They were typically detected in discrete events that correlated with ocean regions of marine productivity (e.g. DOY 79, 82, and 86). Figure 2.3b also displays the measured SO_2 mixing ratio. Several sharp increases in $[SO_2](g)$ are observed, and these are predominantly due to flow passing over the Miyakejima volcano during the First Volcano and Pre-Frontal + Volcano air masses. The episodic spikes in SO_2 during the Post-Frontal Continental air mass are also believed to be from volcanic plumes. Note that from the Polluted Marine air mass through the rest of the study there was always $SO_2(g)$ available to interact with the aerosol

phase, and produce sulfate compounds, for example. No unique particle types were observed during these volcanic events that would indicate the emission of primary particles from the volcano. The lack of a correlation between the $SO_2(g)$ mixing ratio and the variations of the mineral dust particle counts indicates that the volcano is not producing inorganic particles that were misclassified as mineral dust. The same is true for poor correlations with $SO_2(g)$ and the carbonaceous particle types.

The lack of other unique particle classes detected during this study is notable. In a wide variety of environments other particle classes including amines, polycyclic aromatic hydrocarbons (PAH), and unique metal particle classes have been observed. Negligible mass concentrations of PAHs were measured during the RHB's cruise (Simoneit et al., 2004a). Carbon-nitrogen function groups only accounted for between 3-15% of the total organic carbon measured (Bates et al., 2004). As previously mentioned, Ca-EC and V-EC classes are often observed from vehicle and ship combustion engines, but were not observed here, even when the smaller ART-2a clusters were examined. The dominance of sea salt and mineral dust particles in this study may be a large cause of this behavior, as these composed the vast majority of particles clusters produced by the ART-2a algorithm. The RHB was also sampling at a significant distance and thus several hours to days of transport time from all major anthropogenic aerosol sources, as opposed to in a large urban area. Some of these unique particle types such as the amines may have evaporated during transport from their formation sources to the RHB, and the unobserved particle classes may have also coagulated with other particle types during transport, which obscured their unique signals. Evaporation followed by secondary processing and condensation onto other particle classes may also explain the surprisingly low abundance of the OC particle class, this is elaborated upon further below.

2.4.4   Particle class size distributions

The converging nozzle aerosol inlet used on the ATOFMS for this study has a particle transmission curve that scales as D_a^3 to a maximum at ~1.7 um, and then decreases for larger particle sizes. The ATOFMS particle counts can be scaled to co-located aerosol size distribution measurements to correct for this transmission curve and derive the ambient size distribution and absolute particle number concentrations of the detected individual particles (Qin et al., 2006). This was performed for a few example time periods during which the combined SMPS-APS number size distribution was relatively constant for several consecutive hours. The relative ATOFMS particle class fractions were multiplied by the average ambient particle concentration determined from the aerosol size distribution between 0.20 and 3.0 μm in 0.10 μm size bins during that period. This produces an aerosol size distribution in which each size bin displays the ambient concentrations of the various principal particle classes.

These classified size distributions for periods during the Polluted Marine, Pre-Frontal + Volcano, and Dust Storm air masses are shown in Figure 2.4. The number size distribution in the accumulation mode had a typically observed number mode that varies between 100-200 nm in all three periods. The Dust Storm produced somewhat elevated supermicron number concentrations, however the overall number size distribution were not significantly different. Further discussion of the aerosol's size distribution during these periods is provided by Bates et al. (2004). Even in the Polluted Marine environment when the RHB was in the middle of the Pacific Ocean, the submicron mode is dominated by anthropogenic carbonaceous particles and continental mineral dust. Sea salt particles only composed 11-33% of particles in each size bin between 0.20 and 1.0 μm, while carbonaceous particles and mineral dust comprised between 28-59% and 22-46%, respectively. This results in significant number concentrations of carbonaceous and mineral dust particles over the Pacific Ocean. The significant
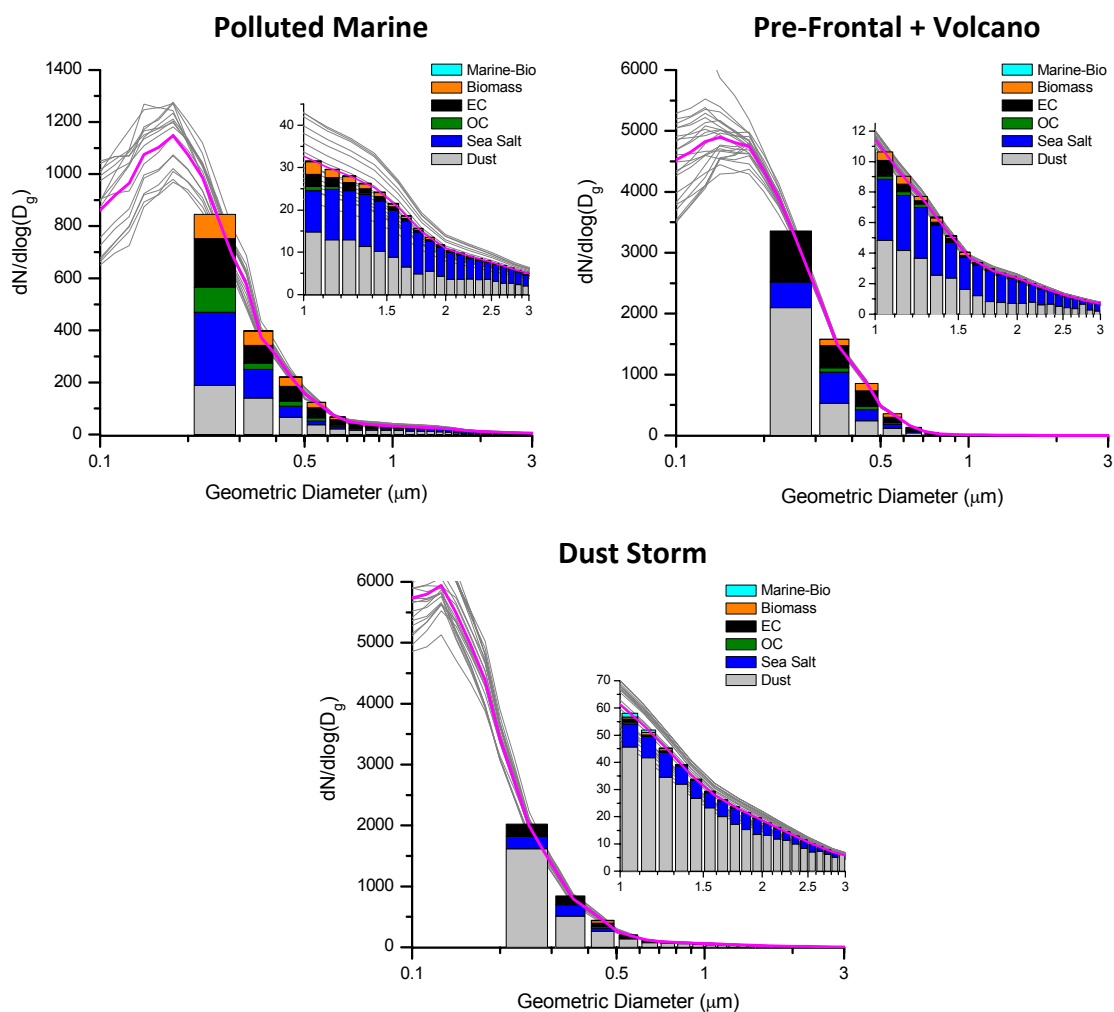
Figure 2.4. Particle class fractions of the aerosol number distribution in periods during the Polluted Marine (DOY 86.48-86.79), Pre-Frontal + Volcano (DOY 98.45-98.91), and Dust Storm (DOY 103.50-103.91) air masses. Thin grey lines are the combined size distribution determined every 30 minutes, and the thick pink line is the average of these. Supermicron size distribution is shown in the inset.

concentration of non-sea salt particles is indicative of long-range pollutant transport to the marine boundary layer. The supermicron mode is dominated by mineral dust and sea salt particles in all three of the displayed periods, with a particularly large contribution during the Dust Storm, and a coincident decrease in the sea salt number concentrations. The submicron number concentrations during the Pre-Frontal + Volcano and Dust Storm air masses were also dominated by mineral dust particles, and an appreciable concentration of EC particles.

2.4.5 Single-particle mixing state evaluation: inorganic components

The presence of predominantly secondary aerosol components that had become internally mixed with individual particles was evaluated by searching for specific ion peaks in the particle's mass spectrum. The peaks used for these queries are listed in Table 2.1. A relative peak area search is employed to account for variations in the laser energy absorbed from particle-to-particle, which affects the absolute peak areas produced (Gross et al., 2000). These peak searches were performed on a subset of each particle class that only contained dual-polarity spectra with no mis-calibrated peaks ("good-dual"). For sea salt and mineral dust particles 83% and 68% produced a properly calibrated dual-polarity spectrum, respectively. For these two classes the fractions of particles found to contain various compounds were scaled by a ratio of the total class counts to the good-dual class counts. This assumes that there is no significant chemical bias between mineral dust or sea salt particles that produce a good-dual ion spectrum and those that do not. This assumption is justified by the observation of the large fraction of single-polarity and/or mis-calibrated mass spectra produced from mineral dust and sea salt laboratory aerosol standards that both have and have not been reacted with acidic vapors to simulate atmospheric processing in simulated laboratory conditions.

Conversely, the lack of a negative ion mass spectrum from carbonaceous (EC, OC, and K-biomass) particles has been found to be predominantly controlled by the water content of the particles that is controlled by the presence of secondary hygroscopic material mixed with the particles, such as soluble inorganic salts. A large amount of water in these particle types will suppress the formation of negative ions in the ion plume produced by LDI (Neubauer et al., 1998). This has recently been confirmed by coupled chemical-optical measurements of individual particles by the ATOFMS. The light scattering optical properties of positive-ion EC, OC, and K-biomass particles ("pos-only") were found to be almost

identical to particles with a dual-ion mass spectrum whose negative ion mass spectrum contained significant signals from secondary hygroscopic compounds including nitrate and sulfate (Moffet et al., 2008b). This caused the particles to have optical properties corresponding to wet, spherical particles. Therefore, within the EC, OC, and K-biomass particle classes, any particle that had a positive-ion only mass spectrum is classified as "aged" and assumed to contain significant amounts of hygroscopic secondary material including inorganic salts (e.g. nitrate and sulfate compounds), and/or water soluble organic carbon, and water. The fractions of EC, OC, and K-biomass particles found to contain various compounds are scaled by a factor equal to the class's total particle counts divided by the sum of the good-dual plus pos-only class counts.

For mineral dust particles the production of a negative ion mass spectrum has not been observed in laboratory experiments to be strongly influenced by the water content of the particle and therefore this assumption is not supported for dust particles. Sea salt particles are initially composed of soluble hygroscopic compounds and therefore the lack of a negative-ion spectrum cannot be used to infer their mixing state with secondary compounds.

The ion peaks listed in Table 2.1 represent the most significant secondary aerosol components that are expected and commonly observed to compose the largest fractions of secondary aerosol mass. Nitrate and sulfate are the major inorganic products of various gas-to-particle conversion processes involving heterogeneous/multiphase chemistry of nitrogen and sulfur oxides that produce nitrate and sulfate salts as their stable end products. Titration of the nitric and sulfuric acid products by ammonia gas produces ammonium nitrate, ammonium bisulfate, and ammonium sulfate. Reactions of HNO_3 and H_2SO_4 with NaCl in sea salt and mineral dust, and with $CaCO_3$ and other carbonates in mineral dust particles, displaces HCl(g) and CO_2 to the gas phase and forms $NaNO_3$, Na_2SO_4, $Ca(NO_3)_2$, $CaSO_4$ and other products in the particle

phase (Gard et al., 1998; Krueger et al., 2004). Similar reactions can occur with KCl and similar salts in biomass particles, producing KNO_3 and K_2SO_4 as particulate products (Li et al., 2003). Coagulation or condensation of ammonium nitrate and ammonium sulfate onto preexisting particles also mixes these particles with secondary aerosol material. While particles including sea salt, mineral dust, and combustion particles can contain nitrate and/or sulfate at their emission source, the concentrations of primary nitrate and sulfate are a small fraction of the nitrate and sulfate compound mass that forms during atmospheric processing. Therefore nitrate and sulfate, as well as ammonium, are regarded as secondary aerosol components in this analysis since all the particles measured, excluding sea salt, had experienced at least several hours of atmospheric transport from their emission sources to the RHB.

2.4.6   Mixing state of secondary inorganic aerosol components

The principal particle class fractions detected in the six broad air masses are shown in Figure 2.5 as a function of particle diameter. Overlain on each particle class is the fraction that was internally mixed with nitrate or sulfate, with nitrate + ammonium or sulfate + ammonium, with nitrate + sulfate, or with nitrate + sulfate + ammonium. Ammonium is indicated by a green colored pattern. "Aged" particles are EC, OC, or K-biomass particles that produced a positive-ion only mass spectrum and contained significant amounts of secondary hygroscopic material such as nitrate, sulfate, ammonium, and/or WSOC, causing the particles to absorb large amounts of water. Size bins that contained fewer than 30 classified particles in a particular air mass are excluded to avoid poor counting statistics. The size-segregated secondary total aerosol mass of ammonium, nitrate, and nss-sulfate are also shown, obtained from co-located filter measurements. These indicate the degree and nature of predominantly anthropogenic pollution in each air mass. Combined with the single-particle mixing state data

Figure 2.5. Size-resolved mixing state of principal particle classes with major secondary aerosol components: sulfate, nitrate, ammonium, and mixtures thereof, in the six broad air masses. The size-segregated secondary aerosol mass sampled by the cascade impactor is also included. The legend is provided below.

Particle Class
- Marine-Bio
- Biomass
- EC
- OC
- Sea Salt
- Mineral Dust

Mixing State
- Amm + Nitr
- Nitrate
- Amm + Nitr + Sulph
- Nitr + Sulf
- Amm + Sulf
- Sulfate
- Aged
- Non-mixed

Secondary Aerosol Mass
- Sulfate
- Nitrate
- Ammonium

Figure 2.5.

First Volcano & Marine

Pre-Frontal + Volcano

Figure 2.5. continued

Figure 2.5. continued
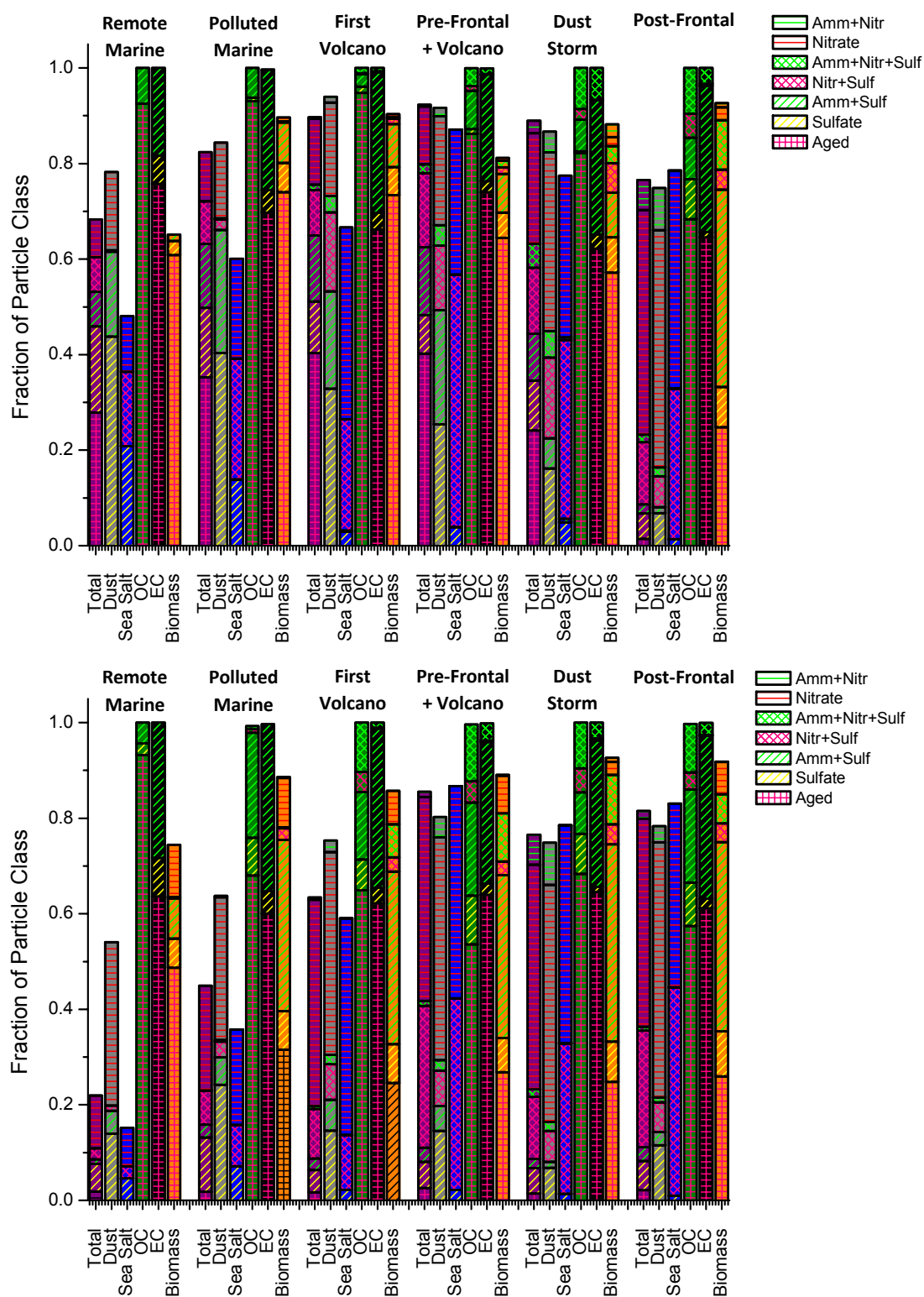
Figure 2.6. Particle fractions of primary particle classes mixed with various secondary inorganic components in submicron (top) and supermicron (bottom) particles in different air masses.
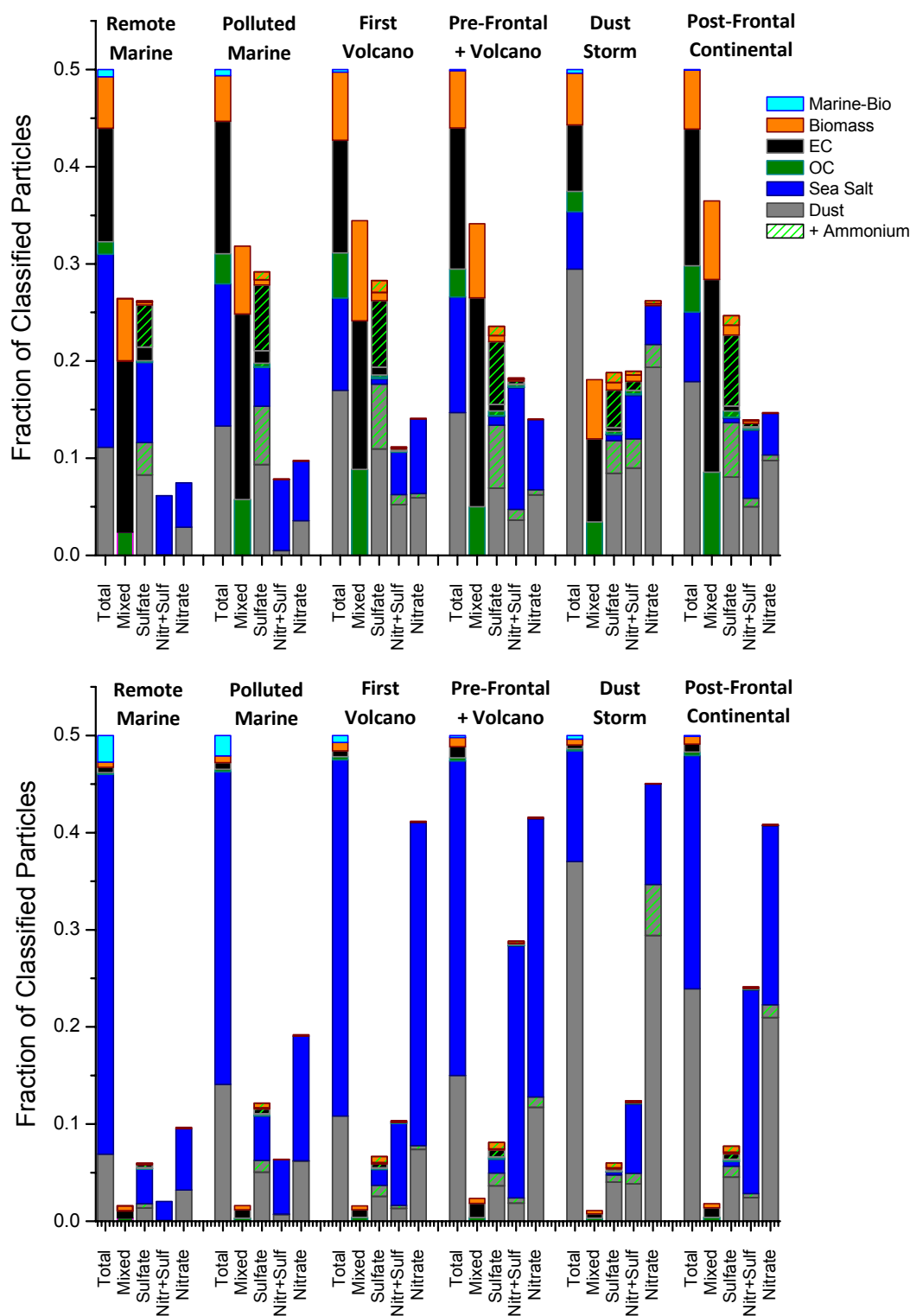
Figure 2.7. Particle fractions of secondary inorganic components mixed with various primary particle classes in different air masses. The total column represents the fractions of all primary particle classes, regardless of their mixing state, and has been divided by 2. Green pattern indicates the particles were also mixed with ammonium.

these figures indicate what particle classes and mixing states contained the majority of the sampled inorganic aerosol mass in the aerosol ensemble filter measurements.

The same data shown in Figure 2.5 is summarized using the same classification scheme for the total submicron and supermicron particle size ranges in Figures 2.6 and 2.7 to facilitate comparisons between the different air masses. These figures display the aerosol mixing state information in different but complementary manners. Figure 2.6 shows the mixing state of each principal particle class with secondary inorganics to explore to what degree each particle class was mixed with various inorganic compounds. The total height of each column indicates the fraction of each particle class that was classified as mixed with any of the secondary inorganics, while the Total column indicates the overall mixing state of all the particles in that size and air mass. Figure 2.7, however, displays the distribution of each secondary inorganic compound across the different principle particle classes. This demonstrates what particle classes each secondary inorganic compound was predominantly mixed with. The height of each column displays the fraction of total particles (all classes) mixed with that secondary compound. The Total column shows the total principal particle class fractions in that air mass and has been divided by 2 for display purposes.

The total fraction of particles classified as mixed with any secondary inorganic increased as the RHB approached Japan during the first four air masses. This is evident in the submicron particles (68% increasing up to 92%) and particularly in the supermicron particles (22% increasing up to 87%) (Figure 2.6). The fraction of mineral dust particles in both size ranges also increases during the cruise towards the Asian continent (Figure 2.7).

In the four pre-Dust Storm air masses the mineral dust particles are a significant fraction of both the submicron (22-34%) and supermicron (14-30%) particle types (Fig. 2.7). The dust was mixed to a highly variable degree with sulfate, nitrate, and ammonium. Sulfate

and ammonium + sulfate are more dominant in submicron dust, while nitrate is more prevalent in supermicron dust particles. There was a larger fraction of unmixed dust particles in the largest supermicron size bins. Sea salt particles display a wide range of mixing with secondary inorganics, and the fraction of mixed sea salt particles increased dramatically as the RHB approached Japan and sampled increasingly polluted air, from 47% to 86% for submicron and from 15% to 87% for supermicron sea salt particles. Sea salt is mixed with either sulfate or nitrate, and mostly with sulfate + nitrate when the sea salt is highly aged in the First Volcano & Marine and Pre-Frontal + Volcano air masses. In the Marine and Polluted Marine air masses only sea salt particles contained nitrate + sulfate, but in the later air masses mineral dust and to a small degree the carbonaceous particle classes were also classified as mixed with nitrate + sulfate (Fig. 2.6). Similar to the mineral dust, the smaller sea salt particles are generally more highly mixed with nitrate and/or sulfate than the larger sea salt particles. Sea salt particles never contained ammonium.

All of the four pre-Dust Storm air masses contained significant fractions of carbonaceous particles in the submicron mode, even in the clean Remote Marine air mass which had low pollution levels and had not experienced continental influence for more than 5 days. The number fractions of the three carbonaceous particle classes were quite constant in both size ranges in the first four air masses (Fig. 2.7). Particularly notable is the large degree of mixing of these carbonaceous particles with secondary inorganic compounds (Figs. 2.5 & 2.6). Virtually 100% of the (small overall fraction) of OC particles are "aged" and likely mixed with significant amounts of sulfate (and possibly ammonium) as this dominated the submicron secondary aerosol mass. The high submicron sulfate mass loading in the Pre-Frontal + Volcano air mass was caused by mixing with a $SO_2(g)$ rich plume from the Miyakejima volcano (Bates et al., 2004). Essentially 100% of the EC particles are also

classified as either "aged' or mixed with sulfate + ammonium in both size ranges in the first four air masses (Fig. 2.6).

The K-biomass particles display a similar but smaller and much more variable degree of mixing as the OC and EC particles, classified as either "aged", mixed with sulfate, or sulfate + ammonium. The total fraction of K-biomass particles that were mixed ranges from 65% to 91% in the submicron range, and from 74% to 90% for supermicron particles. The K-biomass particles are somewhat less mixed with ammonium compared to EC particles. A small fraction of the supermicron K-Biomass particles are mixed with nitrate (3-10%), while EC was never classified as mixed only with nitrate. The K-biomass particles and to a lesser extent EC particles are increasingly mixed with nitrate + sulfate + ammonium in the supermicron range in the later more polluted air masses.

The mixing state of the Marine-Bio particles cannot be evaluated using this method because they never produced negative-ion mass spectra. Their largest contributions to the total particle class fractions are seen in the supermicron sizes during the Remote Marine and Polluted Marine air mass periods.

The arrival of the dust frontal produced large changes in the relative contributions of the principal particle types in both size ranges (Figs. 2.5 & 2.7), though the mixing state of each separate particle class was not drastically different compared to the pre-frontal air masses (Fig 2.6). The mineral dust particles were clearly the dominant particle class in both size ranges and showed increased degrees of mixing with ammonium along with sulfate in submicron dust and with nitrate in supermicron dust. The major change in the aerosol mixing state upon the dust front arrival was a dramatic shift of secondary nitrate being primarily mixed with sea salt particles to being mixing with mineral dust, particularly in the supermicron range (Fig. 2.7). In the Pre-Frontal air mass 69% of the supermicron particles

classified as mixed with nitrate were sea salt compared to 31% mineral dust, versus 76% in mineral dust particles and 23% in sea salt during the Dust Storm air mass. The particle class fractions mixed with sulfate or sulfate + nitrate has smaller increased contributions from mineral dust particles by the dust storm; mineral dust particles accounted for more than 60% of the submicron particles classified as these mixing states in the Dust Storm air mass. The fraction of sulfate + nitrate supermicron particles mixed with sea salt was greatly reduced during the Dust Storm. The submicron dust also displayed higher fractions of dust mixed with both nitrate + sulfate, along with a smaller fraction of nitrate + sulfate + ammonium. Despite the large degree of mixing with secondary inorganics there was still a sizeable fraction of unmixed mineral dust, 23% of total dust particles in the supermicron size range and 12% in the submicron range (Fig. 2.6).

Although its overall contribution was greatly reduced, sea salt particles continued to be substantially mixed with nitrate and nitrate + sulfate, but unlike the mineral dust still did not exhibit any mixing with ammonium. The fraction of sea salt particles mixed with sulfate but not nitrate was also extremely small, while there were notable fractions of sea salt + sulfate in the Marine and Polluted Marine air masses. While the overall contributions from carbonaceous particle types were greatly reduced during the dust event they continued to be highly mixed with nitrate + sulfate + ammonium. Nearly 100% of the EC and OC particles continued to be mixed with secondary inorganics, particularly sulfate + ammonium, in both size ranges (Fig. 2.6). The OC particles displayed a greater degree of mixing with nitrate in addition to sulfate + ammonium, compared to the EC which was less mixed with nitrate. About 90% of the K-Biomass particles were mixed with inorganics in both size ranges, a slightly higher fraction than in the preceding Pre-Frontal air mass.

The Post-Frontal air mass following the dust storm saw a return of the overall particle class fractions to similar to what was observed in the Pre-Frontal air mass, however the contributions from mineral dust particles in both size ranges are still elevated (Fig. 2.7). The total sulfate, nitrate, and ammonium aerosol mass loadings are significantly reduced compared to the Dust Storm air mass (Fig. 2.5). The supermicron dust particles are no longer substantially mixed with ammonium, however the submicron dust continues to be mixed with sulfate + ammonium to a large degree. Carbonaceous particles returned to their prefrontal abundance in the submicron mode and continue to be mixed to very large degrees with sulfate or classified as "aged". Once again the K-biomass particles display a somewhat smaller degree of mixing than the EC or OC particles do. The EC particles are the most highly mixed with sulfate + ammonium, while OC and K-biomass particles are mixed with both sulfate and/or nitrate.

The typical particle types that the secondary inorganic compounds were mixed with can be summarized as follows from Figure 2.7. In the submicron mode sulfate was mixed with all five particle classes, but was somewhat enriched in the carbonaceous particle types when the total particle class fractions are considered. Sulfate mixed with carbonaceous particles was also almost always also mixed with ammonium, while sulfate in sea salt never contained ammonium, and ammonium was only found in ~20-50% of dust particles with sulfate. Particles mixed with nitrate + sulfate were predominantly sea salt and mineral dust, and nitrate was also primarily found in these two particle types. Carbonaceous particles comprised a very small fraction of the nitrate-containing particles. Particles mixed with nitrate were also mixed with ammonium much less frequently than particles mixed with sulfate. EC particles were the most frequently classified as "aged", but K-biomass and OC also made significant contributions (mineral dust and sea salt cannot fall under this classification by definition). The

"aged" particles were likely highly mixed with sulfate, as it was the major secondary inorganic component in the submicron aerosol mass, and ammonium and WSOC may have also contributed. This further adds to the enrichment of sulfate with the carbonaceous particle types. The total fractions of submicron particles mixed with sulfate (and ammonium) or classified as "aged" are much larger than the nitrate + sulfate or nitrate mixed total fractions. This is expected due to the sulfate and ammonium aerosol mass being maximized in the submicron mode.

The major differences observed in the supermicron particles is the dominance of particles mixed with nitrate and nitrate + sulfate, which is always larger than the sulfate or "aged" particle mixing state fractions. The total fraction of supermicron particles mixed with nitrate is also much more variable than the submicron fraction mixed with sulfate, and dramatically increases in the more highly polluted air masses. Similar to the submicron nitrate + sulfate, and nitrate-containing particles, nitrate and nitrate + sulfate are primarily mixed with supermicron sea salt and dust. The fraction of supermicron particles mixed with ammonium is very low, regardless of the other inorganics they are mixed with. One exception is during the Dust Storm air mass, where mineral dust contained a notable fraction of dust mixed with nitrate + ammonium. The small fraction of supermicron particles mixed with sulfate continues to be distributed between the five particle classes, with some enrichment in the carbonaceous particle classes again observed.

Ammonium was never found to be mixed with particles that did not also contain nitrate and/or sulfate, except for a few discrete periods when a small fraction of mineral dust was mixed with ammonium but not nitrate or sulfate. This is attributed to dust particles that were acidified by accumulating secondary $HCl(g)$, a topic that is explored in more detail in Chapter 3.

2.4.7   Single-particle mixing state evaluation: organic components

Oxidation of organic carbon vapors followed by gas-to-particle conversion mixes secondary organic aerosol (SOA) with pre-existing particles. The SOA components can continue to react in the condensed phase with both gaseous and particulate phase reactants. Homogeneous nucleation of SOA can also cause new particle formation events and produce particles that are predominantly composed of SOA. Coagulation with organic-containing particles mixes other particle types with organic components. Due to the large degree of fragmentation experienced by organic compounds during LDI, molecular ions are infrequently detected which makes it difficult to assign a particular organic carbon peak to either a primary or secondary organic aerosol parent compound. Oxidized organic carbon aerosol (OOA) compounds are typically associated with SOA, however OOA can also be present in particles at their emission sources, such as in vehicular and biomass-burning emissions. Therefore, caution is required in attributing all OOA to SOA. In this analysis, three major organic carbon ion peaks are used to evaluate the mixing state of organic carbon with various particle types. The C_3H^+ (m/z +37) ion is commonly observed in the ATOFMS mass spectra of various organic compounds in pure and mixed particles (Silva and Prather, 2000; Spencer and Prather, 2006). It is a major peak in some of the OC particle clusters, though not in the one shown in Figure 2.2. The C_3H^+ peak is a good almost universal marker for organic carbon compounds in general, be they primary or secondary, and they may or may not contain various oxygenated functional groups. A similarly observed universal peak at m/z +27 ($C_2H_3^+$) was not used here because of interference from aluminum common to mineral dust particles, given the large abundance of dust particles in this study. The $C_2H_3O^+$ (m/z +43) peak is the best ATOFMS universal marker for oxidized carbon. Its abundance typically correlates with ambient ozone concentrations (which produce OOA), as well as with the aerosol mass spectrometer's (AMS)

m/z +44 (CO_2^+) marker for OOA. It is used here to find particles containing OOA and is likely predominantly present due to SOA compounds, but the presence of OOA from POA components (e.g. levoglucosan in biomass burning particles) should not be neglected. Finally the oxalate peak (m/z -89), from oxalic acid, is a marker for organic diacids. Oxalic acid is typically the dominant component of aerosol water soluble organic carbon (WSOC), as was observed in this study (Mochida et al., 2003b). It can be produced through gas-phase photochemistry, aqueous chemistry, and in-cloud processing. There is debate regarding the primary production of oxalic acid in vehicular exhaust (Huang and Yu, 2007). Chapter 5 presents a detailed examination of the mixing state of oxalic acid during ACE-Asia, finding it is predominantly mixed with mineral dust and sea salt particles, in both submicron and supermicron size ranges, and was produced via photochemistry and gas-to-particle partitioning. Here the oxalate peak is used to identify particles containing organic acids, which in this study are predominantly produced by SOA formation.

2.4.8   Mixing state of organic aerosol components

Analogous to the analysis of the mixing state of inorganic aerosol components, the mixing state of organic components is evaluated from two different perspectives. In Figure 2.8 the particle class fractions of all particles containing one of the three OC markers are displayed for submicron and supermicron size ranges in the six broad air masses. The total height of each column represents the total fraction of particles containing that marker. The Total column displays the total particle class fractions in that air mass and has been divided by 2 and 10 for display purposes for the submicron and supermicron sizes, respectively. The fractions of each principal particle class that contained one of the three OC markers, or combinations of these, are shown in Figure 2.9. The height of each column is the total fraction

of that particle class mixed with OC compounds, and the Total column represents the total fraction of all classified particles mixed with OC.

Submicron particles were most frequently mixed with the general OC marker (C_3H^+), followed by OOA and diacids. The fraction of particles containing these components increased as the RHB approached Japan, with a notable exception during the Dust Storm air mass (Fig. 2.8). These trends are expected given that the C_3H^+ marker is the most general OC marker of the three while the diacid marker corresponds to a specific molecular parent ion, oxalate. The relative distribution of the C_3H^+ marker between the EC, OC, K-biomass and mineral dust particle classes was very constant in all of the air masses excluding the Dust Storm, in which the total fraction of particles containing the C_3H^+ was reduced but the relative contribution from mineral dust particles increased. The presence of the C_3H^+ ion in the carbonaceous particle types (EC, OC, and K-biomass) is likely due to POA compounds that exist at these particles' emission sources. In Figure 2.9, almost 100% of the sub- and supermicron EC particles contained the C_3H^+ marker (in addition to other OC components). A smaller fraction of OC particles actually contained the C_3H^+ peak compared to EC, but almost 100% of the OC particles had at least one of the three OC markers, as would be expected. Comparing the EC to OC particle classes in Figure 2.8, the EC particles were generally more mixed with the C_3H^+ marker and with OOA (m/z +43), while the OC particles contained less C_3H^+, but were more frequently mixed with OOA and diacids. The OC particles virtually always contained the OOA marker, either on its own or along with the C_3H^+ and/or oxalate peak, in both size ranges and all air masses.

The fractions of K-biomass particles mixed with organic components were much more variable than the EC and OC particles. The K-biomass fraction mixed with any of the three OC components varied between 70% and 86% for submicron K-biomass, with no systematic

113

Figure 2.8. Distribution of organic carbon markers amongst the principal particle types in submicron (top) and supermicron (bottom) particles. Total refers to all particles in that size and air mass and has been divided by 2 for submicron and by 10 for supermicron size ranges.

Figure 2.9. Principle particle class fractions containing combinations of organic carbon markers in different air masses for submicron (top) and supermicron (bottom) particles. Total refers to all particles in that size and air mass.
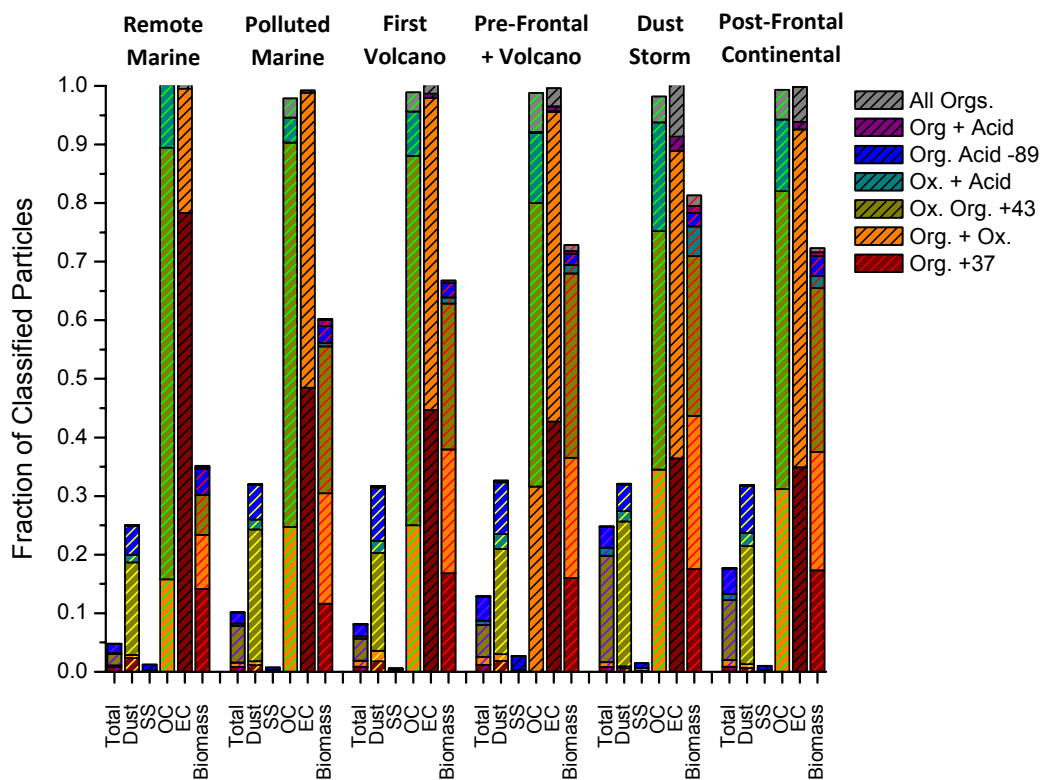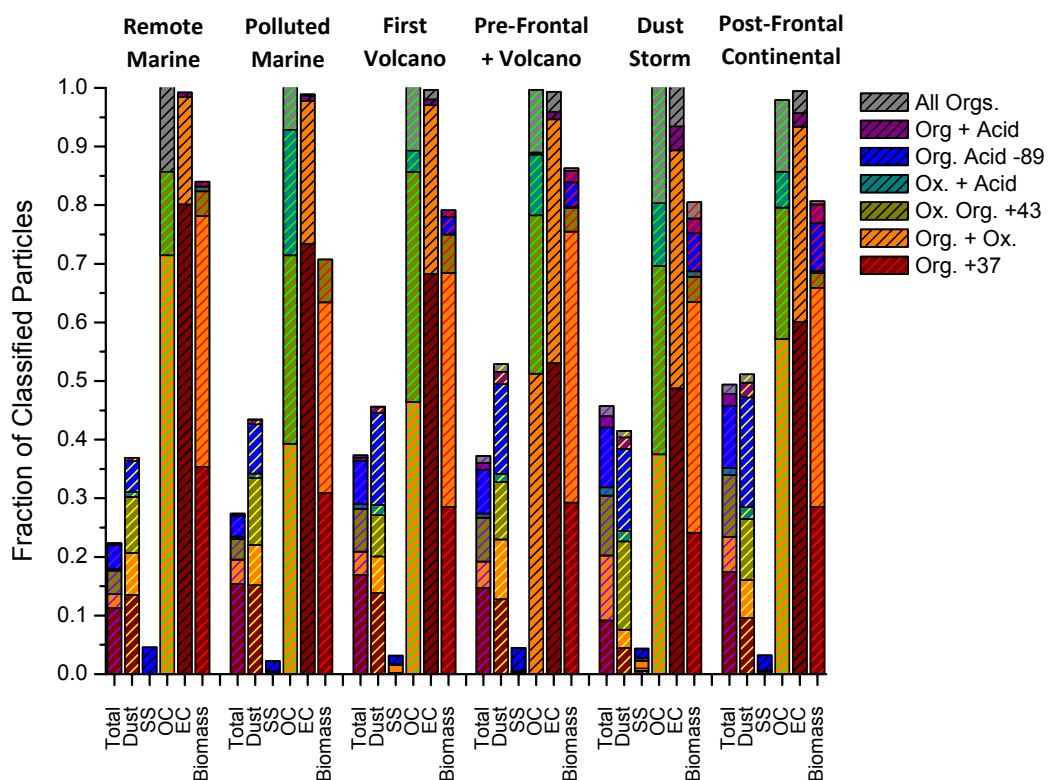
increase as the RHB approached Japan (Fig 2.9). The supermicron K-biomass's mixing with OC was even more variable, ranging from 36% to 82%, with a clear increase as the RHB approached Japan. This suggests that a significant fraction of the OC components internally mixed with the K-biomass particles was secondary in nature, causing this temporal variability, particularly in the supermicron size range. Supermicron biomass particles had similar proportions of the different types of OC components, being predominantly mixed with the C_3H^+ marker, and/or OOA. The OC component fractions in the submicron biomass were more variable, with a notable increase in the fraction of biomass mixed with the oxalate diacid in the later air masses near Japan.

Mineral dust particles were also mixed with organic compounds. In this case the majority of the OC can be safely assumed to be secondary in nature, because Asian dust particles collected from their desert source regions and analyzed by the ATOFMS did not contain any of the three OC peaks used in this analysis. Accordingly, the fraction of dust particles mixed with OC is much smaller than the carbonaceous particle classes, and this fraction is also relatively constant between air masses. The total fraction of dust particles containing any of the OC components varied between 37% and 52% for submicron and between 25% and 33% for supermicron particles (Fig. 2.9). The OC mixed with dust was also composed of the oxalate diacid to a much larger extent than in the carbonaceous particles.

The only notable OC compound found mixed with sea salt particles is oxalate. While sea salt particles can contain POA from the organic ocean surface microlayer (Simoneit et al., 2004a), these organic compounds are typically not detected when analyzed by the ATOFMS. Therefore OC peaks found in sea salt particles are almost exclusively secondary in origin. While the fraction of total sea salt particles mixed with oxalate is very small (< 4%) (Figure

2.9), the contribution of sea salt to the particle types mixed with oxalate is quite significant in the supermicron size range, particularly in the Pre-Frontal airmass (Figure 2.8).

2.4.9 Indirect evidence of a large "pure" sulfate particle event in a volcanic plume

The ATOFMS can detect virtually all potential atmospheric particle types using LDI with a 266 nm UV laser pulse. Particles composed purely of ammonium sulfate, sulfuric acid, and other simple inorganic sulfate compounds are the major exception to this as these compounds do not have an appreciable absorption cross section at 266 nm (Kane and Johnston, 2000). Thompson et al. (1997) found that pure sulfuric acid particles were only ionized at a wavelength of 157 nm and not longer wavelengths, and speculated that this could result in SPMS instruments being unable to detect very pure sulfuric acid particles during ambient sampling. This behavior was in fact observed while sampling with an ATOFMS during the Atlanta Supersite Experiment (Wenzel et al., 2003). The presence of a significant concentration of pure submicron sulfate particles was inferred in that study from a dramatic decrease in the ATOFMS's particle hit rate coupled with an increased particle light scattering event rate. This is caused by the large light scattering cross section and extremely small absorption cross section of pure sulfate particles.

Similar correlations indicating a significant concentration of pure submicron sulfate particles were observed in one brief distinct period during the ACE-Asia campaign, towards the end of the Pre-Frontal + Volcano air mass. A sharp decrease in the ATOFMS particle hit rate was correlated with an increase in the submicron aerosol light scattering and a decrease in the aerosol light absorption, these are shown in Figure 2.10. While any particle type that does not absorb UV or visible light could explain this behavior, pure ammonium sulfate/bisulfate or sulfuric acid particles are the most likely candidates as they are composed of the most
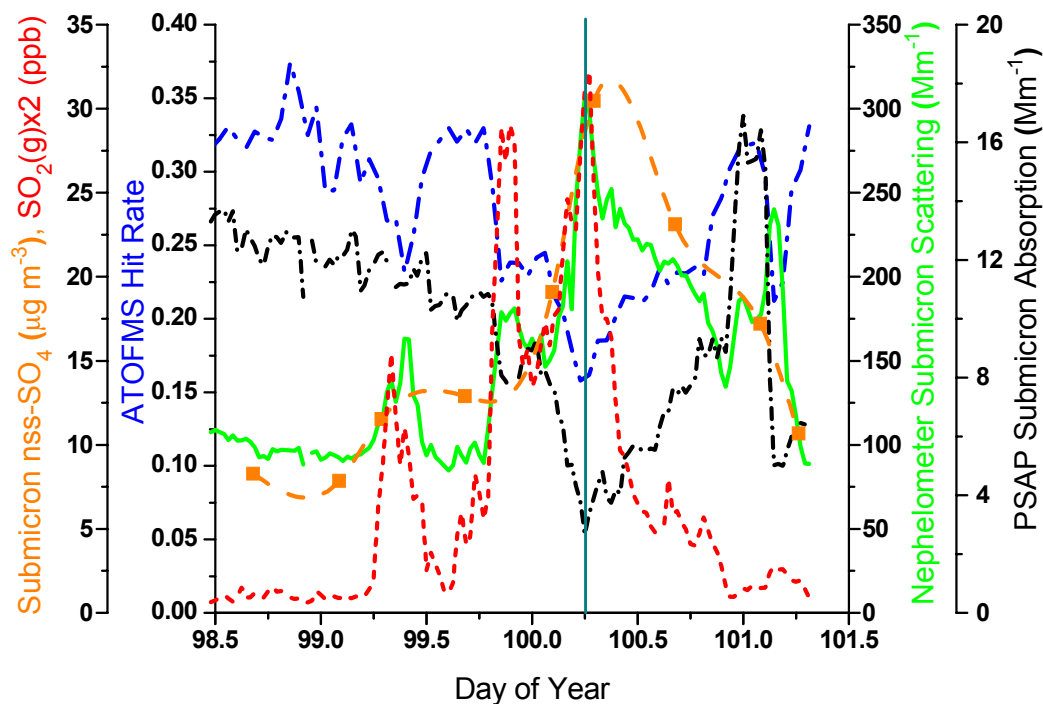
Figure 2.10. Variations in the submicron nss-sulfate aerosol mass, ATOFMS particle hit rate, and aerosol light scattering (550 nm) and absorption measured by a nephelometer and PSAP, respectively. The correlations at DOY 100.25 (green vertical line) indicate the presence of a significant fraction of relatively pure sulfate particles in the Pre-Frontal + Volcano air mass just prior to the dust front that arrived on DOY 100.8.

abundant inorganic compounds typically measured in submicron aerosol samples. This is supported by the coincident increase in the submicron sulfate aerosol mass and the $SO_2(g)$ mixing ratio (from the Miyakejima volcano) at the same time that the ATOFMS hit rate and aerosol light scattering sharply increased (Fig. 2.10). The aerosol size distribution displayed a brief ultrafine mode centered first at ~20 nm from DOY 100.21-100.31 and then centered at ~60 nm from DOY 100.32-100.34. During this period the major mode in the number size distribution occurred at ~250 nm. These discrete ultrafine modes in the aerosol's size distribution further support the hypothesis that a significant number of relatively pure sulfate particles produced from homogeneous nucleation were present, and decreased the ATOFMS

hit rate as they grew above the 200 nm lower limit of the instrument's particle transmission curve.

This event lasted for approximately 7 hours, from DOY 100.2-100.5, before all of these indicators rapidly returned back to values similar to those measured before this event. The major dust frontal arrived a few hours later on DOY 100.83. While this presents very strong indirect evidence for significant pure sulfate particles during this period, recall that sulfate was also found mixed with other particle types in the Pre-Frontal + Volcano air mass. Of the total submicron particles, 24% were classified mixed with sulfate, 18% mixed with nitrate + sulfate, and 34% as "aged", likely due to mixing with sulfate (and ammonium), and the sulfate mixed to varying degrees with all the particle classes (Fig. 2.7). This was the only period in which the ATOFMS exhibited a significant and episodic decrease in its particle hit rate. Similar correlations were not observed either during the First Volcano air mass, or in the volcanic plumes sampled during the Post-Frontal air mass.

2.4.10 Summary and basis of the aerosol mixing state

In this section, some of the major features of the observed aerosol mixing state are summarized and the probable atmospheric processing mechanisms that produced these results are discussed. Submicron particles overall were more highly mixed with both inorganic and organic (predominantly secondary) compounds than the supermicron particles were (Figs. 2.7 & 2.9). This is likely the product of two main effects: the longer atmospheric lifetime of submicron particles, and the more substantial atmospheric processing of submicron particles via heterogeneous chemistry, condensation, and coagulation. Particles in the accumulation mode (D_a = 100-1000 nm) typically have the longest atmospheric lifetimes, while supermicron particles experience faster rates of gravitational settling. Therefore, the submicron particles measured in the early air masses far from the continent may have experienced longer periods

of atmospheric processing than the supermicron particles. Furthermore, the rates of heterogeneous reactions, coagulation, and condensation are typically greater for submicron particles compared to supermicron, leading to a greater extent of atmospheric processing.

Particles mixed with sulfate, ammonium, and sulfate + nitrate were more prevalent in submicron particles, while particles mixed with nitrate were more significant in supermicron particles. This is caused by some of the same processes discussed above. Submicron particles typically experience greater atmospheric processing due to their larger surface area to volume ratios. Sulfate tends to maximize in submicron particles because its formation is largely limited by diffusional uptake of $SO_2(g)$ and thus maximizes at the aerosol's surface area maximum (Song and Carmichael, 1999). This is typically in the submicron mode, as was observed during the ACE-Asia campaign (Bates et al., 2004). Nitrate products such as nitric acid and ammonium nitrate are semivolatile while sulfate products have very low vapor pressures. Sulfuric acid is also a stronger acid than nitric acid. Therefore nitrate can be displaced from submicron particles by sulfuric acid, and partition to larger, less acidified particles (Song and Carmichael, 1999). Nitrate also accumulates in supermicron particles, particularly in this study, because the major alkaline aerosol particles (mineral dust and sea salt) dominate the supermicron mode. This also contributes to nitrate primarily mixing with mineral dust and sea salt particles, and less with carbonaceous particles (Fig. 2.7).

Ammonium accumulates in particles either by titrating secondary acids that form in the particles, or by condensation of ammonium salts. Both these processes favor ammonium mixing with submicron particles, as they are typically more highly acidified, and because ammonium sulfate formation is thermodynamically favored versus ammonium nitrate – sulfate is maximized in the submicron mode.

EC and OC particles were virtually always mixed with secondary inorganics, particularly sulfate and ammonium, in both size ranges, and all air masses (Fig. 2.6). The extremely high and invariable fraction of mixed OC and EC particles indicates that these particles become mixed quickly near their emission sources, and do not lose significant amounts of these inorganic compounds during long range transport. The presence of inorganic compounds in these particles at their sources could also explain these results. However, other source characterization studies and ambient measurements near combustion sources have observed much larger variability in the mixing state of EC and OC particles that does not support this hypothesis (Moffet et al., 2008a; Toner et al., 2008). All of the EC particles, and a large fraction of the OC are produced by combustion, from vehicles in particular. These primary particles typically have initial diameters between ~50-100 nm (Bond et al., 2006). The particles detected by ATOFMS are larger than 200 nm, and are likely the result of the primary EC and OC particles growing by coagulation and mixing with secondary material, such as ammonium sulfate. Considering this it is expected that a large fraction of the EC and OC particles would contain secondary inorganic compounds, particularly as these measurements were made at least several hours from large combustion sources of these particles.

The K-biomass particles, however, were less mixed with inorganic species than the EC and OC particles, and this fraction was highly variable between the different air masses (Fig. 2.6). This indicates that the inorganic compounds mixed with the biomass particles do not exist in the particles at their source to a great extent, and that they also experienced less atmospheric processing relative to the EC and OC particles. An explanation for the large variability in the mixed fractions is the larger primary size of biomass particles compared to EC and OC from combustion. Biomass particles have a wide range of initial particle diameters

based on their fuel sources and burning conditions, but typically peak between 100 and 600 nm (Bond et al., 2006). Reid et al. (2005) reported an average count medium diameter of ~130 nm for fresh biomass smoke. The larger primary size of biomass particles will result in the ATOFMS observing a greater fraction of biomass particles that have not grown significantly through mixing with secondary inorganic material. Therefore, not all of the detected biomass particles will be mixed with inorganic compounds and the temporal variability can be attributed to variations in the degree of secondary processing experienced by the biomass particles during transport.

The very small overall fraction of submicron OC particles measured compared to EC and K-biomass is notable. This has been observed in other environments in which the majority of anthropogenic aerosols sampled are due to long-range transport (Guazzotti et al., 2001a; Spencer et al., 2008). A likely explanation for this is that a significant number of OC particles evaporated during transport. The OC particles could also not have grown large enough to be detected by the ATOFMS, but this is not supported by the significant fraction of EC particles observed, and the very high degree of mixing with inorganics observed fro the EC and OC particles. ATOFMS measurements near typical sources of OC particles typically observe much higher number fractions of submicron OC in this size range (Liu et al., 2003; Moffet et al., 2008a; Pastor et al., 2003). Oxidation of the evaporated OC compounds followed by their condensation onto other pre-existing particle types (Robinson et al., 2007) could explain the high degree of mixing observed for the various particle classes with OC components. Between 22-49% of submicron and 5-18% of the total supermicron particles were mixed with OC (Fig. 2.9), and the low fraction of OC particles made only small contributions to these total particle numbers (Fig. 2.8).

The major difference between the mixing state of organic carbon components with submicron and supermicron particles is that while the general C_3H^+ OC marker was the most abundant in the submicron mode, the oxalate diacid peak was found as often or more frequently than C_3H^+ in the supermicron particles (Fig. 2.8). However, the fraction of supermicron particles mixed with OC was much less than for the submicron particles (Fig. 2.9) (note the different y-axis scales in Fig. 2.8). OC aerosol number and mass are generally maximized in the submicron aerosol size range (Bates et al., 2004), due to their primary combustion and secondary gas-to-particle conversion origins. The larger contribution to OC from oxalate in supermicron particles reflects the secondary nature of the diacid compounds that in this environment largely partitioned to the alkaline mineral dust and sea salt particles, which were maximized in the supermicron size range (Chapter 5). This caused the supermicron OC compounds to be dominated by oxalate, a major component of SOA. Even in the supermicron mode the C_3H^+ and OOA components were still largely mixed with the carbonaceous particle types, with smaller contributions from mineral dust and almost no sea salt. This is a very different mixing state from supermicron oxalate, it was almost exclusively mixed with dust and sea salt particles (Fig. 2.8).

2.5 Conclusions

The mixing state of individual aerosol particles with inorganic and organic components exhibited larger variations between principle particle classes, particle size, and in different air masses. In particular, sulfate was predominantly mixed with submicron particles and did not exhibit a strong bias for particular particle types. Nitrate, however, was mixed to a greater extent with supermicron particles and was significantly enriched with inorganic particle classes: mineral dust and sea salt. The dust storm caused the vast majority of nitrate to be found in mineral dust particles. Ammonium was mostly mixed with submicron particles

with sulfate-containing particles. EC and OC particles were always mixed with secondary inorganics, sulfate and ammonium in particular, in both size ranges. K-biomass particles were less mixed and contained relatively more nitrate than the EC and OC particles did. While submicron particles were mixed to a greater extent with organic components, organic diacids were enriched in supermicron particles with mineral dust and sea salt in particular.

The mixing state observed in the ACE-Asia aerosol has numerous implications for the aerosol's physicochemical properties and direct and indirect effects. The very high degree of mixing of EC with sulfate and ammonium will produce an aerosol with a much smaller single-scattering albedo compared to an externally mixed EC and ammonium sulfate aerosol, resulting in a significantly larger positive radiative forcing (Bond et al., 2006; Jacobson, 2001; Ramanathan and Carmichael, 2008). Accumulation of secondary inorganics by EC and OC can also increase these particles' ability to act as CCN and nucleate warm clouds (Petters et al., 2006a; Pierce et al., 2007). Formation of nitrate salts in mineral dust particles can convert initially insoluble mineral compounds such as calcite into soluble hygroscopic products. This will increase the warm cloud-nucleation potential of these mineral particles (Gibson et al., 2006a) and is investigated experimentally in Chapter 7. However, the formation of sulfate and oxalate products in the mineral dust particles can prevent the formation of soluble salts in the mineral dust particles, and thus shut down this pathway for the conversion of insoluble minerals into soluble salts. This phenomenon is discussed in detail in Chapter 6.

The arrival of the dust front was observed to substantially shift secondary aerosol mass into the elevated fraction of supermicron particles caused by the dust event (Arimoto et al., 2006; Tang et al., 2004b). This reduced the total fraction of submicron particles classified as "aged" or mixed with sulfate while increasing the fraction of supermicron particles mixed with nitrate (Fig. 2.7). Similarly, the fraction of submicron particles mixed with the general

OC marker or with OOA decreased during the dust event. By redistributing secondary aerosol mass from the greater number of submicron particles into the smaller number (but larger mass) of supermicron particles, the aerosol's overall hygroscopicity was reduced. However, the light absorption by the submicron aerosol was increased because a large fraction of reflective secondary aerosol mass had been shifted to the supermicron mode (Arimoto et al., 2006).

2.6 Acknowledgements

2.7 References

Arimoto, R., Kim, Y. J., Kim, Y. P., Quinn, P. K., Bates, T. S., Anderson, T. L., Gong, S., Uno, I., Chin, M., Huebert, B. J., Clarke, A. D., Shinozuka, Y., Weber, R. J., Anderson, J. R., Guazzotti, S. A., Sullivan, R. C., Sodeman, D. A., Prather, K. A., and Sokolik, I. N.: Characterization of Asian Dust during ACE-Asia, Global And Planetary Change, 52 (1-4), 23-56, 2006.

Bates, T. S., Quinn, P. K., Coffman, D. J., Covert, D. S., Miller, T. L., Johnson, J. E., Carmichael, G. R., Uno, I., Guazzotti, S. A., Sodeman, D. A., Prather, K. A., Rivera, M., Russell, L. M., and Merrill, J. T.: Marine boundary layer dust and pollutant transport associated with the passage of a frontal system over eastern Asia, J. Geophys. Res., 109 (D19), doi:10.1029/2003JD004094, 2004.

Bauer, S. E., Balkanski, Y., Schulz, M., Hauglustaine, D. A., and Dentener, F.: Global modeling of heterogeneous chemistry on mineral aerosol surfaces: Influence on tropospheric ozone chemistry and comparison to observations, J. Geophys. Res., 109 (D2), doi:10.1029/2003JD003868, 2004.

Bian, H. S., and Zender, C. S.: Mineral dust and global tropospheric chemistry: Relative roles of photolysis and heterogeneous uptake, J. Geophys. Res., 108 (D21), doi:10.1029/2002JD003143, 2003.

Bond, T. C., and Bergstrom, R. W.: Light absorption by carbonaceous particles: An investigative review, Aerosol Sci. Technol., 40 (1), 1-41, 2006.

Bond, T. C., Habib, G., and Bergstrom, R. W.: Limitations in the enhancement of visible light absorption due to mixing state, J. Geophys. Res., 111 (D20), doi:10.1029/2006JD007315, 2006.

Cahill, C. F.: Asian aerosol transport to Alaska during ACE-Asia, J. Geophys. Res., 108 (D23), doi:10.1029/2002JD003271, 2003.

Choi, M. Y., and Chan, C. K.: The effects of organic species on the hygroscopic behaviors of inorganic aerosols, Environ. Sci. Technol., 36 (11), 2422-2428, 2002.

Chung, S. H., and Seinfeld, J. H.: Global distribution and climate forcing of carbonaceous aerosols, J. Geophys. Res., 107 (D19), 2002.

Dentener, F. J., and Crutzen, P. J.: Reaction Of N2O5 On Tropospheric Aerosols - Impact On The Global Distributions Of Nox, O3, And OH, J. Geophys. Res., 98 (D4), 7149-7163, 1993.

Duce, R. A., Unni, C. K., Ray, B. J., Prospero, J. M., and Merrill, J. T.: Long-range atmospheric transport of soil dust from Asia to the tropical North Pacific - temporal variability, Science, 209 (4464), 1522-1524, 1980.

Furutani, H., Dall'osto, M., Roberts, G. C., and Prather, K. A.: Assessment of the relative importance of atmospheric aging on CCN activity derived from field observations, Atmos. Environ., 42 (13), 3130-3142, 2008.

Gard, E. E., Kleeman, M. J., Gross, D. S., Hughes, L. S., Allen, J. O., Morrical, B. D., Fergenson, D. P., Dienes, T., Galli, M. E., Johnson, R. J., Cass, G. R., and Prather, K. A.: Direct observation of heterogeneous chemistry in the atmosphere, Science, 279 (5354), 1184-1187, 1998.

Gibson, E. R., Hudson, P. K., and Grassian, V. H.: Aerosol chemistry and climate: Laboratory studies of the carbonate component of mineral dust and its reaction products, Geophys. Res. Lett., 33 (13), doi:10.1029/2006GL026386, 2006.

Gong, S. L., Zhang, X. Y., Zhao, T. L., McKendry, I. G., Jaffe, D. A., and Lu, N. M.: Characterization of soil dust aerosol in China and its transport and distribution during 2001 ACE-Asia: 2. Model simulation and validation, Journal Of Geophysical Research-Atmospheres, 108 (D9), doi:10.1029/2002JD002633, 2003.

Gross, D. S., Galli, M. E., Silva, P. J., and Prather, K. A.: Relative sensitivity factors for alkali metal and ammonium cations in single particle aerosol time-of-flight mass spectra, Anal. Chem., 72 (2), 416-422, 2000.

Guazzotti, S. A., Coffee, K. R., and Prather, K. A.: Continuous measurements of size-resolved particle chemistry during INDOEX-Intensive Field Phase 99, J. Geophys. Res., 106 (D22), 28607-28627, 2001.

Guazzotti, S. A., Suess, D. T., Coffee, K. R., Quinn, P. K., Bates, T. S., Wisthaler, A., Hansel, A., Ball, W. P., Dickerson, R. R., Neususs, C., Crutzen, P. J., and Prather, K. A.: Characterization of carbonaceous aerosols outflow from India and Arabia: Biomass/biofuel burning and fossil fuel combustion, J. Geophys. Res., 108 (D15), doi:10.1029/2002JD003277, 2003.

Hearn, J. D., and Smith, G. A.: Ozonolysis of mixed oleic acid/n-docosane particles: The roles of phase, morphology, and metastable states, J. Phys. Chem. A, 111 (43), 11059-11065, 2007.

Huang, X.-F., and Yu, J. Z.: Is vehicle exhaust a significant primary source of oxalic acid in ambient aerosols?, Geophys. Res. Lett., 34, L02808, doi:10.1029/2006GL028457, 2007.

Huebert, B. J., Bates, T., Russell, P. B., Shi, G. Y., Kim, Y. J., Kawamura, K., Carmichael, G., and Nakajima, T.: An overview of ACE-Asia: Strategies for quantifying the relationships between Asian aerosols and their climatic impacts, Journal Of Geophysical Research-Atmospheres, 108 (D23), doi:10.1029/2003JD003550, 2003a.

Huebert, B. J., Bates, T., Russell, P. B., Shi, G. Y., Kim, Y. J., Kawamura, K., Carmichael, G., and Nakajima, T.: An overview of ACE-Asia: Strategies for quantifying the relationships between Asian aerosols and their climatic impacts, J. Geophys. Res., 108 (D23), doi:10.1029/2003JD003550, 2003b.

Jacobson, M. Z.: Strong radiative heating due to the mixing state of black carbon in atmospheric aerosols, Nature, 409 (6821), 695-697, 2001.

Jaffe, D., Anderson, T., Covert, D., Kotchenruther, R., Trost, B., Danielson, J., Simpson, W., Berntsen, T., Karlsdottir, S., Blake, D., Harris, J., Carmichael, G., and Uno, I.: Transport of Asian air pollution to North America, Geophysical Research Letters, 26 (6), 711-714, 1999.

Kane, D. B., and Johnston, M. V.: Size and composition biases on the detection of individual ultrafine particles by aerosol mass spectrometry, Environ. Sci. Technol., 34 (23), 4887-4893, 2000.

Krueger, B. J., Grassian, V. H., Cowin, J. P., and Laskin, A.: Heterogeneous chemistry of individual mineral dust particles from different dust source regions: the importance of particle mineralogy, Atmos. Environ., 38 (36), 6253-6261, 2004.

Li, J., Posfai, M., Hobbs, P. V., and Buseck, P. R.: Individual aerosol particles from biomass burning in southern Africa: 2, Compositions and aging of inorganic particles, J. Geophys. Res., 108 (D13), doi:10.1029/2002JD002310, 2003.

Liu, D. Y., Prather, K. A., and Hering, S. V.: Variations in the size and chemical composition of nitrate-containing particles in Riverside, CA, Aerosol Sci. Technol., 33 (1-2), 71-86, 2000.

Liu, D. Y., Wenzel, R. J., and Prather, K. A.: Aerosol time-of-flight mass spectrometry during the Atlanta Supersite Experiment: 1. Measurements, J. Geophys. Res., 108 (D7), doi:10.1029/2001JD001562, 2003.

McFiggans, G., Artaxo, P., Baltensperger, U., Coe, H., Facchini, M. C., Feingold, G., Fuzzi, S., Gysel, M., Laaksonen, A., Lohmann, U., Mentel, T. F., Murphy, D. M., O'Dowd, C. D., Snider, J. R., and Weingartner, E.: The effect of physical and chemical aerosol properties on warm cloud droplet activation, Atmos. Chem. Phys., 6, 2593-2649, 2006.

Mochida, M., Kawamura, K., Umemoto, N., Kobayashi, M., Matsunaga, S., Lim, H. J., Turpin, B. J., Bates, T. S., and Simoneit, B. R. T.: Spatial distributions of oxygenated organic compounds (dicarboxylic acids, fatty acids, and levoglucosan) in marine aerosols over the western Pacific and off the coast of East Asia: Continental outflow of organic aerosols during the ACE-Asia campaign, J. Geophys. Res., 108 (D23), doi:10.1029/2002JD003249, 2003.

Moffet, R. C., de Foy, B., Molina, L. T., Molina, M. J., and Prather, K. A.: Measurement of ambient aerosols in northern Mexico City by single particle mass spectrometry, Atmos. Chem. Phys., 8, 4499-4516, 2008a.

Moffet, R. C., Qin, X. Y., Rebotier, T., Furutani, H., and Prather, K. A.: Chemically segregated optical and microphysical properties of ambient aerosols measured in a single-particle mass spectrometer, J. Geophys. Res., 113 (D12), doi:10.1029/2007JD009393, 2008b.

Muhle, J., Lueker, T. J., Su, Y., Miller, B. R., Prather, K. A., and Weiss, R. F.: Trace gas and particulate emissions from the 2003 southern California wildfires, J. Geophys. Res., 112 (D3), 2007.

Neubauer, K. R., Johnston, M. V., and Wexler, A. S.: Humidity effects on the mass spectra of single aerosol particles, Atmos. Environ., 32 (14-15), 2521-2529, 1998.

Pastor, S. H., Allen, J. O., Hughes, L. S., Bhave, P., Cass, G. R., and Prather, K. A.: Ambient single particle analysis in Riverside, California by aerosol time-of-flight mass spectrometry during the SCOS97-NARSTO, Atmos. Environ., 37, S239-S258, 2003.

Petters, M. D., Prenni, A. J., Kreidenweis, S. M., DeMott, P. J., Matsunaga, A., Lim, Y. B., and Ziemann, P. J.: Chemical aging and the hydrophobic-to-hydrophilic conversion of carbonaceous aerosol, Geophys. Res. Lett., 33 (24), doi:10.1029/2006GL027249, 2006.

Pierce, J. R., Chen, K., and Adams, P. J.: Contribution of primary carbonaceous aerosol to cloud condensation nuclei: processes and uncertainties evaluated with a global aerosol microphysics model, Atmos. Chem. Phys., 7 (20), 5447-5466, 2007.

Qin, X., and Prather, K. A.: Impact of biomass emissions on particle chemistry during the California Regional Particulate Air Quality Study, International Journal Of Mass Spectrometry, 258 (1-3), 142-150, 2006.

Qin, X. Y., Bhave, P. V., and Prather, K. A.: Comparison of two methods for obtaining quantitative mass concentrations from aerosol time-of-flight mass spectrometry measurements, Anal. Chem., 78 (17), 6169-6178, 2006.

Quinn, P. K., Coffman, D. J., Bates, T. S., Welton, E. J., Covert, D. S., Miller, T. L., Johnson, J. E., Maria, S., Russell, L., Arimoto, R., Carrico, C. M., Rood, M. J., and Anderson, J.: Aerosol optical properties measured on board the Ronald H. Brown during ACE-Asia as a function of aerosol chemical composition and source region, J. Geophys. Res., 109 (D19), doi:10.1029/2003JD004010, 2004.

Ramanathan, V., and Carmichael, G.: Global and regional climate changes due to black carbon, Nat. Geosci., 1 (4), 221-227, 2008.

Rebotier, T. P., and Prather, K. A.: Aerosol time-of-flight mass spectrometry data analysis: A benchmark of clustering algorithms, Analytica Chimica Acta, 585 (1), 38-54, 2007.

Reid, J. S., Koppmann, R., Eck, T. F., and Eleuterio, D. P.: A review of biomass burning emissions part II: intensive physical properties of biomass burning particles, Atmos. Chem. Phys., 5, 799-825, 2005.

Robinson, A. L., Donahue, N. M., Shrivastava, M. K., Weitkamp, E. A., Sage, A. M., Grieshop, A. P., Lane, T. E., Pierce, J. R., and Pandis, S. N.: Rethinking organic aerosols: Semivolatile emissions and photochemical aging, Science, 315 (5816), 1259-1262, 2007.

Schauer, J. J., Rogge, W. F., Hildemann, L. M., Mazurek, M. A., and Cass, G. R.: Source apportionment of airborne particulate matter using organic compounds as tracers, Atmos. Environ., 30 (22), 3837-3855, 1996.

Seinfeld, J. H., Carmichael, G. R., Arimoto, R., Conant, W. C., Brechtel, F. J., Bates, T. S., Cahill, T. A., Clarke, A. D., Doherty, S. J., Flatau, P. J., Huebert, B. J., Kim, J., Markowicz, K. M., Quinn, P. K., Russell, L. M., Russell, P. B., Shimizu, A., Shinozuka, Y., Song, C. H., Tang, Y. H., Uno, I., Vogelmann, A. M., Weber, R. J., Woo, J. H., and Zhang, X. Y.: ACE-ASIA - Regional climatic and atmospheric chemical effects of Asian dust and pollution, Bulletin Of The American Meteorological Society, 85 (3), 367-380, 2004.

Silva, P. J., Liu, D. Y., Noble, C. A., and Prather, K. A.: Size and chemical characterization of individual particles resulting from biomass burning of local Southern California species, Environ. Sci. Technol., 33 (18), 3068-3076, 1999.

Silva, P. J., and Prather, K. A.: Interpretation of mass spectra from organic compounds in aerosol time-of-flight mass spectrometry, Anal. Chem., 72 (15), 3553-3562, 2000.

Simoneit, B. R. T., Kobayashi, M., Mochida, M., Kawamura, K., Lee, M., Lim, H. J., Turpin, B. J., and Komazaki, Y.: Composition and major sources of organic compounds of

aerosol particulate matter sampled during the ACE-Asia campaign, J. Geophys. Res., 109 (D19), 2004.

Song, C. H., and Carmichael, G. R.: The aging process of naturally emitted aerosol (sea-salt and mineral aerosol) during long range transport, Atmos. Environ., 33 (14), 2203-2218, 1999.

Song, X. H., Hopke, P. K., Fergenson, D. P., and Prather, K. A.: Classification of single particles analyzed by ATOFMS using an artificial neural network, ART-2A, Anal. Chem., 71 (4), 860-865, 1999.

Spencer, M. T., Holecek, J. C., Corrigan, C. E., Ramanathan, V., and Prather, K. A.: Size-resolved chemical composition of aerosol particles during a monsoonal transition period over the Indian Ocean, J. Geophys. Res., 113 (D16), 2008.

Spencer, M. T., and Prather, K. A.: Using ATOFMS to determine OC/EC mass fractions in particles, Aerosol Sci. Technol., 40 (8), 585-594, 2006.

Spencer, M. T., Shields, L. G., and Prather, K. A.: Simultaneous measurement of the effective density and chemical composition of ambient aerosol particles, Environ. Sci. Technol., 41 (4), 1303-1309, 2007.

Sun, J. M., Zhang, M. Y., and Liu, T. S.: Spatial and temporal characteristics of dust storms in China and its surrounding regions, 1960-1999: Relations to source area and climate, Journal Of Geophysical Research-Atmospheres, 106 (D10), 10325-10333, 2001.

Tang, Y. H., Carmichael, G. R., Kurata, G., Uno, I., Weber, R. J., Song, C. H., Guttikunda, S. K., Woo, J. H., Streets, D. G., Wei, C., Clarke, A. D., Huebert, B., and Anderson, T. L.: Impacts of dust on regional tropospheric chemistry during the ACE-Asia experiment: A model study with observations, J. Geophys. Res., 109 (D19), doi:10.1029/2003JD003806, 2004a.

Tang, Y. H., Carmichael, G. R., Seinfeld, J. H., Dabdub, D., Weber, R. J., Huebert, B., Clarke, A. D., Guazzotti, S. A., Sodeman, D. A., Prather, K. A., Uno, I., Woo, J. H., Yienger, J. J., Streets, D. G., Quinn, P. K., Johnson, J. E., Song, C. H., Grassian, V. H., Sandu, A., Talbot, R. W., and Dibb, J. E.: Three-dimensional simulations of inorganic aerosol distributions in east Asia during spring 2001, J. Geophys. Res., 109 (D19), doi:10.1029/2003JD004201, 2004b.

Thomson, D. S., Middlebrook, A. M., and Murphy, D. M.: Thresholds for laser-induced ion formation from aerosols in a vacuum using ultraviolet and vacuum-ultraviolet laser wavelengths, Aerosol Sci. Technol., 26 (6), 544-559, 1997.

Thornton, J. A., Braban, C. F., and Abbatt, J. P. D.: N2O5 hydrolysis on sub-micron organic aerosols: the effect of relative humidity, particle phase, and particle size, Phys. Chem. Chem. Phys., 5 (20), 4593-4603, 2003.

Thulasiraman, S., O'Neill, N. T., Royer, A., Holben, B. N., Westphal, D. L., and McArthur, L. J. B.: Sunphotometric observations of the 2001 Asian dust storm over Canada and the US, Geophys. Res. Lett., 29 (8), doi:10.1029/2001GL014188, 2002.

Toner, S. M., Shields, L. G., Sodeman, D. A., and Prather, K. A.: Using mass spectral source signatures to apportion exhaust particles from gasoline and diesel powered vehicles in a freeway study using UF-ATOFMS, Atmos. Environ., 42 (3), 568-581, 2008.

Wenzel, R. J., Liu, D. Y., Edgerton, E. S., and Prather, K. A.: Aerosol time-of-flight mass spectrometry during the Atlanta Supersite Experiment: 2. Scaling procedures, J. Geophys. Res., 108 (D7), 2003.

Zhang, R. Y., Khalizov, A. F., Pagels, J., Zhang, D., Xue, H. X., and McMurry, P. H.: Variability in morphology, hygroscopicity, and optical properties of soot aerosols during atmospheric processing, Proc. Natl. Acad. Sci. USA, 105 (30), 10291-10296, 2008.

Chapter 3

Direct observations of the atmospheric processing of Asian mineral dust

3.1 Synopsis

The accumulation of secondary acids and ammonium on individual mineral dust particles during ACE-Asia has been measured with an online single-particle mass spectrometer, the ATOFMS. Changes in the amounts of sulfate, nitrate, and chloride mixed with dust particles correlate with air masses from different source regions. The uptake of secondary acids was dependent on the individual dust particle mineralogy; nitrate accumulated on calcium-rich dust while sulfate accumulated on aluminosilicate-rich dust. Oxidation of S(IV) to S(VI) by iron in the aluminosilicate dust is a probable explanation for this enrichment of sulfate, which has important consequences for the fertilization of remote oceans by soluble iron. This study shows the segregation of sulfate from nitrate and chloride in individual dust particles for the first time. A transport and aging timeline provides an explanation for the observed segregation. The data indicates that sulfate became mixed with the dust first. This suggests that the transport pathway is more important than the reaction kinetics in determining which species accumulate on mineral dust. Early in the study, dust particles in volcanically influenced air masses were mixed predominately with sulfate. Dust mixed with chloride then dominated over sulfate and nitrate when a major dust front reached the R.V. Ronald Brown. The rapid increase in chloride on dust is hypothesized to have been caused by mixing with HCl(g) released from acidified sea salt particles induced by the heterogeneous reaction of volcanic $SO_2(g)$, prior to the arrival of the dust front. The amount of ammonium mixed with

dust correlated strongly with the total amount of secondary acid reaction products in the dust. Submicron dust and ammonium sulfate were internally mixed, contrary to frequent reports that they exist as external mixtures. The size distribution of the mixing state of dust with these secondary species validates previous mechanisms of the atmospheric processing of dust and generally agrees with simulated aerosol chemistry from the STEM-2K3 model. This series of novel results has important implications for improving the treatment of dust in global chemistry models and highlights a number of key processes that merit further investigation through laboratory and field studies.

3.2 Introduction

Major dust storm events typically develop in China in the spring, brought about by cold frontal systems and the Mongolian cyclonic depression (Sun et al., 2001). The Gobi Deserts in Mongolia and northern China, and the Taklimakan Desert in western China, are the two dominant source regions of dust in east Asia. Once lofted to high altitudes, dust can then become entrained in the jet stream and may be transported long distances over the Pacific Ocean to North America (Cahill, 2003; Duce et al., 1980; Jaffe et al., 1999; Thulasiraman et al., 2002). The Asian Pacific Regional Aerosol Characterization Experiment (ACE-Asia) in 2001 was designed to study the impact these spring dust events have on the physical, chemical and radiative properties of the Asian aerosol as it is transported over the mainland and the Pacific Ocean (Huebert et al., 2003a; Seinfeld et al., 2004). Chapter 2 presented an overview of the changes in particle types and their chemistry observed during ACE-Asia from the R/V Ronald H. Brown. Here the chemistry and atmospheric processing of the Asian mineral dust particles observed during the cruise is investigated in detail.

As discussed in Chapter 1, mineral dust particles experience a wide range of atmospheric processing during transport. Heterogeneous reactions and the addition of secondary aerosol compounds to mineral dust particles can significantly alter the dust particle's physicochemical properties and thus their climate and biogeochemical impacts. These reactions also alter the atmosphere's chemical composition and trace gas budgets. Asian mineral dust particles are particularly interesting due to their high calcite content (Jeong, 2008; Krueger et al., 2004; Nishikawa et al., 2000). Calcite ($CaCO_3$) is a highly alkaline compound that readily undergoes chemical reactions with atmospheric acids such as $NO_x(g)$, $SO_2(g)$, $HNO_3(g)$, and $HCl(g)$, and organic acids (Prince et al., 2008; Santschi and Rossi, 2006; Usher et al., 2003a; Vlasenko et al., 2006). Therefore, Asian mineral dust particles are an excellent particle type for investigating heterogeneous chemistry and atmospheric processing. The results presented here further investigate the chemical aging of the Asian mineral dust particles during ACE-Asia as mixing occurs with trace gases, and natural and anthropogenic aerosols. Our analysis provides new insights into the competitive uptake of different secondary acids by mineral dust and the role that the varying mineralogy of dust plays in these processes, processes that are now being incorporated into chemical models (Krueger et al., 2004; Laskin et al., 2005a; Matsuki et al., 2005a; Matsuki et al., 2005b; Tang et al., 2004b).

3.3 Experimental methods

3.3.1 Shipboard aerosol sampling

A transportable aerosol time-of-flight mass spectrometer (ATOFMS) located on the R/V Ronald H. Brown (RHB) was used to characterize the size and chemical composition of individual particles in real-time during the ACE-Asia campaign, as described in Chapter 2.

The ATOFMS used in this study used a converging nozzle inlet and could effectively detect particles with aerodynamic diameters between 0.2 and 3.0 μm. The spectra from the individual particles were sorted by the ART-2a algorithm and classified following the methods discussed in Chapter 2. The RHB left Hawaii on 16 March 2001 (DOY 75) and spent 10 days in transit to Japan. From DOY 90-99 the RHB circled around the southern end of Japan and into the Sea of Japan. On DOY 99 the RHB turned around and headed south out of the Sea of Japan through the Straits of Korea, finally docking at Yokosuka, Japan on DOY 110. More details on the RHB's cruise track, the air masses it sampled are available and Chapter 2 and in Bates et al. (2004).

A wide variety of mineral dust samples from Asian desert regions were collected in 2001. Mass spectra from each dust sample were obtained after the campaign by placing each dust sample into a flask in a sonicator to create a suspension of dust particles under nitrogen gas flow. The aerosol was then directed into the ATOFMS inlet for analysis and at least 2400 single-particle mass spectra were collected per sample.

3.3.2 Filtering criteria

The mineral dust particles classified by the ART-2a algorithm were further filtered to remove incorrectly classified biomass-burning particles and internal mixtures of dust and sea salt. As dust particles are transported through the troposphere they can become internally mixed with other particle types such as sea salt, particularly via cloud processing if the dust aerosol passes through a cloudy region. The fraction of mineral dust particles internally mixed with sea salt has been reported to be as high as 85% after transport through marine regions (Andreae et al., 1986b; Fan et al., 1996; Niimura et al., 1998; Zhang et al., 2003a). To focus only on the mixing of secondary acid products with mineral dust particles, the contributions of

chloride, nitrate, and sulfate from internal mixing of dust with sea salt were excluded by removing dust particles containing the $^{81}[Na_2^{35}Cl]^+$ ion.

Particles produced by biomass burning typically produce intense $^{39}K^+$ signals, in addition to organic and elemental carbon fragments. The presence of large metal ion peaks such as $^{39}K^+$ can cause biomass particles to be incorrectly placed in mineral dust clusters by the ART-2a algorithm. To correct for this, the mineral dust particles sorted by ART-2a were further filtered using a peak area $^{27}Al^+ > 5000$ criteria to eliminate incorrectly sorted biomass particles. The $^{27}Al^+$ criteria was chosen because Al is generally regarded as the most common single marker for mineral dust particles (Gao and Anderson, 2001; Mori et al., 2003; Nishikawa et al., 1991; Usher et al., 2003a) and is readily detected in mineral dust by ATOFMS (Guazzotti et al., 2001a; Silva et al., 2000). From previous source studies, we have determined that biomass particles do not produce peak areas > 5000 at m/z 27 from $^{27}[C_2H_3]^+$ or other organic fragments.

Mineral dust particles that were internally mixed with sea salt were queried using a peak area > 100 units for $^{81}[Na_2^{35}Cl]^+$ criterion. The $[Na_2Cl]^+$ ion is an ideal marker for various particle types internally mixed with sea salt (Guazzotti et al., 2001a) that was not present in the Asian dust source spectra. The final set of properly-calibrated dust particles that satisfied both the $^{27}Al^+ > 5000$ and $^{81}[Na_2^{35}Cl]^+ < 100$ peak area criteria is herein referred to as "filtered dust particles". Using this criterion, the fraction of mineral dust particles internally mixed with sea salt was determined to be $15 \pm 9.5\%$ on average over the course of the entire study. Before the dust front the fraction of dust particles internally mixed with sea salt was as high as 40%. While this degree of mixing is lower than previous single-particle filter-based measurements in this region (Fan et al., 1996; Zhang et al., 2003a), a high degree of dust-sea salt mixing is typically caused by cloud processing. If the dust-laden air mass did not pass through a dense

convective cloud system before reaching the RHB, this would explain the lower level of internal mixing. This may also be explained by the 0.2–3.0 µm particle size range measured by the ATOFMS. The mixing of a dust particle with sea salt has been shown to increase the dust particle's diameter by ~0.4-0.8 µm (Zhang and Iwasaka, 2004) and the peak in the number-weighted size distribution of mixed dust and sea salt particles is typically near or above 3 µm (Zhang et al., 2003a). During the ACE-Asia dust event, the coarse-mode volume distribution peaked at ~4.0 µm (Bates et al., 2004), implying that a large fraction of the internally mixed dust and sea-salt particles, if present, likely had diameters > 3.0 µm and were therefore not detected by ATOFMS.

3.4 Results and discussion

3.4.1 Mineral dust mass spectra

A total of 731,309 single-particle mass spectra were collected over the course of the campaign. Out of all of these particles, 220,806 were classified as mineral dust upon sorting the particles into chemically similar groups using the ART-2a clustering algorithm (Song et al., 1999). The assignment as dust is based on similarities to source dust mass spectra discussed below, as well as those presented in Silva et al. (2000) and Guazzotti et al. (2001a). The average mass spectrum for filtered mineral dust particles detected during the dust storm frontal passage (DOY 100.8-101.3) is shown in Figure 3.1. The height of each peak indicates the fraction of particles for which each ion was detected, while the color corresponds to the peak area range measured for that fraction of particles. Metals and metal oxides from minerals typical of dust particles are clearly evident in both the positive and negative ion spectra and their peak assignments are listed in Table 3.1, based on previous ATOFMS measurements
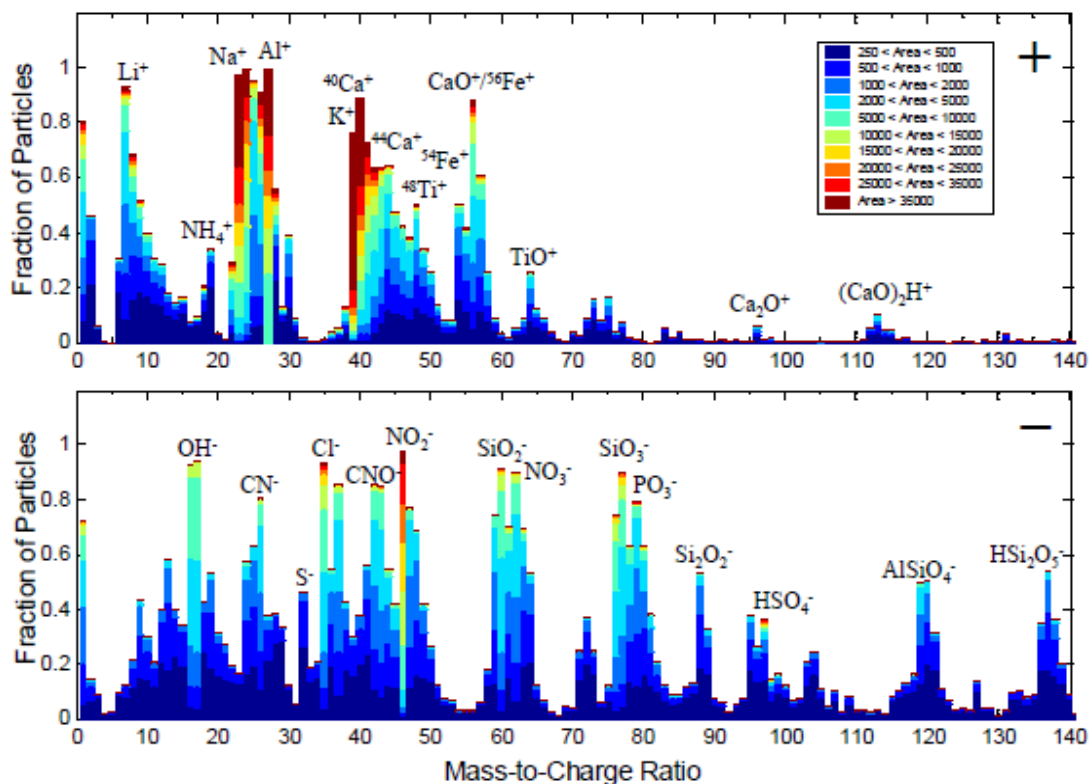
Figure 3.1. Atmospherically processed mineral dust. Average digital mass spectrum of all 3634 filtered mineral dust particles detected during the dust front's passage over the RHB from DOY 101-101.3. Peaks are assigned to the most likely ions for dust particles (Table 3.1). The digital mass spectrum displays the fraction of particles that produced a peak area for each ion within a specified range. It reflects the range and homogeneity in the ion signal produced for a particular ion by an ensemble of particles.

(Guazzotti et al., 2001a; Guazzotti et al., 2001b; Pastor et al., 2003; Silva et al., 2000). The ART-2a sorting algorithm split the dust particles into 23 particle clusters out of the 60 largest clusters, further evidence for the wide range of dust mineralogy at the single particle level. These Asian dust particles represent a complex mixture of numerous different minerals, as reported by previous studies (Andronova et al., 1993; Clarke et al., 2004; Gao and Anderson, 2001; Jeong, 2008; Krueger et al., 2004; Pye, 1987; Trochkine et al., 2003; Yuan et al., 2004).

The large fraction (> 80%) of particles containing calcium marker ions (m/z +40, +56, +96) agrees with the high calcium carbonate fraction typical of Asian mineral dust (Jeong and

Chun, 2006). Krueger et al. (2004) reported the chemical composition of China Loess

determined by EDX to be 39% Ca, 31% Si, 13% Mg, 7% Al, 4% Na, 3% Fe, and 1% K

Table 3.1. Ion assignments for commonly observed peaks from mineral dust particles and secondary species.

Mass-to-charge ratio	Most probable ion assignment
Mineral dust	
+7	Li^+
+23	Na^+
+27	Al^+
+28	Mg^+
+39	$^{39}K^+$
+40	Ca^+
+41	$^{41}K^+$ or $[Na(H_2O)]^+$
+48	Ti^+
+54	$^{54}Fe^+$
+56	$^{56}Fe^+$ or $[CaO]^+$
+64	$[TiO]^+$
+96	$[Ca_2O]^+$
+112	$[Ca(O)_2]^+$
+113	$[Ca(O)_2H]^+$
-16	O^-
-17	$[OH]^-$
-26	$[CN]^-$
-42	$[CNO]^-$
-43	$[AlO]^-$
-60	$[AlO(OH)]^-$ or $[SiO_2]^-$
-63	$[PO_2]^-$
-76	$[AlO_2(OH)]^-$ or $[^{28}SiO_3]^-$
-77	$[^{29}SiO_3]^-$ or $[H^{28}SiO_3]^-$
-79	$[PO_3]^-$
-88	$[SiO_2]^-$ or $[FeO]^-$
Secondary species	
+18 *	$[NH_4]^+$
+30	NO^+
-32	S^-
-35 *	$^{35}Cl^-$
-37	$^{37}Cl^-$
-46	$[NO_2]^-$
-48	$[SO]^-$
-62 *	$[NO_3]^-$
-64	$[SO_2]^-$
-80	$[SO_3]^-$
-97 *	$[HSO_4]^-$

* indicates the principle ions used to measure ammonium, chloride, nitrate, or sulfate in mineral dust particles

(atomic percent). Ca was determined to be mostly from carbonate minerals including calcite ($CaCO_3$) and dolomite ($CaMg(CO_3)_2$). Jeong (2008) determined the single-particle mineralogy of individual Asian dust particles from their source to be predominantly clay aggregates (48%) that were often mixed with nanosized calcite, followed by particles of quartz (22%), plagioclase (11%), coarse calcite (6%), and K-feldspar (5%). The fraction of carbonate in Asian dust has been reported to range from 1-12% by mass (Andronova et al., 1993; Derbyshire et al., 1998; Honda et al., 2004; Nishikawa et al., 2000). The carbonate anion, CO_3^{-2}, generally occurs in low abundance in the mass spectrum and is obscured by the more abundant isobars $[Si_2O_2]^-$ and $[AlO_2H]^-$ at m/z -60 in mineral particles. Thus, carbonate from calcite and dolomite cannot be directly determined using m/z -60. The presence of $CaCO_3$ can be reliably inferred from Ca-containing cations including $^{40}Ca^+$, $^{56}[CaO]^+$, $^{96}[Ca_2O]^+$, and $^{113}[(CaO)_2H]^+$. The $^{56}[CaO]^+$ cation is likely formed via $[CaCO_3]^+ \rightarrow [CaO]^+ + CO_2$ (Bruynseels and Van Grieken, 1983).

The mass spectra contain ions corresponding to ammonium, chloride, nitrate, or sulfate, ions referred to as "secondary species". The principal ions used throughout this paper to study each of these four secondary species are indicated by an asterisk (*) in Table 3.1. These peaks provide evidence of the accumulation of secondary species by mineral dust, as discussed below. Some of these species could be present in the dust at the source as minerals such as halite (NaCl) and gypsum ($CaSO_4$). Falkovich et al. (2001) found sulfate (not from gypsum) in Saharan dust particles which they determined was not due to atmospheric processing. Thus, they concluded that other sources of sulfate such as deposition by rain or runoff added sulfate to the dust's surface. These processes could also be adding sulfate to the Asian dust described herein. As shown later, the ambient aged dust particles had very large ion

gnals and temporal variations for sulfate, indicating that the vast majority of the sulfate accumulated on the dust during atmospheric transport.

Asian dust samples from various source regions were collected during ACE-Asia and analyzed using an ATOFMS to create reference spectra of unprocessed mineral dust. The mass spectra of source dust particles from regions such as Zhenbettai (Shaanxi Province, China), Dunhuang (Gansu Province, China), and the CJ13 Certified Reference Asian Mineral Dust (Gansu Province, China) (Nishikawa et al., 2000) were collected and compared to those of ambient mineral dust sampled during ACE-Asia. These represent likely sources of the mineral dust particles carried aloft from mainland China to the Sea of Japan during ACE-Asia (Gong et al., 2003a). Similarities between mineral cations and anions for both source and ambient dust particles, as listed in Table 3.1, are readily apparent. However, when compared to the ambient dust spectra, the source dust particles have much lower frequencies and ion intensities from the secondary species ammonium, chloride, nitrate, and sulfate. Typical ranges of peak areas for secondary species measured in the source and aged dust are given below. Thus, the source dust spectra provide a benchmark for the very low background amounts of these secondary species in Asian dust, a threshold above which peak areas and detection frequencies can serve as indications of atmospheric processing during transport.

What follows is a summary of typical ion peak areas measured by the ATOFMS for various chemical species in mineral dust particles. Peaks with areas < 25 are generally considered to be in the noise. For the secondary inorganic species, an area < 500 is not considered large and is of the magnitude that can be measured in source dust spectra. This does not apply to ammonium, however, which is not commonly measured in the source dust with a peak area > 50. A peak area > 20,000 for secondary inorganics is a very large value that is never observed in the source dust and is not commonly seen in the ambient aged dust

spectra. Thus, it reflects a very large amount of a secondary inorganic species, likely due to extensive aging. Peak areas up to and exceeding 40,000 have been observed (see Figure 3.1 for example). The peak area of 5000, though not yet quantified, represents a significant amount of secondary inorganic material beyond that detected in any source sample. A list of typical peak areas used to search for various particulate species in ATOFMS data is given in Liu et al. (2003). Table 3.1 lists ion assignments for peaks commonly observed by the ATOFMS from mineral dust particles.

3.4.2 Campaign timeline and air mass history

Over the course of the campaign, the RHB sampled air arriving from a wide variety of source regions, as identified by Bates et al. (2004). We use time periods corresponding to the same source regions herein. Mineral dust particles were commonly detected during the pre-frontal Marine and Polluted Korea & Japan periods in low concentrations. From DOY 99.3-100.5 (UTC) the RHB sampled air that had passed over the Miyakejima volcano and Japan and a distinct dust layer was observed at an altitude of 5 km (Polluted Volcano period). A major dust storm reached the RHB on DOY 100.8 in the western Sea of Japan (Dust Front period). Upper level trajectories were from the north China/Mongolia desert region, while low-level trajectories extended across Korea and China. The passage of the front brought elevated levels of dust to the ship. The sub-10 μm dust concentrations reached 140 μm m^{-3} on DOY 102. From DOY 100 to 104 mineral dust composed 8-31% of submicron and up to 80% of supermicron mass (Arimoto et al., 2006). Dust continued to dominate the aerosol behind the front. From DOY 101.8-103.4, both upper and lower level trajectories crossed Korea and north China/Mongolia (Dust & Korea period). From DOY 103.4-104.5 the RHB was in the Korean Strait and sampling air that came out of north China/Mongolia and had passed over Shanghai (Dust & Shanghai period).

3.4.3 Detection of secondary inorganic species in dust particles

Nitrate, sulfate, and chloride were the most commonly observed anions in the mineral dust and correspond to the products expected from mineral dust particles that have mixed with secondary acids, as well as acid anhydrides including N_2O_5, SO_2, NO_x, etc. Although the exact mechanism that leads to the accumulation of these secondary species cannot be determined from this study, the presence of chloride, nitrate, and sulfate on dust is most likely due to the formation of hydrochloric, nitric, and sulfuric acids on the dust. This could be the result of reactive gases (e.g. SO_2, NO_2) adsorbing on the dust and then being oxidized to their acidic forms, or from the direct uptake of acidic gases (e.g. HCl, HNO_3, H_2SO_4) or their ammonium salts (e.g. NH_4NO_3, $(NH_4)_2SO_4$). After the acids formed/adsorbed on the dust, they can be fully or partially neutralized by alkaline species in the dust (e.g $CaCO_3$) or by alkaline gases (e.g. NH_3). The ions formed from these secondary species by the ATOFMS cannot directly indicate if the species are acidic (i.e. protonated) or not. Therefore, we will refer to them as "secondary acid products" or simply "secondary acids" throughout our discussion, indicating that the chloride, nitrate, and sulfate found on the dust were most likely initially due to the formation/accumulation of secondary acids on the dust. The products of secondary species that reacted with mineral dust and other particle types are evaluated using the ions listed in Table 3.1. For this analysis chloride, nitrate, and sulfate were primarily determined using peaks at m/z -35, -62 and -97, respectively. The peak at $^{62}[NO_3]^-$ is used instead of the $^{46}[NO_2]^-$ nitrate fragment because m/z -62 is not detected in the Asian dust source spectra. Thus, by using m/z -62 to detect nitrate in dust, we preclude any significant contribution from nitrate (or nitrite) that is already present in the dust before it is injected into the atmosphere. Recall that mixed dust-sea salt particles have been filtered out of the analysis.
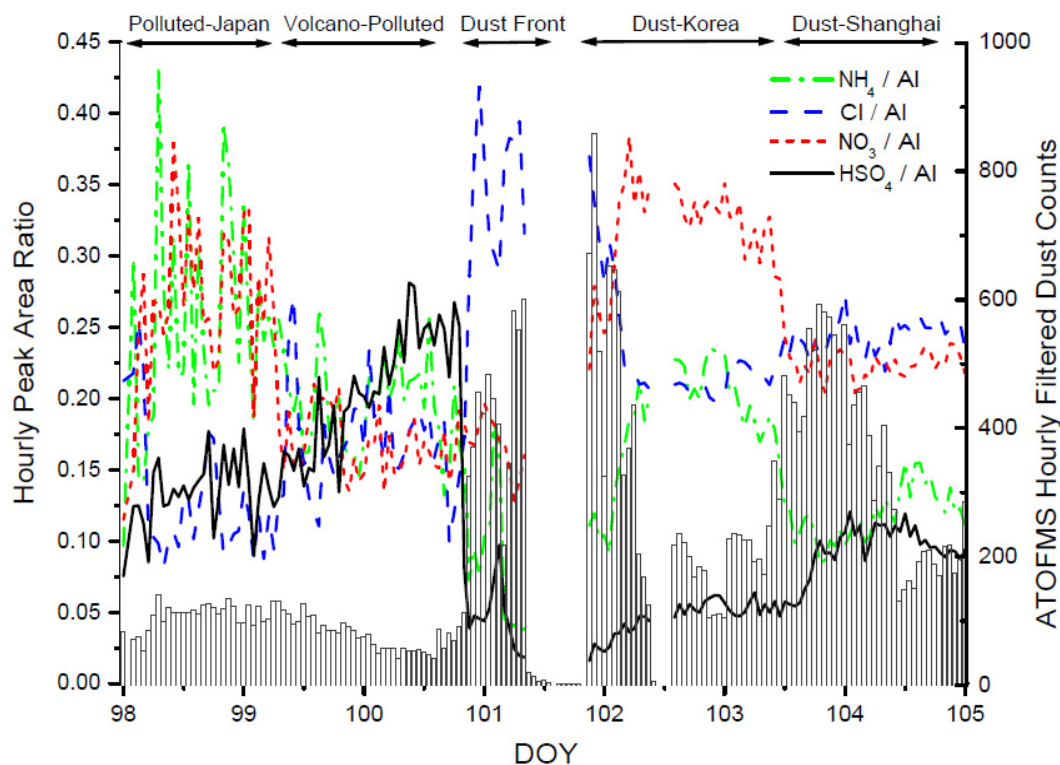
Figure 3.2. Temporal evolution of secondary species in Asian mineral dust sampled aboard the RHB. Hourly averaged single-particle peak area ratios (lines) from all filtered dust particles for four major secondary species: NH_4^+ (m/z = 18/m/z = 27), Cl^- (m/z = -35/m/z = 27), NO_3^- (m/z = -62/m/z = 27), and HSO_4^- (m/z = -97/m/z = 27). Total hourly ATOFMS dust particle counts (bars) are also displayed. Time periods corresponding to different air mass source regions as described by Bates et al. (2004) are indicated. All times are in UTC.

The average mass spectrum for filtered mineral dust particles detected during the dust storm frontal passage (DOY 100.8-101.3) is shown in Figure 3.1. Peaks typical of mineral dust particles discussed above and listed in Table 3.1 are clearly evident, and a large increase is observed in the fraction of particles producing ions indicative of secondary acid products including m/z +30, -35, -46, -62, -80, and -97. These peaks were not significant in the source dust spectra. Changes in the relative amounts of four secondary inorganic species in the mineral dust particles are evaluated by averaging the peak area ratio for each species from all filtered dust particles detected in one hour, as shown in Figure 3.2 for DOY 98-105, encompassing the prefrontal and postfrontal time periods. The peak area for a particular m/z is

divided by that particle's peak area at m/z 27 (Al^+) to account for shot-to-shot variations in the LDI laser power and the amount of laser energy absorbed by each particle. The peak area ratio is evaluated for each individual particle before the hourly average is calculated. Al was chosen as an internal standard because it is the most commonly detected species in mineral dust by ATOFMS and has been shown to remain stable as a function of particle size during atmospheric transport (Arimoto et al., 2006; Guazzotti et al., 2001a; Mori et al., 2003; Silva et al., 2000). The relative sensitivities of the ATOFMS to different compounds in mineral dust and other matrices have not been thoroughly evaluated. If, however, the particle matrix is not changing significantly, as is the case for the Asian mineral dust particles discussed in this paper, then it is valid to compare the intensity of a particular peak from one particle to another and draw conclusions about the relative amounts of that specific species present in each particle.

3.4.4   Temporal evolution of secondary species in Asian dust

The principal peak area ratios for four major secondary species, ammonium, chloride, nitrate, and sulfate are plotted in Figure 3.2. Gaps in the data occurred when aerosol sampling was suspended due to instrument maintenance or when the aerosol inlet was shut off during ship exhaust contamination periods. The total hourly ATOFMS dust particle counts are also displayed and indicate when the first dust front reached the RHB on DOY 100.8. To estimate the fraction of mineral dust particles internally mixed with chloride, nitrate, or sulfate, a peak area criterion > 5000 units for either $^{35}Cl^-$, $^{62}[NO_3]^-$ or $^{97}[HSO_4]^-$ was used to define a mineral dust particle as significantly mixed with one of these secondary species. This subset will be referred to as "reacted dust particles". This peak area criterion was chosen because it is much larger than peak areas for these ions in the original Asian source dust and ensures that only mineral dust particles that have become significantly aged during transport will be selected.
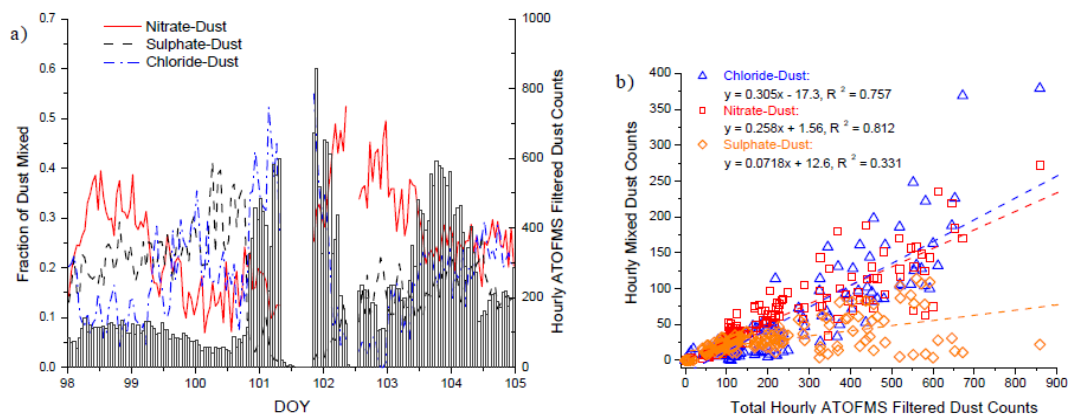
Figure 3.3. Percentage of dust particles mixed with secondary acids. (a) Average hourly fraction (lines) of filtered dust particles defined as mixed with the indicated secondary acid product using the peak area > 5000 criteria for $^{35}Cl^-$, $^{62}[NO_3]^-$ or $^{97}[HSO_4]^-$. The total filtered dust particle hourly counts are also displayed for reference (bars). (b) Scatter plot of the hourly counts of dust mixed with one of the three secondary acid products versus the total hourly ATOFMS dust counts, and their least-squares fits.

The mass fraction of each acid corresponding to a peak area of 5000 has not yet been determined and is the subject of ongoing laboratory studies. This peak area is relatively large and thus these results represent a conservative estimate of the degree to which mineral dust particles were processed and mixed with nitrate, chloride, and/or sulfate. Figure 3.3 shows the results of this classification for the prefrontal and postfrontal periods. From DOY 98-105, the average (± 1σ) fractions of dust particles mixed with nitrate, sulfate, or chloride were 25.9 ± 9.6%, 17.5 ± 8.5%, and 18.4 ± 10.5, respectively.

The fraction of dust particles classified as mixed with each of the four secondary species is shown for each time period in Figure 3.4. The hatched portion of the column indicates the fraction of dust particles that contained both a secondary acid product (e.g. nitrate) <u>and</u> ammonium. These mixing state statistics differ from the preliminary results presented in Arimoto et al. (2006). In that paper, the same criteria were used, but dust mixed with sea salt was not excluded from the analysis in order to present a picture of the fraction of dust mixed with acid products regardless of their source. Here we exclude dust internally
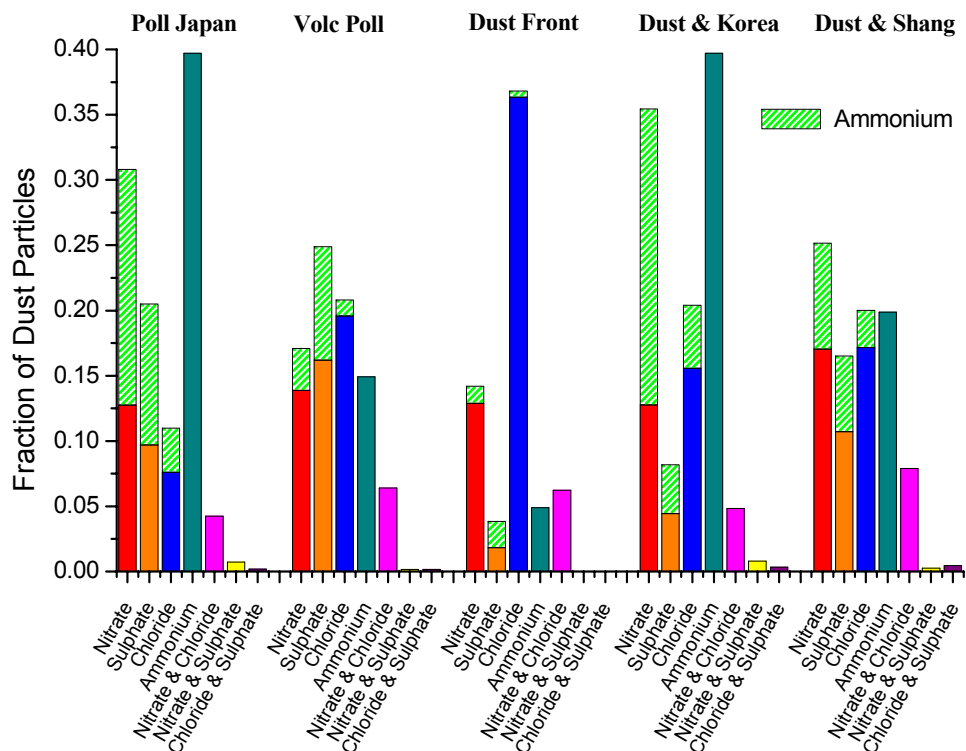
Figure 3.4. Fractions of mineral dust particles internally mixed with major secondary inorganic species in different air masses. A peak area > 5000 was used to define dust particles as mixed with chloride, nitrate, and sulfate, and a peak area > 1000 for ammonium. Dust particles mixed with sea salt have been excluded. The hatched portion of the column represents the fraction of dust particles mixed with a particular secondary acid that also contained ammonium (peak area > 1000).

mixed with sea salt to focus only on the role of secondary species produced in the atmosphere through chemical reactions.

Previous analyses of Asian mineral dust particles near their source show they typically have low concentrations of nitrate, sulfate and chloride (Andronova et al., 1993; Arimoto et al., 2004; Matsuki et al., 2005a; Mori et al., 2003; Nishikawa et al., 1991; Trochkine et al., 2003; Yuan et al., 2004; Zhang and Iwasaka, 1999). Thus, we conclude that these mineral dust particles accumulated secondary acids as they were transported from the desert regions over the polluted mainland and marine regions to the RHB, by either direct heterogeneous uptake, cloud processing, or coagulation with other secondary-containing aerosols such as ammonium

nitrate/sulfate particles. From DOY 98 to 105, a substantial, though highly variable fraction of mineral dust was mixed with the secondary species chloride, nitrate, or sulfate (Figs. 3.3 & 3.4). Just before the dust front, from DOY 100-100.8, there were elevated levels of both sulfate and ammonium corresponding to the Polluted Volcano air mass. From approximately DOY 100.8-102, the relative amount of chloride in the mineral dust increased dramatically, coinciding with the arrival of the dust front, while the amount of ammonium simultaneously decreased. The amount of nitrate and ammonium both increased noticeably from DOY 102-103.5. Dividing the peak areas of these species by a stable dust component, aluminum, provides further evidence for a secondary source of these four species. If these compounds were present in the dust particles at the source, we would expect their peak area ratios to remain constant as long as the dust source regions were not changing over short time periods. Clear temporal changes in the relative amounts of the secondary species associated with the dust are evident. Similar changes were also observed for these same species in the bulk mass concentration measurements of the dust-impacted air masses reported by Bates et al. (2004) and Quinn et al. (2004).

The presence of chloride in dust not due to mixtures with sea salt has only recently been reported (Zhang and Iwasaka, 2001). A very large increase in the chloride area ratio in dust (Fig. 3.2) was observed during the dust front's arrival, along with an increase in the total chloride mass concentration by a factor of nine (Arimoto et al., 2006; Bates et al., 2004). As discussed in detail in Chapter 4, the availability of HCl(g) for reaction with the mineral dust was likely strongly influenced by the release of SO_2(g) from the nearby Miyakejima volcano. The sea salt particles in the prefrontal air mass were highly aged and resulted in a depletion of $77 \pm 12\%$ of the total chloride in the sea salt (Bates et al., 2004). Thus, there were likely elevated levels of HCl(g) in the marine boundary layer just prior to the dust front's arrival.

This liberated HCl(g) then mixed with the incoming dust front as it subsided while there were depleted levels of HNO_3(g) and SO_2/H_2SO_4(g), due to their prior reaction with sea salt, permitting substantial chloride uptake onto the mineral dust. Figures 3.2 and 3.3 clearly show an increase in the amount of chloride in dust and a simultaneous decrease in the amount of nitrate and sulfate in dust during the Dust Front period. Had nitrate and/or sulfate formed on the dust particles during the dust front, this would have displaced much of the chloride to the gas-phase, or prevented its uptake in the first place. Thus, we hypothesize that the significant uptake of chloride by dust during the dust front occurred due to both the reduced mixing ratios of NO_y and SO_x, caused by their prior reaction with sea salt in the prefrontal air mass, and the subsequent release of HCl(g) from the highly aged sea salt particles (see Chapter 4 for a complete discussion).

In Figure 3.3b the hourly counts of dust mixed with one of the secondary species are plotted versus the total hourly dust counts measured by ATOFMS. Sulfate-dust has a very weak dependence on the total dust counts while nitrate-dust and chloride-dust have much stronger correlations over the DOY 98-105 time period. Thus, the mixing of dust with sulfate does not appear to be controlled by the total dust concentrations available, while the number of dust particles mixed with nitrate or chloride increases with increasing total dust concentrations. An explanation for this behavior is that sulfate becomes preferentially mixed with dust. This could be the result of dust reacting with SO_2/H_2SO_4 more efficiently, and/or because the dust plume encounters elevated sulfate precursors before encountering nitrate and chloride precursors. If dust mixes with sulfate first and becomes acidified then, in general, nitrate and chloride will only be able to become significantly mixed with dust if there is an abundance of additional, mostly unreacted dust surface area available for reaction with nitrate and chloride precursors. There would therefore be a dependence on total dust loadings for

nitrate- and chloride-dust, as shown in Figure 3.3b. The degree to which the mineral dust becomes internally mixed with a particular acid is likely predominantly controlled by the history of the air mass.

3.4.5   Mixing state of secondary acids in mineral dust

Nitrate- and sulfate-dust together accounted for 13,754 particles from DOY 98-105, yet only 142 (1.03%) of these dust particles satisfied the peak area > 5000 criterion for <u>both</u> $^{62}[NO_3]^-$ and $^{97}[HSO_4]^-$. Thus, significant amounts of both nitrate and sulfate did not accumulate on the same mineral dust particles. Similarly, only 98 out of 12,272 (0.80%) chloride-dust and sulfate-dust particles satisfied the peak area criteria for both $^{35}Cl^-$ and $^{97}HSO_4^-$, demonstrating that secondary chloride and sulfate were also externally mixed in the mineral dust. Nitrate and chloride, however, were present in the same mineral dust particles to a large extent; 14.8% of chloride-dust and nitrate-dust particles had peak areas > 5000 for both $^{35}Cl^-$ and $^{62}NO_3^-$. Recall that dust mixed with sea salt was excluded from this analysis and thus cannot account for this result. Further mixing state statistics for prefrontal and postfrontal air masses are provided in Figure 3.4, demonstrating the very low fractions of dust particles that contained significant amounts of both sulfate and nitrate or chloride in several different air masses.

The relative amounts of the three secondary species on all reacted dust particles during two time periods are shown in Figure 3.5. In the ternary plot, a dust particle containing primarily sulfate would appear at the top vertex, primarily nitrate at the right vertex, and primarily chloride at the left vertex. For both the Dust Front period (Fig. 3.5a) and the pre-frontal Polluted Volcano period (Fig. 3.5b), two broad groups of particles are evident in the ternary plots. The majority of particles lie along the bottom nitrate-chloride axis, indicating a wide range of internal mixing between nitrate and chloride in individual dust particles. A
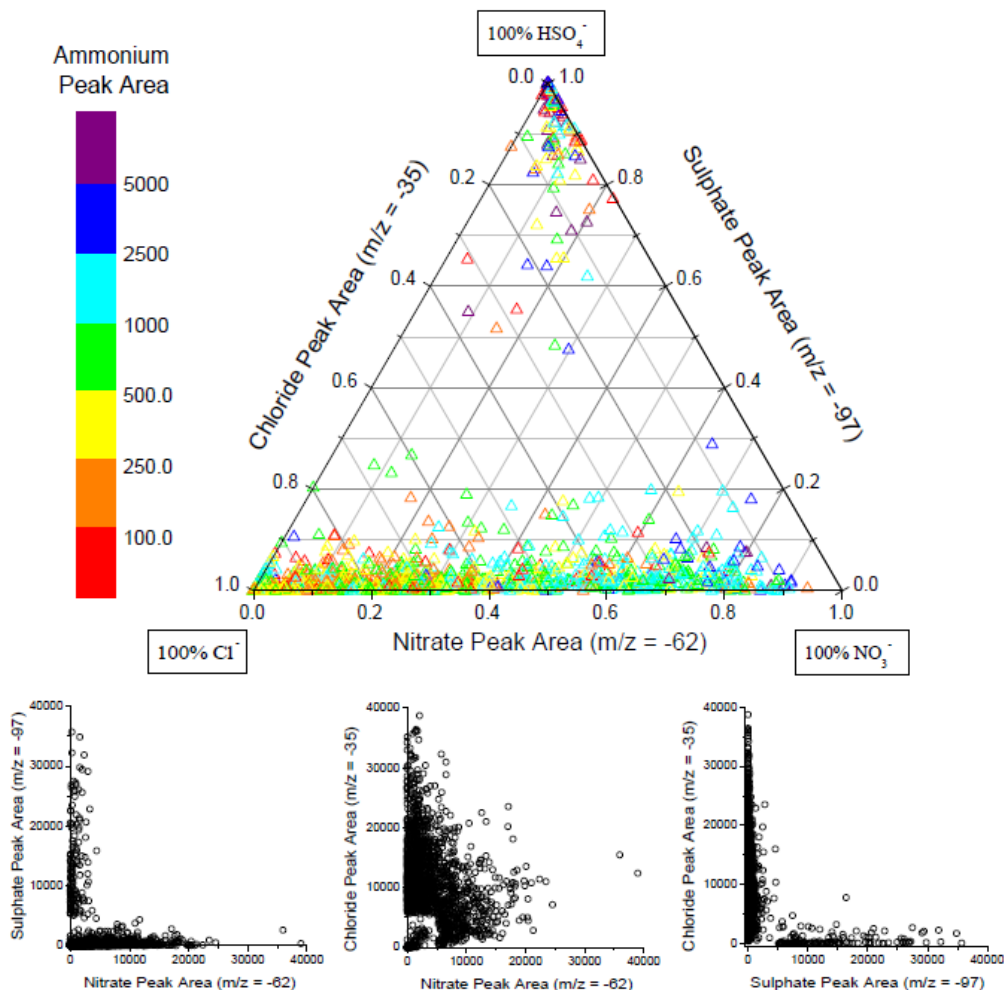
Figure 3.5a. The ternary plot (top) shows the relative distribution of peak areas for secondary chloride, nitrate, and sulfate in filtered mineral dust particles defined as "mixed" with either of the three acid products and detected during the Dust Front period (DOY 101-101.3). Each point is produced from a single dust particle's mass spectrum, 1768 in total are plotted. The symbol color corresponds to the absolute peak area of ammonium for each dust particle. The scatter plots (below) for pairs of secondary acid products are taken from the same data set and show the same trends as the ternary plot but on an absolute peak area scale.

smaller but still substantial group of particles is found at the top sulfate vertex, indicating that

these dust particles contain primarily sulfate and relatively little nitrate or chloride. The lack of

a significant number of particles lying along the sulfate-chloride or sulfate-nitrate axes, or

found in the centre of the ternary plot, further demonstrates that sulfate in aged mineral dust

particles is externally mixed from both nitrate and chloride. This is true for dust particles that contain significant amounts of secondary acid products. Nitrate and sulfate are found in the same dust particle but with peak areas much lower than the 5000 threshold, representing less chemically aged dust. The color of each point reflects that dust particle's ammonium absolute peak area. The largest ammonium signals were found in dust particles also containing nitrate or sulfate while chloride-dust particles had lower but still significant amounts of ammonium. The ternary plots of dust particles detected during the Polluted Volcano and Dust Front periods share these general features but there are more particles from the sulfate-only group in the Polluted Volcano period and more in the nitrate-chloride group during the Dust Front period. This agrees with the temporal changes displayed in Figures 3.2 & 3.3 that show a larger fraction of sulfate-dust before the dust front and a larger nitrate-dust and chloride-dust fraction during the dust storm. The PMEL filter mass measurements show similar temporal behavior for these species (Bates et al., 2004).

This segregation of sulfate from nitrate and chloride is further demonstrated by the scatter plots (bottom) in Figure 3.5a for the Dust Front period. The ternary plots show the relative partitioning of the absolute peak area signals for dust particles between the three major secondary acid peaks (with areas > 5000). The scatter plots, however, show the absolute areas for a set of two secondary acids for the same set of reacted dust particles used to generate the ternary plot. The large number of particles found along either axis in the sulfate-nitrate and sulfate-chloride scatter plots agrees with the segregation of sulfate from nitrate and chloride shown in the ternary plot. The large number of particles found near the centre of the nitrate-chloride scatter plot, however, further supports the substantial and variable internal mixing of these two secondary acids in the mineral dust. The reduced number of particles
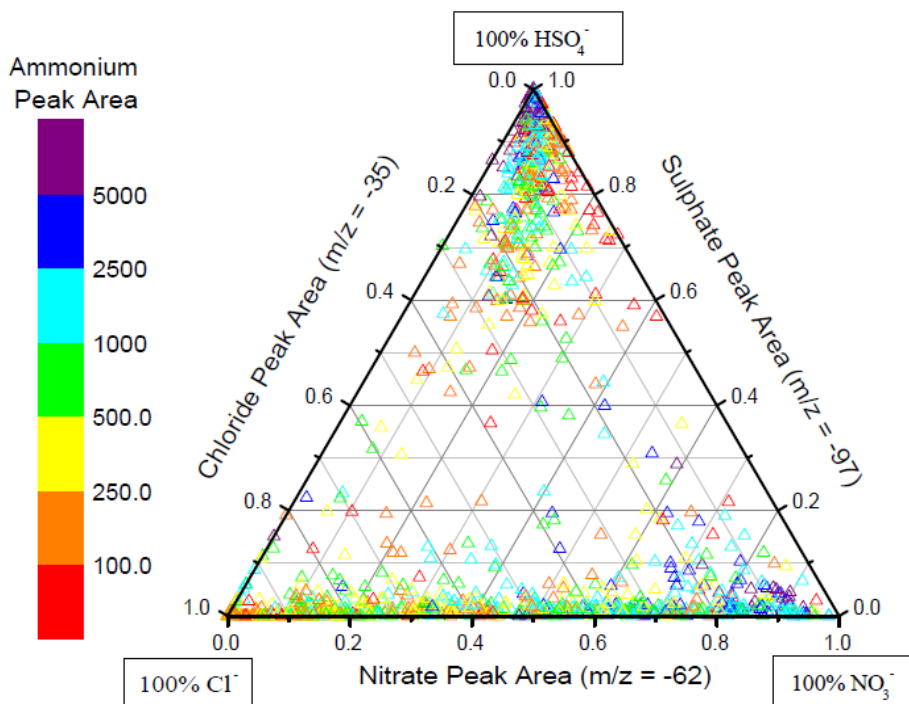
Figure 3.5b. As for Fig. 3.5a above but for dust particles detected during the Polluted Volcano period (DOY 99.3-100.5). Each point is produced from a single dust particle's mass spectrum, 1361 in total are plotted.

around the origin is caused by the peak area > 5000 criterion for $^{35}Cl^-$, $^{62}NO_3^-$, or $^{97}HSO_4^-$.

Very similar results were also found for the Polluted Volcano period (not shown).

3.4.6 Uptake of ammonia by acidified dust

In general, mineral dust shifts ammonia from the particle to gas phase by changing the aerosol from a cation- to anion-limited state due to the presence of alkaline species such as calcium carbonate (Song and Carmichael, 1999; Tang et al., 2004b). Mineral dust that has accumulated secondary acids can be a sink for ammonia, as a result of either direct uptake from the gas-phase, coagulation with ammonium sulfate/nitrate-containing particles (Mori et al., 1998), or heterogeneous nucleation (Korhonen et al., 2003). The acid can be present after reacting with and neutralizing the alkaline carbonates in the dust, or also by physisorption to the dust surface without chemical reaction. In the case of physisorption, ammonia can react
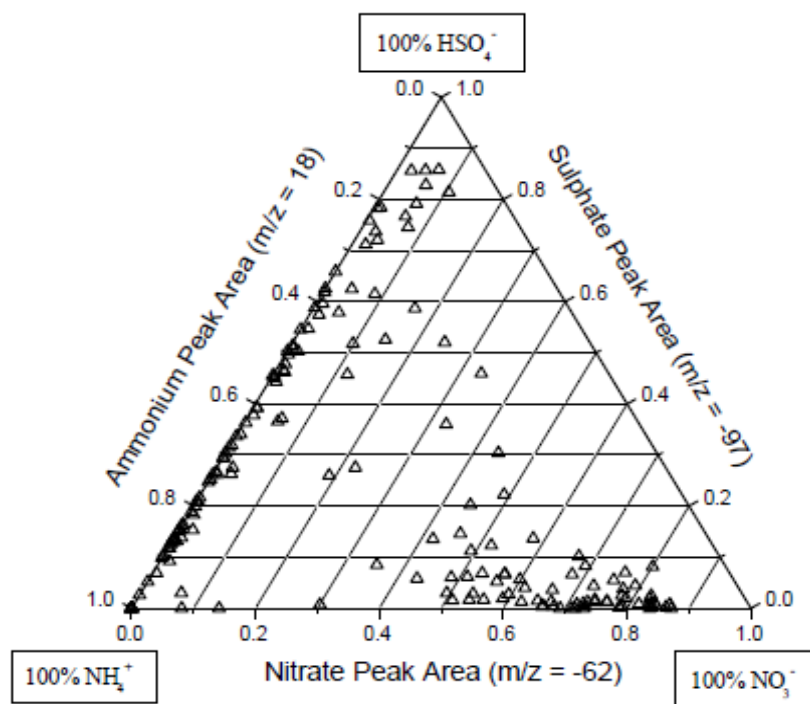
Figure 3.6. Relative distribution of absolute peak areas for nitrate, sulfate, and ammonium in nitrate-dust or sulfate-dust satisfying a peak area for m/z 18 > 1000, detected during the Polluted Volcano period. 364 dust particles are displayed.

with the acid on the surface without the prior consumption of alkalinity. The contributions of both processes should be explored, though likely reaction with alkaline carbonates accelerates the uptake of acids over simple physisorption.

The presence of ammonium nitrate and/or ammonium sulfate in individual mineral dust particles is demonstrated in Figure 3.6. The large cluster of particles lying along the ammonium-sulfate axis on the left indicates the presence of ammonium sulfate in mineral dust particles, while the smaller cluster of particles along the bottom ammonium-nitrate axis represents ammonium nitrate in dust. The fact that these particles appear primarily along one of these two axes indicates that the ammonium sulfate- or ammonium nitrate-dust particles do not also contain a significant nitrate or sulfate signal, respectively. This is expected based on the external mixing of nitrate and sulfate in dust presented above. The much larger spread in

the ammonium sulfate dust particles along the ammonium-sulfate axis compared to the ammonium nitrate cluster may be due to the variable $NH_4:SO_4$ molar ratio caused by partitioning between $(NH_4)_2SO_4$, NH_4HSO_4, and H_2SO_4.

Dust mixed with ammonium was queried using a peak area > 1000 for $^{18}[NH_4]^+$ criterion. Since a particle should first contain some acidic species in order for ammonia to partition to it, we would predict that the number of dust particles that contained ammonium would increase when the number of particles containing nitrate or sulfate increased. This would also be true if the mixing of dust with ammonium was caused by coagulation with or heterogeneous nucleation by ammonium nitrate/sulfate particles. Figure 3.7 shows how the fraction of reacted dust particles that contained ammonium tracked the temporal changes in the fractions of dust particles mixed with either nitrate or sulfate. The linear correlations between the hourly counts of dust that contained ammonium nitrate/sulfate and those that were mixed with nitrate/sulfate showed excellent agreement with R^2 = 0.808 and 0.814, respectively (Fig. 3.7 insets). This is an impressive degree of correlation considering that these queries were performed on all reacted dust particles, regardless of mineralogy, for seven days of ambient sampling which included several changes in the air mass source regions. The slopes of these correlations indicate the average fraction of nitrate-dust or sulfate-dust particles which also contained ammonium over this time period were 43% and 32%, respectively.

To investigate if ammonium was only associated with dust particles which also contained nitrate, sulfate, or chloride, all filtered dust particles with a peak area > 1000 for $^{18}[NH_4]^+$ were queried, returning 8870 particles for DOY 98-105. 4208 of these were dust particles also mixed with nitrate, 1846 were mixed with sulfate, and 1087 were mixed with chloride. Together dust mixed with one or more of the three acids accounted for 73% of the ammonium-containing dust. The remaining ammonium-dust particles can be explained by
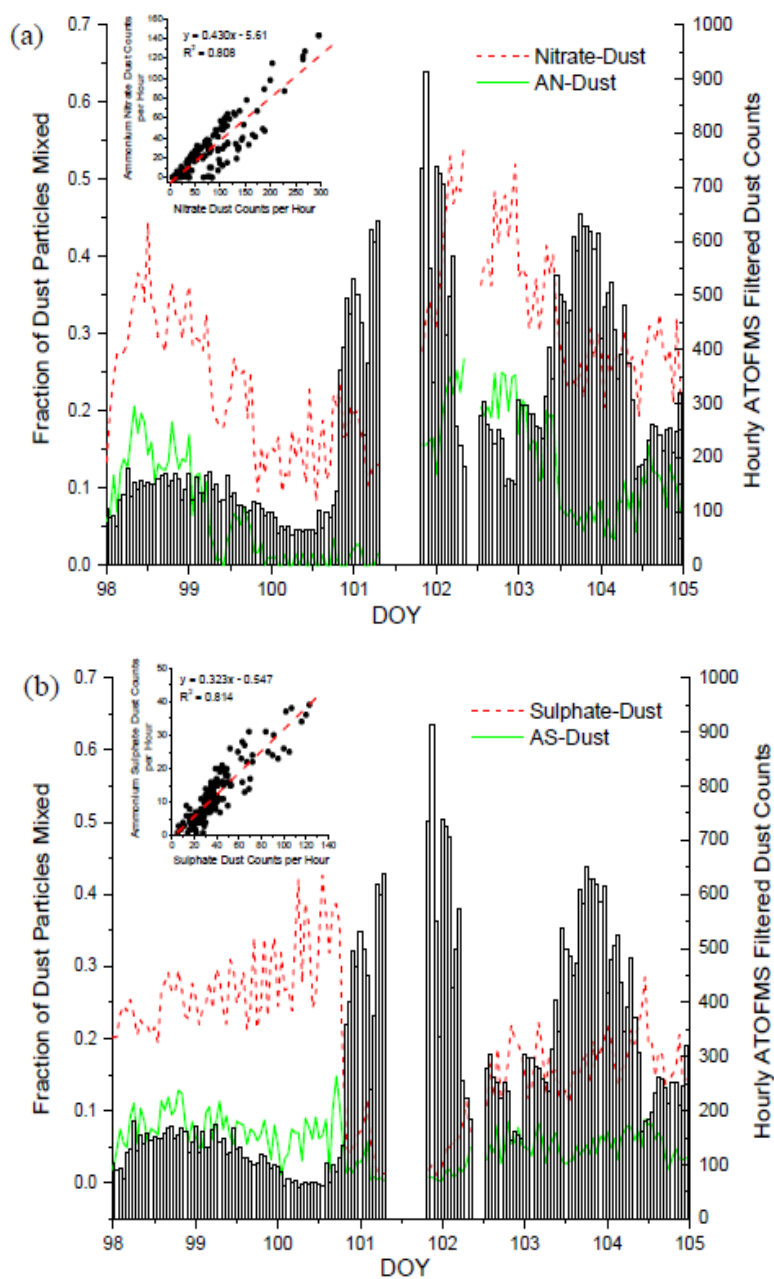
Figure 3.7. The fractions of filtered dust particles (lines) classified as mixed with (a) nitrate or ammonium nitrate; (b) sulfate or ammonium sulfate; and the total hourly filtered dust counts (bars). Scatter plots (insets) show the correlation between hourly counts of nitrate/sulfate dust and ammonium nitrate/sulfate dust. The slope of the linear fit indicates the average hourly fraction of nitrate- or sulfate-dust that was also mixed with ammonium.

having significant signals for chloride, nitrate, and sulfate (i.e. peak area > 1000) that did not exceed the 5000 peak area threshold. More detailed statistics of the mixing state of dust with ammonium and secondary acids are given in Figure 3.4. There were no indications in the average mass spectra that the ammonium was present in dust particles that did not also contain secondary acids to some extent. This was also confirmed by peak area searches within this subset. Therefore, ammonium was only found in dust particles that also contained acidic species such as nitric, sulfuric, and, to a lesser extent, hydrochloric acids.

The temporal correlations of chloride-dust and dust mixed with both ammonium and chloride (not shown), thus containing ammonium chloride, were not as significant as those for ammonium sulfate or ammonium nitrate. There were two time periods when ammonium chloride-dust was detected and these both occurred when chloride-dust dominated. The largest of these was from DOY 108.88-102.38 (Dust & Korea period) when 29.8% of the 1087 total ammonium chloride-dust particles were detected over just 13 hours. From DOY 103.0-105.0 (Dust & Shanghai period) 52.4% were detected. There were no significant counts of ammonium chloride-dust during the first Dust Front period (DOY 101) when the initial large increase in chloride-dust occurred.

We are not able to directly determine the degree to which available alkalinity in the dust has been neutralized by the secondary acids. However, we do find that ammonium was only in dust particles that also contained secondary acids in the form of nitrate, sulfate or, to a lesser extent, chloride. Taking the sum of the nitrate ($m/z = -62/27$) and sulfate ($m/z = -97/27$) hourly peak area ratios as a measure of the available acid in the dust and plotting this versus ammonium ($m/z = 18/27$) in Figure 3.8 reveals a strong temporal trend between the amount of acid in the dust and the amount of ammonium, as expected. Note the strong anti-correlation of ammonium and the two other acids with chloride ($m/z = -35/27$) in the dust, particularly on
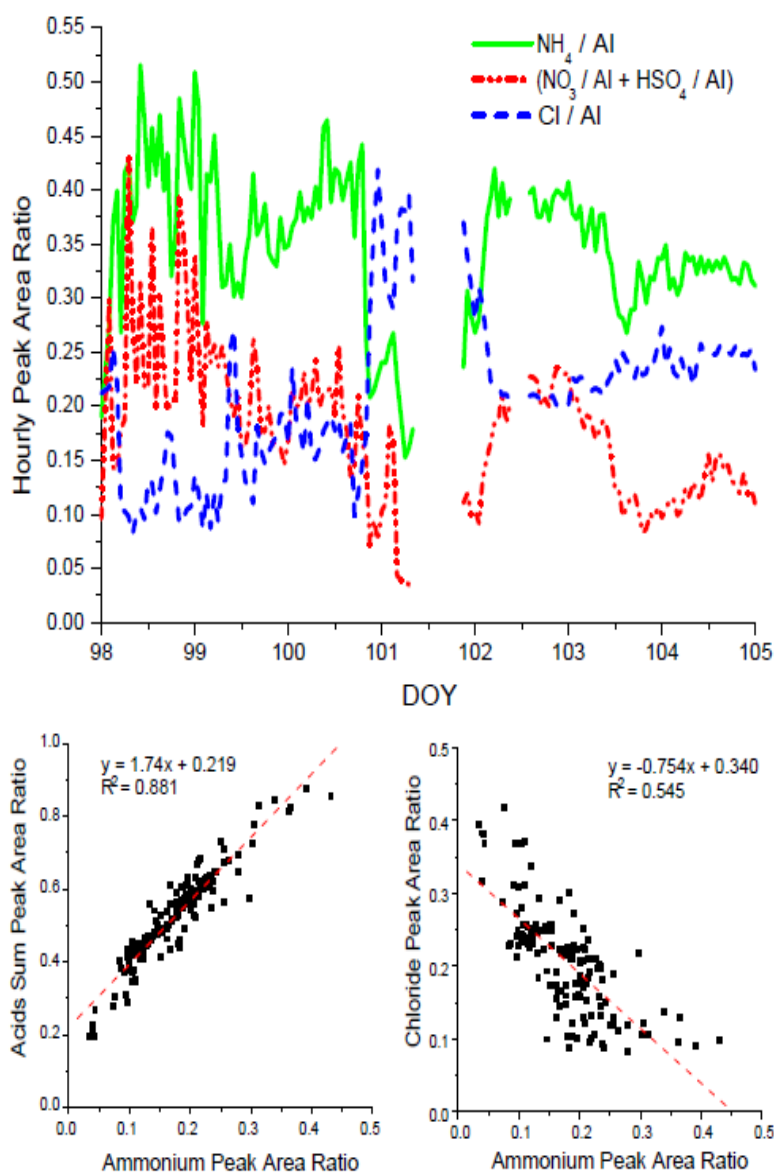
Figure 3.8. Correlation between ammonium and acids in dust. Top: Hourly peak area ratios for ammonium (18/27), chloride (-35/27) and the sum of nitrate (-62/27) plus sulfate (-97/27) for all filtered dust particles from DOY 98-105. Bottom: Scatter plots of the correlation between ammonium and sum of chloride + nitrate + sulfate hourly peak area ratios for this time period (left), the hourly peak area ratios of chloride and ammonium (right), and the corresponding least-squares linear fits.

DOY 101. However, on DOY 104 the peak area ratios for chloride, and the two acids all

stabilize. The degree of correlation between the hourly peak area ratios for nitrate + sulfate,

and ammonium has a $R^2 = 0.574$.

In the troposphere, ammonium sulfate is the most stable and thus preferred ammonium salt, followed by ammonium nitrate. Ammonium chloride, while the least preferred, is also a realistic ammonium salt in the troposphere. Dust containing ammonium chloride was detected during two distinct time periods (DOY 108.88-102.38 and 103.0-105.0). Thus, the amount of ammonium in dust should track the amount of chloride, in addition to sulfate and nitrate on dust. This should be especially true when the stronger sulfuric and nitric acids are not available to neutralize ammonia first, as was the case for the Dust Front period. If chloride is also included in the sum of the peak area ratios (Fig. 3.8), the R^2 is greatly improved from 0.574 to 0.881. This result was found despite the strong anti-correlation between the peak area ratio of chloride and ammonium. This could reflect the fact that ammonium chloride-dust was only detected in two periods and at low concentrations, the first of which occurred when both sulfate-dust and nitrate-dust were greatly reduced. Thus, by including chloride, this time period of ammonium mixed with dust that would not be explained by sulfate or nitrate was captured. The overall anti-correlation of chloride and ammonium on dust may simply be a reflection of an anti-correlation of $HCl(g)$ and $NH_3(g)$ mixing ratios, as the two likely have very different sources for this area. It does not necessarily reflect an inefficient process for ammonia to react with dust acidified by HCl.

The internal mixing of $(NH_4)_2SO_4$, NH_4NO_3, and NH_4Cl with dust is a significant finding that has previously been reported from ATOFMS ambient measurements in Riverside, California (Noble and Prather, 1996b), but not for dust storm events. Heterogeneous nucleation of $(NH_4)_2SO_4$ on dust can produce ammonium sulfate coatings around dust and suppress the growth of ammonium sulfate particles to detectable sizes (Korhonen et al., 2003). Several researchers have frequently stated that ammonium sulfate measured in submicron particles during dust storms are due to ammonium sulfate particles externally mixed from dust

(Jordan et al., 2003; Mori et al., 2003; Song et al., 2005; Tang et al., 2004b). We have clearly demonstrated that ammonium sulfate was internally mixed with dust particles during ACE-Asia, particularly in the submicron dust (Fig. 3.6). Thus, the assumption of externally mixed ammonium sulfate and dust particles during ACE-Asia at sea level should be re-evaluated. In the future, single particle measurements can be used to unambiguously determine the exact aerosol mixing state.

3.4.7   Effect of dust mineralogy on chemical processing

The role that dust particle mineralogy plays in its interactions with secondary acids and their precursors was investigated by comparing dust particles with high amounts of Ca to dust with high amounts of Al. These types broadly represent dust particles rich in calcite or aluminosilicates, respectively. This was achieved by searching within the filtered dust for particles with a relative peak area > 10% for either $^{27}Al^+$ or $^{40}Ca^+$. Together these two types of dust account for 55.2 ± 5.7% of the total filtered dust counts. Clear differences between these two types of dust are shown in the temporal changes of the hourly peak area ratios for the three major secondary acid reaction products in Figure 3.9. Most notable is a large spike in the sulfate area ratio at DOY 100.5 in the high-Al dust that does not occur in the high-Ca dust. The sulfate peak area ratio also increases from DOY 103.5-105 in the high-Al dust but remains mostly unchanged in the high-Ca dust. There are also noticeable differences in the increases in the chloride area ratio from DOY 101-102 for the two types of dust. The majority of chloride uptake during the Dust Front period, beginning on DOY 100.8, took place on the high-Ca dust particles, suggesting reaction with calcite in the dust.

These results imply that sulfate is more strongly associated with aluminosilicate-rich dust particles while nitrate and chloride are more associated with calcite-rich dust. Figure 3.10 provides further evidence for this mineralogy dependence. The ternary plot displays the
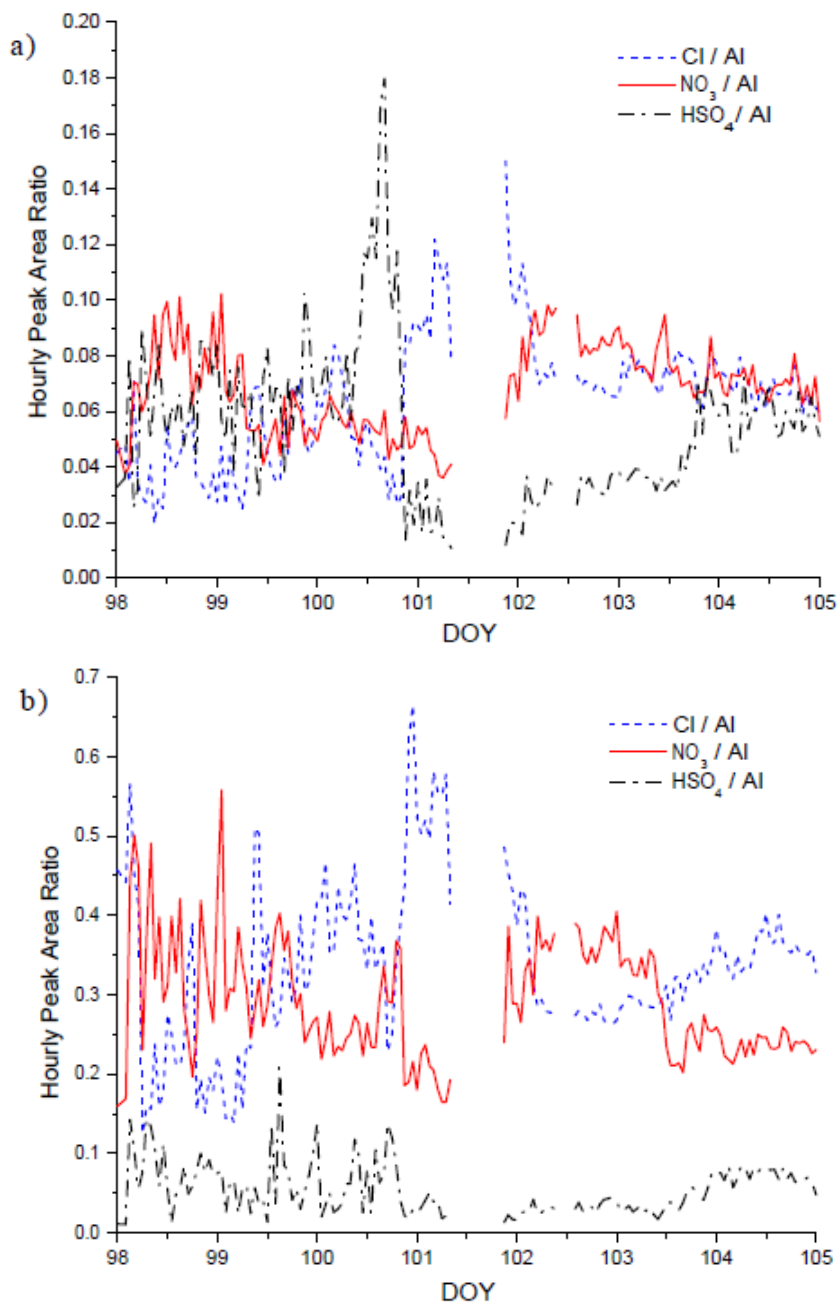
Figure 3.9. Hourly peak area ratios of the three major secondary acid reaction products: chloride, nitrate and sulfate, for filtered dust particles with large ion signals for Al (a) or Ca (b).

relative distribution of three major dust mineral components: aluminum, calcium, and iron. The ^{54}Fe isotope was selected for iron to avoid interference from ^{56}[CaO]$^+$. Reacted dust particles detected during the Dust & Shanghai period are displayed in both Figures 3.10a and

3.10b. In Fig. 3.10a, the symbol color corresponds to the sulfate absolute peak area while in Fig. 3.10b, the color corresponds to the nitrate absolute peak area. Only dust particles containing relatively large amounts of nitrate or sulfate (peak area > 5000) are displayed. These two figures show dramatically different mixing behavior for nitrate versus sulfate and are virtually complete opposites of one and other. This reflects the segregation of large amounts of nitrate and sulfate in dust particles, as discussed above. The sulfate-rich dust particles predominantly lie near the aluminum vertex and extend towards the iron vertex, indicating an association with aluminosilicate-dust particles and their associated enriched iron content (Jickells and Spokes, 2001). The nitrate-dust particles are mostly located towards the calcium vertex, being associated with calcite- and dolomite-rich and dust. An analogous ternary plot using the chloride peak area (not shown) displays very similar behavior to the nitrate ternary plot (Fig. 3.10b), with the largest chloride peak areas being found on Ca-rich dust particles, while Al-rich particles contain much lower chloride signals. The processes that cause this behavior are discussed below.

The carbonate portion of Asian mineral dust is typically considered to be the principle component controlling the uptake of acidic vapors by dust due to its alkalinity (Song and Carmichael, 1999; Song and Carmichael, 2001; Tang et al., 2004b). Both HNO_3 and HCl are mineral acids with an acidic proton that can be readily neutralized upon reaction with alkaline species such as carbonate. SO_2 however, is an acid anhydride and does not contain acidic protons until it is hydrated and oxidized to S(VI). The strong association of nitrate and chloride with calcium-rich dust could be due to the ability of HNO_3, HCl and other precursors to react with carbonates through simple acid-base chemistry. SO_2, not initially containing any acidic protons, is unable to react with calcium carbonates in this direct manner. This would explain why sulfate is not enriched in calcium-rich dust. Since our data suggest that sulfate
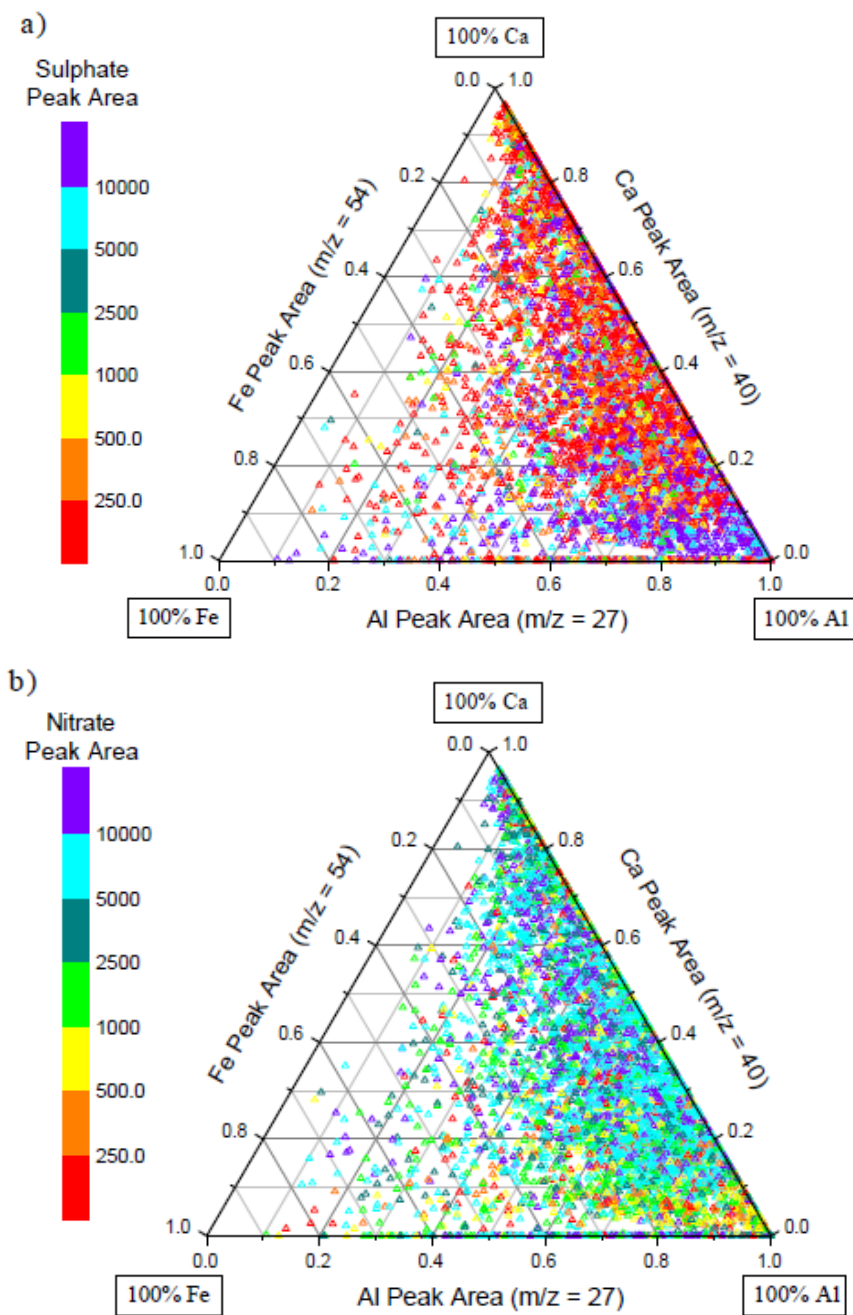
Figure 3.10. Relative distribution of peak areas for three major mineral components, Fe, Ca, and Al, for reacted dust particles detected during the Dust & Shanghai period. The same 5812 dust particles are displayed in both figures with the symbol colour corresponding to the sulfate absolute peak area (a), or the nitrate absolute peak area (b).

accumulates in the dust first, it appears sulfate will react with the mineral component for which it has the highest affinity. We propose that the association of sulfate with Al- and Fe-rich dust is due to the iron-catalyzed oxidation of SO_2 to H_2SO_4 (Brandt and Vaneldik, 1995; Qi et al., 2006; Rani et al., 1992; Yermakov and Purmal, 2003). The majority of the oxidation by this process is thought to occur in the aqueous phase containing dissolved metal ions (i.e. a homogeneous reaction), but the role of surface-catalyzed heterogeneous reactions involving metals may also play an important role (Brandt and Vaneldik, 1995; Rani et al., 1992). The solubility of the metal ions is a key factor controlled by the aerosol's pH and the presence of organic compounds that could chelate the metals. The solubility of iron in dust aerosols is an important but poorly understood factor at present (Jickells et al., 2005; Luo et al., 2005). The rate of this reaction is accelerated at higher pH and thus this sulfate formation pathway is self-quenching. The alkaline nature of Asian mineral dust could enhance the role of iron in the oxidation of sulfur by buffering the pH and increasing this pathway's reaction rate compared to other major pathways such as oxidation by H_2O_2. Relativity humidity has been found to be an important factor for the uptake of acids by dust in both lab and recent field studies (Al-Hosney and Grassian, 2005; Goodman et al., 2001; Krueger et al., 2003; Laskin et al., 2005a; Matsuki et al., 2005b; Ullerstam et al., 2002), however our data set does not allow us to directly investigate this important issue.

3.4.8   Mechanism of secondary acid uptake: size dependence

The distribution of secondary species as a function of dust particle size provides important insights into the mechanisms for the accumulation of acids in dust. The mechanism that is outlined here is based on that of Bassett and Seinfeld (1984b) and Song and Carmichael (1999). In general, the accumulation of sulfate by particles through reaction with SO_2/H_2SO_4 is diffusion limited. Thus, it occurs preferentially in the particle size mode with the greatest

surface area, which is typically the accumulation mode (D_a = 0.1–1.0 μm). As sulfuric acid is essentially non-volatile and a stronger acid than both nitric or hydrochloric acid, the accumulation of sulfuric acid in a particle will prevent additional uptake of HCl, HNO_3, NO_2, etc. These gases will instead react with the less-acidic supermicron dust that represents a larger alkaline sink by mass for these acids. The accumulation of sulfuric acid in submicron dust will also displace any pre-existing nitrate or chloride back to the gas-phase as these are weaker acids and more volatile than H_2SO_4. Nitric acid and hydrochloric acid in the gas-phase can then re-partition to supermicron dust particles that have not already been acidified (Song and Carmichael, 2001). Thus, the irreversible uptake of SO_2 and H_2SO_4 is kinetically limited while the uptake of the more-volatile HCl and HNO_3 is thermodynamically controlled. Therefore, sulfate will accumulate in submicron dust while nitrate and chloride will accumulate in supermicron dust particles. The uptake of ammonia is typically determined by the preceding SO_2/H_2SO_4 uptake, and thus ammonium predominantly accumulates in submicron dust.

Evidence for this uptake mechanism occurring in the aged mineral dust detected during ACE-Asia is presented by the distribution of the peak area ratios for these secondary species as a function of particle size in Figure 3.11a. The average peak area ratios for sulfate and ammonium clearly peak in the submicron filtered dust particles. Nitrate and chloride both peak in the supermicron dust particle mode. Despite the high loading of supermicron dust during the dust front, the largest aerosol surface area mode was still in the accumulation mode (Bates et al., 2004; Quinn et al., 2004). Similar results are shown in Figure 3.11b, this time plotting the fraction of filtered dust particles previously classified as mixed with chloride, nitrate, sulfate (peak area > 5000), or ammonium (peak area > 1000) as a function of size. Again, sulfate-dust peaks in the submicron mode while nitrate- and chloride-dust peak in the
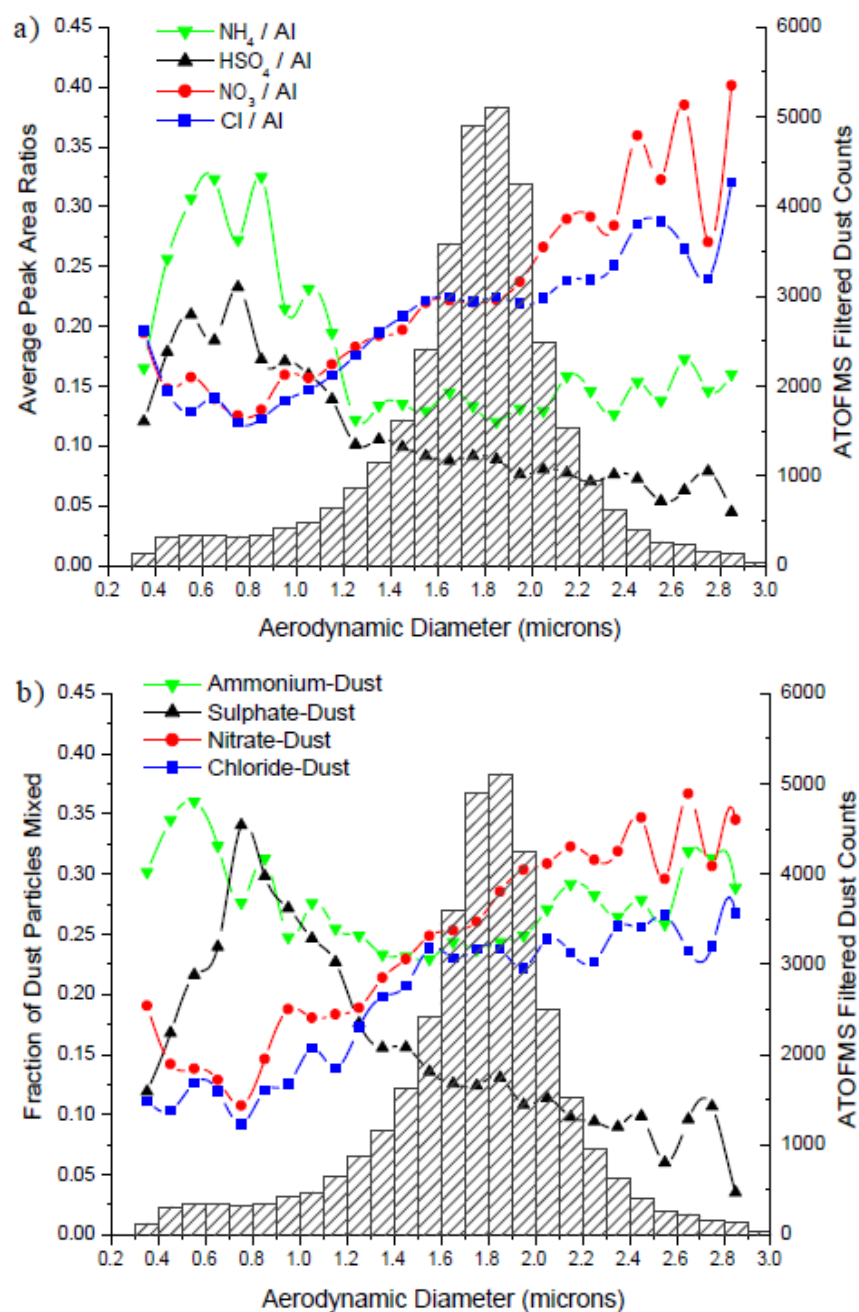
Figure 3.11. Size distributions of secondary species in mineral dust particles. (a) Average single-particle peak area ratios (lines) for four major secondary species from all filtered dust particles detected from DOY 98-105. (b) Fraction of filtered dust particles (lines) classified as mixed with one of the four major secondary species. The size distribution of the set of particles used to generate both figures is also displayed (columns) and reflects the inlet efficiency of the ATOFMS, and not the actual size distribution of the aerosol population.

supermicron. Ammonium-dust has two modes, the largest in the submicron mode along with sulfate-dust and a smaller one in the supermicron mode along with nitrate and chloride-dust. Taken together, these size plots indicate that ammonium accumulates in both the submicron sulfate-dust and the supermicron nitrate/chloride-dust, but the relative amount of ammonium per dust particle is greater in the submicron sulfate-dust mode.

The results suggest that the submicron dust particles were very acidic due to mixing with sulfuric acid early during transport. This prevented the substantial mixing of nitrate and chloride in the submicron dust particles when the dust plume later encountered elevated NO_y and HCl. This also suggests that there was not enough ammonia to neutralize all of the sulfuric acid in the dust. The bulk mass concentration of ammonium was relatively constant from DOY 98-105 while that of nitrate and sulfate varied significantly and were elevated in the post-frontal dust air masses, exceeding ammonium (Bates et al., 2004). The internal mixing of nitrate and chloride (Fig. 3.5) is a result of the greater alkaline mass in the supermicron dust that can neutralize both acids and allow them to exist internally mixed to some degree in the same dust particle. The volatile nature of these two inorganic species allows them both to be displaced to the gas-phase, if displacement is occurring, and then re-partition back to the supermicron dust particles where they are less volatile.

Similar size-distributions of secondary species in Asian mineral dust have been reported previously from the analysis of collected filter samples and in modeling studies (Bates et al., 2004; Mori et al., 2003; Nishikawa et al., 1991; Ooki and Uematsu, 2005a; Tang et al., 2004b; Wu and Okada, 1994; Zhang et al., 2000). However, our results are the first to show the size distribution of secondary species exclusively for individual aged mineral dust particles. We also have the ability to exclude the influence of internally mixed dust and sea salt particles. The 0.10 μm size resolution provided by the ATOFMS measurements is another

significant advantage over filter-based methods. Together these factors result in a unique and important set of results that directly confirm aerosol model predictions of mineral dust aging mechanisms.

3.4.9 Segregation of sulfate from nitrate and chloride

To the best of my knowledge, this is the first report of the segregation of sulfate from nitrate and chloride in individual mineral dust particles that have experienced extensive atmospheric aging and transport (Figs. 3.5 & 3.10). Murphy and Thomson (1997) reported the external mixture of chloride and sulfate in individual ambient particles (not limited to dust) detected at Idaho Hill and also found that sulfate and nitrate were usually, but not always, found in separate particles. Zhang et al. (2000) detected coarse and fine mode single particles collected on filters in coastal China that were internally mixed with sulfate and nitrate. These particles also typically contained mineral elements indicative of dust. Using similar methods, significant fractions of Asian dust particles collected in Japan were also found to contain both nitrate and sulfate (Zhang et al., 2003a). In both these reports, the detection of nitrate and sulfate in each particle was purely qualitative and the detection limits for nitrate and sulfate on the coated collection substrates were 10^{-14} and 10^{-17} g, respectively. Thus, a mineral dust particle containing even a small amount of nitrate and/or sulfate would be reported as internally mixed with nitrate and sulfate.

The aging mechanism presented in Chapter 3.4.8 can be used to explain the segregation of sulfate from nitrate and chloride in dust. As sulfate is non-volatile and the strongest acid, it will prevent the accumulation of other weaker acids once it has formed in the mineral dust. The segregation therefore indicates that sulfate accumulated in the dust first. This could be the result of a faster kinetic rate for the formation of sulfate in dust compared to

nitrate and chloride, and/or the dust plume encountering sulfate precursors prior to those of nitrate and chloride.

Numerous laboratories studies have measured reaction probabilities for various acidic gases with mineral dust surfaces. Most of these have involved reacting the dust with one gas at a time, though Ooki and Uematsu (2005a) reacted Asian dust particles with ambient Tokyo air containing acidic gases (e.g. SO_2, NO_2, HNO_3, and HCl). In general, the reaction probabilities for HNO_3 with dust are found to be several orders of magnitude higher than for NO_2 or SO_2 (Hanisch and Crowley, 2001; Ullerstam et al., 2003; Underwood et al., 2001b; Usher et al., 2003a; Vlasenko et al., 2006). The study of Ooki and Uematsu (2005a) is the only one we are aware of that has studied the reaction of HCl(g) with dust particles. They found that the dust predominantly reacted with HNO_3 (48%) and HCl (40%), and not with SO_2 (12%); no reaction probabilities were determined. Santschi and Rossi (2006) measured the reaction probability for HCl(g) on calcite to be 0.1, which was the same value they found for HNO_3 and SO_2. They stressed the role that adsorbed water plays in the kinetics.

While HNO_3 and HCl exhibit much higher reaction probabilities than SO_2 or NO_2, the latter two gases are typically present in much higher concentrations in the lower atmosphere than either HNO_3 or HCl, and thus the actual rate of reaction of these four gases with dust may be quite similar. The fact that sulfate appears to accumulate first in the aged dust (Fig. 3.3b) despite the fact that the reaction probability for SO_2 with dust is 1-2 orders of magnitude less than for HNO_3 or HCl indicates that kinetics is not the major factor controlling which acids the dust reacts with preferentially. Zhang et al. (2003a) concluded that the formation of sulfate on Asian dust is more efficient than for nitrate based on a much greater abundance of dust particles that contained sulfate than nitrate. They attributed this to the greater concentrations

of SO_2 than NO_x in East Asia and to the non-volatile nature of sulfuric acid compared to the more volatile nitric acid; both of these factors are discussed further below.

In general, the emissions of SO_2 are greater than of NO_x in east Asia. This difference is most pronounced in the interior due to SO_2 emissions from industrial activity and coal power plants (Akimoto and Narita, 1994; Streets et al., 2003; Tang et al., 2004b). The emissions of NO_x are greatest in the large urban areas near the coast, but still do not exceed those of SO_2. Finally, the mixing ratios of HCl will be greatest in the polluted marine boundary layer primarily due to the release of HCl from acidified sea salt particles (Tang et al., 2004b). Thus, it is reasonable to assume that mineral dust particles being transported eastward from the interior by a cold front first encounter elevated SO_2, followed by both SO_2 and NO_x in polluted coastal regions, and finally elevated HCl once over marine areas. This causes sulfate to mix with dust first, before nitrate or chloride, and explains the weak dependence of sulfate-dust concentrations on the total dust loadings (Fig. 3.3b). Interaction of dust with SO_2 from coal burning was also used to explain the strong association between sulfate and single dust particles measured in Japan, recently reported by Matsumoto et al. (2006). Despite the numerous laboratory findings that HNO_3 reacts with dust more rapidly than SO_2 does, sulfate accumulates in the dust first because it encounters elevated SO_2 early in its transport history.

The displacement of nitrate and chloride back to the gas-phase due to the uptake of SO_2/H_2SO_4, a stronger acid, is one possible explanation for the segregation of sulfate in mineral dust from nitrate and chloride in dust presented in Figure 3.5. Mineral dust that has accumulated enough SO_2/H_2SO_4 to neutralize any alkaline components of the dust (likely $CaCO_3$) and acidify the particle will also prevent any further uptake of nitric or hydrochloric acids by that dust particle. If uptake of sulfate versus nitrate and chloride were a displacement

process, numerous dust particles should appear between the 100% HSO_4^- vertex and the 100% NO_3^- or 100% Cl^- vertex. Figure 3.5 clearly shows a lack of significant numbers of particles in these areas. This indicates that the earlier mixing of dust with sulfate precursors was the likely cause of this segregation, not displacement. The chemical mineralogy of dust also plays an important role in determining which acids will preferentially react with dust. Together these processes explain the segregation of sulfate from nitrate and chloride in dust particles.

3.4.10 Comparison with STEM-2K3 regional model and modeling recommendations

The regional transport model, STEM-2K3, was employed to simulate the evolution of aerosol size and composition in east Asia during the ACE-Asia campaign. The extensive results of these simulations in relation to the Asian dust event are described by Tang et al. (Tang et al., 2004a; 2004b). A good comparison of ATOFMS data and STEM-2K3 simulations for the degree of sea salt aging has already been reported (Tang et al., 2004b). The model simulation captures the shift in particulate nitrate from aged sea salt to dust particles that we observed when the dust front arrived. Regarding mineral dust chemistry, the simulations find the presence of Asian dust enhances the production of sulfate and nitrate and increases the supermicron fraction of these species, due to the large size of the dust particles. The production of sulfate increases by 10-40%, with much of this additional sulfate forming in supermicron particles. More than 80% of nitrate and 10-30% of sulfate is found to exist in the supermicron mode (all particle types) during dust events. This agrees with the size distributions we presented in Figure 3.11. The model and other observations also find ammonium is restricted to the submicron mode, which is mostly in agreement with our single-particle dust results. Figure 3.11b shows that a small fraction of supermicron dust contains ammonium. The simulations find that the concentration of nitrate is more sensitive to dust

loadings than that of sulfate. This agrees with our finding that nitrate-dust (and chloride-dust) is more sensitive to total dust concentrations than sulfate-dust is (Fig. 3b). Tang et al. (2004b) also discuss the importance of the elevated SO_2 emissions in the interior of China (Sichuan basin), which leads to higher concentrations of sulfate in the interior, while nitrate and ammonium are maximized in the east towards the coast. They find that sulfate loadings exceed nitrate throughout most of the region, due to the significantly higher SO_2 emissions, which are a factor of 3 larger (by mass) than NO_x emissions. This agrees with the timeline we presented in Section 3.9 in which dust encounters elevated SO_2 before NO_x and HCl, which explains the dust-loading dependence in Figure 3.3b and the segregation of sulfate from nitrate and chloride (Fig. 3.5). In general, the simulations from the STEM-2K3 model are in excellent agreement with our single-particle dust observations, especially in determining the size distributions of secondary inorganic species in dust-impacted aerosol.

One area where the ATOFMS field data and the model simulations disagree concerns the formation of ammonium on dust. Tang et al. (2004b) state "if NH_3 concentrations are in excess of that needed to neutralise sulfate, then NH_4NO_3 can exist in the fine mode, even in the presence of dust." However, our data strongly indicate that a large fraction of the dust aerosol was largely acidic (Figs. 3.3, 3.4 & 3.11), especially for submicron dust, based on the segregation of sulfate and nitrate from each other. Regardless, 42% of the sulfate-dust and 31% of the nitrate-dust was also internally mixed with ammonium, on average. This implies that while there was not enough ammonia to neutralise all the acid in the dust, ammonia still partitioned to the aged dust to a significant extent. Jordan et al. (2003) drew a similar conclusion from their TRACE-P data as Tang et al. did, arguing against the association of ammonium with nitrate and sulfate in the presence of dust. We have demonstrated that

ammonium is internally mixed with nitrate and sulfate in the dust-impacted aerosol, suggesting a re-evaluation of these previous statements.

Many studies, including this one, have shown the importance that dust mineralogy plays in affecting atmospheric chemistry reaction pathways. The STEM-2K3 model accounted for this by assuming a certain fraction of the calcium carbonate in the dust was available for reaction. This remains an important but still uncertain parameter. More detailed descriptions that capture the heterogeneity of the chemical composition of dust at the single-particle level are required to more accurately model its chemistry, though this will be computationally expensive. Our observations of sulfate being segregated from nitrate and chloride in dust indicate that it is not accurate to treat dust as one internally mixed component in aerosol models. The role that relative humidity and the availability of carbonate, iron, and other reactive dust components for reaction play in the chemical kinetics remain important issues under investigation that need to be incorporated into aerosol chemical models. As the STEM-2K3 model has done, it is important to accurately model not only the dust composition and kinetic rates, but also the spatial distributions of gas emissions and the timeline that the aerosol encounters these reactants. As our observations suggest, the concentrations and order in which the dust reacts with various gaseous pollutants can be more important than the reaction kinetics alone.

3.5 Conclusions

ATOFMS measurements of individual dust particles during ACE-Asia show significant fractions of the dust were internally mixed with secondary acids and ammonium. To my knowledge, this is the first report of the segregation of sulfate from nitrate and chloride in individual dust particles. The sulfate appears to accumulate in the dust before nitrate and

chloride. These results are explained by a transport timeline in which the dust plume encounters elevated $SO_2(g)$ in the interior near the dust source before mixing with $NO_y(g)$ and $HCl(g)$ in coastal areas. The significant uptake of chloride (not from sea salt agglomeration) by dust was caused by reaction with $HCl(g)$ released from acidified sea salt. The prior reaction of nitrate and sulfate precursors with sea salt particles reduced the availability for nitrate and sulfate to form on dust while simultaneously releasing $HCl(g)$. Laboratory studies of the competitive reaction of various acidic gases with mineral dust particles are required to investigate the novel segregation results reported here. This segregation and preferential temporal uptake of secondary acids has important implications for the accurate modeling of the troposphere's gas and particle phase composition during dust events. This must be accounted for when modeling the evolution of dust particles during atmospheric transport and processing as it will affect the ability of aged dust to react further with trace gases, and alter the atmospheric lifetime of dust.

Nitrate and chloride were enriched in supermicron dust while sulfate and ammonium were enriched in the submicron mode. This size distribution of secondary acids in dust provides direct evidence in support of model mechanisms of mineral dust aging, using single-particle measurements of size-segregated dust particles not mixed with sea salt to confirm these models' predictions. Ammonium was only found in dust particles also containing secondary acids and the amount of ammonium strongly correlated with the sum of acids in the dust. Ammonium salts were internally mixed with dust particles, especially in the submicron mode, contrary to previous suggestions that submicron ammonium sulfate is externally mixed from dust. Based on these findings, the common assumption that submicron ammonium sulfate and mineral dust particles are externally mixed should be revisited.

The mixing of dust with secondary acids and ammonium has significant implications for the chemical composition of the troposphere, as well as the chemical, physical and optical properties of dust laden aerosol populations and their subsequent climactic effects. The reaction of NO_y and SO_x species with dust can cause significant changes in the partitioning of trace reactive species between the gas and particle phase (Tang et al., 2004a). The uptake of hydrochloric acid by mineral dust has recently been demonstrated in this and previous reports (Murphy et al., 2006; Ooki and Uematsu, 2005a; Zhang and Iwasaka, 2001)[1] and must also be considered in models of tropospheric chemistry. Mixing of secondary acids and ammonium with supermicron-dominated dust in dust plumes causes a shift of these species from submicron to supermicron particles. During ACE-Asia, this led to a decrease in the overall hygroscopicity of the aerosol population and removed aerosol mass from the optically efficient accumulation size mode (Arimoto et al., 2006; Carrico et al., 2003a; Quinn et al., 2004). The addition of soluble material to dust can modify its CCN and IN ability, thus changing the cloud formation properties and lifetime of dust aerosols. Mixing dust with secondary species can also alter the dust's direct radiative properties (Bauer and Koch, 2005; Conant et al., 2003). The segregation of nitrate from sulfate in dust particles will also impart different physical and chemical properties to the aged dust. For example, calcium nitrate is highly soluble and readily deliquesces (Gibson et al., 2006b), while calcium sulfate is very hygroscopic but rather insoluble. This has important implications for the solubility and phase of aged dust particles in the atmosphere.

During ACE-Asia, dust also scavenged semivolatile organic compounds, shifting them from the submicron to supermicron size range (Clarke et al., 2004). This had the interesting and important result of decreasing the scattering efficiency of the submicron particles and thus increasing the absorption efficiency of the black carbon dominated

submicron aerosol (Arimoto et al., 2006). The partitioning of sulfate and nitrate to supermicron-dominated dust had a similar effect. The internal mixing of dust particles with elemental and/or organic carbon is an important issue which we did not discuss here. Uptake of organic diacids by the Asian dust is presented in Chapter 5, while the mixing state of the dust with elemental carbon and other species was presented in Chapter 2.

By comparing the temporal evolution of secondary acids in dust particles of varying mineralogy, clear differences between high-Al and high-Ca dust particles were found. Sulfate was highly associated with aluminosilicate- and iron-rich dust while nitrate mixed with calcium-rich dust. This further supports lab studies which suggest mineralogy plays a role in dictating the types of reactions dust undergoes in the atmosphere. This could be due to different rates of reaction/formation of different acids with specific crustal minerals. The fact that the uptake of acids displayed a strong mineralogical dependence is further evidence for heterogeneous uptake of the acids. If the secondary acids had become mixed with the dust primarily through coagulation, cloud processing, or heterogeneous nucleation, we would not expect such a strong dependence on the dust's mineralogy (Matsuki et al., 2005a). The effect of mineralogy deserves further attention in laboratory studies, particularly using authentic dust samples of varying composition. The dependence of the dust reactivity on its composition should also be incorporated into regional and global chemistry models (Krueger et al., 2004; Tang et al., 2004b).

The alkaline calcium carbonate neutralized nitric and hydrochloric acid, leading to the accumulation of nitrate and chloride in calcium-rich dust. We propose that the sulfate association is due to the iron-catalyzed oxidation of S(IV) to S(VI) in the iron- and aluminosilicate-rich dust particles (Deguillaume et al., 2005; Qi et al., 2006; Rani et al., 1992; Zhuang et al., 1992). This process has important implications for the fertilization of remote

oceans and subsequent climate system feedbacks (Duce, 1995; Jickells et al., 2005; Meskhidze et al., 2003). Iron is a key nutrient controlling biological productivity in high-nutrient low-chlorophyll (HNLC) ocean regions. Mineral dust that deposits in the oceans is the major source of iron to these remote regions (Jickells et al., 2005). However, it is believed that it is the amount of soluble iron in the dust particles, as opposed to the total iron content, which governs the fertilization of the oceans (Jickells et al., 2005; Luo et al., 2005). The solubility of iron in dust particles can be increased as the particles become acidified by atmospheric processing and the accumulation of secondary acids (Zhu et al., 1992), such as has been shown extensively here. Submicron dust particles can be transported over longer distances than larger dust particles due to their longer atmospheric lifetimes. The accumulation of sulfate in submicron dust we demonstrated will therefore have important implications for the transport of acidified dust particles containing soluble iron to remote ocean regions (Baker and Jickells, 2006; Luo et al., 2005). Nitrate that has accumulated in mineral dust due to atmospheric processing is another important soluble nutrient for the oceans (Baker et al., 2003; Prospero and Savoie, 1989).

Fertilization of HNLC ocean regions by soluble iron in dust increases ocean productivity, phytoplankton in particular, causing a wide variety of climate feedbacks. For example, this could increase the uptake of carbon dioxide by marine organisms and also lead to increased DMS ocean emissions and thus increased cloud cover according to the CLAW hypothesis (Charlson et al., 1987; Duce, 1995; Turner et al., 2004). The resulting climate changes (wind speeds and patterns, precipitation) can then affect the production and transport of aeolian crustal material to the oceans in the first place. Our observations of mineral dust processing by pollutant gases present an important link between anthropogenic emissions and the chemistry of naturally-occurring mineral dust particles. These interactions with

anthropogenic pollutants alter the impacts that a <u>naturally</u> produced aerosol has on the atmosphere, oceans, and climate.

3.6 Acknowledgements

3.7 References

Akimoto, H., and Narita, H.: Distribution of SO_2, NO_x and CO_2 emissions from fuel combustion and industrial activities in Asia with 1-degrees-x1-degrees resolution, Atmos. Environ., 28 (2), 213-225, 1994.

Al-Hosney, H. A., and Grassian, V. H.: Water, sulfur dioxide and nitric acid adsorption on calcium carbonate: A transmission and ATR-FTIR study, Physical Chemistry Chemical Physics, 7 (6), 1266-1276, 2005.

Andreae, M. O., Charlson, R. J., Bruynseels, F., Storms, H., Vangrieken, R., and Maenhaut, W.: Internal mixture of sea salt, silicates, and excess sulfate in marine aerosols, Science, 232 (4758), 1620-1623, 1986.

Andronova, A. V., Gomes, L., Smirnov, V. V., Ivanov, A. V., and Shukurova, L. M.: Physicochemical Characteristics Of Dust Aerosols Deposited During The Soviet-American Experiment (Tajikistan, 1989), Atmospheric Environment, Part A: General Topics, 27 (16), 2487-2493, 1993.

Arimoto, R., Kim, Y. J., Kim, Y. P., Quinn, P. K., Bates, T. S., Anderson, T. L., Gong, S., Uno, I., Chin, M., Huebert, B. J., Clarke, A. D., Shinozuka, Y., Weber, R. J., Anderson, J. R., Guazzotti, S. A., Sullivan, R. C., Sodeman, D. A., Prather, K. A., and Sokolik, I. N.: Characterization of Asian Dust during ACE-Asia, Global And Planetary Change, 52 (1-4), 23-56, 2006.

Arimoto, R., Zhang, X. Y., Huebert, B. J., Kang, C. H., Savoie, D. L., Prospero, J. M., Sage, S. K., Schloesslin, C. A., Khaing, H. M., and Oh, S. N.: Chemical composition of atmospheric aerosols from Zhenbeitai, China, and Gosan, South Korea, during ACE-Asia, J. Geophys. Res., 109 (D19), doi:10.1029/2003JD004323, 2004.

Baker, A. R., and Jickells, T. D.: Mineral particle size as a control on aerosol iron solubility, Geophysical Research Letters, 33 (L17608), doi: 10.1029/2006GL026557, 2006.

Baker, A. R., Kelly, S. D., Biswas, K. F., Witt, M., and Jickells, T. D.: Atmospheric deposition of nutrients to the Atlantic Ocean, Geophys. Res. Lett., 30 (24), doi:10.1029/2003GL018518, 2003.

Bassett, M. E., and Seinfeld, J. H.: Atmospheric equilibrium-model of sulfate and nitrate aerosols. 2. Particle-size analysis, Atmospheric Environment, 18 (6), 1163-1170, 1984.

Bates, T. S., Quinn, P. K., Coffman, D. J., Covert, D. S., Miller, T. L., Johnson, J. E., Carmichael, G. R., Uno, I., Guazzotti, S. A., Sodeman, D. A., Prather, K. A., Rivera, M., Russell, L. M., and Merrill, J. T.: Marine boundary layer dust and pollutant transport associated with the passage of a frontal system over eastern Asia, J. Geophys. Res., 109 (D19), doi:10.1029/2003JD004094, 2004.

Bauer, S. E., and Koch, D.: Impact of heterogeneous sulfate formation at mineral dust surfaces on aerosol loads and radiative forcing in the Goddard Institute for Space Studies general circulation model, J. Geophys. Res., 110 (D17), doi:10.1029/2005JD005870, 2005.

Brandt, C., and Vaneldik, R.: Transition-metal-catalyzed oxidation of sulfur(IV) oxides - atmospheric-relevant processes and mechanisms, Chem. Rev., 95 (1), 119-190, 1995.

Bruynseels, F. J., and Van Grieken, R. E.: Molecular ion distributions in laser microprobe mass spectrometry of calcium oxide and calcium salts, Spectrochimica Acta, Part B: Atomic Spectroscopy, 38B (5-6), 853-8, 1983.

Cahill, C. F.: Asian aerosol transport to Alaska during ACE-Asia, J. Geophys. Res., 108 (D23), doi:10.1029/2002JD003271, 2003.

Carrico, C. M., Kus, P., Rood, M. J., Quinn, P. K., and Bates, T. S.: Mixtures of pollution, dust, sea salt, and volcanic aerosol during ACE-Asia: Radiative properties as a function of relative humidity, Journal Of Geophysical Research-Atmospheres, 108 (D23), doi:10.1029/2003JD003405, 2003.

Charlson, R. J., Lovelock, J. E., Andreae, M. O., and Warren, S. G.: Oceanic phytoplankton, atmospheric sulfur, cloud albedo and climate, Nature, 326 (6114), 655-661, 1987.

Clarke, A. D., Shinozuka, Y., Kapustin, V. N., Howell, S., Huebert, B., Doherty, S., Anderson, T., Covert, D., Anderson, J., Hua, X., Moore, K. G., McNaughton, C., Carmichael, G., and Weber, R.: Size distributions and mixtures of dust and black carbon aerosol in Asian outflow: Physiochemistry and optical properties, J. Geophys. Res., 109 (D15), doi:10.1029/2003JD004378, 2004.

Conant, W. C., Seinfeld, J. H., Wang, J., Carmichael, G. R., Tang, Y. H., Uno, I., Flatau, P. J., Markowicz, K. M., and Quinn, P. K.: A model for the radiative forcing during ACE-Asia derived from CIRPAS Twin Otter and R/V Ronald H. Brown data and comparison with observations, J. Geophys. Res., 108 (D23), doi:10.1029/2002JD003260, 2003.

Deguillaume, L., Leriche, M., Desboeufs, K., Mailhot, G., George, C., and Chaumerliac, N.: Transition metals in atmospheric liquid phases: Sources, reactivity, and sensitive parameters, Chem. Rev., 105 (9), 3388-3431, 2005.

Derbyshire, E., Meng, X. M., and Kemp, R. A.: Provenance, transport and characteristics of modern aeolian dust in western Gansu Province, China, and interpretation of the Quaternary loess record, Journal of Arid Environments, 39 (3), 497-516, 1998.

Duce, R. A., Sources, distributions, and fluxes of mineral aerosols and their relationship to climate, in *Aerosol forcing of climate*, edited by Charlson, R.J., and J., H., John Wiley & Sons Ltd., Chichester, England, 1995.

Duce, R. A., Unni, C. K., Ray, B. J., Prospero, J. M., and Merrill, J. T.: Long-range atmospheric transport of soil dust from Asia to the tropical North Pacific - temporal variability, Science, 209 (4464), 1522-1524, 1980.

Falkovich, A. H., Ganor, E., Levin, Z., Formenti, P., and Rudich, Y.: Chemical and mineralogical analysis of individual mineral dust particles, Journal of Geophysical Research-Atmospheres, 106 (D16), 18029-18036, 2001.

Fan, X. B., Okada, K., Niimura, N., Kai, K., Arao, K., Shi, G. Y., Qin, Y., and Mitsuta, Y.: Mineral particles collected in China and Japan during the same Asian dust-storm event, Atmospheric Environment, 30 (2), 347-351, 1996.

Gao, Y., and Anderson, J. R.: Characteristics of Chinese aerosols determined by individual-particle analysis, Journal Of Geophysical Research-Atmospheres, 106 (D16), 18037-18045, 2001.

Gibson, E. R., Hudson, P. K., and Grassian, V. H.: Aerosol chemistry and climate: Laboratory studies of the carbonate component of mineral dust and its reaction products, Geophysical Research Letters, 33 (13), doi:10.1029/2006GL026386, 2006.

Gong, S. L., Zhang, X. Y., Zhao, T. L., McKendry, I. G., Jaffe, D. A., and Lu, N. M.: Characterization of soil dust aerosol in China and its transport and distribution during 2001 ACE-Asia: 2. Model simulation and validation, Journal Of Geophysical Research-Atmospheres, 108 (D9), doi:10.1029/2002JD002633, 2003.

Goodman, A. L., Bernard, E. T., and Grassian, V. H.: Spectroscopic study of nitric acid and water adsorption on oxide particles: Enhanced nitric acid uptake kinetics in the presence of adsorbed water, J. Phys. Chem. A, 105 (26), 6443-6457, 2001.

Guazzotti, S. A., Coffee, K. R., and Prather, K. A.: Continuous measurements of size-resolved particle chemistry during INDOEX-Intensive Field Phase 99, Journal Of Geophysical Research-Atmospheres, 106 (D22), 28607-28627, 2001a.

Guazzotti, S. A., Whiteaker, J. R., Suess, D., Coffee, K. R., and Prather, K. A.: Real-time measurements of the chemical composition of size-resolved particles during a Santa Ana wind episode, California USA, Atmospheric Environment, 35 (19), 3229-3240, 2001b.

Hanisch, F., and Crowley, J. N.: Heterogeneous reactivity of gaseous nitric acid on Al_2O_3, $CaCO_3$, and atmospheric dust samples: A Knudsen cell study, Journal of Physical Chemistry A, 105 (13), 3096-3106, 2001.

Honda, M., Yabuki, S., and Shimizu, H.: Geochemical and isotopic studies of aeolian sediments in China, Sedimentology, 51 (2), 211-230, 2004.

Huebert, B. J., Bates, T., Russell, P. B., Shi, G. Y., Kim, Y. J., Kawamura, K., Carmichael, G., and Nakajima, T.: An overview of ACE-Asia: Strategies for quantifying the relationships between Asian aerosols and their climatic impacts, Journal Of Geophysical Research-Atmospheres, 108 (D23), doi:10.1029/2003JD003550, 2003.

Jaffe, D., Anderson, T., Covert, D., Kotchenruther, R., Trost, B., Danielson, J., Simpson, W., Berntsen, T., Karlsdottir, S., Blake, D., Harris, J., Carmichael, G., and Uno, I.: Transport of Asian air pollution to North America, Geophysical Research Letters, 26 (6), 711-714, 1999.

Jeong, G. Y.: Bulk and single-particle mineralogy of Asian dust and a comparison with its source soils, J. Geophys. Res., 113 (D2), doi:10.1029/2007JD008606, 2008.

Jeong, G. Y., and Chun, Y.: Nanofiber calcite in Asian dust and its atmospheric roles, Geophys. Res. Lett., 33 (L24802), doi:10.1029/2006GL028280, 2006.

Jickells, T. D., An, Z. S., Andersen, K. K., Baker, A. R., Bergametti, G., Brooks, N., Cao, J. J., Boyd, P. W., Duce, R. A., Hunter, K. A., Kawahata, H., Kubilay, N., laRoche, J., Liss, P. S., Mahowald, N., Prospero, J. M., Ridgwell, A. J., Tegen, I., and Torres, R.: Global iron connections between desert dust, ocean biogeochemistry, and climate, Science, 308 (5718), 67-71, 2005.

Jickells, T. D., and Spokes, L. J., Atmopspheric iron inputs to the oceans, in *The biogeochemistry of iron in seawater*, edited by Turner, D.R., and Hunter, K.A., John Wiley & Sons Ltd., Chichester, England, 2001.

Jordan, C. E., Dibb, J. E., Anderson, B. E., and Fuelberg, H. E.: Uptake of nitrate and sulfate on dust aerosols during TRACE-P, J. Geophys. Res., 108 (D21), doi:10.1029/2002JD003101, 2003.

Korhonen, H., Napari, I., Timmreck, C., Vehkamaki, H., Pirjola, L., Lehtinen, K. E. J., Lauri, A., and Kulmala, M.: Heterogeneous nucleation as a potential sulphate-coating mechanism of atmospheric mineral dust particles and implications of coated dust on new particle formation, J. Geophys. Res., 108 (D17), doi:10.1029/2003JD003553, 2003.

Krueger, B. J., Grassian, V. H., Cowin, J. P., and Laskin, A.: Heterogeneous chemistry of individual mineral dust particles from different dust source regions: the importance of particle mineralogy, Atmospheric Environment, 38 (36), 6253-6261, 2004.

Krueger, B. J., Grassian, V. H., Laskin, A., and Cowin, J. P.: The transformation of solid atmospheric particles into liquid droplets through heterogeneous chemistry: Laboratory insights into the processing of calcium containing mineral dust aerosol in the troposphere, Geophys. Res. Lett., 30 (3), doi:10.1029/2002GL016563, 2003.

Laskin, A., Iedema, M. J., Ichkovich, A., Graber, E. R., Taraniuk, I., and Rudich, Y.: Direct observation of completely processed calcium carbonate dust particles, Faraday Discussions, 130, 453-468, 2005.

Liu, D. Y., Wenzel, R. J., and Prather, K. A.: Aerosol time-of-flight mass spectrometry during the Atlanta Supersite Experiment: 1. Measurements, J. Geophys. Res., 108 (D7), doi:10.1029/2001JD001562, 2003.

Luo, C., Mahowald, N. M., Meskhidze, N., Chen, Y., Siefert, R. L., Baker, A. R., and Johansen, A. M.: Estimation of iron solubility from observations and a global aerosol model, J. Geophys. Res., 110 (D23), doi:10.1029/2005JD006059, 2005.

Matsuki, A., Iwasaka, Y., Shi, G. Y., Chen, H. B., Osada, K., Zhang, D., Kido, M., Inomata, Y., Kim, Y. S., Trochkine, D., Nishita, C., Yamada, M., Nagatani, T., Nagatani, M., and Nakata, H.: Heterogeneous sulfate formation on dust surface and its dependence on mineralogy: Balloon-borne observations from ballon-borne measurements in the surface of Beijing, China, Water, Air, and Soil Pollution: Focus, 5, 101-132, 2005a.

Matsuki, A., Iwasaka, Y., Shi, G. Y., Zhang, D. Z., Trochkine, D., Yamada, M., Kim, Y. S., Chen, B., Nagatani, T., Miyazawa, T., Nagatani, M., and Nakata, H.: Morphological and chemical modification of mineral dust: Observational insight into the heterogeneous uptake of acidic gases, Geophysical Research Letters, 32 (22), 2005b.

Matsumoto, J., Takahashi, K., Matsumi, Y., Yabushita, A., Shimizu, A., Matsui, I., and Sugimoto, N.: Scavenging of pollutant acid substances by Asian mineral dust particles, Geophys. Res. Lett., 33 (7), doi:10.1029/2006GL025782, 2006.

Meskhidze, N., Chameides, W. L., Nenes, A., and Chen, G.: Iron mobilization in mineral dust: Can anthropogenic SO_2 emissions affect ocean productivity?, Geophys. Res. Lett., 30 (21), doi:10.1029/2003GL018035, 2003.

Mori, I., Nishikawa, M., and Iwasaka, Y.: Chemical reaction during the coagulation of ammonium sulphate and mineral particles in the atmosphere, Science of the Total Environment, 224 (1-3), 87-91, 1998.

Mori, I., Nishikawa, M., Tanimura, T., and Quan, H.: Change in size distribution and chemical composition of kosa (Asian dust) aerosol during long-range transport, Atmospheric Environment, 37 (30), 4253-4263, 2003.

Murphy, D. M., Cziczo, D. J., Froyd, K. D., Hudson, P. K., Matthew, B. M., Middlebrook, A. M., Peltier, R. E., Sullivan, A., Thomson, D. S., and Weber, R. J.: Single-particle mass spectrometry of tropospheric aerosol particles, J. Geophys. Res., 111 (D23), doi:10.1029/2006JD007340, 2006.

Murphy, D. M., and Thomson, D. S.: Chemical composition of single aerosol particles at Idaho Hill: Negative ion measurements, J. Geophys. Res., 102 (D5), 6353-6368, 1997.

Niimura, N., Okada, K., Fan, X. B., Kai, K., Arao, K., Shi, G. Y., and Takahashi, S.: Formation of Asian dust-storm particles mixed internally with sea salt in the atmosphere, Journal of the Meteorological Society of Japan, 76 (2), 275-288, 1998.

Nishikawa, M., Hao, Q., and Morita, M.: Preparation and evaluation of certified reference matreials for asian mineral dust, Global Environ. Res., 4 (1), 103-113, 2000.

Nishikawa, M., Kanamori, S., Kanamori, N., and Mizoguchi, T.: Kosa aerosol as eolian carrier of anthropogenic material, Science Of The Total Environment, 107, 13-27, 1991.

Noble, C. A., and Prather, K. A.: Real-time measurement of correlated size and composition profiles of individual atmospheric aerosol particles, Environ. Sci. Technol., 30 (9), 2667-2680, 1996.

Ooki, A., and Uematsu, M.: Chemical interactions between mineral dust particles and acid gases during Asian dust events, Journal Of Geophysical Research-Atmospheres, 110 (D3), doi:10.1029/2004JD004737, 2005.

Pastor, S. H., Allen, J. O., Hughes, L. S., Bhave, P., Cass, G. R., and Prather, K. A.: Ambient single particle analysis in Riverside, California by aerosol time-of-flight mass spectrometry during the SCOS97-NARSTO, Atmospheric Environment, 37, S239-S258, 2003.

Prince, A. P., Kleiber, P. D., Grassian, V. H., and Young, M. A.: Reactive uptake of acetic acid on calcite and nitric acid reacted calcite aerosol in an environmental reaction chamber, Phys. Chem. Chem. Phys., 10 (1), 142-152, 2008.

Prospero, J. M., and Savoie, D. L.: Effect of continental sources on nitrate concentrations over the Pacific-Ocean, Nature, 339 (6227), 687-689, 1989.

Pye, K., Aeolian dusts and dust deposits, Academic Press, San Diego, 1987.

Qi, J., Feng, L., Li, X., and Zhang, M.: An X-ray photoelectron spectroscopy study of elements on the surface of aerosol particles Journal Of Aerosol Science, 37 (2), 218-227, 2006.

Quinn, P. K., Coffman, D. J., Bates, T. S., Welton, E. J., Covert, D. S., Miller, T. L., Johnson, J. E., Maria, S., Russell, L., Arimoto, R., Carrico, C. M., Rood, M. J., and Anderson, J.: Aerosol optical properties measured on board the Ronald H. Brown during ACE-

Asia as a function of aerosol chemical composition and source region, Journal Of Geophysical Research-Atmospheres, 109 (D19), 2004.

Rani, A., Prasad, D. S. N., Madnawat, P. V. S., and Gupta, K. S.: The role of free-fall atmospheric dust in catalyzing autoxidation of aqueous sulfur-dioxide, Atmospheric Environment, Part A: General Topics, 26 (4), 667-673, 1992.

Santschi, C., and Rossi, M. J.: Uptake of CO_2, SO_2, HNO_3 and HCl on calcite ($CaCO_3$) at 300 K: Mechanism and the role of adsorbed water, Journal Of Physical Chemistry A, 110 (21), 6789-6802, 2006.

Seinfeld, J. H., Carmichael, G. R., Arimoto, R., Conant, W. C., Brechtel, F. J., Bates, T. S., Cahill, T. A., Clarke, A. D., Doherty, S. J., Flatau, P. J., Huebert, B. J., Kim, J., Markowicz, K. M., Quinn, P. K., Russell, L. M., Russell, P. B., Shimizu, A., Shinozuka, Y., Song, C. H., Tang, Y. H., Uno, I., Vogelmann, A. M., Weber, R. J., Woo, J. H., and Zhang, X. Y.: ACE-ASIA - Regional climatic and atmospheric chemical effects of Asian dust and pollution, Bulletin Of The American Meteorological Society, 85 (3), 367-380, 2004.

Silva, P. J., Carlin, R. A., and Prather, K. A.: Single particle analysis of suspended soil dust from Southern California, Atmospheric Environment, 34 (11), 1811-1820, 2000.

Song, C. H., and Carmichael, G. R.: The aging process of naturally emitted aerosol (sea-salt and mineral aerosol) during long range transport, Atmospheric Environment, 33 (14), 2203-2218, 1999.

Song, C. H., and Carmichael, G. R.: Gas-particle partitioning of nitric acid modulated by alkaline aerosol, J. Atmos. Chem., 40 (1), 1-22, 2001.

Song, C. H., Maxwell-Meier, K., Weber, R. J., Kapustin, V., and Clarke, A.: Dust composition and mixing state inferred from airborne composition measurements during ACE-Asia C130 Flight #6, Atmospheric Environment, 39 (2), 359-369, 2005.

Song, X. H., Hopke, P. K., Fergenson, D. P., and Prather, K. A.: Classification of single particles analyzed by ATOFMS using an artificial neural network, ART-2A, Anal. Chem., 71 (4), 860-865, 1999.

Streets, D. G., Bond, T. C., Carmichael, G. R., Fernandes, S. D., Fu, Q., He, D., Klimont, Z., Nelson, S. M., Tsai, N. Y., Wang, M. Q., Woo, J. H., and Yarber, K. F.: An inventory of gaseous and primary aerosol emissions in Asia in the year 2000, J. Geophys. Res., 108 (D21), doi:10.1029/2002JD003093, 2003.

Sun, J. M., Zhang, M. Y., and Liu, T. S.: Spatial and temporal characteristics of dust storms in China and its surrounding regions, 1960-1999: Relations to source area and climate, Journal Of Geophysical Research-Atmospheres, 106 (D10), 10325-10333, 2001.

Tang, Y. H., Carmichael, G. R., Kurata, G., Uno, I., Weber, R. J., Song, C. H., Guttikunda, S. K., Woo, J. H., Streets, D. G., Wei, C., Clarke, A. D., Huebert, B., and Anderson, T. L.: Impacts of dust on regional tropospheric chemistry during the ACE-Asia experiment: A model study with observations, J. Geophys. Res., 109 (D19), doi:10.1029/2003JD003806, 2004a.

Tang, Y. H., Carmichael, G. R., Seinfeld, J. H., Dabdub, D., Weber, R. J., Huebert, B., Clarke, A. D., Guazzotti, S. A., Sodeman, D. A., Prather, K. A., Uno, I., Woo, J. H., Yienger, J. J., Streets, D. G., Quinn, P. K., Johnson, J. E., Song, C. H., Grassian, V. H., Sandu,

A., Talbot, R. W., and Dibb, J. E.: Three-dimensional simulations of inorganic aerosol distributions in east Asia during spring 2001, J. Geophys. Res., 109 (D19), doi:10.1029/2003JD004201, 2004b.

Thulasiraman, S., O'Neill, N. T., Royer, A., Holben, B. N., Westphal, D. L., and McArthur, L. J. B.: Sunphotometric observations of the 2001 Asian dust storm over Canada and the US, Geophys. Res. Lett., 29 (8), doi:10.1029/2001GL014188, 2002.

Trochkine, D., Iwasaka, Y., Matsuki, A., Yamada, M., Kim, Y. S., Nagatani, T., Zhang, D., Shi, G. Y., and Shen, Z.: Mineral aerosol particles collected in Dunhuang, China, and their comparison with chemically modified particles collected over Japan, Journal of Geophysical Research-Atmospheres, 108 (D23), doi:10.1029/2002JD003268, 2003.

Turner, S. M., Harvey, M. J., Law, C. S., Nightingale, P. D., and Liss, P. S.: Iron-induced changes in oceanic sulfur biogeochemistry, Geophys. Res. Lett., 31 (14), doi:10.1029/2004GL020296, 2004.

Ullerstam, M., Johnson, M. S., Vogt, R., and Ljungstrom, E.: DRIFTS and Knudsen cell study of the heterogeneous reactivity of SO_2 and NO_2 on mineral dust, Atmospheric Chemistry And Physics, 3, 2043-2051, 2003.

Ullerstam, M., Vogt, R., Langer, S., and Ljungstrom, E.: The kinetics and mechanism of SO_2 oxidation by O_3 on mineral dust, Physical Chemistry Chemical Physics, 4 (19), 4694-4699, 2002.

Underwood, G. M., Song, C. H., Phadnis, M., Carmichael, G. R., and Grassian, V. H.: Heterogeneous reactions of NO_2 and HNO_3 on oxides and mineral dust: A combined laboratory and modeling study, J. Geophys. Res., 106 (D16), 18055-18066, 2001.

Usher, C. R., Michel, A. E., and Grassian, V. H.: Reactions on mineral dust, Chem. Rev., 103 (12), 4883-4939, 2003.

Vlasenko, A., Sjogren, S., Weingartner, E., Stemmler, K., Gaggeler, H. W., and Ammann, M.: Effect of humidity on nitric acid uptake to mineral dust aerosol particles, Atmos. Chem. Phys., 6, 2147-2160, 2006.

Wu, P. M., and Okada, K.: Nature of coarse nitrate particles in the atmosphere - A single particle approach, Atmos. Environ., 28 (12), 2053-2060, 1994.

Yermakov, A. N., and Purmal, A. P.: Iron-catalyzed oxidation of sulfite: From established results to a new understanding, Progress In Reaction Kinetics And Mechanism, 28 (3), 189-255, 2003.

Yuan, H., Rahn, K. A., and Zhuang, G.: Graphical techniques for interpreting the composition of individual aerosol particles, Atmospheric Environment, 38 (39), 6845-6854, 2004.

Zhang, D. Z., and Iwasaka, Y.: Nitrate and sulfate in individual Asian dust-storm particles in Beijing, China in spring of 1995 and 1996, Atmospheric Environment, 33 (19), 3213-3223, 1999.

Zhang, D. Z., and Iwasaka, Y.: Chlorine deposition on dust particles in marine atmosphere, Geophys. Res. Lett., 28 (18), 3613-3616, 2001.

Zhang, D. Z., and Iwasaka, Y.: Size change of Asian dust particles caused by sea salt interaction: Measurements in southwestern Japan, Geophysical Research Letters, 31 (15), doi:10.1029/2004GL020087, 2004.

Zhang, D. Z., Iwasaka, Y., Shi, G. Y., Zang, J. Y., Matsuki, A., and Trochkine, D.: Mixture state and size of Asian dust particles collected at southwestern Japan in spring 2000, Journal Of Geophysical Research-Atmospheres, 108 (D24), doi:10.1029/2003JD003869, 2003.

Zhang, D. Z., Shi, G. Y., Iwasaka, Y., and Hu, M.: Mixture of sulfate and nitrate in coastal atmospheric aerosols: individual particle studies in Qingdao (36 degrees 04 ' N, 120 degrees 21 ' E), China, Atmospheric Environment, 34 (17), 2669-2679, 2000.

Zhu, X., Prospero, J. M., Millero, F. J., Savoie, D. L., and Brass, G. W.: The solubility of ferric ion in marine mineral aerosol solutions at ambient relative humidities, Marine Chemistry, 38 (1-2), 91-107, 1992.

Zhuang, G. S., Yi, Z., Duce, R. A., and Brown, P. R.: Link between iron and sulfur cyces suggested by detection of Fe(II) in remote marine aerosols, Nature, 355 (6360), 537-539, 1992.

Chapter 4

Mineral dust is a sink for chlorine in the marine boundary layer

4.1 Synopsis

Dust particles affect the budgets of important atmospheric traces gases by providing a surface on which heterogeneous reactions can occur. The uptake of soluble species on dust alters the physical, chemical, and optical properties and the overall ability of dust to act as cloud condensation and ice nuclei. It is commonly assumed that all measured chloride in particulate filter samples is associated with sea salt particles and any chloride in dust occurs as the result of internal mixtures of sea salt and dust particles, formed by cloud processing. Here we show high temporal resolution single-particle data demonstrating the direct uptake of chlorine by dust via heterogeneous reaction with $HCl(g)$. This reaction added significant amounts of chlorine to the dust particles during a major Asian dust storm, representing 4-9% of the individual dust particle mass. Up to $65\pm4\%$ of the dust particles contained chlorine due to this heterogeneous reaction during the dust front. Ignoring this process leads to an overestimation of sea salt concentrations from bulk measurements, and an underestimation of the degree of sea salt aging. The uptake of chloride will change the pH and hygroscopic properties of the dust and thus can influence the budgets of other reactive gases. Including this heterogeneous process in atmospheric measurements and chemical transport models will improve our ability to predict the atmosphere's composition and radiation budget with greater accuracy.

4.2 Introduction

Atmospheric dust particles are a major component of tropospheric aerosol mass. They play significant but still poorly understood roles in atmospheric chemistry, radiative transfer, biogeochemistry, and warm and cold cloud formation, as discussed in Chapter 1. The international ACE-Asia field campaign was conducted in 2001 to investigate the effect of spring Asian dust storms on east Asia's atmosphere and climate (Arimoto et al., 2006; Huebert et al., 2003b; Seinfeld et al., 2004). An ATOFMS made online single-particle measurements of the Asian aerosol during the R/V Ronald Brown's cruise from Hawaii to the Sea of Japan during the campaign. Chapter 2 presented an overview of the particle types and chemistry observed during the cruise, including the impact of the major dust storm encountered on April 10, 2001. Chemical changes induced in the mineral dust particles by atmospheric processing were described in detail in Chapter 3. Here the unique observation of secondary chlorine in the aged Asian dust particles is investigated in detail.

Uptake and/or formation of nitrate and/or sulfate on mineral dust particles during transport has been observed in different locations (Bates et al., 2004; Fan et al., 1996; Jordan et al., 2003; Laskin et al., 2005a; Matsuki et al., 2005b), as well as in laboratory studies (Usher et al., 2003a), and has been studied in several aerosol modeling efforts (Bauer et al., 2004; Dentener et al., 1996; Tang et al., 2004a; Tang et al., 2004b). Associations of sulfate and nitrate with mineral dust particles, from sorption and/or oxidation, or cloud processing, affect the local cooling effect of the aerosols and modify the ability of the mineral particles to become cloud condensation nuclei (CCN) and ice nuclei (IN), also altering the lifetime of the dust particles (DeMott et al., 2003a; Fan et al., 2004; Gibson et al., 2006a; Levin et al., 1996; Rudich et al., 2002b). Although the occurrence of sulfate and nitrate in dust particles has been previously observed, the presence of chloride in these particles has not been reported until

recently (Arimoto et al., 2006; Murphy et al., 2006; Zhang and Iwasaka, 2001),as it could only be unambiguously confirmed using single particle analysis.

Asian mineral dust particles have the potential of neutralizing acidic species due to their intrinsic alkaline buffer capacity (Matsuki et al., 2005b; Nishikawa, 2000; Tang et al., 2004b; Usher et al., 2003a). Zhang and Iwasaka (2001) previously reported the presence of chloride in Asian mineral dust particles. They suggested it was not due to internal mixtures of sea salt and dust but instead caused by heterogeneous reactions of chlorine gases with dust particles. Here we provide further evidence for this process with greater time and size-resolution and with supporting evidence from other measurements and modeling efforts made during the ACE-Asia campaign. This chapter builds on the observations described in Chapter 3 by examining the possible sources of the chlorine-gases in detail and provides strong evidence for HCl(g) released from aged sea salt as the primary source of secondary chloride in dust. Results from simulations with the STEM-2K3 chemical transport model support the field observations. We discuss the numerous atmospheric implications of this heterogeneous reaction.

4.3 Experimental methods

4.3.1   Single particle analysis

Numerous shipboard measurements were taken onboard the RHB downwind of the Asian continent to contribute to the regional characterization of aerosol properties during the ACE-Asia campaign (Bates et al., 2004; Huebert et al., 2003b). Measurements of the size and chemical composition of individual aerosol particles were carried out in real-time with a transportable aerosol time-of-flight mass spectrometer (ATOFMS) aboard the RHB, as

described in Chapter 2. ATOFMS data on the size and chemical composition of a total of 731,309 particles was collected. Results presented here correspond to the single particle analysis of particles with aerodynamic diameter (D_a) between 1.0 and 3.0 μm.

4.3.2 Aerosol chemical model

The evolution of the chemical composition of the Asian aerosol was simulated using the STEM-2K3 regional chemical transport model (Tang et al., 2004b). This was developed from STEM-2K1 by adding an online aerosol thermodynamic module, SCAPE II (Simulating Composition of Atmospheric Particles at Equilibrium) (Kim and Seinfeld, 1995), for calculating gas-particle equilibrium concentrations among inorganic aerosol ions and their gaseous precursors. Meteorological fields were provided by the RAMS meteorological model and gas-phase chemistry was simulated by the SAPR99 atmospheric chemical mechanism. Tang et al. (2004b) described the framework of STEM-2K3 and its performance during the TRACE-P (TRAnsport and Chemical Evolution over the Pacific) and ACE-Asia experiments. The model analysis includes inorganic aerosols in four size bins (in aerodynamic diameter): 0.1μm-0.3μm, 0.3μm-1.0μm, 1.0μm-2.5μm, and 2.5μm-10μm; the later two (supermicron) size bins are the focus of this paper.

4.3.3 PMEL filter measurements

A wide variety of bulk chemical composition measurements were made by NOAA's Pacific Marine Environmental Laboratory (PMEL) of the same aerosol sampled by the ATOFMS aboard the Ronald Brown. Reported mass concentrations for total supermicrometer particles and for chloride in supermicrometer particles during the time periods used for this study were obtained from the NOAA PMEL data server (http://saga.pmel.noaa.gov/data/). A

cascade impactor was used to separate the collected aerosol into filter samples of particles <1.1 μm, and particles 1.1-10.0 μm in aerodynamic diameter, at 55% relative humidity. Samples were collected over approximately 4-6 hour intervals. A wide variety of cations and anions were determined for each sample by ion chromatography, as described by Bates et al. (2004).

4.4 Results and discussion

During the course of the ACE-Asia IFO, a major dust storm developed over China from April 4-14, 2001 (Day of Year (DOY) 94.0 to 104.0), caused by a frontal zone from northern China/Mongolia. The dust front was carried aloft above the boundary layer before subsiding back into the marine boundary layer. This event brought highly elevated concentrations of dust to the RHB starting on DOY 100.8 (10 April 2001, 19:12 UTC) in the western Sea of Japan (Bates et al., 2004). Air mass back trajectories and model simulations of dust emissions are shown in Figure 4.1. The dust aerosol properties sampled onboard the RHB reflected a northern high desert source region for the dust particles (Bates et al., 2004; Uno et al., 2004). This episode resulted in the long range transport of dust particles to the continental US (Jaffe et al., 2003). The aerosol sampled in the Sea of Japan by the RHB was a complex mixture of sea salt, mineral dust, carbonaceous species, and secondary products including ammonium, chloride, nitrate, and sulfate (Chapter 2).

4.4.1   Single particle analysis of dust storm particles

Single particle ion analysis with an ATOFMS allowed for classification of mineral dust particles according to specific metal ion combinations in the mass spectra (Guazzotti et al., 2001a; Guazzotti et al., 2001b; Silva et al., 2000). Association of dust particles with other
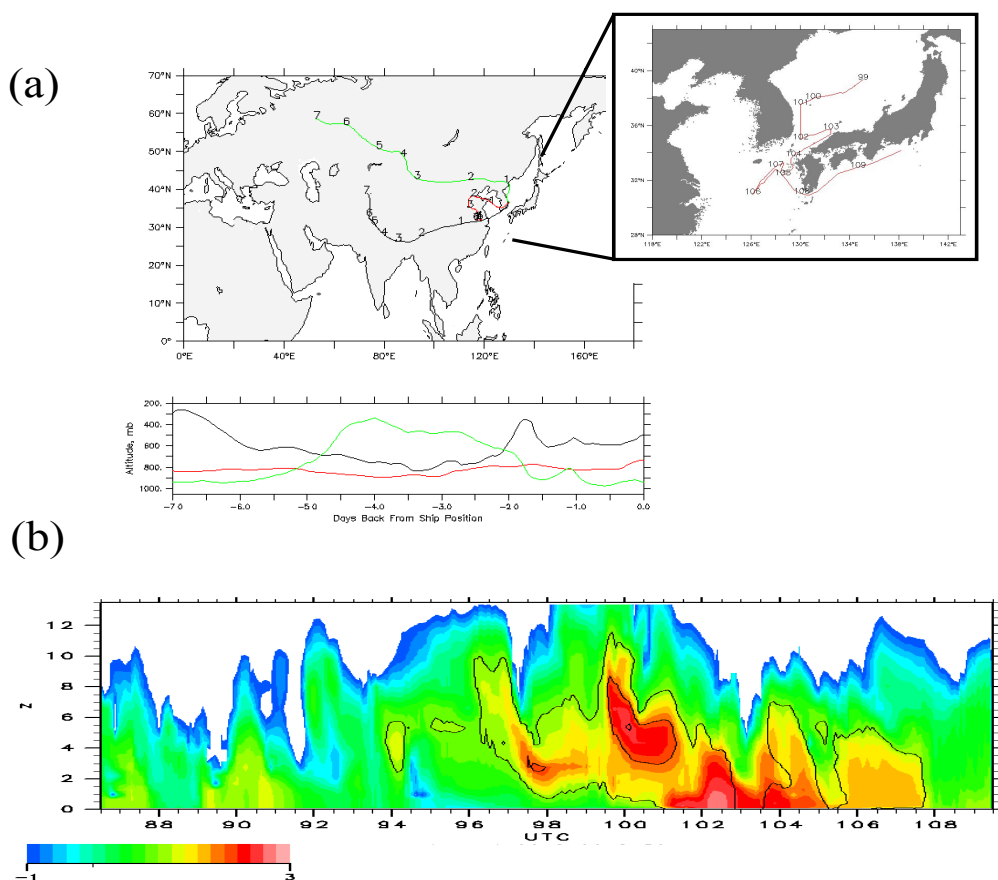
Figure 4.1. Simulations of the 2001 Asian dust storm source regions and trajectories. **(a)** Back-trajectory clusters of air masses arriving at the NOAA R/V Ronald H. Brown location at different altitudes on DOY 101.5. Upper level trajectories are from the North China and Mongolia dust region (Bates et al., 2004; Gong et al., 2003b; Uno et al., 2004). The air mass arriving to the surface (green line) had influence from the Gobi Desert which was carried aloft before subsiding into the boundary layer around DOY 100.8. The back trajectories (available at http://saga.pmel.noaa.gov/data/) were calculated using the NOAA ARL Hybrid Single-Particle Lagrangian Integrated Trajectory (HYSPLIT 4) model (http://www.arl.noaa.gov/ready/hysplit4.html). **Inset:** ACE-Asia NOAA R/V Ronald H. Brown cruise track for DOY 99.0-110.0 (Sea of Japan). **(b)** CFORS model simulation of dust mass concentration (DOY 86.0-110.0) showing the influence of emissions from the Taklimakan desert and Gobi desert. The colour contours represent total dust concentrations in μg/m^3 on a log$_{10}$ basis (e.g., $3 = 10^3$). Lines are equivalent to contour values of 1, 2, and 2.5. The y-axis is altitude above sea level (km). During the period DOY 99-104, the dust originating from the Taklimakan desert was above ~3km, while the Gobi desert dust was at low altitudes (vertical scale in km).
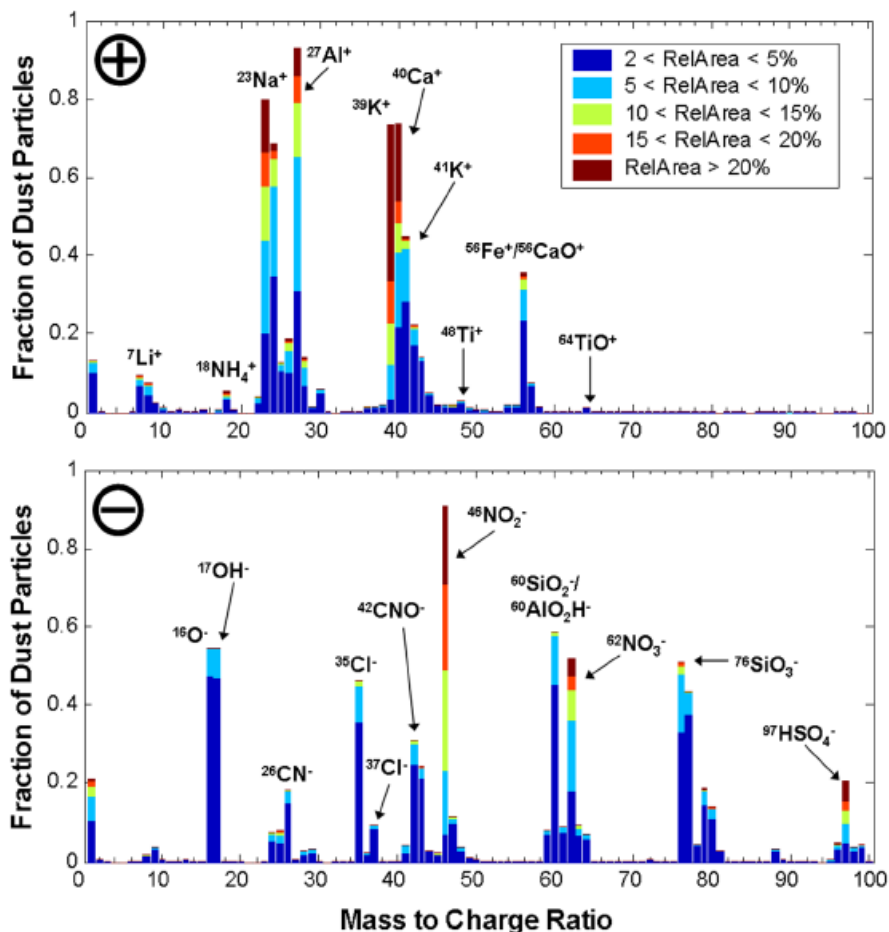
Figure 4.2. Average positive (top) and negative (bottom) ion mass spectra for the principal dust particle type sampled during ACE-Asia. Dust internally mixed with sea salt has been excluded. The y-axis represents the fraction of dust particles containing a peak at the specified mass-to-charge ratio. The colored bars represent the intensity (expressed as relative area) of the corresponding peaks in the mass spectra. In the negative ion mass spectrum, peaks assigned to $^{35}Cl^-$, $^{37}Cl^-$, $^{46}NO_2^-$, $^{62}NO_3^-$, $^{80}SO_3^-$, and $^{97}HSO_4^-$ indicate the presence of chloride, nitrate, and sulfate in this particle class, and represent atmospheric processing of the dust during transport.

secondary aerosol constituents (e.g. sulfate, nitrate, chloride) was determined from the corresponding negative ion mass spectra (Fig. 4.2). The dust particles observed during this dust event showed chemical characteristics consistent with Asian mineral dust, i.e., high calcium content (most likely calcium carbonate close to the source region). ATOFMS results demonstrate nitrate and sulfate uptake by dust particles, with as much as 60-80% of the

nitrate- and sulfate-containing particles in the supermicrometer size range being associated with mineral dust during this dust event (Arimoto et al., 2006; Bates et al., 2004; Tang et al., 2004b). These mineral dust particles provide surface sites for scavenging reactive gases and heterogeneous reactions that lead to the formation of sulfate and nitrate, consistent with previous observations (Arimoto et al., 2006; Bates et al., 2004; Jordan et al., 2003; Matsuki et al., 2005b; Okada et al., 1990; Ooki and Uematsu, 2005b).

4.4.2   Dust associations with chlorine

The major reaction product of chlorine-containing gases with dust is particulate-chloride. Associations/reactions between dust particles and chlorine are indicated by the presence of ion peaks at m/z -35 and -37 in the single dust particle mass spectra (Fig. 4.2), corresponding to $^{35}Cl^-$ and $^{37}Cl^-$, respectively. The peak area ratio of chlorine to aluminum provides an indication of the relative amount of chloride present in each dust particle since the ratio is evaluated with respect to aluminum, a primary dust component. Peak area ratios are used in place of absolute area values to avoid implicit instrumental uncertainties associated with laser shot-to-shot variations and with the number of molecules desorbed/ionized during each ion-forming process in the source region of the mass spectrometer. As shown in Figure 4.3, there is a significant increase in the Cl/Al peak area ratio starting on DOY 100.8 when the dust front arrived, indicating an increasing amount of chloride in the dust particles.

The increase in the relative amount of chloride in dust particles could be the result of (1) the arrival of an air mass transporting dust particles with a naturally high chloride content, (2) coagulation between sea salt and dust particles via cloud processing, and/or (3) uptake/reaction of chlorine-containing trace gases (e.g. HCl(g)) with dust. Although chloride can be present in the dust source regions, its contribution to the chemical composition of dust
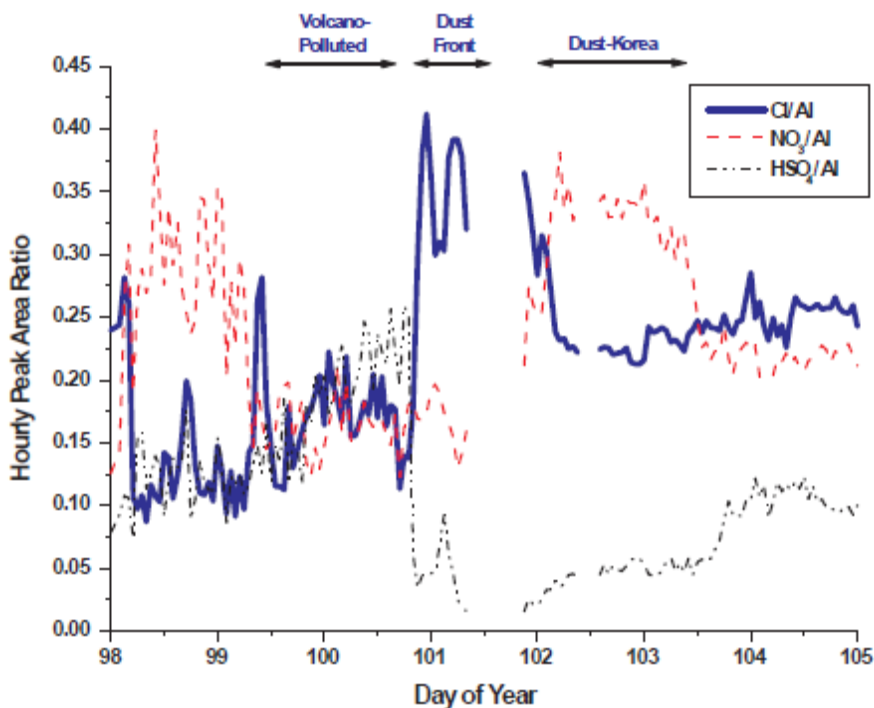
Figure 4.3. Temporal evolution of secondary acid products in sampled Asian dust. Shown is the hourly average of the peak area ratio between peaks at different mass-to-charge ratios (m/z) for individual dust particles (D_a = 1-2.5 μm) during the pre- and post-frontal periods of the ACE-Asia research cruise. The hourly average is evaluated from the area ratios first determined for each dust particle. Results correspond to the dust particles belonging to the class presented in Figure 4.2, and represent the evolution of the peak areas of chloride (m/z= -35), nitrate (m/z = -62), and sulfate (m/z= -97), divided by the aluminum peak area (m/z = +27). Internal mixtures of dust and sea salt are excluded. Gaps in the data occurred when aerosol sampling was suspended. From DOY 99.3-100.5 air mass back-trajectories indicated flow over the Miyakejima volcano and Japan. Time period labels refer to air-mass back trajectories presented in Bates et al. (2004).

particles in the Chinese interior is generally low (~0.4% mass) (Arimoto et al., 2004; Xu et al., 2004; Zhang and Iwasaka, 2001). The large temporal changes in the Cl/Al peak area ratio (Fig. 4.3) in dust particles provide evidence for a secondary (gas-phase) source of the chloride. If chloride was already present in the dust at the source, this area ratio would remain relatively constant. The peak area ratio between different metals and aluminum was used to investigate if the observed increase in the chloride content in dust was due to the arrival of an air mass transporting dust particles with naturally high chloride content in the original source dust. The

obtained values for the peak area ratios between potassium (m/z= 39), sodium (m/z = 23), and aluminum (m/z =27) (Fig. 4.4) do not follow the same temporal trends as those observed for the chloride/aluminum ratio (Fig. 4.3). There are only small variations in the K/Al and Na/Al area ratios and no clear trends. Thus, the elemental composition of the dust particles during the time period under consideration did not change substantially, suggesting the source region of the dust did not change significantly during this period. Therefore, the presence of chloride in these particles is almost certainly not due to an influx of dust particles from different source regions with naturally high chloride content.

Mixtures of dust and sea salt particles have been previously observed in several locations such as Nagasaki (Fan et al., 1996; Niimura et al., 1998) and Kumamoto (Japan) (Zhang et al., 2003b), as well as over the ocean (Andreae et al., 1986a; Okada et al., 1990). These internal mixtures modify the hygroscopic properties of the mineral dust particles, and consequently their removal rate by wet scavenging, as well as their cloud nucleating ability. Peaks at m/z 81 and 83 in the single particle mass spectra, corresponding to $Na_2^{35}Cl^+$ and $Na_2^{37}Cl^+$, can be used as indicators of dust particles internally mixed with sea salt (Gard et al., 1998; Guazzotti et al., 2001a). The relative contributions to the total dust particles resulting from sea salt and dust agglomeration, and those resulting from reaction with chlorine gases, can be distinguished using these sea salt indicators. In these calculations, it is assumed that: 1) all chloride-containing dust particles with peaks at m/z 81 and 83 represent associations between sea salt and dust; 2) all dust particles with no detectable peaks at m/z 81 and 83 are indicative of dust particles with no sea salt, and 3) therefore, peaks at m/z -35 and -37 in such particles represent the presence of chloride due to its existence at the dust source or due to heterogeneous reactions.
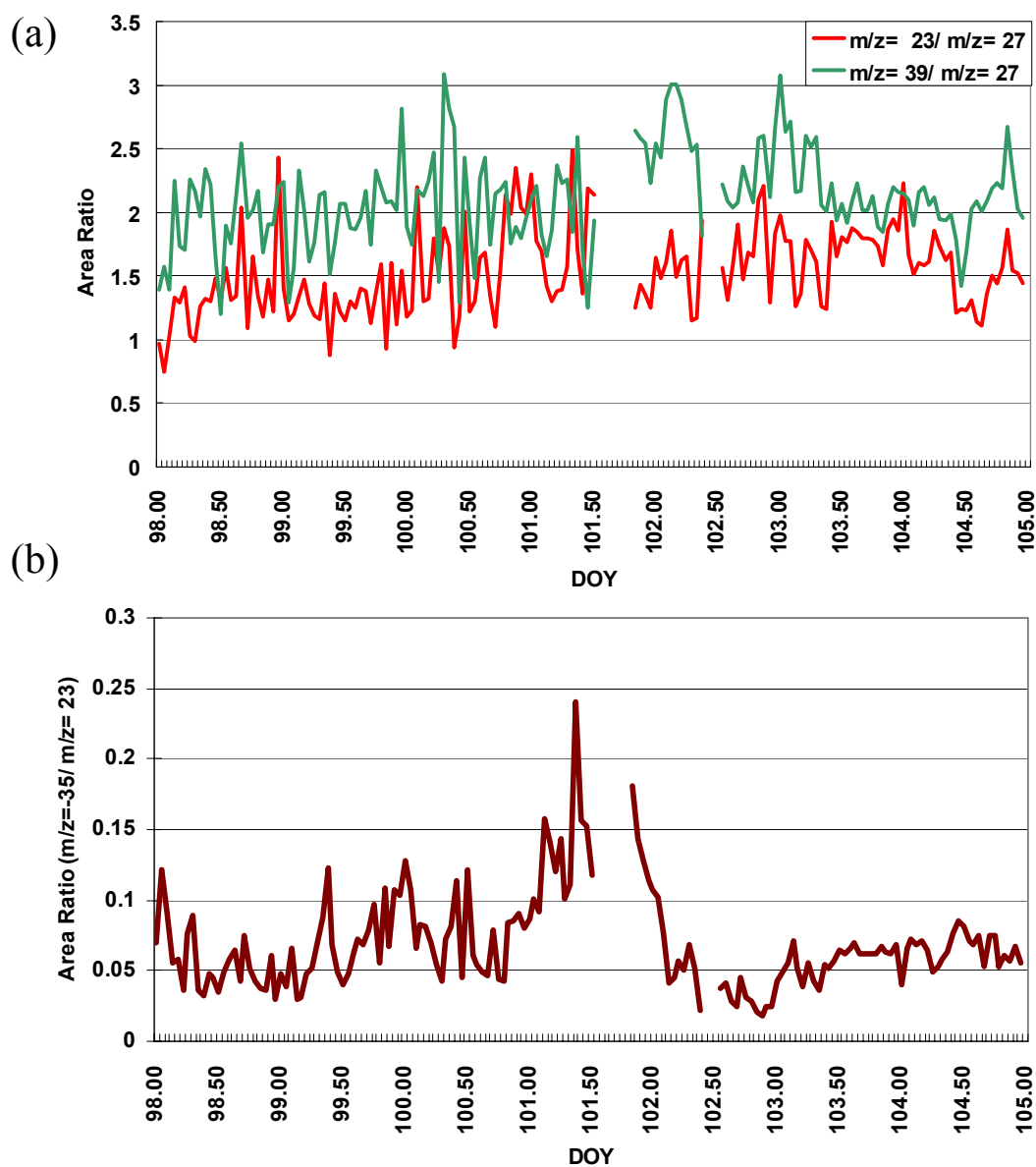
Figure 4.4. Temporal evolution of peak area ratios for dust particles presented in Figure 4.2, sampled during the ACE-Asia research cruise (DOY 98.0-105.0). **a)** Area ratio between peaks at mass-to-charge ratios m/z= +23 (Na) or m/z= +39 (K), and m/z = +27 (Al), representing principal mineral dust components. The lack of major temporal changes indicates that the dust mineralogy was not changing significantly during this period. **(b)** Area ratio between peaks at mass-to-charge ratios m/z= -35 (Cl) and m/z= +23 (Na).

As shown in Figure 4.5, the number fraction of dust particles detected containing chloride due to heterogeneous reactions increases significantly when the dust front arrives on DOY 100.8, representing as much as $65 \pm 4\%$ of the dust particles during the time period DOY 100.8-102.9. The detected number of particles representing agglomeration between sea salt and dust does not change considerably during these time periods, with an overall contribution of $13\pm2\%$ of the total dust between DOY 100.8-102.0, and $24\pm4\%$ over the period DOY 103.4-104.4 (Fig. 4.5b). In addition, the peak area ratio of Cl/Na dramatically increased between DOY 100.8-102.0 (Fig. 4.4). As presented in Bates et al. (2004) and in Chapter 2, during the post-frontal time period sea salt particles were not largely associated with sulfate and/or nitrate and therefore the expected Cl/Na area ratio in sea salt particles should be close to the one observed for unreacted sea salt particles and remain relatively constant. Therefore, if the chloride was due to internal mixtures with fresh sea-salt, the Cl/Na ratio would be expected to remain constant. If the sea salt had been depleted of some chloride due to aging by gaseous pollutants, the Cl/Na ratio would decrease. However, an <u>increase</u> in the -35/+23 (Cl/Na) area ratio in dust particles is observed starting on DOY 100.8 (Fig. 4.4), with similar trends as observed for the -35/+27 (Cl/Al) area ratio (Fig. 4.3), suggesting chloride deposition on these dust particles occurred via uptake of chlorine gases.

The relative contribution from sea salt-dust associated particles is much higher when the overall number of dust particles is lower. For example, as many as $40\pm6\%$ of the dust particles were associated with sea salt during the prefrontal period from DOY 99.0-100.0 (Fig. 4.5b). The association of dust and sea salt particles most likely occurs through cloud processing (Andreae et al., 1986a; Fan et al., 1996; Niimura et al., 1998; Okada et al., 1990). Therefore, when dust concentrations are extremely high (as in the case of the dust storm experienced during ACE-Asia), it is reasonable to expect that the relative contribution from
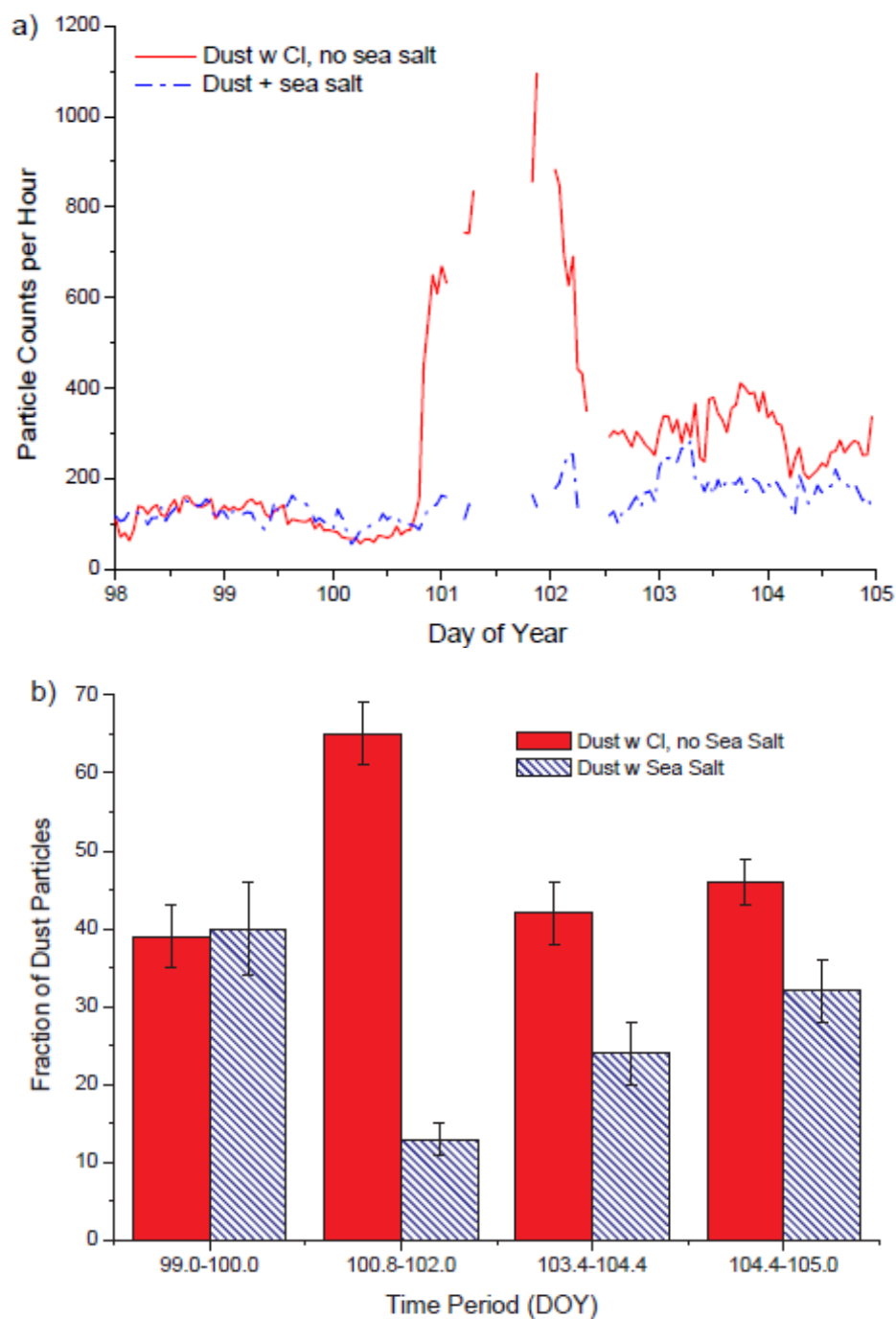
Figure 4.5. Contributions from supermicrometer dust particles containing chloride due to heterogeneous reaction, and dust particles associated with sea salt. **(a)** Temporal evolution (1-hour resolution) for the time period DOY 98.0-105.0. **(b)** Overall contributions to the total number of dust particles detected for different time periods. Error bars are 1 s.d. of the hourly percentages of the two types of dust.

sea salt-dust associated particles would decrease unless substantial cloud processing takes place to accommodate the elevated number of dust particles. Reported values for dust-sea salt coagulation, determined by SEM images of collected particles, range between 16 and 100% (Andreae et al., 1986a; Fan et al., 1996; Niimura et al., 1998; Ooki and Uematsu, 2005b; Zhang et al., 2003b) depending on location, transport, and meteorological conditions. The reduction in the fraction of dust mixed with sea salt during the period of the increased Cl/Al area ratio, along with all the other evidence presented above, clearly indicates that the source of chlorine was a gas-phase reactant that deposited chloride on the mineral dust through a heterogeneous process.

4.4.3   Possible sources of reactive chlorine gases

The chlorine-containing gases that reacted with the mineral dust particles most likely originated from one of the following sources (Keene et al., 1999): 1) HCl(g) released from sea salt particles after their reaction with acidic nitrogen and/or sulfur oxides (Gard et al., 1998; McInnes et al., 1994), 2) volcanic emissions, 3) anthropogenic activities such as fossil fuel combustion, or 4) oceanic methyl chloride. Here evidence is presented which suggests that the major contribution was brought about by HCl(g) released from chemically aged sea salt particles.

Prior to the frontal passage that led to high loadings of dust at the RHB, sea salt particles were substantially depleted of chloride due to heterogeneous reactions, and the majority (50-60%) of the supermicrometer nitrate- and sulfate- was present in sea salt (Bates et al., 2004; Tang et al., 2004b). This was caused by elevated $SO_2(g)$ concentrations transported to the area from the nearby Miyakejima volcano which depleted 77±12% of the total chloride from the sea salt (Bates et al., 2004). Uptake of $SO_2(g)$ by sea salt particles,

followed by its aqueous-phase oxidation to $H_2SO_4(aq)$ (Clegg and Toumi, 1998; Sievering et al., 1992) is likely the dominant mechanism that led to the acidification of aged sea salt in the polluted-volcanic air mass. The passage of the dust front changed the distribution of nitrate and sulfate from being mostly associated with sea salt particles, to the majority (60-80%) of nitrate and sulfate being on dust particles (with intrinsic alkaline properties) after DOY 100.8 (Bates et al., 2004). Sea salt particles in the post-frontal dust air mass were no longer highly associated with nitrate and sulfate and thus were not strongly acidified. The partial or total depletion of the majority of chloride from sea salt particles prior to the frontal passage would release HCl(g) to the marine atmosphere. Thus, it is very likely that dust particles, arriving from aloft (Fig 4.1) (Bates et al., 2004; Uno et al., 2004), encountered concentrations of HCl(g) at elevated levels adequate for heterogeneous processing. Kajino *et al.* (2005) reported increased concentrations of HCl(g) in the marine boundary layer of east Asia due to the acidification of sea salt particles by volcanic $SO_2(g)$. The reaction of HCl(g) with the alkaline $CaCO_3$-containing dust can be represented by the following reaction equation (Kelly and Wexler, 2005b), leading to the accumulation of secondary chloride on dust:

$$2\ HCl(g) + CaCO_3(s) \rightarrow CaCl_2(aq) + H_2O(aq) + CO_2(g) \qquad \text{(R4.1)}$$
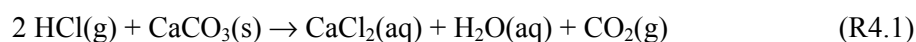
While the release of HCl(g) from sea salt was primarily caused by volcanic SO_2 emissions, there is no evidence for a direct volcanic source of chlorine that reacted with the mineral dust. The area ratio -97/+27, representing sulfate, increases starting on DOY 99.6, but decreases after DOY 100.8 when the dust front arrives (Fig. 4.3). This tracks the increase in SO_2 emissions attributed to volcanic sources and indicates reactions of sulfur oxides with dust particles (Bates et al., 2004). The reduced sulfate and nitrate peak area ratios during the dust front, from DOY 100.8-102.5, indicate that there was not a major influence from volcanic or anthropogenic emissions during this period of substantial increase in the chlorine peak area

ratio. The $SO_2(g)$ concentration was also reduced compared to the pre-frontal volcanic period (Bates et al., 2004). The direct volcanic contribution to $HCl(g)$ during this time was likely not substantial based on a recent report of water soluble species (e.g. Cl^-) analyzed in aerosols and precipitation after the Miyakejima volcanic eruption (Kajino et al., 2005). The Cl/Al area ratio, representing chloride in the dust particles, shows a small increase during the volcanic period but is actually anti-correlated with sulfate for the dust front time period (DOY 100.8-102.5) when chlorine in dust dramatically increased. We attribute the decrease in the HSO_4/Al peak area ratio in dust upon the dust front's arrival to a large decrease in $[SO_2(g)]$ from ~6.5 ppb to ~0.5 ppb (Bates et al., 2004), reducing the availability of sulfate precursors. Thus, the chloride present in dust particles during this time period was not caused by a direct volcanic release of chlorine.

The two remaining possible sources of chlorine in dust can be largely excluded as major contributors. Anthropogenic sources of chlorine include coal combustion, biomass burning, and incinerators (Keene et al., 1999). As the dust plume was transported from the source regions, the aerosol had the opportunity to interact with anthropogenic pollutants. An anthropogenic chlorine source would not explain the temporal spike of chlorine in dust when the dust front subsided into the polluted boundary layer (Figs. 4.3 & 4.4), unless the chlorine was being released in large amounts from a localized point source whose emissions became mixed with the dust front. However, without measurements of $HCl(g)$ on the RHB, we cannot rule out an intense point source of chlorine gases. Chlorine from an anthropogenic non-point source would be present with the dust for a longer period of time as the dust was mixed with anthropogenic pollution from DOY 101-105, but this was not observed. The decreased sulfate and nitrate peak areas in dust (Fig. 4.3) during the dust front, however, indicate a diminished anthropogenic influence during this period. This can be explained by the high altitude

trajectory that the dust front followed before subsiding into the polluted marine boundary layer (Fig. 4.1), thus avoiding substantial direct mixing with anthropogenic emissions during transport. After the dust front period, the air mass trajectories changed to pass over the more polluted regions of Korea and then Shanghai, with consequent increases in the nitrate and sulfate peak area ratios in dust (Chapter 3). We rule out chlorine uptake from reaction with oceanic methyl chloride because this gas is not highly acidic or reactive with mineral surfaces and would not cause the high temporal variability observed in the relative amount of chloride in dust. Therefore, we conclude that the major source of chlorine that reacted with the mineral dust was caused by $HCl(g)$ released from sea salt particles acidified by H_2SO_4, formed from the oxidation of volcanic $SO_2(g)$.

Recent laboratory studies have shown that Asian mineral dust particles react more frequently with HCl than SO_2 (Ooki and Uematsu, 2005b). However, the accumulation of sulfate in Asian dust appears to occur before nitrate and chloride mix with dust due to higher SO_2 concentrations in the interior near the dust sources (see Chapter 3). The acidification of dust by sulfuric acid (from SO_2 oxidation), producing sulfate, will prevent additional reaction between dust and $HCl(g)$ and could also displace HCl back to the gas-phase since H_2SO_4 is a stronger acid than HCl and is non-volatile. These processes explain our previous observations of chloride and nitrate being internally mixed with dust but segregated from dust particles containing sulfate. Reduced mixing ratios of sulfate and nitrate precursor gases (e.g. NO_x, HNO_3, SO_2, H_2SO_4), due to their prior uptake on sea salt particles, most likely contributed to the substantial chlorine uptake by dust particles. As shown in Figure 4.3, coincident with the increase in the chloride peak area ratio, a significant decrease was observed in the peak area ratios corresponding to nitrate ($m/z = -62/+27$), and sulfate ($m/z = -97/+27$) in dust. The decrease in sulfate and nitrate in dust when chloride peaked during the dust front indicates that

the dust was not highly mixed with these stronger acids, thus permitting extensive reaction of the mostly unreacted dust with HCl(g). Thus, the reduced availability of sulfate and nitrate precursors and their diminished presence in dust during the dust front passage allowed for the substantial uptake of chlorine by dust.

4.4.4   Estimates of chloride mass contributions to dust

Based on bulk filter measurements, the average amount of Cl in supermicron particles during the ACE-Asia campaign was 2.9 ug/m^3, ranging from 0.1-11.79 ug/m^3. During the spike of chloride in dust, the amount of supermicron Cl increased substantially by a factor of 9 and peaked at 5.09 ug/m^3 (DOY 101.26-101.37), while total supermicron mass was 113.68 ug/m^3. ATOFMS single particle data evaluated the percentage of supermicrometer chloride-containing particles that were classified as dust (not mixed with sea salt), and the percentage of all the supermicrometer particles that were dust. The mass concentrations of supermicron chloride and total particle mass were then multiplied by these percentages to estimate the fraction of dust particle mass that was chloride. Our single-particle measurements show that the majority of Cl was associated with dust particles during the dust front. Thus, the majority of the Cl mass measured during this time period was associated with dust, not sea salt, and we can estimate the chloride mass fraction in dust. From DOY 101.26-101.37, 60.1% of supermicron particles were mineral dust. The fraction of chloride-containing particles that was dust depends on the peak area criterion used to classify a particle as containing chloride. For this period, the fraction was 63.1% using a criterion of peak area m/z -35 > 100, and 81.3% using area > 5000. This results in a mass percentage of chloride in supermicrometer dust particles between 4.7% and 6.1% (e.g. for area > 100, chloride mass fraction = 63.1%*5.09 ug/m^3 ÷ 60.1%*113.68 ug/m^3 = 4.7%) for DOY 101.26 to 101.37, the second spike of chloride

in dust (Fig. 4.3). Further details and more examples for this calculation are provided in the Appendix, below.

These mass percentages are significantly higher than the percentage (by weight) of chloride in dust samples from relevant Asian source regions that we determined to be 0.005-0.02% by ion chromatography. Previous reports show the chloride mass fraction in dust-dominated aerosols measured in the interior of China in Yulin (Xu et al., 2004) and Zhenbeitai (Arimoto et al., 2004) was ~0.4%. This suggests that a significant amount of chloride was added to the dust via heterogeneous reactions. Analysis of reference Asian mineral dust indicates an average calcium content of 5.8% (Nishikawa, 2000). If the calcium carbonate originally present in these samples reacts completely with HCl, then the maximum chloride content after reaction would be ca. 10.3% by mass. Thus, the 4.7-6.3% chloride content estimated for dust particles observed during this field study strongly supports that the mineral dust particles were significantly transformed by heterogeneous reactions with HCl(g).

4.4.5   Chemical transport model simulations of dust-impacted aerosol chemistry

Chemical transport modeling results presented in Figure 4.6 predict a significant mass increase in particulate chloride from the heterogeneous reaction of HCl(g) with mineral dust. Displayed in Figure 4.6 are results from simulation runs including and omitting dust emissions, thus showing the direct effect of dust chemistry on the overall aerosol chemical composition. During the dust event periods observed on the RHB the majority of supermicron particulate mass was due to mineral dust particles (Bates et al., 2004). The simulation results clearly demonstrate a significant increase in the concentration of supermicron chloride when mineral dust chemistry is included, indicating a strong association between secondary chloride and dust. However, the simulated chloride mass concentrations are much lower than the

measured bulk chloride mass concentrations (a maximum value of 1.03 μg m^{-3} for the "total

model Cl" output, compared to 5.09 μg m^{-3} from filter measurements). This highlights the

need to improve the representation of further heterogeneous chlorine chemistry mechanisms

and kinetics in future chemical transport models. Some models currently in use, such as the

one used for the evaluation described herein (Tang et al., 2004b), include the mechanism for
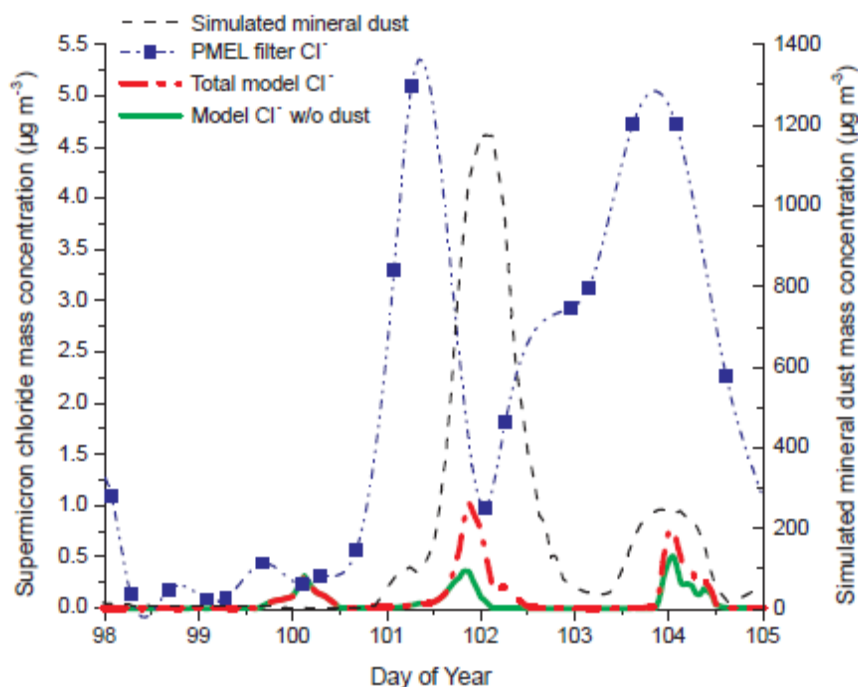
Figure 4.6. Model simulations of supermicron chloride compared with bulk filter measurements. STEM-2K3 model simulation outputs display the mass concentration of supermicron chloride. The total amount of chloride is compared for simulations with (Total model Cl$^-$) and without (Model Cl w/o dust) mineral dust emissions, revealing the contributions from mineral dust chemistry. The simulated mineral dust mass concentration is shown and captured several of the dust events observed on the RHB. Also plotted is the total amount of bulk particulate-chloride measured in filter samples analyzed by PMEL (points with a spline-fit). Bulk filter measurements of Cl$^-$ and other anions in aerosols were made aboard the RHB over 4-6 hour intervals (Bates et al., 2004). The bulk filter analysis measures anions in all particle types, analogous to the model output for the "Total model Cl" simulation plotted. Both the model and PMEL filter data is for particles between 1.0 μm and 10.0 μm in diameter. The time period for the arrival of the dust front obtained from the STEM-2K3 model lags approximately 6 hours behind the in-situ observed increase in the dust concentrations (probably due to differences in modeled wind fields and timing of dust emissions) (Tang et al., 2004b).

chlorine release from aged sea salt particles. The STEM-2K3 model captured the depletion of chloride from sea salt that was observed on the RHB just prior to the dust front (Bates et al., 2004; Tang et al., 2004b). STEM-2K3 uses measured meteorological fields to describe the model's atmospheric dynamics. Even though the air mass trajectory at the RHB changed by ca. 180° from the Polluted-Volcano to the Dust Front period on DOY 100.8, the observations and STEM-2K3 results both indicate that the incoming dust front still encountered an atmosphere enriched in HCl(g). Recall that the dust front arrived from aloft before entering the marine boundary layer. The large increase in particulate-chloride predicted by the model simulation agrees with our hypothesis that the marine boundary layer was enriched in HCl(g) when the dust front subsided from aloft. No volcanic sources of HCl(g) are included in the model and the dust front's modeled high-altitude trajectory would prevent substantial mixing with localized anthropogenic HCl(g) emissions. Therefore, the observed increase in modeled chloride associations with dust most likely arises from chlorine released from sea salt.

4.4.6 Atmospheric relevance and potential impacts

The results presented above demonstrate that the chemistry of reactive chlorine, sulfur, and nitrogen compounds can be altered by the presence of Asian mineral dust particles in the marine boundary layer, as previous studies have indicated (Bates et al., 2004; Dentener et al., 1996; Jordan et al., 2003; Ooki and Uematsu, 2005b). The substantial uptake of chlorine from HCl(g) reacting with dust reported here is still a relatively new finding that needs to be included in more detail in chemical transport models and investigated in laboratory studies. To my knowledge there are only two laboratory studies that have considered the reaction of HCl(g) with dust or minerals. Santschi and Rossi (2006) measured a high reaction probability of 0.1 for HCl(g) reacting with calcite ($CaCO_3$), a major mineral component of Asian dust.

Ooki and Uematsu (2005b) found that Asian dust reacted efficiently with HCl(g) in ambient air in Tokyo. Most prior laboratory studies have focused on the interactions of HNO_3, NO_x, and SO_2 with mineral dust surfaces (Cwiertny et al., 2008; Usher et al., 2003a). Building on the previous results described in Chapter 3, it has been shown that the reaction of HCl(g) with mineral dust is an important process in the atmosphere and involves complicated competitive and/or exclusionary interactions with other reactants such as HNO_3 and SO_2. To improve our understanding of mineral dust reactions with acidic gases, these competitive processes should be investigated further by laboratory and field studies.

Neglecting this chlorine heterogeneous dust chemistry invalidates a cascade of general assumptions commonly made by atmospheric scientists, with important consequences. For example, it is common practice in the scientific community to consider sea salt particles as the sole contributors to sodium and chloride in bulk aerosol samples. Measured mass concentrations of Na and Cl, together with reported Cl/Na molar (or mass) ratios in seawater, are used to calculate sea salt aerosol concentrations (i.e. [sea salt] = $[Cl^-]$ + $[Na^+]$ x 1.47), as well as contributions from other species, such as non-sea-salt sulfate and nitrate (e.g., nss-sulfate = total sulfate – $([SO_4^{2-}]/[Na^+])_{sea\ salt}$ x $[Na^+]_{measured}$) (Bates et al., 2004). This procedure yields accurate results in cases without elevated dust concentrations. However, when substantial amounts of chloride are present in dust, the contribution of chloride from sea salt particles will be overestimated, and therefore the degree of aging of sea salt particles will be underestimated.

Ignoring the deposition of chlorine species onto mineral dust particles could increase uncertainties in the estimates of radiative forcing since dust particles are very important contributors to net global forcing (Satheesh and Moorthy, 2005; Sokolik et al., 2001; Tegen et al., 1996). For example, the uptake of chloride by dust particles can increase their

hygroscopicity (similar to when nitrate is deposited on dust particles) making them more efficient CCN, increasing their rate of wet scavenging, and modifying their ice nuclei properties (Fan et al., 2004; Kelly et al., 2007; Levin et al., 1996; Perry et al., 2004; Sokolik et al., 2001). This deposition could also change the intrinsic optical behavior (and consequently the net radiative forcing) of these particles after their enhanced water uptake. It has been shown that the optical properties of mineral dust particles are strongly dependent on their composition, morphology, and mixing state (Gibson et al., 2006a; Lafon et al., 2006; Laskin et al., 2005a; Sokolik and Toon, 1999).

In certain oceanic regions far from land, where specific trace metals are limiting nutrients, deposition of mineral dust can affect primary productivity of phytoplankton (Jickells et al., 2005) and therefore affect nitrogen fixation and CO_2 uptake, and the release of biogases, some of which are climatically relevant (Jickells et al., 2005). A consequence of an increase in phytoplankton is increased dimethyl sulfide (DMS) emissions to the atmosphere. As described in the CLAW hypothesis (Charlson et al., 1987), a feedback loop involving marine phytoplankton, sulfate aerosols, and cloud albedo, could affect the Earth's climate. The solubility and bio-availability of the trace metals present in dust, such as iron, is strongly dependent on acidity and could be altered by the presence of acidic chlorine in the dust particles, therefore affecting ocean productivity (Jickells et al., 2005).

The uptake of chlorine species onto dust particles modifies the chlorine chemistry budget in the marine boundary layer, thus altering the overall HCl cycle and the cycles of important species involved in these heterogeneous reactions (such as SO_x, NO_y, ClO_x, and O_3). As shown herein, HCl(g) released from acidified sea salt particles can deposit onto mineral dust particles present in the marine atmosphere. This can alter the long-range transport of chlorine in the atmosphere since mineral dust particles can act as non-negligible carriers of

chloride, and therefore affect the local chlorine balance as well as the deposition of acids with its consequent effects on several ecosystems (Jordan et al., 2003). HCl(g) could also diminish later uptake of nitrogen- and sulfur-containing species onto the mineral dust particles by neutralizing the alkalinity of dust. These processes will therefore affect the chemical budgets of ClO_x, NO_x, and SO_x species in the marine boundary layer.

4.5 Conclusions

The uptake of chlorine by mineral dust particles in the marine boundary layer due to heterogeneous reactions involving HCl(g) was demonstrated. Online single-particle analysis allows the exclusion of chloride contributions to dust caused by internal mixtures of dust and sea salt particles. The release of HCl(g) from acidified sea salt particles, from reaction with H_2SO_4 after uptake of volcanic SO_2(g), is hypothesized to have resulted in much larger than normal concentrations of HCl(g) available for reaction with dust particles. The uptake of SO_2(g) and NO_x(g) by sea salt prior to the dust front's arrival reduced the availability of sulfate and nitrate precursors, thus allowing the elevated HCl(g) to react unimpeded with the alkaline mineral dust. Simulations of aerosol chemistry from the STEM-2K3 model support this hypothesis and agree with our observations of substantial chlorine uptake by mineral dust during the dust front. This chemical process has important implications for the budgets of ClO_x, NO_x, SO_x, and O_3 in the marine boundary layer, the atmospheric processing and lifetime of dust, and the long-range transport of chlorine. The enrichment of chloride in mineral dust can invalidate estimates of sea salt aerosol concentrations and aging derived from filter measurements. Uptake of chlorine by dust can potentially alter the direct and indirect climate forcings of mineral dust particles (Chapter 6) and their role as nutrient vectors to remote ocean

regions. Global chemical models must therefore include this reaction to produce a more accurate description of atmospheric chemistry and climate.

4.6 Acknowledgments

4.7 Appendix: Calculation of chloride mass fraction in dust by combining ATOFMS and PMEL data

Single-particle measurements made with the ATOFMS are used to determine the fractions of chloride-containing particles that are mineral dust (not mixed with sea salt), and the fraction of total particles that are mineral dust. This is performed for particles with an aerodynamic diameter (D_a) of 1.0-3.0 um, the upper size range of the ATOFMS. These fractions are then used to apportion the bulk mass concentrations determined by PMEL filter measurements of supermicron (D_a = 1.0-10.0 um) chloride and total particle mass that are

from mineral dust. The raw data is available at http://saga.pmel.noaa.gov/data/. Lognormal distributions were assumed for mass and number concentrations, and therefore the relationship between the two is expressed as: $dV/d(logD) = ((\pi*D^3)/6)*(dN/d(log(D)))$ (Seinfeld and Pandis, 1998). Using mass and number ratios for the same size range allows cancellation of terms and produces a direct relationship between ratios of particle numbers and particle mass. All chlorine-containing dust particles were assumed to have the same amount of chloride.

For the period of interest (DOY 101.26-101.37), total supermicron mass concentration was 113.68 ug/m^3 and 60.1% of the single particles were determined to be mineral dust not mixed with sea salt. Thus 68.3 ug/m^3 of the supermicron mass is estimated to be mineral dust. The chloride mass concentration was 5.09 ug/m^3 and the fraction of chlorine-containing particles classified as mineral dust depends on the peak area criterion selected to classify a particle as being mixed with Cl (m/z = -35). This criterion is somewhat arbitrary as the mass fraction of chloride that produces a given peak area in various particle types is not yet known. However, a good knowledge of the range of peak areas produced from a wide variety of artificial and ambient aerosols is known from over a decade of measurements with ATOFMS (e.g. (Liu et al., 2003)). Table 4.1 below lists the fraction of chloride-containing particles classified as mineral dust for a wide range of Cl peak area criteria. This fraction is then used to estimate the mass fraction of a dust particle that is secondary chloride. For example, a peak area criterion of > 1000 produces a chloride-dust fraction of 73.6%. Multiplying this fraction by the total chloride mass (5.09 ug/m^3) produces an estimated 3.75 ug/m^3 of chloride in dust. The chloride mass fraction in dust is therefore 3.75 ug/m^3 ÷ 68.3 ug/m^3 = 5.5%.

Despite the large range in peak area thresholds used, the estimates of chloride mass fraction in dust is quite tight, from 4.6 to 6.3%. The lowest and highest peak areas likely represent overly extreme criteria and are only presented to illustrate the low sensitivity of the

calculation to this threshold. The fact that the fraction of chloride-dust and thus chloride mass fraction in dust increases with increasing Cl area threshold indicates that the particles with the highest chloride peak areas, and thus largest amounts of chloride, are dominated by mineral dust particles.

ATOFMS measurements included particles up to 3.0 μm, while the filter measurements went up to 10 μm. Thus, we must assume that the ATOFMS measurements from 1.0-3.0 μm represent the dust particles from 3.0-10.0 μm as well. Dust particles larger than 3.0 μm will likely contain less chloride (due to smaller surface area to volume ratio) but the fraction of particulate mass due to dust will be larger. Therefore, the fraction of mass that is chloride should be smaller for the larger dust particles.

Table 4.1. Calculation of chloride mass fraction in aged dust particles.

Cl⁻ Peak Area Threshold	Cl-Containing Particles	Cl-Dust Particles	Cl-Dust Fraction	Cl-Dust Mass	Dust Mass	Cl-Dust Mass Fraction
50	1384	852	0.616	3.133	68.287	4.59%
100	1340	846	0.631	3.214	68.287	4.71%
250	1255	832	0.663	3.374	68.287	4.94%
1000	1005	740	0.736	3.748	68.287	5.49%
5000	406	330	0.813	4.137	68.287	6.06%
10000	154	131	0.851	4.330	68.287	6.34%

4.8 References

Andreae, M. O., Charlson, R. J., Bruynseels, F., Storms, H., Van Grieken, R., and Maenhaut, W.: Internal mixture of sea salt, silicates, and excess sulfate in marine aerosols, Science, 232 (4758), 1620-1623, 1986.

Arimoto, R., Kim, Y. J., Kim, Y. P., Quinn, P. K., Bates, T. S., Anderson, T. L., Gong, S., Uno, I., Chin, M., Huebert, B. J., Clarke, A. D., Shinozuka, Y., Weber, R. J., Anderson, J. R., Guazzotti, S. A., Sullivan, R. C., Sodeman, D. A., Prather, K. A., and Sokolik, I. N.: Characterization of Asian Dust during ACE-Asia, Global and Planetary Change, 52 (1-4), 23-56, 2006.

Arimoto, R., Zhang, X. Y., Huebert, B. J., Kang, C. H., Savoie, D. L., Prospero, J. M., Sage, S. K., Schloesslin, C. A., Khaing, H. M., and Oh, S. N.: Chemical composition of atmospheric aerosols from Zhenbeitai, China, and Gosan, South Korea, during ACE-Asia, J. Geophys. Res., 109 (D19), doi:10.1029/2003JD004323, 2004.

Bates, T. S., Quinn, P. K., Coffman, D. J., Covert, D. S., Miller, T. L., Johnson, J. E., Carmichael, G. R., Uno, I., Guazzotti, S. A., Sodeman, D. A., Prather, K. A., Rivera, M., Russell, L. M., and Merrill, J. T.: Marine boundary layer dust and pollutant transport associated with the passage of a frontal system over eastern Asia, J. Geophys. Res., 109 (D19), doi:10.1029/2003JD004094, 2004.

Bauer, S. E., Balkanski, Y., Schulz, M., Hauglustaine, D. A., and Dentener, F.: Global modeling of heterogeneous chemistry on mineral aerosol surfaces: Influence on tropospheric ozone chemistry and comparison to observations, J. Geophys. Res., 109 (D2), doi:10.1029/2003JD003868, 2004.

Charlson, R. J., Lovelock, J. E., Andreae, M. O., and Warren, S. G.: Oceanic phytoplankton, atmospheric sulfur, cloud albedo and climate, Nature, 326 (6114), 655-661, 1987.

Clegg, N. A., and Toumi, R.: Non-sea-salt-sulphate formation in sea-salt aerosol, J. Geophys. Res., 103 (D23), 31095-31102, 1998.

Cwiertny, D. M., Young, M. A., and Grassian, V. H.: Chemistry and photochemistry of mineral dust aerosol, Annual Review of Physical Chemistry, 59, 27-51, 2008.

DeMott, P. J., Cziczo, D. J., Prenni, A. J., Murphy, D. M., Kreidenweis, S. M., Thomson, D. S., Borys, R., and Rogers, D. C.: Measurements of the concentration and composition of nuclei for cirrus formation, Proc. Natl. Acad. Sci. USA, 100 (25), 14655-14660, 2003.

Dentener, F. J., Carmichael, G. R., Zhang, Y., Lelieveld, J., and Crutzen, P. J.: Role of mineral aerosol as a reactive surface in the global troposphere, J. Geophys. Res., 101 (D17), 22869-22889, 1996.

Fan, S. M., Horowitz, L. W., Levy, H., and Moxim, W. J.: Impact of air pollution on wet deposition of mineral dust aerosols, Geophys. Res. Lett., 31 (2), doi:10.1029/2003GL018501, 2004.

Fan, X. B., Okada, K., Niimura, N., Kai, K., Arao, K., Shi, G. Y., Qin, Y., and Mitsuta, Y.: Mineral particles collected in China and Japan during the same Asian dust-storm event, Atmos. Environ., 30 (2), 347-351, 1996.

Gard, E. E., Kleeman, M. J., Gross, D. S., Hughes, L. S., Allen, J. O., Morrical, B. D., Fergenson, D. P., Dienes, T., Galli, M. E., Johnson, R. J., Cass, G. R., and Prather, K. A.: Direct observation of heterogeneous chemistry in the atmosphere, Science, 279 (5354), 1184-1187, 1998.

Gibson, E. R., Hudson, P. K., and Grassian, V. H.: Aerosol chemistry and climate: Laboratory studies of the carbonate component of mineral dust and its reaction products, Geophys. Res. Lett., 33 (13), doi:10.1029/2006GL026386, 2006.

Gong, S. L., Zhang, X. Y., Zhao, T. L., McKendry, I. G., Jaffe, D. A., and Lu, N. M.: Characterization of soil dust aerosol in China and its transport and distribution during 2001 ACE-Asia: 2. Model simulation and validation, J. Geophys. Res., 108 (D9), doi:10.1029/2002JD002633, 2003.

Guazzotti, S. A., Coffee, K. R., and Prather, K. A.: Continuous measurements of size-resolved particle chemistry during INDOEX-Intensive Field Phase 99, J. Geophys. Res., 106 (D22), 28607-28627, 2001a.

Guazzotti, S. A., Whiteaker, J. R., Suess, D., Coffee, K. R., and Prather, K. A.: Real-time measurements of the chemical composition of size-resolved particles during a Santa Ana wind episode, California USA, Atmos. Environ., 35 (19), 3229-3240, 2001b.

Huebert, B. J., Bates, T., Russell, P. B., Shi, G. Y., Kim, Y. J., Kawamura, K., Carmichael, G., and Nakajima, T.: An overview of ACE-Asia: Strategies for quantifying the relationships between Asian aerosols and their climatic impacts, J. Geophys. Res., 108 (D23), doi:10.1029/2003JD003550, 2003.

Jaffe, D., McKendry, I., Anderson, T., and Price, H.: Six 'new' episodes of trans-Pacific transport of air pollutants, Atmos. Environ., 37 (3), 391-404, 2003.

Jickells, T. D., An, Z. S., Andersen, K. K., Baker, A. R., Bergametti, G., Brooks, N., Cao, J. J., Boyd, P. W., Duce, R. A., Hunter, K. A., Kawahata, H., Kubilay, N., laRoche, J., Liss, P. S., Mahowald, N., Prospero, J. M., Ridgwell, A. J., Tegen, I., and Torres, R.: Global iron connections between desert dust, ocean biogeochemistry, and climate, Science, 308 (5718), 67-71, 2005.

Jordan, C. E., Dibb, J. E., Anderson, B. E., and Fuelberg, H. E.: Uptake of nitrate and sulfate on dust aerosols during TRACE-P, J. Geophys. Res., 108 (D21), doi:10.1029/2002JD003101, 2003.

Kajino, M., Ueda, H., Satsumabayashi, H., and Han, Z. W.: Increase in nitrate and chloride deposition in east Asia due to increased sulfate associated with the eruption of Miyakejima Volcano, J. Geophys. Res., 110 (D18), doi:10.1029/2005JD005879, 2005.

Keene, W. C., Khalil, M. A. K., Erickson, D. J., McCulloch, A., Graedel, T. E., Lobert, J. M., Aucott, M. L., Gong, S. L., Harper, D. B., Kleiman, G., Midgley, P., Moore, R. M., Seuzaret, C., Sturges, W. T., Benkovitz, C. M., Koropalov, V., Barrie, L. A., and Li, Y. F.: Composite global emissions of reactive chlorine from anthropogenic and

natural sources: Reactive Chlorine Emissions Inventory, J. Geophys. Res., 104 (D7), 8429-8440, 1999.

Kelly, J. T., Chuang, C. C., and Wexler, A. S.: Influence of dust composition on cloud droplet formation, Atmos. Environ., 41 (14), 2904-2916, 2007.

Kelly, J. T., and Wexler, A. S.: Thermodynamics of carbonates and hydrates related to heterogeneous reactions involving mineral aerosol, J. Geophys. Res., 110 (D11), doi:10.1029/2004JD005583, 2005.

Kim, Y. P., and Seinfeld, J. H.: Atmospheric gas-aerosol equilibrium. 3. Thermodynamics of crustal elements Ca^{2+}, K^+, and Mg^{2+}, Aerosol Sci. Technol., 22 (1), 93-110, 1995.

Lafon, S., Sokolik, I. N., Rajot, J. L., Caquineau, S., and Gaudichet, A.: Characterization of iron oxides in mineral dust aerosols: Implications for light absorption, J. Geophys. Res., 111 (D21), 2006.

Laskin, A., Iedema, M. J., Ichkovich, A., Graber, E. R., Taraniuk, I., and Rudich, Y.: Direct observation of completely processed calcium carbonate dust particles, Faraday Discuss., 130, 453-468, 2005.

Levin, Z., Ganor, E., and Gladstein, V.: The effects of desert particles coated with sulfate on rain formation in the eastern Mediterranean, Journal Of Applied Meteorology, 35 (9), 1511-1523, 1996.

Liu, D. Y., Wenzel, R. J., and Prather, K. A.: Aerosol time-of-flight mass spectrometry during the Atlanta Supersite Experiment: 1. Measurements, J. Geophys. Res., 108 (D7), doi:10.1029/2001JD001562, 2003.

Matsuki, A., Iwasaka, Y., Shi, G. Y., Zhang, D. Z., Trochkine, D., Yamada, M., Kim, Y. S., Chen, B., Nagatani, T., Miyazawa, T., Nagatani, M., and Nakata, H.: Morphological and chemical modification of mineral dust: Observational insight into the heterogeneous uptake of acidic gases, Geophys. Res. Lett., 32 (22), doi:10.1029/2005GL024176, 2005.

McInnes, L. M., Covert, D. S., Quinn, P. K., and Germani, M. S.: Measurements of chloride depletion and sulfur enrichment in individual sea-salt particles collected from the remote marine boundary-layer, J. Geophys. Res., 99 (D4), 8257-8268, 1994.

Murphy, D. M., Cziczo, D. J., Froyd, K. D., Hudson, P. K., Matthew, B. M., Middlebrook, A. M., Peltier, R. E., Sullivan, A., Thomson, D. S., and Weber, R. J.: Single-particle mass spectrometry of tropospheric aerosol particles, J. Geophys. Res., 111 (D23), doi:10.1029/2006JD007340, 2006.

Niimura, N., Okada, K., Fan, X. B., Kai, K., Arao, K., Shi, G. Y., and Takahashi, S.: Formation of Asian dust-storm particles mixed internally with sea salt in the atmosphere, Journal of the Meteorological Society of Japan, 76 (2), 275-288, 1998.

Nishikawa, M., Hao, Q., Morita, M.: Preperation and evaluation of certified reference materials for Asian mineral dust, Global Environmental Research 4, 103-113, 2000.

Okada, K., Naruse, H., Tanaka, T., Nemoto, O., Iwasaka, Y., Wu, P. M., Ono, A., Duce, R. A., Uematsu, M., Merrill, J. T., and Arao, K.: X-ray spectrometry of individual Asian dust-storm particles over the Japanese islands and the north Pacific-Ocean, Atmos. Environ., 24 (6), 1369-1378, 1990.

Ooki, A., and Uematsu, M.: Chemical interactions between mineral dust particles and acid gases during Asian dust events, J. Geophys. Res., 110 (D3), doi:10.1029/2004JD004737, 2005.

Perry, K. D., Cliff, S. S., and Jimenez-Cruz, M. P.: Evidence for hygroscopic mineral dust particles from the Intercontinental Transport and Chemical Transformation Experiment, J. Geophys. Res., 109 (D23), doi:10.1029/2004JD004979, 2004.

Rudich, Y., Khersonsky, O., and Rosenfeld, D.: Treating clouds with a grain of salt, Geophys. Res. Lett., 29 (22), doi:10.1029/2002GL016055, 2002.

Santschi, C., and Rossi, M. J.: Uptake of CO_2, SO_2, HNO_3 and HCl on calcite ($CaCO_3$) at 300 K: Mechanism and the role of adsorbed water, J. Phys. Chem. A, 110 (21), 6789-6802, 2006.

Satheesh, S. K., and Moorthy, K. K.: Radiative effects of natural aerosols: A review, Atmos. Environ., 39 (11), 2089-2110, 2005.

Seinfeld, J. H., Carmichael, G. R., Arimoto, R., Conant, W. C., Brechtel, F. J., Bates, T. S., Cahill, T. A., Clarke, A. D., Doherty, S. J., Flatau, P. J., Huebert, B. J., Kim, J., Markowicz, K. M., Quinn, P. K., Russell, L. M., Russell, P. B., Shimizu, A., Shinozuka, Y., Song, C. H., Tang, Y. H., Uno, I., Vogelmann, A. M., Weber, R. J., Woo, J. H., and Zhang, X. Y.: ACE-ASIA - Regional climatic and atmospheric chemical effects of Asian dust and pollution, Bulletin Of The American Meteorological Society, 85 (3), 367-380, 2004.

Seinfeld, J. H., and Pandis, S. N., Atmospheric Chemistry & Physics, John Wiley & Sons, Inc., New York, 1998.

Sievering, H., Boatman, J., Gorman, E., Kim, Y., Anderson, L., Ennis, G., Luria, M., and Pandis, S.: Removal of sulfur from the marine boundary-layer by ozone oxidation in sea-salt aerosols, Nature, 360 (6404), 571-573, 1992.

Silva, P. J., Carlin, R. A., and Prather, K. A.: Single particle analysis of suspended soil dust from Southern California, Atmos. Environ., 34 (11), 1811-1820, 2000.

Sokolik, I. N., and Toon, O. B.: Incorporation of mineralogical composition into models of the radiative properties of mineral aerosol from UV to IR wavelengths, J. Geophys. Res., 104 (D8), 9423-9444, 1999.

Sokolik, I. N., Winker, D. M., Bergametti, G., Gillette, D. A., Carmichael, G., Kaufman, Y. J., Gomes, L., Schuetz, L., and Penner, J. E.: Introduction to special section: Outstanding problems in quantifying the radiative impacts of mineral dust, J. Geophys. Res., 106 (D16), 18015-18027, 2001.

Tang, Y. H., Carmichael, G. R., Kurata, G., Uno, I., Weber, R. J., Song, C. H., Guttikunda, S. K., Woo, J. H., Streets, D. G., Wei, C., Clarke, A. D., Huebert, B., and Anderson, T. L.: Impacts of dust on regional tropospheric chemistry during the ACE-Asia experiment: A model study with observations, J. Geophys. Res., 109 (D19), doi:10.1029/2003JD003806, 2004a.

Tang, Y. H., Carmichael, G. R., Seinfeld, J. H., Dabdub, D., Weber, R. J., Huebert, B., Clarke, A. D., Guazzotti, S. A., Sodeman, D. A., Prather, K. A., Uno, I., Woo, J. H., Yienger, J. J., Streets, D. G., Quinn, P. K., Johnson, J. E., Song, C. H., Grassian, V. H., Sandu, A., Talbot, R. W., and Dibb, J. E.: Three-dimensional simulations of inorganic aerosol

distributions in east Asia during spring 2001, J. Geophys. Res., 109 (D19), doi:10.1029/2003JD004201, 2004b.

Tegen, I., Lacis, A. A., and Fung, I.: The influence on climate forcing of mineral aerosols from disturbed soils, Nature, 380 (6573), 419-422, 1996.

Uno, I., Satake, S., Carmichael, G. R., Tang, Y. H., Wang, Z. F., Takemura, T., Sugimoto, N., Shimizu, A., Murayama, T., Cahill, T. A., Cliff, S., Uematsu, M., Ohta, S., Quinn, P. K., and Bates, T. S.: Numerical study of Asian dust transport during the springtime of 2001 simulated with the Chemical Weather Forecasting System (CFORS) model, J. Geophys. Res., 109 (D19), doi:10.1029/2003JD004222, 2004.

Usher, C. R., Michel, A. E., and Grassian, V. H.: Reactions on mineral dust, Chem. Rev., 103 (12), 4883-4939, 2003.

Xu, J., Bergin, M. H., Greenwald, R., Schauer, J. J., Shafer, M. M., Jaffrezo, J. L., and Aymoz, G.: Aerosol chemical, physical, and radiative characteristics near a desert source region of northwest China during ACE-Asia, J. Geophys. Res., 109 (D19), doi:10.1029/2003JD004239, 2004.

Zhang, D. Z., and Iwasaka, Y.: Chlorine deposition on dust particles in marine atmosphere, Geophys. Res. Lett., 28 (18), 3613-3616, 2001.

Zhang, D. Z., Iwasaka, Y., Shi, G. Y., Zang, J. Y., Matsuki, A., and Trochkine, D.: Mixture state and size of Asian dust particles collected at southwestern Japan in spring 2000, J. Geophys. Res., 108 (D24), doi:10.1029/2003JD003869, 2003.

Chapter 5

Investigations of the diurnal cycle and mixing state of

oxalic acid in individual particles in Asian aerosol outflow

5.1 Synopsis

The mixing state of oxalic acid was measured in Asian outflow during ACE-Asia by direct shipboard measurements using a single-particle mass spectrometer (ATOFMS). Oxalic and malonic acids were found to be predominantly internally mixed with mineral dust and aged sea salt particles. A persistent diurnal cycle of oxalic acid in mineral dust occurred for over 25 days in marine, polluted marine, and dust storm air masses. The preferential enrichment of diacids in mineral dust over carbonaceous particles, and their diurnal behavior, indicate a photochemical source of the diacids. Oxalate in dust was only detected simultaneously with elevated aged dust particle counts. This suggests that the diurnal production of diacids most likely results from episodic atmospheric processing of the polluted dust aerosol. We propose a mechanism to explain these observations in which the photochemical oxidation of VOCs is followed by partitioning of the diacids and precursors to the alkaline Asian dust, with subsequent heterogeneous and aqueous oxidation. Our data indicate that the particulate diacids were produced over just a few hours close to the source; no significant production or destruction appears to have occurred during long-range transport to the ship. No evidence of extensive cloud processing of the sampled aerosol was found. This mixing state of diacids has important implications for the solubility and cloud nucleation properties of the dominant fraction of water-soluble organics, and the bioavailability of iron in dust.

5.2 Introduction

Dicarboxylic acids (DCAs, or diacids) represent a significant portion of the organic fraction of aerosols yet their sources and atmospheric behavior remain highly uncertain. Diacids are typically the most dominant fraction of water soluble organic carbon (WSOC) measured in aerosols in a wide variety of environments (Huang and Yu, 2007; Kanakidou et al., 2005; Kawamura and Ikushima, 1993). Oxalic acid (C_2), followed by malonic (C_3) and succinic acid (C_4), are usually the most abundant DCAs (Chebbi and Carlier, 1996; Huang and Yu, 2007; Kanakidou et al., 2005; Kawamura and Ikushima, 1993; Mochida et al., 2003a; Mochida et al., 2003b). Diacids have received a great deal of attention due to their high water solubility, which results in these compounds being very CCN active, and thus likely affecting cloud formation (Abbatt et al., 2005; Ervens et al., 2005; Kanakidou et al., 2005; Prenni et al., 2001). Dicarboxylic acids may play a role in the solubility and aqueous photochemistry of transition metals in aerosols (Deguillaume et al., 2005; Jickells et al., 2005).

The sources and atmospheric behavior of dicarboxylic acids are still under investigation. Diacids can be directly emitted from automobiles and biomass burning (Chebbi and Carlier, 1996; Kanakidou et al., 2005), though recently primary vehicular emissions have been called into question (Huang and Yu, 2007; Wang et al., 2006). Photochemistry and in-cloud processing are two major secondary production pathways under investigation. A large fraction of DCAs are believed to be produced from photochemical oxidation of precursor VOCs including aromatic hydrocarbons and cyclic alkenes (Chebbi and Carlier, 1996; Mochida et al., 2003a). Recently, in-cloud production of DCAs through aqueous oxidation and photochemistry was demonstrated as an efficient mechanism for diacid production in cloud droplets (Ervens et al., 2004; Sorooshian et al., 2006; Warneck, 2003; Yu et al., 2005). There have been several reports of indirect evidence for photochemical production of diacids, but

little direct evidence. Indirect evidence includes observations of a diurnal cycle of diacids in Tokyo (Kawamura and Yasui, 2005), during transport from Tokyo to mountainous regions (Satsumabayashi et al., 1990), correlation of diacid mass and oxidant concentrations in summer (Kawamura and Ikushima, 1993), and the formation of diacids during polar sunrise in the Arctic (Kawamura et al., 2005). All of these studies are based on bulk aerosol filter measurements with 3-hour or 1-day sampling times. Here the first report of hourly temporal counts of single-particles that contain oxalic and larger diacids is presented. These measurements were made on board the NOAA R/V Ronald H. Brown (RHB) during its cruise from Hawaii to the Sea of Japan during the ACE-Asia campaign (March 17 to April 18, 2001). Several massive dust storms that mixed with anthropogenic pollution, volcanic, and marine air were observed as the aerosol was transported eastward from the continent (Bates et al., 2004). In Chapter 2 the chemical composition of the ACE-Asia aerosol was described and Chapters 3 & 4 investigated the atmospheric processing of the Asian dust by inorganic acids and ammonia(Sullivan et al., 2007a; Sullivan et al., 2007b). Here the distribution of dicarboxylic acids in single-particles classified by type (i.e. mixing state) in the polluted Asian aerosol is investigated to better understand the production mechanisms of these important components of WSOC.

5.3 Experimental methods

5.3.1 Shipboard aerosol sampling

The aerosol was sampled as described in Chapter 2 aboard the RHB during its research cruise from Hawaii to Japan. An ATOFMS with a nozzle inlet was used for online single-particle analysis of the aerosol, as described in Chapter 1. The ATOFMS employed during ACE-Asia was capable of efficiently detecting particles between D_a 0.2 and 3.0 μm

The air masses and meteorology encountered during the cruise have been described in Chapter 2 and further details are given by Bates et al. (2004); a brief summary is given below.

The RHB sampled relatively clean marine air free of continental influence during its cruise from Hawaii to Japan (DOY 75-84, Remote Marine). On DOY 84.25 Asian influenced air was first sampled (Marine), and from DOY 88.75-91 volcanic emissions were sampled as the RHB passed by the Miyakejima volcano. Increasingly polluted air was sampled up to DOY 99 (Polluted Marine), when a large volcanic air mass mixed with anthropogenic pollution from DOY 99.3-100.5 (Polluted Volcanic). A massive dust front reached the RHB in the Sea of Japan at DOY 100.8 (Dust Front), and dust continued to dominate, mixing with pollution from Korea (DOY 101.8-103.4) and Shanghai (DOY 103.4-104.5) (Polluted Dust). Polluted continental air with reduced dust concentrations continued from DOY 105-109 (Polluted Continental). Further details on the air masses sampled and their origins are given by Bates et al. (2004).

5.3.2 Analysis of single-particle data

A total of 731,309 single-particle mass spectra were collected over the course of the campaign. The particle clusters produced by the ART-2a sorting algorithm were classified into major particle types based on previous ATOFMS source characterization studies and field measurements (see Chapter 2). The 60 largest particle clusters, representing over 90% of the total particles, were classified as mineral dust, aged sea salt, fresh sea salt, organic carbon, elemental carbon, K-biomass (K-rich particles from biomass burning), or other/unknown. The presence or absence of secondary aerosol species such as nitrate, sulfate, and ammonium was not used as part of this classification, except in the case of dust and sea salt particles. Sea salt particles were divided into "aged" and "fresh" by the presence of large nitrate and/or sulfate peaks in the cluster's average mass spectrum. These peaks indicate chemical aging from

heterogeneous reactions with acidic gases (Guazzotti et al., 2001a). Mineral dust particles were sub-classified as "aged" if they satisfied a peak area criterion for chloride (m/z -35), nitrate (m/z -62), sulfate (m/z -97) > 5000, or ammonium (m/z 18) > 1000 (Chapter 3). Particles containing dicarboxylic acids were queried by searching for the conjugate anion [M-H]$^-$ of different DCAs, including oxalic acid (C$_2$, m/z -89, oxalate), malonic acid (C$_3$, m/z -103), and succinic acid (C$_4$, m/z -117). These anions were selected based on analysis of pure and mixed dicarboxylic acid aerosols standards (Silva and Prather, 2000).

5.4   Results and discussion

5.4.1   Detection of dicarboxylic acids in single-particles

Dicarboxylic acids, in particular oxalic acid, were frequently detected in single-particles in the complex Asian aerosol. Oxalate-containing particles were queried by an m/z -89 > 0.5% relative area criterion. A criterion of 0.8% or 1.0% relative area produces virtually identical temporal patterns, but with reduced hourly counts. The temporal distributions are divided into particles with aerodynamic diameters (D$_a$) less than and greater than 1 μm to eliminate the bias of the ATOFMS nozzle inlet towards supermicron particles, causing submicron particles to be under-sampled. Each size range thus represents the relative counts of different particle types and not the actual atmospheric concentrations. The hourly particle counts indicate the relative atmospheric concentrations of single particle types containing oxalic acid.

The hourly counts of oxalate-containing particle types over the course of the campaign are shown in Figure 5.1 and display several interesting features. Oxalic acid is found almost exclusively in mineral dust particles, for both sub- and supermicron diameters. There is one prolonged time period when a significant fraction of oxalic acid is found in aged

Figure 5.1. Hourly counts of particles containing oxalic acid as a function of principal particle class for (a) submicron (0.2μm > Da > 1.0μm) and (b) supermicron (1.0μm > Da > 3.0μm) particle sizes. Hourly counts of aged mineral dust particles mixed with either nitrate or sulfate (>5% relative area) are also shown. Note that different colors are used for sulfate-dust to improve clarity (pink in a, yellow in b). (c) Hourly fraction of total particles containing oxalate. Letters correspond to different air masses: Remote Marine (RM), Marine (M), Polluted Marine (PM), Polluted Volcanic (PV), Dust Front (DF), Polluted Dust (PD), and Polluted Continental (PC).
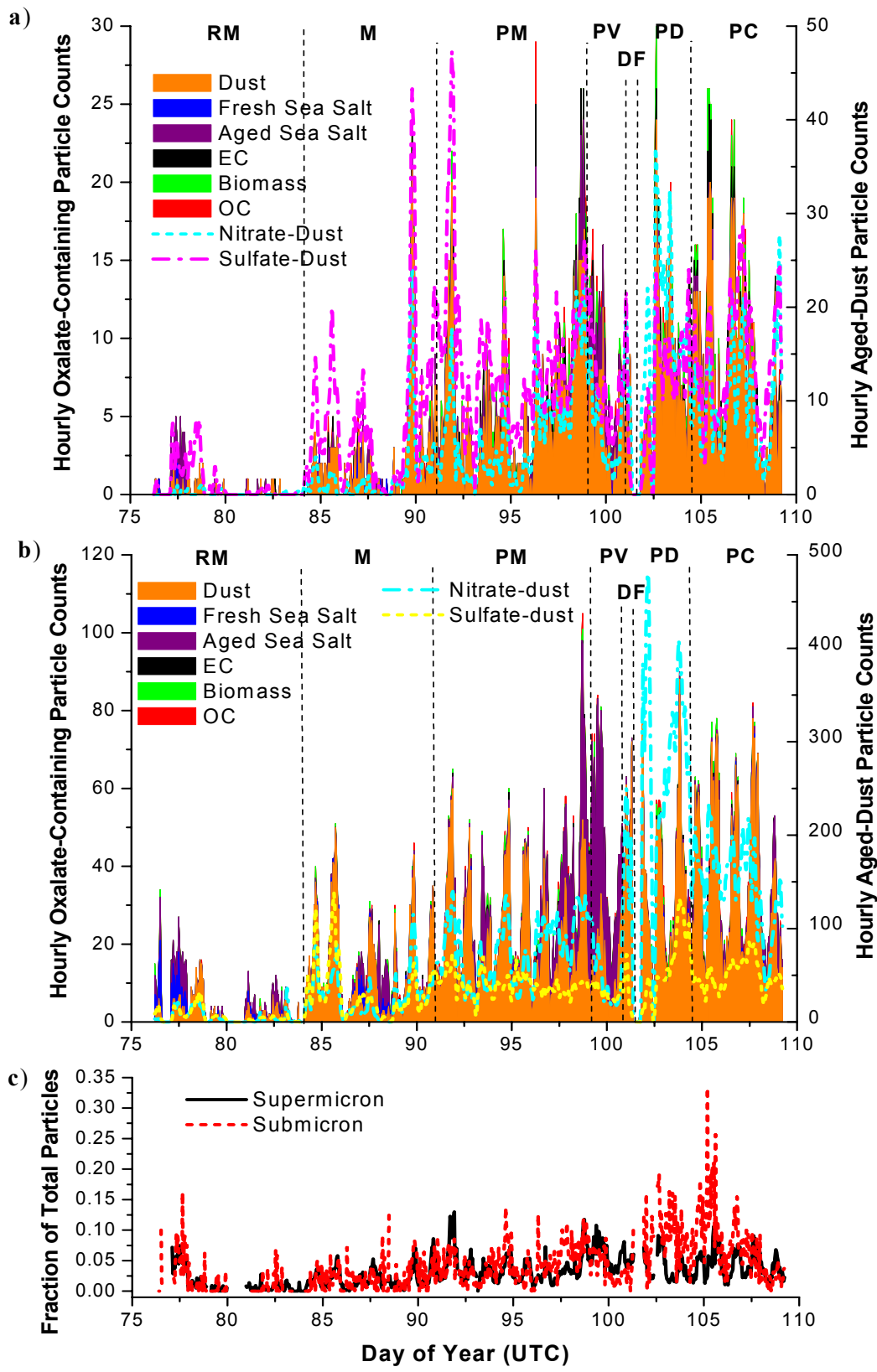
sea salt particles, from DOY 96.5-100.0, in the Polluted Marine & Volcanic air masses prior to the dust front. The hourly counts of sub- and supermicron particles containing oxalic acid increase significantly as the RHB approaches Japan and samples increasingly polluted air. The average single-particle peak areas for diacids across all particle types also increase during the approach (Fig. 5.2). These correspond to an increase in particulate diacid mass measured from simultaneous filter measurements (see below).

To our knowledge this is the first measurement of diacids in individual particles in real-time. The direct observation of oxalic acid being predominantly associated with individual mineral dust particles, and to a lesser degree with aged sea salt particles, is a significant finding. Diacids have previously been found to be associated with mineral dust and sea salt particles (Kerminen et al., 1999; Mochida et al., 2007; Mochida et al., 2003c; Neususs et al., 2002), but not with the size and temporal resolution presented here. Only a few measurements of organic acids in individual particles have been reported (Falkovich et al., 2004a; Maria et al., 2004; Russell et al., 2002). The strong association of the diacids with these inorganic particle types, as opposed to carbonaceous particles, is a reflection of the secondary nature of the diacids. The counts of dust particles containing nitrate or sulfate are also displayed in Figure 5.1. Whenever there is a diurnal spike of oxalate-containing particles there is also a corresponding increase in the nitrate- and/or sulfate-dust counts. This reflects the anthropogenic pollutant origin of these three secondary species.

Figure 5.1 clearly shows that the temporal distribution of oxalic acid in mineral dust and sea salt particles is virtually the same for both submicron and supermicron particles. The hourly counts for submicron particles are lower than for supermicron particles due to the higher overall transmission of supermicron-sized particles by the ATOFMS. There is no significant enrichment of oxalic acid in carbonaceous particle types (organic carbon, elemental
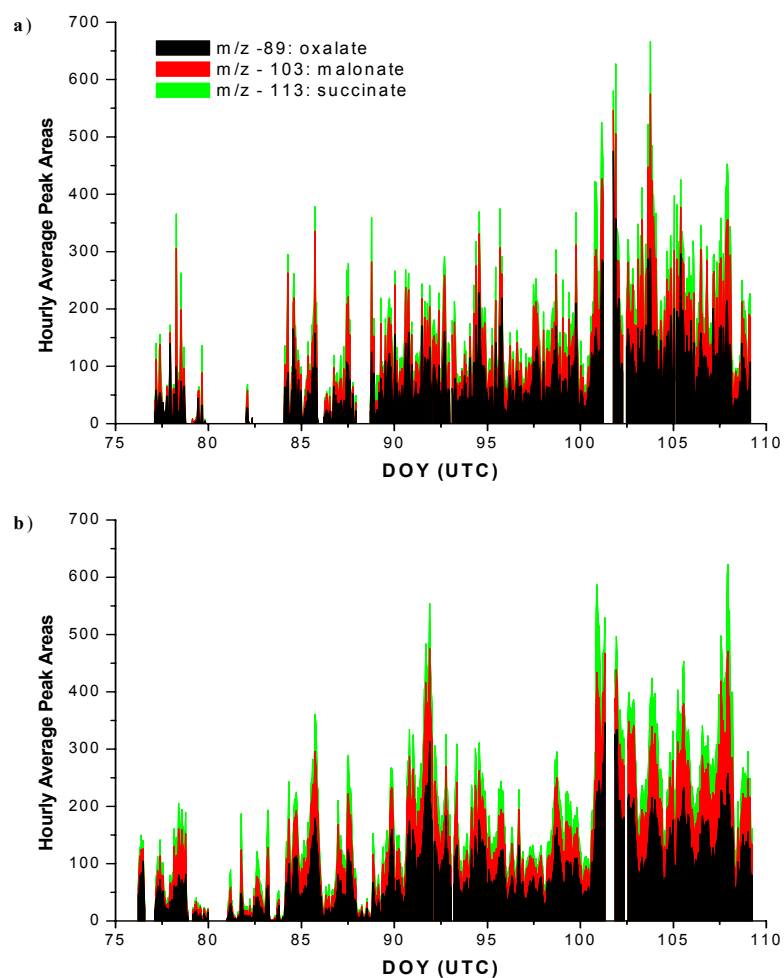
Figure 5.2. Peak areas for the three smallest dicarboxylic acids in all particle types for (a) submicron ($0.2\mu m > Da > 1.0\mu m$) and (b) supermicron ($1.0\mu m > Da > 3.0\mu m$) particle sizes. The ion peak area from the single particles is averaged for every hour and the three peak areas are stacked. Hours with fewer than 10 particle counts are excluded. The peak areas of the three diacids display a diurnal cycle and increase in magnitude as the RHB moves from the Pacific Ocean towards Japan and into the Sea of Japan.

carbon, and K-biomass) in the submicron sizes, where the majority of organic carbon mass is typically found. The temporal trends of oxalic acid in mineral dust, and to a lesser degree sea salt, display a clear diurnal cycle that persists for over 25 days of measurements in a wide variety of air masses. Figure 5.1c shows that the increases in oxalate-particle counts correspond to increases in the fraction of total particles containing oxalate. This behavior is

not explained by diurnal variations (from boundary layer height changes, for example) in the total particle concentration.

5.4.2   Mixing state of dicarboxylic acids

The distributions of particle numbers between the major particles classes for three broad air mass conditions (Remote Marine, Polluted Marine, Polluted Dust) are shown in Figure 5.3. Supermicron particles are dominated by fresh and aged sea salt during marine and polluted marine air masses, respectively. A massive dust storm that originated in the Gobi and Taklimakan deserts resulted in mineral dust being the dominant supermicron particle type sampled from DOY 100.8-105.0, the Dust Front and Polluted Dust air masses (Bates et al., 2004). Mineral dust was also enriched in submicron particles during this period. These trends are similar for both size ranges, with carbonaceous particle classes being enriched in the submicron size range. Notable background levels of dust in sub- and supermicron sized particles were detected in the pre-frontal Remote Marine and Polluted Marine air masses. Searches for oxalate were performed in particles that produced both a positive and negative mass spectrum, however a significant fraction of classifiable particles produced only a positive-ion spectrum. Figure 5.3 compares total to oxalate-containing particle class fractions in dual-ion only particles. Carbonaceous particle types represent a higher fraction of total particles in the positive-ion plus dual-ion particles than in the dual-ion only subset. Therefore the actual contribution from carbonaceous particles to the total particle types is larger, particularly in the submicron, than is indicated in Figure 5.3, but these positive-ion particles cannot be searched for diacids. However, this does not seriously impact the analysis of the diacid mixing state; further details are given below.

Figure 5.3 also displays the number fractions for oxalate-containing particle classes. This permits a direct comparison of the total particle class fractions for each air mass to the
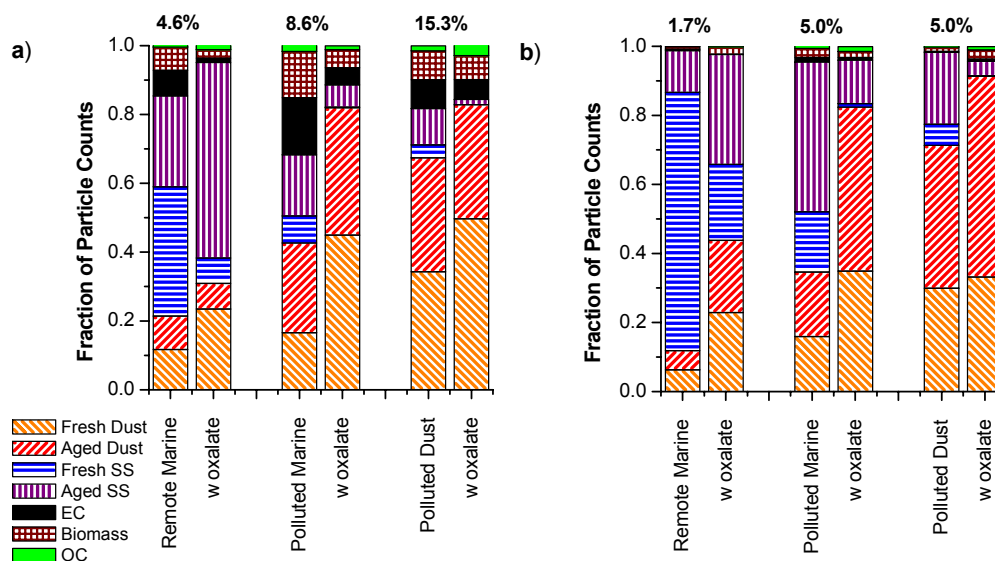
Figure 5.3. Particle class fractions for total particles (left columns) and oxalate-containing particles (right columns) for (a) submicron and (b) supermicron size ranges in different air masses: Remote Marine (DOY 75.0-84.0), Polluted Marine (DOY 91.0-94.0), and Polluted Dust (DOY 101.0-104.5). Percentages above each left column indicate the fraction of total particles that contained oxalic acid for that air mass; the right column represents these factions. Only particles that produced a dual-ion spectrum were used for both analyses.

particle class fractions containing oxalic acid. Between 4.6% and 15.3% of submicron, and 1.7% and 5.0% of supermicron particles were mixed with oxalic acid. These are very large fractions when one considers that oxalic acid, though a major component of WSOC, is just one compound composing a small fraction of total aerosol mass. In both size ranges and all three environments, oxalic acid is predominantly enriched in mineral dust particles to varying degrees. For example, in the Remote Marine air mass only 12% of supermicron particles were mineral dust and 87% were sea salt, but 44% of oxalate-particles were classified as mineral dust and 54% as sea salt. Similar large enrichments of oxalate in mineral dust are evident in the sub- and supermicron Polluted Marine particle classes. While oxalic acid was also frequently associated with aged sea salt particles, an enrichment of oxalic acid in sea salt is not observed. In fact the opposite occurred with oxalate being enriched in mineral dust instead of

sea salt, even when the majority of particles in the air mass are sea salt, such as during the Remote and Polluted Marine periods.

The formation of ions from a particle's chemical components via laser desorption/ionization is dependent on each particle's matrix. Thus, it is possible that oxalic acid is preferentially detected in mineral dust and sea salt particles and this causes the segregation observed in Figure 5.3. However, the ATOFMS has readily detected oxalic acid in a wide variety of particle types in this (Fig. 5.1) and other studies. For example, oxalate was detected in biomass, dust, organic carbon, sea salt, and vanadium-rich particle types in Mexico City during MILAGRO (2006) (Moffet et al., 2008a). During a Santa Ana dust event in Riverside, CA, the ATOFMS did not detect an enrichment of oxalate in mineral dust particles (unpublished results). The fact that oxalate is detected in all major particle types during the course of the study suggests ATOFMS provides a representative picture of the relative concentrations of oxalate in the various organic and inorganic particle types. Analysis of single-particles by X-ray microscopy has observed organic acids in Saharan mineral dust particles in Israel (Falkovich et al., 2004a) and over the Caribbean Sea (Russell et al., 2002), and in Asian dust particles sampled at 1580m during ACE-Asia (Maria et al., 2004). In all cases the carboxylic acids were found in organic surface coatings around the dust.

5.4.3 Contribution of carbonaceous particle types to total particle class fractions

The use of dual-ion only particles (those that produce a positive and negative mass spectrum) to search for diacids and compare total and oxalate-containing particle class fractions (Fig. 5.3) leads to an under representation of carbonaceous particle types (elemental carbon, organic carbon, and K-rich biomass burning particles) in the total particle class fractions, as briefly discussed above. As the diacid markers are present in the negative ion

spectrum, only particles producing both a positive and negative ion spectrum can be both classified and queried for diacids. However, when both positive-ion and dual-polarity classified particles are considered, the relative contributions of carbonaceous particle types are increased compared to dual-ion only particle class fractions. Figure 5.4 displays the class fractions of principal particle types for positive-ion plus dual-ion particles versus dual-ion only particles for the three air masses presented in Figure 5.3. The carbonaceous particle types are clearly under represented in the dual-ion only particles, particularly in the submicron particles. For this study, mineral dust and sea salt particles had a higher propensity of producing a dual-ion mass spectrum. However, it has been observed in numerous field studies that the probability of a particular particle class (e.g. sea salt, organic carbon, K-biomass) producing a dual-ion spectrum is predominantly the result of random instrumental factors such as how a particular particle interacts with the desorption/ionization laser pulse. In this dataset,
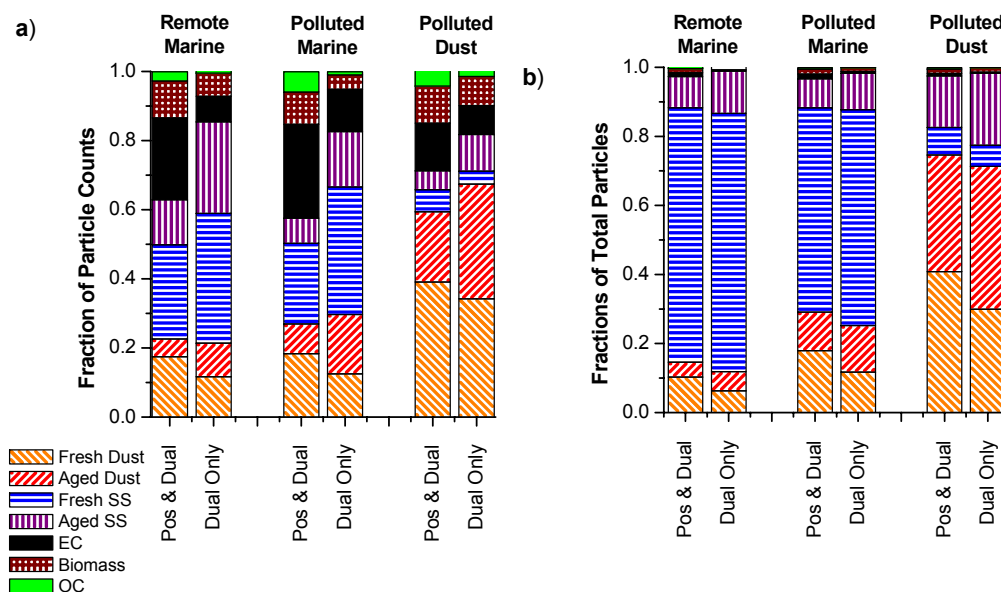
Figure 5.4. Principle particle class fractions for particles with positive-ion plus dual-ion mass spectra (left columns) compared to dual-ion only particles (right columns). The air masses correspond to those shown in Figure 5.3. a) submicron particle classes, b) supermicron particle classes.

typically 45-53% of detected submicron and 70-80% of detected supermicron particles produced both a positive and negative ion spectrum. We typically find one cluster of dual-ion particles whose positive ion mass spectrum exactly matches another positive-ion only cluster's positive ion mass spectrum. In other words, these two clusters were produced from particles with virtually identical chemistry, but one set produced both a positive and negative ion spectrum, while the other only a positive-ion spectrum. The only clear factor that we have observed to alter the probability that a particle produces a negative ion spectrum is the particle's water content. Very hydrated hygroscopic particles tend to decrease the formation of negative ions in the mass spectrometer as the water molecules suppress the negative ion formation process (which occurs in the ion plume via electron attachment with electrons produced from the formation of cations during ionization) (Neubauer et al., 1998). As the aerosol sampled aboard the RHB was controlled to 55% RH, this should not be a factor in this dataset. Therefore, the frequency with which a particular particle class contains an anion of interest, such as nitrate or oxalate for example, will be accurately reflected by the dual-ion only particles. This issue is discussed here to better explain our data analysis methods and to not produce a false impression that carbonaceous particle types were not a significant fraction of the sampled aerosol.

5.4.4 Comparison with aerosol filter measurements

Other research groups collected filter samples for offline analysis of the same aerosol that the ATOFMS sampled. Mochida et al. (2003b) used a high volume sampler for 3-6 hour bulk measurements of the major oxygenated organic compounds in aerosols. An 11-stage MOUDI sampler allowed size-resolved measurements of organic compounds in 4-day aerosol samples (Mochida et al., 2007; Mochida et al., 2003c). Oxalic acid was the most abundant DCA measured in $PM_{2.5}$ during the RHB cruise (70% of total DCA mass), followed by

malonic (13 wt%) and succinic (10 wt%) acid. The concentrations of total particulate-DCAs increased as the RHB approached Japan, from < 100 ng m^{-3} in the Pacific Ocean, to > 1 µg m^{-3} while in the Sea of Japan and East China Sea. The highest concentrations of diacids were measured during DOY 95-101, in the Polluted Volcanic & Marine air masses just prior to the dust front. Overall, DCAs composed 19.0 ± 4.8% of total particulate organic mass (POM) in the RHB aerosol. FT-IR measurements of the same aerosol found the organic acid fraction to vary from 4.2% to 34% of POM during the cruise (Bates et al., 2004). The increase of DCA mass as the RHB approached Japan agrees with the increase in the hourly counts of sub- and supermicron particles containing oxalic acid (Fig. 5.1) and increased diacid peak areas (Fig. 5.2).

Size-segregated measurements of DCA mass revealed a significant supermicron mode in pre-frontal marine (Mochida et al., 2003c), and post-frontal polluted-dust air masses (Mochida et al., 2007). Mochida et al. (2003c) reported a mass enrichment of C_2-C_4 DCAs in supermicron particles sampled aboard the RHB in marine air prior to the dust event. They attributed this to the uptake of diacid gases by sea salt particles, or heterogeneous oxidation of gaseous/dissolved organic precursors. The observations of oxalic and malonic acids in fresh and aged sea salt particles reported here agree with their finding. However, even in remote marine air that was 5 days transport from the continent, significant numbers of supermicron mineral dust particles were still detected (Fig. 5.3). As Asian dust particles are more alkaline than sea salt particles, they are likely a better sink for organic diacids than sea salt particles are. It is very feasible that a significant fraction of the supermicron diacid mass in the remote marine air mass was associated with mineral dust and not sea salt. Oxalic acid was highly enriched in the small fraction of mineral dust particles in the marine air (Fig. 5.3). More recently Mochida et al. reported a supermicron maximum in diacid mass during the dust

events aboard the RHB, attributing this to uptake/formation on mineral dust and sea salt particles (Mochida et al., 2007). This is in agreement with the direct observations of the mixing state of diacids reported here.

5.4.5 Mineral dust containing diacids

Over the entire study, 10.2% of the total dust particle spectra contained an oxalic acid ion peak above the 0.5% relative area criterion. The average digitized mass spectrum of these oxalate-containing mineral dust particles is shown in Figure 5.5. Metal ions typical of mineral dust particles are readily observed, as previously described in Chapter 3. The color stack of the
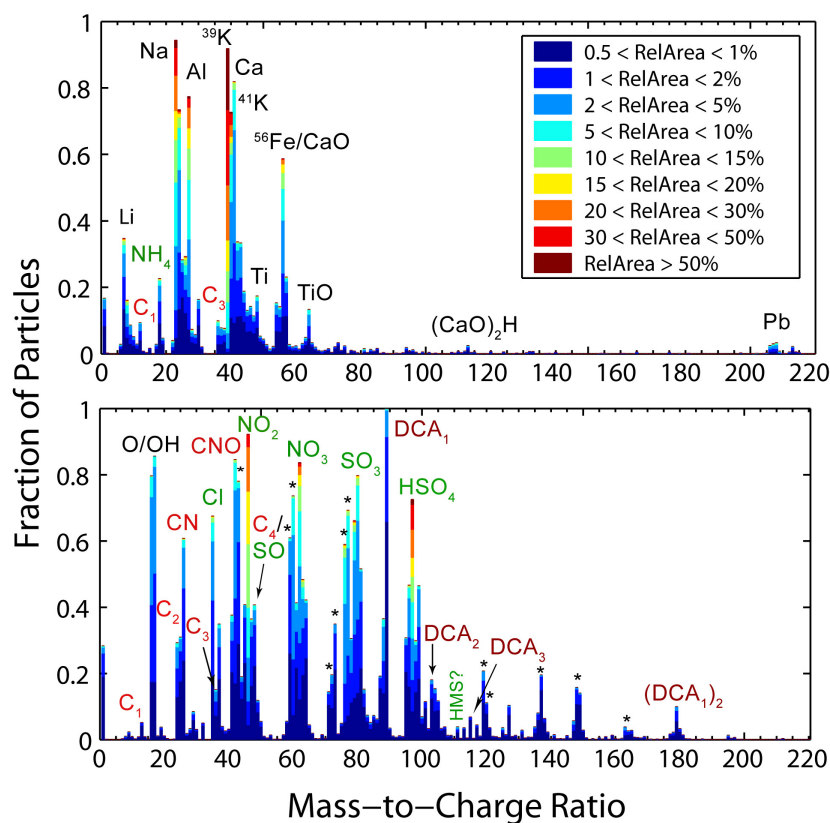
Figure 5.5. Average digitized mass spectrum of oxalate-containing dust particles sampled over the entire study. Positive-ions (top) and negative-ions (bottom) are shown. Black labels and asterisks indicate mineral dust components, dark red are diacids (DCA_n), bright red are other carbonaceous components, and green are secondary inorganic species as discussed in Chapter 3. The presence of lead is likely due to mixing with anthropogenic pollution.

-89 ion peak demonstrates that oxalate in dust particles produced a relative peak area of 2% or greater in ~10% of oxalate-dust particles. While the mass of oxalic acid per dust particle that produces a peak area of this magnitude has yet to be determined, based on concurrent filter measurements, this represents a significant amount of oxalic acid. The small peak at m/z -179 can be attributed to the oxalic acid dimer $[(C_2O_4H)_2H]^-$ which is commonly observed in the spectra of oxalic acid standards. This is further evidence that the peak at m/z -89 in dust is predominantly from oxalic acid. Mineral dust samples collected from various Chinese loess sources did not produce a significant ion signal at m/z -89 in the ATOFMS. Similarly, Mochida et al. (2003b) measured very low concentrations of diacids in a standardized Asian mineral dust sample and concluded that Asian dust is not a direct source of DCAs. Smaller peaks at m/z -103 and -117 correspond to the molecular ions from malonic and succinic acids. The lower relative peak areas and detection frequencies most likely reflects the reduced abundance of these larger diacids, as determined by bulk filter measurements (Mochida et al., 2003b). High mass peaks typically attributed to organic oligomers and other macromolecules were not obserbed in the spectra, indicating that the oxalate and other DCAs were not ion fragments from larger organic molecules. Other peaks from elemental and/or organic carbon species in dust particles are labeled. Secondary inorganic species such as sulfate, nitrate, chloride, ammonium, and lead are also present in the oxalate-containing dust, indicating a large fraction of the dust particles have undergone extensive aging (Chapter 3). This processing by acids likely neutralized much of the alkaline carbonate in the dust, driving some of the diacid mass to partition to less aged dust particles as shown in Figure 5.3.

5.4.6   Particulate diacids sources

The sources of dicarboxylic acids in aerosols are still under investigation. The major potential pathways include photochemical oxidation of gaseous VOCs, particle-phase

oxidation, particularly during in-cloud processing, and primary emission from biomass burning and other combustion sources. The strong and persistent diurnal cycle of particulate oxalic acid, and its enrichment in mineral dust is a good indication that photochemistry is driving the formation of this organic acid in the particle-phase. This can be the result of both gas-phase photochemical production of diacids, and the heterogeneous/aqueous (photo)oxidation of diacid precursors that have partitioned to the particles.

Measurements of gas-phase DCAs were made in series with the particle-phase mass measurements on the RHB and found that the majority of C_2 to C_5 DCA mass was in the particle-phase (Mochida et al., 2003b). Over 70% of oxalic acid was in the particle-phase, implying that a substantial amount of gas-phase oxalic acid was present. The gas-phase oxalic acid was likely the product of photo-oxidation of aromatic hydrocarbons, cyclic alkenes, and other yet unidentified precursors (Mochida et al., 2003a). Kerminen et al. (1999) concluded that gas-phase oxalic acid was the dominant source of oxalate in particles in the Arctic during summer. Mochida et al. concluded that gas-phase diacids are a likely source of the diacids measured in the Asian aerosol (Mochida et al., 2007; Mochida et al., 2003c). Glyoxal is a well known precursor for oxalic acid through aqueous-phase processing, and could also be a precursor for gas-phase oxalic acid. Glyoxal has also been recently measured and linked to photochemical oxidation, and has a short lifetime versus photolysis (Volkamer et al., 2005). The production of gas-phase and particulate diacids from photochemical oxidation of VOCs has been observed in smog chamber experiments (e.g. Kalberer et al., 2000; Volkamer et al., 2008) and warrants further investigation.

The observation that total DCA concentrations, counts of particles containing oxalate (Fig. 5.1), and diacid peak areas (Fig. 5.2) increased as the RHB approached the Asian continent indicates that anthropogenic emissions, likely from industrial and residential fossil

and wood-fuel combustion, are the principle sources of DCAs and their precursors in the continental outflow from east Asia (Mochida et al., 2003a). The correlation between nitrate- and sulfate-dust with oxalate-particle counts further support this (Fig. 5.1). An increase in DCA mass was not observed when air mass trajectories indicated transport from open biomass-burning regions in south and southeast Asia (Mochida et al., 2003b). Therefore, the contribution to DCAs from biomass-burning particles is expected to be low for this study, as our data in Figure 5.1 indicates. Mochida et al. (2003b) concluded that anthropogenic emissions of DCAs in east Asia and photo-oxidation of their precursors were the major sources of the measured DCAs undergoing long-range transport from the continent to the RHB. The strong correlation of DCA mass with (nss)-sulfate and nitrate mass that they report is further evidence of an anthropogenic continental source of the DCAs.

5.4.7   Persistent diurnal cycle of diacids

The diurnal cycle of oxalic acid persists for over 25 days of sampling in remote, polluted, and dust-impacted marine air masses. Figure 5.6 explores the diurnal cycle of dicarboxylic acids in further detail by focusing on the last 10 days of the cruise. This period is characterized by the end of the Polluted Volcanic air mass, followed by the Dust Front & Polluted Dust (DOY 100.8-105.0), and then Polluted Continental air. The diurnal cycle of oxalic and malonic acids generally track each other in both mineral dust and sea salt particles. Plotting in local time (UTC +9) reveals that the daily spike in particles containing the two DCAs typically occurred at night. This is surprising because we expect photochemical production of DCAs to maximize in the afternoon when the solar flux is the highest. Aqueous production of diacids during elevated humidity at night is possible, however ambient RH measured on the RHB did not have a nocturnal maximum. The RH typically varied between 50 and 95%, with no obvious day-night cycle (Fig. 5.6). Therefore, the aerosol water content
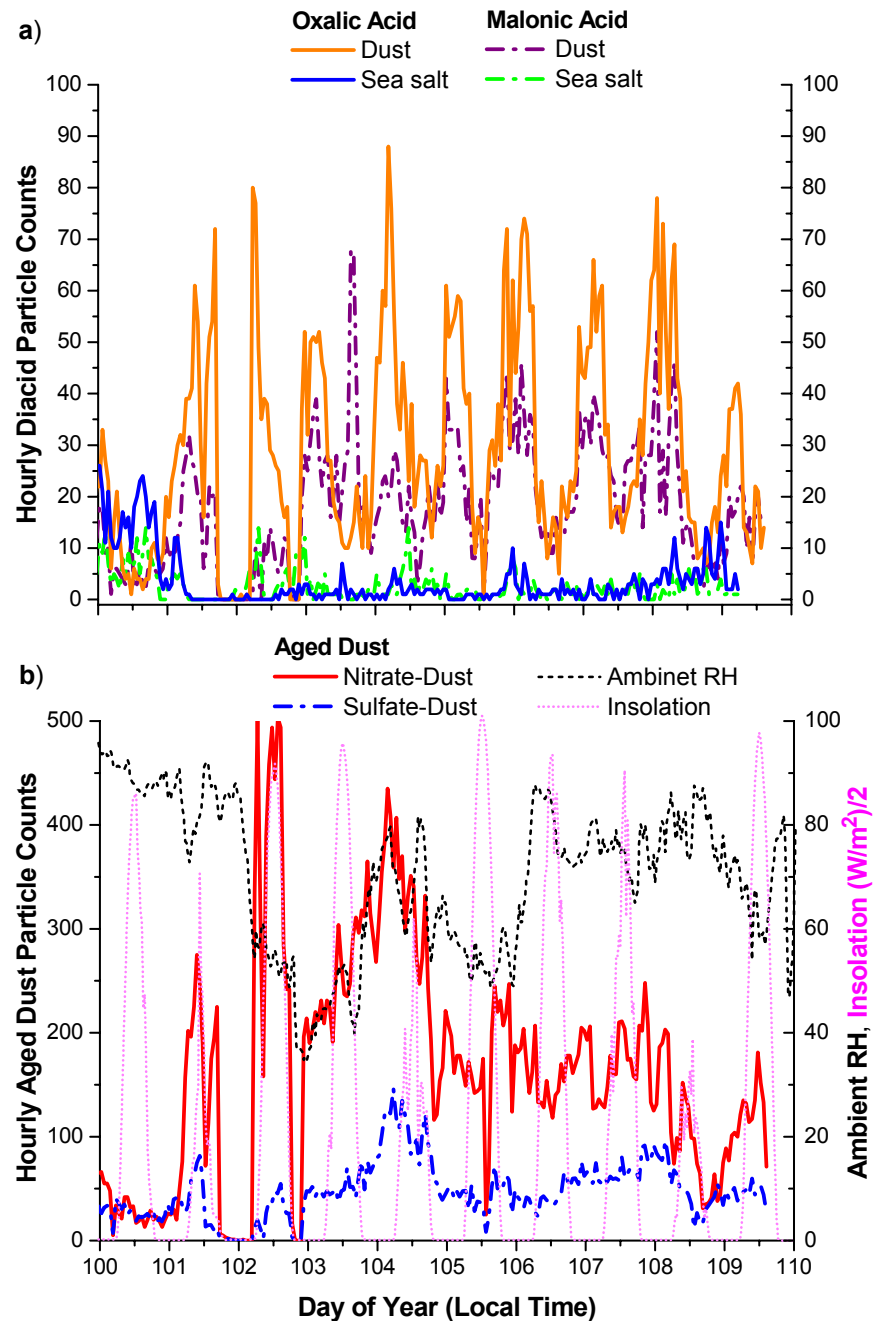
Figure 5.6. Hourly counts of supermicron particles containing oxalic or malonic acid in the three major particle classes. Aged and fresh sea salt particles have been merged into one class for this figure; the majority of diacids were associated with aged and not fresh sea salt. Also shown are the hourly counts of supermicron aged dust particles mixed with nitrate or sulfate (relative area > 5%). The dotted pink line is the solar flux measured on the RHB (right axis), and the dotted black line the ambient RH. An example air mass back trajectory for this period is provided in Figure 5.7.

should not be a major limiting factor in the production of diacids in this environment. The counts of oxalate-containing particles do not correlate with RH in Figure 5.6, nor are they correlated with ambient temperature. However, the ambient RH measured on the RHB does not necessarily reflect the humidity conditions experienced by the particles during transport.

Oxalate-particles were only detected concurrently with elevated nitrate- and sulfate-dust counts (Figs. 5.1 & 5.6). This indicates their occurrence only in air masses that had experienced extensive heterogeneous processing. Oxalate could be produced as the air mass passed through polluted regions and experienced extensive heterogeneous processing, likely enhanced by photochemistry. As oxalate was only detected when dust containing nitrate and/or sulfate was also present these three secondary species probably share a common source and/or production mechanism. The higher temporal correlation of oxalate- and nitrate-dust, particularly in supermicron particles (Fig. 5.1), suggests a predominantly photochemical source of these compounds. Measurements of CO, SO_2, O_3, and total dust counts do not indicate the periodic arrival of polluted-dust air masses at the RHB, so this is not a likely explanation for the diurnal pattern. The formation pathways of all three secondary species can be strongly enhanced by photochemistry. The sources and spatial distribution of their precursors are not necessarily the same, however. In the previous analysis of secondary acids in the mineral dust particles (Chapter 3), it was concluded that sulfate was added to the dust before nitrate, likely as a result of elevated $SO_2(g)$ in the interior from coal-burning power plants. Therefore, the correlation of oxalate, nitrate, and sulfate in the dust particles is most likely caused by the photochemically-driven production of these three acids.

A plausible cause for the nighttime maximum of diacids is the transport time for particles that have accumulated diacids to reach the RHB. Production of DCAs in particles likely occurs at some distance away from the RHB during the afternoon when photochemistry
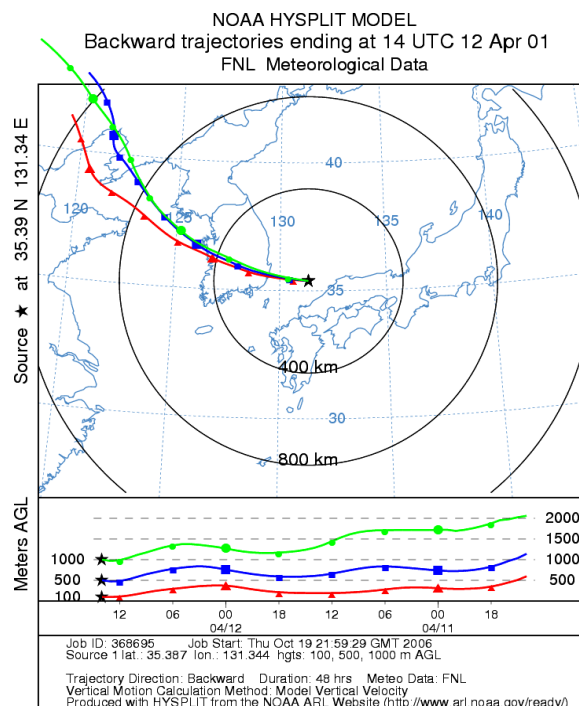
Figure 5.7. Air mass back trajectory for the RHB at DOY 102.6 (UTC) from the NOAA HYSPLIT model (http://www.arl.noaa.gov/ready.html). Symbols are for 6 hour intervals. This corresponds to the time period displayed in Figure 5.6. The back trajectory shows that the air mass was moving over South Korea at low altitude 6-8 hours prior to reaching the RHB in the Sea of Japan.

is most active. The DCA-containing particles are then transported to the RHB without any significant accumulation of additional DCA mass when photochemistry has turned off. One daily spike in mineral dust containing oxalic and malonic acids began around DOY 103.0 (12:00am local time, Fig. 5.6). The HYSPLIT back trajectory shows that 6-10 hours prior (2pm-6pm local time) to reaching the RHB the air mass was passing over South Korea at low altitude (Fig. 5.7). Thus, the dust-laden air mass had mixed with polluted continental air during periods of active photochemistry that likely contained oxalic and malonic acid precursors. In general, the time lag between the production of DCAs through photochemistry in the afternoon, partitioning of the DCAs and precursors to the particle-phase, and then transport of these particles to the RHB can explain the diurnal spike of DCA-containing
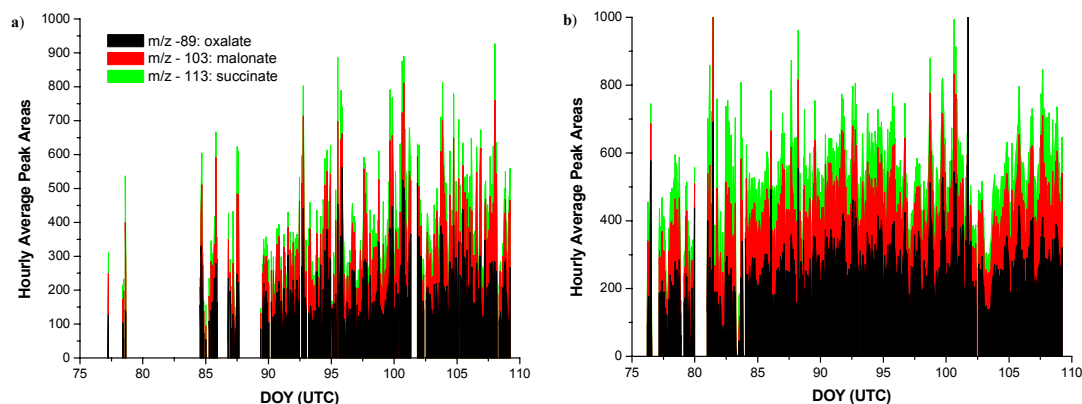
Figure 5.8. Peak areas for the three smallest dicarboxylic acids in mineral dust particles <u>only</u> for (a) submicron ($0.2\mu m > D_a > 1.0\mu m$) and (b) supermicron ($1.0\mu m > D_a > 3.0\mu m$) particle sizes. The ion peak area from the single particles is averaged for every hour and the three peak areas are stacked. Hours with fewer than 10 particle counts are excluded. The peak areas of the three diacids display a diurnal cycle. However, the magnitude of the average single dust-particle diacid peaks areas remain relatively constant as the RHB approaches Japan from the Pacific Ocean.

particles near midnight on most days. If photochemical production of gas-phase diacids and precursors, and their partitioning, occurs over just a few hours, a sharp diurnal cycle would result. While the air mass typically passed over polluted continental regions during the time period in Figure 5.6, the back trajectories reaching the RHB frequently changed and thus the timing of the diurnal cycle displayed in Figures 5.1 and 5.6 is quite variable but typically peaked at night.

The diacid peak areas in only dust are displayed in Figure 5.8. These clearly demonstrate the diurnal cycle also observed in all particle types (Fig 5.2). While the average peak areas of diacids from all single-particles increased as the RHB approached Japan (Fig. 5.2) the diacid peak areas from only mineral dust were much more constant, even when the RHB was several days away from the continent (Fig. 5.8). As the dust particles all originated from Asia, the consistent diacid peak areas in dust indicate that the majority of diacid mass was added to the dust near the continent. Therefore, the dust particles did not experience significant gain or loss of diacid mass during long-range transport over the Pacific Ocean to

the RHB. Mochida et al. (Mochida et al., 2003b) concluded that there was insignificant production or destruction of DCAs during long-range transport to the RHB and that their major sink is through deposition. This is all consistent with the timeline and mechanism presented above.

5.4.8   Evidence against photochemical destruction of diacids during transport

Another possible explanation for the nighttime diacid peak is a photochemical loss of particulate diacids during the day (Staikova et al., 2005). Figure 5.6 shows that the counts of oxalate-containing particles are generally anti-correlated with the solar irradiance measured on the RHB. However, there are some periods where the oxalate-particles peak during the day (DOY 101 & 102, for example). Oxalate and other diacids can form photochemically-active complexes with metals such as iron in mineral dust; this could enhance the photolysis of diacids. One might expect the different diacid-metal complexes to have varying formation and photochemical constants and therefore different photolysis rates. Based on the consistency of diacid mass ratios, Mochida et al. (2003b) concluded that the short diacids ($<C_6$) are stable end products and that their major sink is through deposition, not chemical decomposition. This is supported by the constant diacid peak areas in mineral dust shown in Figure 3.8. We also did not observe a systematic change in the ratio of oxalate-to-malonate-containing particles with distance from the continent. The correlations of the diurnal oxalate-dust peaks with spikes in the nitrate- and-sulfate-dust counts (Figs. 3.1 & 3.6) further support our hypothesis that the nighttime diacids peak was instead primarily caused by the transport time lag from polluted regions containing diacids precursors undergoing photochemistry to the RHB. While the photochemistry of diacids and their metal complexes certainly warrants further investigation, it is unlikely to be the major cause of the observed diurnal cycle.

5.4.9   Lack of evidence for significant cloud processing of the sampled aerosol

Glyoxylic, glycolic, pyruvic, and acetic acids are likely intermediates from the aqueous phase oxidation of oxalic acid precursors (Carlton et al., 2007; Ervens et al., 2004; Warneck, 2003). Their presence or absence in oxalate-containing particles can be used as an indication of substantial aqueous phase chemistry occurring via aqueous oxidation in wet/deliquesced particles, or during in-cloud processing. Organic acids are typically detected as their conjugate anion, [M-H]$^-$, in the ATOFMS. The following anions were searched for: glyoxylate (m/z -57), glycolate (m/z -75), acetate (m/z -59), and pyruvate (m/z -87). These species are also expected to fragment to anions including CH_3CO^- (m/z -43) and CH_3CO^- (m/z -45). However, both oxalic and malonic acid standards produce appreciable signals at these two peaks, and m/z -43 experiences significant interference from AlO$^-$; thus we did not include these possible fragments in our analysis. Of these compounds only acetate has major known interferences at m/z -59 from $^{59}[MgCl]^-$ or $^{59}[AlO_2]^-$; though interferences from unidentified ions, especially from organic fragments, are possible at any of these mass-to-charge ratios. Examining Figure 3.5 for the presence of these peaks reveals that only m/z -59 and m/z -87 are present to any significant degree in the oxalate-containing dust particles. The peak at m/z -59 is almost certainly predominantly due to aluminosilicates (e.g. AlO_2) that are commonly observed in mineral dust particles and indicated by an asterisk in Figure 3.5. The peak at m/z -87 could be due to pyruvate, though the lack of ion peaks corresponding to glyoxylate and glycolate tends to suggest against this. These species could be present in low concentrations (i.e. lower than oxalic and malonic acids which are stable end-products) and thus not be detected. None of these species were reported in the filter analyses of the same aerosol (Mochida et al., 2003b; Mochida et al., 2007; Simoneit et al., 2004b). Hydroxymethane sulfonate (HMS, $HOCH_2SO_3^-$, m/z -111) can be used as a tracer for

fog/cloud processing of single-particles analyzed by ATOFMS (Qin and Prather, 2006; Whiteaker and Prather, 2003). Figure 3.5 displays a very small ion peak at m/z -111, the principle anion normally observed from HMS. A peak at m/z -111 with a relative area > 0.5% was found in only 5.6% of all oxalate-containing particles. The lack of significant signals from indicators of aqueous oxidation indicates that the aerosol had not undergone extensive cloud processing. Therefore the oxalate was most likely formed through a different pathway.

To reach the RHB in the Pacific Ocean and Sea of Japan the Asian mineral dust particles, in general, are lofted to several kilometers and carried eastward and can then subside into the marine boundary layer. This type of transport phenomenon is what brought highly elevated dust concentrations to the RHB during the dust front's arrival on DOY 100.8 (Bates et al., 2004). Therefore, the dust particles traveled for several days well above the polluted boundary layer and it is in this environment that the aerosol could experience the majority of any in-cloud processing cycles. The atmosphere at these altitudes was generally found be very dry by the Twin Otter and C-130 aircraft flights in the region as part of the ACE-Asia campaign. Schmid et al. (2003) state "The Twin Otter water vapor results reveal a relatively dry atmosphere during ACE-Asia with all CWV [columnar water vapor] < 1.5 cm and ρ_w [water vapor density] < 12 g/m3. The C-130 aircraft encountered similarly dry conditions with the exception of a flight on 30 April 2001 (Redemann et al., 2003)." Water vapor typically dropped off rapidly above the marine boundary layer, which was located between 1-2 km. Yoon and Kim (2006) show vertical profiles of RH from C-130 flights during ACE-Asia, demonstrating the rapid decrease in RH < 30% above the boundary layer.

In the analysis of the mixing of inorganic acids with mineral dust particles during ACE-Asia (Chapter 3), we concluded that cloud processing was likely not a major contributor to the atmospheric processing of the dust (Chapter 3 & 4). This was based on the size

distributions of sulfate, nitrate, and chloride in the dust particles, the segregation of sulfate from nitrate and chloride in individual particles, the mineralogical dependence of the associations of the acids with the dust, and the relatively small fraction of internally mixed dust and sea salt particles. The aerosol size distribution measured on the RHB from DOY 95.0-105.0 also showed evidence of minimal cloud processing, based on the lack of a clear minimum between modes in the submicron number size distribution (Bates et al., 2004). Such a minimum however could be masked in the polluted aerosol. Prior to DOY 95.0 the aerosol size distribution indicated a higher degree of cloud processing of the marine air by the presence of such a minimum in the submicron size distribution, i.e. the Hoppel minimum (Hoppel et al., 1986). However, it was only when polluted continental air began to reach the RHB (about DOY 84.25) that the mass (Mochida et al., 2003b; Mochida et al., 2003c) and number concentrations of diacids increased dramatically (Fig. 3.1).

Associations of oxalate and sulfate are typically used to indicate cloud processing as the major source of diacid production due to the efficient sulfate production pathway via in-cloud oxidation. If the oxalic acid is primarily produced through chemistry in cloud droplets during repeated cloud growth and dissipation cycles, then oxalate and sulfate should be internally mixed in the resulting particles and share a similar size distribution. Figure 3.9 displays the averaged single-particle peak areas of oxalate, malonate, sulfate, and nitrate as a function of particle size in dust particles sampled in different air masses. This indicates the relative amounts of each secondary species in individual particles of varying size. In all cases the size distribution of oxalate and sulfate are not correlated and appear to be in fact anti-correlated. The oxalate signal maximizes above 1 micron, similar to nitrate, while the sulfate signal drops to a minimum in the supermicron particles. This corresponds to the maximum in sulfate mass in submicron particles while nitrate mass is typically maximized in the
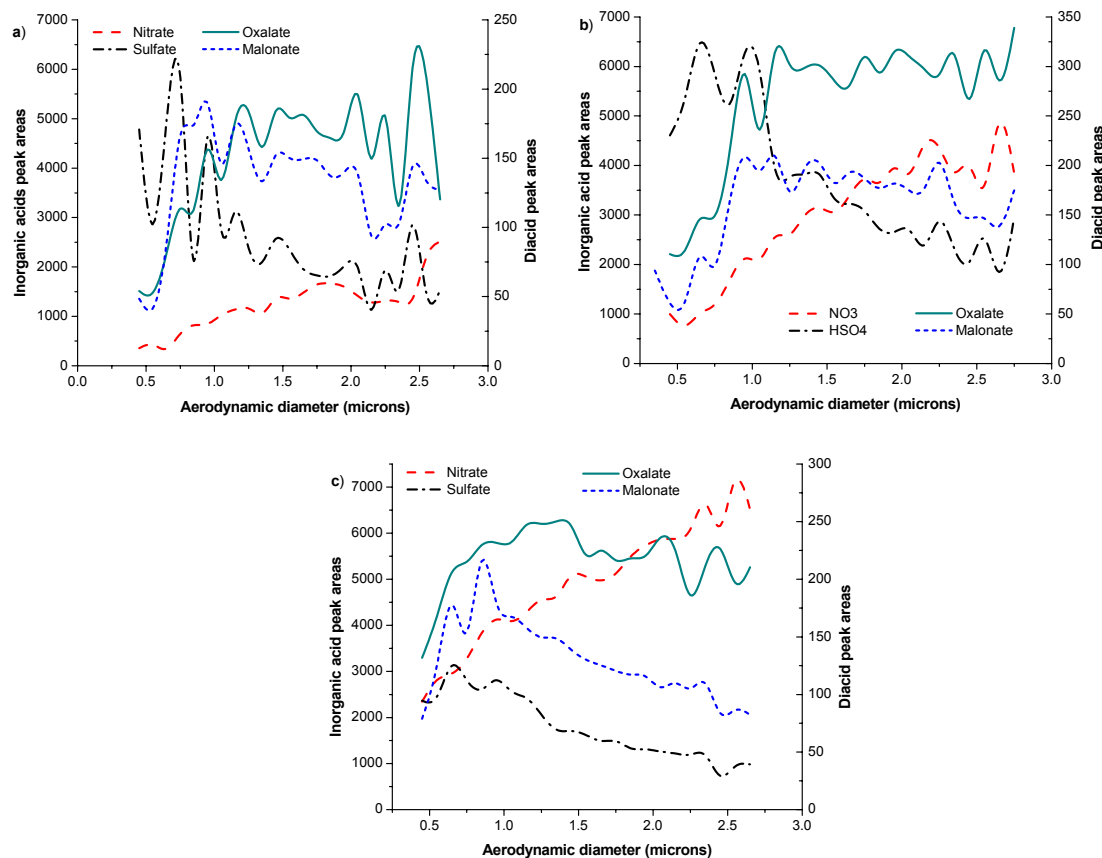
Figure 5.9. Average single-particle peak areas of secondary inorganic acids and organic diacids as a function of particle size in (a) Marine, (b) Polluted Marine, and (c) Polluted Dust air masses. These represent the relative amount of the various species in individual particles with respect to size.

supermicron (Bates et al., 2004). For the entire cruise, 50.2% of all the particles that contained oxalic acid (relative area > 0.5%) also contained sulfate (relative area > 2%). For mineral dust particles <u>only</u> this value is 54.4%. Thus there is not a strong correlation between oxalate-containing particles and sulfate, and this does not change when only mineral dust particles are studied. Repeating the same analysis for mixtures of oxalate and nitrate (relative area > 2%) found that 51.5% of all oxalate-particles and 54.4% of all oxalate-dust particles contained nitrate. The lack of a strong association of oxalate and sulfate is further evidence against cloud processing as the major production pathway of diacids in the ACE-Asia aerosol sampled at sea

level. Aqueous phase chemistry occurring in wet/deliquesced particles could still be contributing to the formation of diacids, but there is no evidence that cloud processing is the major production pathway in this dataset. Different mechanisms may be dominating in different size ranges, with aqueous production perhaps being a significant contributor to sulfate and diacid production in the smallest size ranges reported here.

5.4.10 Summary of evidence for photochemical production of diacids

Our observations of a persistent diurnal enrichment of diacids in mineral dust in both sub- and supermicron particles is best explained by photochemical production of gas-phase DCAs and their precursors, followed by partitioning to the particle-phase. Subsequent aqueous/photochemistry in the particles may also contribute. The strong diurnal pattern is likely driven by solar flux. The fact that oxalate-dust particles were only detected simultaneously with elevated nitrate- and sulfate-dust indicates that the diurnal cycle was the result of episodic heterogeneous processing of the mineral dust particles. This is best explained by gas-phase and heterogeneous/aqueous photochemistry.

As a gas-phase acid, oxalic acid and other DCAs should behave similarly to nitric acid, a secondary inorganic acid also produced through photochemistry (Mochida et al., 2007). Thus, the DCAs, as well as their precursors, will partition to the particle types to which they have the highest affinity. The extensive mixing of nitric and hydrochloric acid with the alkaline Asian dust measured on the RHB has already been described in Chapters 3 & 4. Nitrate and chloride preferentially formed in calcium-rich dust particles, attributed to the reaction of their gaseous precursors with calcium carbonate mineral particles. The diacids and their precursors were experiencing similar chemistry by selectively partitioning to alkaline mineral dust particles, and sea salt particles in some cases. Accelerated production caused by transition metal chemistry in the mineral dust particles may also have contributed. The size

distributions of the nitrate and oxalate peak areas are very similar and both peak in supermicron particles (Fig. 3.9). Available surface area is another important factor in gas-particle partitioning. Figure 3.3 shows that the number fraction of diacid-particles associated with mineral dust is much larger than the number fraction of total dust particles in a given air mass, and therefore the availability of different particle types alone cannot explain the observed mixing state.

The preferential enrichment of DCAs in these two particles types is further evidence of a predominantly gas-phase source of the organic acids and precursors, followed by partitioning and heterogeneous/aqueous chemistry. We distinguish between aqueous (photo)chemistry occurring in hydrated/deliquesced aerosols and aqueous oxidation occurring in cloud droplets. The chemistry of the original particle is a much stronger influence on gas-particle partitioning during aqueous processing of hydrated aerosols than in highly diluted cloud droplets. Thus, an alkaline particle type such as mineral dust would be expected to have a high affinity for acidic gases during aqueous processing, while water solubility and Henry's Law coefficients drive gas-particle partitioning in cloud droplets. In-cloud processing would therefore distribute the DCAs more evenly among particle types of a similar size and would not produce an extended diurnal cycle. Additional evidence against in-cloud diacid production previously discussed include the dissimilar peak areas of oxalate and sulfate as a function of particle size, the lack of significant signals from hydroxymethane sulfonate (m/z -111), glyoxylic acid (m/z -57), or glycolic acid (m/z -75), and the lack of a Hoppel minimum between modes in the submicron size distribution (Bates et al., 2004). Aqueous chemistry in hydrated particles may have contributed however there was no correlation between diacids and ambient RH (Fig. 5.6).

5.4.11 Atmospheric implications

The diurnal cycle and mixing state of dicarboxylic acids we report herein presents strong evidence that photochemical production of gas-phase diacids and their precursors was the dominant source of DCAs in outflow from east Asia. However, several recent studies have provided convincing evidence that in-cloud processing is responsible for the majority of diacid production in certain environments (Sorooshian et al., 2006; Yu et al., 2005). Therefore, it appears that the dominant diacid production mechanism is highly dependent on the environmental conditions and that gas-phase photochemistry, heterogeneous and aqueous phase reactions, and in-cloud production are all viable pathways. Further study is required to determine the factors that control which mechanism dominates in a particular environment.

The preferential formation of dicarboxylic acids in mineral dust and sea salt particles has important implications for the physicochemical properties of this large and important fraction of organic aerosol mass. The size shift of diacid mass from submicron sulfate and carbonaceous-dominated aerosols to supermicron dust and sea salt-dominated particles will alter the lifetime, cloud-aerosol interactions, and radiative effects of diacid aerosol mass (Kanakidou et al., 2005). Diacids have received a great deal of attention due to their suspected importance in droplet activation and cloud formation (Abbatt et al., 2005; Ervens et al., 2005; Kanakidou et al., 2005; Prenni et al., 2001). However, the association of these diacids with mineral dust and sea salt, as we have reported here, could significantly alter their solubility and hygroscopicity. Diacids readily chelate divalent cations such as Ca^{+2}, which is enriched in Asian dust, forming mostly insoluble complexes. Similar chemistry can occur in sea salt particles and their naturally occurring Mg^{+2} and Ca^{+2} content (Mochida et al., 2003c). The formation of these metal-diacid complexes will lower the solubility of a highly water soluble fraction of aerosol mass, possibly decreasing the hygroscopic growth and cloud activation

properties of particles containing diacids. The hygroscopicity of oxalic acid and calcium oxalate particles is investigated in Chapter 6.

Diacids can also complex and undergo important photochemical interactions with transition metals such as Fe^{+2}/Fe^{+3}, present in Asian mineral dust particles (Deguillaume et al., 2005). This photochemical coupling can produce radical oxidants, oxidize oxalic acid to CO_2, and convert Fe(III) to Fe(II). As Fe(II) and Fe-organic complexes are more soluble and bioavailable than Fe(III), this chemistry could have important effects on the delivery of bioavailable nutrients from chemically aged mineral dust particles to remote high nutrient low chlorophyll ocean regions. Fertilization of such ocean regions increases biological productivity with associated CO_2 uptake from the atmosphere and the release of climate-active gases such as DMS (Jickells et al., 2005).

5.5 Conclusions

The mixing state of diacids in individual particles in Asian pollution outflow was investigated during the ACE-Asia campaign. The diacids were found primarily in mineral dust and aged sea salt particles, as opposed to carbonaceous particle types, in both submicron and supermicron particles. The enrichment of the diacids in these particle types was ascribed to a photochemical production mechanism in which gas-phase diacids, and their precursors, partition to alkaline mineral dust and sea salt particles. Further photochemical and aqueous chemical reactions in the particle-phase may have also contributed to diacid production. It appears that the majority of diacid production occurs within a few hours of transport from the continent, with little additional production or loss of diacids observed during long-range transport. This mechanism is in sharp contrast to the more commonly invoked in-cloud diacid production pathway. The importance of both mechanisms deserves further study and

consideration in a wide range of environments. The enrichment of diacid aerosol mass in mineral dust and sea salt particles may have important consequences for the solubility, hygroscopicity, distribution, and lifetime of the dominant component of water soluble organic carbon aerosol mass.

5.6 Acknowledgements

5.7 References

Abbatt, J. P. D., Broekhuizen, K., and Kumal, P. P.: Cloud condensation nucleus activity of internally mixed ammonium sulfate/organic acid aerosol particles, Atmos. Environ., 39 (26), 4767-4778, 2005.

Bates, T. S., Quinn, P. K., Coffman, D. J., Covert, D. S., Miller, T. L., Johnson, J. E., Carmichael, G. R., Uno, I., Guazzotti, S. A., Sodeman, D. A., Prather, K. A., Rivera, M., Russell, L. M., and Merrill, J. T.: Marine boundary layer dust and pollutant transport associated with the passage of a frontal system over eastern Asia, J. Geophys. Res., 109 (D19), doi:10.1029/2003JD004094, 2004.

Carlton, A. G., Turpin, B. J., Altieri, K. E., Seitzinger, S., Reff, A., Lim, H.-J., and Ervens, B.: Atmospheric oxalic acid and SOA production from glyoxal: Results of aqueous photooxidation experiments, Atmos. Environ., In Press, doi:10.1016/j.atmosenv.2007.05.035, 2007.

Chebbi, A., and Carlier, P.: Carboxylic acids in the troposphere, occurrence, sources, and sinks: A review, Atmos. Environ., 30 (24), 4233-4249, 1996.

Deguillaume, L., Leriche, M., Desboeufs, K., Mailhot, G., George, C., and Chaumerliac, N.: Transition metals in atmospheric liquid phases: Sources, reactivity, and sensitive parameters, Chem. Rev., 105 (9), 3388-3431, 2005.

Ervens, B., Feingold, G., Frost, G. J., and Kreidenweis, S. M.: A modeling study of aqueous production of dicarboxylic acids: 1. Chemical pathways and speciated organic mass production, J. Geophys. Res., 109 (D15), doi:10.1029/2003JD004387, 2004.

Ervens, B., Feingold, G., and Kreidenweis, S. M.: Influence of water-soluble organic carbon on cloud drop number concentration, J. Geophys. Res., 110 (D18), doi:10.1029/2004JD005634, 2005.

Falkovich, A. H., Schkolnik, G., Ganor, E., and Rudich, Y.: Adsorption of organic compounds pertinent to urban environments onto mineral dust particles, J. Geophys. Res., 109 (D2), doi:10.1029/2003JD003919, 2004.

Guazzotti, S. A., Coffee, K. R., and Prather, K. A.: Continuous measurements of size-resolved particle chemistry during INDOEX-Intensive Field Phase 99, J. Geophys. Res., 106 (D22), 28607-28627, 2001.

Hoppel, W. A., Frick, G. M., and Larson, R. E.: Effect Of Nonprecipitating Clouds On The Aerosol Size Distribution In The Marine Boundary-Layer, Geophys. Res. Lett., 13 (2), 125-128, 1986.

Huang, X.-F., and Yu, J. Z.: Is vehicle exhaust a significant primary source of oxalic acid in ambient aerosols?, Geophys. Res. Lett., 34, L02808, doi:10.1029/2006GL028457, 2007.

Jickells, T. D., An, Z. S., Andersen, K. K., Baker, A. R., Bergametti, G., Brooks, N., Cao, J. J., Boyd, P. W., Duce, R. A., Hunter, K. A., Kawahata, H., Kubilay, N., laRoche, J., Liss, P. S., Mahowald, N., Prospero, J. M., Ridgwell, A. J., Tegen, I., and Torres, R.:

Global iron connections between desert dust, ocean biogeochemistry, and climate, Science, 308 (5718), 67-71, 2005.

Kalberer, M., Yu, J., Cocker, D. R., Flagan, R. C., and Seinfeld, J. H.: Aerosol formation in the cyclohexene-ozone system, Environ. Sci. Technol., 34 (23), 4894-4901, 2000.

Kanakidou, M., Seinfeld, J. H., Pandis, S. N., Barnes, I., Dentener, F. J., Facchini, M. C., Van Dingenen, R., Ervens, B., Nenes, A., Nielsen, C. J., Swietlicki, E., Putaud, J. P., Balkanski, Y., Fuzzi, S., Horth, J., Moortgat, G. K., Winterhalter, R., Myhre, C. E. L., Tsigaridis, K., Vignati, E., Stephanou, E. G., and Wilson, J.: Organic aerosol and global climate modelling: a review, Atmos. Chem. Phys., 5, 1053-1123, 2005.

Kawamura, K., and Ikushima, K.: Seasonal-changes in the distribution of dicarboxylic-acids in the urban atmosphere, Environ. Sci. Technol., 27 (10), 2227-2235, 1993.

Kawamura, K., Imai, Y., and Barrie, L. A.: Photochemical production and loss of organic acids in high Arctic aerosols during long-range transport and polar sunrise ozone depletion events, Atmos. Environ., 39 (4), 599-614, 2005.

Kawamura, K., and Yasui, O.: Diurnal changes in the distribution of dicarboxylic acids, ketocarboxylic acids and dicarbonyls in the urban Tokyo atmosphere, Atmos. Environ., 39 (10), 1945-1960, 2005.

Kerminen, V. M., Teinila, K., Hillamo, R., and Makela, T.: Size-segregated chemistry of particulate dicarboxylic acids in the Arctic atmosphere, Atmos. Environ., 33 (13), 2089-2100, 1999.

Maria, S. F., Russell, L. M., Gilles, M. K., and Myneni, S. C. B.: Organic aerosol growth mechanisms and their climate-forcing implications, Science, 306 (5703), 1921-1924, 2004.

Mochida, M., Kawabata, A., Kawamura, K., Hatsushika, H., and Yamazaki, K.: Seasonal variation and origins of dicarboxylic acids in the marine atmosphere over the western North Pacific, J. Geophys. Res., 108 (D6), doi:10.1029/2002JD002355, 2003a.

Mochida, M., Kawamura, K., Umemoto, N., Kobayashi, M., Matsunaga, S., Lim, H. J., Turpin, B. J., Bates, T. S., and Simoneit, B. R. T.: Spatial distributions of oxygenated organic compounds (dicarboxylic acids, fatty acids, and levoglucosan) in marine aerosols over the western Pacific and off the coast of East Asia: Continental outflow of organic aerosols during the ACE-Asia campaign, J. Geophys. Res., 108 (D23), doi:10.1029/2002JD003249, 2003b.

Mochida, M., Umemoto, N., Kawabata, A., Lim, H. J., and Turpin, B. J.: Bimodal size distributions of various organic acids and fatty acids in the marine atmosphere: Influence of anthropogenic aerosols, Asian dusts and sea spray off the coast of East Asia, J. Geophys. Res., 112 (D15209), doi:10.1029/2006JD007773, 2007.

Mochida, M., Umemoto, N., Kawamura, K., and Uematsu, M.: Bimodal size distribution of C-2-C-4 dicarboxylic acids in the marine aerosols, Geophys. Res. Lett., 30 (13), doi:10.1029/2003GL017451, 2003c.

Moffet, R. C., de Foy, B., Molina, L. T., Molina, M. J., and Prather, K. A.: Measurement of ambient aerosols in northern Mexico City by single particle mass spectrometry, Atmos. Chem. Phys., 8, 4499-4516, 2008.

Neubauer, K. R., Johnston, M. V., and Wexler, A. S.: Humidity effects on the mass spectra of single aerosol particles, Atmos. Environ., 32 (14-15), 2521-2529, 1998.

Neususs, C., Gnauk, T., Plewka, A., Herrmann, H., and Quinn, P. K.: Carbonaceous aerosol over the Indian Ocean: OC/EC fractions and selected specifications from size-segregated onboard samples, J. Geophys. Res., 107 (D19), 2002.

Prenni, A. J., DeMott, P. J., Kreidenweis, S. M., Sherman, D. E., Russell, L. M., and Ming, Y.: The effects of low molecular weight dicarboxylic acids on cloud formation, J. Phys. Chem. A, 105 (50), 11240-11248, 2001.

Qin, X., and Prather, K. A.: Impact of biomass emissions on particle chemistry during the California Regional Particulate Air Quality Study, International Journal Of Mass Spectrometry, 258 (1-3), 142-150, 2006.

Redemann, J., Masonis, S. J., Schmid, B., Anderson, T. L., Russell, P. B., Livingston, J. M., Dubovik, O., and Clarke, A. D.: Clear-column closure studies of aerosols and water vapor aboard the NCAR C-130 during ACE-Asia, 2001, J. Geophys. Res., 108 (D23), doi:10.1029/2003JD003442, 2003.

Russell, L. M., Maria, S. F., and Myneni, S. C. B.: Mapping organic coatings on atmospheric particles, Geophysical Research Letters, 29 (16), doi:10.1029/2002GL014874, 2002.

Satsumabayashi, H., Kurita, H., Yokouchi, Y., and Ueda, H.: Photochemical formation of particulate dicarboxylic-acids under long-range transport in central Japan, Atmos. Environ., Part A, 24 (6), 1443-1450, 1990.

Schmid, B., Hegg, D. A., Wang, J., Bates, D., Redemann, J., Russell, P. B., Livingston, J. M., Jonsson, H. H., Welton, E. J., Seinfeld, J. H., Flagan, R. C., Covert, D. S., Dubovik, O., and Jefferson, A.: Column closure studies of lower tropospheric aerosol and water vapor during ACE-Asia using airborne Sun photometer and airborne in situ and ship-based lidar measurements, J. Geophys. Res., 108 (D23), doi:10.1029/2002JD003361, 2003.

Silva, P. J., and Prather, K. A.: Interpretation of mass spectra from organic compounds in aerosol time-of-flight mass spectrometry, Anal. Chem., 72 (15), 3553-3562, 2000.

Simoneit, B. R. T., Kobayashi, M., Mochida, M., Kawamura, K., Lee, M., Lim, H. J., Turpin, B. J., and Komazaki, Y.: Composition and major sources of organic compounds of aerosol particulate matter sampled during the ACE-Asia campaign, J. Geophys. Res., 109 (D19), doi:10.1029/2004JD004598, 2004.

Sorooshian, A., Varutbangkul, V., Brechtel, F. J., Ervens, B., Feingold, G., Bahreini, R., Murphy, S. M., Holloway, J. S., Atlas, E. L., Buzorius, G., Jonsson, H., Flagan, R. C., and Seinfeld, J. H.: Oxalic acid in clear and cloudy atmospheres: Analysis of data from International Consortium for Atmospheric Research on Transport and Transformation 2004, J. Geophys. Res., 111 (D23), doi:10.1029/2005JD006880, 2006.

Staikova, M., Oh, M., and Donaldson, D. J.: Overtone-induced decarboxylation: A potential sink for atmospheric diacids, J. Phys. Chem. A, 109 (4), 597-602, 2005.

Volkamer, R., Molina, L. T., Molina, M. J., Shirley, T., and Brune, W. H.: DOAS measurement of glyoxal as an indicator for fast VOC chemistry in urban air, Geophys. Res. Lett., 32 (8), doi:10.1029/2005GL022616, 2005.

Volkamer, R., Ziemann, P. J., and Molina, M. J.: Secondary organic aerosol formation from acetylene (C2H2): seed effect on SOA yields due to organic photochemistry in the aerosol aqueous phase, Atmos. Chem. Phys. Discuss., 8, 14841-14892, 2008.

Wang, H., Kawamura, K., Ho, K. F., and Lee, S. C.: Low molecular weight dicarboxylic acids, ketoacids, and dicarbonyls in the fine particles from a roadway tunnel: possible secondary production from the precursors, Environ. Sci. Technol., 40 (20), 6255-6260, 2006.

Warneck, P.: In-cloud chemistry opens pathway to the formation of oxalic acid in the marine atmosphere, Atmos. Environ., 37 (17), 2423-2427, 2003.

Whiteaker, J. R., and Prather, K. A.: Hydroxymethanesulfonate as a tracer for fog processing of individual aerosol particles, Atmos. Environ., 37 (8), 1033-1043, 2003.

Yoon, S. C., and Kim, J.: Influences of relative humidity on aerosol optical properties and aerosol radiative forcing during ACE-Asia, Atmos. Environ., 40 (23), 4328-4338, 2006.

Yu, J. Z., Huang, X. F., Xu, J. H., and Hu, M.: When aerosol sulfate goes up, so does oxalate: Implication for the formation mechanisms of oxalate, Environ. Sci. Technol., 39 (1), 128-133, 2005.

Chapter 6

Hygroscopicity and cloud nucleation properties of calcium mineral dust particles

6.1 Synopsis

Atmospheric mineral dust particles can alter cloud properties and thus climate by acting as cloud condensation nuclei (CCN) that form warm cloud droplets through hygroscopic growth. The CCN activation properties of various calcium mineral dust particles were studied experimentally to investigate the consequences of our previous field observations showing the segregation of sulfate from nitrate and chloride between individual aged Asian dust particles (Chapter 3). Each mineral's observed hygroscopicity was primarily controlled by its solubility, which determines the degree to which the intrinsic hygroscopicity can be expressed. Trace amounts of soluble hygroscopic material mixed with insoluble mineral particles can significantly increase the apparent hygroscopicity. Insoluble minerals including calcium carbonate, representing fresh unprocessed dust, and calcium sulfate, representing atmospherically processed dust, had similarly small apparent hygroscopicities. Their activation is accurately described by deliquescence limitation and corresponded to a low apparent hygroscopicity, κ_{app}, of ~0.001. Highly soluble calcium chloride and calcium nitrate, representing atmospherically processed mineral dust particles, were much more hygroscopic, activating similar to ammonium sulfate with κ_{app} ~0.5. Notably, the particle generation method strongly impacted the results of this study. Calcium carbonate and calcium oxalate monohydrate particles were significantly more hygroscopic when generated by atomization from water versus dry-generation. This behavior is attributed to the formation of metastable

hydrates. These results indicate that the common assumption that all mineral dust particles become more hygroscopic and CCN-active after atmospheric processing should be revisited.

6.2 Introduction

Atmospheric aerosols affect the formation, growth, and lifetime of clouds by acting as cloud condensation nuclei (CCN) which provide seeds for cloud droplet formation (McFiggans et al., 2006). Increased number concentrations of CCN, from anthropogenic activities, can increase cloud brightness (Twomey, 1977), change cloud lifetime (Albrecht, 1989), and suppress (Lohmann and Feichter, 2005; Rosenfeld et al., 2001) or enhance (Petters et al., 2006b) precipitation (Rosenfeld et al., 2008). The interactions of aerosols and clouds remain the largest uncertainties in our ability to understand and predict the affect that anthropogenic activities have on regional and global climate change (IPCC, 2007). A particle's ability to absorb enough water such that it activates and becomes a cloud droplet is governed primarily by its size and soluble hygroscopic chemical content (McFiggans et al., 2006; Petters and Kreidenweis, 2008). Particles composed of compounds with a large *intrinsic* hygroscopicity (when fully dissolved) but low solubility will therefore display a low observed *apparent* hygroscopicity. Therefore, the size-resolved chemical composition and mixing state of atmospheric aerosols, and a detailed knowledge of how different compounds interact with water, are required to accurately predict how a realistic aerosol population will undergo cloud nucleation (Andreae and Rosenfeld, 2008; McFiggans et al., 2006).

Most inorganic salts present in aerosols (e.g. $(NH_4)_2SO_4$, NaCl) are hygroscopic and CCN-active at sub 100 nm diameters and typical cloud supersaturations. However, the role of insoluble and slightly soluble inorganic salts should be considered and studied for their CCN activation properties (Kelly et al., 2007). The conversion of insoluble salts to more soluble

compounds through heterogeneous and multiphase reactions is of particular interest, and is described in Chapter 7. Mineral dust particles are the most atmospherically relevant example of these types of inorganic systems. To date, only a few laboratory studies have been reported of the CCN properties of model mineral dust particles (Gibson et al., 2007; Gibson et al., 2006a). Koehler et al. (2007) measured the first CCN activation curves of an authentic dust sample, salt-rich playa dust from Owens (dry) Lake in California. Vlasenko et al. (2005) reported that Arizona test dust had very small subsaturated hygroscopic growth. A few studies have recently been reported probing the role that ambient mineral dust particles play in contributing to aerosol hygroscopicity and CCN formation (Carrico et al., 2003b; Perry et al., 2004; Roberts et al., 2006; Shi et al., 2008).

Mineral dust close to the source region is composed of a large and variable mixture of different minerals. This can include insoluble aluminosilicate clays (e.g. kaolinite, montmorilinite, illite), metal oxides (e.g. hematite, silica), carbonates (e.g. calcite, dolomite), and sparingly soluble gypsum ($CaSO_4 \cdot 2H_2O$), as well as soluble halite ($NaCl$) salts (Jeong, 2008; Krueger et al., 2004; Shi et al., 2005). These mineral components often undergo chemical reactions during atmospheric transport, such as reactions with $SO_2(g)$ to produce sulfate, $HCl(g)$ producing chloride, and nitrogen oxides such as $NO_2(g)$, $HNO_3(g)$, and $N_2O_5(g)$ to produce nitrate compounds {Usher, 2003 #314; Krueger, 2004 #316}. Uptake of organic compounds such as carboxylic acids by dust is also possible (Falkovich et al., 2004b), as described in Chapter 5. Kelly et al. (2007) recently reported theoretical calculations predicting a wide range of CCN properties due to the differing water soluble fraction of the various components of mineral dust. As described in Chapters 3 & 4, mineral dust particles can also accumulate soluble material through internal mixing with sea salt particles during cloud processing, and condensation of compounds including ammonium nitrate and sulfate.

Calcite ($CaCO_3(s)$) is generally regarded to be the most chemically reactive mineral component in aeolian dust particles (Laskin et al., 2005a; Tang et al., 2004b; Usher et al., 2003a). It can be found in the form of individual mostly-calcite particles, and also as calcite nanofibers distributed throughout mineral dust particles (Jeong and Chun, 2006). Its strong alkaline nature causes it to react readily with acidic gases such as HNO_3, HCl, and SO_2. This converts calcium carbonate to other calcium salts such as calcium nitrate, calcium chloride, and calcium sulfate, respectively. The conversion of insoluble calcium carbonate to deliquescent calcium nitrate through reaction with nitric acid vapor was first demonstrated in laboratory experiments by Krueger et al. (2004; 2003) and has also been observed in recent field studies (Laskin et al., 2005a; Matsuki et al., 2005b; Shi et al., 2008). Gibson et al. (2006a) demonstrated the large effect that this conversion has on the CCN activation of laboratory calcium mineral particles; the critical supersaturation of 100 nm pure calcium nitrate particles was measured to be 0.11%, compared to ~0.55% for atomized calcium carbonate particles. Calcite aerosol is commonly generated through atomization of the "insoluble" powder in water, for studies of the aerosol's chemical reactivity, hygroscopicity, and morphology (Gibson et al., 2007; Gibson et al., 2006a; Hatch et al., 2008; Liu et al., 2008a; Vlasenko et al., 2006). The results presented here demonstrate that wet-generation of insoluble mineral powders produces serious method artifacts that cause the particles to be much more hygroscopic than predicted by their low solubility.

The addition of soluble material such as nitric and sulfuric acids and the conversion of carbonates to more soluble compounds during atmospheric processing of mineral dust particles is commonly believed to increase the CCN activity of these particles (e.g. Fan et al., 2004; Gibson et al., 2006a; Levin et al., 1996; Perry et al., 2004; Roberts et al., 2006). Single-particle measurements of atmospherically processed mineral dust particles during ACE-Asia

revealed that nitrate and sulfate were not found in relatively large amounts in the same individual dust particles (Chapter 3). We hypothesized that this segregated mixing state of secondary acids could impart very different physicochemical properties to individual aged dust particles, particularly in terms of their interaction with water, due to the large solubility differences between some sulfate and nitrate salts. Oxalic acid was also found to be enriched in the Asian mineral dust particles and it is hypothesized that the formation of oxalate complexes with divalent cations such as Ca^{2+} could reduce the solubility of the dominant fraction of water soluble organic carbon (Chapter 5). Both of these hypotheses are explored herein through laboratory studies of the CCN activation properties of various pure calcium minerals as proxies for fresh and completely processed calcium carbonate particles.

6.3 Experimental methods

6.3.1 Aerosol generation

Commercially available calcium salts were used to generate particles for these experiments. They included two $CaCO_3$ powders (J.T. Baker, 99.9%; Solvay, uncoated ultrafine Socal® 31, unstated purity), $CaSO_4$ (Aldrich, 99%), $Ca(NO_3)_2$ (Alfa Aesar, 99.0+%), $CaCl_2 \cdot 2H_2O$ (Aldrich, 98+%), $CaC_2O_4 \cdot H_2O$ (Alfa Aesar, 99+%), and $C_2O_4H_2$ (Aldrich, 99+%). The wet-generation method involved atomization of aqueous solutions or suspensions using high purity N_2 at 2-3 Lpm, and then passing the aerosol through three silica gel diffusion driers to reduce the RH below 5%. Calcium nitrate ($Ca(NO_3)_2$), calcium chloride ($CaCl_2$), and oxalic acid ($C_2O_4H_2$) solutions were made by mixing 0.15 g powder into 150 mL milli-Q water (>18.2 MΩ). Calcium sulfate ($CaSO_4$), calcium carbonate ($CaCO_3$), and calcium oxalate monohydrate ($CaC_2O_4 \cdot H_2O$) suspensions were made by mixing 0.050 g of powder into 150 mL milli-Q water. Dry generation, used for $CaSO_4$, $CaCO_3$, and $CaC_2O_4 \cdot H_2O$, involved

placing several grams of powder in an Erlenmeyer flask with a Teflon-coated stir bar. A piece of Teflon tubing was passed through a silicone stopper with a plastic pipette tip fitted on the end. When nitrogen gas was passed through the tubing a jet of gas was produced and directed at the powder, while the stir bar or vortex shaker agitated the dry powder. The suspended aerosol was sampled through a 3/8" o.d. stainless steel (s.s.) tube at the top of the flask and then directed into a second Erlenmeyer flask through a s.s. tube with a right angle bend to help remove supermicron particles. The remaining aerosol was transferred to a ~17 L s.s. residence chamber to which dilution nitrogen gas of 2.0-8.0 Lpm was added. The aerosol sample was drawn from two 3/8" o.d. s.s. tubes that protruded slightly into the chamber and then combined into one flow. Size distributions of the generated aerosol were performed with a Scanning Mobility Particle Sizer (SMPS, TSI, Model 3010 CPC and 3081 DMA) and Aerodynamic Particle Sizer (APS, TSI, Model 3321).

6.3.2   CCN activation curve measurement

For both generation methods the dry aerosol was sent to a differential mobility analyzer (DMA, Model 3081, TSI inc.) for size selection. The aerosol was first passed through a Kr-85 bipolar neutralizer to achieve charge equilibrium. An aerosol sample flow rate of 1.0 or 1.5 Lpm was used, with a sheath flow rate of 10.0 or 15.0 Lpm. A 10:1 sheath/sample flow ratio was used whenever possible; however a lower sheath/sample flow ratio was required to select particles as large as 500 nm. The pseudo-monodisperse aerosol was then sent to a flow splitter and transferred to a condensation particle counter (CPC, Model 3010 or 3007, TSI Inc.) and a cloud condensation nuclei counter (CCNc). A small excess aerosol flow of ~0.2 Lpm was vented through a HEPA filter to eliminate any large pressure or flow imbalances. Conductive silicone tubing was used to transport the aerosol and minimize wall losses.

6.3.2.1 CCN counter operation and calibration

The CCNc is a miniature continuous-flow streamwise thermal-gradient CCN chamber constructed at Scripps Institution of Oceanography based on the design of Roberts and Nenes (2005), and is described in Chapter 1. Briefly, the aerosol sample is exposed to a well-defined and controlled water supersaturation. This supersaturation is primarily a function of the column's thermal gradient (dT), and the total flow rate. Particles that are able to absorb water and grow to optical diameters > 1 µm are detected by an optical particle counter (OPC) at the end of the column and are counted as CCN. Calibration of the supersaturation (SS) as a function of column temperature gradient (dT) was performed monthly using dried ammonium sulfate particles atomized from a 1.0 g/L solution of ammonium sulfate (Sigma, 99.999%) and determining activation diameter as a function of column dT. The linear fits of SS to column dT typically had R^2 > 0.995. Column temperature gradients of 2.0 to 15.0 °C generated SS of approximately 0.08 to 1.1%. Further details are given in Chapter 1.

6.3.2.2 Data analysis and fitting

CCN activation curves were generated either by scanning across dry particle diameter (D_{dry}) at a fixed SS, or by scanning SS (through changing dT) at a fixed dry diameter. Both the CCNc and CPC record 1-second averaged data, which were averaged to one minute for calculation of the CCN/CN ratio. For both SS and size scans we determined the dry (critical activation) diameter (D_{dry} or D_{ca}) or critical supersaturation (s_c) by first scaling all ratios to the maximum observed CCN/CN ratio, for large sizes/high supersaturations. The contribution from larger multiply charged particles was then removed following Rose et al (2008). A Boltzman sigmoid curve of the form

$$y = \frac{A_1 - A_2}{1 + e^{(x - x_o)/dx}} - A_2 \qquad (6.1)$$

was used to fit the activation curve, where y is the CCN/CN ratio, A_1 is the minimum value, A_2 is the maximum value, dx is the rate of change, and x_o is the midpoint between A_1 and A_2. The data were fit such that A_1 corresponded to the CCN/CN ratio of the multiply charged particles at small sizes/supersaturations, and A_2 is set to the scaled maximum CCN/CN ratio of ~1.0. Thus, x_o corresponds to the CCN/CN = 0.5 midpoint typically used to define the critical supersaturation or diameter of the singly-charged particles of interest. We note that this technique is more accurate for SS scans, because the fraction of multiply charged particles larger than the selected dry diameter is constant for all points, and the assumption of constant composition with size, implicit in diameter scans, is not as important. SS scans are slower than size scans, however, because the column must equilibrate to the new temperature gradient, and thus size scans were used for some experiments. The contributions of multiply charged particles to the activation curve in size scans can be explicitly calculated using the inversion proposed by Petters et al (2007). Although we did not use that method to reduce all of our size-scan data, we verified via spot checks that our simpler method did not give significantly different results from the full inversion.

6.3.2.3 Error analysis

The major sources of uncertainty in determining the CCN activation properties, critical supersaturation (s_c) and dry (critical activation) diameter (D_{dry} or D_{ca}), are primarily due to the calibration of the CCNc's supersaturation, and errors in selecting a monodisperse aerosol with the DMA. The SS uncertainty was estimated from the linear fit of the CCNc calibration as 3%. Uncertainty in size selection was estimated as 5%, including variations in particle shape factor and flow rates, and by measuring the size distribution of the pseudo-monodisperse size-selected aerosol with a second SMPS system. The error reported for the

fitted hygroscopicity parameter, κ (see below), was estimated from one standard deviation of the κ values determined from the individual s_c-D_{dry} pairs for each system.

6.3.3 Single-particle analysis

6.3.3.1 Single-particle mass spectrometry (SPMS)

An ultrafine aerosol time-of-flight mass spectrometer (UF-ATOFMS) SPMS was used to analyze the chemical composition of individual aerosol particles between D_a = 100-400 nm used in these experiments. This instrument uses an aerodynamic lens to focus submicron particles into a collimated beam that increases their detection efficiency. The design, operation, and capabilities of this instrument are described in Chapter 1.

6.3.3.2 Scanning electron microscopy/energy dispersive x-ray analysis (SEM/EDX)

Atomized particle samples were collected on carbon-coated copper substrates (Carbon type-B, 400 mesh Cu, Ted Pella Inc.). The substrates were placed on the lower stages of a micro-orifice uniform deposition impactor (MOUDI, Model 110, MSP Corp.). The atomized aerosol was diluted with dry nitrogen gas and directly pulled into the MOUDI. Collection was performed for several hours to collect the required particle density. In some cases the stages of the MOUDI were manually rotated every 15 minutes during collection. SEM/EDX analysis was performed with a FEI XL30 digital field emission gun environmental SEM. The microscope is equipped with an EDAX spectrometer (model PV7761/54 ME, EDAX, Inc.) that has an Si(Li) detector and an ATW2 window. The spectrometer allows X-ray detection from elements higher than beryllium (Z > 4). Further details are provided by Liu et al. (2008a).

6.3.3.3 Environmental scanning electron microscopy (ESEM)

To monitor the effects of increased relative humidity on the particle morphology, the FEI XL30 microscope was placed in the environmental mode (ESEM) which allows imaging with up to ~15 Torr of water vapor present in the chamber. The temperature of the sample platform (Peltier stage) was maintained at 2 °C. Hygroscopic transformations of individual particles were recorded using computer video recorder software while the water vapor pressure within the cell increased from < 0.1 to 5.2 Torr (98% RH). With ESEM the choice of the imaging conditions is a trade-off between required strength of the beam to remain well focused throughout water vapor (high energy and high current) and the desire to minimize its damage to the particles (low energy and low current). Conditions of an accelerating voltage of 10–15 keV, beam current of 150 pA, and fast scanning (line time 1.68 ms, 1452 lines per frame) were found to be optimal in a previous study (Hoffman et al., 2004) and thus were used here.

6.3.4 Bulk chemical analysis

6.3.4.1 Ion chromatography

A Metrohm-Peak MIC-2 Advanced System was used for cation and anion analysis of the soluble components of the calcite powders used. 0.050 g of powder was placed in 150 mL of milli-Q water for variable lengths of time. 5.0 mL aliquots were removed and filtered with 0.2 µm nylon syringe filters (Fisher Scientific) before being injected into the IC. Atomized samples were generated with ultra pure nitrogen (~3 Lpm) initially for the first few hours but not overnight or thereafter. Syringe and syringe filter blanks were well below the samples' concentrations. Cation analysis was performed using a Metrosep C 2 (Metrohm-Peak) separation column. The mobile phase was 4.0 mmol/L tartaric acid/0.75 mmol/L dipicolinic acid at a flow rate of 1.0 mL/min. Anion analysis was performed using chemical suppression

and a Metrosep A Supp 5 (Metrohm-Peak) separation column. The mobile phase was 3.2 mmol/L Na_2CO_3/1.0 mmol/L $NaHCO_3$ at a flow rate of 0.7 mL/min.

6.3.4.2 Inductively coupled plasma mass spectrometry (ICP-MS)

The soluble components of the calcite powders were also determined by ICP-MS. 0.050 g of powder was placed in 10.0 mL of water and then sonicated for 2-3 hours several times a day over five days. The samples were then filtered and the aqueous extract analyzed. To another set of samples 0.50 mL of conc. nitric acid was added to completely dissolve the powder. An Agilent 4500 series ICP-MS (Agilent Technology, Inc.) was used for these measurements. Detection limits of this instrument are at the sub-parts-per-trillion level for most elements. However, detection limit for Ca^{2+} is higher (~15 ppb conservatively) because of the interference from the Ar carrier gas. Blank levels for all reported elements were < 0.010 mg/L except for Ca, which was < 0.50 mg/L.

6.4   Results and discussion

6.4.1   Hygroscopicity parameter

All of the experimental data is expressed in terms of the hygroscopicity parameter, κ, introduced by Petters and Kreidenweis (2007), which describes a particle's water activity, a_w, via

$$\frac{1}{a_w} = 1 + \kappa \frac{V_s}{V_w},$$

(6.2)

where V_s is the volume of the dry particle mass and V_w is the volume of water. A choice of dry diameter (D_{dry}) and κ enable calculation of the expected supersaturation − wet diameter relationship ("Köhler curve"):

$$S(D) = \frac{D^3 - D_{dry}^3}{D^3 - D_{dry}^3(1-\kappa)} \exp\left(\frac{A}{D}\right), \tag{6.3}$$

where S is the water saturation ratio over the aqueous droplet, D is the droplet diameter, and A = 2.1×10^{-9} m is a constant evaluated for a surface tension of 0.072 J m^{-2} (pure water) and temperature of 298.15 K. The κ term captures the Raoult effect while the A term describes the Kelvin effect in Eq. 6.3. The maximum in the curve described by Eq. 6.3 is identified as the critical saturation ratio for activation of the chosen dry diameter (critical supersaturation, s_c = S-1). The best-fit hygroscopicity parameter that describes the observed behavior of test particles can be determined using Eq. 6.3 by computing Köhler curves for iterations of κ until the modeled s_c for a selected dry diameter matches the experimentally observed s_c. κ increases with increasing hygroscopicity, from 0 to a maximum of ~ 1.4; NaCl has κ = 1.2, for example. Further details regarding this hygroscopic parameter are given in Chapter 1. We denote the κ value that is derived from measured s_c-D_{dry} pairs and Eq. 6.3 as apparent hygroscopicity, or κ_{app}, while the κ value that is obtained from Eq. 6.2 is the intrinsic hygroscopicity, or κ_{intr}, for an aqueous particle. Apparent and intrinsic hygroscopicities are equal when the particle is fully dissolved at the water content relevant to CCN activation. The apparent hygroscopicity can be considered as a compound's intrinsic hygroscopicity expressed according to its solubility limit constraint.

It is important to properly distinguish between the roles of solubility and hygroscopicity. While hygroscopicity determines the ability of a particle to uptake water, only the compound's dissolved volume fraction contributes to hygroscopic growth and the Raoult effect in Eq. 6.3. Insoluble but wettable components contribute to particle growth and activation via water condensation by increasing the particle's size and thus reducing the Kelvin effect in Eq. 6.3. Therefore, particles composed of intrinsically hygroscopic but

insoluble compounds will exhibit a very small apparent hygroscopicity and poor CCN activity. As many of the minerals used in this study have limited solubility in water, an extension of Eq. 6.3 proposed by Petters and Kreidenweis (2008) is applied, wherein the following equations are used to compute κ:

$$\kappa_{sum}(D) = \sum_i \varepsilon_i \kappa_i H(x_i)$$

$$x_i = \left(\left(D/D_{dry}\right)^3 - 1\right) C_i / \varepsilon_i \qquad (6.4\text{a-c})$$

$$H(x_i) = \begin{cases} x_i & x_i < 1 \\ 1 & x_i > 1 \end{cases}$$

Eqs. 6.4a-c have been written to allow for multiple components, i, where ε_i is the volume fraction of component i in the dry particle, C_i the solubility of i in water (expressed as volume compound per unit volume of water), and H is an index for the fraction of component i that has dissolved, x_i. In Eq. 6.4a the individual κ_i are intrinsic hygroscopicities for each compound and $\kappa_{sum}(D)$ is used in Eq. 6.3 to find the maximum of the Köhler curve. It is important to distinguish $\kappa_{sum}(D)$ which varies with droplet size, D, and the associated water content, from the constant κ_{app}, which is fit to observed s_c-D_{dry} pairs.

Figure 6.1 shows representative Köhler growth curves computed from Eqs. 6.3-6.4 for two of the sparingly soluble minerals studied in this work, $CaCO_3$ and $CaSO_4$, using the properties listed in Table 6.1. The curves demonstrate that, for species with limited solubility, some ranges of D represent water contents that are insufficient to dissolve the entire compound present in the dry particle. Both of these 200 nm particle types are predicted to activate at s_c ~1%, the critical supersaturation required for an insoluble and thus nonhygroscopic but wettable particle (κ_{app} ~0) of the selected dry diameter. The large s_c is the result of the compound's low solubility which results in deliquescence relative humidity exceeding the critical supersaturation of an equivalent metastable solution droplet. Such
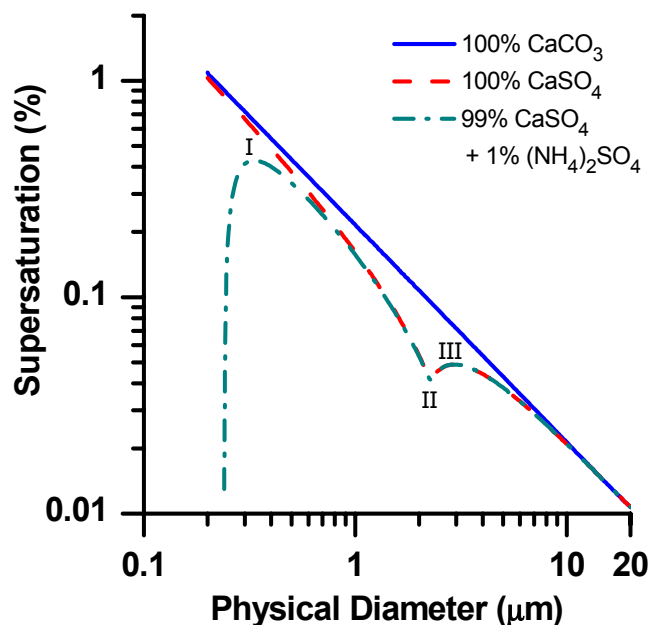
Figure 6.1. Theoretical κ-Köhler droplet growth curves for 200 nm dry $CaCO_3$ and $CaSO_4$ particles calculated using Eqs. (6.3-6.4). A mixed 200 nm particle composed of 99% $CaSO_4$ and 1% $(NH_4)_2SO_4$ ($\kappa_{intr} = 0.6$, $C = 0.43$) by volume is also shown. The solubilities and intrinsic hygroscopicities (κ_{intr}) used are from Table 6.1. I: activation of the mixed particle before $CaSO_4(s)$ has fully dissolved, II: complete dissolution of $CaSO_4$, III: activation of the entire deliquesced mixed $CaSO_4(aq) + (NH_4)_2SO_4(aq)$ particle.

particles thus activate under a deliquescence-limitation as the deliquescence water supersaturation, S_{Del}, exceeds that predicted by Köhler theory for aqueous particles, S_K (Kreidenweis et al., 2006).

Whether a particle expresses its "intrinsic hygroscopicity" κ_{intr} at activation, or activates at some "apparent hygroscopicity", κ_{app}, depends on κ_{intr}, solubility, particle phase, and initial dry diameter. The apparent hygroscopicity is that which is expected to manifest both experimentally and in the atmosphere. Figure 6.2 shows the apparent hygroscopicity that would be deduced from a measured s_c-D_{dry} pair as a function of the solubility of the primary compound in the particle. The two cases are for an intrinsic hygroscopicity of $\kappa_{intr} = 1.0$ (left panel) and $\kappa_{intr} = 0.050$ (right panel). The contours show that as the solubility increases a

larger fraction of its intrinsic hygroscopicity will be observed as its apparent hygroscopicity, until the solubility limit is exceeded and the full intrinsic hygroscopicity is expressed. We show calculations for three particle sizes: 0.010, 0.10, and 1.0 μm. The smallest particle sizes have a reduced apparent hygroscopicity at relatively high solubilities. This is because the higher supersaturations required to deliquesce smaller particles, due to an increased Kelvin effect, are interpreted as lower hygroscopicity (Kreidenweis et al., 2006). Thus, for a solubility at which larger particles may express their $\kappa_{app} = \kappa_{intr}$ during activation, the critical supersaturation observed for smaller particles might appear close to the $\kappa_{app} = 0$ isoline (Kelvin limit for insoluble but wettable particles). The larger the intrinsic hygroscopicity of the primary component, the smaller the solubility at which this deliquescence limitation is observed. The presence of sufficiently soluble contaminant that is in solution reduces the solubility where intrinsic and apparent hygroscopicities diverge, as shown by the grey lines in Fig. 6.2. The presence of the 1% $\kappa_{intr} = 0.6$ contaminant limits the smallest apparent κ value than can be observed experimentally; for the cases considered here, this limit is at $\kappa_{app} = 0.006$ (= 0.6 × 1%, Eq. (6.4a)). The contaminant also allows the intrinsic hygroscopicity of the primary component to be expressed at lower solubilities than for single-component particles. This is because the presence of the soluble contaminant assures that there is always some water associated with the particle that can dissolve at least a portion of the limited-solubility primary component. We note that the presence of the trace contaminant also modifies the apparent hygroscopicity observed when the particle is fully dissolved at activation. For the case where the primary component was assumed to have $\kappa_{intr} = 0.05$, the observed hygroscopicity at complete dissolution is slightly larger ($\kappa_{app} = 0.0555$) in the presence of the contaminant, as predicted from the mixing rule for κ (Eq. (6.4a)).
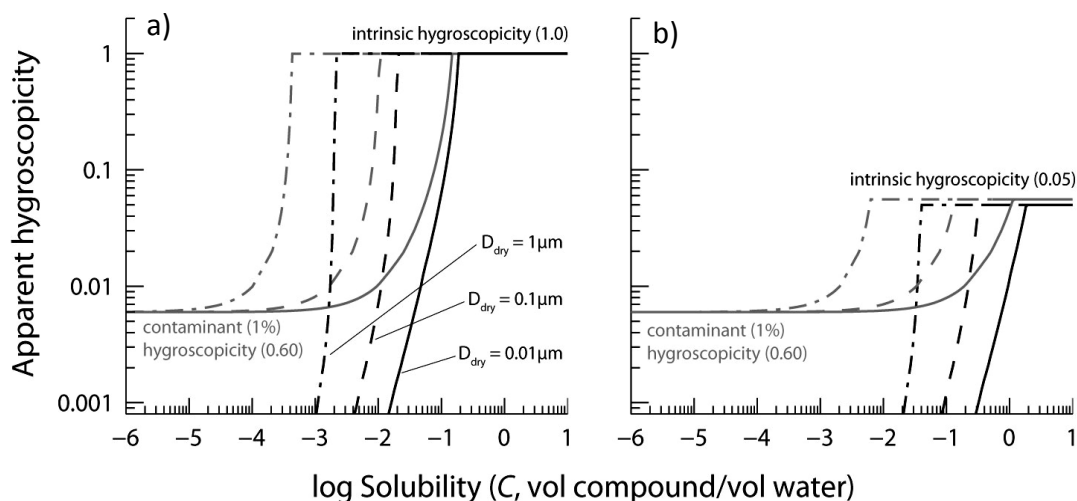
Figure 6.2. Predicted apparent hygroscopicity contours for particles composed of a principle compound with κ_{intr} = 1.0 (a) or 0.050 (b) as a function of the compound's solubility, C, and dry particle size. Grey contours are for mixed particles composed of 99% volume principle compound and 1% contaminant with κ = 0.60 and $C = \infty$.

The effect of a 1% by volume $(NH_4)_2SO_4$ impurity on the Köhler curve for a 200 nm $CaSO_4$ particle is shown in Figure 6.1. The presence of this soluble and hygroscopic minor component removes the deliquescence-limitation experienced by pure $CaSO_4$ because the mixed particle activates before the $CaSO_4$ core dissolves. This reduces s_c from 1.03% to 0.429%, occurring at the first maximum in the growth curve (point I), and κ_{app} at activation is increased from 0 to 0.0075. The second maximum occurs after the $CaSO_4$ core has fully dissolved (at point II) and corresponds to the activation of the completely aqueous $(NH_4)_2SO_4/CaSO_4$ mixed particle (point III). This is analogous to the descriptions of the Köhler curve used to model activation of limited-solubility components in mixed organic-inorganic particles (Bilde and Svenningsson, 2004; Broekhuizen et al., 2004; Petters and Kreidenweis, 2008; Shulman et al., 1996).

Based on Fig. 6.2, we delineate three solubility regimes: 1) "sufficiently soluble compounds" are those that have C > ~0.1 and are soluble enough that $\kappa_{app} = \kappa_{intr}$ for all dry

particle sizes. Therefore $CaCl_2$, $Ca(NO_3)_2$, and $C_2O_4H_2$ are expected to activate according to κ_{intr}. 2) "Sparingly soluble compounds" are those where κ_{app} can take any value between ~0 and κ_{intr}. An approximate range is $10^{-4} < C < 10^{-1}$. 3) "Insoluble compounds" are those for which κ_{app} ~0 always applies, i.e. $C < ~10^{-4}$. $CaCO_3$, $CaSO_4$, and $CaC_2O_4 \cdot H_2O$ (Table 6.1) are thus not expected to express their large intrinsic hygroscopicities, either experimentally or during cloud nucleation. As particles composed of low solubility compounds undergo reactions/processes both in the laboratory and atmosphere that either convert the compounds into more soluble forms, or add soluble hygroscopic material to the particles, the modified particles will express a larger apparent hygroscopicity.

The intrinsic hygroscopicity of a limited-solubility compound, expressed once it is fully dissolved, is difficult to measure, but it can be approximated assuming Raoult's Law applies:

$$\kappa_{intr} = \frac{\nu \cdot \rho_s \cdot M_w}{\rho_w \cdot M_s}, \tag{6.5}$$

where ρ is the density and M the molecular weight of the solute, s, and of water, w, and ν is the number of ions and molecules produced when one molecule of the solute completely dissociates (i.e. van 't Hoff factor). Table 6.1 summarizes the properties of the calcium salts considered here. It includes estimates of the intrinsic and apparent hygroscopicities of each compound, the latter estimated for a 200 nm particle, a typical particle size used in this work, and an amount of soluble contaminant equivalent to the compound's stated purity.

6.4.2 Experimentally determined hygroscopicities

Representative experimentally determined activation curves for each compound are shown in Figures 6.3-6.5. Figures 6.3 and 6.4 demonstrate fits to SS-scans used to obtain critical supersaturations for fixed dry diameters, and Figure 6.5 shows fits to size scans used to
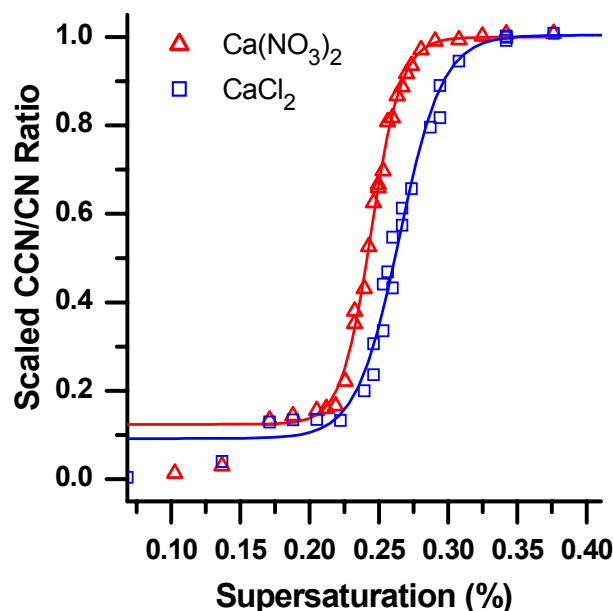
Figure 6.3. CCN activation curves for atomized calcium chloride and calcium nitrate from supersaturation scans of 75.0 nm mobility diameter particles. Lines are sigmoidal fits between the scaled lower and upper plateaus. The CCN column's supersaturation is derived from the column's temperature gradient (dT) by calibration with ammonium sulfate aerosol.

obtain critical dry diameters at fixed SS. All of the D_{dry}-s_c data obtained in this study, and the best-fit κ for each data point, are listed in Table 6.2. Averaged observed values of κ_{app} are summarized for each compound in Table 6.1.

For calcium chloride and calcium nitrate, only wet-generated particles were studied. Because these compounds are sufficiently soluble, it is expected that $\kappa_{app} = \kappa_{intr}$ listed in Table 6.1. The observed s_c-D_{dry} relationships of both particle types are $\kappa_{app} = 0.48 \pm 0.07$ and $\kappa_{app} = 0.51 \pm 0.07$, respectively, similar to ammonium sulfate ($\kappa_{app} = 0.61$). These particles were likely composed of their most stable hydrates after atomization and drying: $CaCl_2 \cdot 2H_2O$ and $Ca(NO_3)_2 \cdot 4H_2O$. As indicated in Table 6.1, the calculated intrinsic κ values for the hydrated compounds are lower than for the anhydrous compounds, and correspond well to the measurements. These results also compare reasonably well with those of Gibson et al. (2006a)

for calcium nitrate. Gibson et al. found $s_c = 0.11\%$ and estimated the dry diameter of their 100 nm particles to be 89 nm due incomplete particle drying, corresponding to $\kappa_{app} = 1.25$ (Table 6.2).

Calcium carbonate and calcium sulfate were studied using two different particle generation methods: atomization from an aqueous suspension/solution, and resuspension of the dry powder. Dry-generated Baker $CaCO_3$ produced a much broader activation curve than did the other dried powders, with no clear multiply-charged plateau (Figure 6.4). This made these curves more difficult to fit and accurately determine the critical supersaturation; the estimates shown in Table 6.1 give $\kappa_{app} = 0.0078 \pm 0.0036$. Dry-generated Solvay $CaCO_3$ corresponded to very low CCN-activity particles with $\kappa_{app} = 0.0011 \pm 0.0004$, and dry-generated $CaSO_4$ particles to $\kappa_{app} = 0.0016 \pm 0.0005$. All three particle types approach the expected behavior of insoluble particles which activate according to the Kelvin effect only
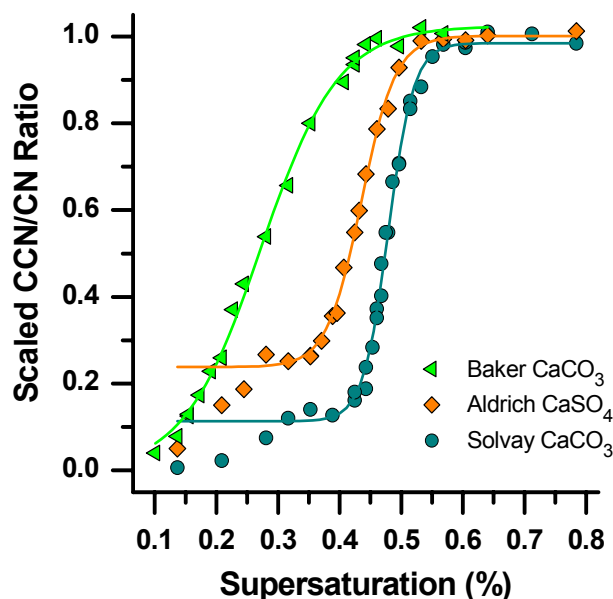
Figure 6.4. CCN activation curves of dry-generated Solvay calcium carbonate, Baker calcium carbonate, and Aldrich calcium sulfate aerosol obtained by scanning supersaturation of 300.0 nm dry mobility diameter particles. Lines are sigmodal fits to each curve. Note the lack of a multiply-charged plateau in the Baker $CaCO_3$ data.
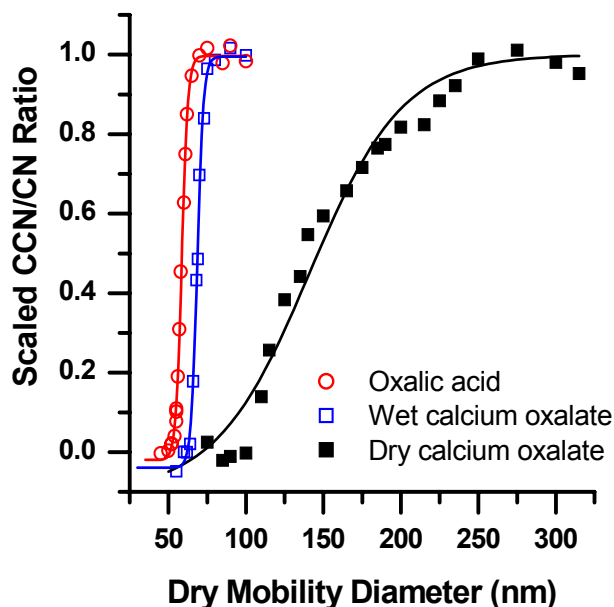
Figure 6.5. CCN activation curves from scanning size at 0.363% SS of atomized oxalic acid, and calcium oxalate monohydrate using wet-generation (open squares) and dry-generation (solid squares). The CCN/CN ratio for the multiply-charged plateau has been subtracted from each curve and the data rescaled so that all data sets span the same range on the y-axis.

(κ_{app} = 0). Small amounts of sufficiently soluble contaminants (1% by volume) increase apparent hygroscopicity above 0, as shown in Figs. 6.2 & 6.6. The small κ_{app} of ~0.001 for these dry-generated particles indicates that they likely contained only small quantities of sufficiently soluble impurities (< 1%), such as inorganic salts.

Wet-generated CaSO$_4$ particles exhibited a somewhat larger κ_{app} = 0.0045 ± 0.0012 than the dry-generated particles, but small amounts of hygroscopic impurities can explain these differences. From the results, we conclude that CaSO$_4$ has a sufficiently low solubility that its CCN activation behavior can be approximated as that of an insoluble component (κ_{app} = 0). In contrast, the wet-generated Baker CaCO$_3$ particles were much more CCN-active than the dry-generated particles, with κ_{app} = 0.020 ± 0.0035 compared to κ_{app} = 0.0078 ± 0.0036 for

dry. The atomized Baker calcite became significantly more CCN-active as it remained in the water, eventually producing particles with $\kappa \sim 0.1$ one day after the powder was added to the water. Atomized Solvay $CaCO_3$ did not exhibit these large changes in hygroscopicity with time, but did display unusual behavior that indicated that there were two different chemical systems present in the atomized aerosol. Particles smaller than ~ 100 nm had $\kappa_{app} > 0.1$, while larger particles resembled the dry-generated Solvay $CaCO_3$ with a slightly larger $\kappa_{app} < 0.005$. These unexpected results are explored more fully below.

To investigate the CCN activity of calcium-rich dust particles internally mixed with organic diacids, such as those observed during ACE-Asia (Chapter 5), activation curves were determined for calcium oxalate monohydrate ($CaC_2O_4 \cdot H_2O$, COH) particles from both dry- and wet-generation. The dry-generated COH produced broad activation curves, similar to the dry-generated Baker $CaCO_3$ (Fig. 6.5). As a result these curves are more difficult to fit, introducing greater uncertainty into the determination of the critical dry diameter or supersaturation. Dry-generated COH had $\kappa_{app} = 0.048 \pm 0.013$. When calcium oxalate monohydrate is atomized from water the particles produced are much more CCN active, with $\kappa_{app} = 0.34 \pm 0.02$. The shift to more CCN-active particles caused by atomization from water is likely due to the formation of metastable calcium oxalate hydrates with increased solubility (Brecevic et al., 1989) whose states become locked into during the rapid particle drying process before CCN analysis. This may result in the atomized particles remaining deliquesced even after being dried to $< 5\%$ RH by the diffusion driers, and thus requiring much lower supersaturations (higher κ_{app}) to activate.

CCN activation curves were also determined for oxalic acid particles atomized from water and yielded $\kappa_{app} = 0.50 \pm 0.05$. This value is close to that expected for oxalic acid

Table 6.1. Properties of minerals[a] studied in this work, including predicted and measured hygroscopicities.

compound	ρ	M_s	ν	S (25°C)	C	predicted κ		experimental κ_{app} (this work)		notes
	g cm⁻³	g mol⁻¹		g L⁻¹	vol sol / vol water	Raoult κ_{intr}^b	calc κ_{app}^c	wet gen.	dry gen.	
CaCl₂	2.15	110.98	3	813	0.38	1.05	1.04	0.48 ± 0.07		0
CaCl₂·2H₂O	1.85[d]	147.02	3	813	0.44	0.68	0.68			1
Ca(NO₃)₂	2.5	164.09	3	1440	0.576	0.82	0.82	0.51 ± 0.07		2
Ca(NO₃)₂·4H₂O	1.86[d]	236.09	3	1440	0.774	0.43	0.43			0
CaSO₄	2.96	136.14	2	2.05	6.9×10⁻⁴	0.78	0.0084	0.0045 ± 0.0012	0.0016 ± 0.0005	0
CaSO₄·2H₂O	2.32	172.20	2	2.05	8.8×10⁻⁴	0.49	0.0078			3
CaCO₃ (calcite)	2.71	100.09	2	0.0058[e]	2.1×10⁻⁶	0.97	0.00072	0.020 ± 0.0035	0.0078 ± 0.0036	4
						0.97	0.0068	0.2 to 0.002[f]	0.0011 ± 0.0004	5
CaC₂O₄	2.2	128.10	2	0.0061	2.8×10⁻⁶	0.62	0.0060	0.34 ± 0.02	0.048 ± 0.013	0
CaC₂O₄·H₂O	2.12[d]	146.12	2	0.0061	2.9×10⁻⁶	0.52	0.0060			6
C₂O₄H₂	1.90	90.04	3	143[g]	7.5×10⁻²	1.14	1.14	0.50 ± 0.05		3
C₂O₄H₂·2H₂O	1.653	126.07	3	143[g]	8.7×10⁻²	0.71	0.71			0

[a] Density and solubility taken from the CRC Handbook of Physics and Chemistry, 88th Edition, except where noted below.
[b] Calculated using Eq. 6.5.
[c] For 200 nm particles of specified compound, with 0.1%–2% impurity (see notes) having $\kappa_{intr} = 0.6$ and infinite solubility.
[d] Manufacturer stated value.
[e] Plummer and Busenberg (1982).
[f] Apparent hygroscopicity highly variable with particle size.
[g] From http://www.wikipedia.org

Notes:
0. Assumed purity of 99%
1. Aldrich, 98+%
2. Alfa Aesar, 99.0+%
3. Aldrich, 99+%
4. J.T. Baker, 99.9%
5. Solvay, assumed purity 99%
6. Alfa Aesar

dihydrate particles (Table 6.1). Koehler et al. (2006) also observed that hygroscopicity was generally most consistent with the formation of the dihydrate in typical laboratory atomization/drying processes. The small measured hygroscopicity of dry COH compared to oxalic acid is attributed to its low solubility (0.0061 g L^{-1}), which is similar to that of calcium carbonate (0.0058 g L^{-1}). Therefore, COH should produce particles with hygroscopicity near κ_{app} ~0.001, similar to that measured for dry Solvay calcium carbonate. The particles would have to contain mass fractions of soluble contaminants on the order of > 10% to exhibit κ_{app} = 0.048 ± 0.013. It is possible that dissolved calcium oxalate may be surface active and therefore reduce the surface tension at the air-solute interface, thus decreasing the activation barrier. We calculate that a large reduction in surface tension from 0.072 J m^{-2} (pure water) to 0.029 J m^{-2} would be required to produce particles with κ_{app} = 0.048. This reduction in surface tension is much larger than that typically determined for surface active organic compounds considered in CCN activation (Facchini et al., 2000). For example, adipic acid, azelaic acid, and succinic acid have surface tensions of 0.064, 0.061, and 0.065 J m^{-2}, while nonanoic acid has a surface tension of 0.030 J m^{-2} (Broekhuizen et al., 2004). Nancollas and Wu (1998) measured the surface tension of COH to be 0.0324 J m^{-2} using a thin layer wicking method. As this is close to the surface tension we calculated to be necessary to match observations, reduced surface tension may explain the higher-than-expected apparent hygroscopicity of the dry calcium oxalate monohydrate.

Figure 6.6 compares the CCN properties of the dry- and wet-generated calcium mineral particles described above in s_c-D_{dry} space with κ isolines overlain. Dry-generated $CaCO_3$ and $CaSO_4$ demonstrated low apparent hygroscopicity and thus poor CCN activation potential, approaching the κ = 0 isoline. $CaCl_2$, $Ca(NO_3)_2$, and $C_2O_4H_2$ approach the hygroscopicity of $(NH_4)_2SO_4$ (κ_{app} = 0.61). Dry-generated $CaC_2O_4 \cdot H_2O$ has κ_{app} ~0.048 ±

Table 6.2. CCN activation properties and hygroscopicities of calcium minerals from wet- and dry-generation.

compound	*	D_{dry} (nm)	s_c (%)	κ_{app}[a]	*	D_{dry} (nm)	s_c (%)	κ_{app}[a]
		wet-generated				dry-generated		
$CaCl_2 \cdot 2H_2O$	S	75.0	0.265	0.46				
	S	100.0	0.173	0.45				
	S	125.0	0.126	0.44				
	D	154.0	0.078	0.58				
$Ca(NO_3)_2$	S	75.0	0.244	0.55				
	S	100.0	0.171	0.47				
	S	125.0	0.126	0.44				
	D	152.0	0.078	0.64				
	b	89	0.110	1.25				
$CaSO_4$	D	182.5	0.626	0.0035	S	150.0	0.885	0.0024
	D	211.6	0.487	0.0042	S	200.0	0.683	0.0015
	D	290.9	0.280	0.0059	D	213.5	0.640	0.0014
					S	300.0	0.435	0.0013
Solvay $CaCO_3$	D	63.6	0.614	0.14	S	150.0	0.938	0.0018
	S	100	0.265	0.194	S	200.0	0.730	0.0011
	S	200	0.505	0.0047	D	232.1	0.640	0.0009
	S	300	0.396	0.0018	S	250.0	0.580	0.0009
					S	300.0	0.479	0.0008
Baker $CaCO_3$	D	116.5	0.626	0.0194	S	200.0	0.341	0.013
	D	138.4	0.487	0.0197	S	250.0	0.328	0.0067
	D	140.4	0.427	0.0253	D	254.1	0.281	0.0093
	D	212	0.28	0.0171	S	300.0	0.272	0.0057
					D	396.8	0.209	0.0041
OMYA $CaCO_3$	b	100.0	~0.55[b]	0.043				
$Ca(C_2O_4) \cdot H_2O$	D	68.6	0.363	0.32	S	100.0	0.487	0.056
	S	100.0	0.201	0.34	D	123.63	0.363	0.054
	S	125.0	0.138	0.37	D	140.28	0.363	0.036
					S	150.0	0.253	0.062
					S	200.0	0.224	0.033
$C_2O_4H_2$	S	50.0	0.449	0.54				
	D	58.6	0.363	0.52				
	S	100.0	0.176	0.44				

*Scan type: S, supersaturation scan; D, dry diameter scan.

[a] Single-parameter apparent hygroscopicity, κ_{app}, derived from CCN activation curves.

[b] Data from Gibson et al. (2006a); s_c estimated from their Figure 3.

0.013, but when atomized from aqueous solution behaves similar to sufficiently soluble inorganic compounds, with $\kappa_{app} = 0.34 \pm 0.02$.

In Figure 6.6, isolines are also included for pure $CaCO_3$ and $CaSO_4$, and their mixtures with a hygroscopic soluble contaminant with $\kappa_{intr} = 0.6$ and $C = 0.43$, representative of ammonium sulfate (and similar to calcium chloride, calcium nitrate, or oxalic acid), that take into account limited solubility (Eq. 6.4). The volume fraction of contaminant increases from right to left. Since almost no $CaCO_3$ has dissolved in all these cases, the activation lines obtained for these mixed particles are almost completely determined by the sufficiently
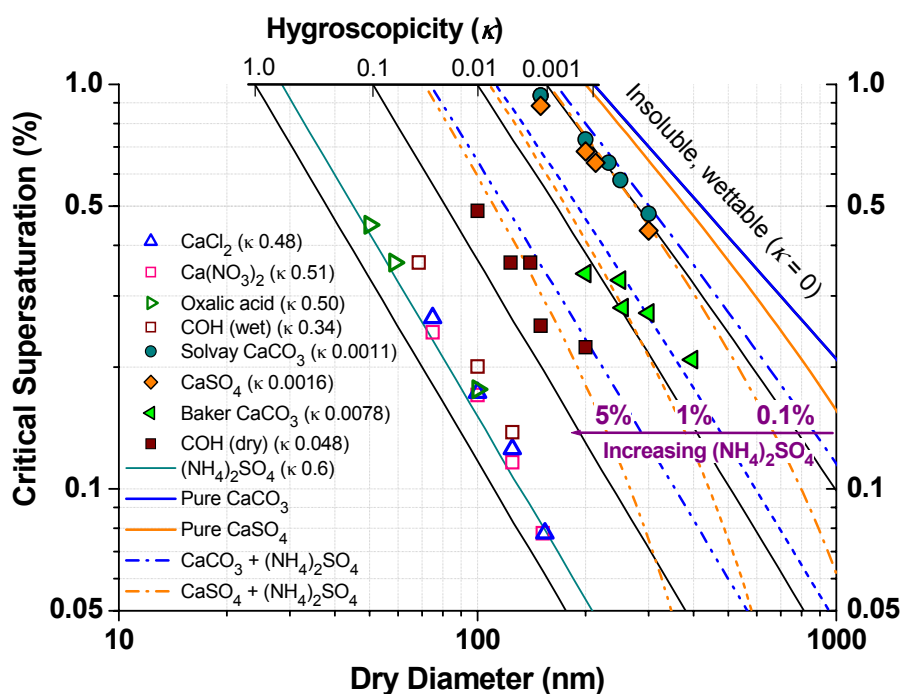
Figure 6.6. s_c-D_{dry} relationships with κ isolines overlain for dry-generated sparingly soluble calcium minerals (solid symbols) and atomized soluble salts (open symbols), and oxalate compounds from dry- and wet-generation. The best-fit κ_{app} values from Table 6.1 are also listed. Also displayed are predicted κ isolines for pure $CaCO_3$ particles (blue lines, $\kappa_{intr} = 0.97$, $C = 2.1 \times 10^{-6}$) and $CaSO_4$ particles (orange lines, $\kappa_{intr} = 0.78$, $C = 6.9 \times 10^{-4}$), and their internal mixtures (dashed lines) with varying volume fractions of ammonium sulfate ($\kappa_{intr} = 0.6$, $C = 0.43$). 100% $CaCO_3$ lies along the $\kappa = 0$ isoline, and the fraction of $(NH_4)_2SO_4$ increases from right to left. The theoretical isoline for pure $(NH_4)_2SO_4$ ($\kappa_{app} = 0.6$) is also shown.

soluble substance alone. Our measurements of dry-generated $CaCO_3$ are consistent with the presence of very small volume fractions of soluble hygroscopic material, which produce a detectable increase in the particle's hygroscopicity and a subsequent decrease in its critical supersaturation (Gibson et al., 2007; Kelly et al., 2007; Roberts et al., 2002).

6.4.3 CCN activation curves of atomized calcium minerals

Calcite aerosol has commonly been produced through the atomization of a saturated suspension of the powder in water which is then dried. Due to the very low solubility of calcite, the atomization has been assumed to cause little or no changes to the chemistry of the particles (Gibson et al., 2007). However, the CCN activation curves that are presented below indicate that in fact very large changes in the chemistry, solubility, and hygroscopicity of calcite particles can be induced when they are placed in water. These cause the larger than expected apparent hygroscopicities reported above for the atomized insoluble calcium minerals.

6.4.3.1 Solvay calcite

The calcium carbonate powder obtained from Solvay is an ultrafine uncoated powder. It was chosen because it has a very small manufacturer listed primary particle diameter of ~25 nm and therefore produces high particle concentrations (>1000 cm^{-3}) below 200 nm. It is generally very difficult to find or prepare mineral powders that produce significant particle concentrations smaller than ~250 nm, which is required for CCN studies. However, as this powder is manufactured for industrial applications, its purity (not stated) may be lower than that of the ACS reagent-grade Baker $CaCO_3(s)$; possible contaminants in the powder are investigated in a following section. A size-scan activation curve of the atomized Solvay $CaCO_3(s)$ is shown in Figure 6.7a. This curve displays very unusual and unexpected behavior, with a large decrease in the CCN/CN ratio *above* 100 nm to a local minimum. The CCN/CN
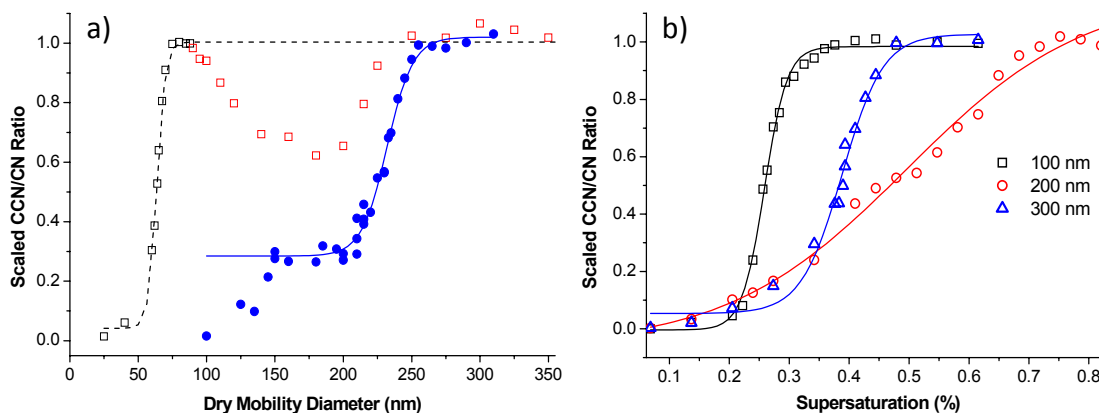
Figure 6.7. CCN activation curves for wet-generated Solvay calcium carbonate from (a) scanning size at 0.614% SS (open squares) and (b) scanning supersaturation for three dry diameters. Activation curve from size-scan of dry-generated Solvay $CaCO_3$ at 0.640% SS (solid circles) is also shown in (a) for comparison (data from Part 1). The sigmoid curve (dashed line) in (a) is fit to the black data points of 80 nm diameter and smaller.

ratio then increases again with larger particle size to a second maximum plateau. This behavior was observed in three separate experiments. This appears to be the result of the superposition of two separate activation curves from two very different systems: a very hygroscopic system at small particle sizes < 80 nm, and a much less hygroscopic system at larger sizes. The second activation curve that occurs for sizes > 200 nm is similar to that previously obtained from dry-generation of the Solvay $CaCO_3$ (solid symbols in Fig. 6.7a), but somewhat more hygroscopic.

The three major regions of the size-scan in Figure 6.7a (100, 200, and 300 nm) were size selected for SS-scans to determine the critical supersaturation (s_c) of each size (Fig. 6.7b). The curves have very different slopes and critical supersaturations. The 100 nm mode, corresponding to the first maximum in Fig. 6.7a, has the smallest critical supersaturation (0.265%) and the steepest curve. The activation curve for 100 nm particles lies to the left of both the 200 nm and 300 nm curves. The critical supersaturations for 200 nm (0.505%) and 300 nm (0.396%) particles are both <u>larger</u> than for 100 nm, which is very unusual. In a chemically homogenous aerosol population the critical supersaturation should decrease with

increasing particle size. s_c of the 300 nm mode is smaller than the 200 nm mode, as would be expected for a well-behaved system. When compared to the dry-generated Solvay results, the critical supersaturation of the wet generated 200 nm particles is significantly smaller (0.505% compared to 0.730%) while the difference for 300 nm particles is less (0.396% versus 0.479% for wet and dry, respectively) (Table 6.1). While the atomized Solvay CaCO$_3$ particles did not display a constant hygroscopicity versus size, the < 100 nm particles can be described by κ_{app} ~0.1-0.2, while the > 200 nm particles correspond to κ_{app} ~0.002-0.005 and approach that of dry-generated Solvay CaCO$_3$ (κ_{app} = 0.0011 ± 0.0004) .

6.4.3.2 *Baker calcite*

The CCN properties of another calcite powder, from J.T. Baker, were also studied. This high purity powder (99.9%) is coarser than the Solvay powder, with an average particle diameter of ~25 μm. CCN activation curves obtained for the Baker CaCO$_3$ display much different behavior than the Solvay CaCO$_3$. Activation curves for wet-generated Baker CaCO$_3$ at three different SS are shown in Figure 6.8 from size scans. These activation curves lack the
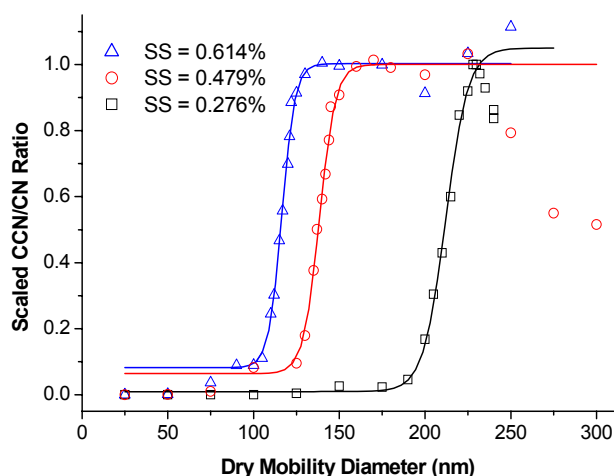
Figure 6.8. CCN activation curves for wet-generated Baker calcium carbonate from size scans of "fresh" Baker calcium carbonate just added to water at three different supersaturations.

unusual shape produced by the Solvay $CaCO_3$ (Fig. 6.7a), though the CCN/CN ratio does decrease for particle sizes larger than ~225 nm for the 0.28% and 0.48% SS cases. However, the total CN counts were very low (< 20 particles/cm^3) at sizes larger than 200 nm and thus this observation has a larger degree of uncertainty and could not be explored further.

The hygroscopicity of wet-generated Baker $CaCO_3$ ($\kappa = 0.020 \pm 0.0035$) is significantly larger than those produced by dry-generation ($\kappa = 0.0078 \pm 0.0036$), and was also observed to dramatically increase as the Baker calcite powder continued to sit in water. This was confirmed by measuring repeated CCN activation curves of the same Baker $CaCO_3$
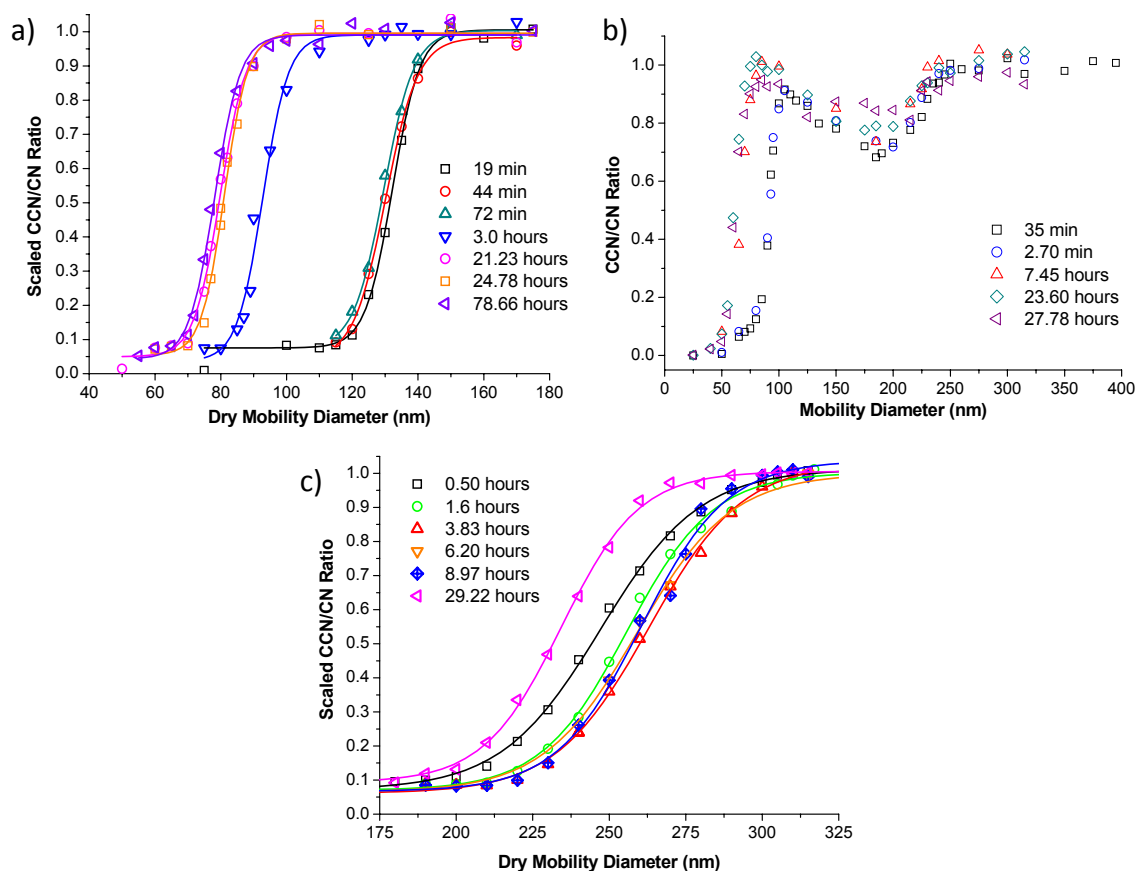
Fi**gure 6.9.** Repeated CCN activation curves via size scans of (a) atomized Baker $CaCO_3$ powder at 0.427% SS, (b) atomized Solvay $CaCO_3$ at 0.640% SS, and (c) atomized $CaSO_4$ at 0.427% SS, as they continued to sit in water. The time is the midpoint of the CCN scan after the powder was first added to water.

sample as it continued to be atomized from a suspension in water. Size scans were employed as they are faster than SS scans, they are shown in Figure 6.9a. The black points and line is for the first activation scan, started a few minutes after the dry powder was placed in water. A stir bar was used to resuspend any powder that had settled out and a constant flow of 3.0 lpm $N_2(g)$ was used for atomization during the scan. Calcite has a solubility of 0.0058 g/L (Plummer and Busenberg, 1982) while the solution used was 0.333 g/L and solid powder was observed to remain for both $CaCO_3$ powders for at least several days after the powder was added to water. Figure 6.9a clearly shows the activation curve for Baker $CaCO_3(s)$ shifted to the left (smaller critical dry diameter) with time spent in water. The critical dry diameter of the first scan was determined to be 132.0 nm at 0.427% SS, while that after 78 hours was 78.2 nm. The shift appears to maximize after ~21 hours, with no further large shifts exhibited, and corresponds to κ_{app} ~0.16.

Similar repeated CCN scans were also performed for Solvay $CaCO_3$ powder as it sat in water (Fig. 6.9b). In this case the more-hygroscopic sub-100 nm particles became significantly more hygroscopic over time by shifting to smaller activation diameters. The super-100 nm particles, however, did not display any significant systematic shifts with time.

6.4.3.3 Calcium sulfate

Calcium sulfate particles were also generated by atomization from water. At a concentration of 0.050 g powder in 150 mL water (0.333 g/L) the solution is below the solubility limit of $CaSO_4$ (2.05 g/L) and the powder was observed to completely dissolve in the water after several minutes. The aqueous particles were subsequently dried to < 5% RH before being size-selected. Unlike the wet-generated calcite powders, atomized $CaSO_4$ particles were not significantly more hygroscopic when dry-generated. The s_c-D_{dry} relationships indicate that these particles have relatively low hygroscopicity with $\kappa_{app} = 0.0045$

± 0.0012 for wet-generated and κ_{app} = 0.0016 ± 0.0005 for dry-generated $CaSO_4$ (Table 6.1). The activation curves of wet-generated calcium sulfate displayed no unusual behavior (Fig. 6.9c), unlike the wet-generated calcium carbonate particles. Although there are shifts in the curves with time their magnitude is much smaller than that observed for the wet-generated Baker $CaCO_3$. There is also no clear systematic shift to smaller activation diameters for $CaSO_4$. The initial activation diameter of atomized $CaSO_4$ was 247.1 nm at 0.427% SS. All the scans up to 8 hours after the $CaSO_4$ powder was added to water had slightly larger activation diameters, up to 263.0 nm. The scan after 29 hours was the only one with a smaller activation diameter of 234.4 nm. The temporal variations in the activation diameters are likely not due to fluctuations in the CCNc's column SS. Repeated size scans of atomized highly soluble calcium nitrate particles at 0.407% SS produced virtually identical activation curves with D_{ca} = 53.54 ± 0.25 nm (1σ) from 4 scans. Therefore, a conservative estimate in the precision of the CCNc is D_{ca} ± 0.50 nm (2σ), which is much smaller than the variation displayed in Figure 6.9.

The observed changes in particle hygroscopicity induced when low solubility calcium minerals particles are produced by atomization from water are compared in s_c-D_{dry} space in Figure 6.10. Measurements of dry-generated Solvay $CaCO_3$ particles are also displayed for comparison. The s_c-D_{dry} pairs from the highly CCN-active sub-100 nm wet-generated Solvay $CaCO_3$ particles are nearly as hygroscopic as the very hygroscopic soluble calcium nitrate and chloride particles, corresponding to κ_{app} ~0.1-0.2. The larger diameter Solvay $CaCO_3$ pairs, however, are orders of magnitude less hygroscopic and approach the κ_{app} = 0.001 isoline that the dry-generated Solvay $CaCO_3$ lies along. This indicates that there are two very different chemical systems present in the atomized Solvay $CaCO_3$ aerosol and that their relative abundance changes dramatically as a function of particle size. Fresh atomized Baker $CaCO_3$
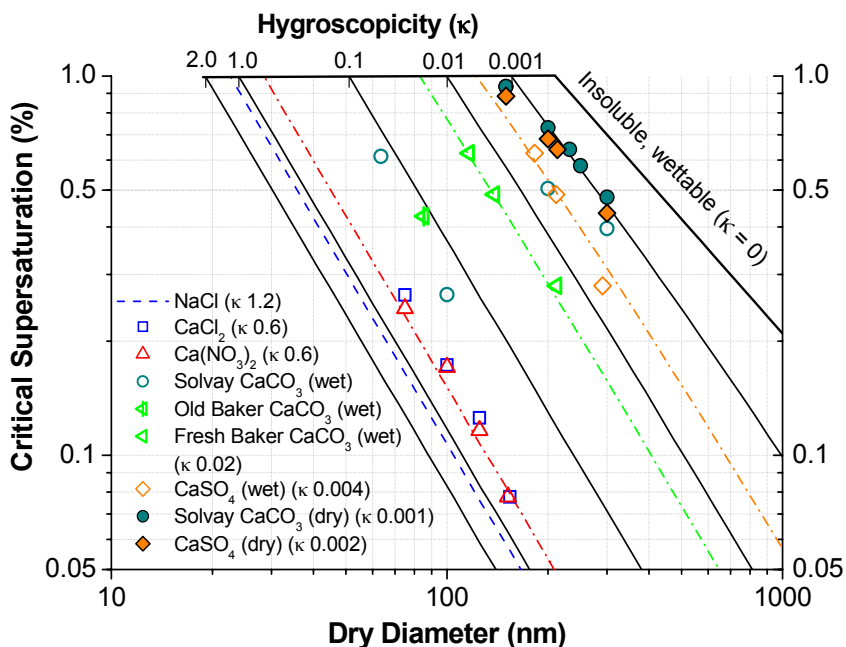
Figure 6.10. s_c-D_{dry} relationships with κ isolines overlain for dry-generated (solid symbols) and wet-generated (open symbols) calcium minerals. "Fresh" Baker CaCO$_3$ refers to powder just added to water while "old" Baker CaCO$_3$ is a sample of powder that had been in water for over 3 days. Dashed lines correspond to κ isolines that best fit the associated data points as listed in the legend.

particles had a consistent hygroscopicity of $\kappa_{app} = 0.020 \pm 0.0035$, compared to $\kappa_{app} = 0.0078 \pm 0.0072$ for dry-generated particles. However, the atomized particle's hygroscopicity increased up to $\kappa_{app} \sim 0.16$ after the Baker CaCO$_3$ powder had been in water for 24 hours. Atomized CaSO$_4$ was only slightly more hygroscopic than dry-generated CaSO$_4$, with $\kappa_{app} = 0.0045 \pm 0.0012$ versus $\kappa_{app} = 0.0016 \pm 0.0005$, respectively.

6.4.4 Characterization of calcium mineral powders and possible contaminants

Physical and chemical analysis of particles from both calcite powders was performed to determine possible causes for the unexpected hygroscopic behavior presented above. The atomized and bulk calcite particles were investigated using scanning electron microscopy (SEM) coupled with energy dispersive X-ray analysis (EDX). Single-particle analysis was also performed using an aerosol time-of-flight mass spectrometer (ATOFMS). Soluble
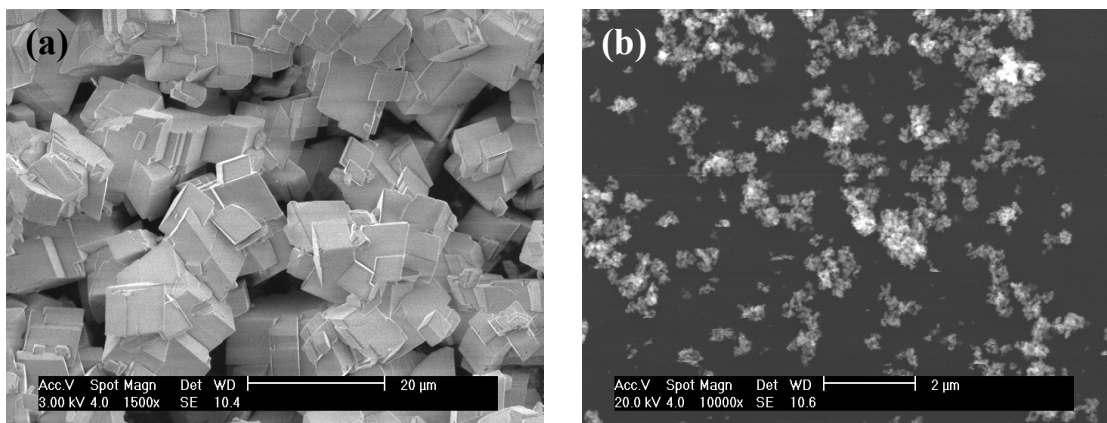
Figure 6.11. SEM images of (a) Baker and (b) Solvay dry calcite powders dispersed onto substrates. Note the different magnification and scale.

contaminants that dissolve from the powder into water were analyzed using ion chromatography (IC) and inductively-coupled plasma mass spectrometry (ICP-MS).

6.4.4.1 SEM/EDX measurements

SEM images of the bulk powders dispersed on the substrates are shown in Figure 6.11. Very large differences between the size and shape of the two calcite powders are readily evident. The Baker $CaCO_3$ powder is composed of very large, smooth crystalline particles with a relatively low surface area to volume ratio. This agrees with the manufacturer's stated average particle diameter of ~25 μm. The Solvay $CaCO_3$, however, is composed of small irregularly shaped fractal particles that are aggregates of very small nanoparticles. The small size corresponds to the stated average particle size of ~25 nm. These particles are not smooth and have a much higher surface area to volume ratio. The very different sizes and morphologies of the two calcite powders will result in the Solvay $CaCO_3$ dissolving and achieving equilibrium with the aqueous phase much faster than the Baker $CaCO_3$ will. In both powders the EDX spectra did not reveal any elements apart from Ca and O. EDX can generally detect elements in greater than 1% atomic abundance.
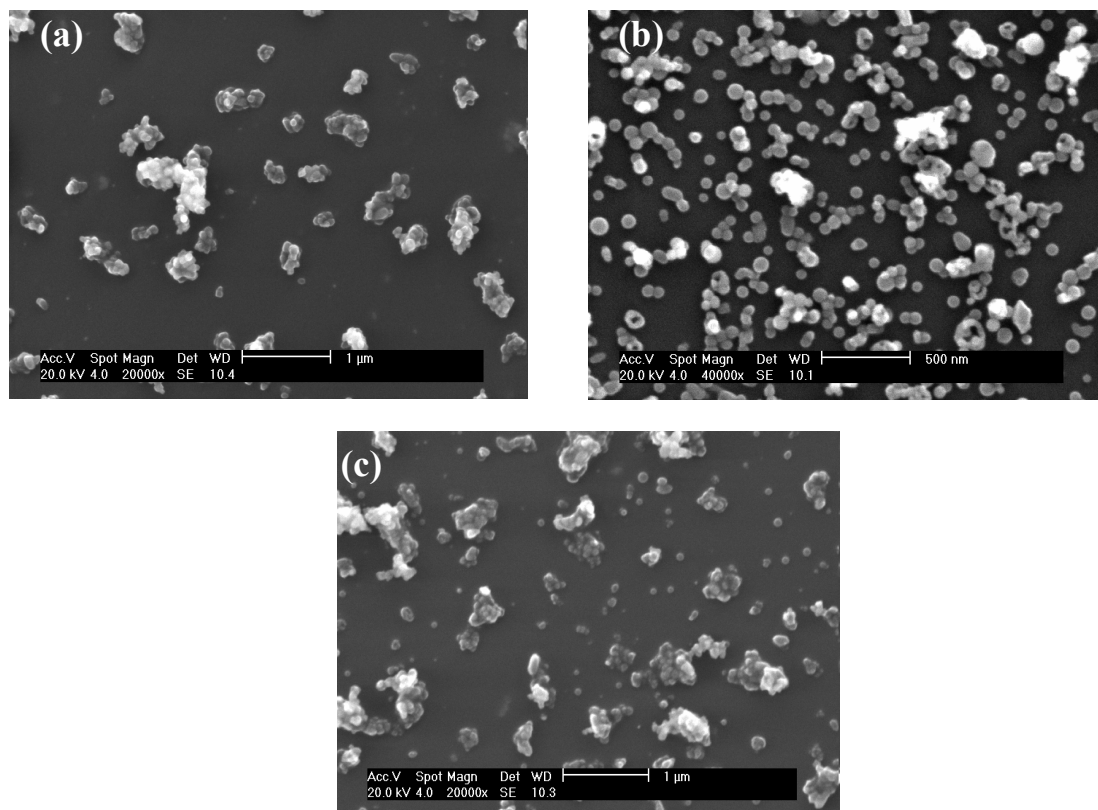
Figure 6.12. SEM images of atomized Baker calcite particles collected on substrates (a) shortly after the powder was added to water and (b) up to two hours after being added to water, and (c) atomized Solvay calcite. Note the different magnification and scale.

The size and morphology of the atomized Baker $CaCO_3$ particles was observed to change over time as the dried atomized particles were continuously deposited on the substrate. The MOUDI sampler was manually rotated during sampling to capture this behavior. Figure 6.12 displays SEM images of atomized Baker $CaCO_3$ particles from two different positions on the same TEM grid, representing particles deposited up to two hours apart. The particles in Fig. 6.12a are larger and more irregularly shaped than those collected later, shown in Fig. 6.12b, which are smaller and highly spherical. Atomized Solvay $CaCO_3$ particles were composed of a mix of larger nonspherical and smaller spherical particles (Fig. 6.12c) and this was not observed to change significantly with collection time.

6.4.4.2 Hygroscopic growth of atomized CaCO₃ from ESEM analysis

The hygroscopic properties of atomized Baker CaCO$_3$ particles collected on substrates was also investigated using environmental SEM (ESEM) analysis by exposing the particles to increasingly higher RH. The changes in the particle's morphology are shown in Figure 6.13. Above ~95% RH the atomized Baker CaCO$_3$ particles are observed to absorb water and become more spherical as the particles are continuously exposed to RH ~98-100%. Eventually the stage absorbs multilayers of water and becomes flooded, however the CaCO$_3$ particles are not observed to completely dissolve at this point.

The hygroscopic behavior of the newly formed particles with round morphology was probed in an ESEM experiment. Figure 6.13 shows the microscopy images of these particles
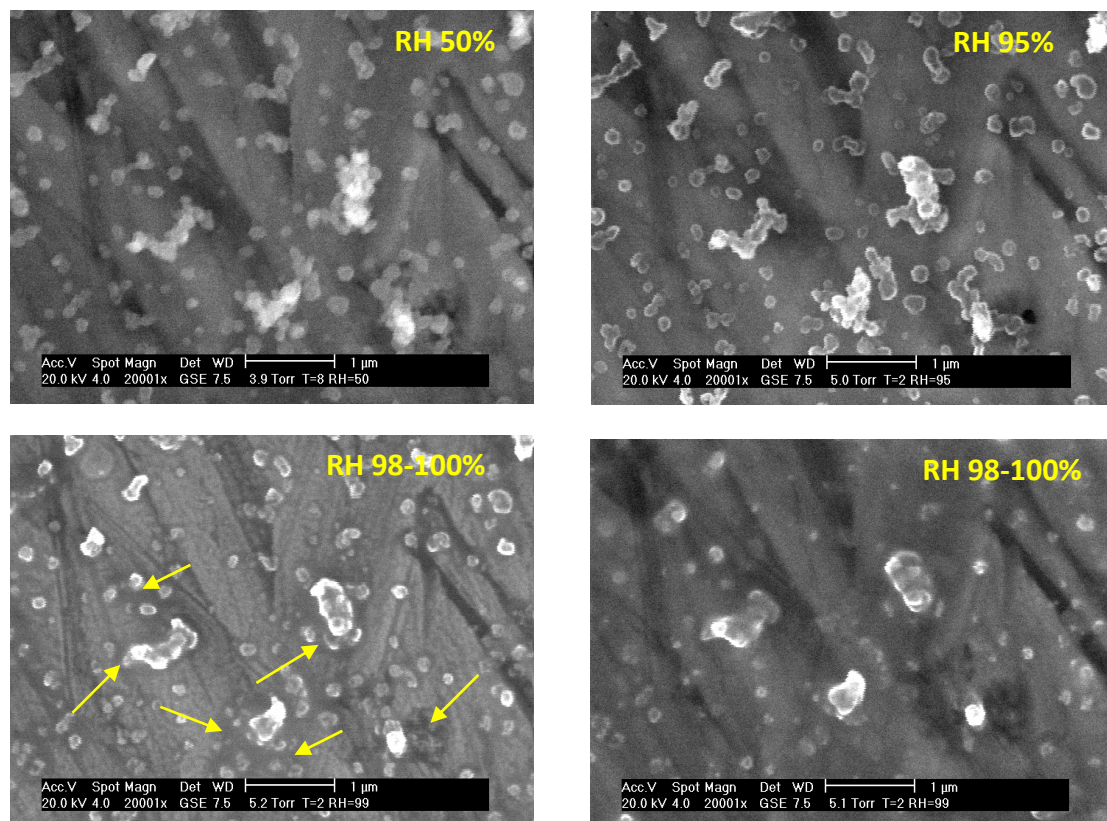
Figure 6.13. ESEM images of newly formed spherical particles produced in atomization of the Baker CaCO$_3$ powder suspended in water. Images are taken at increasing relative humidity of 50%, 95% and approaching 100% RH, respectively. Arrows point to observed initial morphology changes at 98-100% RH.

captured at different RH. The two images taken at 50% and 95% RH are nearly identical and indicate no visible changes in particle morphology. The changes in particle morphology are observed at 98-100% RH which are initially evident by the blurring and ''melting'' of particle edges as indicated by arrows in the corresponding image. At that point, capturing of the sample image becomes highly unstable and within a few moments instant activation and unrestrained, spontaneous growth of water over the particles has been revealed by quick disappearance of particle images and blurring of the entire field–of-view area. This ESEM experiment indicates that the new spherical particles exhibit hygroscopic properties of "sparingly soluble material" and activate at some apparent hygroscopicity (κ_{app}), albeit lower than that characteristic for soluble inorganic salt particles with distinct deliquescence points. This observation is consistent with the CCN measurements presented and discussed above that can be explained now by the apparent hygroscopicity of the newly formed particles.

6.4.4.3 ATOFMS single-particle analysis

The chemical composition of individual calcite aerosol particles was analyzed by single-particle mass spectrometry performed with an UF-ATOFMS. Particles from both wet and dry-generation were analyzed. No clear indications of soluble contaminants such as inorganic salts were observed in the mass spectrum of either powder. The mass spectra of wet and dry-generated particles were also very similar. Examples of mass spectra obtained from wet-and dry-generated Solvay $CaCO_3$ particles are shown in Figure 6.14. The dry-generated particle spectrum is dominated by ions from Ca, Mg, and Al compounds that are commonly observed in mineral dust particles analyzed by ATOFMS (Chapter 3). $CaCO_3$ cannot be directly observed by this method as it undergoes the following decomposition after ionization: $[CaCO_3]^+ \rightarrow [CaO]^+ + CO_2(g)$. $CaCO_3$ is therefore indirectly observed via the dominant Ca^+, CaO^+, $CaOH^+$, and Ca_2O^+ ions evident in Fig. 6.14. The Mg peak is likely from dolomite
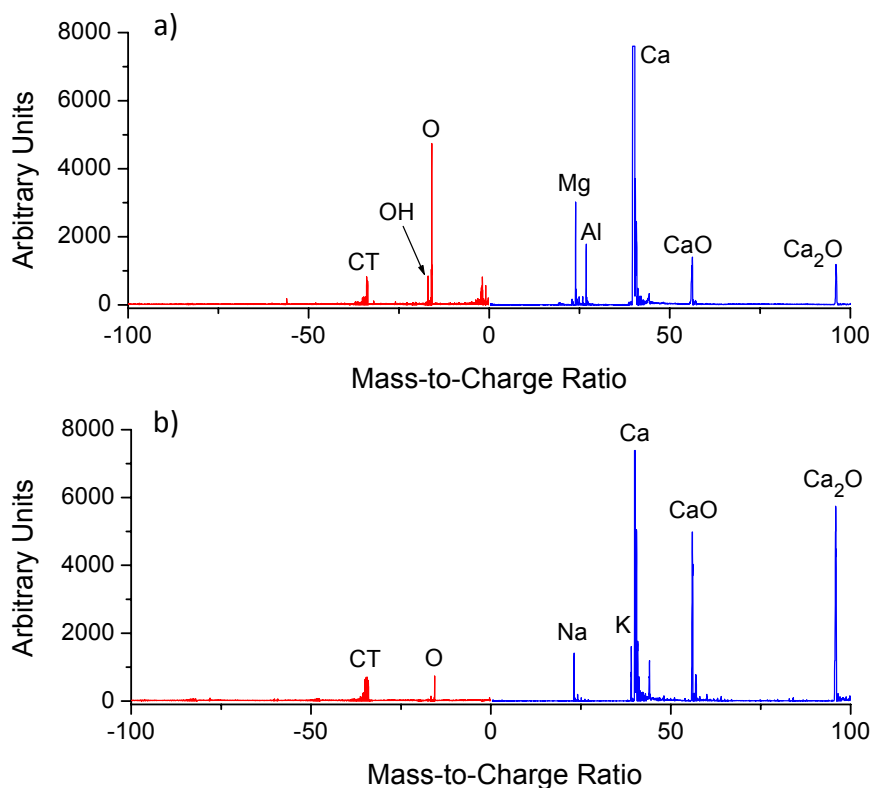
Figure 6.14. Single-particle dual-polarity UF-ATOMFS mass spectrum of mobility diameter selected (a) 150 nm dry-generated and (b) 200 nm atomized Solvay $CaCO_3$ particles. Likely peak identities are listed. Crosstalk (CT) indicates interference from intense ion signals from the positive ion channel and should be ignored.

$(MgCa(CO_3)_2)$. Note that similar features were observed in the ICP-MS analysis of the dissolved Solvay calcite powder, discussed below. The small ion signals from Na^+ and K^+ in the atomized particle spectrum and indicate small amounts of contaminants either present in the original powder or that become added to the particles during sample preparation and particle generation. The poorly-resolved peaks in the negative ion spectra marked "crosstalk" are caused by intense positive ion signals interfering with the negative ion detector and should be ignored. It is important to note that apart from very small signals from Na^+ and K^+ that there are no indications that the particles contain significant amounts of soluble contaminants such as inorganic salts (e.g. $NaCl$, KNO_3, Na_2SO_4, etc.). The ATOFMS is generally highly

sensitive to inorganic salts due to the cations' low ionization energies and anions' high electron affinities. Trace amounts of soluble carbonates including Na_2CO_3 and K_2CO_3 are possibilities. Similar features were observed for Baker calcite particles but these were dominated by $CaCO_3$ fragments and contained much smaller peaks from Mg and Al compounds.

6.4.4.4 Soluble contaminants

The atomic composition of soluble material in the bulk calcite powders measured using ICP-MS is listed in Table 6.3. As expected, calcium is the dominant soluble element. The Solvay calcite also produced appreciable amounts of magnesium, likely from dissolved dolomite $(CaMg(CO_3)_2)$. The small amount of Na is presumably from inorganic salts such as Na_2SO_4, NaCl, or Na_2CO_3. The Baker calcite extract contained only calcium and a very small amount of magnesium, as expected for this higher purity chemical. The compositions of the solutions after the powder was dissolved by concentrated nitric acid are very similar to the aqueous extracts. For both the acidified Solvay and Baker calcite samples, the concentration of

Table 6.3. Concentration of elements (mg/L) in aqueous extracts of calcite powders determined by ICP-MS.

Element	Powder suspended in H_2O		Powder suspended in H_2O/HNO_3	
	Baker	*Solvay*	*Baker*	*Solvay*
Al	0	0.208	0.06	1.136
Br	0.006	0.001	0.011	0.012
Ca	4.536	4.14	1611.523	1780.384
Cl	0	0	0	0
Fe	0	0	0	0.908
K	0	0.046	0	0
Mg	0.006	2.087	0.179	12.867
Mn	0	0	0	0.055
Na	0	0.773	0.004	1.682
P	0	0	0	0
S	0	0	0	0
Si	0	0.237	2.857	1.627
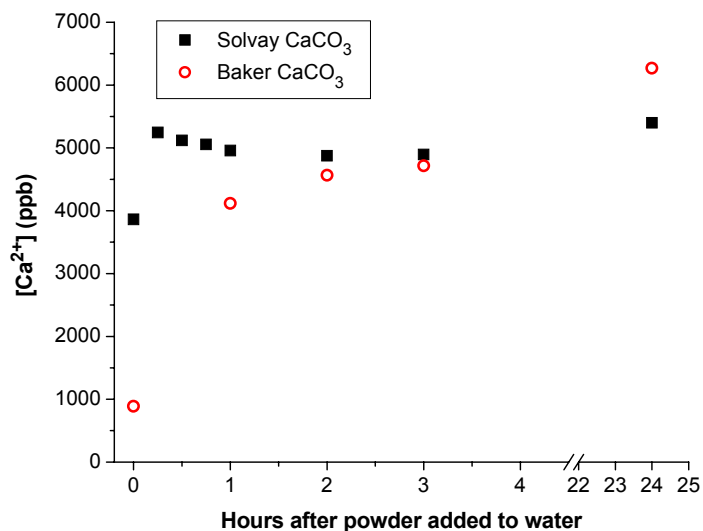
Figure 6.15. Concentration of dissolved calcium ions as the Solvay and Baker $CaCO_3$ powder were left in water. Note the break in the x-axis scale.

Ca is at least 100 times that of Mg and more than 1000 times greater than the concentration of the other measured elements, Na, Fe, Al, Si, and K. Therefore, the bulk compositions of both calcite powders is at least 99% $CaCO_3$, however the Solvay calcite contained more dissolved elements in its unacidifed aqueous extract.

The aqueous extracts of both calcite powders as they were atomized with nitrogen gas were also measured over time using IC to determine soluble cations and anions. The concentration of Ca^{2+} in the aqueous extracts over time is shown in Figure 6.15. As expected, the concentration of Ca^{2+} increased over time as more of the calcite dissolved while the system approached equilibrium. However, the rate at which $[Ca^{2+}]$ increased was much faster for Solvay $CaCO_3$ compared to Baker $CaCO_3$. The Solvay Ca^{2+} concentration stabilized in less than one hour while the Baker $CaCO_3$'s Ca^{2+} concentration had continued to increase up to 24 hours after the powder was added to water.

6.4.5 CCN activation of dry-generated calcite after exposure to water vapor

Solvay calcite particles were dry-generated and then exposed to water vapor with humidified nitrogen gas in a small flow tube for ~5 seconds. The particles were then sent through three diffusion driers before the CCN activation curve was measured. Figure 6.16 displays activation curves after the dry 200nm calcite particles were exposed to 47% and 72% RH, compared to no water vapor exposure. Clear shifts to more active particles with smaller critical supersaturations are evident as the RH is increased. Analysis of the humidified particles via ATOFMS revealed no changes in the particle's mass spectrum from the addition of contaminants.

6.4.6 Changes induced by atomization from water: hydrate formation

Large increases in the hygroscopicity of calcite particles were observed when atomized from water. These changes were found to vary with particle size (Solvay calcite) and
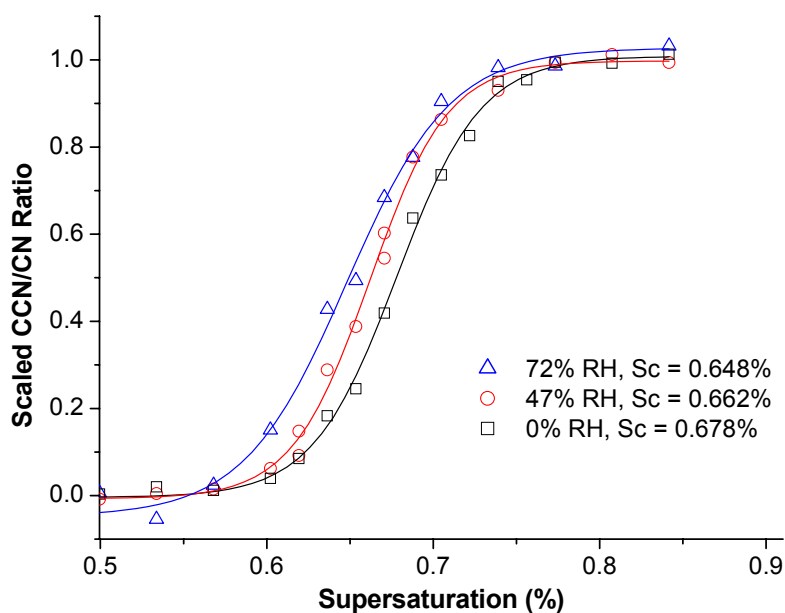
Figure 6.16. CCN activation curves of 200 nm dry-generated Solvay calcite particles after exposure to varying relative humidity for less than 5 seconds. Each curve has been rescaled so they all span the same y-axis range.

time spent in water (Baker calcite). In all cases the atomized calcite particles were more hygroscopic than those produced using dry-generation. Particles generated by atomization can have soluble substances that dissolve from the bulk material concentrate on the smaller particles due to a smaller initial particle core to droplet volume ratio when atomized. Koehler et al. (2007) observed this behavior when dust from Owen's (dry) lake was atomized versus generated dry and also for atomized Arizona test dust (Koehler, 2007). In both cases placing the dust samples in water caused the particles to be more homogenous and have much higher hygroscopicity, similar to inorganic salts such as sodium sulfate and ammonium sulfate. This was presumably caused by soluble components present in a fraction of the heterogeneous dust particles dissolving and then being distributed across all the particles contained in the droplets when the solution was atomized. We expected to find that the atomization process introduced increased amounts of soluble inorganic salts such as NaCl to the wet-generated calcite particles and that this might explain some of the behavior we observed. However, the analysis of the soluble fractions and bulk calcite powders with a variety of methods described above did not reveal any significant amounts of soluble contaminants in the bulk powders or atomized particles that would explain this behavior. The atomized Solvay and aged Baker CaCO$_3$ particles with κ_{app} ~0.1 would require the presence of > 15% by volume soluble hygroscopic contaminant with κ_{app} = 0.60. This large degree of contamination was not observed in any of the single-particle or bulk analysis described above. Therefore, another mechanism is presumably the cause of the increased hygroscopicity.

The hygroscopicity changes resulting from atomization are likely the result of secondary aqueous chemistry involving sparingly soluble calcium carbonate itself. Calcite has a very low solubility (0.0058 g L^{-1}) (Plummer and Busenberg, 1982) and therefore a small but

non-negligible fraction of $CaCO_3$ is expected to dissolve when the powder is placed in water. Multiphase reactions involving $CaCO_3$ can also take place, including:

$$CaCO_3(s) + CO_2(aq) + H_2O \rightleftharpoons 2\ Ca(HCO_3)_2(aq) \qquad \text{(R6.1)}$$

$$CaCO_3(s) + H_2O \rightleftharpoons Ca(OH)_2(aq) + CO_2(aq) \qquad \text{(R6.2)}$$
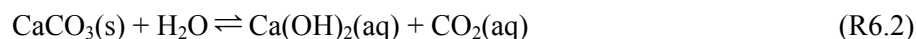
The milli-Q water used in these experiments is stored in a large container and replaced weekly. Therefore the water will have contained $CO_2(aq)$ from dissolved atmospheric $CO_2(g)$ to promote R6.1. Dissolution of $CO_2(g)$ will also cause the water to be slightly acidic, down to a pH of ~5.6 if fully equilibrated with atmospheric $CO_2(g)$. Reactions R6.1 and R6.2 (and others), in addition to the initial acidity of the water, will all lead to further dissolution of $CaCO_3(s)$.

The atomized droplets would thus have been a mixture of any small (submicron) original calcite powder particles plus $CaCO_3(aq)$, $Ca(HCO_3)_2(aq)$, $Ca(OH)_2(aq)$ and their dissociated ions. After atomization the particles experienced rapid drying in a series of three silica gel diffusion driers. This method is assumed to produce dry $CaCO_3(s)$ particles. Based on the CCN results and the possible multiphase chemistry discussed above we propose that the particles produced are in fact a mixture of original primary calcite plus secondary calcium carbonate hydrates. These hydrates form during the rapid particle drying process and may be solid or possibly exist in a metastable liquid state. Note that calcium bicarbonate, $Ca(HCO_3)_2$, is only stable in the aqueous phase and is therefore not expected to be present if the dried particles effloresce. Calcium hydroxide, however, is a likely component of the dried atomized particles.

Calcium carbonate can precipitate in six known forms, three metastable hydrates and three anhydrous polymorphs. Their properties are summarized in Table 6.4. In order of increasing stability and thus decreasing solubility, they are: amorphous calcium carbonate,

Table 6.4. Properties of known forms of calcium carbonate.

Form	Formula	pK$_{sp}$ (25°C)	C^b	Appearance
Calcite	$CaCO_3$	8.480[1]	2.14x10^{-6}	rhombohedral crystals
Aragonite	$CaCO_3$	8.336[1]	2.53x10^{-6}	rhombohedral crystals
Vaterite	$CaCO_3$	7.913[1]	4.11x10^{-6}	supermicron spherulites
Monohydrocalcite	$CaCO_3 \cdot H_2O$	7.212[2]	1.09x10^{-5}	supermicron spheres
Ikaite	$CaCO_3 \cdot 6H_2O$	6.779[3]	3.14x10^{-5}	rhombohedral crystals
Amorphous	$CaCO_3 \cdot 1H_2O^a$	6.393[4]	2.79x10^{-5}	non-crystalline submicron spheres
	$CaCO_3 \cdot 20H_2O^a$	6.393[4]	1.08x10^{-4}	

Sources: [1](Plummer and Busenberg, 1982), [2](Brecevic and Nielsen, 1993), [3](Kralj and Brecevic, 1995), [4](Brecevic and Nielsen, 1989).
[a]Number of water molecules in amorphous $CaCO_3$ is not known, thus two cases are estimated.
[b]Solubility in volume solute per unit volume water, following Petters & Kreidenweis (2008). Density = 2.71 used in all cases.

calcium carbonate hexahydrate (ikaite), calcium carbonate monohydrate (monohydrocalcite), vaterite, aragonite, and calcite (Brecevic and Kralj, 2007; Kralj and Brecevic, 1995; Plummer and Busenberg, 1982). The first three are metastable hydrates while the last three are anhydrous polymorphs. Calcite is the most stable and dominant form at the Earth's surface conditions. In general, the least stable amorphous calcium carbonate precipitates first from a supersaturated solution, and then converts in succession through the more stable hydrates and then polymorphs (Brecevic and Kralj, 2007). The dominant $CaCO_3$ form that precipitates can be strongly influenced by the presence of other metals (magnesium in particular), sea water, and organic compounds, for example (Brecevic and Kralj, 2007). Brooks et al. (1950) found that the formation of metastable calcium carbonate phases was promoted by increasing the rate of precipitation. Amorphous calcium carbonate and calcium carbonate hexahydrate precipitate as spherical crystals. Vaterite particles are also spherules and irreversibly convert to the more

stable polymorphs, aragonite at high temperatures and calcite at lower temperatures, when in contact with water. Calcium carbonate monohydrate, aragonite, and calcite form non-spherical crystalline precipitates (Brecevic and Kralj, 2007).

As the droplets atomized from the calcite solution are rapidly dried in the diffusion driers they will become highly supersaturated in $CaCO_3$(aq), thus promoting precipitation of solid phases of $CaCO_3$(s). Extensive research into the factors and mechanisms that control the precipitation process has indicated that they are a strong function of precipitation rate, thermodynamic conditions, and concentrations of other compounds. As the precipitation conditions experienced by the $CaCO_3$(aq) droplets are not readily comparable to those commonly reported in the literature we can only speculate as to the form of the solid calcium carbonate phase that was produced. Since the metastable hydrates form first during precipitation, and their production is favored by fast precipitation rates (Brecevic and Kralj, 2007; Brooks et al., 1950) it is reasonable to assume that the particles were largely composed of metastable calcium carbonate hydrates. While the hydrates, and vaterite, are quickly converted to the stable aragonite and calcite anhydrous polymorphs, the rapid drying process may have removed the water required for this conversion to take place at these timescales. The spherical morphology of the atomized Baker $CaCO_3$ also suggests that metastable hydrates and/or vaterite were the dominant forms. Finally, the increased apparent hygroscopicity of the atomized $CaCO_3$ particles is best explained by the increased solubility of $CaCO_3$; the metastable hydrates and vaterite are all more soluble than calcite (Table 6.4) (Brecevic and Kralj, 2007).

6.4.7   Production of secondary $CaCO_3$ particles via atomization

The particles diameters studied here for CCN activation are typically smaller than 300 nm. The sizes of the original particles in the Baker calcite powder are much larger, ~25 μm. It
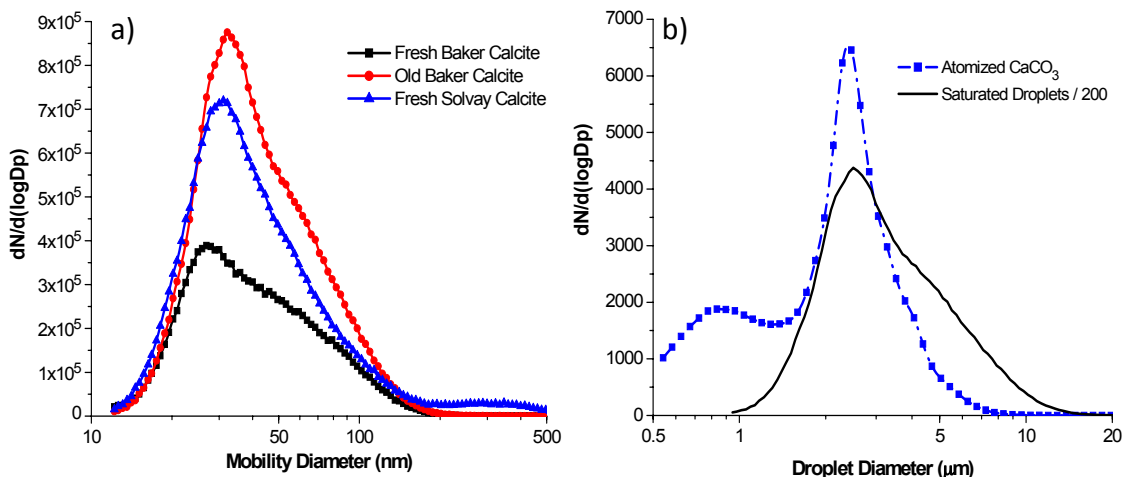
Figure 6.17. (a) SMPS size distributions of dried atomized Baker calcite powder just added to water ("Fresh") and that had been in water for 24 hours ("Old"), and Fresh Solvay calcite. (b) APS size distribution of wet atomized droplets from Old Baker calcite solution (blue dashed line and squares) and calculated size distribution of saturated $CaCO_3(aq)$ droplets required to produce the dried Old Baker calcite spectrum in (a) (solid black line).

is doubtful that there are significant concentrations of submicron particles in the Baker powder to produce the observed particle concentrations when the powder is atomized. The atomized particles are thus likely the result of secondary compounds which formed from the precipitation of dissolved $CaCO_3$ and other compounds, as discussed above, during the atomization and particle drying process. However, given the very low solubility of $CaCO_3$ the original atomized droplet would need to be significantly large to contain enough dissolved solute to produce the dried submicron residual particles. To test this hypothesis the size distribution of dried atomized Baker calcite particles was compared to the size distribution of the atomized droplets before drying. These are shown in Figure 6.17. The size of a saturated atomized $CaCO_3(aq)$ droplet required to produce each SMPS size bin of the dried calcite aerosol after the droplet has been completely dried was also calculated using simple solubility limitations for calcite (0.0058 g L^{-1}), the result is also shown in Figure 6.17b. The overlap between the calculated size distribution of the atomized droplets from the dried residual

aerosol and the actual size distribution of the atomized droplets is excellent. This confirms that the atomized droplets were large enough to produce the observed dried Baker calcite aerosol if the droplet residual is composed entirely of dissolved $CaCO_3$. Therefore, it is possible that the atomized Baker $CaCO_3$ particles in fact contained no original primary calcite particles and that they are completely composed of secondary calcium carbonates (metastable hydrates and vaterite) that formed during the particle atomization and drying process. Note that the size distribution of the atomized Baker $CaCO_3$ also narrows and the particle concentration increases as the powder ages in the water.

6.4.8 Effect of increased solubility on CCN activation of $CaCO_3$ aerosol

The decrease in the critical supersaturation of size-selected $CaCO_3$ particles induced by the formation of more soluble metastable hydrates was predicted using κ-Köhler theory that accounts for a compound's limited solubility (Eq. 6.3-6.4) (Petters and Kreidenweis, 2008). The inputs used were D_{dry} = 200 nm, κ_{intr} = 1.0 (for dissolved $CaCO_3$), and the solubility of $CaCO_3$, C, was varied between 2.14×10^{-6} and 1.08×10^{-4} volume solute/volume water based on the published solubilities of the six known forms of $CaCO_3$ (Table 6.4). In the case of amorphous $CaCO_3$ the number of water molecules associated with this form, n, is not known and thus $n = 1$ and $n = 20$ were both used. Figure 6.18 displays the predicted critical supersaturation of $CaCO_3$ for this range of solubility. Even though the solubility spans four orders of magnitude, s_c is only reduced from 1.055% for calcite (least soluble), to 1.044% for amorphous $CaCO_3 \cdot 20H_2O$ (most soluble). Figure 6.18 indicates that s_c only begins to significantly decrease for $C > 10^{-3}$, which is 10 times more soluble than the most soluble known metastable hydrate. Figure 6.2 demonstrates how a compound's solubility only has a large effect on the particle's apparent hygroscopicity over a narrow range of C. For C smaller than this range the particle activates as though it is completely insoluble ($\kappa_{app} = 0$), according
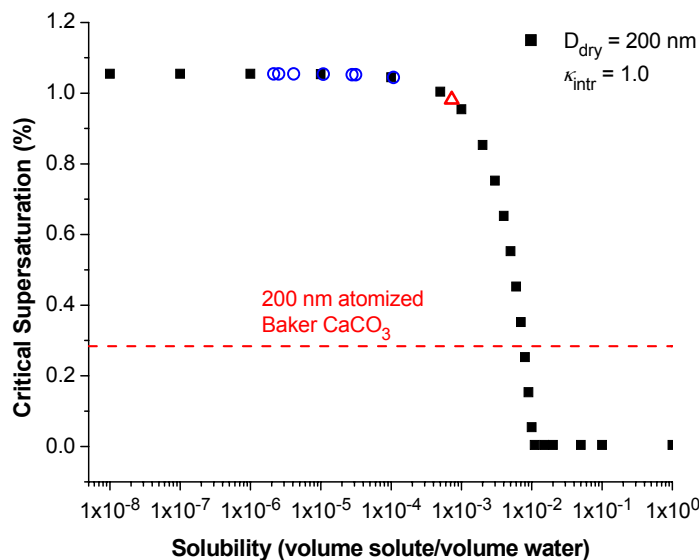
Figure 6.18. Predicted s_c from κ-Köhler theory for calcium carbonate as a function of solubility. $D_{dry} = 200$ nm and $\kappa_{intr} = 1.0$ for dissolved $CaCO_3(aq)$. Open blue circles correspond to the published solubilities of the six known forms of calcium carbonate and the red triangle that of $Ca(OH)_2$. The dashed line corresponds to s_c of a 200 nm atomized fresh Baker $CaCO_3$ particle ($\kappa_{app} = 0.020 \pm 0.0035$).

to its deliquescence-limited s_c. For *C* larger than this range the particle behaves as if completely soluble and dissolved, and its apparent hygroscopicity comes close to its intrinsic hygroscopicity, i.e. that of a completely soluble particle as predicted by traditional Köhler theory.

The dashed line in Figure 6.18 represents the s_c (0.284%) of a 200 nm fresh atomized Baker $CaCO_3$ particle based on its experimentally measured apparent hygroscopicity, $\kappa_{app} = 0.020 \pm 0.0035$. This critical supersaturation is well below that predicted using the known solubilities of the various metastable hydrates. Therefore, the increased solubility produced by the formation of the metastable hydrates is not sufficient to produce the observed decrease in the critical supersaturation of atomized Baker $CaCO_3$ and the subsequent increase in hygroscopicity. Theory predicts that the solubility of amorphous $CaCO_3 \cdot 20\,H_2O$ would still be too low to remove the deliquescence-limit to activation. It is possible that the published

solubilities do not accurately describe the metastable hydrates that form in the atomized and dried particles. These compounds are formed under very different conditions then those used in the published literature. Given the variable structure and water content of *amorphous* $CaCO_3$ it is reasonable to assume that the metastable hydrates that formed in our experiments are more soluble than those produced under different conditions. If the atomized particles did not completely effloresce during particle drying and contained some liquid-state compounds, these would also cause an increased apparent hygroscopicity. ESEM analysis demonstrated that aged atomized Baker $CaCO_3$ particles partially dissolved near 98% RH, supporting an increased particle solubility. $Ca(OH)_2$ may also have formed in the atomized particles and it is more soluble than calcite (1.60 g/L vs. 0.00058 g/L). The predicted s_c of 200 nm $Ca(OH)_2$ is also shown in Figure 6.18 and is still too high to explain the observations.

Wet-generated calcite particles displayed significantly different hygroscopic behavior than when dry-generated (Fig. 6.10). The very hygroscopic sub-100 nm Solvay $CaCO_3$ particles are attributed to the production of metastable calcium carbonate hydrates formed by precipitation. These hydrates are much more soluble than the nearly insoluble original calcite particles and thus produce highly hygroscopic particles. The primary particle size of the original Solvay $CaCO_3$ powder is ~55 nm. The sub-100 nm particles should contain a greater volume fraction of secondary hydrates as they will become concentrated into the smaller particles during atomization and drying. This agrees with the observation that the sub-100 nm Solvay particle's hygroscopicity increased notably with time in water, while the larger particles did not. The larger > 100 nm particles contain a higher fraction of the original calcite and therefore activate similar to the dry-generated Solvay $CaCO_3$. The dissolution of trace soluble contaminants into water and their concentration onto smaller particles during atomization may also contribute to this large difference in hygroscopicity versus particle size,

though no evidence of large soluble contaminants was observed. The lack of large changes in the hygroscopicity of the Solvay calcite with time is attributed to the very small primary particle size and high surface area of the powder. This enables the Solvay calcite to reach a steady state with the aqueous phase much more quickly than the coarser Baker calcite powder can.

Atomized Baker $CaCO_3$ was also more CCN-active compared to dry-generation and its hygroscopicity increased with time spent in water. The dissolution of small amounts of calcium carbonate and the subsequent formation of calcium carbonate hydrates also explains this behavior. The Baker $CaCO_3$ powder is much coarser than the Solvay powder, with an average particle diameter of ~25 μm. Unlike the Solvay $CaCO_3$, there will be almost no original submicron atomized Baker $CaCO_3$ particles, as presented above (Fig. 6.17). Therefore, all the atomized Baker $CaCO_3$ particles must be produced by secondary calcium carbonate (and other trace salts) that has dissolved, been atomized, and then precipitated during drying. This produces particles composed of the residues of mixtures of small partially dissolved original $CaCO_3$ particles and their secondary hydrates. The increase in κ_{app} caused by atomization is much smaller than for the Solvay calcium carbonate because the dry-generated Baker powder starts at a larger κ_{app} than the Solvay does. However, after 3 days in water the Baker calcium carbonate's hygroscopicity increased from $\kappa_{app} = 0.020 \pm 0.0035$ to ~0.16, which is virtually the same hygroscopicity of the sub-100 nm atomized Solvay calcium carbonate particles (Fig. 6.10). The large size and low surface area of the original Baker $CaCO_3$ particles causes the powder to dissolve and reach saturation more slowly than the ultrafine Solvay powder does. This explains the large increase in the hygroscopicity of wet-generated Baker $CaCO_3$ over time as it continued to sit in water.

The small change in κ_{app} observed for wet- versus dry-generated calcium sulfate may be explained by the similarly low solubility of anhydrite ($CaSO_4$) and its most stable hydrate, gypsum ($CaSO_4 \cdot 2H_2O$). At 25 C gypsum is only slightly less soluble and thus more stable than anhydrite, while the hemihydrate ($CaSO_4 \cdot \frac{1}{2}H_2O$) is metastable and much more soluble than both (Freyer and Voigt, 2003). This is the opposite of $CaCO_3$, whose hydrates are all less stable than the original calcite. There may be little difference in the measured CCN activation for wet- versus dry-generation of $CaSO_4$ because both $CaSO_4$ and $CaSO_4 \cdot 2H_2O$ have almost the same low solubility and presumably similar deliquescence RHs. At the concentrations used the $CaSO_4$ suspension was below the solubility limit and all the powder was observed to dissolve after a few minutes. Therefore, similar to the Baker calcite, the dried atomized $CaSO_4$ particles will also be completely secondary, forming from the aqueous calcium sulfate and its hydrates that compose the droplets.

6.5 Atmospheric implications

6.5.1 Interplay between chemical mixing state and hygroscopicity of calcium mineral particles

The interplay between chemical mixing state and solubility is summarized in Table 6.5, which lists the solubilities of various cation–anion pairs for typical mineral dust components. Sparingly soluble and insoluble compounds are indicated with shading. The estimated intrinsic hygroscopicities via Raoult's law (Eq. 6.5) are all > 0.4. However, the large differences in solubility affect whether the observed apparent hygroscopicity of each compound reflects its intrinsic hygroscopicity, or approaches $\kappa_{app} = 0$, during activation. Our experiments for calcium salts confirm the expected links between solubilities and observed apparent hygroscopicities, with calcium carbonate, sulfate and oxalate approximately

described by $\kappa_{app} = 0$. Although we did not measure them, based on our findings for calcium minerals, we expect the CCN activities of magnesium carbonate and oxalate to also approach $\kappa_{app} = 0$. Other forms of magnesium minerals, calcium nitrate and chloride, and all of the potassium, sodium, and ammonium compounds, are sufficiently soluble that we expect them to exhibit hygroscopic behavior similar to ammonium sulfate, i.e. $\kappa_{app} = \kappa_{intr}$. Note that sulfate and oxalate compounds represent atmospherically processed forms of mineral dust and yet are not always soluble enough to express their large intrinsic hygroscopicities. The experimental CCN data summarized in Figure 6.6 are in direct agreement with these expected trends in apparent hygroscopicity.

The atmospheric processing of mineral dust particles is typically expected to increase their hygroscopicity and CCN activity (e.g. Fan et al., 2004; Gibson et al., 2006a; Levin et al., 1996; Perry et al., 2004; Roberts et al., 2006). This is because heterogeneous reactions with reactive gases including nitric, hydrochloric, and sulfuric acids can convert insoluble carbonates into sparingly or sufficiently soluble compounds. However, few field or laboratory studies have been conducted to validate this. From these laboratory measurements of the hygroscopicity of various calcium minerals, it is shown that one common mineral representative of chemically aged dust particles – calcium sulfate – has poor CCN activation potential, behaving similarly to calcium carbonate which is a proxy for fresh unaged mineral dust. Another proxy for aged dust, calcium oxalate monohydrate, has only moderate CCN activity. Thus, it is possible for mineral dust particles to undergo extensive chemical reactions during atmospheric transport and yet remain non-hygroscopic, due to the formation of low solubility products (Table 6.5). It is therefore incorrect to assume that all mineral dust particles will become more hygroscopic and CCN-active during the course of atmospheric processing. The predominant chemical reaction must be known to reliably predict the resulting

hygroscopicity of the aged mineral dust particles. If calcite-rich dust particles instead react with nitrate or chloride precursors, such as NO_x, HNO_3, N_2O_5, HCl, etc., the resulting calcium nitrate and chloride salts are highly hygroscopic and will result in more CCN-active aged dust particles. The initial mineralogy of the mineral dust particles also exerts significant influence

Table 6.5. Solubilities,[a] estimated intrinsic hygroscopicities,[b] and measured apparent hygroscopicities of various inorganic salts.[c]

	Ca^{2+}	Mg^{2+}	K^+	Na^+	NH_4^+
CO_3^{2-}	S = 0.0058	1.8^{20}	1110	307	1000^{15}
	$\kappa = 0.97 / 0.001^d$	1.30	0.90	1.30	0.84^*
SO_4^{2-}	2.05 ($2H_2O$)	357	120	281	764
	$0.49 / 0.002^d$	0.80	0.83	$1.03 / 0.80^e$	$0.72 / 0.61^e$
NO_3^-	1440 ($4H_2O$)	712	383	912	2130
	$0.43 / 0.51^d$	0.84	0.88	$0.96 / 0.88^e$	$0.77 / 0.67^e$
Cl^-	813 ($2H_2O$)	560	355	360	395
	$0.68 / 0.48^d$	1.32	0.89	$1.34 / 1.28^e$	1.02
Oxalate$^-$	0.0061^{20} (H_2O)	0.38	364^{20}	36.1	52.0
	$0.52 / 0.048^d$	0.79^*	0.42	0.94	0.65

[a] All solubilities (g L^{-1}) taken from the CRC Handbook of Chemistry and Physics, 88th edition, for 25 °C except (*) from http://www.wikipedia.org. Superscript indicates solubility at T other than 25 °C.
[b] Calculated with Eq. 6.5 using values listed in Table 6.1 or else in the CRC Handbook.
[c] Data for the most stable hydrate was used when known. The hydrate form is indicated by (xH_2O) where x is the number of water molecules in the hydrate.
[d] Measured apparent hygroscopicity from this work, from dry-generated particles when available.
[e] Hygroscopicity measured from CCN activation experiments summarized by Petters and Kreidenweis (2007).

on this process. While sulfate and oxalate calcium salts are insoluble, their sodium, potassium, and magnesium salts are not (Table 6.5). Therefore mineral dust particles composed of magnesium, potassium, and sodium carbonates would be predicted to form hygroscopic particles upon reaction with SO_2 and oxalic acid (magnesium oxalate is sparingly soluble, however).

Shi et al. (2008) have recently reported the differing hygroscopicities of individual supermicron Asian mineral dust particles collected in Japan. They observed that dust particles that did not contain sulfate or nitrate (i.e. unreacted dust) and sulfate-rich dust particles (i.e. aged dust) did not experience hygroscopic growth even at 90% RH. Nitrate-rich dust particles, however, appeared to deliquesce at as low as 15% RH, as has been previously reported (Krueger et al., 2003; Laskin et al., 2005a). Our laboratory experiments agree with their field measurements and demonstrate a segregated hygroscopicity state caused by the segregated chemical mixing state of sulfate from nitrate and chloride in individual aged dust particles (Chapter 3).

Calcium oxalate monohydrate was observed to be significantly less hygroscopic than oxalic acid. Oxalic acid is typically the dominant component of water soluble organic aerosol mass and has been studied as a large potential contributor to aerosol hygroscopicity and CCN activity (Kanakidou et al., 2005; Prenni et al., 2001). In the Asian aerosol sampled during ACE-Asia oxalic acid was predominantly internally mixed with mineral dust particles (Chapter 5). This mixing state could result in the oxalate forming low solubility complexes with divalent cations such as Ca^{2+} that are enriched in Asian dust. This would reduce the solubility of the oxalic acid and this could in turn reduce the apparent hygroscopicity and CCN-activity of oxalate-containing particles, as we observed here. The conversion of calcium carbonate to calcium oxalate through reaction with oxalic acid will also reduce the mass of $CaCO_3$ available to be converted to more hygroscopic forms such as $CaCl_2$ and $Ca(NO_3)_2$. When calcium oxalate monohydrate particles were generated by atomization from water the particles were much more hygroscopic than when generated dry. This was attributed to the formation of metastable calcium oxalate hydrates with increased solubility even after particle drying.

In discussing the CCN activation potential of atmospheric mineral dust particles, we must also consider the role of ammonium internally mixed with dust, which was observed during ACE-Asia (Chapter 3). Ammonium was frequently internally mixed with aged mineral dust particles and appeared to have formed through neutralizing secondary acids that had accumulated in the dust. Ammonium was most strongly associated with sulfate, as expected due to the stability of ammonium sulfate. If a small fraction of the sulfate is in the form of $(NH_4)_2SO_4$ instead of $CaSO_4$, this can increase the dust particle's hygroscopicity due to the higher solubility of $(NH_4)_2SO_4$ (Fig. 6.6). During ACE-Asia, sulfate-rich mineral dust particles were primarily associated with iron- and aluminosilicate-rich mineral particles, while nitrate and chloride were enriched in calcite-rich particles (Chapter 3). However, an appreciable fraction of Ca-rich dust particles did contain smaller but still significant sulfate signals. These likely represent particles that are primarily calcium sulfate, while the aged Fe/Al-rich dust particles with larger sulfate and ammonium signals are indicative of dust particles internally mixed with ammonium sulfate. Based on the laboratory CCN data presented above, these two chemical forms of aged sulfate-dust particles would have very different CCN-activity. The observation of Shi et al. (2008) of aged sulfate-rich mineral dust particles that remained non-hygroscopic is further confirmation that this is a realistic physiochemical state for aged dust particles in the atmosphere. For nitrate- and chloride-rich aged dust particles, however, the precise chemical form of these acid reaction products will be less important because most atmospherically-relevant nitrate and chloride salts are sufficiently soluble and hygroscopic, regardless of their associated cation (Table 6.5) (Kelly et al., 2007). The addition of trace amounts of water soluble species (e.g. $(NH_4)_2SO_4$) exerts the largest increase in CCN activity on dust particles that are initially non-hygroscopic and insoluble. Hence, the chemical pathways associated with atmospheric aging effectively dictate the activation potential of

atmospheric dust particles. Our findings provide further motivation for the need to determine both the mixing state and relative amounts of various secondary species in individual mineral dust and other particle types to accurately predict the aged aerosol's hygroscopicity and CCN-activity.

In this discussion, the important role of particle hygroscopicity in determining other significant particle properties was not emphasized. Particulate-phase water alters the dust particle's size, refractive index, and shape, which affect the radiative properties of dust and thus their direct climate effects (Satheesh and Moorthy, 2005). The water content of hygroscopic dust particles may provide a medium for multiphase chemical reactions and change the solubility of important components in mineral dust such as iron. Finally, the increased CCN activity of some aged mineral dust particles will also increase their rate of wet scavenging which affects the environmental mass balance and transport of mineral dust (Fan et al., 2004).

6.5.2 Increased hygroscopicity caused by wet-generation method artifact

Calcite aerosol generated by atomization from water has been used in numerous studies of the chemical kinetic, hygroscopic, and morphological properties of atmospheric calcium carbonate particles (Gibson et al., 2007; Gibson et al., 2006a; Hatch et al., 2008; Liu et al., 2008a; Vlasenko et al., 2006). While it has been assumed that the very low solubility of calcite powder would result in minimal changes to the compound when a saturated solution is atomized, the results presented here clearly indicate a large increase up to a factor of 100 in the hygroscopicity of two calcite powders produced by atomization. In addition to increasing the particle's hygroscopicity, their reaction kinetics with acidic gases may also be altered due to the changes in morphology and hygroscopicity and by the presence of strongly bound water and hydrates. The surface chemistry of calcite particles is understood to consist of hydroxyl

and carbonate groups due to the dissociative absorption of water, producing $Ca(OH)(CO_3)$ (Liu et al., 2008a). Under dry conditions H_2CO_3 may also be present but rapidly dissociates into CO_2 and H_2O in the presence of water. H_2CO_3 has been identified as an important intermediate in the reaction of calcite surfaces with acidic gases (Al-Hosney and Grassian, 2004). The presence of water on the surface is also important in the dissociation of reactants such as HNO_3 and enhancement of ion mobility (Al-Hosney and Grassian, 2005). Considering that atomization of calcite aerosol likely creates strongly bound water in addition to metastable hydrates in the dried particles, this effect should be considered when evaluating previous studies performed on atomized calcite aerosols.

Gibson et al. (2006a) recently reported CCN activation measurements of calcium carbonate and calcium nitrate aerosol. They concluded that the large increase in a dust particle's CCN activity due to conversion of calcium carbonate to calcium nitrate from reaction with nitric oxides could convert non-hygroscopic dust particles into highly hygroscopic particles. The findings reported here are in agreement with this; the hygroscopicity of calcium nitrate ($\kappa_{app} = 0.51 \pm 0.07$) is about 500 times greater than dry-generated calcite aerosol ($\kappa_{app} = 0.0011 \pm 0.0004$). However, Gibson et al. produced their calcium carbonate aerosol by atomization from water and thus produced particles that were more hygroscopic than pure $CaCO_3$ is predicted to be, as we also observed. Their calcium carbonate had s_c ~0.55 for $D_{dry} = 100$ nm (κ_{app} ~0.043), while a 100 nm $CaCO_3$ particle should activate at SS ~2.0% (Kelly et al., 2007), if the $\kappa = 0$ line in Figure 6.6 is extrapolated back to 100 nm. The wet-generated Baker $CaCO_3$ particles were similarly too CCN-active ($\kappa_{app} = 0.020 \pm 0.0035$). This results in the increased hygroscopicity due to the conversion of calcium carbonate to calcium nitrate during atmospheric processing being even larger than that previously reported by Gibson et al. (2006a). For example, the s_c of a 100 nm dry diameter

$CaCO_3$ particle should be 2.0% compared to the much smaller s_c of 0.17% for pure calcium nitrate. This decrease in s_c of 1.83% SS (absolute) is much larger than the previously reported decrease of ~0.44% SS (0.55% - 0.11%) by Gibson et al. (2006a). Therefore the increased hygroscopicity and CCN-activity of calcium carbonate aerosol that has been converted to calcium nitrate is about 40 times larger than previously determined, when $CaCO_3$ of a properly low original solubility is considered.

Gibson et al. (2006a) also performed hygroscopic growth experiments on their atomized $CaCO_3$ particles via subsaturated HTDMA experiments. They observed no hygroscopic growth up to the maximum tested RH of 85%, yet their $CaCO_3$ particles were more hygroscopic than expected in supersaturated conditions during their CCN activation experiments. The formation of metastable hydrates that are more soluble than calcite but still have deliquescence RHs ~100% is the best explanation for this observation. This would cause the particles to have very different apparent hygroscopicities when measured under sub- and supersaturated conditions. The presence of significant amounts of soluble contaminants would not agree with their observations as their solubility should cause them to have DRH well below 100%. The contaminants would therefore increase the apparent hygroscopicity of the particles in the HTDMA experiments, which was not observed.

Our observations of an increased apparent hygroscopicity after dry-generated calcite aerosol was briefly exposed to water vapor indicates that bulk aqueous-phase chemistry is not required to produce the observed changes in hygroscopicity. The calcium carbonate metastable hydrates formed during the atomization and particle drying process appear to also form from exposure to water vapor. These metastable states could then be locked into when the humidified particles are subsequently dried before CCN analysis. This is further evidence for metastable hydrates as opposed to soluble contaminants causing the increased apparent

hygroscopicity of the atomized $CaCO_3$. This has potentially important and previously unreported consequences for the hygroscopicity and CCN activation of $CaCO_3$ containing atmospheric mineral dust particles. Exposure to water vapor could provide an atmospheric pathway that increases the apparent hygroscopicity (by increasing its solubility) of insoluble calcite aerosol without the need for reaction with acidic gases. This phenomenon and its possible atmospheric implications warrant further study.

6.6 Conclusions

The CCN activation properties of various pure calcium minerals were measured as proxies for fresh and atmospherically aged Ca-rich mineral dust particles. A single-parameter for particle hygroscopicity, κ, was used to interpret the experimental data. We found two general states of particle hygroscopicity:

1. Sufficiently soluble minerals, i.e. $CaCl_2$ and $Ca(NO_3)_2$, that are hygroscopic (κ_{app} ~0.5) and have critical supersaturations similar to $(NH_4)_2SO_4$ ($\kappa_{app} = 0.61$).

2. Insoluble minerals, i.e. $CaCO_3$ and $CaSO_4$, with low apparent hygroscopicity (κ_{app} ~0.001), poor CCN activation ability, and critical supersaturations consistent with a deliquescence-limitation (Kelvin limit).

Calcium oxalate monohydrate was moderately CCN active and more hygroscopic ($\kappa_{app} = 0.048$) than its solubility and intrinsic hygroscopicity would predict (perhaps caused by a large reduction in the surface tension), but still significantly less hygroscopic than oxalic acid ($\kappa_{app} = 0.50$). Calcium oxalate particles generated by atomization from water had much larger hygroscopicity ($\kappa_{app} = 0.34$) than dry-generated particles. The large increase in apparent hygroscopicity is attributed to the formation of metastable hydrates with higher solubility. A similar effect was observed for atomized calcium carbonate particles which were much more

hygroscopic than dry-generated $CaCO_3$, displaying hygroscopicities of $\kappa_{app} > 0.1$, 100 times more hygroscopic than when generated dry. Accounting for this results in the expected increase in the hygroscopicity of $CaCO_3$ mineral dust particles that have been atmospherically processed to $Ca(NO_3)_2$ or $CaCl_2$ being 40 times larger than previously reported. We concluded that the atomized particles are predominantly composed of secondary $CaCO_3$ metastable hydrates, and contain little to none of the original calcite powder. This data demonstrates that generation of mineral (and other) particles by atomization from water may produce a range of products with highly varying hygroscopicities, due to the potential formation of metastable hydrates with increased solubility and thus higher apparent hygroscopicity.

As shown here, the chemical form of the reactive gases which produce secondary products that become mixed with and react with the dust must be known to accurately predict the hygroscopicity and CCN activity of the resulting mineral mixture. As demonstrated in Table 6.5, it is incorrect to assume that all chemical reactions that process dust in the atmosphere produce soluble reaction products that increase the dust's CCN ability. Insoluble reaction products such as calcium sulfate are frequently observed in aged mineral dust particles, have low CCN-activity, and should also be considered (Kelly et al., 2007; Shi et al., 2008).

6.7 Acknowledgements

SEM/EDX/ESEM analysis at Pacific Northwest National Laboratory, and his colleague Odeta Qafoku performed the ICP-MS analysis.

Publication Acknowledgment

The contents of Chapter 6 compose part of a submitted manuscript: Sullivan RC, Moore MJK, Petters MD, Kreidenweis SM, Roberts GC, and Prather KA, Hygroscopicity and cloud nucleation ability of calcium mineral dust particles – 1. Importance of chemical mixing state, submitted to *Journal of Physical Chemistry A*; and a manuscript in preparation: Sullivan RC, Moore MJK, Petters MD, Kreidenweis SM, Qafoku O, Laskin A, Roberts GC, and Prather KA, Hygroscopicity and cloud nucleation ability of calcium mineral dust particles – 2. Effect of water and hydrate formation, to be submitted to *Journal of Physical Chemistry A*.

6.8 References

Al-Hosney, H. A., and Grassian, V. H.: Carbonic acid: An important intermediate in the surface chemistry of calcium carbonate, J Am Chem Soc, 126 (26), 8068-8069, 2004.

Al-Hosney, H. A., and Grassian, V. H.: Water, sulfur dioxide and nitric acid adsorption on calcium carbonate: A transmission and ATR-FTIR study, Phys. Chem. Chem. Phys., 7 (6), 1266-1276, 2005.

Albrecht, B. A.: Aerosols, Cloud Microphysics, and Fractional Cloudiness, Science, 245 (4923), 1227-1230, 1989.

Andreae, M. O., and Rosenfeld, D.: Aerosol–cloud–precipitation interactions. Part 1. The nature and sources of cloud-active aerosols Earth Science Reviews, 89 (1-2), 13-41, 2008.

Bilde, M., and Svenningsson, B.: CCN activation of slightly soluble organics: the importance of small amounts of inorganic salt and particle phase, Tellus Series B-Chemical And Physical Meteorology, 56 (2), 128-134, 2004.

Brecevic, L., and Kralj, D.: On calcium carbonates: from fundamental research to application, Croat. Chem. Acta, 80 (3-4), 467-484, 2007.

Brecevic, L., Kralj, D., and Garside, J.: Factors Influencing the Distribution of Hydrates in Calcium-Oxalate Precipitation, J. Cryst. Growth, 97 (2), 460-468, 1989.

Brecevic, L., and Nielsen, A. E.: Solubility of Amorphous Calcium-Carbonate, J. Cryst. Growth, 98 (3), 504-510, 1989.

Brecevic, L., and Nielsen, A. E.: Solubility of Calcium-Carbonate Hexahydrate, Acta Chem. Scand., 47 (7), 668-673, 1993.

Broekhuizen, K., Kumar, P. P., and Abbatt, J. P. D.: Partially soluble organics as cloud condensation nuclei: Role of trace soluble and surface active species, Geophys. Res. Lett., 31 (1), doi:10.1029/2003GL018203, 2004.

Brooks, R., Clark, L. M., and Thurston, E. F.: Calcium Carbonate and Its Hydrates, Philosophical Transactions of the Royal Society of London Series a-Mathematical and Physical Sciences, 243 (861), 145-167, 1950.

Carrico, C. M., Kus, P., Rood, M. J., Quinn, P. K., and Bates, T. S.: Mixtures of pollution, dust, sea salt, and volcanic aerosol during ACE-Asia: Radiative properties as a function of relative humidity, J. Geophys. Res., 108 (D23), doi:10.1029/2003JD003405, 2003.

Facchini, M. C., Decesari, S., Mircea, M., Fuzzi, S., and Loglio, G.: Surface tension of atmospheric wet aerosol and cloud/fog droplets in relation to their organic carbon content and chemical composition, Atmos. Environ., 34 (28), 4853-4857, 2000.

Falkovich, A. H., Schkolnik, G., Ganor, E., and Rudich, Y.: Adsorption of organic compounds pertinent to urban environments onto mineral dust particles, J. Geophys. Res., 109 (D2), doi:10.1029/2003JD003919, 2004.

Fan, S. M., Horowitz, L. W., Levy, H., and Moxim, W. J.: Impact of air pollution on wet deposition of mineral dust aerosols, Geophys. Res. Lett., 31 (2), doi:10.1029/2003GL018501, 2004.

Freyer, D., and Voigt, W.: Crystallization and phase stability of CaSO4 and CaSO4-based salts, Mon. Chem., 134 (5), 693-719, 2003.

Gibson, E. R., Gierlus, K. M., Hudson, P. K., and Grassian, V. H.: Generation of internally mixed insoluble and soluble aerosol particles to investigate the impact of atmospheric aging and heterogeneous processing on the CCN activity of mineral dust aerosol, Aerosol Sci. Technol., 41 (10), 914-924, 2007.

Gibson, E. R., Hudson, P. K., and Grassian, V. H.: Aerosol chemistry and climate: Laboratory studies of the carbonate component of mineral dust and its reaction products, Geophys. Res. Lett., 33 (13), doi:10.1029/2006GL026386, 2006.

Hatch, C. D., Gierlusa, K. M., Schuttlefielda, J. D., and Grassian, V. H.: Water adsorption and cloud condensation nuclei activity of calcite and calcite coated with model humic and fulvic acids, Atmos. Environ., 42 (22), 5672-5684, 2008.

Hoffman, R. C., Laskin, A., and Finlayson-Pitts, B. J.: Sodium nitrate particles: physical and chemical properties during hydration and dehydration, and implications for aged sea salt aerosols, Journal of Aerosol Science, 35 (7), 869-887, 2004.

IPCC, Climate Change 2007: The Physical Science Basis. Contribution of Working Group I to the Fourth Assessment Report of the Intergovernmental Panel on Climate Change, Cambridge University Press, Cambridge, 2007.

Jeong, G. Y.: Bulk and single-particle mineralogy of Asian dust and a comparison with its source soils, J. Geophys. Res., 113 (D2), doi:10.1029/2007JD008606, 2008.

Jeong, G. Y., and Chun, Y.: Nanofiber calcite in Asian dust and its atmospheric roles, Geophys. Res. Lett., 33 (L24802), doi:10.1029/2006GL028280, 2006.

Kanakidou, M., Seinfeld, J. H., Pandis, S. N., Barnes, I., Dentener, F. J., Facchini, M. C., Van Dingenen, R., Ervens, B., Nenes, A., Nielsen, C. J., Swietlicki, E., Putaud, J. P., Balkanski, Y., Fuzzi, S., Horth, J., Moortgat, G. K., Winterhalter, R., Myhre, C. E. L., Tsigaridis, K., Vignati, E., Stephanou, E. G., and Wilson, J.: Organic aerosol and global climate modelling: a review, Atmos. Chem. Phys., 5, 1053-1123, 2005.

Kelly, J. T., Chuang, C. C., and Wexler, A. S.: Influence of dust composition on cloud droplet formation, Atmos. Environ., 41 (14), 2904-2916, 2007.

Koehler, K., The impact of natural dust aerosol on warm and cold cloud formation, Colorado State University, Fort Collins, 2007.

Koehler, K. A., Kreidenweis, S. M., DeMott, P. J., Prenni, A. J., Carrico, C. M., Ervens, B., and Feingold, G.: Water activity and activation diameters from hygroscopicity data - Part II: Application to organic species, Atmos. Chem. Phys., 6, 795-809, 2006.

Koehler, K. A., Kreidenweis, S. M., DeMott, P. J., Prenni, A. J., and Petters, M. D.: Potential impact of Owens (dry) Lake dust on warm and cold cloud formation, J. Geophys. Res., 112 (D12), D12210, doi:10.1029/2007JD008413, 2007.

Kralj, D., and Brecevic, L.: Dissolution Kinetics and Solubility of Calcium-Carbonate Monohydrate, Colloid Surf. A-Physicochem. Eng. Asp., 96 (3), 287-293, 1995.

Kreidenweis, S. M., Petters, M. D., and DeMott, P. J.: Deliquescence-controlled activation of organic aerosols, Geophys. Res. Lett., 33 (6), L06801, doi:10.1029/2005GL024863, 2006.

Krueger, B. J., Grassian, V. H., Cowin, J. P., and Laskin, A.: Heterogeneous chemistry of individual mineral dust particles from different dust source regions: the importance of particle mineralogy, Atmos. Environ., 38 (36), 6253-6261, 2004.

Krueger, B. J., Grassian, V. H., Laskin, A., and Cowin, J. P.: The transformation of solid atmospheric particles into liquid droplets through heterogeneous chemistry: Laboratory insights into the processing of calcium containing mineral dust aerosol in the troposphere, Geophys. Res. Lett., 30 (3), doi:10.1029/2002GL016563, 2003.

Laskin, A., Iedema, M. J., Ichkovich, A., Graber, E. R., Taraniuk, I., and Rudich, Y.: Direct observation of completely processed calcium carbonate dust particles, Faraday Discussions, 130, 453-468, 2005.

Levin, Z., Ganor, E., and Gladstein, V.: The effects of desert particles coated with sulfate on rain formation in the eastern Mediterranean, Journal Of Applied Meteorology, 35 (9), 1511-1523, 1996.

Liu, Y., Gibson, E. R., Cain, J. P., Wang, H., Grassian, V. H., and Laskin, A.: Kinetics of heterogeneous reaction of CaCO3 particles with gaseous HNO3 over a wide range of humidity, J. Phys. Chem. A, 112 (7), 1561-1571, 2008.

Lohmann, U., and Feichter, J.: Global indirect aerosol effects: a review, Atmos. Chem. Phys., 5, 715-737, 2005.

Matsuki, A., Iwasaka, Y., Shi, G. Y., Zhang, D. Z., Trochkine, D., Yamada, M., Kim, Y. S., Chen, B., Nagatani, T., Miyazawa, T., Nagatani, M., and Nakata, H.: Morphological and chemical modification of mineral dust: Observational insight into the heterogeneous uptake of acidic gases, Geophys. Res. Lett., 32 (22), doi:10.1029/2005GL024176, 2005.

McFiggans, G., Artaxo, P., Baltensperger, U., Coe, H., Facchini, M. C., Feingold, G., Fuzzi, S., Gysel, M., Laaksonen, A., Lohmann, U., Mentel, T. F., Murphy, D. M., O'Dowd, C. D., Snider, J. R., and Weingartner, E.: The effect of physical and chemical aerosol properties on warm cloud droplet activation, Atmos. Chem. Phys., 6, 2593-2649, 2006.

Nancollas, G. H., and Wu, W. J.: The surface, interfacial and electrokinetic properties of biominerals, J. Dispersion Sci. Technol., 19 (6-7), 723-738, 1998.

Perry, K. D., Cliff, S. S., and Jimenez-Cruz, M. P.: Evidence for hygroscopic mineral dust particles from the Intercontinental Transport and Chemical Transformation Experiment, J. Geophys. Res., 109 (D23), doi:10.1029/2004JD004979, 2004.

Petters, M. D., and Kreidenweis, S. M.: A single parameter representation of hygroscopic growth and cloud condensation nucleus activity, Atmos. Chem. Phys., 7 (8), 1961-1971, 2007.

Petters, M. D., and Kreidenweis, S. M.: A single parameter representation of hygroscopic growth and cloud condensation nucleus activity - Part 2: Including solubility, Atmos. Chem. Phys., 8, 6273–6279, 2008.

Petters, M. D., Prenni, A. J., Kreidenweis, S. M., and DeMott, P. J.: On measuring the critical diameter of cloud condensation nuclei using mobility selected aerosol, Aerosol Sci. Technol., 41 (10), 907-913, 2007.

Petters, M. D., Snider, J. R., Stevens, B., Vali, G., Faloona, I., and Russell, L. M.: Accumulation mode aerosol, pockets of open cells, and particle nucleation in the remote subtropical Pacific marine boundary layer, J. Geophys. Res., 111 (D2), doi:10.1029/2004JD005694 2006.

Plummer, L. N., and Busenberg, E.: The Solubilities of Calcite, Aragonite and Vaterite in Co2-H2o Solutions between 0-Degrees-C and 90-Degrees-C, and an Evaluation of the Aqueous Model for the System Caco3-Co2-H2o, Geochimica Et Cosmochimica Acta, 46 (6), 1011-1040, 1982.

Prenni, A. J., DeMott, P. J., Kreidenweis, S. M., Sherman, D. E., Russell, L. M., and Ming, Y.: The effects of low molecular weight dicarboxylic acids on cloud formation, J. Phys. Chem. A, 105 (50), 11240-11248, 2001.

Roberts, G., Mauger, G., Hadley, O., and Ramanathan, V.: North American and Asian aerosols over the eastern Pacific Ocean and their role in regulating cloud condensation nuclei, J. Geophys. Res., 111 (D13), doi:10.1029/2005JD006661, 2006.

Roberts, G. C., Artaxo, P., Zhou, J. C., Swietlicki, E., and Andreae, M. O.: Sensitivity of CCN spectra on chemical and physical properties of aerosol: A case study from the Amazon Basin, J. Geophys. Res., 107 (D20), doi: 10.1029/2001JD000583, 2002.

Roberts, G. C., and Nenes, A.: A continuous-flow streamwise thermal-gradient CCN chamber for atmospheric measurements, Aerosol Sci. Technol., 39 (3), 206-221, 2005.

Rose, D., Gunthe, S. S., Mikhailov, E., Frank, G. P., Dusek, U., Andreae, M. O., and Pöschl, U.: Calibration and measurement uncertainties of a continuous-flow cloud condensation nuclei counter (DMT-CCNC): CCN activation of ammonium sulfate and sodium chloride aerosol particles in theory and experiment, Atmos. Chem. Phys., 8, 1153-1179, 2008.

Rosenfeld, D., Lohmann, U., Raga, G. B., kulmala, M., Fuzzi, S., Reissell, A., and Andreae, M. O.: Flood or Drought: How Do Aerosols Affect Precipitation?, Science, 321 (5894), 1309-1313, 2008.

Rosenfeld, D., Rudich, Y., and Lahav, R.: Desert dust suppressing precipitation: A possible desertification feedback loop, Proc. Natl. Acad. Sci. USA, 98 (11), 5975-5980, 2001.

Satheesh, S. K., and Moorthy, K. K.: Radiative effects of natural aerosols: A review, Atmos. Environ., 39 (11), 2089-2110, 2005.

Shi, Z., Zhang, D., Hayashi, M., Ogata, H., Ji, H., and Fujiie, W.: Influences of sulfate and nitrate on the hygroscopic behaviour of coarse dust particles, Atmos. Environ., 42 (4), 822-827, 2008.

Shi, Z. B., Shao, L. T., Jones, T. P., and Lu, S. L.: Microscopy and mineralogy of airborne particles collected during severe dust storm episodes in Beijing, China, J. Geophys. Res., 110 (D1), doi:10.1029/2004JD005073, 2005.

Shulman, M. L., Jacobson, M. C., Charlson, R. J., Synovec, R. E., and Young, T. E.: Dissolution behavior and surface tension effects of organic compounds in nucleating cloud droplets, Geophys. Res. Lett., 23 (3), 277-280, 1996.

Tang, Y. H., Carmichael, G. R., Seinfeld, J. H., Dabdub, D., Weber, R. J., Huebert, B., Clarke, A. D., Guazzotti, S. A., Sodeman, D. A., Prather, K. A., Uno, I., Woo, J. H., Yienger, J. J., Streets, D. G., Quinn, P. K., Johnson, J. E., Song, C. H., Grassian, V. H., Sandu, A., Talbot, R. W., and Dibb, J. E.: Three-dimensional simulations of inorganic aerosol distributions in east Asia during spring 2001, J. Geophys. Res., 109 (D19), doi:10.1029/2003JD004201, 2004.

Twomey, S.: Influence of Pollution on Shortwave Albedo of Clouds, Journal of the Atmospheric Sciences, 34 (7), 1149-1152, 1977.

Usher, C. R., Michel, A. E., and Grassian, V. H.: Reactions on mineral dust, Chem. Rev., 103 (12), 4883-4939, 2003.

Vlasenko, A., Sjogren, S., Weingartner, E., Gaggeler, H. W., and Ammann, M.: Generation of submicron Arizona test dust aerosol: Chemical and hygroscopic properties, Aerosol Sci. Technol., 39 (5), 452-460, 2005.

Vlasenko, A., Sjogren, S., Weingartner, E., Stemmler, K., Gaggeler, H. W., and Ammann, M.: Effect of humidity on nitric acid uptake to mineral dust aerosol particles, Atmos. Chem. Phys., 6, 2147-2160, 2006.

Chapter 7

Timescale for hygroscopic conversion of mineral dust particles through heterogeneous reaction with nitric acid

7.1 Synopsis

Atmospheric heterogeneous reactions can potentially convert non-hygroscopic aerosol particles into hygroscopic and thus CCN-active particles, with important climatic consequences. Size-selected calcite particles were reacted with controlled amounts of nitric acid vapor over a range of relative humidities between 0 and 75% in an aerosol flow tube to study the conversion of non-hygroscopic calcium carbonate into soluble and very hygroscopic calcium nitrate. The rate of increase in the hygroscopicity of an initially insoluble aerosol undergoing a heterogeneous reaction is derived from simultaneous measurements of individual particle chemistry and CCN activation curves for the first time. The reacted particles' chemistry was determined with an ultrafine aerosol time-of-flight mass spectrometer (UF-ATOFMS) while the particles' hygroscopicity was determined through measuring CCN activation curves and fit to a single parameter of hygroscopicity, κ. As reported by several previous reports, the reaction is rapid and was observed to be accelerated at elevated relative humidity for low HNO_3 exposures. At low to moderate HNO_3 exposures the increase in the reacted particles' hygroscopicity is a linear function of their exposure to $HNO_3(g)$. The experimentally observed rate of hygroscopic conversion from reactions performed at 50% RH constrained a simple but accurate kinetic model. This predicts that calcite particles will be rapidly converted into very hygroscopic particles ($\kappa_{app} > 0.1$) within 5 hours for low HNO_3 mixing ratios (10 pptv) and in less than 30 minutes for 1000 pptv HNO_3. This suggests that the

hygroscopic conversion of the calcite component of mineral dust aerosol will be limited by the availability of nitric acid vapor and not by the available atmospheric reaction time between nitric acid and mineral dust aerosol.

7.2 Introduction

Mineral dust particles undergo chemical reactions during atmospheric transport. These modify the physicochemical properties of the dust particles, by adding secondary aerosol mass to the particles, for example. Calcite ($CaCO_3$) and other carbonates are generally regarded as the most chemically reactive components of mineral dust, due to their high alkalinity and propensity to undergo reaction with acidic vapors (Krueger et al., 2004; Laskin et al., 2005b; Tang et al., 2004b; Usher et al., 2003a). Calcite is distributed to a large and variable degree between individual dust particles. It can be found in the form of individual mostly-calcite particles, and also as calcite nanofibers distributed throughout mineral dust particles (Jeong and Chun, 2006). China loess dust and Saudi coastal dust samples were found to contain significant amounts of $CaCO_3$ in 20 to 40% of the particles (Laskin et al., 2005b). Kinetic studies have determined the reaction probability of calcite particles or powders to be very high in reactions with acidic vapors including N_2O_5, HNO_3, HCl, formic acid, and acetic acid (Al-Hosney et al., 2005; Karagulian et al., 2006; Liu et al., 2008a; Prince et al., 2007; Prince et al., 2008; Santschi and Rossi, 2006; Vlasenko et al., 2006). The role of relative humidity and surface bound water is particularly important in driving these reactions (Al-Hosney and Grassian, 2004; Liu et al., 2008a; Prince et al., 2007). The conversion of insoluble calcium carbonate into soluble products including calcium nitrate and calcium chloride is of particular interest as a pathway for transforming mineral dust into hygroscopic particles capable of nucleating warm cloud droplets, as discussed in Chapter 6. Completely processed calcium

nitrate particles have been previously observed in laboratory experiments and field measurements (Krueger et al., 2003; Laskin et al., 2005a; Matsuki et al., 2005b). The single-particle analysis of aged Asian mineral dust particles described in Chapter 3 found that secondary nitrate and chloride were enriched in supermicron calcium-rich dust particles.

The hygroscopicity and cloud nucleating ability of calcium nitrate particles has been investigated theoretically by Kelly et al. (2007), and measured experimentally by Gibson et al. (2006a) and in Chapter 6; the particles are very soluble and hygroscopic, with κ_{app} = 0.51. Recently Liu et al. (2008b) used micro-Raman spectroscopy to study the phase transitions and hygroscopic growth of calcium nitrate and mixed calcium carbonate/nitrate particles. The observed transitions were significantly different from those expected based on bulk thermodynamics, highlighting the need to study these processes in individual particles. Above 10% RH the calcium nitrate particles exist as stable droplets that experience continuous hygroscopic growth. This low deliquescence point is attributed to the formation of an amorphous calcium nitrate hydrate. Between 7-10% RH an undetermined phase transition occurs, likely the formation of a solid amorphous hydrate, but no evidence for actual efflorescence has been observed in this or other studies. Surprisingly, the mixed $CaCO_3/Ca(NO_3)_2$ particles displayed the same hygroscopic properties as pure $Ca(NO_3)_2$, with no effect of $CaCO_3$ observed (Liu et al., 2008b). Laskin et al. (2005b) found calcium nitrate particles to deliquesce between 8-10% RH while Tang and Fung (1997) observed the phase transition to occur between 10-12% RH. Gibson et al. (2006a) observed similar phase transitions in atomized calcium nitrate particles. Gibson et al. (2007) also generated mixed $CaCO_3/Ca(NO_3)_2$ particles from an aqueous suspension of the two salts to study the hygroscopicity of the mixed particles. For 200 nm $CaCO_3$ particles containing 1% $Ca(NO_3)_2$ they found s_c = 0.29 ± 0.02%, and for 5% $Ca(NO_3)_2$ s_c = 0.20 ± 0.02%, compared to s_c = 0.37

± 0.02% for unmixed $CaCO_3$ particles. These were the only critical supersaturations they reported for mixed $Ca(NO_3)_2/CaCO_3$ particles; the change in hygroscopicity and s_c as a function of the nitrate fraction was not derived from the experimental data.

The heterogeneous reaction between solid calcite and gaseous nitric acid proceeds as follows:

$$CaCO_3(s) + 2HNO_3 \rightarrow Ca(NO_3)_2(s,aq) + H_2CO_3(aq) \qquad (R7.1)$$

$$\rightarrow Ca(NO_3)_2(aq) + CO_2(g)\uparrow + H_2O \qquad (R7.2)$$
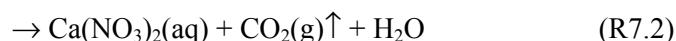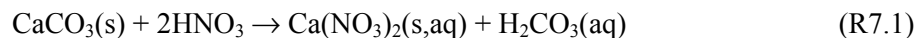
to produce the soluble and very hygroscopic calcium nitrate product. The reaction rate has been found to be accelerated by increased relative humidity, particularly above 10% RH, the deliquescence point of the calcium nitrate product (Liu et al., 2008a; Prince et al., 2007; Santschi and Rossi, 2006).

Laskin et al. (2005b) observed that $CaCO_3$ particles, and authentic dust samples containing carbonates, formed highly hygroscopic particles after reaction with $HNO_3(g)$ that rapidly grew by water uptake above 9-11% RH. Liu et al. (2008a) recently reported the detailed kinetics of $HNO_3(g)$ reacting with isolated $CaCO_3$ particles on a substrate in a flow reactor. They found that the reaction obeyed a pseudo-first order rate law. RH significantly enhanced the reaction probability, γ; at 10% RH $\gamma \geq 0.003$, while at 80% RH $\gamma \geq 0.21$ (Liu et al., 2008a). Vlasenko et al. (2006) found γ for $HNO_3(g)$ uptake on Arizona test dust aerosol (which contains ~5% calcite) in flow tube experiments to range from 0.022 at 12% RH to 0.113 at 73% RH.

Field observations of the atmospheric processing of mineral dust particles by secondary inorganic and organic acids during the ACE-Asia campaign are described in Chapters 3-5. These reactions can modify the dust particles' hygroscopicity and thus change their cloud nucleation properties. Chapter 6 describes experiments investigating the role that

dust mineralogy, mixing state, and solubility have on the hygroscopicity of fresh and chemically aged dust particles. Here aerosol flow tube experiments are described in which dust particles are exposed to controlled amounts of nitric acid and the resulting changes in the particle's chemistry and hygroscopicity are simultaneously determined.

7.3 Experimental methods

The experiments involved the dry-generation of calcite particles which were size selected, conditioned to a particular RH, and sent into the entrained aerosol flow reactor where they were exposed to $HNO_3(g)$. After reaction, the particles passed through an annular denuder, three particle driers, and were then analyzed by a UF-ATOFMS and a CCNc to measure the chemical composition and hygroscopicity of the particles, respectively. A schematic of the experimental setup is shown in Figure 7.1 and more details are provided below.

7.3.1   Particle generation

Solvay uncoated ultrafine Socal® 31 calcite powder (unstated purity) was used to generate the $CaCO_3$ aerosol. This powder was chosen due to its very small particle size, facilitating the generation of high concentrations of submicron aerosol, and because it was found to have a very low apparent hygroscopicity when generated dry, as described in Chapter 6. The powder was placed in an Erlenmeyer flask placed inside an ultrasonic water bath. The sonicator helped to distribute the powder throughout the flask, to shake off powder that had accumulated on the walls, and to possibly break up aggregates that had formed. A side arm near the bottom of the flask passed a piece of Teflon tubing attached to a plastic pipette tip towards the powder. A jet of nitrogen gas of 1-2 sLpm was directed from the tip towards the powder as the flask was held at a ~30° angle. The suspended aerosol was sampled through a
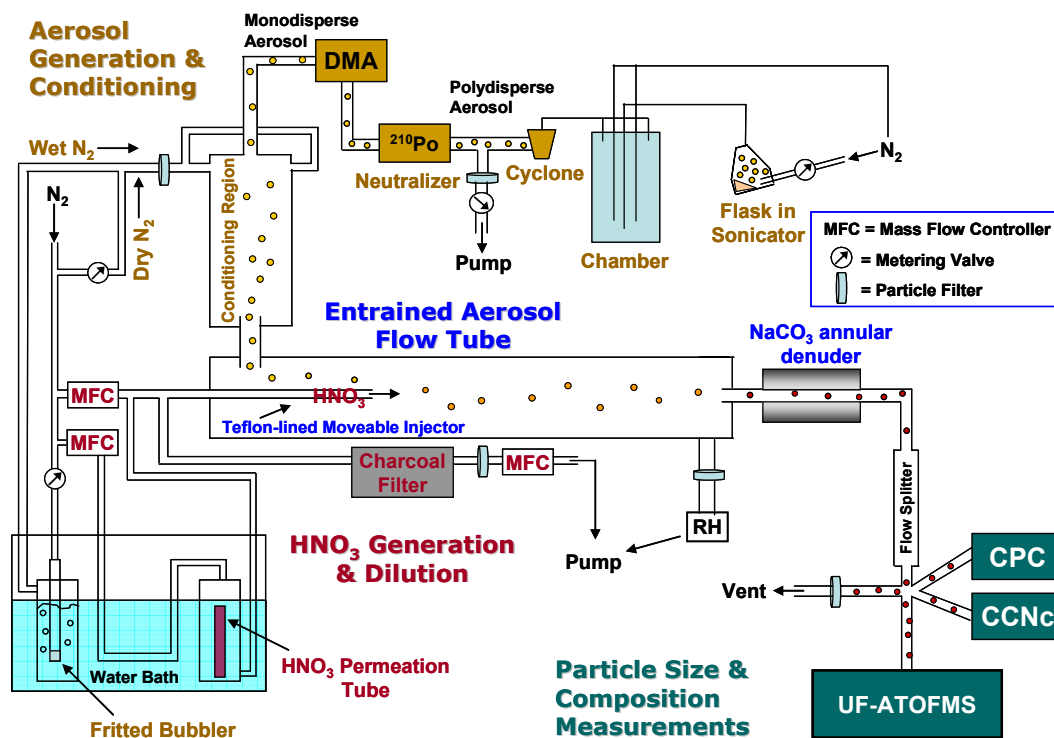
Figure 7.1. Schematic of entrained aerosol flow reactor for heterogeneous reactions of nitric acid vapour with powder and dust aerosol, and single-particle chemical analysis and CCN activation curve measurement.

3/8" o.d. stainless steel (s.s.) tube at the top of the flask and then directed into a second Erlenmeyer flask through a s.s. tube with a right angle bend to remove larger particles. The remaining aerosol was transferred to a ~ 17 L s.s. residence chamber to which dilution nitrogen gas of 2.0-8.0 sLpm was added. The aerosol sample was drawn from two 3/8" o.d. s.s. tubes that protruded slightly into the chamber and then combined into one flow. A small cyclone (URG-2000-30EQ, URG Corp.) removed larger particles from the aerosol. The cyclone has a stated cutoff of 1 μm at 5 sLpm flow, and ~0.8 μm at 10 sLpm flow. A vacuum pump removed a large portion of the aerosol flow exiting the cyclone such that 1.50 sLpm passed through a Po-210 aerosol neutralizer before entering the Kr-85 neutralizer of the differential mobility analyzer (DMA) (TSI Model 3081). The DMA's sheath flow was set at 15.0 sLpm to produce the recommended sheath-to-aerosol flow ratio of 10.0. The voltage was

set to select particles with D_m = 200.0 nm. While the calcite particles are non-spherical no attempt was made to correct for this because the empirical correction factors are not known for this powder. The 1.50 sLpm pseudo-monodisperse aerosol was then sent to the aerosol flow tube. Pure calcium nitrate particles were generated by atomizing an aqueous solution of 0.15g $Ca(NO_3)_2$ (Alfa Aesar, 99.0+ %) dissolved in 150 ml of milli-Q water (>18.0 MΩ). Wet-generated calcite particles were generated by atomizing a suspension of 0.050 g Solvay $CaCO_3$ powder in 150 mL milli-Q water. The droplets were subsequently dried to < 5% RH by a series of three diffusion driers and then size-selected as described above.

7.3.2   Entrained aerosol flow reactor

The aerosol flow tube is based on the design of Thornton et al. (2003). The pseudo-monodisperse aerosol flow first entered a short conditioning tube to which a variable mix of dry and humidified nitrogen gas was added to equilibrate the aerosol with the selected RH. The conditioned aerosol then entered the kinetic flow tube at a right angle. The glass flow tube was coated with halocarbon wax to reduce the loss of $HNO_3(g)$ and make the partitioning of HNO_3 more controllable. Nitric acid vapor was generated from a calibrated permeation tube (Kin-Tek Laboratories, Inc.), stored in a temperature controlled water bath (Neuman et al., 2003). The permeation tube had a manufacturer calibrated emission rate of 507 ng/min at 30.0 C. A constant flow of 1.0 lpm N_2 passed through the glass permeation tube holder. Upstream of this a variable flow of 0.5-5.0 sLpm dilution N_2 could be added, and an oil-less vacuum pump was used to pull a variable 0.5-5.0 sLpm from this diluted HNO_3 flow. In this way the HNO_3 concentration and total injector flow was controlled, typically between 0.1 and 0.4 sLpm, and up to 1.0 sLpm.
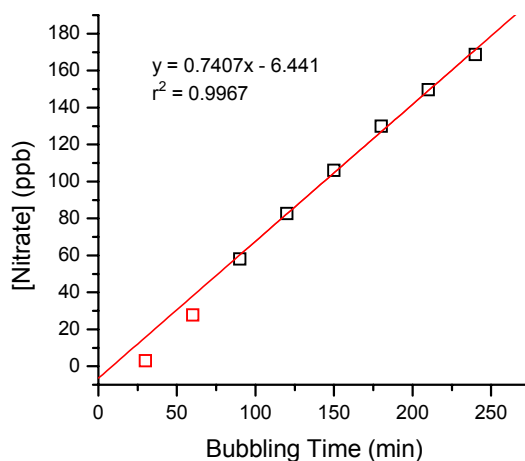
Figure 7.2. Calibration of HNO_3 permeation tube emission rate by bubbling gas stream into carbonate buffer and measuring $[NO_3^-]$ by ion chromatography in aliquots every 30 minutes. The first two aliquots (red symbol) are excluded from the linear fit.

The permeation tube's emission rate was empirically measured by bubbling 1.0 sLpm nitrogen gas from the HNO_3 source through the Teflon injector line into 500 mL of $Na_2CO_3/NaHCO_3$ buffer. 5.0 mL aliquots were removed every 30 minutes and the concentration of nitrate was determined using ion chromatography, as described in Chapter 6. The measured HNO_3 emission rate, the slope of the line displayed in Figure 7.2, was found to equal 370.4 ng/min. The first two aliquots are excluded to eliminate the effect of HNO_3 ad/desorbing from the Teflon injection line placed in the water, and to allow the system to reach steady-state. The measured HNO_3 emission rate is 73% of the manufacturer calibrated rate. This difference is attributed to irreversible loss of HNO_3 in the permeation tube holder and the lines and fittings between the source and end of the injection line. The permeation tube was 6 months old when used in these experiments which may also contribute to the reduced emission rate.

The $HNO_3(g)$ flow entered the kinetics flow tube through a Teflon-lined stainless steel moveable injector to reduce the surface loss of HNO_3 (Neuman et al., 1999). The position of the injector was adjusted to change the reaction time the particles experienced with the

reactant gas. The reaction time was controlled by the moveable injector's position and by the total aerosol flow rate. The flow tube's [HNO_3] was controlled by the concentration and flow of the HNO_3 source coming through the injector, and by the total aerosol flow rate. The [HNO_3] was calculated from the measured emission rate and the dilution flows, but was not directly measured during the experiments. Nitric acid's stickiness is well documented, and it will adsorb and then desorb from most surfaces (Neuman et al., 1999), and as a result there was likely a significant background of HNO_3 desorbing from the flow tube's coated walls throughout the experiment. The flow tube was equilibrated at the chosen RH, [HNO_3](g) and injector position for typically > 30 minutes before the start of each experiment in an attempt to achieve a steady state concentration of HNO_3(g) in the flow tube close to the predicted concentration. Inevitably, some wall loss of HNO_3 occurred though this was not quantified and is expected to be small due to the repeated passivation of the system.

The flow tube had an inner diameter of 6.1 cm and was 120 cm long. At typical total flow rates of 3 to 7 sLpm, the Reynolds's number was 68 to 160, corresponding to a laminar flow regime. The moveable injector was moved over a limited range of 70 cm such that the aerosol was able to achieve laminar flow and mix with the HNO_3(g). Sufficient mixing time was empirically tested by avoiding an increase in the RH sampled from a side port at the end of the flow tube as the movable injector was pushed forward. The increased RH is caused by insufficient mixing of the dry HNO_3(g) injector flow with the surrounding humidified sheath flow. Reaction times between the aerosol and HNO_3(g) ranged from 3 to 40 seconds, and the calculated flow tube [HNO_3] was varied between 0.50 to 45 ppbv. The flow tube's RH was measured by a hygrometer (Vaisala, HMP45AC, accuracy ± 1.5% RH) connected to the end of the flow tube by nylon tubing, as an oil-less vacuum pump pulled a small flow < 0.5 sLpm through the hygrometer. The flow tube RH was continuously measured and typically varied by

< 3% RH (absolute) over the course of an experiment due to small changes in the various gas and aerosol flow rates.

7.3.3 Particle analysis

After reaction in the flow tube, the particles were passed through an annular denuder (URG Corp., URG-2000-30x242-3CSS) coated with a dried concentrated solution of Na_2CO_3 (Fitz, 2002) to remove gas-phase HNO_3, ending the heterogeneous reaction. This may have also removed an unknown amount of nitric acid that had reversibly partitioned to the particles. The particles were dried to < 5% RH through a series of three silica gel diffusion driers before particle analysis.

The particle's chemical composition was determined online using an ultrafine-aerosol time-of-flight mass spectrometer (UF-ATOFMS) for simultaneous size and chemical analysis of individual particles (Su et al., 2004), as described in Chapter 1. The UF-ATOFMS uses an aerodynamic lens aerosol inlet to focus submicron particles. Typical particle light scattering rates during these experiments were 5-10 Hz. However, pure calcite particles have very low hit rates in the ATOFMS (< 0.1 % typically) due to a small absorption cross section at 266 nm, but the hit rate would increase to ~1-4% after reaction with $HNO_3(g)$. The UF-ATOFMS had a particle hit rate of ~25% for pure 200 nm $Ca(NO_3)_2$ particles, which is typical for this instrument when properly aligned. The experiments were conducted for long enough to collect at least 200 particle mass spectra per reaction and complete the CCN activation curve. This typically took ~1 hour.

The reacted particle's hygroscopicity and CCN-activity were measured under supersaturated conditions using the continuous-flow streamwise thermal-gradient cloud condensation nuclei counter (CCNc) previously described in Chapter 1 (Roberts and Nenes, 2005). As the particle size was held constant, the CCNc's dT was adjusted during the

experiment to change the cloud chamber's supersaturation (SS) and measure activation curves via SS-scans to determine the aerosol's critical supersaturation, s_c. These scans typically took ~45 minutes to complete. The CCNc could produce supersaturations ranging from approx. 0.08 to 1.0% SS for a dT ranging between 2.0 and 15.0 C. The instrument's SS was calibrated versus column dT using ammonium sulfate aerosol, as described in Chapter 1. Total particle counts were measured using a condensation particle counter (CPC, TSI Model 3010). Submicron particle size distributions were measured with a DMA coupled to a CPC in a scanning mobility particle sizer (SMPS) system (see Chapter 1). Aerosol and sheath flow rates of 0.40 and 4.0 sLpm were used for SMPS scans.

The UF-ATOFMS, CCNc, CPC, and hygrometer pulled 0.10, 0.50, 1.0 and < 0.5 sLpm respectively of the flow tube's 3-7 sLpm total aerosol flow. The reacted, dried aerosol particles were transferred to the various instruments through a flow splitter and conductive silicone tubing, and the excess flow was vented to atmosphere to maintain the flow tube near atmospheric pressure.

7.3.4 Single hygroscopicity parameter

The single parameter for particle hygroscopicity, κ, was used to analyze the hygroscopicity measurements made with the CCNc. This parameter has already been described in Chapter 1 and employed extensively in Chapter 6, following the method developed by Petters & Kreidenweis (2007; 2008). The following equation describes the relationship between a growing particle's equilibrium water saturation ratio, S, diameter, D, dry diameter, D_{dry}, and hygroscopicity, κ, and describes the classic Köhler growth curve:

$$S(D) = \frac{D^3 - D_{dry}^3}{D^3 - D_{dry}^3 (1-\kappa)} \exp\left(\frac{A}{D}\right) \tag{7.1}$$

where $A = 2.1\times10^{-9}$ m is a constant evaluated for a surface tension of 0.072 J m^{-2} (pure water) and temperature of 298.15 K. Eqn. 7.1 can be iterated to find κ that matches the particle's experimentally observed critical supersaturation, $s_c = S$ -1, and dry initial diameter, and to predict s_c or D_{dry}, the activation diameter, if κ is known.

Briefly, κ describes a particle's water activity and typically ranges from 1.4 to ~0 for atmospherically relevant systems. Soluble hygroscopic salts have large kappa values, for example NaCl(aq) has $\kappa = 1.2$. Wettable but completely insoluble particles have $\kappa \sim 0$. A plot of the critical supersaturation of identical particles of varying size in log s_c – log D_{dry} space typically yields kappa isolines such that particles lying along one line will all have the same hygroscopicity and thus κ value. As discussed in Chapter 6, it is important to distinguish between solubility and hygroscopicity; only aqueous components can experience hygroscopic growth, regardless of the compound's intrinsic hygroscopicity when it is fully dissolved. Therefore, compounds with high *intrinsic* hygroscopicity but low solubility, such as CaCO$_3$, will experimentally exhibit a low *apparent* hygroscopicity due to this solubility limit. In this discussion apparent hygroscopicity, κ_{app}, is exclusively used, which is the experimentally observed hygroscopicity and is equivalent to the system's intrinsic hygroscopicity under its solubility limit.

7.3.5   Error analysis

The following uncertainties were estimated for the various key parameters determined from the experimental data. The sources of each uncertainty and its estimation are described in the following results section. The uncertainty in the HNO$_3$ exposure is estimated at 25% as [HNO$_3$](g) was not directly monitored during the experiments. This uncertainty is dominated by possible fluctuations in the flow tube's [HNO$_3$], due to the problematic sticky nature of nitric acid which readily ad/desorbs from surfaces. Variations in the flow tube's total flow

were < 5%, based on measurements taken at the beginning and end of each experiment. The ATOFMS nitrate measurement's uncertainty is estimated as 15% based on calibration aerosol standards. The determination of the aerosol's critical supersaturation, s_c, is larger than normal in this case due to the peculiar activation curve shapes. An uncertainty of $s_c \pm 0.02\%$ (absolute) is estimated by varying the parameters of the activation curve sigmoid fits. This translates into an uncertainty in the single hygroscopicity parameter, κ, of $\pm 20\%$ for the range of kappa values observed here.

7.4   Results and discussion

7.4.1   Nitrate measurement in individual reacted calcite particles

The mass spectral data from individual particles obtained by the UF-ATOFMS was used to measure the extent of reaction the $CaCO_3(s)$ particles had experienced with $HNO_3(g)$. The expected product is $Ca(NO_3)_2$. A typical mass spectrum of a reacted calcite particle is shown in Figure 7.3. The positive ions are dominated by $CaCO_3$ fragments including $^{40}Ca^+$, $^{44}Ca^+$, $^{56}[CaO]^+$, $^{96}[Ca_2O]^+$, and smaller peaks from likely contaminants including $^{23}Na^+$, $^{24}Mg^+$, and $^{27}Al^+$. The negative ions also contain peaks from the original calcite particle ($^{16}O^-$, $^{17}OH^-$), but are dominated by fragments of $Ca(NO_3)_2$ at $^{46}[NO_2]^-$ and $^{62}[NO_3]^-$. Nitrate salts in mineral dust particles and calcium-rich particles in particular have been observed to fragment much more favorably to NO_2^- than NO_3^-, while sodium-rich particles, sea salt in particular, tend to favor the NO_3^- fragmentation channel in the ATOFMS. The carbonate anion $[CO_3]^-$ ion is rarely produced by the laser desorption/ionization method; $CaCO_3$ predominantly fragments to $CaO^+ + CO_2(g)$ (Bruynseels and Van Grieken, 1983).

The ion peak areas measured from individual particles represent a semi-quantitative (or relative) measure of the amount of specific compounds in the particle. However, these
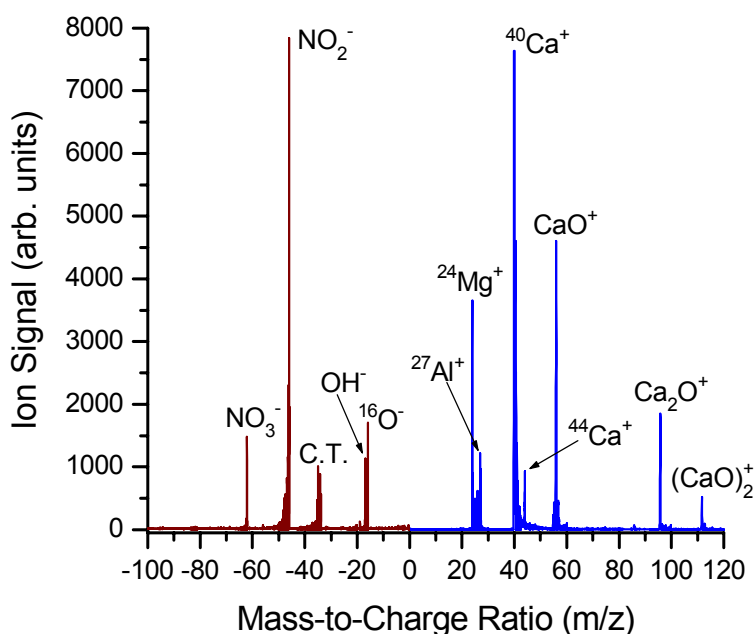
Figure 7.3. Typical dual-polarity single-particle mass spectrum obtained with the UF-ATOFMS of a dry-generated 200 nm calcite particle after exposure to 53.56 ppb s $HNO_3(g)$. The most probable peak identities are listed. C.T. indicates "cross-talk" from the positive ion detector into the negative ion channel and should be ignored.

peak areas can also be strongly influenced by matrix effects, and the amount of laser energy each particle absorbs. The LDI laser has significant shot-to-shot energy variations, and there are hot spots of high energy density in the laser beam's profile which are much larger than the particle itself. These effects when combined can lead to a wide variety of laser energy absorbed between otherwise identical particles (Wenzel and Prather, 2004). The use of relative peak areas or peak area ratios can significantly reduce these particle-to-particle peak area variations and improve the instrument's quantitative abilities. $Ca(NO_3)_2$ has a much larger absorption cross section at 266 nm than $CaCO_3$, and therefore particles containing $Ca(NO_3)_2$ will tend to absorb more laser energy and thus produce larger ion signals than pure $CaCO_3$ particles. This effect is shown in Figure 7.4a, which displays the peak areas of $^{40}[Ca]^+$ and $^{56}[CaO]^+$ versus particle size for size-selected pure $CaCO_3$ and $Ca(NO_3)_2$ particles analyzed by the UF-ATOFMS. The absolute ion peak areas of both ions are significantly larger at all
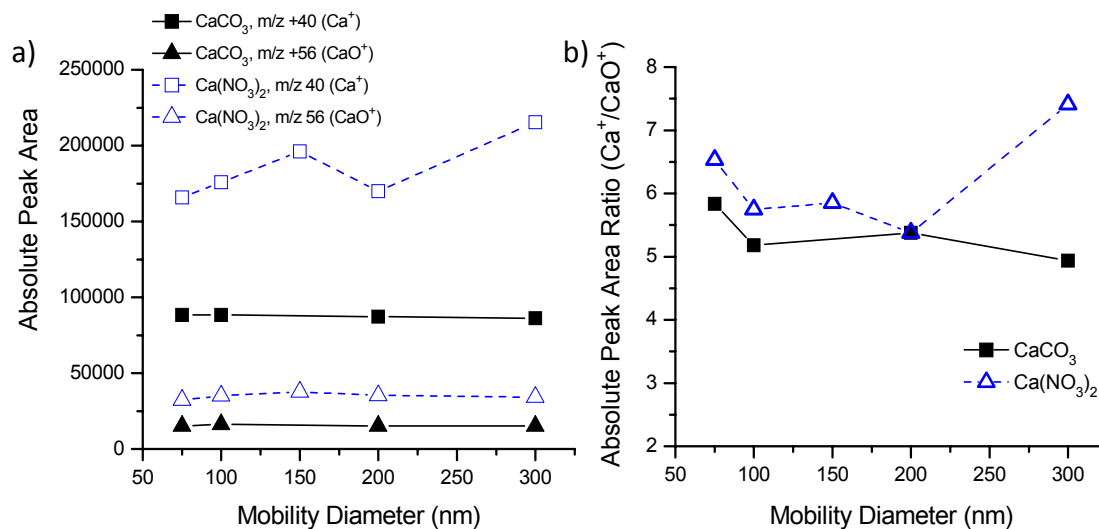
Figure 7.4. (a) Absolute ion peak areas measured from size-selected pure $CaCO_3$ and $Ca(NO_3)_2$ particles in the UF-ATOFMS. (b) Absolute peak area ratio (m/z +40/m/z +56) of the same pure particles.

particle sizes for $Ca(NO_3)_2$ compared to $CaCO_3$. The density of $Ca(NO_3)_2 \cdot 4H_2O$ (previous studies have indicated that the tetrahydrate is the dominant form in atomized and dried calcium nitrate particles, see Chapter 6) is 1.86 g/cm^3 versus 2.71 g/cm^3 for calcite. The molar fraction of Ca in $Ca(NO_3)_2 \cdot 4H_2O$ is 17.0% versus 40.0% for $CaCO_3$. Combining these two factors, a dry $Ca(NO_3)_2 \cdot 4H_2O$ particle contains only ~29% Ca present in a dry $CaCO_3$ particle of the same size. Therefore, the larger calcium ion signals produced from calcium nitrate particles is best explained by the larger UV absorption cross section of $Ca(NO_3)_2 \cdot 4H_2O$ compared to $CaCO_3$. This means that as $CaCO_3$ particles are converted to $Ca(NO_3)_2$, the particles should absorb more laser energy and produce larger overall ion signals. This bias can be accounted for by dividing the peaks areas of interest by the absolute peak area of the CaO^+ fragment (produced from $CaCO_3$ and $Ca(NO_3)_2$) at m/z +56. Figure 7.4b demonstrates that by dividing the Ca^+ ion signal by the CaO^+ ion signal for both pure $CaCO_3$ and $Ca(NO_3)_2$ particles that the ratio is very similar across all particle sizes for both particle types. For particles of 200 nm or smaller the Ca^+/CaO^+ ratios are within 12% of each other. The reason
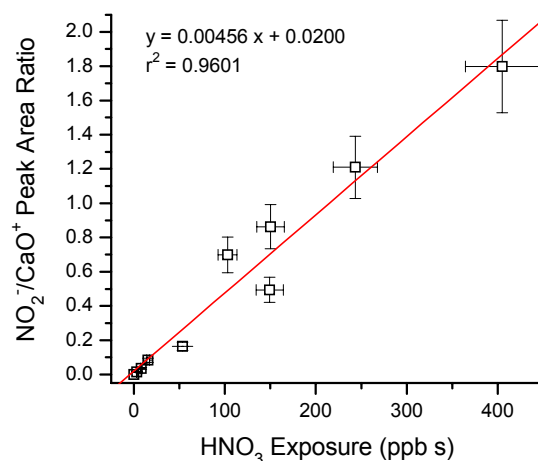
Figure 7.5. ATOFMS absolute NO$_2^-$/CaO$^+$ peak area ratio (m/z -46 / m/z +56) from reacted calcite particles at 50% RH as a function of HNO$_3$ exposure (= [HNO$_3$](g) × reaction time).

for the large difference for the 300 nm particles is likely caused by the incomplete desorption of particles of this size. This could affect the ion fragmentation patterns during the LDI process and produce the anomalous peak area ratio compared to the ratio from smaller particles that are completely desorbed. As 200 nm particles were used for these experiments, this indicates that this ion ratio method can be used to largely eliminate the signal bias caused by the differing absorption cross sections of the particles as they undergo conversion from CaCO$_3$ to Ca(NO$_3$)$_2$.

Following the above methodology, the ion peak area of the major nitrate fragment, ^{46}[NO$_2$]$^-$, was divided by the [CaO]$^+$ peak area for calcite particles after reaction with HNO$_3$(g) to measure the extent of nitrate formation in the particles. The nitrate peak areas in pure calcite particles are essentially zero. The [NO$_2$]$^-$/[CaO]$^+$ peak area ratio for all reactions performed at 50% RH are shown in Figure 7.5. The correlation between the ATOFMS measurement of nitrate in the individual particle versus the HNO$_3$ exposure is very high (r^2 = 0.96). The HNO$_3$ exposure is the product of the [HNO$_3$] (ppb) × reaction time (s) used for each reaction. This assumes a pseudo-first order rate law, which has been observed in previous studies of this

system (Liu et al., 2008a), as discussed further below. This excellent correlation indicates that this is a reliable method for determining the relative amounts of nitrate formed in the individual calcite particles due to heterogeneous reaction with HNO_3(g). Based on the analysis presented in Figure 7.4, which showed that the NO_2^-/CaO^+ peak area ratio was within 12% for $Ca(NO_3)_2$ particles of different sizes, an uncertainty of 15% is assigned to the ATOFMS nitrate measurement. The HNO_3 exposure uncertainty is estimated as 25% due to variations in the predicted flow tube [HNO_3](g) from surface loss, and small fluctuations in the flow tube's total flow rate, and dilution flows. Similar correlations between the ATOFMS nitrate measurement and HNO_3 exposure were found for reactions at 0% and 75% RH.

7.4.2 CCN activation curves of reacted calcite aerosol

The CCN activation curves measured for unreacted calcite versus calcite particles after various HNO_3 reaction conditions, all at 50% RH, are shown in Figure 7.6. The activation curves are coded by their HNO_3 exposure (ppb s) and clearly shift towards the left (smaller critical supersaturations) after increasing exposure to nitric acid vapor, as expected. Note that exposing dry-generated calcite aerosol to water vapor, without nitric acid, was also observed to slightly decrease the critical supersaturation of the calcite particles, as discussed in Chapter 6. Therefore, the reacted calcite aerosol is compared to an unreacted control that had been exposed to the same RH of 50% but without nitric acid. An unusual feature of the reacted activation curves is the loss of a clear multiply-charged plateau, which can still be clearly seen in the RH 50% unreacted particles control curve. This plateau is caused by the presence of particles with 2 or more electrical charges that have the same mobility diameter as singly-charged 200 nm particles but much larger volume equivalent diameters (Petters et al., 2007). As particles of the same composition but larger size activate at smaller s_c according to Köhler theory, these large multiply-charged particles activate at a low SS in the CCNc and produce
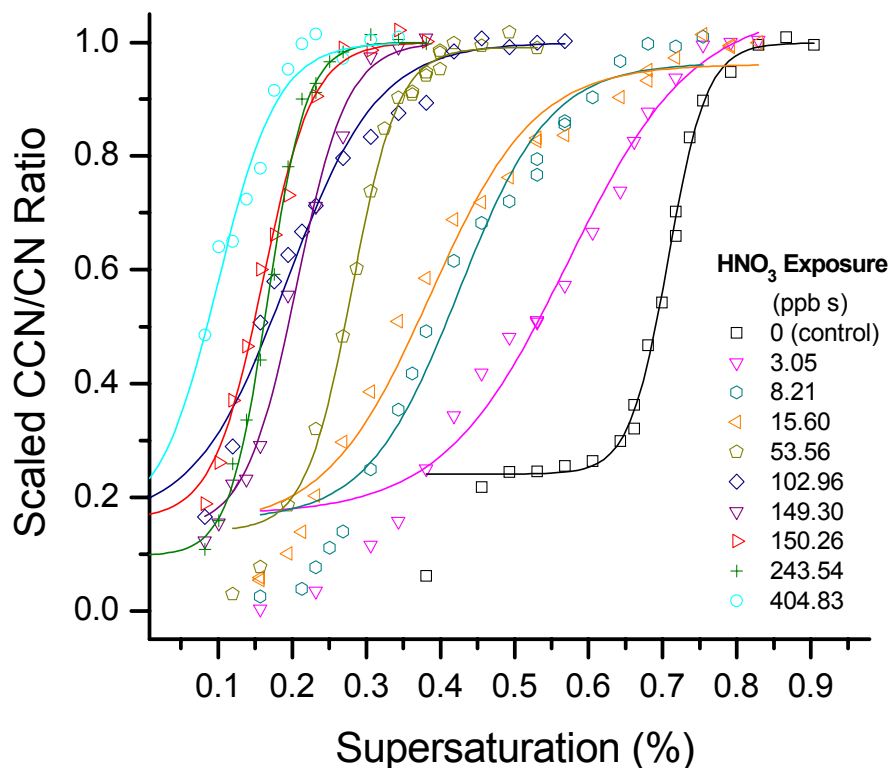
Figure 7.6. CCN activation curves of unreacted and reacted calcite aerosol at 47% RH. The sigmoid fits are constrained by the SMPS size distribution, shown in Fig. 7.7.

the plateau at CCN/CN ~0.25 in Figure 7.6. However, this plateau is quickly lost even under the smallest HNO₃ exposures, even though there should still be an appreciable fraction of multiply-charged particles in the pseudo-monodisperse aerosol exiting the flow tube. The lack of a clear minimum plateau makes it more difficult to accurately fit the activation curves with the sigmoid curve described in Chapter 6, defined as:

$$y = \frac{A_1 - A_2}{1 + e^{(x-x_o)/dx}} - A_2 \tag{7.2}$$

where y is the measured CCN/CN ratio, A_1 is the minimum value, A_2 is the maximum value, dx is the rate of change, and x_o is the midpoint between A_1 and A_2. The data is normally fit such that A_1 corresponds to the CCN/CN ratio of the multiply charged particles at small sizes/supersaturations, and A_2 is set to the scaled maximum CCN/CN ratio of ~ 1.0. Thus, x_o
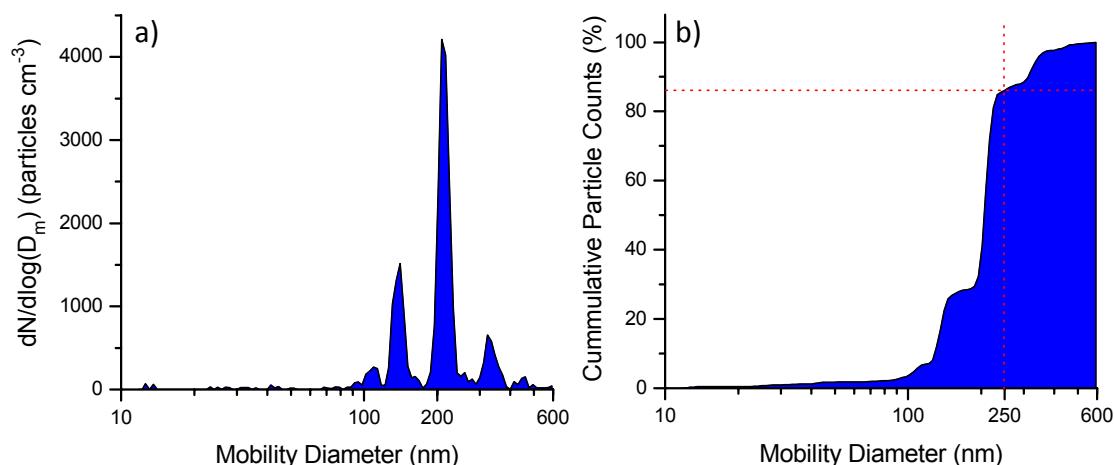
Figure 7.7. (a) Typical SMPS size distribution of size-selected calcite aerosol after reaction in the flow tube. (b) The % cumulative plot is used to determine the fraction of multiply charged particles of $D_m > 250$ nm. The SMPS charge correction was not used here.

corresponds to the CCN/CN = 0.5 midpoint typically used to define the critical supersaturation or activation diameter of the singly-charged particles of interest. The lack of the multiply-charged plateau in the reacted aerosol makes it difficult to empirically constrain A_1 in this fit.

To resolve this issue the contribution of multiply-charged particles in the aerosol exiting the flow tube was directly measured using aerosol size distributions made with an SMPS. The dried and denuded particles were sub-sampled by the SMPS after the flow tube. A typical size distribution is shown in Figure 7.7a. The SMPS software's multiple charge correction was not used here. As expected, the dominant mode is centered around 200 nm which is produced by the original +1 charge 200 nm particles selected by the 1st DMA before the flow tube. The mode to the left are originally +1 200 nm particles that gain a +2 charge in the 2nd DMA. The mode on the right are originally +2 charge particles with $D_m = 200$ nm that only have +1 charge in the 2nd DMA; these represent the larger multiply-charged particles in the aerosol measured by the CCNc. The fraction of multiplied charged particles was evaluated from the cumulative % size distribution shown in Figure 7.7b. The fraction of particles larger than 250 nm was used to determine the fraction of multiply-charged particles in the aerosol

and constrain the value of A_1 in Eqn. 7.2. The resulting sigmoid fits are shown along with the data in Figure 7.6. The uncertainty in the determination of s_c is typically the product of the uncertainty in the CCNc's SS calibration (3%), and in the particle size selection of the DMA ($\leq$ 5%). The lack of a multiply-charged plateau in the activation curve introduces additional uncertainty in the determination of s_c, though this is constrained by the SPMS measurement. The fraction of multiply-charged particles typically varied by 3% (absolute) between experiments. The value of A_1 was varied by $\pm$ 3% (absolute) for several typical activation curves and produced a change in s_c no greater than $\pm$ 0.01% (absolute). A more conservative uncertainty of $s_c \pm 0.02\%$ (absolute) is assigned for the reacted activation curves.

7.4.3 Hygroscopic changes caused by heterogeneous reaction with HNO$_3$

The methods described above to measure the relative amount of nitrate in the reacted calcite aerosol, and to determine their critical supersaturation, s_c, are used to determine the change in the particle's hygroscopicity as a function of particle exposure time to nitric acid vapor. The critical supersaturation of the reacted aerosol at 47% RH is plotted versus the HNO$_3$ exposure in Figure 7.8a. As expected, the critical supersaturation decreases with increasing reaction with nitric acid due to the formation of the highly soluble and hygroscopic Ca(NO$_3$)$_2$ product. However, even at a large HNO$_3$ exposure of 400 ppb s the particles are still not as hygroscopic as expected for fully converted Ca(NO$_3$)$_2$ particles. The scatter in the experimental data may be due to the difficulty in generating highly reproducible concentrations of HNO$_3$(g) in the flow tube. By plotting the critical supersaturation versus the ATOFMS product (nitrate) ion signal intensities, in Figure 7.8b, much of this scatter is eliminated and a clear trend is observed. The large variability observed for two reactions done for ~150 ppb s HNO$_3$ exposure times is particularly improved from Fig. 7.8a. This further validates the ATOFMS nitrate metric as both the ATOFMS and CCNc provide independent
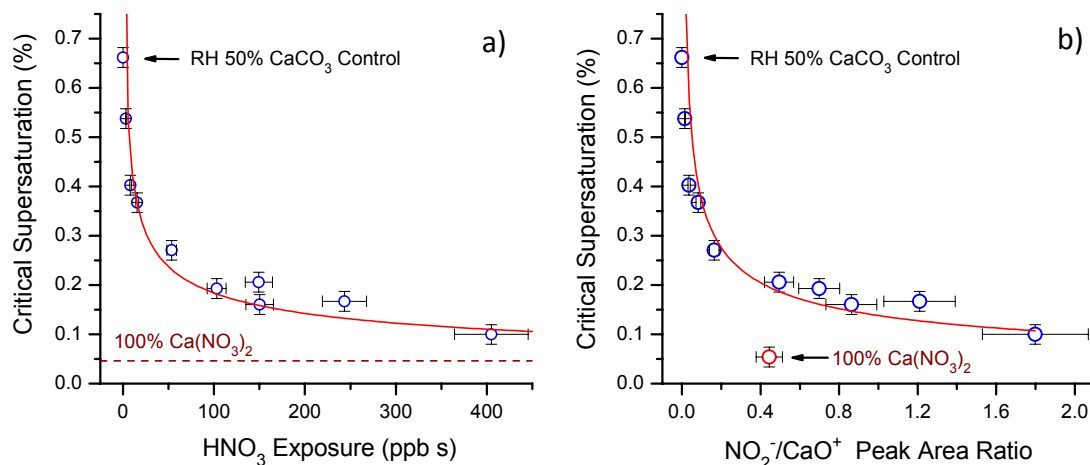
Figure 7.8. Measured critical supersaturation (s_c) of reacted calcite particles at 47% RH versus (a) HNO_3 exposure and (b) ATOFMS NO_2^-/CaO^+ absolute peak area ratio. Data from RH 50% unreacted calcite control and pure 200 nm $Ca(NO_3)_2$ particles are included. A single power law fit (red line) is included as a guide.

measures of the amount of nitrate in the particles, and both agree very well as shown in Figure 7.8b. According to Eqn. 7.1, $s_c = S - 1 \sim 1/\kappa_{app}$, and therefore a simple power law fit is included in Figure 7.8 to help capture the expected relationship between s_c as the particles undergo hygroscopic conversion. κ_{ap} is expected to increase linearly with the reaction extent as discussed below, which is linearly proportional to the HNO_3 exposure and ATOFMS nitrate measurement used in Figure 7.8. The s_c for pure calcium nitrate was predicted using κ-Köhler theory and the previously determined $\kappa_{app} = 0.51$ (see Chapter 6).

Comparing the reacted calcite hygroscopicity data to that of pure $Ca(NO_3)_2$ particles reveals some interesting behavior. While the s_c of the reacted particles at greater than 100 ppb·s HNO_3 exposure did not come close to that of pure calcium nitrate, the ATOFMS nitrate peak area ratio was significantly larger at these exposures for the reacted particles compared to the nitrate ion signals obtained from pure calcium nitrate particles. This indicates that the reacted particles contained more nitrate than pure calcium nitrate particles, yet were not as hygroscopic. The best explanation is that additional HNO_3 had partitioned to the reacted
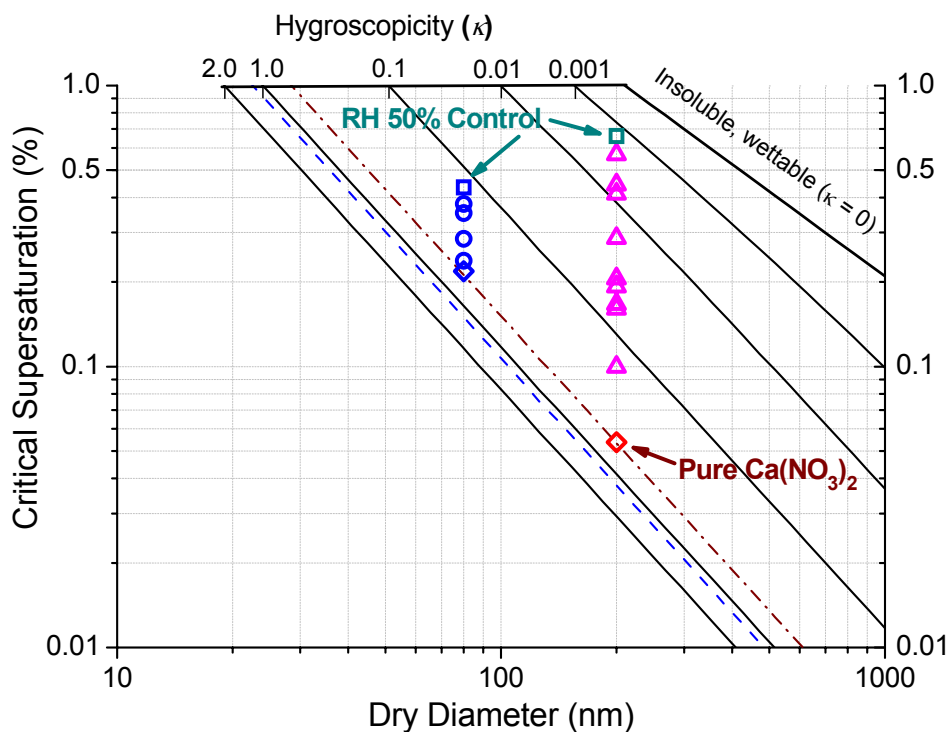
Figure 7.9. Relationship of s_c versus D_{dry} with kappa isolines for pure calcite and calcium nitrate particles, and calcite particles reacted with nitric acid at 50% RH. Pink triangles are dry-generated 200 nm calcite particles, while blue circles are atomized 80 nm calcite particles.

particle's surface but had not reacted with the $CaCO_3$ core. It is possible that HNO_3 produces a significantly larger NO_2^- signal than $Ca(NO_3)_2$ does on a per molecule basis, and HNO_3 would not produce a CaO^+ signal. Therefore condensing HNO_3 on to the particles would dramatically increase the particle's measured $[NO_2]^-/[CaO]^+$ ratio. Further evidence for this is presented in the 0% RH reactions discussed below.

The measured s_c of the reacted particles at 50% RH was converted to the single-hygroscopicity parameter, κ, by iterating Equation 7.1 to match the experimentally measured s_c. The uncertainty in determining κ_{app} is primarily a product of the uncertainty in s_c, estimated as ± 0.02% (absolute). This translates into an uncertainty in $\kappa_{app} \leq \pm 20\%$. The change in apparent hygroscopicity, κ_{app}, is displayed for all the reactions at 50% RH and compared to the

hygroscopicity of unreacted dry-generated calcite aerosol, and pure $Ca(NO_3)_2$ particles (Fig. 7.9). A wide range of hygroscopicity values was experimentally observed, from a minimum $\kappa_{app} = 0.0018$ for unreacted calcite, to a maximum $\kappa_{app} = 0.17$. The hygroscopicity of pure atomized then dried $Ca(NO_3)_2$ particles was previously determined to be $\kappa_{app} = 0.51$ (see Chapter 6). As previously mentioned, we did not observe this large a hygroscopicity experimentally; possible reasons for this are discussed below.

Figure 7.9 also displays similar data obtained by reacting atomized then dried Solvay calcite particles with HNO_3 at 50% RH, similar to the reactions with dry-generated Solvay $CaCO_3$ presented above. As discussed in Chapter 6, atomizing calcite from a suspension in water causes the particle's hygroscopicity to increase dramatically, to $\kappa_{app} \sim 0.2$. This greatly limits the hygroscopicity range that can be accessed experimentally and does not reflect the low initial hygroscopicity of atmospheric calcite particles. Further details on these atomized calcite experiments are not included here, they are briefly mentioned to emphasize the importance of using dry-generated calcite aerosol with an appropriately low initial hygroscopicity to properly model this system.

7.4.4 Reaction mechanism and rate law

To date, there is only one detailed report of the reaction kinetics of calcite particles with nitric acid vapor under moist conditions. All previous reactions were studied under dry vacuum conditions, as summarized by Liu et al. (2008a). Vlasenko et al. (2006) performed one experiment on calcite aerosol at 33% RH, and a more detailed set of experiments on Arizona test dust aerosol. Liu et. al. (2008a) measured the reaction kinetics for 850 nm calcite particles using $[HNO_3](g)$ between 7 and 25 ppb for reaction times of 5 to 300 minutes at 40% RH. Analysis of their kinetic data taken from a wide range of reaction times and HNO_3 concentrations demonstrated that the reaction obeyed a pseudo-first order rate law in which

HNO$_3$ was in large excess. Following Reaction 7.1, the rate of calcium carbonate loss can be expressed by an elementary rate law as:

$$\frac{d[CaCO_3]}{dt} = -k_{II}[CaCO_3][HNO_3]$$

(7.3)

where k_{II} is the second-order rate constant. Under conditions where [HNO$_3$] is large enough to be invariant during the reaction, such as in the conditions used here and by Liu et al., Eqn. 7.3 can be expressed as a pseudo-first order rate law:

$$\frac{d[CaCO_3]}{dt} = -k_I'[CaCO_3]$$

(7.4)

where k_I' is the apparent pseudo first-order rate constant, equal to $k_I' = k_{II}[HNO_3]_\infty$, and [HNO$_3$]$_\infty$ is the relatively high concentration of HNO$_3$ in the flow tube that is not significantly depleted during the reaction. Liu et al. found that [HNO$_3$]/k_I' = constant at low particle densities over their range of [HNO$_3$], justifying the use of the pseudo first-order rate law. Eqn. 7.4 is re-expressed as

$$\frac{d[CaCO_3]}{dt} = -k_{II}[CaCO_3][HNO_3]_\infty$$

(7.5)

 to describe the rate of CaCO$_3$ loss, and concurrent Ca(NO$_3$)$_2$ production, so that the flow tube [HNO$_3$]$_\infty$(g) can be accounted for, recalling that the rate constant was found by Liu et al. to be invariant to [HNO$_3$](g). Following Eqn. 7.5, the concentration of CaCO$_3$ remaining after some reaction time, t, is:

$$[CaCO_3]_t = [CaCO_3]_0 \exp(-k_{II}[HNO_3]_\infty t)$$

(7.6)

where [CaCO$_3$]$_0$ is the original concentration of CaCO$_3$(s). The pseudo-first order rate law implies that the HNO$_3$ exposure, e = [HNO$_3$]t, can be substituted into Eqn. 7.6 because k_{II} does not vary with either parameter. Substituting this into Eqn. 7.6 yields

$$[CaCO_3]_t = [CaCO_3]_0 \exp(-k_{II} e) \qquad (7.7)$$

where k_{II} is the experimentally observed rate constant (ppb^{-1} s^{-1}).

7.4.5 Timescale for hygroscopic conversion

A key outstanding issue is the timescale for different types of atmospheric particles to undergo hygroscopic conversion through a variety of processes, including heterogeneous reactions, such as explored here. The apparent hygroscopicites, κ_{app}, derived for the 50% RH reactions are plotted versus the HNO$_3$ exposure in Figure 7.10 to address this issue. A highly linear correlation is observed with $r^2 = 0.999$ when two obvious outliers are excluded. These outliers also were positioned well off the trend line in Figure 7.8a, and were mostly corrected using the ATOFMS nitrate measurement in Figure 7.8b. This was likely caused by the flow tube [HNO$_3$] being lower than predicted for those experiments. The highly linear correlation further validates the use of the pseudo first-order rate law, as this response is expected for the hygroscopic conversion, as explained below.

The slope obtained from Figure 7.10 can be used to predict the timescale for hygroscopic conversion due to Reaction 7.1. Due to the pseudo-first order rate law that the
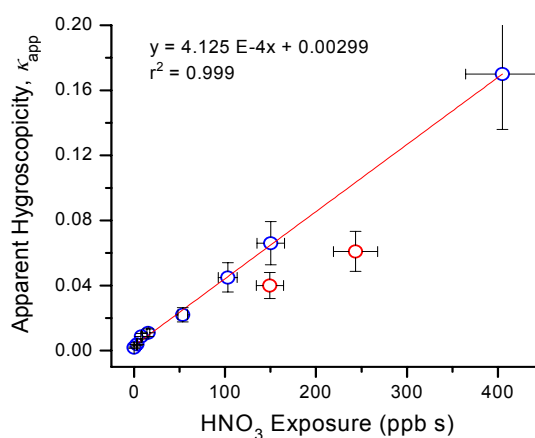

Figure 7.10. Measured apparent hygroscopicity of calcite particles after reaction with nitric acid at 50% RH. The two outliers (red symbol) are not included in the linear fit.

reaction obeys, the rate constant is invariant with [HNO$_3$], and therefore the slope from Figure 7.10 can be extrapolated down to atmospherically relevant nitric acid mixing ratios. Following Equation 7.7, where $e = $ [HNO$_3$]t is the HNO$_3$ exposure, an expression for κ_{app} can be derived as a function of e. Using the volume mixing rule, the reacted particle's apparent hygroscopicity will be equal to:

$$\kappa_{app} = \varepsilon_{Ca(NO_3)_2}\kappa_{Ca(NO_3)_2} + \varepsilon_{CaCO_3}\kappa_{CaCO_3} \tag{7.8}$$

where ε is the volume fraction and κ the apparent hygroscopicity of each component. κ_{app} of pure atomized Ca(NO$_3$)$_2$ was previously determined to be 0.51 in Chapter 6, and pure dry-generated Solvay CaCO$_3$ at 50% RH was determined here to be 0.0018. κ_{CaCO3} can be assumed ~0 to simplify the analysis since it is much less than $\kappa_{Ca(NO3)2} = 0.51$. The volume fraction of calcium nitrate in a partially reacted calcite particle is:

$$\varepsilon_{Ca(NO_3)_2} = \frac{(1-f)MW_{Ca(NO_3)_2}/\rho_{Ca(NO_3)_2}}{fMW_{CaCO_3}/\rho_{CaCO_3} + (1-f)MW_{Ca(NO_3)_2}/\rho_{Ca(NO_3)_2}} \tag{7.9}$$

where f is the volume fraction of CaCO$_3$ remaining in the particle, defined as

$$f = \exp(-k_{II}e) \tag{7.10}$$

from Eqn. 7.7, and MW and ρ are the molecular weight and densities of the two compounds (listed in Chapter 6). Substituting Eqn. 7.10 into 7.9 allows the mixed particle's κ_{app} to be solved as the reaction proceeds. k_{II} is found from the slope of Figure 7.10 and using Eqn. 7.8, treating $\kappa_{CaCO3} \sim 0$ since is it $\ll \kappa_{Ca(NO3)2}$. Therefore, the slope from Figure 7.10 is divided by $\kappa_{Ca(NO3)2} = 0.51$ to account for the hygroscopicity of the reaction product, yielding $k_{II} = 8.09 \pm 1.81 \times 10^{-4}$ ppb^{-1} s^{-1} (the uncertainty is the product of the 10% uncertainty in HNO$_3$ exposure and the 20% uncertainty in κ_{app}). This is similar to the result of Liu et al. (2008a) for the same system, $k'_{obs} = 2.9 \times 10^{-5}$ ppb^{-1} s^{-1} except they used 850 nm particles at 40% RH which likely
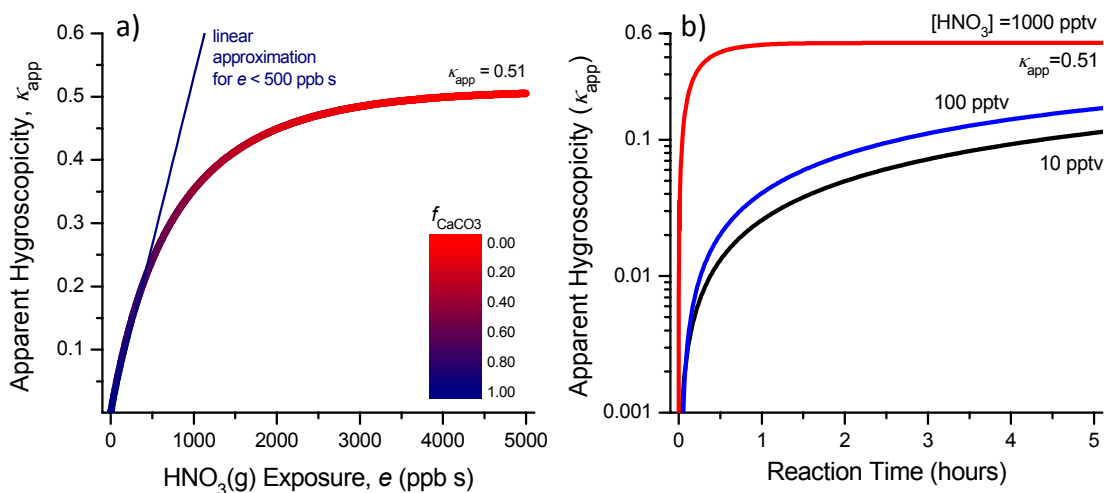
Figure 7.11. (a) Modeled timescale for hygroscopic conversion of 200 nm calcite aerosol due to heterogeneous reaction with nitric acid, constrained by the experimental data in Fig. 7.10. The apparent hygroscopicity increases following a pseudo first-order rate law to a maximum of $k_{app} = 0.51$, that of pure $Ca(NO_3)_2$.. f_{CaCO3} is the fraction of $CaCO_3(s)$ remaining in the particle. The slope of the linear approximation fit to low HNO_3 exposures ($e < 500$ ppb s) is 5.31×10^{-4}. (b) Similar to (a), timescale for hygroscopic conversion following the model in (a) for different atmospheric $[HNO_3]$ mixing ratios.

have a slower reaction rate than the smaller 200 nm particles at 50% RH used here. The reaction rate and thus reaction probability is typically larger for smaller particles in this kinetic regime due to a larger surface area-to-volume ratio. For example, Vlasenko et al. (2006) found $\gamma_{net} = 0.11$ at 33% RH for ~50 nm calcite particles, while Liu et al. (2008a) found $\gamma_{net} = 0.06$ at 40% RH for 850 nm calcite particles.

Using the derived k_{II} in Eqns. 7.9 & 7.10 combined to predict the particle's apparent hygroscopicity versus HNO_3 exposure produces the result shown in Figure 7.11a. A linear relationship between HNO_3 exposure and apparent hygroscopicity is observed for low exposures of $e < \sim 500$ ppb s. The similar linear relationship observed in the experimental data (Fig. 7.10) was obtained from experiments conducted at $e < 410$ ppb s. The modeled apparent hygroscopicity is color coded based on the fraction of original $CaCO_3$ remaining, f. The linear response of κ_{app} to e is observed for $f > \sim 0.7$. Once the reaction has proceeded beyond this

point the linearity will begin to degrade due to the exponential decay of the rate law (Eqn. 7.6). Experimentally, the most reacted particle at $e = 404$ ppb s and $\kappa_{app} = 0.17$ corresponds to $f = 0.67$, i.e. one third of the original calcite had been reacted to produce the calcium nitrate product.

A range of atmospherically relevant $[HNO_3](g)$ values were used to explore the sensitivity of κ_{app} versus e to the nitric acid mixing ratio. Figure 7.11b reveals that even under low $[HNO_3]$ conditions of 10 pptv, the originally non-hygroscopic calcite particles will be converted to highly hygroscopic particles with $\kappa_{app} > 0.1$ within 5 hours of reaction in the atmosphere. Higher $[HNO_3]$ causes the particles to reach $\kappa_{app} > 0.1$ within 3 hours and only 3 minutes for 100 and 1000 pptv, respectively. At all the $[HNO_3]$ studied the calcite particles will have become moderately hygroscopic ($\kappa_{app} > 0.01$) after about 30 minutes reaction time. This analysis also explains why reacted particles with κ_{app} as high as pure calcium nitrate were not observed. As the fraction of $CaCO_3$ consumed decreases exponentially versus HNO_3 exposure, $e > 4000$ ppb s is predicted to be necessary to produce particles with $\kappa_{app} > 0.5$. The flow tube technique limited the HNO_3 exposure to $< \sim 450$ ppb s.

7.4.6 Effect of relative humidity

Numerous reports exist showing the large effect that water vapor has on increasing the kinetics of nitric acid uptake by calcite particles and powders. For example, Liu et al. (2008a) found that the net reaction probability, γ_{net}, increased monotonically with RH, from 0.008 at 10% RH, to 0.21 at 80% RH. Vlasenko et al. (2006) observed a similar RH dependence in the uptake of nitric acid to Arizona test dust, which contains only ~5% $CaCO_3$. The relative humidity effect has been attributed to two principle mechanisms. The first involves the adsorption of water vapor to the calcite surface, and the subsequent formation of hydroxyl

(OH) and bicarbonate (Ca(OH)(CO$_3$H)) functional groups that terminate the calcite's surface. The reaction between calcite and nitric acid vapor is initiated by the exchange of the bicarbonate ligand for nitrate, which produces carbonic acid:

$$Ca(OH)(CO_3H) + HNO_3(g) \rightarrow Ca(OH)(NO_3) + H_2CO_3 \tag{R7.3}$$

Under very dry conditions this reaction can saturate the calcite surface with carbonic acid and prevent the further uptake of nitric acid. However, as carbonic acid is unstable under moist conditions and spontaneously dissociates into carbon dioxide and water, the presence of water vapor allows the nitric acid uptake to proceed past the calcite particle's surface. The adsorbed water also facilitates the dissociation of nitric acid and promotes ion mobility through the quasi-liquid surface layer. Both of these effects further enhance the overall reaction via the acid catalyzed hydrolysis of calcium carbonate:

$$HNO_3(aq) \rightleftharpoons H^+(aq) + NO_3^-(aq) \tag{R7.4}$$

$$H^+(aq) + CaCO_3(s) \rightleftharpoons HCO_3^-(aq) + Ca^{2+}(aq) \tag{R7.5}$$

$$H^+(aq) + HCO_3^-(aq) \rightleftharpoons H_2CO_3(aq) \rightleftharpoons H_2O + CO_2(g)\uparrow \tag{R7.6}$$
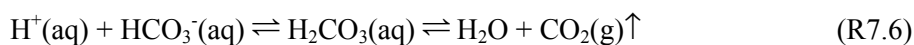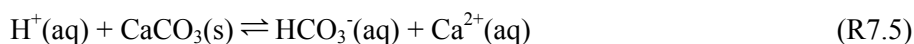
The second mechanism involves the formation of the highly soluble and hygroscopic product, calcium nitrate. Ca(NO$_3$)$_2$ deliquesces around 8-10% RH (Gibson et al., 2006a; Liu et al., 2008b; Tang and Fung, 1997). This observed DRH is much lower than the ~50% RH predicted by bulk thermodynamics for Ca(NO$_3$)$_2$. This is believed to be due to the formation of an amorphous hydrate (Gibson et al., 2006c; Laskin et al., 2005a; Tang and Fung, 1997). The hygroscopic calcium nitrate product absorbs water vapor, which further facilitates the hydrolysis reactions (R7.4-7.6) above, as well as the decomposition of carbonic acid at the calcite surface, to facilitate (R7.3). Combined these processes make the entire calcite core available for reaction with nitric acid vapor that partitions to the aqueous shell surrounding the calcite core. Absorption and dissociation of HNO$_3$, and diffusion through the aqueous shell
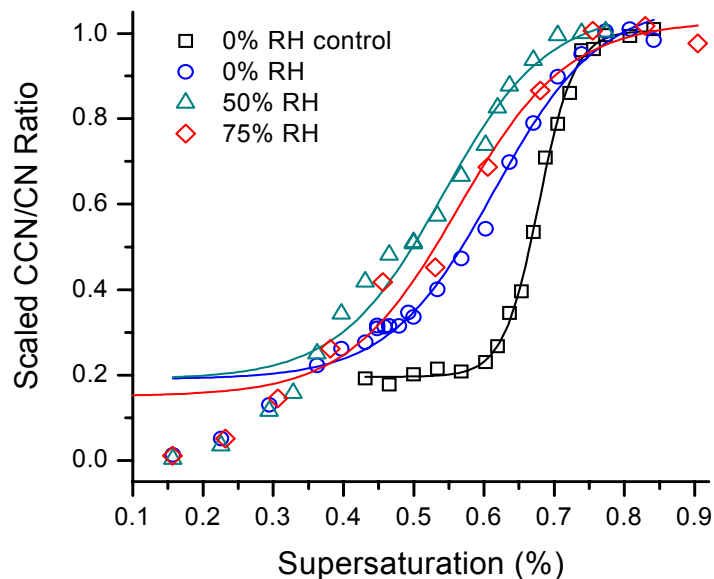
Figure 7.12. CCN activation curves of calcite aerosol after reaction with a low HNO_3 exposure of 3.1 ppb s at varying relative humidity, and unreacted calcite (control). The sigmoid fits were constrained using the SMPS determined multiply-charged fraction.

permit further reaction of the calcium carbonate core in the mixed, partially reacted particle.

Hygroscopic growth at elevated RH will dilute the calcium nitrate product in the shell, which

will reduce the shell's viscosity and thus likely increase diffusion rates and the overall rate of

reaction (Liu et al., 2008a).

The effect of relative humidity was explored by performing the same flow tube

reactions at 0% and 75% RH, in addition to the 50% RH reactions described above. At very

low HNO_3 exposures the water vapor effect is readily demonstrated. Figure 7.12 displays

activation curves for calcite aerosol exposed to 3.1 ppb s $HNO_3(g)$ at the three relative

humidities, compared to an unreacted 0% RH control. The 50% RH activation curve lies to the

left of the 0% RH curve, indicating that the particles were more hygroscopic due to a larger

conversion extent at 50% RH, as expected. The 75% RH curve, however, lies between the

50% and 0% RH curves, as opposed to the left of the 50% RH curve. This indicates that the
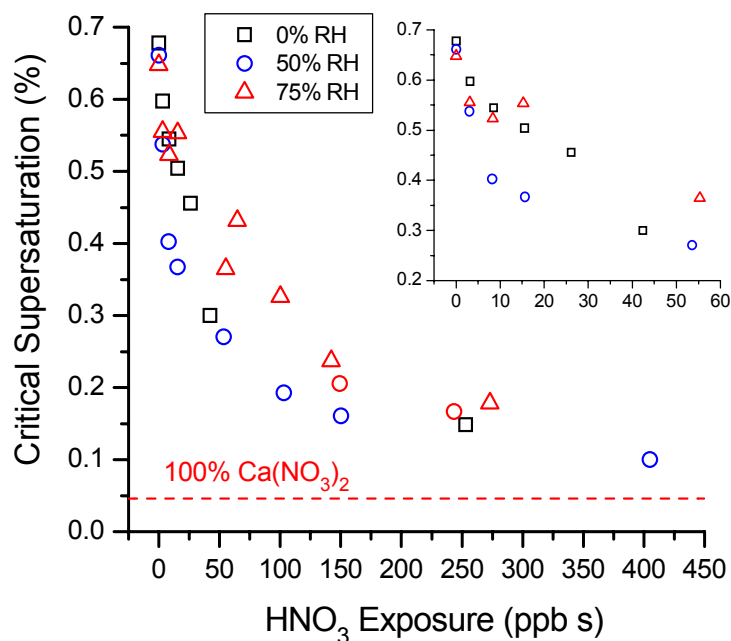
Figure 7.13. Measured critical supersaturation (s_c) versus HNO$_3$ exposure at 0%, 50%, and 75% RH. Inset displays data for low HNO$_3$ exposures where the relative humidity effect is most evident.

calcite particles were less converted and therefore less hygroscopic after reaction at 75% compared to 50% RH.

Data from all experiments conducted at the three RHs are presented in Figure 7.13 over a wide range of HNO$_3$ exposures. Recall that exposing dry-generated calcite aerosol to water vapor caused the particles to become slightly more hygroscopic even without exposure to acidic gases (Chapter 6). The largest difference between the 0% and 50% RH data is seen at low HNO$_3$ exposures below 20 ppb s. A similar trend as observed in Figure 7.12 is evident here; while the 50% RH reacted particles were typically more hygroscopic (smaller critical supersaturations) than the 0% RH reactions, the reactions conducted at 75% RH often produced particles that were less hygroscopic than the 50% RH and sometimes the 0% RH reactions. Liu et al. (2008a) observed the reaction probability to continue to increase smoothly up the maximum RH they studied, 80%. The reasons for the smaller reaction extent and thus lower hygroscopicity for reactions at 75% RH are not clear. A likely explanation is that the

high RH caused an increase in the wall loss of $HNO_3(g)$ to the halocarbon wax coated walls of the flow tube (Neuman et al., 1999), thus decreasing $[HNO_3](g)$ significantly below the predicted value, and causing the HNO_3 exposure to be lower than the 0% and 50% RH experiments.

The overall small effect of RH on the reaction extent and resulting hygroscopicity of the calcite aerosol is likely the result of the high $[HNO_3]$ mixing ratios used, and the very short reaction times accessible with the flow tube technique. The flow tube's $[HNO_3]$ was varied between 0.5 and 45 ppbv. This high concentration was necessary to produce an observable hygroscopic charge after the short less than 40 seconds of reaction time in the flow tube. Liu et al. used a similar range of $[HNO_3]$ in their experiments on much larger 850 nm calcite particles, and much longer reaction times of 5 to 300 minutes. The use of 850 nm particles compared to the 200 nm particles used here required much longer reaction times with HNO_3 to achieve the same degree of conversion by volume observed here. The longer reaction times used by Liu et al. (2008a) are speculated to be the major difference that allowed them to observe the large expected effect of relative humidity on the reaction probability. The high HNO_3 concentrations and short reaction times used here likely overwhelmed any significant enhancement in the reaction kinetics due to water vapor. This is supported by the largest effect of RH being observed at the smallest HNO_3 exposures (Fig. 7.13).

The reactions performed at 0% RH produced a set of interesting results that suggest that under dry conditions the calcite particles became extensively coated by nitric acid that condensed on the partially reacted particles but that much of the HNO_3 was unable to actually react with the $CaCO_3$ core. Figure 7.14 displays two different ATFOMS nitrate measurements, in addition to the usual NO_2^-/CaO^+ peak area ratio that has been used thus far, for the 0% RH reactions. All three indicate that the nitrate signal was close to or larger than that measured
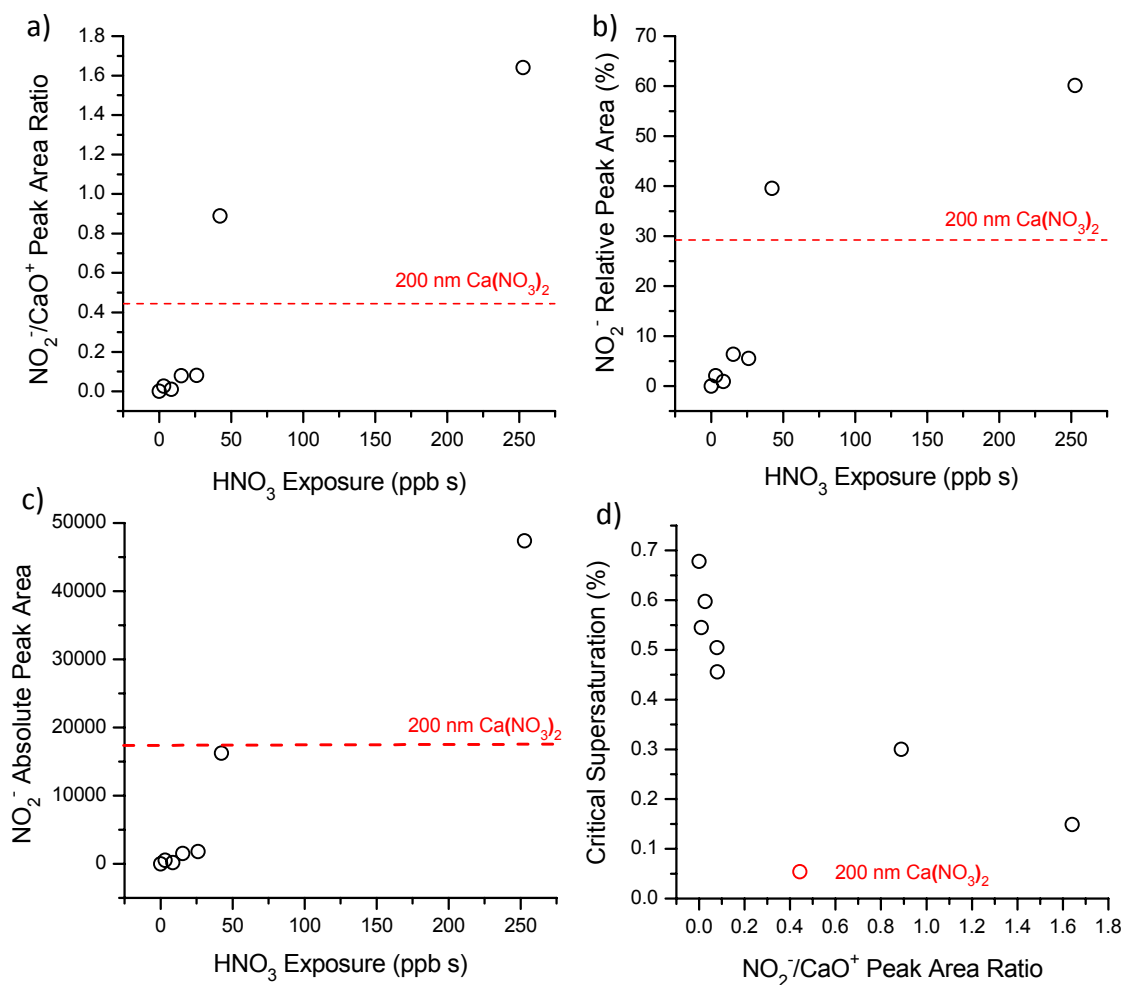
Figure 7.14. (a-c) Three ATOFMS nitrate measurements from calcite particles reacted with nitric acid at 0% RH. Data from pure 200 nm calcium nitrate particles is included. (d) Critical supersaturation (s_c) of the same reacted particles versus the ATOFMS NO_2^-/CaO^+ absolute peak area ratio.

from pure 200 nm $Ca(NO_3)_2$ particles. However, these particles never achieved critical supersaturations as small as pure calcium nitrate, as shown in Figure 7.14d. The critical supersaturation of 200 nm $Ca(NO_3)_2$ particles ($\kappa_{app} = 0.51$) is 0.0537%, below the lower SS limit of the CCNc of ~0.08%. Therefore completely converted calcite particles that were 100% $Ca(NO_3)_2$ would be completely CCN active, precluding the measurement of an activation curve. This was not observed, even at the largest HNO_3 exposure at 0% RH the particles were ~40% CCN-active at SS = 0.089%. However, the ATOFMS nitrate peak areas

were much larger than from pure $Ca(NO_3)_2$ particles. The condensation of relatively large amounts of nitric acid to the surface of the partially reacted particle is the best explanation for this, particularly if HNO_3 produces larger [46][NO_2]$^-$ signals than $Ca(NO_3)_2$ does per molecule. The short reaction times in the flow tube, in addition to the dry conditions, may have limited the ability of the nitric acid reactant to react further with the calcium carbonate core.

7.4.7 Atmospheric implications

As expected, and in agreement with previous laboratory experiments and field observations, calcite mineral particles can be converted to highly hygroscopic particles through heterogeneous reaction with nitric acid vapor. Using the measured range of hygroscopic conversion versus the HNO_3 exposure to constrain a simple kinetic model enables an estimation of the atmospheric timescale for hygroscopic conversion of calcite-containing mineral dust aerosol (Fig. 7.11). Even at a modest HNO_3 mixing ratio of 10 pptv the calcite aerosol will be moderately hygroscopic ($\kappa_{app} > 0.01$) after 30 minutes of reaction and very hygroscopic ($\kappa_{app} > 0.1$) after 5 hours of reaction. Higher HNO_3 mixing ratios significantly reduce the hygroscopic conversion time. A similar conversion can also be caused by other nitrogen oxides including $NO_2(g)$ and $N_2O_5(g)$ (Karagulian et al., 2006; Usher et al., 2003a), and their presence can therefore accelerate this conversion process. This suggests that the conversion of calcite-containing mineral dust aerosol through atmospheric processing will be primarily controlled by the availability of HNO_3, its precursors, and other nitrogen oxides, as opposed to the time the aerosol is in contact with elevated concentrations of $HNO_3(g)$. The fact that the hygroscopic conversion can be accurately described using a simple pseudo first-order kinetic model should facilitate the incorporation of such a process into chemical transport models. An important caveat is that the hygroscopic conversion timescale derived from this data was taken from experiments conducted on 200 nm particles at 50% RH. As

discussed previously, the reaction probability has been shown to be a strong function of RH and particle size. As the reaction probability typically decreases with increasing particle size (Liu et al., 2008a), and 200 nm likely represents a lower size limit for atmospheric dust aerosol populations, the conversion rate estimated here should be viewed as an upper limit for this process, under moist conditions.

The rapid conversion of non-hygroscopic calcite aerosol to soluble and hygroscopic calcium nitrate particles under tropospheric conditions has a wide range of important potential atmospheric implications. As experimentally demonstrated, the process can produce highly CCN-active particles from initially CCN-inactive particles. This increases the atmospheric concentration of potential CCN, with the related consequences of changes in cloud albedo and lifetime, the probability of autoconversion and precipitation, and other microphysical cloud properties. The calcium nitrate particles also have significantly different shapes and optical properties than the original calcite aerosol, and these properties will be affected by the particle's increased hygroscopic growth. The soluble and hygroscopic nature of calcium nitrate will result in the particles existing in a stable aqueous state under tropospheric conditions, thus providing an aqueous medium for other heterogeneous and multiphase reactions to potentially occur in which would not be possible in insoluble calcite particles (e.g. Prince et al., 2008). The rapid uptake of nitric acid by calcite aerosols can have a large impact on the atmospheric balance of important trace gases including HNO_3 and other NO_y species, and the related photochemical ozone cycle (Bauer et al., 2004; Bian and Zender, 2003; Dentener et al., 1996). Finally, the hygroscopic conversion of calcite to calcium nitrate will reduce the lifetime of these aerosols caused by increased rain out due to their increased CCN activity. This has important consequences for the global budget and distribution of

atmospheric mineral dust particles, and the transport of nitrate and other important nutrients to remote ocean regions, for example.

While mineral dust aerosols can contain relatively pure individual calcite particles, calcium and other carbonates such as dolomite $(CaMg(CO_3)_2)$ are frequently found internally mixed to varying degrees with other mineral components, insoluble aluminosilicate clays, for example. These clays typically display much lower reactivity to gases such as NO_2 and HNO_3 than $CaCO_3$ does, and their insolubility causes them to be non-hygroscopic (i.e. κ_{app} ~0). Calcite can also be found in small nanofibers distributed through mineral dust particles (Jeong and Chun, 2006). The results presented here for pure calcite particles can be applied to these mixed particles using the volume mixing rule for κ (Eqn. 7.8). Consider a mineral dust particle composed of 5% calcite by volume, and 95% by a mixture of insoluble aluminosilicate clays and a small fraction of insoluble goethite (α-FeO(OH)). The insoluble fraction can be assumed to have κ_{app} ~0, while the insoluble $CaCO_3$ also has κ_{app} ~0, resulting in an initially completely non-hygroscopic particle. After the calcite component has been fully converted to $Ca(NO_3)_2$ ($\kappa_{app} = 0.51$), the resulting processed dust particle's hygroscopicity can be predicted by

$$\kappa_{app} = \varepsilon_{Ca(NO_3)_2} \kappa_{Ca(NO_3)_2} + \varepsilon_{insol} \kappa_{insol} \tag{7.11}$$

where ε is the volume fraction of the $Ca(NO_3)_2$ and insoluble components, respectively, and κ their respective apparent hygroscopicities. The completely processed particle will have $\kappa_{app} = (0.51\times0.05) + (0\times0) = 0.0255$, and will thus be moderately hygroscopic after complete conversion of the small 5% calcite fraction. Therefore, even small amounts of reactive components can have potentially significant effects on the particle's overall hygroscopicity after atmospheric processing. This analysis assumes that all of the calcite is accessible to reaction with nitric acid, which may not be completely true and should be explored in further studies.

In this discussion, the effects that competing reactions of carbonate minerals with other reactive gases including SO_2 and oxalic acid may have should also be considered. As presented in Chapter 6, the formation of calcium sulfate and calcium oxalate via atmospheric processing will not significantly increase the particle's apparent hygroscopicity due to the low solubility of these compounds. Further, these reactions will consume carbonates and therefore prevent their reaction with nitrogen oxides to produce calcium nitrate, and with $HCl(g)$ to produce calcium chloride; these two pathways would significantly increase the particle's hygroscopicity. As sulfate tends to accumulate in the submicron aerosol mode where surface area is maximized (see Chapter 3), and as it is also this size mode that typically has the largest influence on CCN populations, these competing pathways could impact the ability of nitrogen oxides and chlorine-containing gases to produce significant concentrations of submicron CCN-active mineral dust particles after atmospheric processing. The production of supermicron giant-CCN is still quite likely, however. Chapter 6 also discussed the effect of the condensation of soluble secondary ammonium sulfate and ammonium nitrate salts on the hygroscopicity of mineral dust particles. The various competing chemical pathways and their resulting particle hygroscopicities require further examination using chemical transport and cloud air parcel models to fully evaluate the potential effect of atmospheric processing on the hygroscopicity and cloud-nucleating ability of mineral dust particles.

7.5 Conclusions

The heterogeneous reaction between nitric acid vapor and calcite aerosol produces very hygroscopic particles due to the conversion of insoluble calcium carbonate to soluble and hygroscopic calcium nitrate. The conversion rate extrapolated from the experimental data indicates that the hygroscopic conversion will occur very rapidly under atmospheric

conditions and will be primarily controlled by the availability of nitric acid and other nitrogen oxides gases, as opposed to the reaction time between these gases and the dust aerosol. The dust particles must contain reactive carbonate minerals for this conversion to occur, but even small fractions of carbonates in individual dust particles can lead to moderately hygroscopic particles after complete chemical processing. The applicability of a simple kinetic model to describe the rate of this hygroscopic conversion process should facilitate its incorporation into chemical transport models. Uptake of nitric acid by carbonate mineral particles has a series of important atmospheric consequences including increased number concentrations of CCN-active particles and potentially increased cloud droplet formation (and related climactic effects), reduced lifetime of atmospheric dust particles, altered budget and distribution of important trace gases, and changes to the transport of nitrate and other important nutrients to various ecosystems including remote ocean regions.

The results reported here were obtained from reactions performed under moist conditions (50% RH) on 200 nm calcite particles. They should therefore be regarded as an upper limit to the conversion rate that will occur under tropospheric conditions, as the reaction probability typically decreases with lower RH and larger particle sizes for this system. A significant kinetic enhancement due to increased RH was only observed at the lowest HNO_3 exposures. Higher exposures likely overwhelmed the typically strong influence of water vapor. This effect deserves further study over a wide range of HNO_3 mixing ratios, particle sizes, and relative humidities. The potential for other heterogeneous reactions such as uptake of sulfur dioxide and oxalic acid to compete with nitrogen oxides and chlorine-containing gases for the consumption of carbonate minerals also requires further study. While processing by nitric and hydrochloric acid produce soluble, highly hygroscopic products, sulfur dioxide and oxalic acid produce non-hygroscopic products after reaction with calcium carbonate,

potentially limiting the effect of nitric acid to increase the hygroscopicity of mineral dust aerosol populations.

7.6 Acknowledgements

Meagan Moore helped conduct most of the experimental work described here. Liz Fitzgerald assisted with some of these experiments and performed ancillary CIMS measurements. Markus Petters and Sonia Kreidenweis contributed substantially to the experimental design and the interpretation of the results and data analysis. Greg Roberts provided the CCNc instrument and advice in its operation and experimental design. Jon Abbatt and Joel Thornton provided valuable advice regarding the design and operation of the aerosol flow tube system.

Publication Acknowledgment

The contents of Chapter 7 are part of a manuscript to be submitted, Sullivan, R. C., Moore, M., Petters, M. D., Kreidenweis, S. M., Roberts, G., and Prather, K. A.: Timescale for hygroscopic conversion of mineral dust particles after heterogeneous reaction with nitric acid, 2008, *to be submitted*.

7.7 References

Al-Hosney, H. A., Carlos-Cuellar, S., Baltrusaitis, J., and Grassian, V. H.: Heterogeneous uptake and reactivity of formic acid on calcium carbonate particles: a Knudsen cell reactor, FTIR and SEM study, Phys. Chem. Chem. Phys., 7 (20), 3587-3595, 2005.

Al-Hosney, H. A., and Grassian, V. H.: Carbonic acid: An important intermediate in the surface chemistry of calcium carbonate, J Am Chem Soc, 126 (26), 8068-8069, 2004.

Bauer, S. E., Balkanski, Y., Schulz, M., Hauglustaine, D. A., and Dentener, F.: Global modeling of heterogeneous chemistry on mineral aerosol surfaces: Influence on tropospheric ozone chemistry and comparison to observations, J. Geophys. Res., 109 (D2), doi:10.1029/2003JD003868, 2004.

Bian, H. S., and Zender, C. S.: Mineral dust and global tropospheric chemistry: Relative roles of photolysis and heterogeneous uptake, J. Geophys. Res., 108 (D21), doi:10.1029/2002JD003143, 2003.

Bruynseels, F. J., and Van Grieken, R. E.: Molecular ion distributions in laser microprobe mass spectrometry of calcium oxide and calcium salts, Spectrochimica Acta, Part B: Atomic Spectroscopy, 38B (5-6), 853-8, 1983.

Dentener, F. J., Carmichael, G. R., Zhang, Y., Lelieveld, J., and Crutzen, P. J.: Role of mineral aerosol as a reactive surface in the global troposphere, J. Geophys. Res., 101 (D17), 22869-22889, 1996.

Fitz, D. R., Evaluation of Diffusion Denuder Coatings for Removing Acid Gases from Ambient Air, U.S. Environmental Protection Agency, 2002.

Gibson, E. R., Gierlus, K. M., Hudson, P. K., and Grassian, V. H.: Generation of internally mixed insoluble and soluble aerosol particles to investigate the impact of atmospheric aging and heterogeneous processing on the CCN activity of mineral dust aerosol, Aerosol Sci. Technol., 41 (10), 914-924, 2007.

Gibson, E. R., Hudson, P. K., and Grassian, V. H.: Aerosol chemistry and climate: Laboratory studies of the carbonate component of mineral dust and its reaction products, Geophys. Res. Lett., 33 (13), doi:10.1029/2006GL026386, 2006a.

Gibson, E. R., Hudson, P. K., and Grassian, V. H.: Physicochemical properties of nitrate aerosols: Implications for the atmosphere, J. Phys. Chem. A, 110 (42), 11785-11799, 2006b.

Jeong, G. Y., and Chun, Y.: Nanofiber calcite in Asian dust and its atmospheric roles, Geophys. Res. Lett., 33 (L24802), doi:10.1029/2006GL028280, 2006.

Karagulian, F., Santschi, C., and Rossi, M. J.: The heterogeneous chemical kinetics of N2O5 on CaCO3 and other atmospheric mineral dust surrogates, Atmos. Chem. Phys., 6, 1373-1388, 2006.

Kelly, J. T., Chuang, C. C., and Wexler, A. S.: Influence of dust composition on cloud droplet formation, Atmos. Environ., 41 (14), 2904-2916, 2007.

Krueger, B. J., Grassian, V. H., Cowin, J. P., and Laskin, A.: Heterogeneous chemistry of individual mineral dust particles from different dust source regions: the importance of particle mineralogy, Atmos. Environ., 38 (36), 6253-6261, 2004.

Krueger, B. J., Grassian, V. H., Laskin, A., and Cowin, J. P.: The transformation of solid atmospheric particles into liquid droplets through heterogeneous chemistry: Laboratory insights into the processing of calcium containing mineral dust aerosol in the troposphere, Geophys. Res. Lett., 30 (3), doi:10.1029/2002GL016563, 2003.

Laskin, A., Iedema, M. J., Ichkovich, A., Graber, E. R., Taraniuk, I., and Rudich, Y.: Direct observation of completely processed calcium carbonate dust particles, Faraday Discussions, 130, 453-468, 2005a.

Laskin, A., Wietsma, T. W., Krueger, B. J., and Grassian, V. H.: Heterogeneous chemistry of individual mineral dust particles with nitric acid: A combined CCSEM/EDX, ESEM, and ICP-MS study, J. Geophys. Res., 110 (D10), 2005b.

Liu, Y., Gibson, E. R., Cain, J. P., Wang, H., Grassian, V. H., and Laskin, A.: Kinetics of heterogeneous reaction of CaCO3 particles with gaseous HNO3 over a wide range of humidity, J. Phys. Chem. A, 112 (7), 1561-1571, 2008a.

Liu, Y. J., Zhu, T., Zhao, D. F., and Zhang, Z. F.: Investigation of the hygroscopic properties of $Ca(NO_3)_2$ and internally mixed $Ca(NO_3)_2/CaCO_3$ particles by micro-Raman spectrometry, Atmos. Chem. Phys. Discuss., 9 (10597-10625), 2008b.

Matsuki, A., Iwasaka, Y., Shi, G. Y., Zhang, D. Z., Trochkine, D., Yamada, M., Kim, Y. S., Chen, B., Nagatani, T., Miyazawa, T., Nagatani, M., and Nakata, H.: Morphological and chemical modification of mineral dust: Observational insight into the heterogeneous uptake of acidic gases, Geophys. Res. Lett., 32 (22), doi:10.1029/2005GL024176, 2005.

Neuman, J. A., Huey, L. G., Ryerson, T. B., and Fahey, D. W.: Study of inlet materials for sampling atmospheric nitric acid, Environ. Sci. Technol., 33 (7), 1133-1136, 1999.

Neuman, J. A., Ryerson, T. B., Huey, L. G., Jakoubek, R., Nowak, J. B., Simons, C., and Fehsenfeld, F. C.: Calibration and evaluation of nitric acid and ammonia permeation tubes by UV optical absorption, Environ. Sci. Technol., 37 (13), 2975-2981, 2003.

Petters, M. D., and Kreidenweis, S. M.: A single parameter representation of hygroscopic growth and cloud condensation nucleus activity, Atmos. Chem. Phys., 7 (8), 1961-1971, 2007.

Petters, M. D., and Kreidenweis, S. M.: A single parameter representation of hygroscopic growth and cloud condensation nucleus activity - Part 2: Including solubility, Atmos. Chem. Phys., 8, 6273–6279, 2008.

Petters, M. D., Prenni, A. J., Kreidenweis, S. M., and DeMott, P. J.: On measuring the critical diameter of cloud condensation nuclei using mobility selected aerosol, Aerosol Sci. Technol., 41 (10), 907-913, 2007.

Prince, A. P., Grassian, V. H., Kleiber, P., and Young, M. A.: Heterogeneous conversion of calcite aerosol by nitric acid, Phys. Chem. Chem. Phys., 9 (5), 622-634, 2007.

Prince, A. P., Kleiber, P. D., Grassian, V. H., and Young, M. A.: Reactive uptake of acetic acid on calcite and nitric acid reacted calcite aerosol in an environmental reaction chamber, Phys. Chem. Chem. Phys., 10 (1), 142-152, 2008.

Roberts, G. C., and Nenes, A.: A continuous-flow streamwise thermal-gradient CCN chamber for atmospheric measurements, Aerosol Sci. Technol., 39 (3), 206-221, 2005.

Santschi, C., and Rossi, M. J.: Uptake of CO_2, SO_2, HNO_3 and HCl on calcite ($CaCO_3$) at 300 K: Mechanism and the role of adsorbed water, J. Phys. Chem. A, 110 (21), 6789-6802, 2006.

Su, Y. X., Sipin, M. F., Furutani, H., and Prather, K. A.: Development and characterization of an aerosol time-of-flight mass spectrometer with increased detection efficiency, Anal. Chem., 76 (3), 712-719, 2004.

Tang, I. N., and Fung, K. H.: Hydration and Raman scattering studies of levitated microparticles: Ba(NO(3))(2), Sr(NO3)(2), and Ca(NO3)(2), Journal Of Chemical Physics, 106 (5), 1653-1660, 1997.

Tang, Y. H., Carmichael, G. R., Seinfeld, J. H., Dabdub, D., Weber, R. J., Huebert, B., Clarke, A. D., Guazzotti, S. A., Sodeman, D. A., Prather, K. A., Uno, I., Woo, J. H., Yienger, J. J., Streets, D. G., Quinn, P. K., Johnson, J. E., Song, C. H., Grassian, V. H., Sandu, A., Talbot, R. W., and Dibb, J. E.: Three-dimensional simulations of inorganic aerosol distributions in east Asia during spring 2001, J. Geophys. Res., 109 (D19), doi:10.1029/2003JD004201, 2004.

Thornton, J. A., Braban, C. F., and Abbatt, J. P. D.: N2O5 hydrolysis on sub-micron organic aerosols: the effect of relative humidity, particle phase, and particle size, Phys. Chem. Chem. Phys., 5 (20), 4593-4603, 2003.

Usher, C. R., Michel, A. E., and Grassian, V. H.: Reactions on mineral dust, Chem. Rev., 103 (12), 4883-4939, 2003.

Vlasenko, A., Sjogren, S., Weingartner, E., Stemmler, K., Gaggeler, H. W., and Ammann, M.: Effect of humidity on nitric acid uptake to mineral dust aerosol particles, Atmos. Chem. Phys., 6, 2147-2160, 2006.

Wenzel, R. J., and Prather, K. A.: Improvements in ion signal reproducibility obtained using a homogeneous laser beam for on-line laser desorption/ionization of single particles, Rapid Communications In Mass Spectrometry, 18 (13), 1525-1533, 2004.

Chapter 8

Conclusions

This dissertation focuses on the complex chemical reactions that mineral dust particles experience in the atmosphere. This research was accomplished through a combination of ambient field measurements, novel laboratory studies, and theoretical calculations, all focused on chemical analysis at the single-particle level. The important interplay between the chemical processing of atmospheric dust and their resulting warm cloud nucleation properties was a particular emphasis.

Direct measurements of the atmospheric processing of individual particles during the ACE-Asia campaign near East Asia revealed the important roles that mineralogy and size play in these processes. The dust accumulated both secondary organic and inorganic compounds during its transport from the desert regions in China and Mongolia to the research vessel sampling in the Sea of Japan. Single-particle analysis was able to confirm a previously proposed mechanism for the atmospheric processing of dust particles as a function of size (Song and Carmichael, 1999), while the accumulation of organic acids represents a seldom reported phenomenon that requires further study before it can be incorporated into chemical models.

Changes in the dust's mixing state caused by the observed atmospheric processing would have changed the particles' hygroscopicity and solubility, thus altering their cloud-nucleation properties. Exploring this effect experimentally using various pure minerals as proxies for fresh and aged dust particles confirmed that their solubility and thus apparent hygroscopicity is highly dependent on chemical mixing state. The observation that calcium sulfate (gypsum) has a very poor cloud nucleation potential, similar to calcium carbonate

(calcite), implies that the commonly made assumption that <u>all</u> dust becomes more hygroscopic and thus better CCN due to atmospheric processing should be revisited.

The commonly used atomization method produced large changes in the chemistry and apparent hygroscopicity of insoluble mineral particles. This should be avoided in favor of dry-generation methods in the case of insoluble particles. The effect that this previously unreported method artifact has on the results obtained from previous studies of the chemical kinetics, hygroscopicity, and cloud nucleation properties of mineral particles should also be evaluated. Calcium carbonate also became slightly more hygroscopic upon exposure to just water vapor for a few seconds. This could represent a pathway through which insoluble calcite particles become more soluble and hygroscopic without the need to react with acidic vapors, and deserves further study.

The field observation that sulfate was primarily mixed with submicron dust, and that it existed mostly as calcium sulfate and not ammonium sulfate in calcium-rich dust, coupled with the experimental observations suggest that a large number fraction of atmospherically processed dust particles could remain poor CCN despite the accumulation of sulfate compounds. Similar synergistic field and laboratory observations were made for calcium oxalate, which also has poor CCN potential. While calcium chloride and calcium nitrate are very hygroscopic, they were mostly found in the much smaller overall numbers of supermicron dust particles. As cloud nucleation is a number driven process, this could result in these aged very hygroscopic particles making small contributions to the number population of total CCN, as it is dominated by the submicron mode. These particles could create small but important contributions as very hygroscopic giant CCN, which can stimulate the auto-conversion process leading to precipitation (Rosenfeld et al., 2008; Rudich et al., 2002b).

The timescale for the conversion of insoluble calcium carbonate particles to highly soluble and thus hygroscopic calcium nitrate was observed through novel laboratory experiments to be very rapid, on the order of a few hours under atmospheric nitric acid mixing ratios. This suggests that this important conversion process will be predominantly controlled by the availability of atmospheric nitric acid, as opposed to the available reaction time. Determining the timescales for the analogous conversion of calcium carbonate to calcium sulfate (gypsum) (via reaction with $SO_2(g)$) or calcium oxalate (via reaction with oxalic acid vapor) is worthy of future study.

While the accumulation of secondary soluble compounds by dust and other compounds generally increases their hygroscopicity and thus warm cloud nucleation ability, the same process tends to decrease the ice nucleation ability of the mixed particles. As mineral dust is generally the best ice nucleating particle type observed in field and laboratory studies thus far, the implications of atmospheric aging on the CCN versus IN properties of dust could be quite significant for cloud formation and global climate (DeMott et al., 2003a; DeMott et al., 2003b). While some studies have already indicated that the accumulation of soluble material reduced the IN ability of dust, much work remains in this area (Archuleta et al., 2005; Mohler et al., 2008). Whether calcium sulfate or calcium carbonate represent IN-active particle types due to their low solubility remains to be determined.

8.1 Future work

Until recently, mineral dust has frequently been treated as a single-component entity in models of atmospheric chemistry and climate, such that all dust particles have the same rates of chemical reaction and the same cloud nucleation properties. Recently some models have begun to consider the effect that the variable mineralogy has on these important

processes (Song et al., 2007; Tang et al., 2004a; Tang et al., 2004b). This is an important development in improving the accuracy of these model predictions. Similarly, the effect of dust mineralogy and aging should be considered for model predictions of the effect of dust on cloud nucleation (Kelly et al., 2007). Further laboratory studies conducted under atmospherically relevant conditions, when possible, are needed to provide the required inputs to this models. The effects of relative humidity, particle size, and mineralogy should be particularly emphasized in these studies.

While the research described in this dissertation has helped to answer some of the questions raised by the ACE-Asia field observations, and will provide meaningful parameters for models of atmospheric dust chemistry, more research in this field is required to more fully understand the interactions between dust, atmospheric chemistry, cloud nucleation, and climate change. A brief list of some of the major outstanding questions follows.

1. How do the heterogeneous kinetics of various tropospheric gases vary with dust mineralogy?

2. How do the changes in the hygroscopicity and cloud nucleation properties vary with mineralogy for these same systems?

3. What is the hygroscopic conversion timescale for these systems?

4. How do the ice nucleation properties of the same reacted dust change compared to changes in their warm cloud nucleation properties?

5. How do the physical phase, size, and optical properties of dust change during these reactions?

6. Can the effect of dust particle size on the accumulation of sulfate versus nitrate and chloride be reproduced experimentally under simulated atmospheric conditions?

7. Was the segregation of sulfate from nitrate and chloride in aged dust particles caused primarily by:

    a. sulfate mixing with dust first (transport history)

    b. displacement of nitrate and chloride by sulfate (chemistry)

    c. sulfate reacting with submicron dust first when both sulfate and nitrate precursors were simultaneously present (kinetics)

    d. a combination of these effects or something else?

8. Can the displacement of nitrate and chloride from dust by the formation of sulfuric acid be observed experimentally? Under what conditions does this occur?

9. Can the experimentally determined chemical rates and mechanisms help improve closure between observed and model predicted atmospheric chemistry in dust-impacted ambient aerosol?

10. What is the phase, hygroscopicity, and warm and ice cloud nucleation properties of ambient dust aerosol in different environments, altitudes, and aging history?

11. What is the effect of the accumulation of sulfuric acid, oxalic acid, and other compounds on the oxidation state and solubility of iron in dust? How does this affect the role of dust as a nutrient vector to remote ocean regions?

8.2 References

Archuleta, C. M., DeMott, P. J., and Kreidenweis, S. M.: Ice nucleation by surrogates for atmospheric mineral dust and mineral dust/sulfate particles at cirrus temperatures, Atmos. Chem. Phys., 5, 2617-2634, 2005.

DeMott, P. J., Cziczo, D. J., Prenni, A. J., Murphy, D. M., Kreidenweis, S. M., Thomson, D. S., Borys, R., and Rogers, D. C.: Measurements of the concentration and composition of nuclei for cirrus formation, Proc. Natl. Acad. Sci. USA, 100 (25), 14655-14660, 2003a.

DeMott, P. J., Sassen, K., Poellot, M. R., Baumgardner, D., Rogers, D. C., Brooks, S. D., Prenni, A. J., and Kreidenweis, S. M.: African dust aerosols as atmospheric ice nuclei, Geophys. Res. Lett., 30 (14), doi:10.1029/2003GL017410, 2003b.

Kelly, J. T., Chuang, C. C., and Wexler, A. S.: Influence of dust composition on cloud droplet formation, Atmos. Environ., 41 (14), 2904-2916, 2007.

Mohler, O., Benz, S., Saathoff, H., Schnaiter, M., Wagner, R., Schneider, J., Walter, S., Ebert, V., and Wagner, S.: The effect of organic coating on the heterogeneous ice nucleation efficiency of mineral dust aerosols, Environ. Res. Lett., 3 (2), 2008.

Rosenfeld, D., Lohmann, U., Raga, G. B., kulmala, M., Fuzzi, S., Reissell, A., and Andreae, M. O.: Flood or Drought: How Do Aerosols Affect Precipitation?, Science, 321 (5894), 1309-1313, 2008.

Rudich, Y., Khersonsky, O., and Rosenfeld, D.: Treating clouds with a grain of salt, Geophys. Res. Lett., 29 (22), doi:10.1029/2002GL016055, 2002.

Song, C. H., and Carmichael, G. R.: The aging process of naturally emitted aerosol (sea-salt and mineral aerosol) during long range transport, Atmos. Environ., 33 (14), 2203-2218, 1999.

Song, C. H., Kim, C. M., Lee, Y. J., Carmichael, G. R., Lee, B. K., and Lee, D. S.: An evaluation of reaction probabilities of sulfate and nitrate precursors onto East Asian dust particles, J. Geophys. Res., 112 (D18), doi: 10.1029/2006JD008092 2007.

Tang, Y. H., Carmichael, G. R., Kurata, G., Uno, I., Weber, R. J., Song, C. H., Guttikunda, S. K., Woo, J. H., Streets, D. G., Wei, C., Clarke, A. D., Huebert, B., and Anderson, T. L.: Impacts of dust on regional tropospheric chemistry during the ACE-Asia experiment: A model study with observations, J. Geophys. Res., 109 (D19), doi:10.1029/2003JD003806, 2004a.

Tang, Y. H., Carmichael, G. R., Seinfeld, J. H., Dabdub, D., Weber, R. J., Huebert, B., Clarke, A. D., Guazzotti, S. A., Sodeman, D. A., Prather, K. A., Uno, I., Woo, J. H., Yienger, J. J., Streets, D. G., Quinn, P. K., Johnson, J. E., Song, C. H., Grassian, V. H., Sandu, A., Talbot, R. W., and Dibb, J. E.: Three-dimensional simulations of inorganic aerosol distributions in east Asia during spring 2001, J. Geophys. Res., 109 (D19), doi:10.1029/2003JD004201, 2004b.